Kinetics-based discrimination of reversibly photoswitchable fluorescent labels

Agnès Pellissier-Tanon

SORBONNE UNIVERSITÉ

École doctorale 388 :
Chimie Physique et Chimie Analytique de Paris Centre

Laboratoire PASTEUR - UMR 8640

Pôle de Chimie Bio-Physique

Kinetics-based discrimination of reversibly photoswitchable fluorescent labels

Présentée par

Agnès Pellissier-Tanon

Thèse de doctorat de Chimie-Physique

Dirigée par

Ludovic Jullien

Soutenance publique prévue le 15 décembre 2020

Devant le jury composé de :

M.	Ranieri	Bizzarri	Examinateur
M.	Dominique	Bourgeois	Rapporteur
M.	Ludovic	Jullien	Directeur de Thèse
M.	David	Lacoste	Rapporteur
Mme	Annie	Lemarchand	Examinatrice
Mme	Aurélie	Perrier-Pineau	Examinatrice

List of abbreviations

BAMM	: Bleaching-Assisted Multichannel Microscopy
BSA	: Bovine Serum Albumin
CCD	: Charged-Coupled Device
EGFP	: Enhanced Green Fluorescent Protein
FLIM	: Fluorescence Lifetime Imaging Microscopy
FRET	: Förster Resonance Energy Transfer
FP	: Fluorescent Protein
GFP	: Green Fluorescent Protein
HIGHLIGHT	: PHase-sensItive imaGing of reversibly pHotoswitchable Labels after modulatIon of activating ligHT
LIGHTNING	: Light-tunable tIme-gated readinG-out of pHotocycles for mulTiplexed fluorescence ImagiNG
LED	: Light Emitting Diode
NA	: Numerical Aperture
OLID	: Optical Lock-In Detection
OPIOM	: Out-of-Phase Imaging after Optical Modulation
PBS	: Phosphate-Buffered Saline
PMT	: PhotoMultiplier Tube
RSF	: Reversibly (photo)-Switchable Fluorophore
RSFP	: Reversibly (photo)-Switchable Fluorescent Protein
ROI	: Region Of Interest
SAFIRe	: Synchronously Amplified Fluorescence Imaging Recovery
TRAST	: TRAnsient STate imaging microscopy
UV	: Ultraviolet

Contents

Chapter 1

Introduction

1.1 Imaging living matter

Living matter provides a variety of challenges to the chemist. Cells contain a very large number (more than 10^6) of chemical components whose concentrations vary from 10^{-12} mol.L^{-1} (for DNA) to 10^{-1} mol.L^{-1} (for ions such as Na^+, K^+ or Cl^-) and which exhibit a well-defined heterogeneous spatial distribution. Dynamics are observed at various time scales and do not always reach a steady state. For example, the membrane polarization occurs within a few milliseconds, the dynamics of the metabolites happens at the second time scale, and the actions of transcriptome and proteome occur from minutes to hours. As a consequence, interrogating living cells requires sensitive imaging of a large number of components in real time.

A crucial issue is to image one or several targeted components of the cell without interference from the other components. It is therefore necessary that the target exhibits a specific signature. However, the elemental composition and functional groups of the cell components are essentially the same. An exogenous chemical construct with a specific signature can be introduced by genetic encoding to label a targeted components.[1–3] The properties of the label can therefore be harnessed to improve selective imaging.

Due to high sensitivity of fluorescence, fluorescent labels and in particular fluorescent proteins (FPs) have been widely developed. Light is used to probe and measure the amount of label. Micromolar concentrations of bright fluorophores can be currently detected with a time acquisition of 0.01 s. The present level of performance is not sufficient to analyze the dynamic behavior of low abundance biomolecules (e.g. mRNA and transcription factors) and needs to be improved. In any case, a balance has to be found between sensitivity and temporal resolution.

The heterogeneity of living matter causes differential absorption and light scattering.[4] Moreover the fluorescence emission of the labels may be polluted by light emission from endogenous cell compounds of the cells, a phenomenon known as autofluorescence.[5] Hence overcoming autofluorescence is a challenge for the design of imaging protocols.

Multiplexed fluorescence imaging, which allows simultaneous visualization of a large number of different labels, is currently limited not by labeling but by label discrimination.

1.2 Spectral discrimination

In the usual spectral-based approach, the discrimination of fluorescent labels relies on the choice of absorption and emission wavelengths.[6]

1.2.1 Fluorophores of all colors

Myriads of organic fluorophores are used in biological applications.[7] Their small size makes it possible to label biomolecules without disturbing their biological function. Their versatility is harnessed to meet the specific conditions imposed by biology. As shown in Fig. 1.1, common fluorophores such as fluoresceins, rhodamines, 4,4-difluoro-4-bora-3a,4a-diaza-s-indacene (BODIPY dyes), and cyanines exhibit favorable features: high molar absorption coefficients (25,000−250,000 $M^{-1}cm^{-1}$), moderate-to-high fluorescence quantum yields over a large wavelength range, and often limited photobleaching (irreversible loss of fluorescence).[8–10]

The discovery of the green fluorescent protein (GFP) has revolutionized the field of fluorophores for bioimaging. Thirty years after its discovery in the jellyfish *Aequorea Victoria* ,[11] the first cloning of the GFP gene[12] and its successful expression in both prokaryotic and eukaryotic cells[13] have opened unprecedented opportunities for selectively labeling proteins and visualizing their role in dynamic cellular processes in living systems in real time, e.g. protein expression, localization, translocations, interactions, and degradation.[14] A major effort has been undertaken to engineer brighter fluorescent proteins and to extend their chromatic palette.[15] As shown in Fig. 1.2, it has resulted in a wide palette of fluorescent proteins absorbing and emitting from the UV to the near Infra-Red.[16–24]

1.2.2 Multicolor fluorescence imaging

Despite the developments of organic fluorophores, the width of the absorption and emission bands intrinsically limits the number of discriminatable labels using spectral dis-

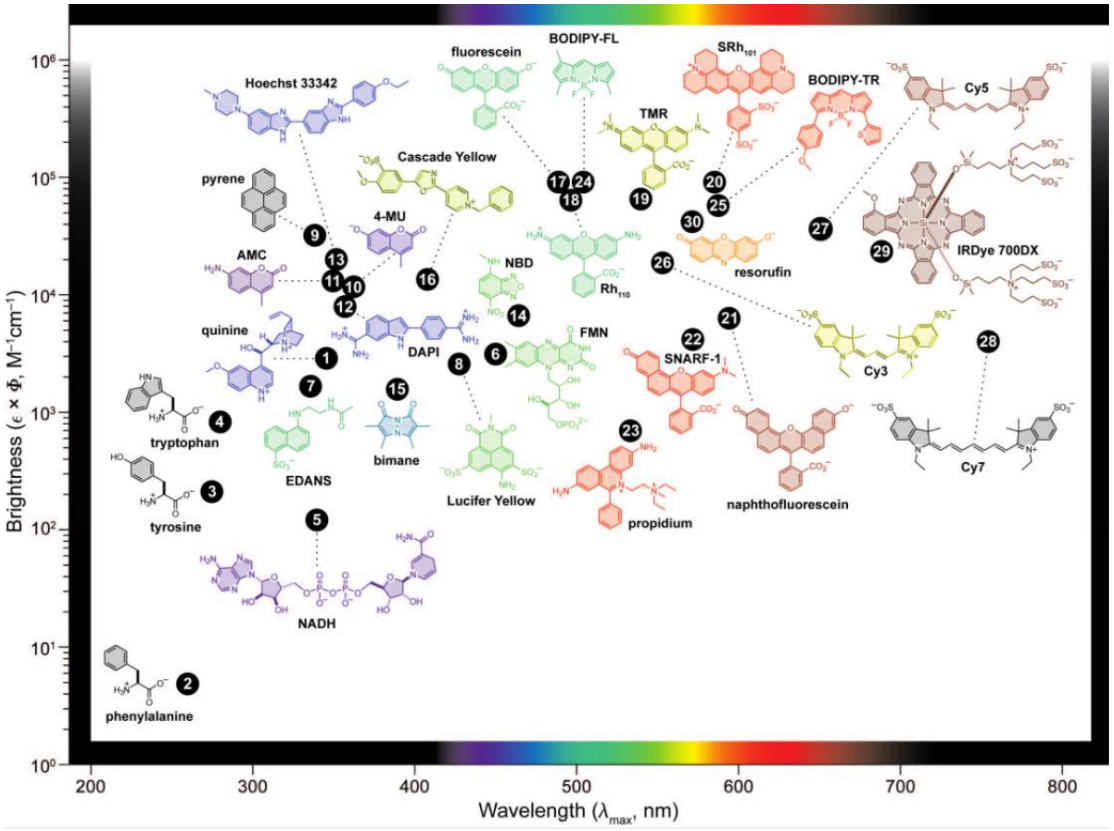

Figure 1.1: Diagram of typical organic fluorescent dyes in the space of maximum emission wavelength and brightness. The color of the chemical formula indicates its wavelength of maximum emission. For clarity, only the fluorophoric moiety of some molecules is shown. Adapted from Lavis *et al.*[9]

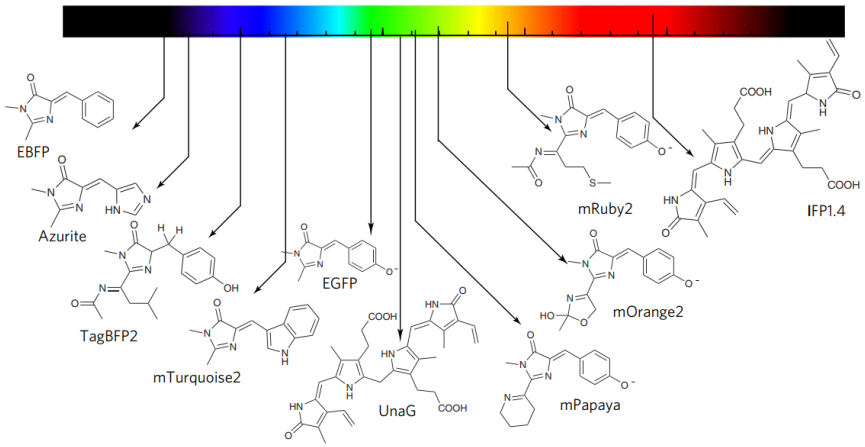

Figure 1.2: Illustration of the maximum absorption wavelength for some of chromophores of FPs covering the whole visible spectrum. Adapted from Dean *et al.*[25]

crimination. An illustration can be found in Fig. 1.3 which displays the distribution in the visible range of four fluorescence emission spectra with a width at half height of 100

nm. Even with a rich hardware of light sources and optical devices, no more than four fluorescent labels can be distinguished without spectral deconvolution.[25]

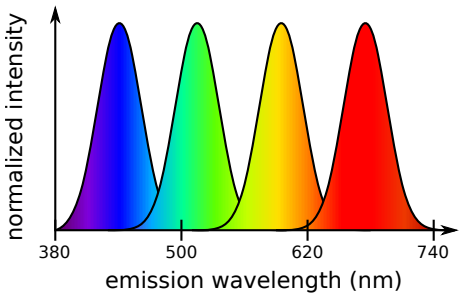

Figure 1.3: Schematic fluorescence emission spectra of four fluorophores with wavelengths of maximal emission spanning the entire visible spectrum. The width at half-height of the spectra is 100 nm.

To exceed this limit, one possibility is to process the fluorescence signal. The two main algorithms of image processing are linear unmixing and spectral phasor analysis.

In linear unmixing, the reference spectra of the fluorophores are first collected. The signal detected in each spectral channel is considered as a linear combination of the contributing fluorophores.[26] The number of detection spectral channels should be at least equal to the number n of fluorophores contained in the sample.[27] The concentration of each fluorophore is obtained by solving a linear system of at least n equations with n unknowns. In the case where more than n spectral channels have been analyzed, the conditions of compatibility between the additional equations lead to an estimate of the accuracy of concentration determination.

The spectral phasor analysis exploits the fundamental frequency of the Fourier transform of the fluorescence spectra.[28,29] For each pixel, the real and imaginary parts of the Fourier transform at the fundamental frequency are used as coordinates in a scatter plot. Discrimination occurs in a 2-dimensional space, without necessitating reference spectra nor numerical procedures.[28] Yet these two data processing methods generate a significant loss of temporal resolution and sensitivity.[30]

1.3 Dynamic contrast

Spectral parameters are not the only features of fluorescent labels which can be used for discrimination purposes. The strength of dynamic contrast is to exploit the kinetic properties of fluorophores in order to distinguish them.[31]

1.3.1 Simple absorption/emission photocycle

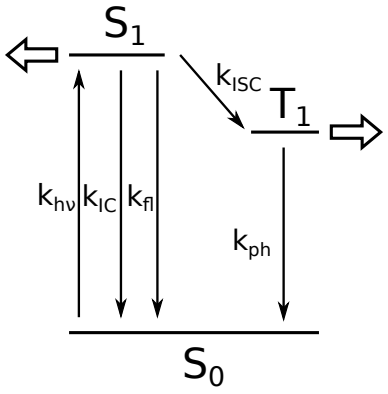

Figure 1.4: Jablonski diagram. Possible transitions between the electronic states of a fluorophore. A fluorophore in the fundamental singlet state S_0 absorbs light ($h\nu$) and yields the first excited singlet state S_1. The state S_1 may relax into S_0, by either nonradiative internal conversion (IC) or fluorescence emission (fl), or yields the first excited triplet state T_1 by inter-system crossing (ISC). The state T_1 relax into the fundamental state S_0 by phosphorescence emission (ph). Various reaction pathways can be further initiated from S_1 and T_1 as suggested by the big open arrows.

Fluorescence emission involves an absorption/fluorescence emission photocycle whose dynamics can be harnessed for discrimination purposes as shown in Fig. 1.4. A fluorophore in the fundamental state S_0 can absorb light with the rate constant $k_{\mathrm{h}\nu}$ up to 10^{15} s^{-1} and reach the first singlet excited state S_1. The relaxation of S_1 towards S_0 occurs either nonradiatively or by fluorescence emission, the two associated rate constants k_{IC} and k_{fl} being in the 10^7-10^{10} s^{-1} range. The triplet state T_1 is reached from S_1 with a rate constant k_{ISC} spanning the 10^8-10^{10} s^{-1} range. Among other pathways T_1 relaxes by phosphorescence emission, with the rate constant k_{ph} in the 1-10^6 s^{-1} range.

Depending on a variety of factors, e.g. temperature, viscosity, pH, solvent polarity, and the presence of fluorescence quenchers, the fluorescence lifetime of common fluorophores ranges from hundreds of picoseconds (e.g. for cyanines) to hundreds of nanoseconds (e.g. for pyrenes) and is generally anticorrelated with the quantum yield of fluorescence.[32] The fluorescent proteins exhibit similar fluorescence lifetimes ranging from 1 to 4 ns.[33] In the purpose of expanding the range of fluorescence lifetimes, long-lived luminophores have been developed, e.g. lanthanide-based luminescent probes,[34] azadioxatriangulenium (ADOTA) fluorophores,[35,36] Ag clusters.[37] Eventually quantum dots often exhibit longer fluorescence lifetimes than organic fluorophores, e.g. 10–100 ns for CdSe nanocrystals protected with a ZnS shell.[38]

The lifetime $1/(k_{\mathrm{IC}} + k_{\mathrm{fl}})$ of the excited state S_1 has been exploited to distinguish fluorophores in Fluorescence Lifetime Imaging Microscopy (FLIM).[39,40] However the narrow lifetime dispersion, spanning one order of magnitude in the nanosecond range, of the bright fluorophores currently used in fluorescence bioimaging has necessitated complex data processing methods.[39,41]

1.3.2 Rich reaction photocycles

Photochemical systems

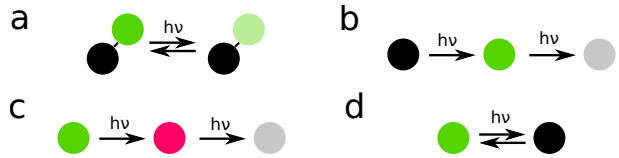

Figure 1.5: Four families of photochemical systems used or potentially exploitable in imaging protocols based on dynamic contrast. **a**: Reversibly photoswitchable FRET system. Under illumination the donor fluorophore (green disk) is quenched by the photochromic acceptor (black disk). **b**: Photoactivation from a dark state (black disk) to a fluorescent state (green disk) and then a bleached state (gray disk). **c**: Photoconversion from a fluorescent (green disk) to a red-shifted fluorescent state (red disk) and then a bleached state (gray disk). **d**: Reversibly photoswitchable fluorophore reversibly switched between a fluorescent state (green disk) and a dark state (black disk).

The dynamics of fluorophores can be even very rich, leading to various characteristic times spanning various orders of magnitude (from ns to s). The excited states, singlet S_1 and triplet T_1, may be the first steps in complex reaction pathways, involving fluorescent and non fluorescent states and often photochemical steps.[42] The many possible reaction pathways induced by light are illustrated by four families of photochemical systems as shown in Figure 1.5:[42]

a If two fluorophores are close enough and if the emission wavelength of one fluorophore matches the absorption wavelength of the other one, a Förster resonance energy transfer (FRET) happens. The fluorescence of the donor fluorophore is quenched by the photochromic acceptor which in turn may become fluorescent.[43] FRET systems have been used in imaging protocols based on dynamic contrast.[44,45]

b In the photoactivatable fluorophores, an illumination irreversibly transforms a dark, i.e. non fluorescent, state into a fluorescent state which in turn is bleached, i.e. irreversibly loses fluorescence.[46]

c The photoconvertible fluorophores are irreversibly photoconverted from a fluorescent state to a red-shifted fluorescent state. Photoconvertible fluorophores end in a dark bleached state.[47]

d Reversibly photoswitchable fluorophores (RSFs) exhibit switches between states of different brightnesses when illuminated at one or two wavelengths.[48–50] A same fluorescent label can generate cycles of fluorescence emission under periodic illumination without significant loss of the fluorescence signal.

Reversibly photoswitchable fluorescent proteins (RSFPs) combine the benefits of the fluorescent proteins (FPs) and the RSFs.[50,51] Dronpa has been the first discovered RSFP in 2004.[52] The 28 kDa Dronpa is made of an 11-stranded beta-barrel surrounding the p-hydroxybenzylidene imidazolinone chromophore.[53] As shown in Fig. 1.6**A**, at neutral pH, the absorption spectrum of Dronpa exhibits a major peak at 503 nm, which is associated with the anionic deprotonated state of the chromophore.[52,54] At lower pH, this peak is converted into a peak at 388 nm, which is associated with the protonated state of the chromophore.[52,54] Illumination at 490 nm followed by illumination at 400 nm induces the same transformations in Dronpa as a decrease of pH followed by an increase, as evidenced by the evolution shown in Fig. 1.6**B** of the absorption spectrum.

As displayed in Figs. 1.6**C**,**D** the emission spectrum of Dronpa displays a predominant peak at 515 nm.[54] As shown in Fig. 1.6**E**, the protonated state of Dronpa is bright and the deprotonated state is dark, which makes Dronpa a negative photoswitcher. The recovery of the bright state can be either spontaneous, (i.e. thermally-driven), with a half time of 14 h in the dark at room temperature, or light-driven under illumination at 388 nm.[52] Dronpa exhibits a low bright-to-dark photoswitching quantum yield (3.2 10^{-4}) and a relatively high dark-to-bright photoswitching quantum yield (3.7 10^{-1}).[52] Several fast-photoswitching mutants of Dronpa have been reported such as Dronpa-2,[55] Dronpa-3,[56] and rsFastLime.[57] Moreover, positive photoswitchers such as Padron have been introduced.[57] In this case the most stable state is not fluorescent.

RSFPs have been successfully employed by different imaging protocols based on dynamic contrast.[58–63]

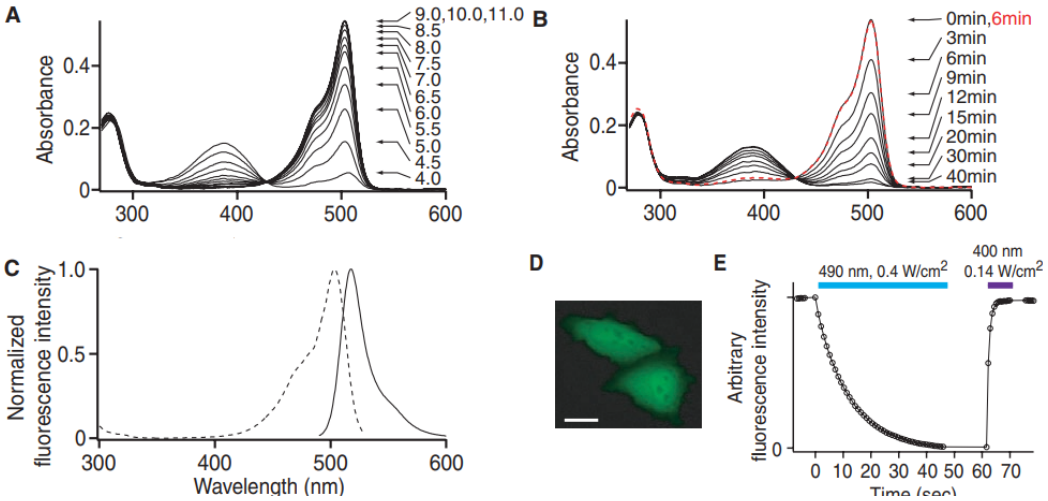

Figure 1.6: Photochromic properties of Dronpa. **A**: pH dependence of Dronpa absorbance. **B**: Irradiation-dependent changes in Dronpa absorbance. Absorbance spectra obtained during irradiation at 490 nm (black) and after irradiation at 400 nm (red) are displayed. **C**: Normalized excitation (dotted line) and emission (solid line) spectra of Dronpa. **D**: Fluorescence micrograph of HeLa cells expressing Dronpa. Scale bar, 20 μm. **E**: Fluorescence evolution of Dronpa in a fixed HeLa cell. During the marked intervals, the cell was continuously illuminated at 490 nm (0.40 W/cm^2) or 400 nm (0.14 W/cm^2) to induce forward photoswitching or backward photoswitching, respectively. Adapted from Ando *et al.*[52]

Discrimination protocols

Several protocols exploit dynamic contrast to image spectrally similar fluorophores. In this section I focus on bleaching-assisted multichannel microscopy (BAMM),[64] transient state imaging microscopy (TRAST),[65–67] optical lock-in detection (OLID),[58] synchronously amplified fluorescence image recovery (SAFIRe),[45,68] and out-of-phase imaging after optical modulation (OPIOM).[62,63,69–71]

Bleaching-assisted multichannel microscopy (BAMM) BAMM exploits the specific kinetic signature of photobleaching under constant illumination. The contribution of each fluorescent label is extracted using linear unmixing methods as shown in Fig. 1.7.[64] BAMM was successfully applied to organic dyes, autofluorescent biomolecules and fluorescent proteins.[64] Up to three spectrally similar fluorophores have been discriminated.

Transient state imaging microscopy (TRAST) TRAST selectively discriminates fluorophores by monitoring illumination of long-lived, photo-induced transient dark states which emerge from the time-averaged fluorescence response to a pulsewave illumina-

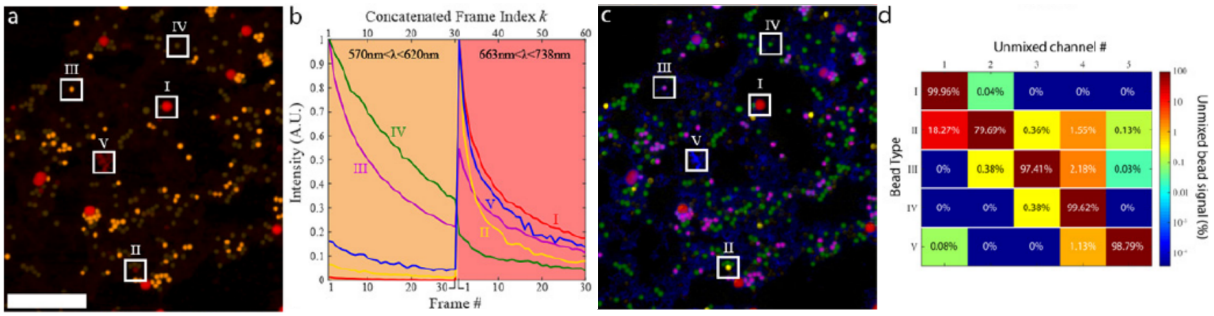

Figure 1.7: Principle of BAMM implemented with fluorescent beads. **a**: The first frame of a 30-frame photobleaching experiment, with each frame consisting of a yellow/red dual spectral channel image of a mixture of 5 different fluorescent beads. Examples of different bead types are boxed and labeled as I-V. Scale bar is 50 μm. **b**: Fluorescence evolution of beads I-V in (**a**), during the photobleaching experiment. Concatenated frames 1-30 correspond to frames 1-30 in the yellow channel (570-620 nm) of image (**a**). Concatenated frames 31-60 correspond to frames 1-30 from the red channel (663-738 nm) of image (**a**). Each bead type has a unique spectral-bleaching "fingerprint". **c**: False-coloured unmixed image of all five bead types. Abundance maps for bead types I-V are coloured red, yellow, purple, green and blue, respectively. **d**: The cross-talk matrix of the unmixing process. Cross-talk is generally low across all bead types except for bead type II into channel 1 (bead type I). This is due to the similarity in their bleaching rates, and low signal from type II beads. For all other bead types, more than 97% of the bead signal is unmixed into the correct channel. Adapted from Orth *et al.*[64]

tion.[65–67] The principle of TRAST is summarized in Fig. 1.8. The image of the targeted label is obtained by the ratio of two images recorded with different excitation pulse widths adapted to the relaxation time of the dark state of interest. TRAST has been used to achieve multiplexed imaging by exploiting the triplet state, which is sensitive to the presence of molecular dioxygen and heavy ions such as iodide.[66]

Optical lock-in detection (OLID) In OLID a periodic light perturbation drives RSFs throughout several cycles of photoswitching.[58] Then the fluorescence evolution is cross-correlated with a reference signal obtained from a small region where only the reversibly photoswitchable fluorophore is present. The signal of the targeted RSF yields a non vanishing cross-correlation coefficient whereas the background, e.g. ambient light, autofluorescence or another reversibly photoswitchable fluorophore, leads to a cross-correlation coefficient close to zero, as illustrated in Fig. 1.9.

The initial OLID observable, the cross-correlation coefficient, is not linearly related to the reversibly photoswitchable fluorophore concentration.[58] To solve this problem, Du *et al.* have introduced the "scope" defined as the difference between the maximum

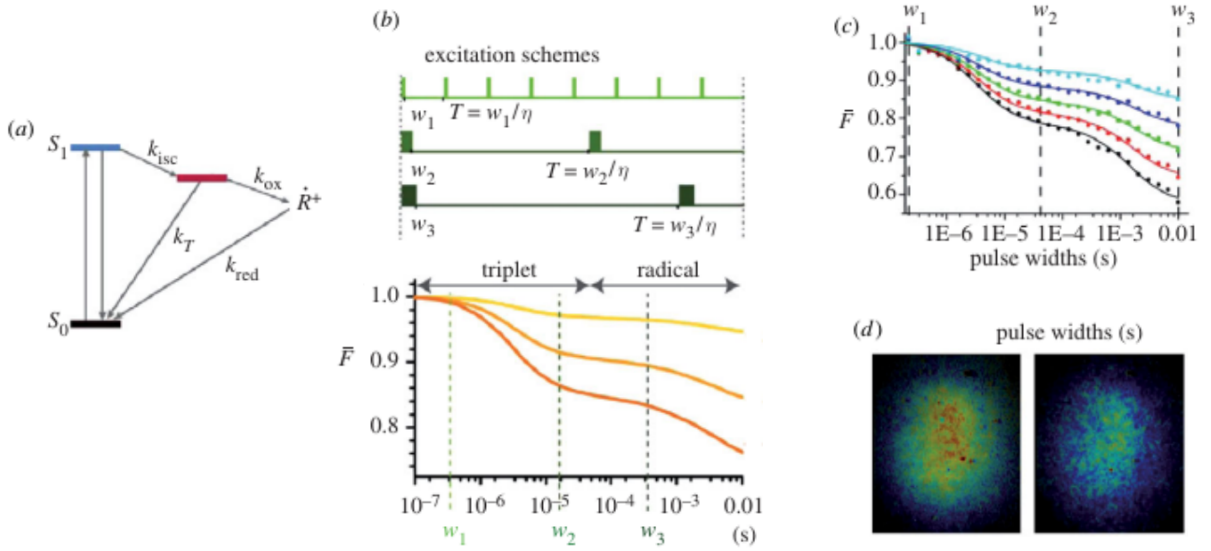

Figure 1.8: TRAST principle. **a**: Simplified state diagram of a typical organic dye molecule, including the ground singlet state (S_0), the first excited singlet state (S_1), the lowest triplet state (T_1) and the oxidized radical state (R^+). The parameters k_{isc}, k_{T}, k_{ox} and k_{red} denote the rate constants for intersystem crossing from S_1 to T_1, relaxation of T_1 to S_0, oxidation of T_1 to R^+, and reduction from R^+ to S_0, respectively. **b**: Measurement principle for TRAST imaging. Pulsewave excitation (top). The fluorescence intensity within a certain region is normalized to 1 for short pulse widths (less than triplet lifetime τ_T), and fluorescence response curves can then be generated for that particular region. In these curves, the fluorescence intensity decreases with increasing pulsewidths because of an increased population build-up in T_1 and thereafter in R^+ (bottom). **c**: Measured fluorescence response curves of the dye Rhodamine 110 in aqueous solution, showing two distinct relaxation processes with increasing pulse widths, which can be attributed to triplet state build-up and photo-oxidation, respectively. **d**: Images showing the triplet state build-up (left) and build-up of the photo-oxidized state R^+ (right). The triplet state image (left) is formed as a ratio of two images recorded with excitation pulse widths $w_1 < \tau_T$ and $w_2 > \tau_T$, but shorter than the build-up time of R^+. The radical state image (right) is formed as a ratio image from images recorded with the pulse width w_2, and a pulse width w_3, longer than the build-up time of R^+. The pulse widths w_1, w_2, and w_3 are indicated in subfigure **c**. Adapted from Widengren *et al.*[67]

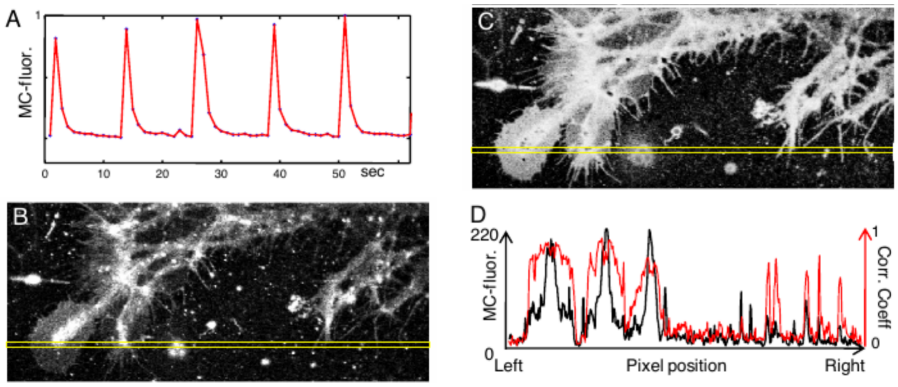

Figure 1.9: Illustration of OLID. **A**: Internal reference signal for the optical switching of C11-nitroBIPS in cells within a Xenopus spinal cord explants measured by using fluorescence of merocyanine (MC). The normalized signal was obtained from a selected region of 5×5 pixels with strongest MC-fluorescence corresponding to 5 cycles of optical switching of the probe and was used in the pixel-by-pixel calculation of the correlation coefficient. **B**: Fluorescence-intensity image of the C11-nitroBIPS stained cells within the Xenopus spinal cord explant. **C**: Correlation image corresponding to subfigure **B**, which used the signal shown in subfigure **A** as a reference signal. **D**: Variation with the pixel position of the relative fluorescence intensity (black) and the correlation coefficient (red) of C11-nitroBIPS associated with the yellow boxed region in subfigures **B** and **C**, respectively. Adapted from Marriott *et al.*[58]

and the minimum fluorescence intensity observed during the experiment.[72,73] The correlation coefficient multiplied by the "scope" enhances the signal-to-noise ratio and gives quantitative information.

A more refined quantitative version of OLID valid in the presence of bleaching has been recently developed.[74] The principle is as follows. Due to periodic illumination, the fluorescence signal is modulated and its Fourier transform is computed. Whereas bleaching contributes to the entire Fourier spectrum, photoswitching only leads to peaks at the excitation frequency and its harmonics. Using this property, the characteristic times of photoswitching and bleaching are extracted. The fluorescence evolution is then correlated to a monoexponential function with the characteristic time of photoswitching. For each pixel, a quantitative information on the concentration of the fluorophore is obtained using the correlation coefficient and the scope.

Synchronously amplified fluorescence imaging recovery (SAFIRe) In SAFIRe, the kinetics of long-lived dark states is exploited. A primary constant illumination leads to fluorescence emission and a secondary red-shifted modulated light drives the transition between fluorescent and dark species, which results in modulated fluorescence intensity.

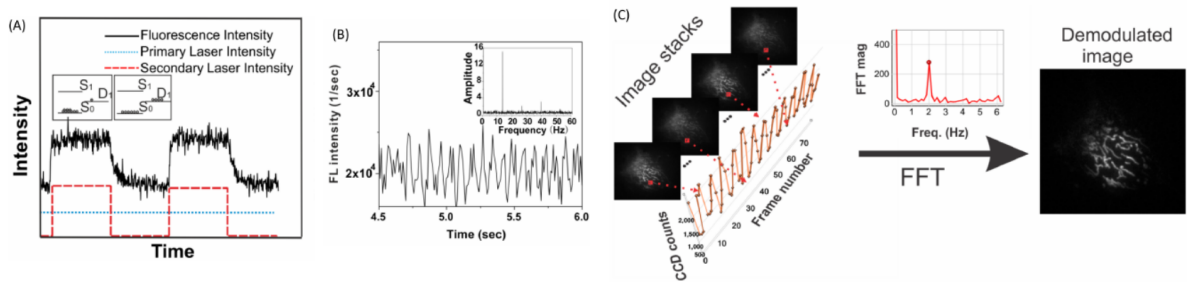

Figure 1.10: SAFIRe imaging principle. **A**: Fluorescence evolution of an optically modulatable blue fluorescent protein (modBFP/H148K) with constant primary excitation at 372 nm and modulated secondary excitation at 514 nm. The insets show Jablonski diagrams illustrating the populations of dark (D_1) and bright (S_0) states during the two half-periods of light modulation. **B**: Fluorescence evolution of aqueous modBFP/H148K with 372 nm primary excitation and 514 nm secondary excitation modulated at 13 Hz. The inset shows the fast Fourier transform (FFT) of the bulk time series, highlighting the modulation frequency encoded in the fluorescence signal. **C**: Analysis of optically modulated fluorescence image stacks by taking the Fourier transform of each pixel's time series. The demodulated image is formed from the peak of the FFT amplitude at each pixel. Adapted from Hsiang *et al.*[45]

The Fourier transform of the oscillating fluorescence signal displays peaks due to the kinetics of the reversibly photoswitchable fluorescent label. The background-free image of the label is obtained from the maximum of the peak of the Fourier transform of the oscillating fluorescence signal.[45,68,75] An illustration of the protocol is shown in Fig.1.10. SAFIRe has been first validated with Ag nanodots,[75] and then with organic fluorophores like xanthene[76] and Cy5.[77] It was later implemented with RSFPs.[59–61] The combination of SAFIRe and FRET dispenses with the secondary red-shifted illumination for dark state depopulation.[44] SAFIRe has been also extended to simple fluorophores by depleting their fluorescent state using stimulated emission induced by a modulated secondary laser at a longer wavelength than the fluorescence emission.[78]

Out-of-phase imaging after optical modulation (OPIOM and Speed OPIOM)
Our group developed a discrimination protocol based on the modulation of illumination. Photochemical systems under modulated illumination are modeled by forced dynamical systems. Interestingly forced dynamical systems often possess resonance phenomena.[79,80] OPIOM has been applied to reversibly photoswitchable fluorophores (RSFs) described by the two-state mechanism[62,69]

$$\text{Bright state} \rightleftharpoons \text{Dark state} \tag{1.1}$$

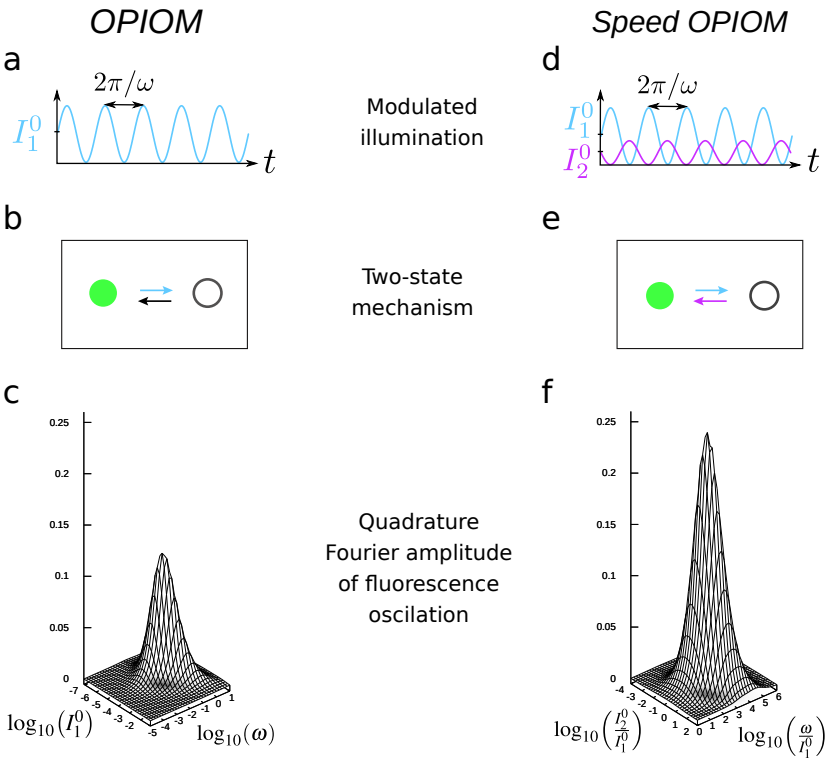

Figure 1.11: Principle of OPIOM (**a**–**c**) and Speed OPIOM (**d**–**f**). **a**: Modulated illumination of mean intensity I_1^0 at the frequency ω and the wavelength $\lambda_1 = 480$ nm. **d**: Double modulation in antiphase. I_1^0 and I_2^0 are the mean light intensities at the wavelengths $\lambda_1 = 480$ nm and $\lambda_2 = 405$ nm, respectively. **b**,**e**: Two-state mechanisms of a negative reversibly photoswitchable fluorophore with a fluorescent most stable state (green disk). Illumination at $\lambda_1 = 480$ nm yields the dark state (black circle). The bright state is recovered either thermally (**b**) or under illumination at $\lambda_2 = 405$ nm (**e**). **c**,**f**: Resonance of the quadrature Fourier amplitude of fluorescence oscillation in the control parameter space (I_1^0, ω) for OPIOM (**c**) and $(I_2^0/I_1^0, \omega/I_1^0)$ for Speed OPIOM (**d**).

The quadrature Fourier amplitude of fluorescence oscillations at the excitation frequency displays an extremum for well-chosen control parameters such as the excitation frequency and the mean light intensity as illustrated in Fig. 3.1.3. The resonance phenomenon occurs when the control parameters of the excitation match the kinetic parameters of photoswitching. In order to facilitate the experimental implementation of OPIOM, user-friendly analytical resonance conditions have been made precise.

The mean feature of OPIOM consists in harnessing resonance properties for dicrimination purposes. In a mixture of several RSFs with different kinetics, adjusting the control parameters to the resonance of the targeted RSF is sufficient to eliminate the contribution of the other RSFs to the quadrature Fourier amplitude. Since the fluorescence emission is directly related to the population of the bright state, the quadrature Fourier amplitude

also gives quantitative information on the amount of the targeted fluorophore. Additionally OPIOM benefits from lock-in amplification, which improves the signal-to-noise ratio.

The OPIOM imaging protocol has been applied to RSFPs.[62,63] In a first attempt, a single light modulation at the wavelength $\lambda_1 = 480$ nm has been used with a thermally-driven backward reaction step. OPIOM has been experimentally validated using green RSFPs in microsystems, mammalian cells, and zebrafish embryos with a wide-field epifluorescence microscope or a single plane illumination microscope.[62] These initial implementations of OPIOM suffer from low values of the rate constant of thermal recovery. Even with the fastest recovering RSFP, Dronpa-3, the image acquisition takes more than 2 minutes.[62]

Since most photoswitched green RSFPs yield the stable state under illumination at the wavelength $\lambda_2 = 405$ nm, a secondary illumination at $\lambda_2 = 405$ nm has been introduced in order to accelerate the recovery process.[63,81] The advanced protocol called Speed OPIOM uses illumination at the two wavelengths $\lambda_1 = 480$ nm and $\lambda_2 = 405$ nm modulated in antiphase.[63] The Speed OPIOM signal is twice higher than the one obtained in the original one-color OPIOM.[63] For both OPIOM and Speed OPIOM, the resonance conditions set two control parameters. Since the second illumination introduces a third control parameter in Speed OPIOM, one control parameter can be chosen at will. This degree of freedom can be used to increase one mean light intensity and consequently reduce the acquisition time. The millisecond timescale has been reached. Experimental validations have evidenced that Speed OPIOM is a powerful protocol for quantitative imaging of RSFs, which can overcome a background of autofluorescence or ambient light.[63] It is as well efficient for multiplexed fluorescence imaging. Using Speed OPIOM our group imaged three spectrally similar RSFPs in 1 s without deconvolution scheme.[63]

1.4 Outline of the manuscript

The state of the art of the discrimination protocols in fluorescence imaging reveals that multiplexing remains challenging even if three or four labels have been successfully imaged, for example using Speed OPIOM. For a long time our research group has been concerned with exploring how the integration of tailored fluorescent probes with well-thought instruments and protocols of signal acquisition could level off current limitations. The rich photochemistry of reversibly photoswitchable fluorophores provides attractive opportunities for dynamic contrast protocols beyond the sole field of superresolution mi-

croscopies.

During my PhD, I designed two fluorescence imaging protocols, which exploit dynamic contrast by exposing reversibly photoswitchable fluorophores to either constant illumination or periodic illumination. I only realized part of what has been a collective effort under the supervision of Ludovic Jullien. I did my PhD in parallel with Raja Chouket's. She did all experiments and part of data processing with another member of the group, Thomas Le Saux. I was in charge of the theoretical part, which includes the study of kinetic models, the design of experimental protocols, and part of data processing under the co-supervision of Ludovic Jullien and Annie Lemarchand (Laboratoire de Physique Théorique de la Matière Condensée, Sorbonne Université).

This collective work gave rise to several reviews. Two short reviews qualitatively present discrimination protocols with a special focus on OPIOM.[82,83] An accepted book chapter provides a more extensive review of imaging protocols, experimental setups, and fluorescent labels.[84]

The manuscript is organized as follows. In chapter 2, I analyze the fluorescence signal of reversibly photoswitchable fluorophores under constant illumination. One of the key ideas in order to take advantage of the complex kinetics of reversibly photoswitchable fluorophores is to change the limiting steps of kinetics by tuning light intensity for different initial conditions. At low intensity the limiting step is a photochemical step while, at sufficiently high intensity, the limiting steps are thermal steps. Our goal is to improve the performance of multiplexing by extracting the largest possible non redundant kinetic information from fluorescence evolution. The question that arises is to find the relevant steps of a photocycle in the experimentally accessible time window.

This concern led me to investigate adiabatic approximations and the elimination of fast variables in a dynamical system. Section 2.1 presents the differential equations governing the evolution of fluorophore concentration and the relationship between concentration and fluorescence evolution. Different methods of elimination of fast variables, the quasi-steady-state approximation and the pre-equilibrium approximation, are detailed in section 2.2. In section 2.3, the quasi-steady-state approximation is applied to reversibly photoswitchable fluorescent proteins (RSFPs) in order to obtain reduced mechanisms valid under four different conditions of illumination. We use the reduced mechanisms to prove that the characteristic times extracted for different illumination conditions offer non redundant information. Section 2.4 presents two methods of data processing: Curve fitting and spectra of characteristic times are used to extract characteristic times of fluorescence

evolution.

The discrimination protocol using constant illumination, further referred to as LIGHTNING, is presented in section 2.5. LIGHTNING is the acronym for Light-tunable tImegated readinG-out of pHotocycles for mulTiplexed fluorescence ImagiNG. An experimental setup* has been developed by our group to investigate the kinetics of 22 RSFPs under constant illumination of various intensities. The fluorescence evolution at a given light intensity is characterized by a single characteristic time. For each RSFP, four different illumination conditions are used to determine four characteristic times, leading to a four-dimensional kinetic fingerprint. Discrimination is performed in the four-dimensional space of the characteristic times by finding the RSFP, among all referenced RSFPs, whose kinetic fingerprint matches the fingerprint of the sample. A sorting algorithm has been implemented to list sets of discriminatable RSFPs for a given experimental accuracy. Our results show that up to 20 out of 22 noncolocalized RSFPs can be discriminated. When no more than two RSFPs contribute to a given fluorescence signal, LIGHTNING is able to discriminate 10 out of 22 RSFPs.

This discrimination protocol is presented in a manuscript that is not yet finalized. Supporting information is given in the appendix A. I was involved in the writing of this manuscript, in particular the theoretical parts found in the supporting information. The experimental setup and the discrimination principle are protected by two patents of which I am co-inventor.[85,86] The predictions of the reduced mechanisms are successfully confronted with the experimental results in section 2.6.

In chapter 3, I analyze the kinetics of reversibly photoswitchable fluorophores (RSF) under modulated illumination with the goal of overcoming the limits of OPIOM and Speed OPIOM. The protocols OPIOM and Speed OPIOM exploit resonance phenomena in photochemical systems submitted to periodic light excitation. Section 3.1 provides the basics of Fourier analysis routinely used in the case of forced systems and the relevance of resonances for discrimination purposes. The resonance conditions links the kinetic parameters of an RSF and the control parameters, e.g. the angular frequency of light

*I have been involved in the design of the optical instrument used to characterize the kinetics of RSFPs. This instrument, which we called a photoswitchometer, has been designed to record the fluorescence emission of liquid samples of RSFPs under constant light from different sources (LED or lasers) over a large range of intensities. Both light excitation and fluorescence detection have been optimized to automate acquisition and signal processing. Equipped with synchronized detectors, the photoswitchometer automatically records in 15 minutes the RSFP fluorescence evolution from an up to 36 μm-wide circular field exposed to homogeneous light at a series of light intensities covering 4 orders of magnitude up to a few hundreds of ein.m^{-2}.s^{-1} (10^4 W/cm^2).

modulation and the mean light intensities. Setting the control parameters at the resonance of a targeted RSF optimizes the contribution of the target to the fluorescence signal and weakens the contributions of all RSFs with other kinetics. OPIOM and Speed OPIOM have been designed for a two-state photoswitching mechanism and only harness the Fourier amplitude of fluorescence oscillations at the fundamental frequency. I have extended the principles of discrimination based on light modulation in two directions.

First, in the framework of the two-state mechanism used in OPIOM, I analyze the Fourier amplitudes of fluorescence oscillations at harmonic frequencies. The theoretical development has been carried out using pure sinewave illumination. I calculated analytical expressions of the amplitudes of the first harmonics. For each harmonics, either the in-phase amplitude or the quadrature amplitude of fluorescence oscillations exhibits at least one resonance in the space of the control parameters. In particular, from the second order, there are two extrema of opposite sign separated by a zero line. When the order of the harmonics increases, the value at the resonance and the width of the resonance peak both decrease. The theoretical predictions I obtained have been experimentally validated by our group. Three RSFPs have been discriminated using the second-order Fourier amplitude. We call the corresponding discrimination protocol HIGHLIGHT for PHase-sensItive imaGing of reversibly pHotoswitchable Labels after modulatIon of activatinG ligHT. Section 3.2 gives the main text of a manuscript devoted to its presentation. I wrote the details of the calculations that constitute the main part of the supporting information given in the appendix B. The principle of HIGHLIGHT has been protected by a patent which I co-invented.[87]

Second, we consider a less simple chemical mechanism. A titration reaction is commonly used in chemistry to quantitatively detect the presence of a targeted species, but few titration reactions are light driven. In order to exploit the benefit of photoswitching species in the framework of titration, we couple a reversible photoswitching step to a titration step. Under periodic illumination, the quadrature Fourier amplitude associated with the fundamental frequency displays a resonance with respect to the angular frequency, the mean light intensity and the total concentration of the titrating species. Two user-friendly protocols of dynamic titration have been proposed. The discrimination protocols of dynamic titration have been published in Physical Chemistry Chemical Physics (PCCP).[88] I wrote the first draft of the corresponding article given in section 3.3.

In chapter 4, I conduct a critical analysis of the discrimination protocols I developed and I put them into perspective in order to highlight their strengths in comparison with

close existing protocols. In section 4.1, I compare LIGHTNING with OLID and in section 4.2, I compare HIGHLIGHT with SAFIRe. Then, section 4.3 is devoted to the comparison between the constant illumination protocol, LIGHTNING, and the modulated illumination protocol, HIGHLIGHT, implemented on RSFPs. Finally, the generalization of both protocols to other photoactivatable chemical systems is discussed in section 4.4.

Concluding remarks and perspectives of the PhD work are given in chapter 5. Supporting information of the manuscripts devoted to LIGHTNING and HIGHLIGHT are given in appendices A and B, respectively.

Chapter 2

Characterization of the kinetics of reversibly photoswitchable fluorescent proteins (RSFPs) for discrimination purposes using constant illumination

A reaction network often involves a large number of chemical species and elementary steps of different kinds whose values of the rate constants generate time evolution occuring over different orders of magnitude, from nanoseconds to hours. Different methods can be used to monitor the progress of a chemical transformation. Many spectroscopic methods, in particular UV-visible absorption, infrared, NMR or fluorescence methods can give access to kinetic information. The observation of a chemical transformation is limited by experimental considerations, e.g. temporal resolution, acquisition time, and sensitivity, preventing the full kinetic information to be gathered. Simplifying a kinetic model and keeping only the relevant chemical species and relevant steps is therefore essential.

We present usual approximations based on timescale analysis which can be used to simplify a kinetic mechanism to report on an experiment. The crudest approximation consists in eliminating all the steps of a chemical mechanism except the slowest one acting as the rate-limiting step. The quasi-steady-state approximation (QSSA) and the pre-equilibrium approximation (PEA) are more refined and eliminate either a chemical species or a reaction step which evolves faster than the others. These approximations have been extensively studied over the last century.[89–93] They all exploit the same idea: Due to the existence of different timescales, the trajectories in the phase space of concentrations or extents are attracted by a low-dimensional invariant manifold in which the evolution

occurs at long times.[94,95] All these methods are based on singular perturbation. As QSSA and PEA use the zeroth order of the expansion, the small parameter does not appear, making it difficult to *a priori* test the validity of the approximation.

2.1 The rate laws

Before illustrating the elimination of fast variables in simple chemical schemes, we consider a general mechanism involving n_s chemical species $\mathrm{C_i}$ engaged in n_r elementary reaction steps

$$\sum_{i=1}^{n_s} \nu_{ij} \mathrm{C_i} \underset{k_{-j}}{\overset{k_j}{\rightleftharpoons}} \sum_{i=1}^{n_s} \nu'_{ij} \mathrm{C_i} \tag{2.1}$$

where ν_{ij} and ν'_{ij} are the left and right stoichiometric coefficients associated with species $\mathrm{C_i}$ and reaction j. The forward and backward rate constants of reaction j for $j = 1, .., n_r$ are denoted k_j and k_{-j}. The system of ordinary differential equations governing the evolution of the n_s concentrations C_i is a coupled system of equations

$$\frac{\mathrm{d}C_i}{\mathrm{d}t} = \sum_{j=1}^{n_r} \left(\nu'_{ij} - \nu_{ij}\right) \left(k_j \prod_{l=1}^{n_s} C_l^{\nu_{lj}} - k_{-j} \prod_{l=1}^{n_s} C_l^{\nu'_{lj}} \right) \tag{2.2}$$

If n_c conservation laws can be written, only $n = n_s - n_c$ concentrations are independent. The system is written in matrix form for the n independent variables

$$\frac{\mathrm{d}\mathbf{C}}{\mathrm{d}t} = f(\mathbf{C}) \tag{2.3}$$

where $\mathbf{C} = \begin{pmatrix} C_1 \\ ... \\ C_n \end{pmatrix}$ is the concentration vector and f is a possibly nonlinear function of the variables. The solution of Eq. (2.3) is highly dependent on the nonlinearities of the function f. The steady state obeys $\frac{\mathrm{d}\mathbf{C}}{\mathrm{d}t} = 0$. The deviation from the steady-state vector $\mathbf{C}^0$ is

$$\tilde{\mathbf{C}} = \mathbf{C} - \mathbf{C}^0 \tag{2.4}$$

Substituting for the concentration vector from Eq. (2.4) into Eq. (2.3) and linearizing around the steady state, we have

$$\frac{\mathrm{d}\tilde{\mathbf{C}}}{\mathrm{d}t} = \mathbf{J}\tilde{\mathbf{C}} \tag{2.5}$$

where the Jacobian matrix is

$$\mathbf{J} = \left(\frac{\partial f(\mathbf{C})}{\partial \mathbf{C}} \right)_{\mathbf{C}=\mathbf{C}^0} \tag{2.6}$$

Equation (2.5) is a linear system of n equations approximately accounting for the dynamics around the steady state. In the case of a linear function f, the Jacobian matrix $\mathbf{J}$ is independent of the steady state and the resolution of Eq. (2.5) gives the exact evolution of the concentrations even far from the steady state. We consider the case where the Jacobian matrix $\mathbf{J}$ has n eigenvalues denoted λ_i for $i = 1, .., n$. The eigendecomposition of the Jacobian matrix $\mathbf{J}$ leads to

$$\mathbf{J} = \mathbf{P}\mathbf{\Lambda}\mathbf{P}^{-1} \tag{2.7}$$

where $\mathbf{\Lambda}$ is a diagonal matrix whose diagonal terms are the eigenvalues and $\mathbf{P}$ is the change of basis matrix. In the eigenbasis, the equations are uncoupled and can be written

$$\frac{\mathrm{d}\gamma_i}{\mathrm{d}t} = \lambda_i \gamma_i \tag{2.8}$$

for $i = 1, .., n$. The vector of the variables in the eigenbasis $\mathbf{\Gamma} = \begin{pmatrix} \gamma_1 \\ ... \\ \gamma_n \end{pmatrix}$ is related to $\tilde{\mathbf{C}}$ through

$$\tilde{\mathbf{C}} = \mathbf{P}\mathbf{\Gamma} \tag{2.9}$$

The solution of Eq. (2.8) is

$$\gamma_i = \gamma_i^{\mathrm{ini}} \exp\left(\lambda_i t\right) \tag{2.10}$$

for $i = 1, .., n$, where γ_i^{ini} is the initial condition of the variable γ_i. At a given time, the state of the system is meaningfully represented by a point in the n-dimension phase space of concentrations. In the same space, the evolution of the system is a curve named trajectory. The evolution of the variables γ_i are uncoupled, which means that a perturbation leads to independent responses of the variables. If the real parts $\mathrm{Re}(\lambda_i)$ of all eigenvalues λ_i for $i = 1, .., n$ are negative, the steady state $\mathbf{C}^0$ is stable. Stable steady states are attractors, i.e. for well-chosen initial conditions the concentrations eventually reach one of the stable steady concentrations: The trajectory converges towards the steady state. If $\mathrm{Re}(\lambda_i) > 0$ for at least one eigenvalue λ_i, the steady state is unstable. The time $\tau_i = 1/ \mid \mathrm{Re}(\lambda_i) \mid$ associated with the variable γ_i characterize the evolution along the i^{th} eigendirection,

a large value of τ_i being associated with a slow variable and a small value with a fast variable. Equation (2.9) written for $t = 0$ gives the relation between the initial conditions γ_i^{ini} for the variables in the eigenbasis and the initial conditions C_i^{ini} for the concentrations, leading in matrix from to

$$\mathbf{\Gamma}^{\text{ini}} = \mathbf{P}^{-1}\tilde{\mathbf{C}}^{\text{ini}} \tag{2.11}$$

The evolution of the concentration C_i is then straightforwardly obtained using Eqs. (2.4,2.9-2.11)

$$C_i = \sum_{j=1}^{n}\sum_{k=1}^{n} P_{ij}P_{jk}^{-1}\tilde{C}_k^{\text{ini}} \exp\left(\lambda_k t\right) + C_i^0 \tag{2.12}$$

where P_{ij} and P_{ij}^{-1} are elements of the matrices $\mathbf{P}$ and $\mathbf{P}^{-1}$, respectively. The concentrations are linear combination of the variables in the eigenbasis. Equation (2.12) shows how each variable γ_i contributes to the evolution of the concentrations.

The law governing the evolution of the extent ξ_j of step j given in Eq. (2.1) is

$$\frac{\mathrm{d}\xi_j}{\mathrm{d}t} = k_j \prod_{l=1}^{n_s} C_l^{\nu_{lj}} - k_{-j} \prod_{l=1}^{n_s} C_l^{\nu'_{lj}} \tag{2.13}$$

We choose that each extent ξ_j vanishes at the steady state. Using Eqs. (2.2,2.13) and integrating we obtain

$$C_i - C_i^0 = \sum_{j=1}^{n_r} \left(\nu'_{ij} - \nu_{ij}\right) \xi_j \tag{2.14}$$

Substituting C_i from Eq. (2.14) into Eq. (2.13), we find

$$\frac{\mathrm{d}\xi_j}{\mathrm{d}t} = k_j \prod_{i=1}^{n_s} \left(\sum_{k=1}^{n_r} \left(\nu'_{ik} - \nu_{ik}\right) \xi_k + C_i^0\right)^{\nu_{ik}} - k_{-j} \prod_{i=1}^{n_s} \left(\sum_{k=1}^{n_r} \left(\nu'_{ik} - \nu_{ik}\right) \xi_k + C_i^0\right)^{\nu'_{ik}} \tag{2.15}$$

The system can be described by two sets of variables, the concentrations and the extents, which are a linear combination of each other. Therefore only n extents are independent. In addition, the linerization method applied to the concentrations can be adapted to the extents. It is worth noting that concentrations and extents share the same characteristic times.

In the case of fluorescent species, the fluorescence intensity I_F under illumination of intensity I at the excitation wavelength λ is related to the concentration C_i according to

$$I_F = I \sum_{i=1}^{n_s} Q_i C_i \tag{2.16}$$

where Q_i is the brightness of species C_i at the wavelength λ. The fluorescence intensity is thus a linear combination of the concentrations which reports on their evolution. Hence fluorescence experiments can be used to explore the kinetics of a chemical network.

The characteristic times τ_i for $i = 1, .., n$ provide relevant kinetic information and timescale analysis plays a major role in my PhD work.

2.2 Elimination of fast variables in chemical kinetics

2.2.1 Rate-limiting step

Several definitions of the rate-limiting step can be found in the literature.[96–98] We choose the following definition, which is relevant for reactions composed of irreversible elementary first-order steps. If one rate constant is much smaller than all the others, the evolution of the concentrations is limited by the step associated with the smallest rate constant. The inverse of the smallest rate constant gives the order of magnitude of the time characterizing the evolution of the concentrations. This crude approximation reduces the chemical mechanism to a single step, called the rate-limiting step. The evolution of the concentrations is then monoexponential. This simplification is used in section 2.5.

2.2.2 Quasi-steady-state approximation (QSSA)

The quasi-steady-state approximation (QSSA) is a well-known method used to reduce chemical mechanisms.[99–102] Qualitatively, when one of the chemical species C_i is much more reactive than the other chemical species, the fast variation of C_i is over at the timescale at which the other chemical species are still evolving. The approximation consists in writing $\frac{dC_i}{dt} = 0$. According to Eq. (2.2) the concentration C_i can then be written as a function of the other concentrations, which reduces by one the number of independent variables in the dynamics. The QSSA is used to eliminate the concentration C_i which is considered as a fast variable and we make precise the validity domain of the approximation.

Fast and slow variables are defined in the eigenbasis i.e. in the vicinity of the steady state. The elimination of C_i can be performed if two conditions are fulfilled. First a variable γ_k in the eigenbasis must be faster than the other variables, i.e.

$$\tau_k \ll \max_{l \neq k} (\tau_l) \tag{2.17}$$

Second the concentration C_i must vary as the fast variable γ_k during the time interval $[0, \tau_k]$. Using the normalized change of basis matrix $\mathbf{P}$ and Eq. (2.9) the condition is written as

$$| \operatorname{Re}(P_{ik}) | \gg \max_{j \neq k} (| \operatorname{Re}(P_{ij}) |) \tag{2.18}$$

According to Eq. (2.18), the slow eigendirections are close to the hyperplan defined by $C_i = C_i^0$. According to the QSSA, the relaxation with the short characteristic time τ_k along the γ_k-axis can be considered as instantaneous. The conditions given in Eqs. (2.17,2.18) involve the rate constants. They are necessary but not sufficient to ensure the validity of the elimination of the variable C_i since they result from a linearization of the equations around the steady state.

Even if these conditions are met, the approximation is not *a priori* valid at the beginning of the evolution of the concentrations. It is valid only after the fast variable γ_k has relaxed. Between 0 and τ_k the trajectories in the phase space of the concentrations are close to the k^{th} eigendirection. After the relaxation of the fast variable γ_k the trajectories evolve on an $(n-1)$-dimensional space called the slow manifold and defined by

$$\frac{\mathrm{d}C_i}{\mathrm{d}t} = 0 \tag{2.19}$$

At the fixed point corresponding to the steady state, the slow manifold is tangent to the vector space spanned by the $n-1$ eigendirections associated with the slow variables, i.e. almost perpendicular to the C_i-axis. On the slow manifold, the concentration C_i slowly evolves and adapts to the evolution of the slow concentrations.

After the elimination of the concentration C_i, the system of differential equations governing the evolution of the other concentrations can be written as a system of dimension $n-1$. If this system of differential equations involves polynomials compatible with the kinetic laws of elementary steps, the evolution of the remaining concentrations can be associated with a new set of chemical reactions. Approximate initial conditions adapted to the reduced mechanism can be defined as the intersection of the slow manifold and the fast direction passing through the initial conditions before elimination. If different characteristic times are still present an analogous process of elimination may be performed on the new chemical mechanism to further reduce the number of variables.

For illustration we consider two examples involving linear and nonlinear equations. We choose two close chemical mechanisms that differ only by one step, being of the first or the second order. Using a chemostat, i.e. a reservoir of some species, limits the number of variables without recourse to laws of conservation.

Example 1

We consider the three-state first-order mechanism further referred to as mechanism 1

$$\mathrm{X} \underset{k_{-1}}{\overset{k_1}{\rightleftharpoons}} \mathrm{Y} \tag{2.20}$$

$$\mathrm{Y} \underset{k_{-2}}{\overset{k_2}{\rightleftharpoons}} \mathrm{A} \tag{2.21}$$

where A is a reservoir of A species also called chemostat. The concentration A of species A is constant. Only the concentrations X and Y associated with chemical species X and Y are independent variables obeying the linear system of ordinary differential equations

$$\frac{\mathrm{d}X}{\mathrm{d}t} = -k_1 X + k_{-1} Y \tag{2.22}$$

$$\frac{\mathrm{d}Y}{\mathrm{d}t} = k_1 X - (k_{-1} + k_2)\, Y + k_{-2} A \tag{2.23}$$

The steady state is $X^0 = \frac{k_{-1}k_{-2}A}{k_1 k_2}$ and $Y^0 = \frac{k_{-2}A}{k_2}$. Following the method detailed in section 2.1 with the Jacobian matrix

$$\mathbf{J} = \begin{pmatrix} -k_1 & k_{-1} \\ k_1 & -(k_{-1} + k_2) \end{pmatrix} \tag{2.24}$$

we obtain the analytical expressions of the evolution of the concentrations, which are valid in the entire concentration phase space due to the linear nature of the equations given in Eqs. (2.22,2.23). In particular the eigenvalues of J_1 are

$$\lambda_1 = \frac{1}{2}\left(-(k_1 + k_{-1} + k_2) + \sqrt{(k_1 + k_{-1} + k_2)^2 - 4k_1 k_2} \right) \tag{2.25}$$

$$\lambda_2 = \frac{1}{2}\left(-(k_1 + k_{-1} + k_2) - \sqrt{(k_1 + k_{-1} + k_2)^2 - 4k_1 k_2} \right) \tag{2.26}$$

and the change of basis matrix is

$$\mathbf{P} = \begin{pmatrix} P_{11} = \frac{k_{-1}}{\sqrt{k_{-1}^2 + (k_1+\lambda_1)^2}} & P_{12} = \frac{k_{-1}}{\sqrt{k_{-1}^2 + (k_1+\lambda_2)^2}} \\ P_{21} = \frac{k_1+\lambda_1}{\sqrt{k_{-1}^2 + (k_1+\lambda_1)^2}} & P_{22} = \frac{k_1+\lambda_2}{\sqrt{k_{-1}^2 + (k_1+\lambda_2)^2}} \end{pmatrix} \tag{2.27}$$

The eigenvalues are real negative number regardless of the values of the rate constants. The steady state is thus stable. Interestingly the rate constant k_{-2} does not appear in the Jacobian matrix and consequently in the eigenvalues and the change of basis matrix. Hence the evolution of the system is independent of the rate constant k_{-2} and only depends on k_1, k_{-1}, and k_2.

The conditions given in Eqs. (2.17,2.18) for the elimination of species Y are written as

$$| \lambda_1 | \leq 10 | \lambda_2 | \tag{2.28}$$

$$| P_{21} | \leq 10 | P_{22} | \tag{2.29}$$

where λ_1 and λ_2 are given in Eqs. (2.25,2.26) and P_{21} and P_{22} in Eq. (2.27). Figure 2.1**a** displays the domain of rate constant space in which the conditions given in Eqs. (2.28,2.29) are met. It is numerically fund to be close to $k_1 \ll k_{-1} + k_2$. The variable γ_2 associated with the largest characteristic time $\tau_2 = 1/ | \lambda_2 |$ is the fast variable and the variable γ_1 associated with the largest characteristic time $\tau_1 = 1/ | \lambda_1 |$ is the slow variable.

According to Eqs. (2.19,2.23) the equation of the slow manifold is

$$k_1 X - (k_{-1} + k_2) Y + k_{-2} A = 0 \tag{2.30}$$

Substituting for the concentration Y from Eq. (2.30) into Eq. (2.22), we obtain the ordinary differential equation governing the evolution of the concentration of species X after elimination of Y

$$\frac{\mathrm{d}X}{\mathrm{d}t} = -\frac{k_1 k_2}{k_{-1} + k_2} X + \frac{k_{-1} k_{-2}}{k_{-1} + k_2} A \tag{2.31}$$

This equation can be associated with the reduced chemical reaction

$$\mathrm{X} \underset{\frac{k_{-1}k_{-2}}{k_{-1}+k_2}}{\overset{\frac{k_1 k_2}{k_{-1}+k_2}}{\rightleftharpoons}} \mathrm{A} \tag{2.32}$$

Approximate initial conditions associated with the reduced mechanism given in Eq. (2.32) can be defined from the initial conditions X^{ini} and Y^{ini} defined for mechanism 1. Using the second column of the change of basis matrix given in Eq. (2.27), we find that the straight line parallel to the fast eigendirection and passing through the point associated with the initial conditions defined for mechanism 1 is given by

$$(k_1 + \lambda_2) \left(X - X^{\mathrm{ini}} \right) - k_{-1} \left(Y - Y^{\mathrm{ini}} \right) = 0 \tag{2.33}$$

Solving the system given by Eqs. (2.30,2.33), we obtain the initial condition X'^{ini} valid for the reduced system

$$X'^{\mathrm{ini}} = \frac{\left((k_1 + \lambda_2) X^{\mathrm{ini}} - k_{-1} Y^{\mathrm{ini}} \right) (k_{-1} + k_2) + k_{-1} k_{-2} A}{(k_1 + \lambda_2) (k_{-1} + k_2) - k_1 k_{-1}} \tag{2.34}$$

Example 2

We consider the nonlinear mechanism further referred to as mechanism 2

$$2\mathrm{X} \underset{k_{-1}}{\overset{k_1}{\rightleftharpoons}} \mathrm{Y} \tag{2.35}$$

$$\mathrm{Y} \underset{k_{-2}}{\overset{k_2}{\rightleftharpoons}} \mathrm{A} \tag{2.36}$$

where A is a chemostat.

Following the laws of chemical kinetics the rate equations for the concentrations X and Y are

$$\frac{\mathrm{d}X}{\mathrm{d}t} = -2k_1X^2 + 2k_{-1}Y \tag{2.37}$$

$$\frac{\mathrm{d}Y}{\mathrm{d}t} = k_1X^2 - (k_{-1} + k_2)\,Y + k_{-2}A \tag{2.38}$$

We obtain the steady state $X^0 = \sqrt{\frac{k_{-1}k_{-2}A}{k_1k_2}}$ and $Y^0 = \frac{k_{-2}A}{k_2}$.

Linearizing around the steady state, we follow the same method involving the Jacobian matrix as previously

$$\mathbf{J} = \begin{pmatrix} -4\kappa\sqrt{\frac{k_{-1}}{k_2}} & 2k_{-1} \\ 2\kappa\sqrt{\frac{k_{-1}}{k_2}} & -(k_{-1}+k_2) \end{pmatrix} \tag{2.39}$$

The eigenvalues are

$$\lambda_1 = \frac{1}{2}\Bigg(-\left(4\kappa\sqrt{\frac{k_{-1}}{k_2}} + k_{-1} + k_2\right) + \sqrt{\left(4\kappa\sqrt{\frac{k_{-1}}{k_2}} + k_{-1} + k_2\right)^2 - 16\kappa\sqrt{k_{-1}k_2}}\Bigg) \tag{2.40}$$

$$\lambda_2 = \frac{1}{2}\Bigg(-\left(4\kappa\sqrt{\frac{k_{-1}}{k_2}} + k_{-1} + k_2\right) - \sqrt{\left(4\kappa\sqrt{\frac{k_{-1}}{k_2}} + k_{-1} + k_2\right)^2 - 16\kappa\sqrt{k_{-1}k_2}}\Bigg) \tag{2.41}$$

and the change of basis matrix is given by

$$\mathbf{P} = \begin{pmatrix} P_{11} = \frac{2k_{-1}}{\sqrt{4k_{-1}^2 + \left(4\kappa\sqrt{\frac{k_{-1}}{k_2}} + \lambda_1\right)^2}} & P_{12} = \frac{2k_{-1}}{\sqrt{4k_{-1}^2 + \left(4\kappa\sqrt{\frac{k_{-1}}{k_2}} + \lambda_2\right)^2}} \\ P_{21} = \frac{4\kappa\sqrt{\frac{k_{-1}}{k_2}} + \lambda_1}{\sqrt{4k_{-1}^2 + \left(4\kappa\sqrt{\frac{k_{-1}}{k_2}} + \lambda_1\right)^2}} & P_{22} = \frac{4\kappa\sqrt{\frac{k_{-1}}{k_2}} + \lambda_2}{\sqrt{4k_{-1}^2 + \left(4\kappa\sqrt{\frac{k_{-1}}{k_2}} + \lambda_2\right)^2}} \end{pmatrix} \tag{2.42}$$

with $\kappa = \sqrt{k_1 k_{-2} A}$. The steady state is stable because the eigenvalues are always real and negative regardless of the values of the rate constants. The evolution of the concentrations depends on three parameters k_{-1}, k_2 and $\kappa = \sqrt{k_1 k_{-2} A}$.

The conditions for the elimination of Y are given in Eqs. (2.28,2.29) where λ_1 and λ_2 are given in Eqs. (2.40,2.41) and P_{21} and P_{22} given in Eq. (2.42). The variable Y can be eliminated if the parameters meet the conditions given in Eqs. (2.28,2.29) as shown in Fig. 2.1**b**. The variable γ_2 and γ_1 are the fast and slow variables, respectively.

According Eqs. (2.19,2.38) the equation of the slow manifold is

$$k_1 X^2 - (k_{-1} + k_2)\, Y + k_{-2} A = 0 \tag{2.43}$$

Substituting for the concentration Y from Eq. (2.43) into Eq. (2.37), we have

$$\frac{\mathrm{d}X}{\mathrm{d}t} = -2\frac{k_1 k_2}{k_{-1} + k_2} X^2 + 2\frac{k_{-1} k_{-2}}{k_{-1} + k_2} \tag{2.44}$$

The associated chemical reaction can be written

$$2\mathrm{X} \underset{\frac{k_{-1}k_{-2}}{k_{-1}+k_2}}{\overset{\frac{k_1 k_2}{k_{-1}+k_2}}{\rightleftharpoons}} \mathrm{A} \tag{2.45}$$

Linearizing around the steady state $X^0 = \sqrt{\frac{k_{-1}k_{-2}A}{k_1 k_2}}$ the reduced mechanism evolve with a characteristic time

$$\tau = \frac{k_{-1} + k_2}{4\kappa\sqrt{k_{-1} k_2}} \tag{2.46}$$

Approximate initial conditions associated with the reduced mechanism given in Eq. (2.45) can be deduced from the initial conditions X^{ini} and Y^{ini} defined for mechanism 2. Using the second column of the change of basis matrix given in Eq. (2.42), we obtain the equation of a straight line parallel to the fast eigendirection and passing through the point associated with the initial conditions of mechanism 2

$$\left(4\kappa\sqrt{\frac{k_{-1}}{k_2}} + \lambda_2\right)\left(X - X^{\mathrm{ini}}\right) - 2k_{-1}\left(Y - Y^{\mathrm{ini}}\right) = 0 \tag{2.47}$$

Solving the system given by Eqs. (2.43,2.47), we obtain the initial condition X'^{ini} of the reduced system

$$X'^{\mathrm{ini}} = \frac{\zeta + \sqrt{\Delta}}{2k_{-1}} \tag{2.48}$$

where $\Delta = \zeta^2 - 4\left(\kappa^2 + k_1 \zeta X^{\mathrm{ini}} - k_1\left(k_{-1} + k_2\right) Y^{\mathrm{ini}}\right)$ and $\zeta = \frac{(k_{-1}+k_2)}{2k_{-1}}\left(4\kappa\sqrt{\frac{k_{-1}}{k_2}} + \lambda_2\right)$

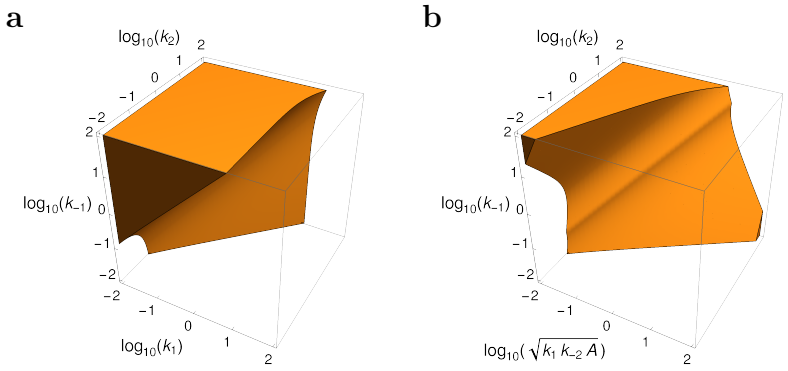

Figure 2.1: Domains of validity of the elimination of species Y for mechanisms 1 (**a**) and 2 (**b**) in the parameter space. The colored volumes are defined by Eqs. (2.28,2.29). The rate constants are expressed in arbitrary units.

Elimination of Y

As shown in Fig. 2.1 mechanisms 1 and 2 lead to very different parameter domains in which the elimination of Y is valid.

Figure 2.2 displays the eigendirections given in Eq. (2.24) (Eq. (2.39), resp.) and the slow manifold given in Eq. (2.30) (Eq. (2.43), resp.) for mechanism 1 (2, resp.). The trajectories in the phase space (X, Y) deduced from the numerical integration of Eqs. (2.20,2.21) for mechanism 1 and Eqs. (2.21,2.35) for mechanism 2 are also shown for rate constant values in the domain where the elimination of the variable Y is valid. For the linear mechanism 1 the slow manifold is a straight line equal to the slow eigendirection. In this case the slow manifold is a vector space. For the nonlinear mechanism 2 the slow manifold is curved but is, as expected, tangent to the slow eigendirection at the steady state. For both mechanisms, the slow eigendirections are quasi-parallel to the X-axis. The trajectories are first parallel to the fast eigendirection, then close to the slow manifold, and reach the stable steady state in the slow eigendirection. The elimination of the variable Y is valid as soon as the trajectories have reached the vicinity of the slow manifold.

The variation of X at large timescales ($t \gg \tau_2$) is correctly described by the reduced mechanisms with the initial conditions given in Eqs. (2.34,2.48). After a period of a few τ_2, the difference between the evolution of X from mechanism 1 (2, resp.) and the reduced mechanism given in Eq. (2.32) (Eq. (2.45), resp.) is less than one per cent.

Fig. 2.3**a** displays the variation of the decimal logarithm of the eigenvalues given in Eqs. (2.40,2.41) with the rate constant k_2 for mechanism 2. The logarithm of the characteristic time given in Eq. (2.46) associated with the reduced mechanism is also displayed. As expected, the variation is similar to the variation of λ_1 for $k_2 > 0.4$. Figure

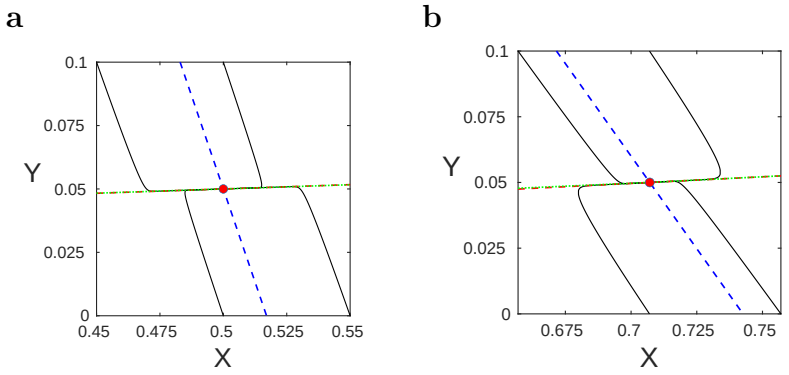

Figure 2.2: Trajectories (black solid lines) in the phase space (X, Y) for mechanisms 1 (**a**) and 2 (**b**), steady state (red disk), eigendirections associated with the fast variable (blue dashed line) and the slow variable (red dashed line) in the eigenbasis, and slow manifold (green dotted line). The trajectories are deduced from the numerical integration of Eqs. (2.22,2.23) for mechanism 1 and Eqs. (2.37,2.38) for mechanism 2. The initial conditions $(X^{\text{ini}}, Y^{\text{ini}})$ are $(0.5, 0), (0.45, 0.1), (0.55, 0), (0.5, 0.1)$ and $(0.707, 0), (0.657, 0.1), (0.757, 0), (0.707, 0.1)$ in arbitrary units (a.u.) for mechanisms 1 and 2, respectively. The parameter values are $k_1 = 0.1$ a.u., $k_{-1} = 1$ a.u., $k_2 = 2$ a.u., and $k_{-2}A = 0.1$ a.u.

2.3**b** shows the variation with k_2 of the elements $\mid P_{21} \mid$ and $\mid P_{22} \mid$ of the change of basis matrix given in Eq. (2.42) of mechanism 2. Whereas the condition $\mid \lambda_1 \mid \ll \mid \lambda_2 \mid$ for the elimination of Y is obeyed for all values of k_2, the condition $\mid P_{21} \mid \ll \mid P_{22} \mid$ is fulfilled only for $k_2 \gg 0.13$. The condition on the elements on the change of basis matrix is more restrictive than the condition on the eigenvalues.

The eigenvalues λ_1 and λ_2 have a typical avoided crossing behavior in the sense of quantum chemistry around $k_2 \simeq 0.4$. An interesting parallel can be drawn with the Born-Oppenheimer approximation which, with the QSSA, is an adiabatic approximation.[89] The Born-Oppenheimer approximation consists in neglecting the fast movements of the electrons and considering only their response to the slower movement of the nuclei. For degenerate energy states the Born-Oppenheimer approximation is not valid. Introducing a perturbation in the non diagonal elements splits the degenerate energy states and leads to an avoided crossing, as in Fig. 2.3**a**. For $k_2 \ll 0.13$, the concentration X essentially varies as γ_2 and Y as γ_1. For $k_2 \gg 0.13$, the reverse is true. Hence the eigenvalues characterizing the variation of X (Y, resp.) are decreasing (increasing, resp.) functions of k_2 in each interval. For $k_2 \simeq 0.4$, X and Y depend on both eigenvalues.

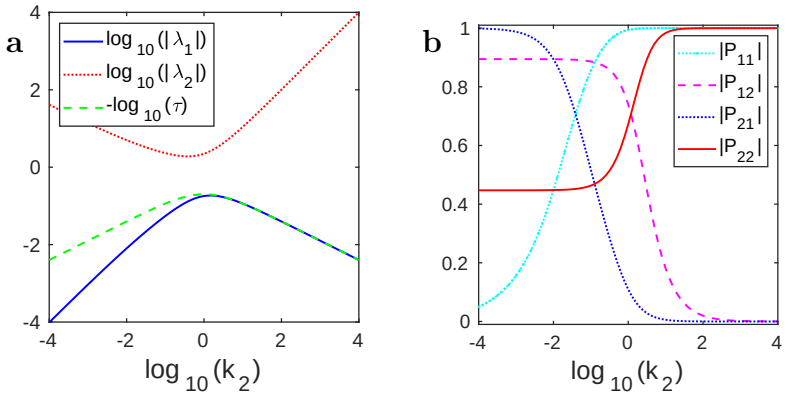

Figure 2.3: **a**: Logarithm of the absolute value of the eigenvalues $\log_{10}(\mid \lambda_1 \mid)$ and $\log_{10}(\mid \lambda_2 \mid)$ of mechanism 2 and $-\log_{10}(\tau)$ of the reduced mechanism associated with mechanisms 2 versus $\log_{10}(k_2)$. **b**: Absolute value of the elements $\mid P_{11} \mid$, $\mid P_{12} \mid$, $\mid P_{21} \mid$, and $\mid P_{22} \mid$ of the change of basis matrix of mechanism 2 versus $\log_{10}(k_2)$. The parameter values are $k_1 = 0.1$ a.u., $k_{-1} = 1$ a.u., and $k_{-2}A = 0.1$ a.u.

2.2.3 Pre-equilibrium approximation (PEA)

The pre-equilibrium approximation (PEA) offers another method of mechanism reduction.[95,103] When a step is much faster than the others, the fast variation of its extent ξ_i can be eliminated at the timescale of the evolution of the other extents. The approximation consists in writing $\frac{\mathrm{d}\xi_i}{\mathrm{d}t} = 0$. This approximation is similar to the QSSA, with the only difference that the eliminated variable is an extent and not a concentration.

The same comments as for the elimination of a concentration can be made for the elimination of an extent. In summary, the extent ξ_i can be eliminated in the vicinity of the steady state if the following conditions are met. First a variable γ_k in the eigenbasis must be faster than the other variables, leading to the condition given in Eq. (2.17). Second the variables γ_k and ξ_i must evolve similarly on the time interval $[0, \tau_k]$, leading to the condition given in Eq. (2.18). The reduced system is valid after the relaxation of the variable γ_k associated with the characteristic time τ_k. In the phase space of the extents, the trajectories are first parallel to the k^{th} eigendirection and then tangent to the slow manifold defined by

$$\frac{\mathrm{d}\xi_i}{\mathrm{d}t} = 0 \tag{2.49}$$

The slow manifold is tangent to the hyperplane defined by $\xi_i = 0$. In some cases the evolution of the non eliminated extents on the slow manifold can be associated with a reduced chemical mechanism and adapted initial conditions can be defined.

The pre-equilibrium approximation is illustrated on the following example.

Example 3

We consider the three-state mechanism further referred to as mechanism 3

$$\mathrm{X} \underset{k_{-1}}{\overset{k_1}{\rightleftharpoons}} \mathrm{Y} \tag{2.50}$$

$$\mathrm{X} + \mathrm{Y} \underset{k_{-2}}{\overset{k_2}{\rightleftharpoons}} \mathrm{A} \tag{2.51}$$

where A is a chemostat. According to the laws of kinetics, the rate laws for the concentrations are

$$\frac{\mathrm{d}X}{\mathrm{d}t} = -k_1 X + k_{-1} Y - k_2 XY + k_{-2} A \tag{2.52}$$

$$\frac{\mathrm{d}Y}{\mathrm{d}t} = k_1 X - k_{-1} Y - k_2 XY + k_{-2} A \tag{2.53}$$

The steady state is $X^0 = \sqrt{\frac{k_{-1}k_{-2}A}{k_1 k_2}}$ and $Y^0 = \sqrt{\frac{k_1 k_{-2} A}{k_{-1} k_2}}$. The extents ξ_1 and ξ_2 are associated with the steps given in Eq. (2.50) and Eq. (2.51), respectively. Using Eq. (2.14) we deduce

$$X - X^0 = -\left(\xi_1 + \xi_2\right) \tag{2.54}$$

$$Y - Y^0 = \xi_1 - \xi_2 \tag{2.55}$$

Following Eq. (2.15), we find

$$\frac{\mathrm{d}\xi_1}{\mathrm{d}t} = k_1 X - k_{-1} Y \tag{2.56}$$

$$\frac{\mathrm{d}\xi_2}{\mathrm{d}t} = k_2 XY - k_{-2} A \tag{2.57}$$

Substituting X and Y from Eqs. (2.54,2.55) into Eqs. (2.56,2.57) we obtain the rate laws for the extents

$$\frac{\mathrm{d}\xi_1}{\mathrm{d}t} = -\left(k_1 + k_{-1}\right)\xi_1 + \left(-k_1 + k_{-1}\right)\xi_2 \tag{2.58}$$

$$\frac{\mathrm{d}\xi_2}{\mathrm{d}t} = k_2\left(-\xi_1^2 + \xi_2^2 + \left(X^0 - Y^0\right)\xi_1 - \left(X^0 + Y^0\right)\xi_2\right) \tag{2.59}$$

We follow the method detailed in section 2.1. The system given in Eqs. (2.58,2.59) is written in matrix form for the Jacobian matrix

$$\mathbf{J} = \begin{pmatrix} -\left(k_1 + k_{-1}\right) & -k_1 + k_{-1} \\ \kappa\frac{\left(-k_1 + k_{-1}\right)}{\sqrt{k_1 k_{-1}}} & -\kappa\frac{\left(k_1 + k_{-1}\right)}{\sqrt{k_1 k_{-1}}} \end{pmatrix} \tag{2.60}$$

with $\kappa = \sqrt{k_2 k_{-2} A}$. The eigenvalues of $\mathbf{J}$ are given by

$$\lambda_1 = \frac{1}{2}\Bigg(-(k_1+k_{-1})\left(1+\frac{\kappa}{\sqrt{k_1 k_{-1}}}\right) + \sqrt{(k_1+k_{-1})^2\left(1+\frac{\kappa}{\sqrt{k_1 k_{-1}}}\right)^2 - 16\kappa\sqrt{k_1 k_{-1}}}\Bigg) \tag{2.61}$$

$$\lambda_2 = \frac{1}{2}\Bigg(-(k_1+k_{-1})\left(1+\frac{\kappa}{\sqrt{k_1 k_{-1}}}\right) - \sqrt{(k_1+k_{-1})^2\left(1+\frac{\kappa}{\sqrt{k_1 k_{-1}}}\right)^2 - 16\kappa\sqrt{k_1 k_{-1}}}\Bigg) \tag{2.62}$$

and the change of basis matrix is

$$\mathbf{P} = \begin{pmatrix} P_{11} = \frac{-k1+k_{-1}}{\sqrt{(-k1+k_{-1})^2+(k_1+k_{-1}+\lambda_1)^2}} & P_{12} = \frac{\kappa(k_1+k_{-1})+\lambda_2\sqrt{k_1 k_{-1}}}{\sqrt{\left(\kappa(k_1+k_{-1})+\lambda_2\sqrt{k_1 k_{-1}}\right)^2+\kappa^2(-k_1+k_{-1})^2}} \\ P_{21} = \frac{k_1+k_{-1}+\lambda_1}{\sqrt{(-k1+k_{-1})^2+(k_1+k_{-1}+\lambda_1)^2}} & P_{22} = \frac{\kappa(-k_1+k_{-1})}{\sqrt{\left(\kappa(k_1+k_{-1})+\lambda_2\sqrt{k_1 k_{-1}}\right)^2+\kappa^2(-k_1+k_{-1})^2}} \end{pmatrix} \tag{2.63}$$

The conditions given in Eqs. (2.17,2.18) for the elimination of the extent ξ_1 are written as

$$\mid \lambda_1 \mid \leq 10 \mid \lambda_2 \mid \tag{2.64}$$

$$\mid P_{11} \mid \leq 10 \mid P_{12} \mid \tag{2.65}$$

where λ_1 and λ_2 are given in Eqs. (2.61,2.62) and P_{11} and P_{12} given in Eq. (2.63). The eigenvalues of $\mathbf{J}$ are negative for all values of the rate constant. Consequently the steady state is stable. The evolution of the system depends on three parameters, k_1, k_{-1}, and $\kappa = \sqrt{k_2 k_{-2} A}$. Figure 2.4 displays the domain of rate constants space in which the conditions given in Eqs. (2.64,2.65) are met. These conditions are numerically close to $\mid k_1 - k_{-1} \mid \ll 1$ and $\sqrt{k_2 k_{-2} A} \leq k_1 + k_{-1}$. In the eigenbasis the variables γ_1 and γ_2 are the fast and slow variables, respectively.

According to Eqs. (2.49,2.56,2.52), the equation of the slow manifold is

$$-(k_1+k_{-1})\,\xi_1 + (-k_1+k_{-1})\,\xi_2 = 0 \tag{2.66}$$

in the phase space of the extents and

$$k_1 X - k_{-1} Y = 0 \tag{2.67}$$

in the phase space of the concentrations. The reduced chemical scheme is straightforwardly given by Eq. (2.51). The variation of the extent is given by Eq. (2.59) and the variation of the concentrations is

$$\frac{\mathrm{d}X}{\mathrm{d}t} = \frac{\mathrm{d}Y}{\mathrm{d}t} = -k_2 XY + k_{-2} A \tag{2.68}$$

Approximate initial conditions X'^{ini} and Y'^{ini} associated with the reduced model are deduced from the initial conditions X^{ini} and Y^{ini} defined for mechanism 3. Using Eqs. (2.54,2.55) and the change of basis matrix given in Eq. (2.63), the equation of the fast eigendirection in the phase space of the concentrations is

$$\left(2k_1\kappa + \lambda_2\sqrt{k_1 k_{-1}}\right)\left(X - X^{\mathrm{ini}}\right) + \left(2k_{-1}\kappa + \lambda_2\sqrt{k_1 k_{-1}}\right)\left(Y - Y^{\mathrm{ini}}\right) = 0 \tag{2.69}$$

We solve the system given by Eqs. (2.67,2.69) and obtain the initial conditions X'^{ini} and Y'^{ini} for the reduced system

$$X'^{\mathrm{ini}} = k_{-1}\frac{2\kappa\left(k_1 X^{\mathrm{ini}} + k_{-1} Y^{\mathrm{ini}}\right) + \lambda_2\sqrt{k_1 k_{-1}}\left(X^{\mathrm{ini}} + Y^{\mathrm{ini}}\right)}{4\kappa k_1 k_{-1} + \lambda_2\left(k_1 + k_{-1}\right)\sqrt{k_1 k_{-1}}} \tag{2.70}$$

$$Y'^{\mathrm{ini}} = k_1\frac{2\kappa\left(k_1 X^{\mathrm{ini}} + k_{-1} Y^{\mathrm{ini}}\right) + \lambda_2\sqrt{k_1 k_{-1}}\left(X^{\mathrm{ini}} + Y^{\mathrm{ini}}\right)}{4\kappa k_1 k_{-1} + \lambda_2\left(k_1 + k_{-1}\right)\sqrt{k_1 k_{-1}}} \tag{2.71}$$

The phase spaces (ξ_1, ξ_2) for the extents and (X, Y) for the concentrations are shown in Fig. 2.5 with rate constant values for which the elimination of the extent ξ_1 is valid. The eigendirections are obtained using Eq. (2.63) and the slow manifold using Eq. (2.66) in the space (ξ_1, ξ_2) and Eq. (2.67) in the space (X, Y). The trajectories are obtained by numerical integration of Eqs. (2.58,2.59) in the phase space (ξ_1, ξ_2) and Eqs. (2.52,2.53) in the phase space (X, Y). As expected, in the phase space of the extents the slow eigendirection and the slow manifold are parallel to the ξ_1-axis. However they are not parallel to any axis in the phase space of the concentrations. In both phase spaces the trajectories are first parallel to the fast eigendirection, then reach the vicinity of the slow manifold, and end at the steady state. The reduced model is valid once the trajectory have reached the vicinity of the slow manifold. The extent ξ_1 has then almost reached its steady value, however both X and Y are still far from their steady values.

The reduced mechanism and the approximate initial conditions given in Eqs. (2.70,2.71) satisfactorily describe the behavior of mechanism 3 at large timescale. After a period of several fast characteristic times, the difference between X and Y deduced from mechanism 3 and the reduced mechanism given in Eq. (2.51) is less than one per cent.

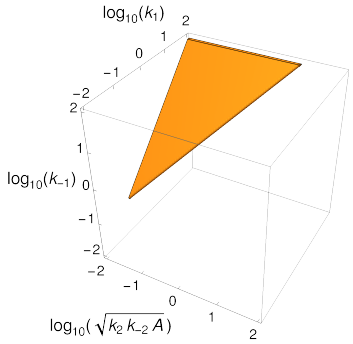

Figure 2.4: Domains of validity of the elimination of extent ξ_2 for mechanism 3 in the parameter space. The colored volumes are defined by Eqs. (2.64,2.65). The rate constants are expressed in arbitrary units.

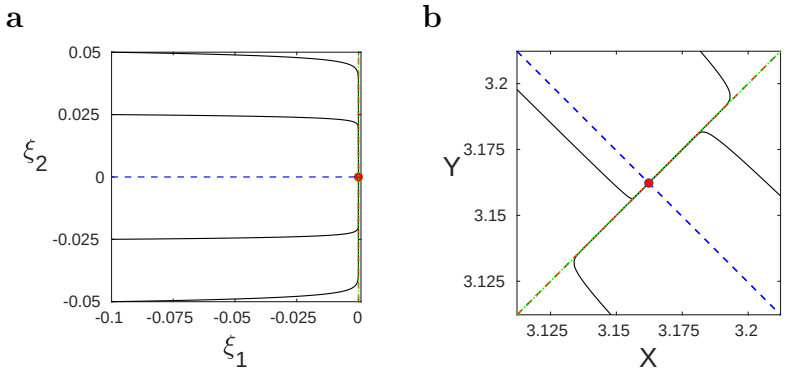

Figure 2.5: Trajectories (black solid lines) in the phase space (ξ_1, ξ_2) (**a**) and (X, Y) (**b**) for mechanism 3, steady state (red disk), eigendirections associated with the fast variable (blue dashed line) and the slow variable (red dashed line) in the eigenbasis, and slow manifold (green dotted line). The trajectories are deduced from the numerical integration of Eqs. (2.58,2.59) (**a**) and Eqs. (2.52,2.53) (**b**). The initial conditions are $(-0.1, 0.05)$, $(-0.1, 0.025)$, $(-0.1, -0.025)$, $(-0.1, -0.05)$, (**a**), $(3.15, 3.11)$, $(3.11, 3.2)$, $(3.175, 3.22)$, $(3.22, 3.15)$ (**b**). The parameter values are $k_1 = 1$ a.u., $k_{-1} = 1$ a.u., $k_2 = 0.01$ a.u., and $k_{-2}A = 0.1$ a.u.

2.3 Application to the reduction of an RSFP mechanism

Our group identified the reversibly photoswitchable fluorescent proteins (RSFPs) as well suited for multiplexing imaging protocols because they offer a rich photocycle with rate constants spanning several orders of magnitude.[104–108]

In the purpose of developing discrimination protocols harnessing the kinetic properties of RSFPs, we are interested in extracting different times characterizing fluorescence evolution. Standard microscopies used in biology, from epifluorescence to confocal microscopies, are typically used to observe photophysical and photochemical processes occuring from 1 μs to tenths of second. Moreover many biological phenomena, such as membrane polarization and some metabolite dynamics, occur in less than a few seconds. These considerations led us to focus on the kinetics of RSFPs in a time window spanning the 1 μs–1 s range.

For each RSFP, we aim at building a kinetic signature composed of non redundant characteristic times. Our answer consists in tuning the light intensity and changing the rate-limiting step. Indeed, the rate constant of a photochemical step is the product of light intensity and cross section. At low intensity kinetics is governed by the slow photochemical step. At sufficiently high intensity, the photochemical step becomes faster than some thermal steps, which in turn become rate limiting.

In this section we apply the quasi-steady-state approximation to a reasonably complex RSFP mechanism in order to highlight the relevant steps for different light intensities in a the 1 μs–1 s time window. We use the orders of magnitude of the photochemical cross sections and thermal rate constants found in the literature or unpublished work of our group to define light intensity regimes associated with non redundant kinetic information.

2.3.1 A seven-state mechanism for RSFPs relevant in the 1 μs–1 s time window

We rely on literature to establish the mechanism given in Fig. 2.6**a** accounting for the photochemical behavior of RSFPs in the 1 μs–1 s time window. We focus on reported steps of isomerization,[104–108] protonation,[104–108] and formation of triplet state.[110] The detailed mechanisms of all RSFPs are not entirely known. We use existing information on more studied RSFPs, such as Dronpa and Dronpa-2, and admit that the other RSFPs obey a similar mechanism. The orders of magnitude of the rate constants are given in

	parameter	order of magnitude
seven-state mechanism		
absorption cross sections[104–109]	ϵ_{11}, ϵ_{22}	10^3-10^4 $m^2.mol^{-1}$
	ϵ_{12}	10^2-10^3 $m^2.mol^{-1}$
singlet relaxation[104–108]	k_{-1}	10^9 s^{-1}
	k_{-2}	10^{11} s^{-1}
isomerization[104–108]	k_B	10^7 s^{-1}
	k_D	10^{10} s^{-1}
inter-system crossing[110]	k_T	10^7 s^{-1}
proton exchange[104–108]	k_C, k_{DA}	10^3-10^6 s^{-1}
back inter-system crossing[110]	k_{TA}	10^3 s^{-1}
thermal isomerization[104–108]	k_{CA}	10^{-4}-10^{-2} s^{-1}
five-state mechanism		
light intensities	I_1, I_2	$\ll 10^5$ ein.m^{-2}.s^{-1}
isomerization cross sections	σ_{11}, σ_{22}	10-10^2 $m^2.mol^{-1}$
	σ_{12}	1-10 $m^2.mol^{-1}$
triplet cross sections	σ_{11}^T	10-10^2 $m^2.mol^{-1}$
	σ_{12}^T	1-10 $m^2.mol^{-1}$
two-state mechanism I_{low}		
light intensity	I_1	$\ll 10^1$-10^2 ein.m^{-2}.s^{-1}
three-state mechanism I_{high}		
light intensity	I_1	$\gg 10^1$-10^5 ein.m^{-2}.s^{-1}
rate constant of step T→B	k_{TB}	1-10^3 s^{-1}
two-state mechanism II_{low}		
light intensities	I_1	~ 0.1 ein.m^{-2}.s^{-1}
	I_2	$\ll 10^1$-10^2 ein.m^2.s^{-1}
four-state mechanism II_{high}		
light intensities	I_1	~ 0.1 ein.m^{-2}.s^{-1}
	I_2	$\gg 10^1$-10^5 ein.m^2.s^{-1}

Table 2.1: Order of magnitude of parameters of the photoisomerization mechanisms of RSFPs.

Tab. 2.1.

The thermodynamically stable Cis-O^- state, denoted A, absorbs light mainly at the wavelength $\lambda_1 = 480$ nm and to a lesser extent at the wavelength $\lambda_2 = 405$ nm forming the singlet excited state A^*[109] from which three reactions paths begin. The Cis-O^- state is recovered (i) by singlet relaxation, (ii) through the triplet state T of the Cis-O^- state involving inter-system crossing,[110] and (iii) by a longer reaction path described below. Isomerization of A^* yields the Trans-O^- state, denoted B, which presumably possesses a similar absorption spectrum and a similar order of magnitude of relaxation rate of its singlet excited state B^* as the Cis-O^- state.[109] Protonation of B leads to the Trans-OH state, denoted C.[104–108] The singlet excited state C^* of the Trans-OH state is only formed

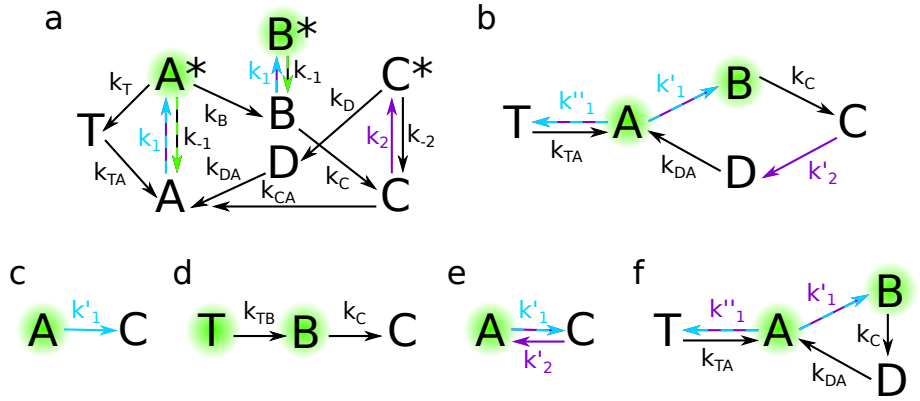

Figure 2.6: Photoisomerization mechanisms of negative RSFPs relevant in the 1 μs–1 s time window. **a**: Seven-state mechanism. **b**: Five-state mechanism relevant in the investigated light intensity range obtained after elimination of the fast variables A*, B*, and C*. **c**: Reduced mechanism valid for low light intensity at $\lambda_1 = 480$ nm and no light at $\lambda_2 = 405$ nm (illumination I_{low}). **d**: Reduced mechanism valid for high light intensity at $\lambda_1 = 480$ nm and no light at $\lambda_2 = 405$ nm (illumination I_{high}). **e**: Reduced mechanism valid for low light intensities at $\lambda_1 = 480$ nm and $\lambda_2 = 405$ nm (illumination II_{low}). **f**: Reduced mechanism valid for low light intensity at $\lambda_1 = 480$ nm and high light intensity at $\lambda_2 = 405$ nm (illumination II_{high}). The order of magnitude of the rate constants and light intensities associated with each case are given in Tab. 2.1. The photochemical rate constants associated with absorption at $\lambda_1 = 480$ nm ($\lambda_2 = 405$ nm, resp.) are cyan (purple, resp.). The thermal rate constants are black. Species with a green halo are bright or acquire brightness due to mechanism reduction.

by absorption at the wavelength $\lambda_2 = 405$ nm. The Cis-O^- state may be directly formed from Trans-OH by thermal isomerization or obtained by light excitation of Trans-OH, isomerization yielding the Cis-OH state denoted D, and deprotonation.[104–108] At neutral pH, the Cis-O^- state and the Trans-OH state are the predominant acid-base states of the cis-trans isomers.[105]

States with lifetimes outside the investigated time window do not appear in the considered seven-state mechanism since they do not contribute to kinetics in the investigated time window. Among the species with a lifetime in the investigated time window, only the triplet state of Cis-O^- was considered. Triplet states of other species, such as the triplet of Trans-OH, could have been considered. Other states could have been included in the mechanism. However, in a minimalist approach, we chose not to include them in the mechanism of RSFPs.

The considered seven-state mechanism possesses both photochemical and thermal steps and is therefore well adapted to changing the rate-limiting steps simply by tuning light intensities.

We consider two different illuminations I and II. In illumination I, a light intensity I_1 at the wavelength $\lambda_1 = 480$ nm is applied to the sample initially in the bright Cis-O$^-$ state. In illumination II, a light intensity I_2 at the wavelength $\lambda_2 = 405$ nm and a small fixed intensity I_1 at the wavelength $\lambda_1 = 480$ nm are applied to the sample initially in the dark Trans-OH state. The complementary illumination at $\lambda_1 = 480$ nm is added to obtain a fluorescent signal since the brightness of the states A and B at the wavelength $\lambda_2 = 405$ nm are small.

The seven-state mechanism given in Fig. 2.6**a** yields the rate laws

$$\frac{\mathrm{d}A}{\mathrm{d}t} = -k_1 A + k_{-1} A^* + k_{CA} C + k_{DA} D + k_{TA} T \tag{2.72}$$

$$\frac{\mathrm{d}A^*}{\mathrm{d}t} = k_1 A - (k_{-1} + k_T + k_B)\, A^* \tag{2.73}$$

$$\frac{\mathrm{d}B}{\mathrm{d}t} = k_B A^* - (k_1 + k_A)\, B + k_{-1} B^* \tag{2.74}$$

$$\frac{\mathrm{d}B^*}{\mathrm{d}t} = k_1 B - k_{-1} B^* \tag{2.75}$$

$$\frac{\mathrm{d}C}{\mathrm{d}t} = k_C B - (k_2 + k_{CA})\, C + k_{-2} C^* \tag{2.76}$$

$$\frac{\mathrm{d}C^*}{\mathrm{d}t} = k_2 C - (k_{-2} + k_D)\, C^* \tag{2.77}$$

$$\frac{\mathrm{d}D}{\mathrm{d}t} = k_D C^* - k_{DA} D \tag{2.78}$$

with the law of conservation of matter $C_{\mathrm{tot}} = A + A^* + B + B^* + C + C^* + D + T$. In Eqs. (2.72–2.78), the photochemical rate constants k_1 and k_2 can be written as

$$k_1 = \epsilon_{11} I_1 + \epsilon_{12} I_2 \tag{2.79}$$

$$k_2 = \epsilon_{22} I_2 \tag{2.80}$$

where ϵ_{11} and ϵ_{12} are the absorption cross sections of A and B at the wavelengths $\lambda_1 = 480$ nm and $\lambda_2 = 405$ nm, respectively and ϵ_{22} is the absorption cross section of C at the wavelength $\lambda_2 = 405$ nm. We assume that only illumination at $\lambda_1 = 480$ nm leads to fluorescence emission. The rate constant k_{-1} takes into account the radiative and non radiative de-excitation of the singlet excited states A* and B*. We neglect the fluorescence of all species except A* and B*[104,105,109] leading to the fluorescence intensity written as

$$I_F = k^F_{A^*} A^* + k^F_{B^*} B^* \tag{2.81}$$

where $k^F_{A^*}$ and $k^F_{B^*}$ are the radiative part of the rate constants k_{-1} associated with the desexcitation of A* and B*, respectively.

Varying the light intensities I_1 and I_2 allows us to explore different kinetic regimes.

2.3.2 Elimination of the singlet excited states – The five-state mechanism

We exploit the very different orders of magnitude of the rate constants and use the quasi-steady-state approximation to reduce the system given in Eqs. (2.72-2.78). The mechanism being composed of first-order steps, the condition of validity for the elimination of a fast chemical species is easy to express: The sum of the rate constants of the steps in which the considered species is a reagent must be large compared to the sum of the rate constants of the steps in which the species is a product. The fastest reactive species are eliminated first and only smaller characteristic times defining the timescale of interest remain. The next fastest species is eliminated until all characteristic times are close within the chosen time range.

According to Tab. 2.1, the fastest species are the singlet excited states A^*, B^*, and C^*. Their elimination is valid if the conditions $k_1 \ll k_{-1} + k_T + k_B$, $k_1 \ll k_{-1}$, and $k_2 \ll k_{-2}+k_D$ are fulfilled, i.e. if the light intensities obey $I_1 \ll k_{-1}/\epsilon_{11}$ and $I_2 \ll k_{-2}/\epsilon_{22}$. Using Tab. 2.1, we find that light intensities smaller than 10^5 ein.m^2.s^{-1} meet these conditions. In addition, the rate constant k_{CA}, which order of magnitude is given in Tab. 2.1, is associated with a slow step whose kinetics is not accessible in the explored time window. This step is therefore ignored. We eliminate the species A^*, B^*, and C^* and obtain the reduced five-state mechanism given in Fig. 2.6**b**. The effective photochemical rate constants are given by

$$k_1' = \sigma_{11} I_1 + \sigma_{12} I_2 \tag{2.82}$$

$$k_1'' = \sigma_{11}^T I_1 + \sigma_{12}^T I_2 \tag{2.83}$$

$$k_2' = \sigma_{22} I_2 \tag{2.84}$$

where $\sigma_{11} = \epsilon_{11} k^B/(k_{-1} + k_T + k_B)$ and $\sigma_{11}^T = \epsilon_{11} k^T/(k_{-1} + k_T + k_B)$ are the isomerization and triplet cross sections of A at the wavelength $\lambda_1 = 480$ nm, $\sigma_{12} = \epsilon_{12} k^B/(k_{-1}+k_T+k_B)$ and $\sigma_{12}^T = \epsilon_{12} k^T/(k_{-1}+k_T+k_B)$ are the isomerization and triplet cross sections of A at the wavelength $\lambda_2 = 405$ nm, and $\sigma_{22} = \epsilon_{22} k^D/(k_{-2} + k_D)$ is the isomerization cross section of C at the wavelength $\lambda_2 = 405$ nm.

Using Eq. (2.81), we write the fluorescence intensity as

$$I_F = (Q_A A + Q_B B)\, I_1 \tag{2.85}$$

where $Q_A = \epsilon_{11} k_{A^*}^F/(k_{-1} + k_T + k_B)$ and $Q_B = \epsilon_{11} k_{B^*}^F/k_{-1}$ are the brightnesses of species A and B.

2.3.3 Reduced mechanisms valid for four different illuminations

The thermal rate constants, k_C, k_{DA}, k_{TA}, involved in the five-state mechanism have close orders of magnitude and are associated with reaction steps which can be observed within the investigated time range. The light intensities I_1 and I_2 set the value of the photochemical rate constants, k_1', k_1'', and k_2'. Consequently the light intensities control which species are sufficiently fast to be eliminated and which reduced mechanism is relevant.

Under illumination I, $I_2 = 0$ which leads to $k_2' = 0$. Hence kinetics does not involve species D nor the rate constants k_2' and k_{DA}. The five-state mechanism becomes a four-state mechanism. In addition, since A is the thermodynamically stable state, the initial condition is assumed to be $A = C_{\text{tot}}$. We reduce then the four-state mechanism for low and high light intensities I_1.

Illumination $\mathbf{I}_{\text{low}}$

We first consider an illumination I_{low} of low light intensity I_1. We assume the light intensity to obey $I_1 \ll \min(k_C/\sigma_{11}, k_{TA}/\sigma_{11}^T)$, such that the conditions $k_1' \ll k_C$ and $k_1'' \ll k_{TA}$ are fulfilled. The orders of magnitude of the parameters given in Tab. 2.1 are used to evaluate the interval of I_1 in which the condition is fulfilled. The fast species B and T are eliminated and the two-state mechanism given in Fig. 2.6**c** is obtained. Using Eq. (2.85), we write the fluorescence intensity as

$$I_F = \left(Q_A + Q_B \frac{k_1'}{k_A} \right) A I_1 \tag{2.86}$$

The fluorescence intensity behaves as the concentration A according to a monoexponential decrease of characteristic time

$$\tau_1 = \frac{1}{k_1'} \tag{2.87}$$

Illumination $\mathbf{I}_{\text{high}}$

Then we consider an illumination I_{high} of high light intensity I_1 such that the condition $I_1 \gg k_{DA}/(\sigma_{11} + \sigma_{11}^T)$, i.e. $k_{CA} + k_{DA} \ll k_1' + k_1''$ is fulfilled. Table 2.1 is used to assess the interval of I_1 in which the condition is fulfilled. The fast species A is eliminated and the three-state thermal mechanism given in Fig. 2.6**d** is obtained. Using Eq. (2.85), we have

$$I_F = \left(Q_A \frac{k_{TA}}{k_1' + k_1''} T + Q_B B \right) I_1 \tag{2.88}$$

Exactly as the fundamental state of a fluorophore is said to be bright, due to the elimination of the fast evolving singlet excited state, some species in reduced mechanisms may be considered bright. The reduction of the seven-state mechanism results in an apparent brightness for the triplet state although the triplet is not intrinsically bright.

The method described in section 2.1 can be used to obtain the analytical expressions of the concentrations and the fluorescence intensity. The fluorescence intensity depends on both T and B which decrease with the two characteristic times

$$\tau_1 = \frac{1}{k_C} \tag{2.89}$$

$$\tau_2 = \frac{k_B + k_T}{k_B k_{TA}} \tag{2.90}$$

Hence, for high enough intensities I_1, fluorescence decreases according to a biexponential law. The characteristic times are independent of I_1 and thermal steps control fluorescence evolution.

Regardless of the value of the light intensity I_1, illumination I yields $C = C_{\text{tot}}$ at the steady state. In the case of illumination II, which occurs after illumination I_{low}, we assume that the steady state is reached when illumination II starts. Consequently we adopt $C = C_{\text{tot}}$ as the initial condition of illumination II. We reduce the five-state mechanism for low and high light intensities I_2.

Illumination II_{low}

We consider an illumination II_{low} of low light intensity I_2 bearing in mind that I_1 is to be fixed around 0.1 ein.m^2.s^{-1}. We assume that the condition $I_2 \ll \min(k_{DA}/\sigma_{22}, k_C/\sigma_{12}, k_{TA}/\sigma_{12}^T)$ is met, so that $k_1' \ll k_C$, $k_1'' \ll k_{TA}$, and $k_2' \ll k_{DA}$. Table 2.1 is used to evaluate the interval of I_2 in which the condition is fulfilled. We eliminate the fast species B, D, and T and obtain the two-state mechanism given in Fig. 2.6**e**. According to Eq. (2.86), the fluorescence intensity behaves like A according to a monoexponential increase of characteristic time

$$\tau_1 = \frac{1}{k_1' + k_2' + k_{CA}} \tag{2.91}$$

Illumination II_{high}

Finally we consider an illumination II_{high} of high light intensity I_2 and $I_1 \sim 0.1$ ein.m^2.s^{-1}. We suppose that the intensity I_2 obeys $I_2 \gg \max(k_{DA}/(\sigma_{12} + \sigma_{12}^T, k_C/\sigma_{22})$, so that $k_{CA} +$

$k_{DA} \ll k_1' + k_1''$ and $k_C \ll k_2'$. Table 2.1 is used to estimate the interval of I_2 in which the condition is fulfilled. The fast species A and C are eliminated and we obtain the four-state mechanism given in Fig. 2.6**f**. The fluorescence intensity is given in Eq. (2.85). The dynamics is described by three independent variables. The method described in section 2.1 can be used to obtain the analytical expressions of the concentrations and the fluorescence intensity. A 3×3 matrix has to be diagonalized and Cardano's method used to obtain the three characteristic times. We introduce a condition of comparison between k_C and k_{DA} in addition to the orders of magnitude given in Tab. 2.1 in order to more easily interpret the results. At the leading order of the expansion in $\max(k_{DA}/k_C, k_1'/k_C, k_1''/k_C, k_{TA}/k_C)$, we find the characteristic times

$$\tau_1 \simeq \frac{1}{k_C} \tag{2.92}$$

$$\tau_2 \simeq \frac{2}{(k_{DA} + k_1' + k_1'' + k_{TA}) + \sqrt{\Delta}} \tag{2.93}$$

$$\tau_3 \simeq \frac{2}{(k_{DA} + k_1' + k_1'' + k_{TA}) - \sqrt{\Delta}} \tag{2.94}$$

with $\Delta = (k_{DA} + k_1' + k_1'' + k_{TA})^2 - 4\,(k_{DA}\,(k_1'' + k_{TA}) + k_1' k_{TA})$. Similarly at the leading order of the expansion in $\max(k_C/k_{DA}, k_1'/k_{DA}, k_1''/k_{DA}, k_{TA}/k_{DA})$ we find

$$\tau_1 \simeq \frac{1}{k_{DA}} \tag{2.95}$$

$$\tau_2 \simeq \frac{1}{k_C} \tag{2.96}$$

$$\tau_3 \simeq \frac{1}{k_1' + k_1'' + k_{TA}} \tag{2.97}$$

The characteristic time τ_1 is smaller than τ_2 and τ_3. Consequently fluorescence evolution is governed at short times by τ_1, then by τ_2, and eventually by τ_3. Starting from the four-state mechanism given in Fig. 2.6**f**, we look for analytical solutions of the concentrations in the form of the sum of three exponential terms. For the initial condition $C = C_{\text{tot}}$, we find that the amplitude associated with τ_1 is negative and the amplitudes associated with τ_2 and τ_3 are positive. Consequently fluorescence first increases and then decreases. Interestingly increasing the I_1 intensity increases the validity domain of the reduced mechanism.

2.3.4 Non-redundancy of the characteristic times acquired under the four different illuminations

Depending on the value of the light intensities, the reaction model of the RSFPs is reducible into various effective mechanisms. The preceding theoretical analysis proposes to probe the kinetics of RSFPs using four illumination regimes which grant access to four different dynamics. In the case of illumination $\mathrm{I}_{\mathrm{low}}$, the characteristic time depends on light intensity I_1 and in the case of illumination $\mathrm{II}_{\mathrm{low}}$, the characteristic time depends on both light intensities I_1 and I_2 which ensures the non redundancy of the two characteristic times at low intensities. At high light intensities, the characteristic times are imposed by thermal steps that differ depending on cases $\mathrm{I}_{\mathrm{high}}$ and $\mathrm{II}_{\mathrm{high}}$ as proven by the two different reduced mechanisms. Hence the four illumination regimes provide at least four non redundant kinetic information on RSFPs.

2.4 Data processing of multiexponential evolution

The preceding section suggests the interest in extracting characteristic times from RSFP fluorescence at different light intensities. The reduction of RSFP mechanism has revealed that fluorescence is adequately described by a multiexponential signal

$$f(t) = \sum_{i=1}^{n} A_i \exp\left(-\lambda_i t\right) \tag{2.98}$$

Analysis of multiexponential signals is a recurring and challenging concern in literature.[111] The problem consists in extracting the number n of components, their characteristic times $1/\lambda_i$ and their amplitudes A_i. The inverse Laplace transform

$$g(\lambda) = \frac{1}{2\pi} \int_{c-i\infty}^{c+i\infty} f(t) \exp\left(\lambda t\right) dt \tag{2.99}$$

gives the distribution function $g(\lambda)$ of the characteristic times when the analytical expression of the function $f(t)$ is known which is not the case when dealing with experimental data.[111] Moreover Eq. (2.99) necessitates integration in the complex plane whereas the values of the function $f(t)$ are only known on the real axis. The distribution function $g(\lambda)$ can be found solving the Laplace integral equation

$$f(t) = \int_{0}^{\infty} g(\lambda) \exp\left(-\lambda t\right) d\lambda \tag{2.100}$$

This equation is a Fredholm integral of the first kind, which is known to be ill posed. Indeed, the distribution function $g(\lambda)$ obtained from the solution of Eq. (2.100) may

not be unique, may not exist, and may not continuously depend on the data. This is a fundamental limitation of exponential analysis. There is also a limit to the maximum resolution capacity of exponential analysis which highly depends on the signal-to-noise ratio. The choice of the number of data points, the time step, and the acquisition time have a major impact on the resolution and the accuracy of a multiexponential analysis.

Among the numerous methods that have been developed in the purpose of multiexponential analysis,[111] we more specifically consider the classical nonlinear least-squares analysis and the less known correlation method.

2.4.1 Curve fitting using nonlinear least-squares analysis

$f_{\exp}(t_i)$, $i = 1, .., N$, denotes the N experimental data points. We assume that the function

$$f(t) = \sum_{i=1}^{n} A_i \exp\left(-\frac{t}{\tau_i}\right) + A_0 \tag{2.101}$$

parametrized by the amplitudes A_i, $i = 0, .., n$, and the characteristic times τ_i, $i = 1, .., n$, describes the data points. The procedure consists in minimizing the function

$$\chi^2 = \sum_{j=1}^{N} \left(f_{\exp}(t_j) - f(t_j)\right)^2 \tag{2.102}$$

by varying the $2n + 1$ parameters. Initial values and increament of the parameters are chosen. The search for the best fit is made by iteration. The existing algorithms differ by the methods of exploration of the parameter space. We used the Levenberg-Marquart algorithm in section 2.5.[112,113]

The initial guess of the parameter values have a big impact on the convergence of the minimization of the function χ. If the estimate is poor the iteration may converge to a local minimum. The robustness of the procedure decreases when the complexity n of the assumed model $f(t)$ increases.

2.4.2 Correlation method - Spectrum of characteristic times

The experimental data points are correlated with a weighting function $W_l(t)$ of parameter l, defined as the decimal logarithm of a characteristic time, over an interval of time increasing with l.[111,114–120]

$$S(l) = \frac{\int_0^{\beta 10^l} \left(f_{\exp}(t) - \langle f_{\exp}(t)\rangle\right)\left(W_l(t) - \langle W_l(t)\rangle\right) dt}{\int_0^{\beta 10^l} \left(e^{-\frac{t}{10^l}} - \langle e^{-\frac{t}{10^l}}\rangle\right)\left(W_l(t) - \langle W_l(t)\rangle\right) dt} \tag{2.103}$$

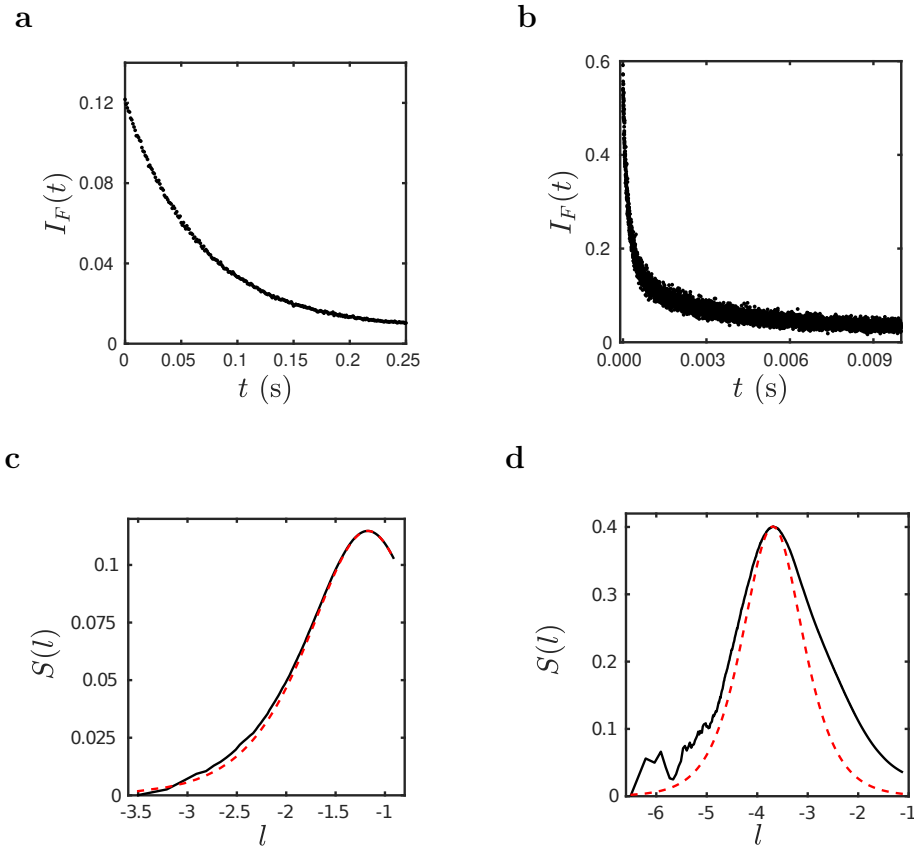

Figure 2.7: Experimental fluorescence evolution $I_F(t)$ (**a**,**b**) and spectra $S(l)$ of the relaxation times (**c**,**d**) of a 20 μM solution of the RSFP Dronpa-2 in pH 7.4 PBS (50 mM sodium phosphate, 150 mM NaCl) at T = 298 K under illumination I at the wavelengths $\lambda_1 = 480$ nm. The solid lines of the spectra are obtained by computing $S(l)$ for the experimental fluorescence evolution $I_F(t)$. The dashed red lines are obtained when replacing $I_F(t)$ by a monoexponential function with the relaxation time associated with the absolute extremum of the spectrum built from the experimental fluorescence evolution. **a**,**c**: Illumination condition $\mathrm{I_{low}}$, $I_1 = 0.23$ Ein.m^{-2}.s^{-1}. **b**,**d**: Illumination condition $\mathrm{I_{high}}$, $I_1 = 128.8$ Ein.m^{-2}.s^{-1}.

The average $\langle\rangle$ represents the integration between 0 and $\beta 10^l$. The value of the parameter β depends on the function $W_l(t)$. The denominator is a normalization condition. Using Eq. (2.103), we obtain a spectrum $S(l)$ of characteristic times. As in lock-in amplification in which the data are correlated to as sine-wave, the spectrum of characteristic times present a better signal-to-noise ratio than the experimental data $f_{\mathrm{exp}}(t)$.[119–121] Due to the construction of the spectrum, the signal-to-noise ratio increases along the l-axis. Figures 2.7 and 2.8 display experimental data of fluorescence evolution of RSFPs submitted to illuminations I and II and the corresponding spectra.

When the fluorescence intensity is a monoexponential function associated with a re-

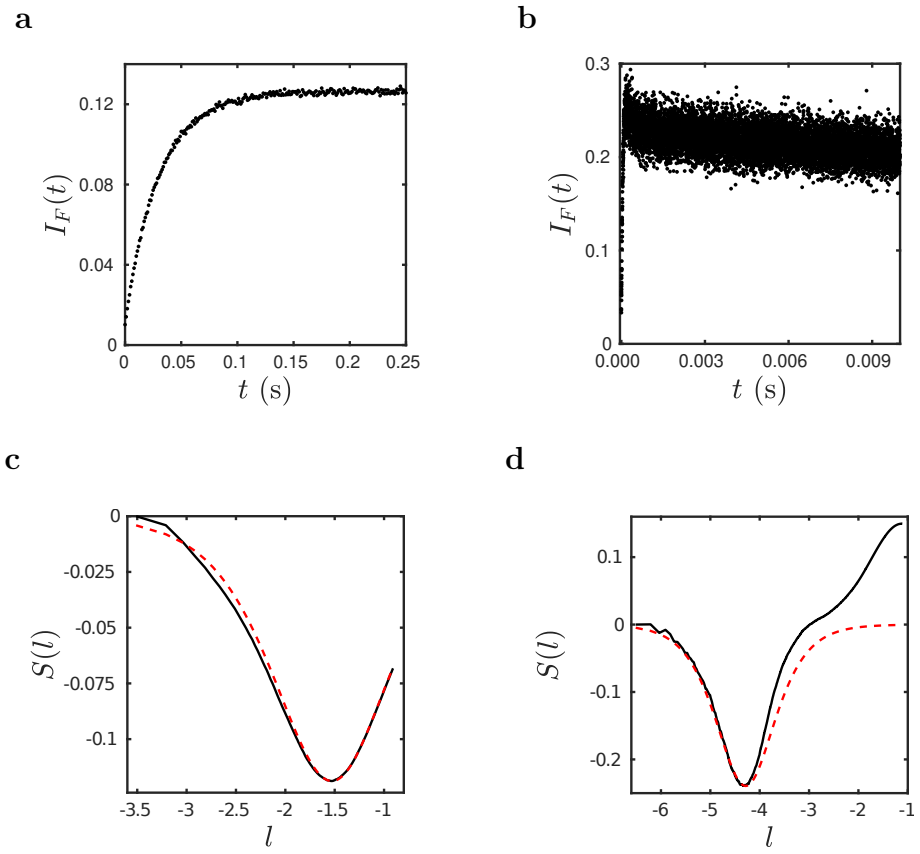

Figure 2.8: Experimental fluorescence evolution $I_F(t)$ (**a**,**b**) and spectra $S(l)$ of the relaxation times (**c**,**d**) of a 20 μM solution of the RSFP Dronpa-2 in pH 7.4 PBS (50 mM sodium phosphate, 150 mM NaCl) at T = 298 K under illumination II at the wavelengths $\lambda_1 = 480$ nm and $\lambda_2 = 405$ nm. The solid lines of the spectra are obtained by computing $S(l)$ for the experimental fluorescence evolution $I_F(t)$. The dashed red lines are obtained when replacing $I_F(t)$ by a monoexponential function with the relaxation time associated with the absolute extremum of the spectrum built from the experimental fluorescence evolution. **a**,**c**: Illumination condition II_{low}, $I_1 = 0.15$ Ein.m^{-2}.s^{-1} and $I_2 = 0.10$ Ein.m^{-2}.s^{-1}. **b**,**d**: Illumination condition II_{high}, $I_1 = 0.15$ Ein.m^{-2}.s^{-1} and $I_2 = 106$ Ein.m^{-2}.s^{-1}.

laxation time τ_1

$$f_{\exp}(t) = A_1 \exp\left(-t/\tau_1\right) + A_0 \tag{2.104}$$

the upper bound of the integral, β, is chosen to ensure that the spectrum $S(l)$ possesses an extremum for $l_1 = \log(\tau_1)$. Due to the chosen normalization, the amplitude of the extremum $S(l_1)$ is equal to the preexponential factor A_1. The sign of the preexponential factor determines the nature of the extremum, a positive factor leading to a maximum and a negative factor leading to a minimum of $S(l)$. When the experimental data points $f_{\exp}$ are not correctly described by a monoexponential function but behaves as a sum of n exponential terms, the spectrum of the relaxation times has one to n extrema.

The spectra of relaxation times can be computed for different choices of the weighing function $W_l(t)$. In the case of a multiexponential function as described in Eq. (2.101), the choice $W_l(t) = e^{-\frac{t}{10^l}}$ is intuitive. The correlation with an exponential is known to produce spectra with broad peaks i.e. a moderate time resolution but little sensitivity to the noise of the experimental data.[119,120] For the exponential correlator, we find $\beta = 3.25$.

The analytical expression of the spectrum $S(l)$ for the monoexponential fluorescence evolution $I_F(t)$ given in Eq. (2.104) is given by

$$S(l) = A_1 \frac{\exp\left(-3.25 \times 10^{l-l_1}\right)\left(1.38 + 1.20 \times 10^{l-l_1}\right) - 1.38 + 3.28 \times 10^{l-l_1}}{10^{l-l_1}\left(1 + 10^{l-l_1}\right)} \tag{2.105}$$

The peak of the spectrum is symmetrical and the full width at half maximum equals 1.4. The logarithm of the relaxation time l has to differ by more than a factor a 1.5 from l_1 for the corresponding spectrum value $S(l)$ to be smaller than 10% of the amplitude $S(l_1)$ of the extremum.

The generalization to a linear combination of exponential functions is straightforward. In the case where the experimental data points $f_{\exp}$ is a sum of two exponential terms with identical prefactors $A_1 = A_2$ and different characteristic times $10^{l_1} < 10^{l_2}$, the spectrum has either one or two extrema. The spectrum shows one or two maxima if the prefactors are positive and one or two minima if the prefactors are negative. If $l_2 - l_1 < 1.1$, the spectrum has a single extremum for l between l_1 and l_2. In this case, the amplitude of the extremum is between $1.3p$ and $2p$. On the contrary, if $l_2 - l_1 > 1.1$, the spectrum has two extrema. If $l_2 - l_1 > 1.7$, the abscissa of the extrema differ from l_1 and l_2 by less than 5%. Moreover, the values of the spectrum associated with the extrema are less than 7% larger than the prefactor $A_1 = A_2$.

For an experimental signal $f_{\exp}$ equal to the difference of two exponential terms with identical prefactors and characteristic times $10^{l_1} < 10^{l_2}$, the spectrum has always one maximum and one minimum. If $l_2 - l_1 > 1.7$, then the abscissa of the extrema differ from l_1 and l_2 by less than 4%. In addition, the amplitudes of the extrema are less than 6% smaller than the prefactor.

In the general case of non identical prefactors, the position of the absolute extremum is close to the characteristic time of the exponential associated with the largest prefactor.

2.4.3 Extraction of a single characteristic time

Regardless of the chosen method, the analysis of a sum of exponential functions is all the more difficult as the characteristic times are close. A balance has to be found between the complexity and the robustness of the solution. Characterizing the evolution of the function $f_{\exp}(t)$ by only one characteristic time favors the robustness of the analysis. This makes sense when the $f_{\exp}(t)$ function is monotonous, i.e. when all amplitudes A_i have the same sign. In this case the spectrum of characteristic times exhibits an absolute extremum, a maximum if f is decreasing and a minimum if $f_{\exp}(t)$ is increasing. The coordinates of this absolute extremum lead to the characteristic time $\tau_1 = 10^{l_1}$ and the amplitude A_1. The curve fitting method can also be used with only 3 parameters, two amplitudes A_0 and A_1 and a characteristic time τ_1.

2.5 Manuscript: Extra kinetic dimensions for fluorescence imaging (LIGHTNING)

Equipped with four illumination regimes revealing the kinetics of reversibly photoswitchable fluorescent proteins (RSFPs) and two data processing methods providing robust characteristic times, we build a four-dimensional kinetic fingerprint of RSFPs. The principle of the discrimination protocol and its implementation using RSFPs are found below in the form of a manuscript in progress. Supporting information can be found in appendix A. The proof of concept has been obtained for non-biological samples. Experimental validation on bacteria is challenging and still in progress. Promising images have already been obtained.

Extra kinetic dimensions for fluorescence imaging

Raja Chouket, Agnès Pellissier-Tanon, *et al*.

Abstract

Due to its sensitivity and versatility, fluorescence is widely used to image labeled biomolecules or cells. However fluorescence imaging is currently limited by label discrimination. Even when their signatures in spectral and lifetime domains are combined, only a few fluorophores can be distinguished. We overcome this limitation by introducing extra kinetic dimensions through multicolor illuminations of reversibly photoswitchable fluorophores (RSFs) at different light intensities. In this expanded space, each RSF is characterized by a unique signature that depends on its intrinsic photochemical and thermal properties. We managed to discriminate and recognize 20 green reversibly photoswitchable fluorescent proteins with similar fluorescence spectra. This strategy considerably expands the multiplexing capabilities of fluorescence imaging.

Introduction

There is a growing demand of quantitative biology to simultaneously image tens of chemical species in a cell or nearby cells within a tissue.[1] Hence powerful genetic engineering strategies have been introduced for labeling biomolecules or cells[2, 3, 4] and the level of multiplexed observation is presently limited by label discrimination.[5] In fluorescence imaging which is valued for its high sensitivity and widespread equipment, 3–4 labels can be currently discriminated. Further increasing this number requires unmixing in the spectral or time domain but at significant cost in terms of photon budget and computation time.[6, 7] In this report, we introduce a simple alternative approach to boost the number of discriminatable fluorophores.

Fluorescence emission reports on a photocycle and the simplest absorption/fluorescence emission photocycle is usually exploited to target a label. It provides two spectral – the excitation and emission wavelengths – and one temporal – the fluorescence lifetime – discriminative dimensions (see Fig.1a). Yet, the broad half width of the absorption/emission bands (50–100 nm) and the narrow lifetime dispersion (in the ns range) of the bright fluorophores intrinsically limit the discriminative power of protocols based on a simple photocycle. Rich photocycles including several

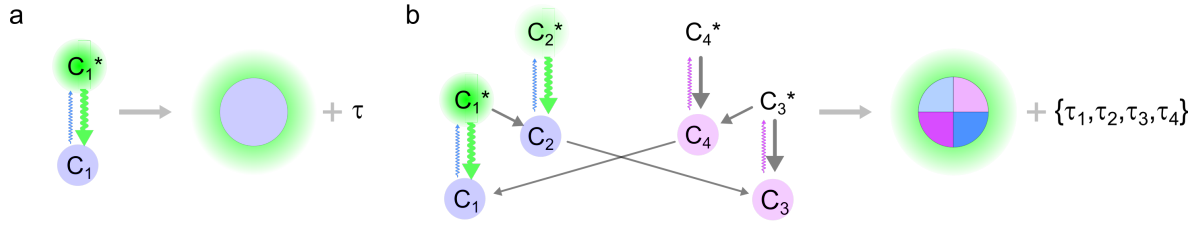

Figure 1: *LIGHTNING opens new kinetic dimensions for multiplexed fluorescence imaging*. **a**: The standard absorption/emission photocycle provides three discriminative dimensions to target a label: its absorption and emission wavelengths, and its fluorescence lifetime; **b**: LIGHTNING exploits the richer photocycle of RSFs, which contains several states photoactivatable at distinct wavelengths. Its interrogation with a multicolored sequence of photoactivating illuminations at various light intensities generates multiple time fluorescence responses and as many characteristic times τ_i. With green RSFPs, we used three wavelengths (488 nm (blue) and 405 nm (purple) at two different light intensities for photocycle activation and 525 nm (green) for fluorescence readout) to generate a kinetic fingerprint of $n = 4$ non-redundant characteristic times, which yields four dimensions for RSFP discrimination.

photochemical and thermal steps are found in reversibly photoswitchable fluorophores (RSFs).[8] Endowed with multiple photoactivatable and bright states and a wide palette of relaxation times (from μs to s), they contain much more discriminative information, which has only been partially explored in multiplexed imaging.[9, 10, 11] In this report, we introduce Light-tunable tIme-gated readinG-out of pHotocycles for mulTiplexed fluorescence ImagiNG (LIGHTNING) which uncovers unprecedented dimensions for RSF discrimination. Hence LIGHTNING considerably increases the number of fluorophores which can be distinguished without any deconvolution nor subtraction schemes.

The LIGHTNING concept

LIGHTNING exploits RSFs, whose photocycle consists of a network of states engaged in first-order light- and thermally-driven reactions (see Fig.1b). Upon light activation of each photoactivatable state, the concentrations of the RSF states – and consequently the RSF fluorescence signal – evolve as a linear combination of exponential terms (see section A4 in SI).[12] The amplitudes and relaxation times of these exponential terms depend on the multiple rate constants of the photocycle reactions. The light intensity affects the rate constants of the photochemical steps but not those of the thermal steps. We exploit this crucial property to change the rate-limiting steps of the photocycle, which enables us to sequentially extract its rich kinetic information.

Since multiexponential data processing is poorly robust,[13] we chose to parameterize each time evolution of the RSF fluorescence signal by a single characteristic time regardless of the

photocycle complexity. Applying n multicolor illuminations at different light intensities yields a set of n non-redundant characteristic times $\{\tau_i\}$, the reference LIGHTNING kinetic fingerprint of each considered RSF (see Fig.1b). Two RSFs are distinguished if the Euclidean distance between their positions in the n-dimensional space of characteristic times $\{\tau_i\}$ is greater than the resolution limit governed by the experimental uncertainty on the characteristic times. Conversely, when the distance between the kinetic fingerprints of a sample and a referenced RSF is smaller than the resolution limit, the presence of this RSF in the sample is ascertained. Therefore, the expansion into new kinetic dimensions relying on intrinsic differences of photochemical and thermal properties enables LIGHTNING to discriminate RSFs without any demanding data processing.

LIGHTNING in action

In order to evaluate the LIGHTNING framework, we used reversibly photoswitchable fluorescent proteins (RSFPs)[14], popularized by super-resolution microscopy.[15, 16, 17, 18] With the aim of exploring LIGHTNING discrimination capacity, we engineered and selected a serials of Skylan[19] mutants differing by the α-amino acid at position 62, 157, 173 respectively, which are endowed with high brightness, high on-off contrast, and various photoswitching kinetics. Completed by members from the series of Dronpa[20] and rsEGFP,[21] they provided 22 spectrally similar green RSFPs (**1**–**22**; see §A1.1.2, Fig. A6a,b, and Tab.A1 in SI). We chose two wavelengths – $\lambda_1 = 488$ nm and $\lambda_2 = 405$ nm – to drive the RSFP photocycle and reversibly photoactivate states of distinct brightnesses. [22, 23, 24, 25, 26] Excitation at λ_1 generates a significant fluorescence signal. An original setup was used to automatically record and analyze the fluorescence response of an RSFP solution exposed to sequences of homogeneous illuminations at λ_1 and/or λ_2 in a few minutes (see §A1.4 in SI).

We first measured the rate constant associated with the thermal relaxation of the photoswitched RSFPs (see Fig. A7–A9; see also Tab. A3 in SI). In addition, for both wavelengths and a long acquisition time, we extracted two light-driven characteristic times from fluorescence evolution, one being at least three orders of magnitude smaller than the other (see Fig.A4 and Fig.A10–A13; see also Tab.A2 in SI). They are in line with fast reversible photoswitching and slow long-term decay of fluorescence.[27, 28] Thus, we identified a time window common to the 22 RSFPs over which illumination drives reversible fluorescence photoswitching without any pronounced detrimental interference of thermal relaxation and long term decay.

Then we submitted RSFP solutions to 1 s-sequences of illuminations for tens of light intensities covering 5 orders of magnitude up to 10^4 W.cm^{-2} (see Fig.A4 and Fig. A14–A35a,b in SI).

Illuminations I and II are defined by constant light of intensity I_1 at λ_1 and constant lights of intensities I_1 and I_2 at λ_1 and λ_2, respectively. Apart from the "positive" switchers **4** and **5**, all studied RSFPs are "negative" switchers[29] for which illumination I drives a fluorescence decay and illumination II promotes a rise of the fluorescence signal (see Fig.2a). The detailed interpretation of the observed fluorescence evolutions will be the subject of another report. We introduced a kinetic filter by adopting a time window for signal acquisition (see §A6.1 in SI) and focused on the part of the fluorescence time evolution exhibiting the largest amplitude (see Fig.2a). Then we robustly retrieved a single characteristic time by (i) correlating the fluorescence evolution with an exponential function and retaining the absolute extremum of the resulting spectrum of relaxation times (see section A5 in SI) or (ii) reducing the fluorescence evolution to a monoexponential function and retaining its relaxation time (see section A6 in SI). Hence we extracted a single characteristic time τ^{I} (τ^{II}, resp.) at each light intensity I_1 (I_2, resp.) of illumination I (II, resp.).

All investigated RSFPs share a qualitatively similar light intensity dependence of the characteristic times. For sufficiently low intensities, $1/\tau^{\mathrm{I}}$ ($1/\tau^{\mathrm{II}}$, resp.) linearly increases with I_1 (I_2, resp.) at λ_1 (λ_2, resp.) and tends to saturate for higher intensities (see Fig.2b and Fig. A14–A35c–f in SI). At the lowest intensities, the photochemical steps limit the rate of the RSFP photocycle and fluorescence evolution is monoexponential. The photoswitching cross sections Σ_1 and Σ_2 are deduced from the slopes of $1/\tau^{\mathrm{I}}$ versus I_1 and $1/\tau^{\mathrm{II}}$ versus I_2, respectively (see section A7 in SI). At the highest intensities, thermal steps intervene in the photocycle rate and τ^{I} and τ^{II} exhibit no significant (or a weaker) dependence on light intensities. The low- and high-intensity regimes are separated by indicative threshold light intensities I_1^c (in the range 40–2 10^3 W.cm^{-2}; 2–80 Ein.m^{-2}.s^{-1}) at λ_1 and I_2^c (in the range 8–3 10^2 W.cm^{-2}; 0.3–10 Ein.m^{-2}.s^{-1}) at λ_2 (see Tab. A3 in SI). For each RSFP, the low intensity regimes $\mathrm{I_{low}}$ and $\mathrm{II_{low}}$ provide two characteristic times $\tau^{\mathrm{I}}_{\mathrm{low}}$ and $\tau^{\mathrm{II}}_{\mathrm{low}}$, respectively, which are independent of the two characteristic times $\tau^{\mathrm{I}}_{\mathrm{high}}$ and $\tau^{\mathrm{II}}_{\mathrm{high}}$ obtained in the regimes of high intensity, $\mathrm{I_{high}}$ and $\mathrm{II_{high}}$, respectively. The $\{\tau^{\mathrm{I}}_{\mathrm{low}}, \tau^{\mathrm{II}}_{\mathrm{low}}, \tau^{\mathrm{I}}_{\mathrm{high}}, \tau^{\mathrm{II}}_{\mathrm{high}}\}$ set defines the LIGHTNING kinetic fingerprint of an RSFP under the four illuminations $\{\mathrm{I_{low}}, \mathrm{II_{low}}, \mathrm{I_{high}}, \mathrm{II_{high}}\}$ (see Fig.2c).

The LIGHTNING discriminatory power

LIGHTNING discrimination involves the kinetic fingerprint of RSFPs in the 4D space of their characteristic times without adverse effects of their similar photoactivating and fluorescence wavelengths (see Fig.3a). Optimal initial conditions before the next illumination are obtained for the ordered sequence $\{\mathrm{I_{low}}, \mathrm{II_{low}}, \mathrm{I_{high}}, \mathrm{II_{high}}\}$ (see Fig.2a). Acquisition time is minimized by choosing

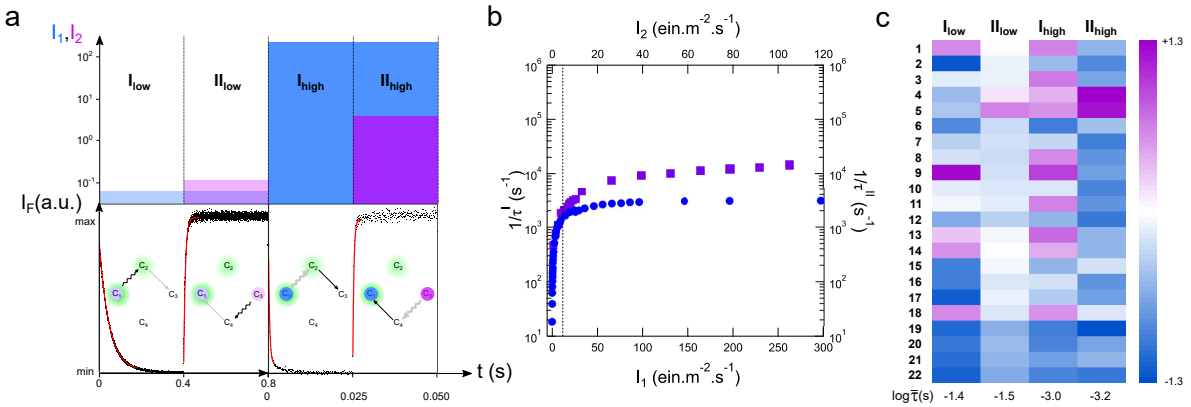

Figure 2: *LIGHTNING in action*. **a**: A sequence of four illuminations $\{\mathrm{I_{low}}, \mathrm{II_{low}}, \mathrm{I_{high}}, \mathrm{II_{high}}\}$ involving lights at the wavelengths $\lambda_1 = 488$ nm (blue) and $\lambda_2 = 405$ nm (purple) at intensities I_1 and I_2 in Ein.m^{-2}.s^{-1}, respectively, yields four fluorescence time series $I_F(t)$ (each scaled by the difference between the maximal and minimal values). RSFP kinetics is governed by distinct photochemical (zigzag arrow) or thermal (standard arrow) rate-limiting steps (in black). The faster the step, the thicker the arrow. C_1 is brighter than C_2 whereas C_3 and C_4 are dark; **b**: Inverse of the characteristic time obtained for illuminations I (blue) (II (purple), resp.) versus light intensity I_1 (I_2, resp.). The vertical dotted line separates two regimes, the low intensity regime $\mathrm{I_{low}}$ ($\mathrm{II_{low}}$, resp.) for which the rate-limiting step is photochemical and the high intensity regime $\mathrm{I_{high}}$ ($\mathrm{II_{high}}$, resp.) for which the rate-limiting step is thermal. The set of the four characteristic times extracted from the four illuminations provides the kinetic fingerprint $\{\tau^{\mathrm{I}}_{\mathrm{low}}, \tau^{\mathrm{II}}_{\mathrm{low}}, \tau^{\mathrm{I}}_{\mathrm{high}}, \tau^{\mathrm{II}}_{\mathrm{high}}\}$ of each RSFP. **c**: Heatmap displaying the deviations from the mean value $\overline{\tau}$ of the characteristic time obtained for each illumination for the 22 investigated RSFPs in decimal logarithmic scale. RSFP = Dronpa-2 (**2**) in **a** and **b**.

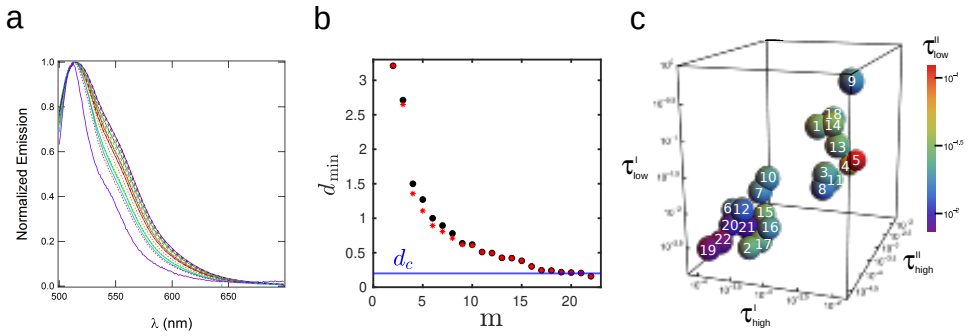

Figure 3: *The LIGHTNING discriminatory power.* **a**: Similar normalized emission spectra of solutions of the RSFPs **1**–**22** illuminated at $\lambda_1 = 488$ nm; **b** Minimum distance between pairs for optimized subsets of RSFPs versus cardinal m of the subsets. The threshold d_c is deduced from the experimental uncertainty on the determination of the characteristic times. The condition $d_{\min} \geq d_c$ fixes the maximum number of discriminatable RSFPs (20 among the 22 investigated RSFPs **1**–**22**); **c**: Representation of the 22 RSFPs in the 4D space $\{\tau^{\mathrm{I}}_{\mathrm{low}}, \tau^{\mathrm{II}}_{\mathrm{low}}, \tau^{\mathrm{I}}_{\mathrm{high}}, \tau^{\mathrm{II}}_{\mathrm{high}}\}$. The volume associated with each RSFP has been fixed by the resolution limit.

the highest possible light intensity adapted to all RSFPs in each regime. Fig.2c and Tab. A4 sum up the resulting $\{\tau^{\mathrm{I}}_{\mathrm{low}}, \tau^{\mathrm{II}}_{\mathrm{low}}, \tau^{\mathrm{I}}_{\mathrm{high}}, \tau^{\mathrm{II}}_{\mathrm{high}}\}$ sets for the 22 RSFPs. Optimized subsets of the most distant RSFPs are determined using the minimum distance $d_{\min}$ between pairs for all subsets of m RSFPs. For each cardinal m, the optimized subset associated with the largest value of $d_{\min}$ is selected (see Fig.3b and §A1.7.1 in SI). In order to evaluate the resolution limit in 15–20 μM solutions of RSFPs, we measured 500 times the kinetic fingerprint of two representative RSFPs (see Figs. A45 and A46a–d; see also Tabs. A7 and A8 in SI). We evaluated that the minimum distance between two discriminatable RSFPs is $d_c = 0.2$ (see §A8.3). Under such experimental conditions LIGHTNING unambiguously distinguishes and identifies 20 among the 22 investigated green RSFPs, as evidenced by the spreading and the lack of overlap of the kinetic fingerprints of 20 RSFPs in the discriminating 4D space (see Fig.3b,c).

The LIGHTNING scope

We consider the scope of LIGHTNING for multiplexed fluorescence imaging. With RSFPs, wide-field LIGHTNING will be relevant for imaging many biological phenomena in real time (acquisition and processing in less than 1 s) with a good signal-to-noise ratio (slight reduction of acquired photons with respect to standard fluorescence imaging; see §A9.1.3). With an optimized acquisition sequence, LIGHTNING will be relevant as well in light scanning (e.g. confocal or light-sheet) microscopies, which are favorably endowed with a wide range of light intensities. Beyond RSFPs, LIGHTNING should be relevant to the multiple fluorophores engaged in photocycles involving

light- and thermally-driven reactions. This includes in particular regular fluorophores generating dark states upon light activation at one (e.g. in xanthens,[9] rhodamines,[30] or fluorescent proteins FPs[31]) or two (e.g. in FPs [32]) wavelengths, which could be discriminated in 2 or 4 dimensions, respectively. Hence, providing that further fluorescence photoswitching information is gathered, LIGHTNING is anticipated to distinguish several tens of fluorophores, which would be attractive for analyzing microbiomes, lineage, or cell connectivity, and for monitoring sensors or gene expression.

Acknowledgments

This work was supported by the ANR (France BioImaging - ANR-10-INBS-04, Morphoscope2 - ANR-11-EQPX-0029, HIGHLIGHT, and dISCern), the Fondation de la Recherche Médicale (FRM DEI201512440), and the Mission Interdisciplinarité du CNRS.

References

[1] R. Weissleder and M. Nahrendorf. Advancing biomedical imaging. *Proc. Natl. Acad. Sci. USA*, 112:14424–14428, 2015.

[2] J. Livet, T. A. Weissman, H. Kang, R. W. Draft, J. Lu, R. A. Bennis, J. R. Sanes, and J. W. Lichtman. Transgenic strategies for combinatorial expression of fluorescent proteins in the nervous system. *Nature*, 450:56–62, 2007.

[3] Maysam Mansouri, Itxaso Bellon-Echeverria, Aurélien Rizk, Zahra Ehsaei, Chiara Cianciolo Cosentino, Catarina S Silva, Ye Xie, Frederick M Boyce, M Wayne Davis, Stephan CF Neuhauss, et al. Highly efficient baculovirus-mediated multigene delivery in primary cells. *Nature Comm.*, 7:11529, 2016.

[4] Yin Cai, M Julius Hossain, Jean-Karim Hériché, Antonio Z Politi, Nike Walther, Birgit Koch, Malte Wachsmuth, Bianca Nijmeijer, Moritz Kueblbeck, Marina Martinic-Kavur, et al. Experimental and computational framework for a dynamic protein atlas of human cell division. *Nature*, 561(7723):411, 2018.

[5] Lu Wei, Zhixing Chen, Lixue Shi, Rong Long, Andrew V Anzalone, Luyuan Zhang, Fanghao Hu, Rafael Yuste, Virginia W Cornish, and Wei Min. Super-multiplex vibrational imaging. *Nature*, 544(7651):465, 2017.

[6] A. Valm, S. Cohen, W. Legant, J. Melunis, U. Hershberg, E. Wait, A. Cohen, M. Davidson, E. Betzig, and J. Lippincott-Schwartz. Applying systems-level spectral imaging and analysis to reveal the organelle interactome. *Nature*, 546:162–167, 2017.

[7] T. Niehörster, A. Löschberger, I. Gregor, B. Krämer, H.-J. Rahn, M. Patting, F. Koberling, J. Enderlein, and M. Sauer. Multi-target spectrally resolved ? multi-tar lifetime imaging microscopy. *Nat. Meth.*, 13:257–262, 2016.

[8] Tyler J. Chozinski, Lauren A. Gagnon, and Joshua C. Vaughan. Twinkle, twinkle little star: Photoswitchable fluorophores for super-resolution imaging. *FEBS Letters*, 588:3603–3612, 2014.

[9] C. I. Richards, J.-C. Hsiang, and R. M. Dickson. Synchronously amplified fluorescence image recovery (SAFIRe). *J. Phys. Chem. B*, 114:660–665, 2010.

[10] J. Widengren. Fluorescence-based transient state monitoring for biomolecular spectroscopy and imaging. *J. R. Soc. Interface*, 7:1135–1144, 2010.

[11] J. Quérard, R. Zhang, Z. Kelemen, M.-A. Plamont, X. Xie, R. Chouket, I. Roemgens, Y. Korepina, S. Albright, E. Ipendey, M. Volovitch, H. L. Sladitschek, P. Neveu, L. Gissot, A. Gautier, J.-D. Faure, V. Croquette, T. Le Saux, and L. Jullien. Resonant out-of-phase fluorescence microscopy and remote imaging overcome spectral limitations. *Nat. Comm.*, 8:969, 2017.

[12] M. Eigen and L. de Mayer. *Relaxation Methods in Techniques of Organic Chemistry*, volume VIII. Interscience Publishers, John Wiley and Sons, 2nd edition, 1963.

[13] A. A. Istratov and O. F. Vyvenko. Exponential analysis in physical phenomena. *Rev. Sci. Instrum.*, 70:1233–1257, 1999.

[14] X. X. Zhou and M. Z. Lin. Photoswitchable fluorescent proteins: ten years of colorful chemistry and exciting applications. *Curr. Opin. Chem. Biol.*, 17:682–690, 2013.

[15] M. Hofmann, C. Eggeling, S. Jakobs, and S. W. Hell. Breaking the diffraction barrier in fluorescence microscopy at low light intensities by using reversibly photoswitchable proteins. *Proc. Natl. Acad. Sci. U. S. A.*, 102:17565–17569, 2005.

[16] E. Betzig, G. H. Patterson, R. Sougrat, O. W. Lindwasser, S. Olenych, J. S. Bonifacino, M. W. Davidson, J. Lippincott-Schwartz, and H. F. Hess. Imaging intracellular fluorescent proteins at nanometer resolution. *Science*, 313:1642–1645, 2006.

[17] P. Dedecker, G. C. H. Mo, T. Dertinger, and J. Zhang. Widely accessible method for superresolution fluorescence imaging of living systems. *Proc. Natl. Acad. Sci. U. S. A.*, 109(27):10909–10914, 2012.

[18] E Hesper Rego, Lin Shao, John J Macklin, Lukman Winoto, Göran A Johansson, Nicholas Kamps-Hughes, Michael W Davidson, and Mats GL Gustafsson. Nonlinear structured-illumination microscopy with a photoswitchable protein reveals cellular structures at 50-nm resolution. *Proc. Nat. Acad. Sci.*, 109(3):E135–E143, 2012.

[19] Xi Zhang, Mingshu Zhang, Dong Li, Wenting He, Jianxin Peng, Eric Betzig, and Pingyong Xu. Highly photostable, reversibly photoswitchable fluorescent protein with high contrast ratio for live-cell superresolution microscopy. *Proc. Nat. Acad. Sci.*, 113:10364–10369, 2016.

[20] R. Ando, H. Mizuno, and A. Miyawaki. Regulated fast nucleocytoplasmic shuttling observed by reversible protein highlighting. *Science*, 306:1370–1373, 2004.

[21] T. Grotjohann, I. Testa, M. Reuss, T. Brakemann, C. Eggeling, S. W. Hell, and S. Jakobs. rsEGFP2 enables fast RESOLFT nanoscopy of living cells. *ELife*, 1, 2012.

[22] Aline Regis Faro, Philippe Carpentier, Gabriella Jonasson, Guillaume Pompidor, Delphine Arcizet, Isabelle Demachy, and Dominique Bourgeois. Low-temperature chromophore isomerization reveals the photoswitching mechanism of the fluorescent protein padron. *J. Am. Chem. Soc.*, 133(41):16362–16365, 2011.

[23] M. M. Warren, M. Kaucikas, A. Fitzpatrick, P. Champion, J. T. Sage, and J. J. van Thor. Ground-state proton transfer in the photoswitching reactions of the fluorescent protein dronpa. *Nat. Comm.*, 4:1461, 2013.

[24] D. Yadav, F. Lacombat, N. Dozova, F. Rappaport, P. Plaza, and A. Espagne. Real-time monitoring of chromophore isomerization and deprotonation during the photoactivation of the fluorescent protein dronpa. *J. Phys. Chem. B*, 119:2404–2414, 2015.

[25] N. Coquelle, M. Sliwa, J. Woodhouse, G. Schiro, V. Adam, A. Aquila, T. R. M. Barends, S. Boutet, M. Byrdin, S. Carbajo, E. De la Mora, R. B. Doak, M. Feliks, F. Fieschi, L. Foucar, V Guillon, M. Hilpert, M. S. Hunter, S. Jakobs, J. E. Koglin, G. Kovacsova, T. J. Lane, B. L, M. Liang, K. Nass, J. Ridard, J. S. Robinson, C. M. Roome, Ruckebusch C., M. Seaberg, M. Thepaut, M. Cammarata, I. Demachy, M. Field, R. L. Shoeman, D. Bourgeois, J. P. Colletier, I. Schlichting, and M. Weik. Chromophore twisting in the excited state of a photo-

switchable fluorescent protein captured by time-resolved serial femtosecond crystallography. *Nat. Chem.*, 10:31–37, 2017.

[26] Sergey P Laptenok, Agnieszka A Gil, Christopher R Hall, Andras Lukacs, James N Iuliano, Garth A Jones, Gregory M Greetham, Paul Donaldson, Atsushi Miyawaki, Peter J Tonge, et al. Infrared spectroscopy reveals multi-step multi-timescale photoactivation in the photoconvertible protein archetype dronpa. *Nat. Chem.*, 10(8):845, 2018.

[27] C. Duan, V. Adam, M. Byrdin, J. Ridard, S. Kieffer-Jaquinod, C. Morlot, D. Arcizet, I. Demachy, and D. Bourgeois. Structural evidence for a two-regime photobleaching mechanism in a reversibly switchable fluorescent protein. *J. Am. Chem. Soc.*, 135:15841–15850, 2013.

[28] Paula J Cranfill, Brittney R Sell, Michelle A Baird, John R Allen, Zeno Lavagnino, H Martijn De Gruiter, Gert-Jan Kremers, Michael W Davidson, Alessandro Ustione, and David W Piston. Quantitative assessment of fluorescent proteins. *Nat. Meth.*, 13(7):557, 2016.

[29] M. Andresen, A. C. Stiel, J. Follig, D. Wenzel, A. Schoenle, A. Egner, C. Eggeling, S. W. Hell, and S. Jakobs. Photoswitchable fluorescent proteins enable monochromatic multilabel imaging and dual color fluorescence nanoscopy. *Nat. Biotech.*, 26:1035–1040, 2008.

[30] T. Sandén, G. Persson, and J. Widengren. Transient state imaging for microenvironmental monitoring by laser scanning microscopy. *Anal. Chem.*, 80:9589–9596, 2008.

[31] Martin Byrdin, Chenxi Duan, Dominique Bourgeois, and Klaus Brettel. A long-lived triplet state is the entrance gateway to oxidative photochemistry in green fluorescent proteins. *J. Am. Chem. Soc.*, 140(8):2897–2905, 2018.

[32] A. E. Jablonski, J.-C. Hsiang, P. Bagchi, N. Hull, C. I. Richards, C. J. Fahrni, and R. M. Dickson. Signal discrimination between fluorescent proteins in live cells by long-wavelength optical modulation. *J. Phys. Chem. Lett.*, 3:3585–3591, 2012.

2.6 Comparison of the experiments with the predictions of the reduced mechanisms of RSFPs

Our goal is not to fully validate the seven-state mechanism of RSFPs proposed in section 2.3. We present some experimental observations, which support the relevance of the reduction of the seven-state mechanism in the investigated 1 μs–0.25 s time window.

The fluorescence evolution of the RSFPs under various illuminations has been recorded during 0.25 s with a sampling interval of 10^{-6} s at best. As a consequence, only reaction steps associated with characteristic times larger than 1 μs and smaller than 0.1 s can be observed. The fluorescence evolutions of all 20 studied negative RSFPs exhibit a qualitatively similar behavior as shown in Figs. S17-S38 of appendix A.

Figures 2.7 and 2.8 of section 2.4.2 display representative fluorescence evolutions and the associated spectra of characteristic times for the low and the high intensity regimes under illuminations I and II, respectively. We build a monoexponential function with a relaxation time equal to the time associated with the absolute extremum of the experimental spectrum. The spectrum associated with this monoexponential function is also shown and referred to as the monoexponential spectrum. In the case where the experimental spectrum has not the same width as the monoexponential spectrum, we conclude that the experimental evolution is at least biexponential. If the experimental spectrum is larger than the monoexponential spectrum, the amplitudes of the two exponential terms have the same sign. Otherwise, they have opposite signs.

In the case of illuminations I_{low} and II_{low}, the experimental spectra shown in Figs. 2.7**c** and 2.8**c** are very close to the built monoexponential spectrum which proves the monoexponential behavior of fluorescence evolution. Figures. S17-S38**e**,**f** of appendix A show that the inverse of the characteristic time is proportional to light intensity in the regimes of low intensities. The two-state mechanisms obtained in section 2.3.3 correctly predict a monoexponential behavior with characteristic times inversly proportional to light intensity: Kinetics is controlled by the photochemical steps in the low intensity regimes. Fluorescence experiments give access to the values of the isomerization cross sections for all investigated RSFPs. As displayed in Tab. S3 of appendix A, the results agree with the orders of magnitude of the values tabulated in the literature.

In the case of illuminations I_{high} and II_{high} the monoexponential approach illustrated in Figs. S17-S38**c**,**d** of appendix A leads to characteristic times nearly independent of light intensity in the range of high experimentally accessible intensities.

As displayed in Fig. 2.7**d**, the experimental spectrum obtained for illumination I_{high} is broader than the corresponding monoexponential spectrum which reveals that fluorescence evolution is at least biexponential with positive pre-exponential factors. The three-state mechanism obtained in section 2.3.3 satisfactorily accounts for a biexponential behavior. However the two characteristic times are sufficiently close and the pre-exponential factors sufficiently different for the spectrum to display a single maximum which justifies the monoexponential approach. As displayed in Tab. S3 of appendix A, the approximated determination of the characteristic time yields the order of magnitude of the characteristic time of the thermal step associated with protonation. Moreover the experimental results support the idea that the Trans-O^- state is fluorescent and the triplet state of the Cis-O^- species plays a non negligible role in kinetics. Indeed releasing either of these hypotheses would lead to a monoexponential evolution.

According to Fig. 2.8**b** fluorescence evolution under illumination II_{high} is not monotonous in the investigated time window. A rapid increase of large amplitude is followed by a slower decrease of smaller amplitude leading to the existence of a maximum. As showed in Fig. 2.8**d**, the spectrum of characteristic times admits a sink narrower than the built monoexponential spectrum revealing the presence of at least two exponential terms with pre-exponential factors of opposite signs in the fluorescence evolution. In addition the spectrum admits a second extremum close to the upper bound of the investigated time window which demonstrates the existence of a third characteristic time. Hence the four-state mechanism obtained in section 2.3.3 correctly accounts for the experimental results. The monoexponential data analysis only exploits the fluorescence increase until the maximum. The associated characteristic time given in Tab. S3 of appendix A is mainly controlled by the thermal proton exchange steps and consequently depends little on light intensity.

In conclusion of this chapter, the seven-state mechanism and the associated reduced schemes in the four illumination regimes provide a satisfying description of the experimental fluorescence evolution of illuminated RSFPs in the investigated time window.

Chapter 3

Kinetics-based discrimination protocols of reversibly photoswitchable fluorophores under modulated illumination

3.1 Chemical systems submitted to periodic forcing

A non-constant illumination can also be used to reveal the kinetics of reversibly photoswitchable fluorescent species. In this section we are interested in the case of periodic illumination. The equations of kinetics in the presence of oscillation of illumination and thus photochemical rate constants are non-autonomous equations, i.e. in which time explicitly appears. In the presence of periodic light excitation, the photochemical system belongs to the class of forced dynamical systems, which has been extensively studied in the case of electrical systems submitted to periodic voltage excitation.[79,80]

3.1.1 Fourier analysis

Specifically we consider sinevawe illuminations of period T. The photochemical rate constants of the general chemical system given in Eq. (2.1) are T-periodic functions of time whereas the thermal rate constants remain constant over time. The method of calculation of the concentrations evolution described in section 2.1 has to be adapted. In particular the Jacobian matrix is a T-periodic function of time. It should be remembered that a T-periodic function $f(t)$ can be written as a Fourier series according to

$$f(t) = a_0 + \sum_{k=1}^{\infty} a_k \cos(k\omega t) + b_k \sin(k\omega t) \tag{3.1}$$

where a_0, a_k, and b_k are the real amplitudes of the Fourier series and $\omega = 2\pi/T$ is the fundamental angular frequency. The function f is defined by the mean a_0, the amplitudes a_1 and b_1 at the fundamental frequency ω and the amplitudes a_k and b_k, $k > 1$, at the harmonic frequencies $k\omega$. Solutions of Eq. (2.5) are sought in a periodic form, using Fourier analysis. The concentration vector $\mathbf{C}$ is written as a Fourier series as given in Eq. (3.1). We cancel the terms in front of the sine and cosine at each order k. We obtain a linear system for the Fourier amplitudes of the concentration vector $\mathbf{C}$.

Since the Fourier series has an infinite number of terms the system has an infinite dimension and another approximation has to be made in order to obtain analytical expressions of the Fourier amplitudes. When the light intensity and thus the rate constants and the Jacobian matrix are modulated with a sufficiently small amplitude α, such an approximation can be an expansion in α. The expansion is all the more valid at large amplitude as we consider many orders in the Fourier series. Then the first Fourier amplitudes can be calculated and the concentration evaluated. Numerical computation can also be performed regardless of the value of the modulation amplitude.

The fluorescence evolution associated with a chemical system submitted to periodic forcing does not simply depends on the concentrations of the species. According to Eq. (2.16) the fluorescence intensity depends on the product of the illumination of intensity $I(t)$ and the concentration evolution $C_i(t)$, both being periodic and written as Fourier series.

3.1.2 Resonance, a tool for discrimination

Resonances can be found in dynamical systems submitted to periodic forcing. The phenomenon of resonance has been extended to stochastic systems.[122] At the molecular scale, chemical reactions are stochastic birth and death processes. Adding a periodic forcing to a chemical network fulfills the requirements of stochastic resonance.

Historically, stochastic resonance has been introduced in the case of a Brownian particle moving in a bistable potential submitted to periodic forcing.[122,123] The amplitude of oscillation of the particle position is optimized when the characteristic time associated with the noise-induced interwell transitions, the mean first-passage time, matches the half period of the forcing.[122,123] Similar resonances have been found in other physical situations. Three basic ingredients are usually observed in a system giving rise to resonance: (i) an energetic activation barrier, (ii) a weak coherent input, such as a periodic signal and (iii) a source of noise that is inherent to the system, or added to the coherent input.[122]

The output signal can be optimized when a given value of the parameters associated with the stochastic processes matches the fundamental frequency or the harmonic frequencies of the input signal.[122,124] In the case of the harmonics the output signal can also vanish for specific values of the parameters.[125,126]

Among the numerous applications of resonance, our group has already worked on optimizing effective diffusive coefficient using oscillations of an electric field in the case of a reaction inducing an important change of size for the chemical species.[127] Resonances are particularly well suited to discrimination purposes when using dynamic contrast. In a mixture, when the frequency of the light modulation matches the kinetics of the targeted reversibly photoswitchable fluorescent label, its contribution to a Fourier amplitude of the fluorescence intensity is maximized while the contribution of interfering species with different kinetics are small. Thus an image of the targeted reversibly photoswitchable fluorescent label can be obtained by tuning the frequency of the light modulation to match the kinetics of the targeted label.

Due to their nonlinearities, the Fourier amplitudes of the fluorescence intensity can also be optimized with respect to other parameters. In the case of a reversibly photoswitchable species, the mean light intensity set the value of the photochemical rate constants. In the case of a nonlinear chemical network, conserved quantities, such as a concentration, which intervene in the kinetics, may also be chosen by the experimentalist. Thus, the variations of the Fourier amplitudes have to be studied in the space of the control parameters, i.e. the parameters whose value can be set by the experimentalist. Our objective has been to find resonance conditions of a Fourier amplitude, i.e. relations between the control parameters and parameters that characterize kinetics as cross sections or rate constants, for which the Fourier amplitude is maximized.

3.1.3 Summary of Out-of-Phase Imaging after Optical Modulation (OPIOM and Speed OPIOM)

In order to highlight my contributions to the design of discrimination methods harnessing light modulation, I summarize the principles of OPIOM and Speed OPIOM developed by the group before my arrival.[62,63,83]

In the framework of OPIOM and Speed OPIOM the kinetics of reversibly photoswitchable fluorescent proteins (RSFPs) is described by a two-state model. This hypothesis is fully justified for low enough light intensities as shown in section 2.3. Using the notations

used in Fig. 2.6, we consider

$$\mathrm{A} \underset{k_2'+k_{CA}}{\overset{k_1'}{\rightleftharpoons}} \mathrm{C} \tag{3.2}$$

with k_1' and k_2' given in Eqs. (2.82,2.84). The two-state model contain a single step and a single dynamical variable due to the law of conservation of matter. Illumination involve sinevawe light intensity at the wavelength λ_i of mean value I_i^0, amplitude α_i, and angular frequency ω according to

$$I_i = I_i^0 \left(1 + \alpha_i \sin\left(\omega t\right)\right) \tag{3.3}$$

Two cases are considered depending on the number of wavelengths involved in the illumination.

In the OPIOM protocol, a modulated illumination at the single wavelength $\lambda_1 = 488$ nm is applied. The control parameters are the mean light intensity I_1^0 and the angular frequency ω. The quadrature Fourier amplitude of fluorescence oscillations at the fundamental frequency displays an optimum in the space (ω, I_1^0) when the control parameters fulfill the conditions

$$\omega = 2k_{CA} \tag{3.4}$$

$$I_1^0 = \frac{k_{CA}}{\sigma_{11}} \tag{3.5}$$

In the Speed OPIOM protocol, a modulated illumination in antiphase at both wavelengths $\lambda_1 = 488$ nm and $\lambda_2 = 405$ nm is considered. The thermal rate constant k_{CA} is neglected with respect to k_2'. The control parameters are the mean light intensities I_1^0 and I_2^0 and the angular frequency ω. The quadrature Fourier amplitude of fluorescence oscillations at the fundamental frequency displays an optimum in the space $(\omega/I_1^0, I_2^0/I_1^0)$ for the following resonance conditions

$$\omega = 2\sigma_{11} I_1^0 \tag{3.6}$$

$$\left(\sigma_{22} + \sigma_{12}\right) I_2^0 = \sigma_{11} I_1^0 \tag{3.7}$$

The Speed OPIOM protocol has been used to discriminate three out of eight RSFPs in biological samples.[63]

During my PhD, I extended the OPIOM discrimination protocol in two directions. First I investigated the presence of resonances in the harmonic Fourier amplitudes of

fluorescence oscillations in a two-state model close to the one given in Eq. (3.2). Then, I implemented the principle of the discrimination method on another chemical system, for which a thermal reaction, a complexation, is made photoactivatable in combination with a reversibly photoswitchable species.

3.2 Manuscript: Resonances of reversibly photoactivatable labels responding to high amplitude light modulation for selective analysis and imaging (HIGHLIGHT)

In OPIOM, the width of the resonance peak of the Fourier amplitude associated with the fundamental frequency sets the number of discriminatable RSFPs. In order to improve the performance of multiplexing, I investigated whether the Fourier amplitudes at harmonic frequencies exhibit resonances, preferably narrower. The theoretical predictions I obtained have been experimentally validated by our group. The results are presented in the form of a manuscript ready for submission. Detailed calculations are given in the supporting information found in appendix B.

Resonances of reversibly photoactivatable labels responding to high amplitude light modulation for selective analysis and imaging

A. Pellissier-Tanon,[a],* R. Chouket,[a],† R. Zhang,[a] A. Espagne,[a]
A. Lemarchand,[b],* V. Croquette,[c],* T. Le Saux,[a],* L. Jullien[a],*

[a] *PASTEUR, Département de chimie, École normale supérieure,*
PSL University, Sorbonne Université, CNRS, 24, rue Lhomond, 75005 Paris, France.
E-mail: Thomas.Lesaux@ens.psl.eu, Ludovic.Jullien@ens.psl.eu

[b] *Sorbonne Université, Centre National de la Recherche Scientifique (CNRS),*
Laboratoire de Physique Théorique de la Matière Condensée (LPTMC)
4, Place Jussieu, Case Courrier 121, 75252 Paris Cedex 05, France.
E-mail: Annie.Lemarchand@sorbonne-universite.fr

[c] *Laboratoire de Physique Statistique, Département de Physique and Département de Biologie,*
École normale supérieure, PSL Research University, F-75005 Paris, France.
E-mail: Vincent.Croquette@ens.fr

Abstract

Dynamic contrast exploits kinetics to discriminate a label against a spectrally interfering background. We submit reversibly photoactivatable labels to sine-wave light of large amplitude and show that Fourier amplitudes of fluorescence oscillations at harmonic frequencies exhibit resonances in the space of the control parameters. Specifically, we evidence that several resonant observables can be simultaneously retrieved from a single experiment by using phase-sensitive detection. This simple and general strategy is used to selectively image four spectrally similar reversibly photoswitchable fluorescent proteins.

*A. Pellissier-Tanon and R. Chouket contributed equally to this work.

1 Introduction

Analysis and imaging aim at identifying, quantifying, and localizing components in mixtures. Non-invasive strategies are adopted in systems which should remain in their native state (e.g. living cells).[1] A specific spectroscopic signature can be exploited to distinguish a target. However, complex media contain a large number of components often bearing similar atoms or functional groups, which hinders spectral target discrimination against the background. The thermodynamics (as used in titrations) or the kinetics of a reaction between the target and a specific reagent can also be harnessed for further discrimination of spectrally similar components. Kinetics is especially attractive since it relies on a high number of discriminative parameters: the rate constants.[1,2]

A kinetics-based strategy has been implemented in light-driven dynamic contrast, which leverages a reversibly photoactivatable label fused with the target. Light is used for both triggering the kinetics of the label photocycle and reading out.[3] Dynamic contrast has found significant developments in multiplexed fluorescence imaging by exploiting the relaxation of reversibly excited[4,5] or photoswitched labels.[6–10] These imaging protocols provide appreciable selectivity but they still demand too wide a span of relaxation times for discrimination, which is inconsistent with imaging the large number of labelled biomolecules needed in advanced bioimaging.[11,12]

Several of these imaging protocols (phase suppression in fluorescence lifetime imaging,[4,5,13] Out-of-Phase Imaging after Optical Modulation–OPIOM[9,10]) exploit phase-sensitive analysis of the response at the fundamental angular frequency of a reversibly photoactivatable label submitted to periodic illumination.[9,10] Selectivity for label discrimination can be improved by using the label response not only at the fundamental frequency but also at the harmonics. This approach has proven extremely fruitful in several fields such as chemical sensing,[14] detection of atoms,[15] subdiffraction-limited imaging,[16,17] electrochemical impedance spectroscopy,[18] or fingerprinting reactive processes.[19–23] In this paper, we derive the periodic fluorescence evolution of a reversibly photoactivatable fluorophore submitted to sine-wave illumination of large amplitude. We demonstrate that a Fourier amplitude at each harmonic frequency exhibits at least one resonance of significant amplitude and determine the relation observed at resonance between the kinetic properties of the label and experimentally-controlled parameters. HIGHLIGHT (pHase-sensItive imaGing of reversibly pHotoactivatable Labels after modulatIon of activatinG ligHT) harnesses this feature, which enhances selectivity over previous protocols only relying on the fundamental angular frequency and provides additional opportunities for highly selective analysis and imaging of spectrally similar labels.

2 HIGHLIGHT principle

We consider a reversibly photoactivatable fluorophore engaged in a light-driven exchange between two states differing by their brightness (see Fig. 1a). The forward photoconversion results from illumination I_1 at wavelength λ_1 and the backward conversion is either spontaneous, e.g. by an emissive or thermally-driven process, or photochemically governed under illumination I_2 at wavelength λ_2, e.g. as in reversibly photoswitchable fluorescent proteins (RSFPs)[24,25] used in the following.[26–29] We analytically and numerically compute the evolution of the concentrations of the fluorophore states and the fluorescence signal under different illumination protocols involving sine-wave light at angular frequency ω (see section B1 in Supporting Information): (i) light modulation at λ_1 without light at λ_2; (ii) light modulation at λ_1 (λ_2, resp.) with constant light at λ_2 (λ_1, resp.) (displayed in Fig. 1a); (iii) antiphase modulation of both lights at λ_1 and λ_2. In all examined cases, fluorescence oscillates at frequency ω. Fourier analysis is performed to extract the n^{th}-order amplitudes at each harmonic frequency $n\omega$ (see Fig. 1a). The Fourier amplitudes are proportional to the total concentration of the photoactivatable fluorophore. Defining the phase of the Fourier amplitudes with respect to the exciting modulated light, the quadrature (for the odd orders) and in-phase (for the even orders) amplitudes exhibit at least one resonance in the space of the control parameters (I_1^0, ω) in (i) or $(I_2^0/I_1^0, \omega/I_1^0)$ in (ii) and (iii), where I_1^0 and I_2^0 are the mean light intensities. The resonant n^{th}-order Fourier amplitudes are further referred to as HIGHLIGHT-n signals. For all illuminations, the HIGHLIGHT-1 signal exhibits a single resonance peak, which is twice as high for illumination (iii) as for the other illuminations. From the second order, the HIGHLIGHT-n signals have a single extremum or two extrema of opposite signs, leading to a line of vanishing amplitude.[30,31] Far from extrema, the HIGHLIGHT-n signals vanish. Importantly the width of a resonance peak decreases as the order n of the harmonics increases without detrimental loss of absolute amplitude evaluated at the extremum. Typically the HIGHLIGHT-n signal decays by a factor of two when n is increased by one. The resonance conditions relate the control parameters and the kinetic properties of a given reversibly photoactivatable fluorophore. Specifically the angular frequency ω is close to the inverse of the photoswitching relaxation time (see section B1 in Supporting Information). Imposing resonant conditions for a target label eliminates the contributions to the HIGHLIGHT-n signals of non-resonant spectrally interfering signals (e.g. other labels, autofluorescence, or ambient light) and provides a selective and quantitative imaging protocol.

The protocol (ii) with light modulation at λ_1 is chosen for its well-suited properties for selective imaging (see Supporting Information). As a representative example of reversibly photoactivatable fluorophore for HIGHLIGHT evaluation, we choose the RSFP Dronpa-2.[32] As a negative photo-

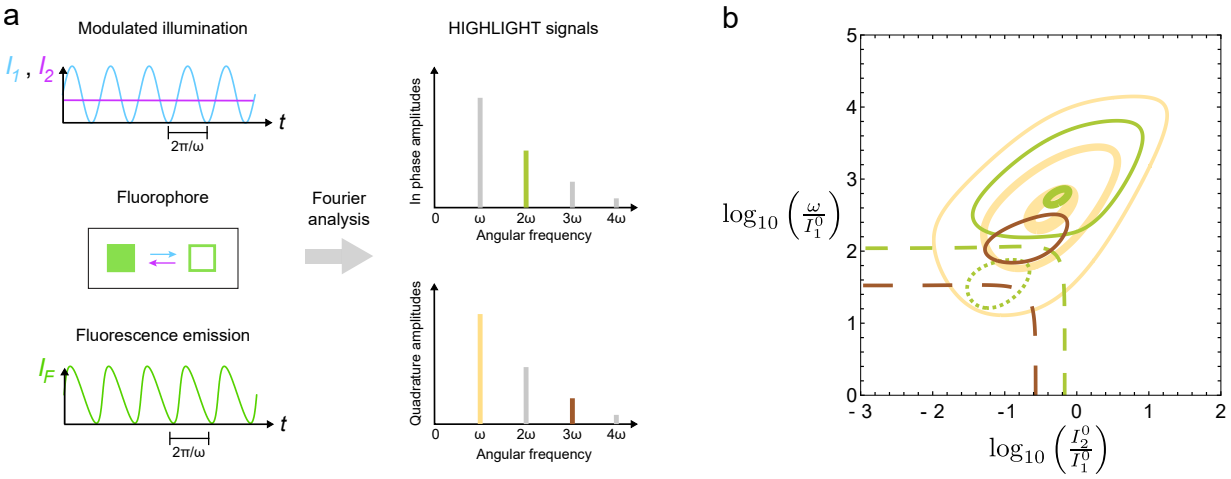

Figure 1: *The HIGHLIGHT principle*. **a**: Application of a sine-wave illumination (here sine-wave light at angular frequency ω and wavelength λ_1 – in blue – and constant light at wavelength λ_2 – in purple) on a reversibly photoactivatable fluorophore generates a periodic fluorescence signal, which provides quadrature and in-phase amplitudes after Fourier analysis; **b**: Contour maps of the HIGHLIGHT-n signals ($n = 1$: yellow; $n = 2$: green; $n = 3$: brown) computated for Dronpa-2 driven by sine-wave light at $\lambda_1 = 480$ nm and constant light at $\lambda_2 = 405$ nm using the photochemical data shown in Tab. B5. Solid (dotted, resp.) lines are associated with positive (negative, resp.) values. Dashed lines are zero lines. The HIGHLIGHT-n signals are scaled by the HIGHLIGHT-1 value at resonance: Thick lines correspond to amplitudes equal to 0.9, medium lines to 0.4, and thin lines to 0.1.

switcher, Dronpa-2 is switched to a dark state by a blue light at $\lambda_1 = 480$ nm and back from the photoswitched dark state to a bright state by purple light at $\lambda_2 = 405$ nm. Fig. 1b displays the computed maps of the HIGHLIGHT-n signals ($n = 1$–3) in the $(I_2^0/I_1^0, \omega/I_1^0)$ space. Interestingly, the resonance condition of the positive peaks of HIGHLIGHT-2 and HIGHLIGHT-3 are close to the resonance condition of HIGHLIGHT-1. The width of the peaks along the ω/I_1^0-axis significantly drops from HIGHLIGHT-1 to HIGHLIGHT-3 without severe decrease of peak amplitude. Hence a single acquisition with a same set of control parameters provides several independent and quantitative observables of increasing selectivity for fluorescence imaging.

3 HIGHLIGHT in action

HIGHLIGHT implementation requires pure sine-wave light sources ensuring that non-linearities revealed by the harmonics result from the response of the reversibly photoactivatable fluorophore and not from harmonic distortion of illumination. Considering the acquisition frequency of the camera and the resonant conditions for RSFPs, we aimed at generating pure sine-wave modulation from Light Emitting Diodes (LEDs) at 1–50 Hz frequencies. Despite a waveform generator deliver-

ing a sinusoidal voltage with less than 0.075% harmonic distortion, we noticed that the modulated light exhibited a detrimental level of harmonic distortion (see Fig.B13a,b and B14a,b), presumably originating from temperature-dependent brightness of the passively cooled LEDs. Hence we introduced a feedback control on the generator bringing harmonic distortion below 1%. Equipped with reliable pure sine-wave illumination, we could illustrate the opportunities provided by the set of HIGHLIGHT-n observables for selective fluorescence imaging.

We first experimentally evaluated the theoretical predictions of the discriminative map displayed in Fig. 1b. We submitted fixed nucleus-labeled U2OS cells (see Fig. 2a) expressing H2B-Dronpa-2 to sine-wave light at $\lambda_1 = 480$ nm and constant light at $\lambda_2 = 405$ nm under fulfilling the HIGHLIGHT-1 resonance conditions using reported photochemical information (see Fig. 2b–h).[10] A lock-in amplifier was used to extract the in-phase and quadrature components leading to HIGHLIGHT-n images with satisfactory signal-to-noise ratios $S/N(n)$ up to $n = 3$: $S/N(1) = 10.2$, $S/N(2) = 11.4$, and $S/N(3) = 6.1$ (see also Fig. B17a–d and Fig. B18a–d for Dronpa-3[33]- and rsFastLime[32,34]-labeled cells, respectively). The HIGHLIGHT-1–3 signals agreed with the theoretical predictions. The measured HIGHLIGHT-2 and -3 signals scaled by the HIGHLIGHT-1 signal were 0.31±0.12 and 0.14±0.16 when 0.35 and 0.10 could be expected, respectively. The signals HIGHLIGHT-1–3 obtained at conditions deviating from the HIGHLIGHT-1 resonance by an order of magnitude along each axis were in agreement with the predictions. In particular, the expected decrease of the width of the peak along the the ω/I_1^0-axis from HIGHLIGHT-1 to HIGHLIGHT-3 was confirmed. Eventually, we observed the vanishing of the HIGHLIGHT-2 and HIGHLIGHT-3 signals and the change of their sign for smaller control parameters than the resonant values along the diagonal.

Harnessing experimentally validated HIGHLIGHT discrimination maps, we showed that HIGHLIGHT selectively imaged a targeted RSFP against a background of spectrally interfering fluorophores. We first targeted Dronpa-2 against EGFP, in microscopy of mammalian cells expressing both fluorophores. The pre-HIGHLIGHT image results from averaging the fluorescence evolution and is similar to an image recorded under constant illumination. Whereas the contributions of Dronpa-2 and EGFP were superimposed in the pre-HIGHLIGHT image (Fig. B19a), only Dronpa-2 contributed to the HIGHLIGHT-1 and HIGHLIGHT-2 images as anticipated from the absence of any resonant photoswitching behavior for EGFP (Fig. B19b). Hence, HIGHLIGHT-1 and -2 efficiently suppressed the signal from spectrally interfering non-photoactive fluorophores.

Then we showed that spectrally similar RFSPs (see Fig. B16) possessing different kinetic properties could be selectively imaged with HIGHLIGHT. We specifically examined the negative photoswitchers Dronpa,[35] Dronpa-2,[32] and rsFastLime,[32,34] which could not be independently im-

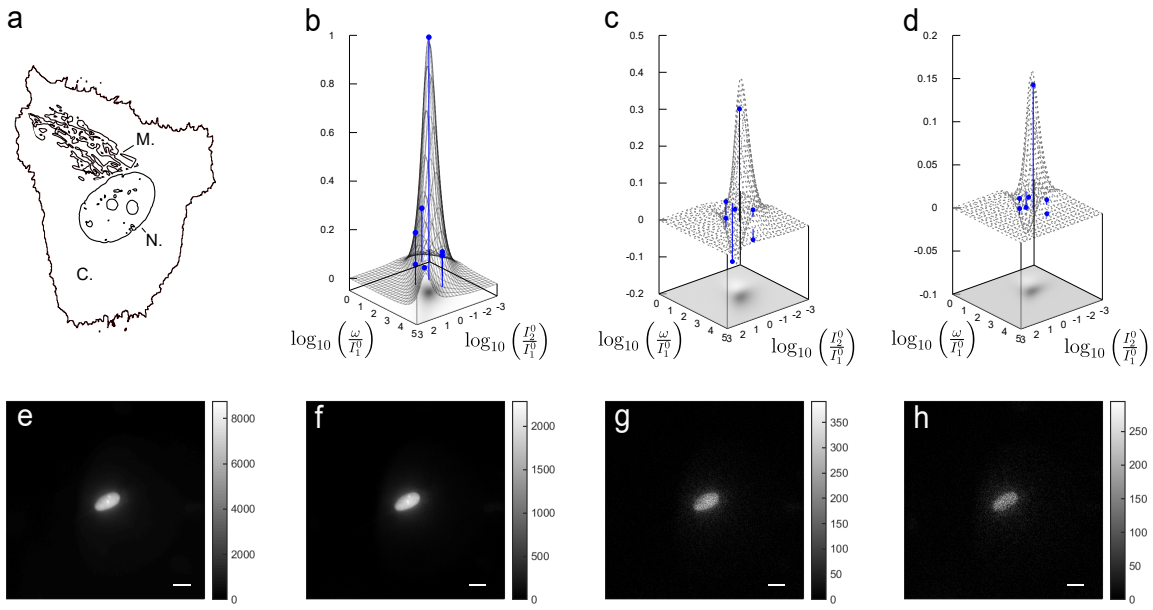

Figure 2: *HIGHLIGHT-n discrimination maps using cell imaging*. **a**: Schematic representation of the imaged cell (N: nucleus; M: mitochondria); **b–d**: Experimental (blue disks) and theoretical (black dots) HIGHLIGHT-1 (**b**), -2 (**c**), and -3 (**d**) signals scaled by HIGHLIGHT-1 value at resonance in the (I_2^0/I_1^0,ω/I_1^0) space for Dronpa-2 under sine-wave light at $\lambda_1 = 480$ nm and constant light at $\lambda_2 = 405$ nm; **e–h**: Pre-HIGHLIGHT (**e**) and HIGHLIGHT-1 (**f**), -2 (**g**), and -3 (**h**) images of Dronpa-2. The level of the HIGHLIGHT-n signals is displayed in the gray scale on the right of each figure. System: Fixed U2OS cells expressing H2B-Dronpa-2 (at the nucleus). The images were recorded at 298 K with scale bars: 10 μm; See Tab. B6 in Supporting Information for the acquisition conditions.

aged using Speed OPIOM.[10] The theoretical predictions for the HIGHLIGHT-n maps of Dronpa and rsFastLime were first determined using light modulation at $\lambda_1 = 480$ nm and constant light at $\lambda_2 = 405$ nm (see Fig. 3a,e,i). Then we imaged a four-chamber microfluidic device, each chamber being filled with a solution of one fluorophore, Dronpa, Dronpa-2, rsFastLime, or EGFP. Three fluorescence evolutions were recorded at the HIGHLIGHT-1 resonance conditions of the three RSFPs, Dronpa, Dronpa-2, and rsFastLime. As expected, the EGFP chamber was again dark in all HIGHLIGHT-n images (see Figs. 3a, e, i). Whereas the HIGHLIGHT-1 image recorded at resonance for Dronpa-2 could almost eliminate the interfering contributions of the two other RSFPs (see Fig. 3c), the HIGHLIGHT-1 images recorded at resonance for Dronpa and rsFastLime encountered strong interferences from rsFastLime and Dronpa-2 respectively (see Fig. 3b and d) as anticipated from significant overlaps in Fig. 3a. This result was expected from the similarity between the HIGHLIGHT-1 and Speed OPIOM imaging protocols. In contrast, HIGHLIGHT-2

could selectively image the three RSFPs under their respective conditions of HIGHLIGHT-1 resonance (see Fig. 3f–h). This result was predicted by the theoretical maps showing that the point associated with the HIGHLIGHT-1 resonant parameter values of Dronpa and rsFastLime lies on the HIGHLIGHT-2 zero line of rsFastLime and Dronpa-2 respectively (see Fig. 3a and e, and d and h). The HIGHLIGHT-2 discrimination of rsFastLime and Dronpa-2 was reproduced in fixed U2OS cells (see Figure B20). Whereas the Pre-HIGHLIGHT (Figure B20a,e) and HIGHLIGHT-1 (Figure B20b,f) images evidenced overlap of the signals from both RSFPs, HIGHLIGHT-2 unambiguously distinguished rsFastLime at the cell membrane from Dronpa-2 at the nucleus (Figure B20c,g). The HIGHLIGHT-3 theoretical map displayed in Fig. 3i predicts a similar behavior to the one obtained with HIGHLIGHT-2. However, the signal-to-noise ratio of the HIGHLIGHT-3 images was too low to reach any definitive conclusion under the present acquisition conditions (see Fig. 3j–l). Hence, when adopting the HIGHLIGHT-1 resonance conditions for acquisition, both HIGHLIGHT-1 and HIGHLIGHT-2 signals can be easily accessed. Moreover HIGHLIGHT-2 emerged as the most attractive observable balancing selectivity with sensitivity for fluorescence imaging of reversibly photoactivatable fluorophores.

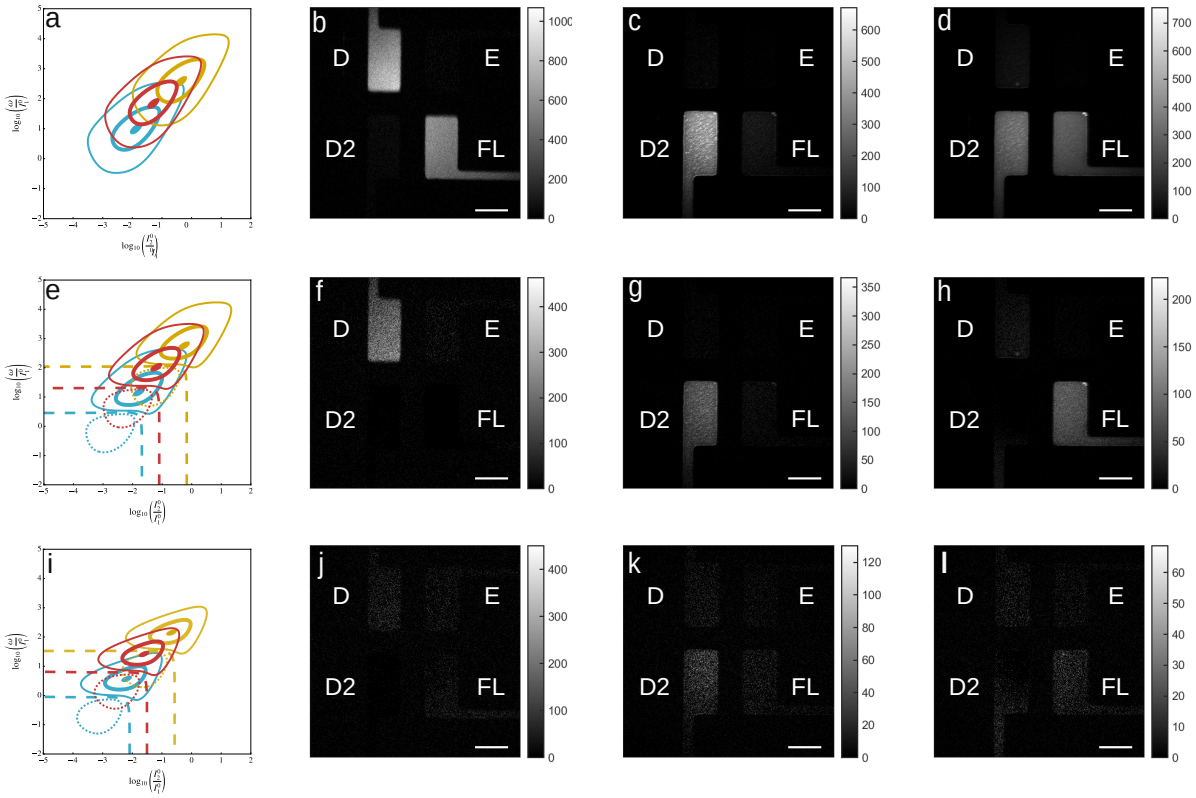

Figure 3: *HIGHLIGHT discriminates distinct four spectrally similar fluorescent proteins*. **a**,**e**,**i**: Contour maps of the scaled HIGHLIGHT-1 (**a**), -2 (**e**), and -3 (**i**) signals under sine-wave light at $\lambda_1 = 480$ nm and constant light at $\lambda_2 = 405$ nm for Dronpa (light blue), Dronpa-2 (yellow), and rsFastLime (red) in the $(I_2^0/I_1^0,\omega/I_1^0)$ space using the data shown in Tab. B5 (see Supporting Information). Solid (dotted, resp.) lines are associated with positive (negative, resp.) values. Dashed lines are zero lines. The HIGHLIGHT-n signals are scaled by the HIGHLIGHT-1 value at resonance: Thick lines correspond to amplitudes equal to 0.9, medium lines to 0.4, and thin lines to 0.1; HIGHLIGHT-n ($n = 1$: **b–d**; $n = 2$: **f–h**; $n = 3$: **i–l**) images of a four-chamber microsystem filled with solutions of Dronpa (D; 2 μM), Dronpa-2 (D2; 8 μM), rsFastLime (FL; 5μM), and EGFP (E; 5 μM) in pH 7.4 BSA-PBS buffer. The images were recorded at 298 K. Scale bars: 100 μm. The control parameters are set at the resonance of HIGHLIGHT-1 Dronpa (**b**,**f**,**j**), Dronpa-2 (**c**,**g**,**k**), and rsFastLime (**d**,**h**,**l**) See Tab. B6 in Supporting Information for the acquisition conditions.

In addition to selective imaging performances, HIGHLIGHT possesses an intrinsic optical sectioning power. Imposing an inhomogeneous spatial profile of illumination allows the HIGHLIGHT resonance conditions to be met only locally, which enables us to easily discard fluorophores out of targeted locations. To evidence this attractive feature, we built an epi-fluorescence imaging system (see subsection B4.5 in the Supporting Information) that delivers coaxial light profiles at 480 and 405 nm spatially decaying over 10 μm from a homogeneously illuminated 15-μm edge octahedron located at the focal plane. This setup was used to image layers of variable thickness of a Dronpa-2

solution with sine-wave light at $\lambda_1 = 480$ nm and constant light at $\lambda_2 = 405$ nm by choosing the values of the control parameters in the octahedron to meet the HIGHLIGHT-1 resonance conditions. Fig. 4a–f displays the Pre-HIGHLIGHT, HIGHLIGHT-1, and -2 images for 4-μm and 120-μm thick samples. For the 4-μm thick sample, the three images do not exhibit any halo around the central bright square as anticipated from the absence of any fluorescence emission out of the focal plane. For the 120-μm thick sample, the Pre-HIGHLIGHT image yields a bright square surrounded by a strong halo, which originates from the contribution of the solution located above and below the octahedron. The HIGHLIGHT-1 and HIGHLIGHT-2 images provide a better defined square with a less pronounced halo since Dronpa-2 experiences out-of-resonance conditions above and below the octahedron. To be quantitative, we measured the Pre-HIGHLIGHT, HIGHLIGHT-1, -2 signals as a function of the sample thickness z. From $z = 0$ to 15 μm, both Pre-HIGHLIGHT and HIGHLIGHT-1, -2 signals linearly increase as expected from homogeneous light distribution within the octahedron (see Fig. 4g). Beyond 15 μm, the Pre-HIGHLIGHT signal still increases with increasing z. In contrast, the HIGHLIGHT-1, -2 signals saturate, which demonstrates their intrinsic optical sectioning power. These conclusions were confirmed when taking into account the spatial dependence of the light intensities in the analytical expressions of the HIGHLIGHT signals. Figs. 4h–j show that the HIGHLIGHT-1 and -2 signals are more focused than the Pre-HIGHLIGHT signal. Similar results were obtained with modulated light at $\lambda_2 = 405$ nm and constant light at $\lambda_1 = 480$ nm (see Fig. B21a–g).

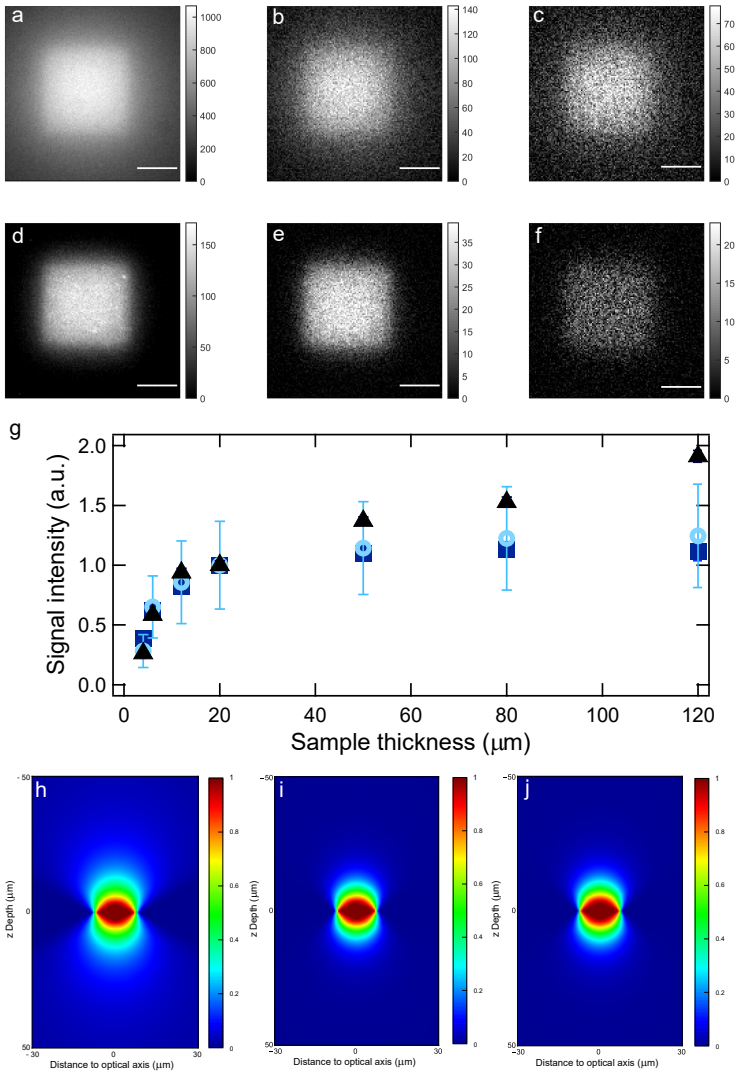

Figure 4: *Optical sectioning power of HIGHLIGHT*. Pre-HIGHLIGHT (**a**,**d**), HIGHLIGHT-1 (**b**,**e**), -2 (**c**,**f**) images of a 10-μM Dronpa-2 solution of thickness 120 μm (**a**–**c**) and 4 μm (**d**–**f**) obtained with an optical setup using coaxial light profiles spatially decaying over 10 μm from a homogeneously illuminated 15-μm edge octahedron. Scale bar: 10 μm; **g**: Pre-HIGHLIGHT (black triangles), HIGHLIGHT-1 (deep blue squares), -2 (light blue circles) signals versus thickness z of the sample for a 10-μM Dronpa-2 solution. The mean signal intensities and the error bars are obtained using spatial averages of the images over a 6-μm square; Spatial dependence of the scaled Pre-HIGHLIGHT (**h**), HIGHLIGHT-1 (**i**), and -2 (**j**) signals after introducing the light profiles in the analytical expressions of the HIGHLIGHT signals. See Tab. B6 in Supporting Information for the acquisition conditions with sine-wave light at $\lambda_1 = 480$ nm and constant light at $\lambda_2 = 405$ nm.

4 Concluding remarks

The development of HIGHLIGHT has been motivated by improving dynamic contrast of reversibly photoactivatable fluorophores engaged in a two-state exchange.[10,13] We harness the resonant be-

havior of the HIGHLIGHT-n signals defined as n^{th} order Fourier amplitudes obtained by phase-sensitive Fourier analysis of fluorescence evolution under periodic illumination. We more specifically adopted pure sine-wave illumination, which is presumably more favorable for discrimination with excellent signal-to-noise ratio from lock-in amplification. Provided that simple photochemical experiments[9,10] have revealed the intensity dependence of the rate constants, the parameters that control illumination can be tuned to maximize the HIGHLIGHT-n signals of a targeted fluorophore and minimize the contributions of spectrally similar mixture components. The control parameter dependence of the HIGHLIGHT-n signals predicted by the theoretical analysis has been experimentally confirmed.

In particular, the HIGHLIGHT-1 signal has a single extremum whereas the HIGHLIGHT-2 signal has two narrower and lower resonance peaks separated by a zero line in the space of control parameters. HIGHLIGHT-1 and Speed-OPIOM[9,10] both harness the 1^{st}-order quadrature Fourier amplitude of fluorescence oscillations. Whereas HIGHLIGHT-1 and Speed-OPIOM efficiently fought against autofluorescence, they both failed to distinguish spectrally similar reversibly photoactivatable fluorophores with closely located resonances. Under such demanding situations, we demonstrated the added value of HIGHLIGHT-2. Without loosing much signal with respect to HIGHLIGHT-1, we independently imaged three RSFPs with similar resonances using the narrower resonance peak and the zero lines of HIGHLIGHT-2.

Moreover we showed that HIGHLIGHT-1 and -2 are intrinsically endowed with optical sectioning,[36,37] which is favorable to the implementation of 3D-fluorescence imaging. Interestingly, independent light beam shaping at both wavelengths is not required (like in REversible Saturable OpticaL Fluorescence Transitions (RESOLFT)[38] for instance) and only the generation of any non uniform light profiles is necessary. The simple illumination scheme of HIGHLIGHT may find promising applications in the context of light scanning (e.g. confocal microscopy) and could simplify the optical setup, reduce its cost, and facilitate its maintenance.

Obtaining several observables in a single experiment is another favorable feature of HIGHLIGHT. We have chosen to harness the Fourier amplitudes with resonant behavior. However all Fourier amplitudes have specific dependencies on the control parameters which could be exploited for example in the framework of machine learning.

Eventually, HIGHLIGHT has been applied to a two-state exchange but can be extended to more complex mechanisms.[39] If the mechanism is known, resonance conditions can be determined leading to analytical expressions, which can be straightforwardly used by experimentalists. For unknown mechanisms, empirical determination of resonances remains possible using numerical determination. It is worth to note that complex mechanisms offer the possibility to exploit a large

number of control parameters to tune different rate constants and get better selectivity for fluorophore discrimination.

5 Acknowledgement

The authors thank S. Jakobs for providing the Dronpa-2 cDNAs. This work was supported by the ANR (France BioImaging - ANR-10-INBS-04, Morphoscope2 - ANR-11-EQPX-0029,, HIGHLIGHT, and dISCern), the Fondation de la Recherche Médicale (FRM DEI201512440), and the Domaine d'Intérêt Majeur Analytics de la Région Ile de France (DREAM).

References

[1] J. Quérard, T. Le Saux, A. Gautier, D. Alcor, V. Croquette, A. Lemarchand, C. Gosse, and L. Jullien. Kinetics of reactive modules adds discriminative dimensions for selective cell imaging. *ChemPhysChem*, 17:1396–1413, 2016.

[2] R. Winkler-Oswatitsch and M. Eigen. The art of titration. From classical end points to modern differential and dynamic analysis. *Angew. Chem. Intl. Ed.*, 18:20–49, 1979.

[3] Raja Chouket, Agnès Pellissier-Tanon, Annie Lemarchand, Agathe Espagne, Thomas Le Saux, and Ludovic Jullien. Dynamic contrast with reversibly photoswitchable fluorescent labels for imaging living cells. *Chemical Science*, 11(11):2882–2887, 2020.

[4] J. R. Lakowicz, H. Szmacinski, K. Nowaczyk, and M. L. Johnson. Fluorescence lifetime imaging of free and protein-bound nadh. *Proc. Natl. Acad. Sci. USA*, 89:1271–1275, 1992.

[5] J. R. Lakowicz, H. Szmacinski, K. Nowaczyk, K. W. Berndt, and M. L. Johnson. Fluorescence lifetime imaging. *Anal. Biochem.*, 202:316–330, 1992.

[6] G. Marriott, S. Mao, T. Sakata, J. Ran, D. K. Jackson, C. Petchprayoon, T. J. Gomez, E. Warp, O. Tulyathan, H. L. Aaron, E. Y. Isacoff, and Y. Yan. Optical lock-in detection imaging microscopy for contrast-enhanced imaging in living cells. *Proc. Natl. Acad. Sci. U. S. A.*, 105:17789–17794, 2008.

[7] J. Widengren. Fluorescence-based transient state monitoring for biomolecular spectroscopy and imaging. *J. R. Soc. Interface*, 7:1135–1144, 2010.

[8] C. I. Richards, J.-C. Hsiang, and R. M. Dickson. Synchronously amplified fluorescence image recovery (SAFIRe). *J. Phys. Chem. B*, 114:660–665, 2010.

[9] J. Quérard, T.-Z. Markus, M.-A. Plamont, C. Gauron, P. Wang, A. Espagne, M. Volovitch, S. Vriz, V. Croquette, A. Gautier, T. Le Saux, and L. Jullien. Photoswitching kinetics and phase-sensitive detection add discriminative dimensions for selective fluorescence imaging. *Angew. Chem. Int. Ed.*, 54:2633–2637, 2015.

[10] J. Quérard, R. Zhang, Z. Kelemen, M.-A. Plamont, X. Xie, R. Chouket, I. Roemgens, Y. Korepina, S. Albright, E. Ipendey, M. Volovitch, H. L. Sladitschek, P. Neveu, L. Gissot, A. Gautier, J.-D. Faure, V. Croquette, T. Le Saux, and L. Jullien. Resonant out-of-phase fluorescence microscopy and remote imaging overcome spectral limitations. *Nat. Comm.*, 8:969, 2017.

[11] R. Weissleder and M. Nahrendorf. Advancing biomedical imaging. *Proc. Natl. Acad. Sci. USA*, 112:14424–14428, 2015.

[12] H. Grecco, S. Imtiaz, and E. Zamir. Multiplexed imaging of intracellular protein networks. *Cytometry Part A*, 2016.

[13] Joseph R Lakowicz and Aleksander Balter. Theory of phase-modulation fluorescence spectroscopy for excited-state processes. *Biophysical chemistry*, 16(2):99–115, 1982.

[14] Satoshi Nakata, Kaori Takemura, and Kayoko Neya. Chemical sensor based on nonlinearity: Principle and application. *Analytical sciences*, 17(3):365–373, 2001.

[15] Robert P Frueholz and Jerry A Gelbwachs. Harmonic saturated spectroscopy for improved atomic detection. *Applied optics*, 19(16):2735–2741, 1980.

[16] Katsumasa Fujita, Minoru Kobayashi, Shogo Kawano, Masahito Yamanaka, and Satoshi Kawata. High-resolution confocal microscopy by saturated excitation of fluorescence. *Physical review letters*, 99(22):228105, 2007.

[17] Masahito Yamanaka, Kenta Saito, Nicholas I Smith, Satoshi Kawata, Takeharu Nagai, and Katsumasa Fujita. Saturated excitation of fluorescent proteins for subdiffraction-limited imaging of living cells in three dimensions. *Interface focus*, 3(5):20130007, 2013.

[18] Fathima Fasmin and Ramanathan Srinivasan. Nonlinear electrochemical impedance spectroscopy. *Journal of The Electrochemical Society*, 164(7):H443–H455, 2017.

[19] H. Berthoumieux, L. Jullien, and A. Lemarchand. Response to a temperature modulation as a signature of chemical mechanisms. *Phys. Rev. E*, 76:056112, 2007.

[20] A. Lemarchand, H. Berthoumieux, L. Jullien, and C. Gosse. Chemical mechanism identification from frequency response to small temperature modulation. *J. Phys. Chem. A*, 116:8455–8463, 2012.

[21] F. Closa, C. Gosse, L. Jullien, and A. Lemarchand. Identification of two-step chemical mechanisms and determination of thermokinetic parameters using frequency responses to small temperature oscillations. *J. Chem. Phys.*, 138:244109, 2013.

[22] F. Closa, C. Gosse, L. Jullien, and A. Lemarchand. Identification of two-step chemical mechanisms using small temperature oscillations and a single tagged species. *J. Chem. Phys.*, 142:174108, 2015.

[23] Philipp Müller and Ive Hermans. Applications of modulation excitation spectroscopy in heterogeneous catalysis. *Industrial & Engineering Chemistry Research*, 56(5):1123–1136, 2017.

[24] D. Bourgeois and V. Adam. Reversible photoswitching in fluorescent proteins : A mechanistic view. *IUBMB Life*, 64:482–491, 2012.

[25] X. X. Zhou and M. Z. Lin. Photoswitchable fluorescent proteins: ten years of colorful chemistry and exciting applications. *Curr. Opin. Chem. Biol.*, 17:682–690, 2013.

[26] H. Bouas-Laurent and H. Dürr. Organic photochromism. *Pure Appl. Chem.*, 73:639–665, 2001.

[27] M.-S. Wang, G. Xu, Z.-J. Zhang, and G.-C. Guo. Inorganic-organic hybrid photochromic materials. *Chem. Commun.*, 46:361–376, 2010.

[28] T. Fukaminato. Single-molecule fluorescence photoswitching : Design and synthesis of photoswitchable fluorescent molecules. *J. Photochem. Photobiol. C : Photochem. Rev.*, 12:177–208, 2011.

[29] S. van de Linde and M. Sauer. How to switch a fluorophore: from undesired blinking to controlled photoswitching. *Chem. Soc. Rev.*, 43:1076–1087, 2014.

[30] Peter Jung and Peter Talkner. Suppression of higher harmonics at noise induced resonances. *Physical Review E*, 51(3):2640, 1995.

[31] Gerhard Schmid and Peter Hänggi. Controlling nonlinear stochastic resonance by harmonic mixing. *Physica A: Statistical Mechanics and its Applications*, 351(1):95–105, 2005.

[32] A. C. Stiel, S. Trowitzsch, G. Weber, M. Andresen, C. Eggeling, S. W. Hell, S. Jakobs, and M. C. Wahl. 1.8 å bright-state structure of the reversibly switchable fluorescent protein Dronpa guides the generation of fast switching variants. *Biochem. J.*, 402:35–42, 2007.

[33] R. Ando, C. Flors, H. Mizuno, J. Hofkens, and A. Miyawaki. Highlighted generation of fluorescence signals using simultaneous two-color irradiation on Dronpa mutants. *Biophys. J.*, 92:L97 – L99, 2007.

[34] M. Andresen, A. C. Stiel, J. Follig, D. Wenzel, A. Schoenle, A. Egner, C. Eggeling, S. W. Hell, and S. Jakobs. Photoswitchable fluorescent proteins enable monochromatic multilabel imaging and dual color fluorescence nanoscopy. *Nat. Biotech.*, 26:1035–1040, 2008.

[35] R. Ando, H. Mizuno, and A. Miyawaki. Regulated fast nucleocytoplasmic shuttling observed by reversible protein highlighting. *Science*, 306:1370–1373, 2004.

[36] José-Angel Conchello and Jeff W Lichtman. Optical sectioning microscopy. *Nature Methods*, 2(12):920, 2005.

[37] T Wilson. Optical sectioning in fluorescence microscopy. *Journal of microscopy*, 242(2):111–116, 2011.

[38] M. Hofmann, C. Eggeling, S. Jakobs, and S. W. Hell. Breaking the diffraction barrier in fluorescence microscopy at low light intensities by using reversibly photoswitchable proteins. *Proc. Natl. Acad. Sci. U. S. A.*, 102:17565–17569, 2005.

[39] Agnès Pellissier-Tanon, Raja Chouket, Thomas Le Saux, Ludovic Jullien, and Annie Lemarchand. Light-assisted dynamic titration: from theory to an experimental protocol. *Physical Chemistry Chemical Physics*, 20(37):23998–24010, 2018.

3.3 Article: Light-assisted dynamic titration: From theory to an experimental protocol

The discrimination protocols OPIOM, Speed OPIOM, and HIGHLIGHT have been implemented for specific reversibly photoswitchable fluorescent labels engaged in a two-state exchange. The three methods are quantitative, i.e. give access to the amount of fluorophore. The chemist is often faced with the determination of the concentration of a non-fluorescent species and uses titration reactions for this purpose. However few titration reactions are light driven. In order to harness the potential of forced photochemical systems in the framework of titration, we consider a titration reaction coupled with a reversibly photoswitching step.[128–130]

Light modulation brings new control parameters, the angular frequency and the mean light intensity, with respect to standard titration.[31,131] The resonance conditions link the control parameters and the kinetic parameters. Due to the larger number of kinetic parameters than thermodynamic parameters, dynamic titration provides better selectivity than standard titration.

The theoretical results I obtained on the extension of the discrimination protocol to a reversibly photoswitchable/complexation system have been published in Phys. Chem. Chem. Phys.[88] The article is given below.

PCCP

PAPER

View Article Online
View Journal | View Issue

Cite this: *Phys. Chem. Chem. Phys.*, 2018, **20**, 23998

Light-assisted dynamic titration: from theory to an experimental protocol†

Agnès Pellissier-Tanon,[a] Raja Chouket,[a] Thomas Le Saux,[a] Ludovic Jullien*[a] and Annie Lemarchand *[b]

Received 21st June 2018,
Accepted 9th September 2018

DOI: 10.1039/c8cp03953d

rsc.li/pccp

In order to design a dynamic titration method, we propose a theoretical model harnessing the kinetic properties of the complexation of the titrated species with a titrating photoswitchable reagent. Forced oscillations of illumination are imposed and concentration oscillations of the targeted species are deduced from the equations of chemical kinetics. We determine analytical expressions of the resonance conditions on the control parameters, angular frequency, mean light intensity, and total concentration of the photoswitchable reagent, which optimize the out-of-phase amplitude of concentration oscillations. A user-friendly protocol of dynamic titration is proposed.

1 Introduction

In analysis or imaging, addressing a targeted component in a mixture without any separation requires selectively reading-out its signature. When a mixture contains many components, exploiting a spectroscopic signature may be too restrictive for discrimination. Indeed, the signals associated with atoms or functional groups exhibit non-vanishing half-widths and are spread over a finite frequency range, which limits the number of discernable components. As an example relevant for fluorescence microscopy,[1] the absorption and fluorescence emission features of the labels currently used in biology suffer from spectral crowding. Only a few labels can be discriminated[2] instead of the several tens which would be desirable for advanced bioimaging,[3,4] multicolored cell labeling,[5–7] and highly multiplexed diagnostic assays.[8,9] Alternative strategies have to be implemented in order to overcome the preceding limitation.

Titration is such a strategy, which has been extensively used in chemistry and biology. In titrations, discrimination of a targeted component relies on its reaction with a selective reagent, which is read-out by an observable (*e.g.* absorbance, fluorescence emission,...) reporting on the extent of the titrating reaction. Most titration protocols exploit chemical equilibrium with respect to the titrating reaction. In those protocols, the observable is constant and its value is governed by the thermodynamic constant of the titrating reaction, which has to be singularized in order to achieve successful contrast of the targeted component against interfering species. Dynamic titrations add a new dimension for discrimination.[10,11] As relaxation methods used in chemical kinetics,[12–16] they exploit the mixture response to a sudden or periodic change of a parameter, which controls the rate of the titrating reaction. In dynamic titrations, the observable is not anymore constant but it is replaced by a temporal series of observable values, which depends on the impact of the perturbation on the titrating reaction. In particular, both the extent and the relaxation time of the titrating reaction govern the response of any mixture component to the perturbation. Consequently, they add a kinetic dimension to the titration protocols relevant at chemical equilibrium and correspondingly make dynamic titrations more selective.

Several control parameters can perturb the rate of a titration reaction.[12,14] Periodic forcing of reaction kinetics *via*, *e.g.* modulation of pressure, temperature, or illumination, is a useful tool to improve the reaction performance, the reaction rate, or to control the selection of a given behavior in complex nonlinear reactions.[17–21] Optimizing the quantity of interest consists in determining resonance conditions relating the parameters associated with external forcing and intrinsic chemical dynamics. Analogous optimization could be obtained using noise instead of a periodic forcing leading to stochastic resonance.[22] Protocols relying on temperature modulations and signal demodulation for selective analysis[23–25] or mechanism unraveling[26–33] have been proposed.

In this manuscript, we consider perturbing the rate of the titration reaction by changing the concentration of its reactants and products. Such a change would most often involve matter transport. However, this approach may bring limitations originating from poor temporal resolution, detrimental convective

[a] *PASTEUR, Département de Chimie, École Normale Supérieure, PSL University, Sorbonne Université, CNRS, 75005 Paris, France. E-mail: ludovic.jullien@ens.fr*
[b] *Sorbonne Université, Centre National de la Recherche Scientifique (CNRS) Laboratoire de Physique Théorique de la Matière Condensée (LPTMC), 4 Place Jussieu, Case Courrier 121, 75252 Paris Cedex 05, France. E-mail: anle@lptmc.jussieu.fr*

† Electronic supplementary information (ESI) available. See DOI: 10.1039/c8cp03953d

flows, or lack of access in the case of compartmentalized systems. We are interested in using light as a fast non-invasive trigger to change the concentration of photoactive species, which is compatible with biological applications.[34] Hence, we consider that the selective reagent used in the titration is reversibly photoswitchable and exchanges between two states respectively reactive and inert towards the mixture components. Our goal is to introduce a highly selective dynamic titration protocol discriminating the mixture components by the rate constants of their reaction with the reactive state of the selective reagent. Interestingly, the same protocol will be as well relevant to add another dimension to discriminate recent biomolecular tags, which non-covalently interact with reversibly photoswitchable reagents to provide fluorescent labels.[35–37]

The paper is organized as follows. In Section 2, we introduce a model of dynamic titration involving a photoswitchable reagent and forced oscillations of illumination. In Section 3, we analytically compute the concentration response of the reactants and products engaged in the light-assisted titrating reaction when they are submitted to modulated illumination of small amplitude. The observable is the out-of-phase amplitude of concentration oscillations of the complex formed by the targeted species and the photoswitchable titrating reagent. The observable displays an optimum in the space of the rate constants. These resonant rate constants are associated with specific values of the control parameters, *i.e.* the angular frequency of illumination modulation, the mean light intensity and the concentration of the photoswitchable reagent. Reciprocally, setting the control parameters to resonant values leads to singularizing the species with kinetic properties of interest. In Section 4, we extract analytical expressions of the control parameters associated with an extremum of the observable. The analytical predictions are numerically checked in Section 5. Section 6 is devoted to the design of the experimental protocol for light-assisted dynamic titration. Section 7 contains the conclusion.

2 The model

We consider the following mechanism accounting for the photochemical isomerization of a reversibly photoswitchable reagent (**1F**, **2F**) and its complexation with a titrated species **R**:

$$\mathbf{1F} \underset{k_{21}^{h\nu}+k_{21}^{\Delta}}{\overset{k_{12}^{h\nu}}{\rightleftharpoons}} \mathbf{2F} \tag{1}$$

$$\mathbf{R} + \mathbf{1F} \underset{k_{-1}^{\Delta}}{\overset{k_{+1}^{\Delta}}{\rightleftharpoons}} \mathbf{1B} \tag{2}$$

In reaction (1), the thermodynamically most stable state **1F** is photochemically converted into the thermodynamically less stable state **2F** at rate constant $k_{12}^{h\nu}$ from which it can relax back to the initial state **1F** either by a photochemically- or a thermally-driven process at rate constant $k_{21}^{h\nu} + k_{21}^{\Delta}$, where $k_{21}^{h\nu}$ and k_{21}^{Δ} are the photochemical and the thermal contributions of the rate constants, respectively. In reaction (2), the state **1F** interacts with the titrated species **R** to yield the bound, fluorescent state **1B**. The thermally-driven on- and off-rate constants, k_{+1}^{Δ} and k_{-1}^{Δ}, are used as discriminative parameters in a dynamic titration protocol.

In this work, the photochemical reaction (1) is used to drive the complexation reaction (2) and reveal its kinetics. Numerous molecular backbones exhibit reversible photoswitching when they are exposed to light.[38–41] The forward and backward photochemical isomerizations of reaction (1) can be light-driven at a same wavelength. Alternatively two distinct wavelengths can be used to respectively govern the forward and backward photochemical processes in many reversibly photoswitchable chromophores (*e.g.* reversibly fluorescent photoswitchable proteins – RSFPs,[42,43] azobenzenes,[44–46] cyanines,[47,48] diarylethenes,[49–51] and spirobenzopyrans[52]). In the following, we distinguish two regimes of illumination. In the first regime, subsequently referred to as the one-color system, we consider that the forward and backward photochemical isomerizations are driven at one wavelength only. In this regime, the thermally-driven backward isomerization associated with the rate constant k_{21}^{Δ} is essential to control the modulation of the extent of reaction (1). In the second regime, subsequently denominated as the two-color system, we assume that the forward and backward photochemical isomerizations are driven at two distinct wavelengths. The thermally-driven backward isomerization is not necessary to control the modulation of the extent of reaction (1) and we restrict the examination of the two-color system to the case $k_{21}^{\Delta} \ll k_{21}^{h\nu}$, *i.e.* to high intensities of illumination.

3 Concentration responses to small oscillations of illumination

We investigate the response of the system to forced oscillations of the rate constants $k_{12}^{h\nu}$ and $k_{21}^{h\nu}$ around their steady values k_{12}^{0} and k_{21}^{0}. Denoting $1B$, R, $1F$, and $2F$ the concentrations in **1B**, **R**, **1F**, and **2F** respectively, we express the laws of conservation of matter

$$R_{\mathrm{tot}} = 1B + R \tag{3}$$

$$F_{\mathrm{tot}} = 1F + 2F + 1B \tag{4}$$

where R_{tot} and F_{tot} denote the total concentrations of the titrated species and the photoswitchable reagent, respectively. The temporal evolution of the concentrations is governed by

$$\begin{aligned}\frac{\mathrm{d}1B}{\mathrm{d}t} &= k_{+1}^{\Delta}1B^2 + k_{+1}^{\Delta}1B2F - \left[k_{+1}^{\Delta}(R_{\mathrm{tot}} + F_{\mathrm{tot}}) + k_{-1}^{\Delta}\right]1B \\ &\quad - k_{+1}^{\Delta}R_{\mathrm{tot}}2F + k_{+1}^{\Delta}R_{\mathrm{tot}}F_{\mathrm{tot}}\end{aligned} \tag{5}$$

$$\frac{\mathrm{d}2F}{\mathrm{d}t} = -k_{12}^{h\nu}1B - \left(k_{12}^{h\nu} + k_{21}^{h\nu} + k_{21}^{\Delta}\right)2F + k_{12}^{h\nu}F_{\mathrm{tot}} \tag{6}$$

In the one-color system, photoswitching is driven at one wavelength. With a one-photon excitation, the photochemical rate constants can be written

$$k_{12}^{h\nu}(t) = \sigma_{12}I(t) \tag{7}$$

$$k_{21}^{h\nu}(t) = \sigma_{21} I(t) \quad (8)$$

where σ_{12} and σ_{21} are the photoswitching cross-sections and $I(t)$ is the light intensity. In the two-color system, photoswitching is driven at two wavelengths with associated light intensities $I_1(t)$ and $I_2(t)$. The rate constants obey

$$k_{12}^{h\nu}(t) = \sigma_{12,1} I_1(t) + \sigma_{12,2} I_2(t) \quad (9)$$

$$k_{21}^{h\nu}(t) = \sigma_{21,1} I_1(t) + \sigma_{21,2} I_2(t) \quad (10)$$

where $\sigma_{12,1}$, $\sigma_{12,2}$, $\sigma_{21,1}$, and $\sigma_{21,2}$ are the photoswitching cross-sections. The thermal rate constant k_{21}^{A} is neglected in front of the photochemical rate constants, implying that the light intensities are large enough.

3.1 Steady-state concentrations

In this section, we consider steady illumination, $I(t) = I^0$ for the one-color system and $I_1(t) = I_1^0$ and $I_2(t) = I_2^0$ for the two-color system. We look for the steady solutions of eqn (5) and (6) for stationary values of the photochemical rate constants

$$k_{12}^0 = \sigma_{12} I^0 \quad (11)$$

$$k_{21}^0 = \sigma_{21} I^0 \quad (12)$$

for the one-color system and

$$k_{12}^0 = \sigma_{12,1} I_1^0 + \sigma_{12,2} I_2^0 \quad (13)$$

$$k_{21}^0 = \sigma_{21,1} I_1^0 + \sigma_{21,2} I_2^0 \quad (14)$$

for the two-color system. We introduce dimensionless steady concentrations

$$\Psi_{1B}^0 = \frac{k_{+1}^{A}}{k_{-1}^{A}} 1B^0 \quad (15)$$

$$\Psi_{2F}^0 = \frac{k_{+1}^{A}}{k_{-1}^{A}} 2F^0 \quad (16)$$

which obey for the one-color system

$$\Psi_{1B}^{02} + \Psi_{1B}^0 \Psi_{2F}^0 - (\zeta_R + \zeta_F + 1)\Psi_{1B}^0 - \zeta_R \Psi_{2F}^0 + \zeta_R \zeta_F = 0 \quad (17)$$

$$-\eta \Psi_{1B}^0 - [\eta(\gamma + 1) + 1]\Psi_{2F}^0 + \eta \zeta_F = 0 \quad (18)$$

Table 1 Expression of the dimensionless parameters ζ_R, ζ_F, η, γ, γ_1, and γ_2 for the one- and two-color systems

	One-color system	Two-color system
ζ_R	$\frac{k_{+1}^{A}}{k_{-1}^{A}} R_{\mathrm{tot}}$	$\frac{k_{+1}^{A}}{k_{-1}^{A}} R_{\mathrm{tot}}$
ζ_F	$\frac{k_{+1}^{A}}{k_{-1}^{A}} F_{\mathrm{tot}}$	$\frac{k_{+1}^{A}}{k_{-1}^{A}} F_{\mathrm{tot}}$
η	$\frac{\sigma_{12} I^0}{k_{21}^{A}}$	$\frac{\sigma_{21,1} I_1^0}{\sigma_{21,2} I_2^0}$
γ	$\frac{\sigma_{21}}{\sigma_{12}}$	
γ_1		$\frac{\sigma_{12,1}}{\sigma_{21,1}}$
γ_2		$\frac{\sigma_{12,2}}{\sigma_{21,2}}$

Table 2 Expression of the parameters e, f, and g for the one- and two-color systems where ζ_F, η, γ, γ_1, and γ_2 are given in Table 1

	One-color system	Two-color system
e	$(\eta(1 + \gamma) + 1)(\eta\gamma + 1)$	$(\eta + 1)(\eta(\gamma_1 + 1) + \gamma_2 + 1)$
f	$\eta((\zeta_R - \zeta_F)(\eta\gamma + 1) + \eta(1 + \gamma) + 1)$	$(\eta\gamma_1 + \gamma_2)((\zeta_R - \zeta_F)(\eta + 1) + \eta(\gamma_1 + 1) + \gamma_2 + 1)$
g	$-\eta^2 \zeta_F$	$-(\eta\gamma_1 + \gamma_2)^2 \zeta_F$

and depend on the four dimensionless parameters ζ_R, ζ_F, η, and γ given in Table 1. The dimensionless steady concentrations are

$$\Psi_{1B}^0 = \zeta_F - \frac{\eta(1 + \gamma) + 1}{\eta} \Psi_{2F}^0 \quad (19)$$

$$\Psi_{2F}^0 = \frac{-f + \sqrt{f^2 - 4eg}}{2e} \quad (20)$$

with e, f, and g given in Table 2.

For the two-color system, eqn (17) and (20) remain unchanged and eqn (18) and (19) are substituted by

$$0 = -(\eta\gamma_1 + \gamma_2)\Psi_{1B}^0 - [\eta(\gamma_1 + 1) + \gamma_2 + 1]\Psi_{2F}^0 + (\eta\gamma_1 + \gamma_2)\zeta_F \quad (21)$$

$$\Psi_{1B}^0 = \zeta_F - \left(1 + \frac{\eta + 1}{\eta\gamma_1 + \gamma_2}\right) \Psi_{2F}^0 \quad (22)$$

where the expressions η, γ_1, and γ_2 are given in Table 1 and e, f, and g are given in Table 2.

3.2 First-order in- and out-of-phase concentration responses

We impose small oscillations of the illumination at the angular frequency ω. For the one-color system, we have

$$I(t) = I^0[1 + \varepsilon \sin(\omega t)] \quad (23)$$

with $\varepsilon \ll 1$. In the two-color system, we propose to either modulate one of the two light intensities $I_1(t)$ and $I_2(t)$ or anticorrelate both of them at the same angular frequency

$$I_1(t) = I_1^0[1 + n_1 \varepsilon \sin(\omega t)] \quad (24)$$

$$I_2(t) = I_2^0[1 + n_2 \varepsilon \sin(\omega t)] \quad (25)$$

where $(n_1,n_2) = (1,0)$ or $(0,1)$ for one modulated light intensity and $(n_1,n_2) = (1,-1)$ for two modulated light intensities. The oscillations of illumination lead to oscillations of the photochemical rate constants

$$k_{12}^{h\nu}(t) = k_{12}^0 + \varepsilon k_{12}^1 \sin(\omega t) \quad (26)$$

$$k_{21}^{h\nu}(t) = k_{21}^0 + \varepsilon k_{21}^1 \sin(\omega t) \quad (27)$$

For the one-color system, we have $k_{12}^1 = k_{12}^0$ and $k_{21}^1 = k_{21}^0$. For the two-color system, the expressions of k_{12}^1 and k_{21}^1 are obtained by introducing eqn (24) and (25) into eqn (9) and (10). We look for solutions of eqn (5) and (6) in the form of first-order expansions

$$1B = 1B^0 + \varepsilon 1B^1 \quad (28)$$

$$2F = 2F^0 + \varepsilon 2F^1, \quad (29)$$

valid for sufficiently small oscillation amplitudes ($\varepsilon \ll 1$). As previously, dimensionless variables and parameters are introduced. The dimensionless first-order amplitudes of concentration oscillation are given by

$$\Psi^1_{1B} = \frac{k^A_{+1}}{k^A_{-1}} 1B^1 \tag{30}$$

$$\Psi^1_{2F} = \frac{k^A_{+1}}{k^A_{-1}} 2F^1 \tag{31}$$

In addition to the notations given in Table 1, we introduce three other dimensionless parameters in Table 3.

Under the hypothesis of small oscillations, eqn (5) and (6) are linearized and written in matrix form

$$\frac{\mathrm{d}\mathcal{X}}{\mathrm{d}\delta} = \mathcal{M}\mathcal{X} + \mathcal{F}\sin(\theta\delta) \tag{32}$$

where the vectors are

$$\mathcal{X} = \begin{pmatrix} \Psi^1_{1B} \\ \Psi^1_{2F} \end{pmatrix} = \mathcal{X}^{\cos}\cos(\theta\delta) + \mathcal{X}^{\sin}\sin(\theta\delta) \tag{33}$$

$$\mathcal{F} = \begin{pmatrix} 0 \\ Nh\Psi^0_{2F} \end{pmatrix} \tag{34}$$

and the matrix is

$$\mathcal{M} = \begin{pmatrix} a & b \\ c & d \end{pmatrix} \tag{35}$$

with a, b, c, d, N, and h given in Table 4. Linearizing the dynamical equations in the limit of small forcing ensures that the analysis is generic: regardless of the specific nonlinearities of chemical kinetics, the following results can be applied. The linear system of equations for the dimensionless concentrations is easily solved in the eigenvector basis in which the equations are decoupled. The eigenvalues of $\mathcal{M}$ are given by

$$\lambda_\pm = \frac{a + d \pm \sqrt{(a-d)^2 + 4bc}}{2} \tag{36}$$

In the eigenvector basis, the dynamical state of the system is given by the vector

$$\mathcal{Y} = \mathcal{P}^{-1}\mathcal{X} \tag{37}$$

Table 3 Expression of the dimensionless parameters κ, θ, and δ for the one- and two-color systems

	One-color system	Two-color system
κ	$\frac{k^A_{-1}}{k^A_{21}}$	$\frac{k^A_{-1}}{\sigma_{21,2}I^0_2}$
θ	$\frac{\omega}{k^A_{21}}$	$\frac{\omega}{\sigma_{21,2}I^0_2}$
δ	$k^A_{21}t$	$\sigma_{21,2}I^0_2 t$

Table 4 Expression of a, b, c, d, N, and h for the one- and two-color systems, where κ is given in Table 3, Ψ^0_{1B} and Ψ^0_{2F} in eqn (19), (20) and (22), and ζ_R, ζ_F, η, γ, γ_1, and γ_2 in Table 1

	One-color system	Two-color system
a	$\kappa(2\Psi^0_{1B} + \Psi^0_{2F} - (\zeta_R + \zeta_F + 1))$	$\kappa(2\Psi^0_{1B} + \Psi^0_{2F} - (\zeta_R + \zeta_F + 1))$
b	$\kappa(\Psi^0_{1B} - \zeta_R)$	$\kappa(\Psi^0_{1B} - \zeta_R)$
c	$-\eta$	$-(\gamma_1\eta + \gamma_2)$
d	$-(\eta(\gamma + 1) + 1)$	$-(\eta(\gamma_1 + 1) + \gamma_2 + 1)$
N	1	$\lvert n_1 - n_2\rvert$
h	1	$\frac{\eta(\gamma_1 - \gamma_2)}{\eta\gamma_1 + \gamma_2}$

where $\mathcal{P}^{-1}$ is the inverse matrix of the change-of-basis matrix

$$\mathcal{P} = \begin{pmatrix} \frac{b}{\sqrt{(\lambda_+ - a)^2 + b^2}} & \frac{b}{\sqrt{(\lambda_- - a)^2 + b^2}} \\ \frac{\lambda_+ - a}{\sqrt{(\lambda_+ - a)^2 + b^2}} & \frac{\lambda_- - a}{\sqrt{(\lambda_- - a)^2 + b^2}} \end{pmatrix} \tag{38}$$

The coordinates of the vector $\mathcal{Y} = \mathcal{Y}^{\cos}\cos(\theta\delta) + \mathcal{Y}^{\sin}\sin(\theta\delta)$ obey the following decoupled equations

$$\frac{\mathrm{d}Y_\pm}{\mathrm{d}\delta} = \lambda_\pm Y_\pm + \alpha_\pm \sin(\theta\delta) \tag{39}$$

with

$$\begin{pmatrix} \alpha_+ \\ \alpha_- \end{pmatrix} = \mathcal{P}^{-1}\mathcal{F} \tag{40}$$

In the eigenvector basis, the solution is

$$Y^{\cos}_\pm = -\frac{\theta\alpha_\pm}{\theta^2 + \lambda_\pm{}^2} \tag{41}$$

$$Y^{\sin}_\pm = -\frac{\lambda_\pm\alpha_\pm}{\theta^2 + \lambda_\pm{}^2} \tag{42}$$

and in the initial basis, we find $\mathcal{X} = \mathcal{X}_+ + \mathcal{X}_-$ with $\mathcal{X}_\pm = \mathcal{P}\mathcal{Y}_\pm$. Bearing all above in mind, we obtain the expression of the dimensionless first-order amplitudes of concentration oscillations for **1B** and **2F**

$$\Psi^{1,\cos}_{1B} = \frac{N\theta b(a+d)h\Psi^0_{2F}}{\theta^4 + \theta^2(a^2 + d^2 + 2bc) + (ad - bc)^2} \tag{43}$$

$$\Psi^{1,\sin}_{1B} = \frac{Nb(ad - bc - \theta^2)h\Psi^0_{2F}}{\theta^4 + \theta^2(a^2 + d^2 + 2bc) + (ad - bc)^2} \tag{44}$$

$$\Psi^{1,\cos}_{2F} = -\frac{N\theta(\theta^2 + a^2 + bc)h\Psi^0_{2F}}{\theta^4 + \theta^2(a^2 + d^2 + 2bc) + (ad - bc)^2} \tag{45}$$

$$\Psi^{1,\sin}_{2F} = \frac{N[\theta^2(2a + d) - a(ad - bc)]h\Psi^0_{2F}}{\theta^4 + \theta^2(a^2 + d^2 + 2bc) + (ad - bc)^2} \tag{46}$$

where the parameters a, b, c, d, N, and h are given in Table 4, the dimensionless steady concentration Ψ^0_{2F} is given in eqn (20), and the dimensionless frequency θ is given in Table 3. The expressions of the dimensionless first-order amplitudes for **1F**

and **R** are obtained using the law of conservation of matter given in eqn (3) and (4).

4 Analytical approach to the optimization of the out-of-phase concentration responses

We wish to introduce a highly selective dynamic titration protocol discriminating the titrated species by the rate constants of their reaction with the photoswitchable reagent. We are concerned with identifying both the observable and the experimental conditions which are the most favorable to fulfill this goal.

The expressions (43)–(46) give access to the amplitudes of the in- and out-of-phase terms of the modulated concentrations. In this paper, we adopt the out-of-phase amplitude of the concentration oscillations to build the observable of a dynamic titration protocol. We focus on the behavior of **1B** among the species involved in the reactions (1) and (2). However, for the sake of completeness, we will also mention the remarkable properties of the species **1F** and **2F**, which could be useful in similar systems. First of all, the out-of-phase amplitude of the concentration oscillations of **1B** is proportional to the total concentration of the titrated species. Then, it is expected to present a band-pass filter behavior for species engaged in the set of reactions (1) and (2), which should facilitate their discrimination. Indeed, species not affected by photochemical reactions do not respond to illumination modulation, whereas light fast-responding species respond in phase with the modulated illumination.

For the one-color system, the first-order amplitudes of the concentration oscillations are controlled by six dimensionless parameters η, γ, ζ_R, ζ_F, κ, and θ, instead of the nine initially introduced parameters, σ_{12}, σ_{21}, I^0, R_{tot}, F_{tot}, k^{Δ}_{-1}, ω, k^{Δ}_{+1}, and k^{Δ}_{21}. For the two-color system, the first-order amplitudes are controlled by seven dimensionless parameters η, γ_1, γ_2, ζ_R, ζ_F, κ, and θ, instead of the eleven initially introduced parameters, $\sigma_{12,1}$, $\sigma_{21,1}$, $\sigma_{12,2}$, $\sigma_{21,2}$, I^0_1, I^0_2, R_{tot}, F_{tot}, k^{Δ}_{-1}, ω, and k^{Δ}_{+1}.

It is essential to recognize the parameters which can be tuned in a titration protocol and the discriminative parameters which are specific to each targeted species. The scaled intensity of illumination, η, and the ratios of the isomerization cross-sections (γ for the one-color system or γ_1 and γ_2 associated with the light intensities I_1 and I_2 for the two-color system) characterize the kinetics of the reversibly photoswitchable reagent. The ratio of the complexation rate constant and photoswitching rate constant, κ, and the thermodynamic dissociation constant, $K_{\mathrm{d}} = k^{\Delta}_{-1}/k^{\Delta}_{+1}$, are associated with the kinetics of the complexation of the targeted species. The parameters γ or γ_1 and γ_2 are imposed by the photoswitchable reagent and κ is set by the couple formed by the photoswitchable reagent and the titrated species. In contrast, the normalized concentration ζ_R of the targeted species, the normalized concentration ζ_F of the photoswitchable reagent, the scaled frequency θ of the forced oscillations, and the scaled intensity of illumination η are monitored by the experimentalist and called control parameters.

4.1 Optimization of $\Psi^{1,\cos}_{1B}$ with respect to the control parameters

In this section, we investigate whether the scaled out-of-phase amplitude of concentration oscillations $\Psi^{1,\cos}_{1B}$ exhibits extrema with respect to the control parameters. We determine analytical expressions of the control parameters associated with an extremum, further referred to as resonant parameter values labeled by an exponent R.

We first optimize $\Psi^{1,\cos}_{1B}$ with respect to the scaled frequency of the forced oscillations, θ. Using eqn (43), we find that $\Psi^{1,\cos}_{1B}$ exhibits a single optimum for a positive value of θ given by

$$\theta^R = \sqrt{\frac{-\left(a^2+d^2+2bc\right)+\sqrt{\left(a^2+d^2+2bc\right)^2+12(ad-bc)^2}}{6}} \tag{47}$$

Then, we consider optimizing $\Psi^{1,\cos}_{1B}(\theta^R)$ with respect to the scaled intensity of illumination, η. The exact expression of η at the optimum could not be extracted in the general case, but it can be analytically retrieved in two experimentally relevant situations: (i) the complexation reaction (2) is much faster than the photoisomerization (1), *i.e.* $\kappa \gg 1$, which amounts to applying the quasi-steady state approximation to species **1B**, (ii) the reaction (1) is much faster than reaction (2), *i.e.* $\kappa \ll 1$, which amounts to applying the quasi-steady state approximation to species **2F**. To leading order, we find

$$\theta^R \simeq \left|\frac{ad-bc}{a}\right|, \quad \kappa \gg 1 \tag{48}$$

$$\theta^R \simeq \left|\frac{ad-bc}{d}\right|, \quad \kappa \ll 1 \tag{49}$$

Interestingly, both limit cases lead to the same value of the out-of-phase amplitude for $\theta = \theta^R$

$$\Psi^{1,\cos}_{1B}\left(\theta^R\right) \simeq \frac{N|b|\Psi^0_{2F}}{2|ad-bc|} \tag{50}$$

Although the expression does not depend on κ, it is nevertheless not valid for $\kappa \simeq 1$. The expression of $\Psi^{1,\cos}_{1B}(\theta^R)$ is still not sufficiently simplified to determine the resonant expression of η. Consequently, we further restrict our analysis to two concentration regimes, $\zeta_R \ll \zeta_F$ and $\zeta_R \gg \zeta_F$, leading to symmetrical expressions obtained by exchanging ζ_R and ζ_F. In order to cover both regimes of approximation, we introduce $\zeta_{\max}$ and $\zeta_{\min}$ for $\sup(\zeta_R,\zeta_F)$ and $\inf(\zeta_R,\zeta_F)$, respectively, and obtain for the one-color system

$$\Psi^{1,\cos}_{1B}\left(\theta^R\right) \simeq \frac{N\eta\zeta_{\min}\zeta_{\max}}{2\left[\eta(\gamma(\zeta_{\max}+1)+1)+\zeta_{\max}+1\right]^2} \tag{51}$$

We find a single optimum with respect to η for

$$\eta^R \simeq \frac{\zeta_{\max}+1}{\gamma(\zeta_{\max}+1)+1} \tag{52}$$

and the out-of-phase amplitude optimized with respect to θ and η is

$$\Psi_{1B}^{1,\cos}(\theta^R,\eta^R) \simeq \frac{N\zeta_{\min}\zeta_{\max}}{8(\gamma(\zeta_{\max}+1)+1)(\zeta_{\max}+1)} \quad (53)$$

Similarly, we find for the two-color system

$$\Psi_{1B}^{1,\cos}(\theta^R) \simeq \frac{N(\gamma_1-\gamma_2)\eta\zeta_{\min}\zeta_{\max}}{2[\eta(\zeta_{\max}+\gamma_1+1)+\zeta_{\max}+\gamma_2+1]^2} \quad (54)$$

$$\eta^R \simeq \frac{\zeta_{\max}+\gamma_2+1}{\zeta_{\max}+\gamma_1+1} \quad (55)$$

$$\Psi_{1B}^{1,\cos}(\theta^R,\eta^R) \simeq \frac{N(\gamma_1-\gamma_2)\zeta_{\min}\zeta_{\max}}{8(\zeta_{\max}+\gamma_1+1)(\zeta_{\max}+\gamma_2+1)} \quad (56)$$

An optimum of $\Psi_{1B}^{1,\cos}(\theta^R,\eta^R)$ with respect to the maximum $\zeta_{\max}$ can be found for the resonant value

$$\zeta_{\max}^R \simeq \sqrt{\frac{\gamma+1}{\gamma}} \quad (57)$$

leading to

$$\Psi_{1B}^{1,\cos}(\theta^R,\eta^R,\zeta_{\max}^R) \simeq \frac{N\zeta_{\min}}{8\sqrt{\gamma}(2\sqrt{\gamma(\gamma+1)}+2\gamma+1)} \quad (58)$$

For the two-color system, we derive

$$\zeta_{\max}^R \simeq \sqrt{(\gamma_1+1)(\gamma_2+1)} \quad (59)$$

$$\Psi_{1B}^{1,\cos}(\theta^R,\eta^R,\zeta_{\max}^R) \simeq \frac{N(\gamma_1-\gamma_2)\zeta_{\min}}{8\left(\sqrt{\gamma_1+1}+\sqrt{\gamma_2+1}\right)^2} \quad (60)$$

4.2 Optimization of $\Psi_{1F}^{1,\cos}$ and $\Psi_{2F}^{1,\cos}$ with respect to the control parameters

An analogous approach is adopted to find approximate expressions for the out-of-phase amplitudes $\Psi_{1F}^{1,\cos}$ and $\Psi_{2F}^{1,\cos}$ of the modulation of **1F** and **2F** concentrations and the associated resonance conditions. Depending on the rates of complexation with respect to photoisomerization described by the κ parameter, different behaviors are obtained. In the case of a slower complexation ($\kappa \ll 1$), we find not one but three extrema in the (θ,η) parameter space. The resonant parameter values associated with a nonvanishing amplitude obey

$$\theta^{R_1} \simeq |d|, \quad \theta^{R_2} \simeq \left|\frac{ad-bc}{d}\right| \quad (61)$$

The first resonance R_1 is associated with the behavior of the photoisomerization subsystem given in eqn (1).[11,53,54] Indeed, in a two-state exchange, the resonant value of the angular frequency is equal to the inverse of the relaxation time of the reaction. Here, the dimensionless parameter d corresponds to $k_{12}^0 + k_{21}^0 + k_{21}^A$ for the scaled parameters. The second resonance R_2 associated with species **1F** and **2F** leads to the same condition (eqn (49)) as for species **1B**.

In the case of a slower photoisomerization ($\kappa \gg 1$), $\Psi_{1F}^{1,\cos}$, and $\Psi_{2F}^{1,\cos}$ exhibit a single extremum at

$$\theta^R \simeq \left|\frac{ad-bc}{a}\right| \quad (62)$$

which corresponds to the resonance condition associated with **1B** given in eqn (48).

5 Numerical approach to the optimization of $1B^{1,\cos}$ with respect to the control parameters

5.1 Behavior in the space of the control parameters

The analytical calculations rely on approximations and provide partial knowledge of the behaviors of the out-of-phase amplitudes. Whereas the analytical θ^R expression is exact, the corresponding η^R expression is not explicit when the rate constants associated with reactions (1) and (2) are comparable ($\kappa \simeq 1$) or when the dimensionless concentrations ζ_R and ζ_F take similar values. In order to validate the approximations, we compare the analytical predictions with numerical solutions. We determine the parameter values associated with optima of the scaled out-of-phase amplitude.

Fig. 1 displays the numerically computed dependence of the out-of-phase amplitude of the **1B** concentration on the control parameters. Experimentally relevant values of γ or γ_1 and γ_2 have been chosen. The **1B** concentration is scaled by its upper value $\min(R_{\text{tot}},F_{\text{tot}})$. Fig. 1a and b evidence the predicted resonant behavior in the (θ,η) space and underline the relevance of the analytical resonant conditions. For the one-color system, the analytical predictions lead to (θ^R = 0.69, η^R = 0.92) while the numerical computations result in (θ^R = 0.69, η^R = 0.79). Similarly, for the two-color system, we analytically obtain (θ^R = 0.41, η^R = 1.43) and numerically find (θ^R = 0.41, η^R = 1.44). For a fixed value of $\zeta_{\min}$, Fig. 1c and d validate the presence of an optimum with respect to $\zeta_{\max}$ for both the one- and two-color systems. The observable needs to be proportional to ζ_R in order to be used in a titration protocol. Hence, ζ_R cannot be imposed by resonance conditions. In the following, we consider the approximation $\zeta_F \gg \zeta_R$ and the resonance with respect to ζ_F. Fig. 1c and d point out the relevance of the analytic expressions to locate the resonance. Specifically, for the one-color system and ζ_R = 0.1, we analytically find ζ_F^R = 1.41 while ζ_F^R = 1.60 is numerically computed. For the two-color system we analytically obtain ζ_F^R = 2.63 to be compared to the numerical value ζ_F^R = 2.87.

The resonant behavior in the (θ,η) space is robust. It is observed for all the values of γ or γ_1 and γ_2 (*e.g.* for any type of photoswitching behavior of the photoswitchable reagent) and of κ (*e.g.* for any ratio of the complexation rate constant and photoswitching rate constant). The resonance phenomenon in the (ζ_R,ζ_F) space is robust as well. For all the investigated values of κ and γ, $1B^{1,\cos}(\theta^R,\eta^R)/\min(R_{\text{tot}},F_{\text{tot}})$ exhibits a maximum $\zeta_F^R > 1$ with respect to ζ_F when $\zeta_R < 1$.

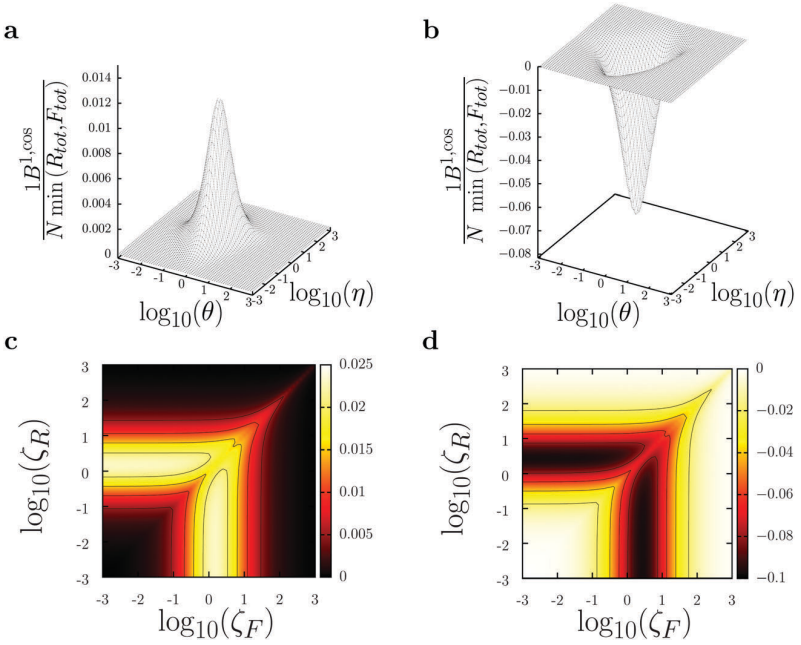

Fig. 1 Numerically computed dependence of the scaled out-of-phase amplitude of the **1B** concentration on the control parameters for the (a and c) one-color system (γ = 1) and (b and d) two-color system (γ_1 = 1/5, γ_2 = 5). (a and b) Dependence of the normalized out-of-phase amplitude $1B^{1,\cos}/N \min(R_{\text{tot}},F_{\text{tot}})$ on the dimensionless angular frequency θ and intensity of illumination η for fixed values of ζ_R = 0.1 (dimensionless concentration of the titrated species), ζ_F = 10 (dimensionless concentration of the photoswitchable reagent), and κ = 0.1 (ratio of complexation and isomerization rate constants). (c and d) Dependence of $1B^{1,\cos}(\theta^R,\eta^R)/N \min(R_{\text{tot}},F_{\text{tot}})$ on ζ_R and ζ_F, for a fixed value of κ = 0.1.

5.2 Behavior with respect to the kinetically fixed parameters

5.2.1 One-color system. We address the case of photoswitchable reagents whose isomerization is driven at one wavelength and study the impact of the parameters γ and κ on the resonance of the out-of-phase amplitude $1B^{1,\cos}$.

We first examine the significance of the photoswitching features expressed by γ on the position of the resonance of $1B^{1,\cos}$ in the (θ,η) space (see Fig. 1a). As shown in Fig. 2a, θ^R does not significantly depend on γ. In contrast, η^R strongly depends on γ (Fig. 2b). In particular, for large γ, η^R is proportional to $1/\gamma$. Then, we analyze the role of γ on the resonance of $1B^{1,\cos}$ in ζ_F for fixed $\zeta_R < 1$ (Fig. 2c). For small γ, ζ_F^R is proportional to $1/\sqrt{\gamma}$ but converges to 1 for large γ. In Fig. S1a–c of the ESI,† we report on the deviations between the analytically and numerically computed values of θ^R, η^R, and ζ_F^R, which originate from the expansion used to derive eqn (52) and (57). As shown in Fig. S1a of ESI,† the introduction of the approximate values of η^R and ζ_F^R into the exact expression of θ^R given in eqn (47) induces a difference between the values retrieved from analytical and numerical computations. It is worth noting that the observed deviations are small compared to the width of the resonance peak where the amplitude drops to half of the resonance value. As a result, the analytical predictions are fully exploitable.

Finally, we study the impact of γ on the amplitude of the resonance of $1B^{1,\cos}(\theta^R,\eta^R,\zeta_F^R)$. Fig. 3a and eqn (58) show that $1B^{1,\cos}(\theta^R,\eta^R,\zeta_F^R)/\min(R_{\text{tot}},F_{\text{tot}})$ is a decreasing function of γ and essentially vanishes for $\gamma > 1$. The maximal $1B^{1,\cos}$ value reaches 14% of $\min(R_{\text{tot}},F_{\text{tot}})$ and 25% of the steady state value $1B^0$.

We examine the effect of the complexation kinetics expressed by the parameter κ on the resonance. As shown in Fig. 2d, θ^R is proportional to κ at small κ values, whereas it does not significantly depend on κ at large κ. This observation was expected from eqn (48) and (49). As anticipated from eqn (52) and (57), η^R and ζ_F^R are essentially independent of κ (Fig. 2e and f). However, a second-order dependence of ζ_F^R on κ is numerically observed when $\gamma \ll 1$. Fig. S1d–f of the ESI,† show that the deviations between the analytically and numerically computed values of θ^R, η^R and ζ_F^R can be neglected.

The out-of-phase amplitude $1B^{1,\cos}(\theta^R,\eta^R,\zeta_F^R)/\min(R_{\text{tot}},F_{\text{tot}})$ does not significantly depend on κ as illustrated in Fig. 3b and eqn (58).

5.2.2 Two-color system. For a two-color system, the kinetic parameters to be considered are γ_1, γ_2, and κ. The choice of the dimensionless parameters has introduced a symmetry breaking in a system initially symmetric with respect to the permutations between the light intensities I_1^0 and I_2^0 and the isomerization cross-sections $(\sigma_{12,1},\sigma_{21,1})$ and $(\sigma_{12,2},\sigma_{21,2})$. It is worth noting that the sign of the amplitude $1B^{1,\cos}$ is imposed by the sign of $\gamma_1 - \gamma_2$. We discuss the results in the case $\gamma_1 < \gamma_2$ leading to a negative amplitude.

We study the impact of the ratios γ_1 and γ_2 of the isomerization cross-sections corresponding to the light intensities I_1^0 and

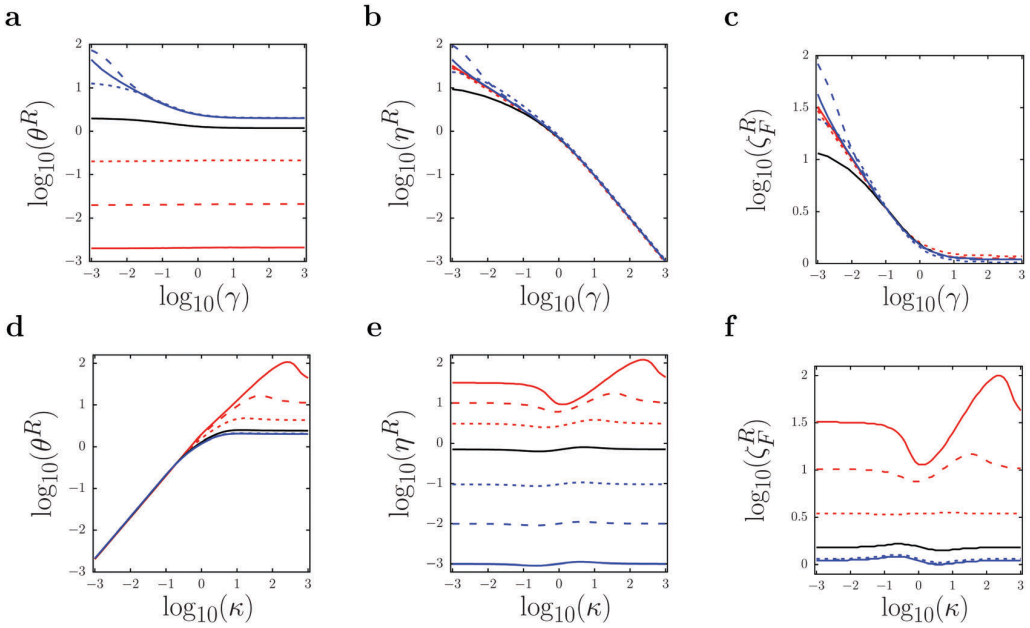

Fig. 2 One-color system. Dependence of the resonant values of the control parameters on γ (ratio of backward and forward photochemical isomerization rate constants) and κ (ratio of complexation and isomerization rate constants). Dependence of (a) θ^R, (b) η^R, (c) ζ_F^R on γ for several fixed values of κ equal to 10^{-3} (red solid line), 10^{-2} (red dashed line), 10^{-1} (red dotted line), 1 (black solid line), 10^1 (blue dotted line), 10^2 (blue dashed line), 10^3 (blue solid line). (d–f) Same caption as in (a–c) by exchanging γ and κ. The numerical computations are performed for a fixed value of ζ_R = 0.1 (dimensionless concentration of the titrated species).

I_2^0 on the position of the resonance $1B^{1,\cos}$ in the control parameter space. Analytical expressions given in eqn (47), (55) and (59) and numerical results both lead to the following conclusions. For $\kappa \gg 1$, θ^R is an increasing function of γ_1 and γ_2, whereas θ^R does not depend on γ_1 and γ_2 for $\kappa \ll 1$. The resonant value η^R is a decreasing function of γ_1 and an increasing function of γ_2. We find that ζ_F^R is an increasing function of γ_1 and γ_2. Fig. 4a–c show the numerical results in the particular case $\gamma_2 = 1/\gamma_1$ which corresponds to reasonable experimental conditions. The comparison between the analytical predictions and the numerical results is made precise in Fig. S2a–c of the ESI,† for $\gamma_2 = 1/\gamma_1$ The analytical results can be used with a satisfying accuracy in a wide parameter range.

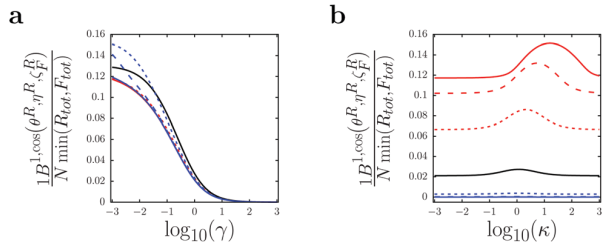

Fig. 3 One-color system. (a) Dependence of the resonant out-of-phase amplitude of oscillations of concentration $1B^{1,\cos}(\theta^R,\eta^R,\zeta_F^R)/N\min(R_{tot},F_{tot})$ on γ for ζ_R = 0.1 and for several fixed values of κ equal to 10^{-3} (red solid line), 10^{-2} (red dashed line), 10^{-1} (red dotted line), 1 (black solid line), 10^1 (blue dotted line), 10^2 (blue dashed line), 10^3 (blue solid line). (b) Same caption as in (a) by exchanging γ and κ.

The impact of γ_1 and γ_2 on the resonance of $1B^{1,\cos}(\theta^R,\eta^R,\zeta_F^R)$ is shown in Fig. 5a in the particular case $\gamma_2 = 1/\gamma_1$. The amplitude is an increasing function of $|\gamma_1 - \gamma_2|$ and reaches a plateau for $|\gamma_1 - \gamma_2| \gg 100$, according to eqn (60). The largest $|1B^{1,\cos}|$ reaches 12.5% of $\min(R_{tot},F_{tot})$ for a single modulated light intensity and 25% of $\min(R_{tot},F_{tot})$ for two modulated light intensities. Similarly, $|1B^{1,\cos}|$ reaches 25% of the steady state value $1B^0$ for a single modulated light intensity and 50% of the steady state value $1B^0$ for two modulated light intensities.

The dependences of θ^R, η^R, and ζ_F^R on κ are similar to the ones that have already been discussed in a one-color system. Fig. 4a–c display the numerical results for $\gamma_2 = 1/\gamma_1$. Fig. S2d–f of the ESI,† show that the discrepancies between the analytically and numerically computed values of θ^R, η^R, and ζ_F^R are small.

The amplitude $1B^{1,\cos}(\theta^R,\eta^R,\zeta_F^R)$ is nearly independent of κ, as displayed in Fig. 5b and in eqn (60).

The behaviors of the one- and two-color systems are similar. However for a two-color system with two modulated light intensities, the optimized amplitude can be doubled with respect to the one of the one-color system.

6 Protocol for light-assisted dynamic titration

The preceding results can be used to propose a highly selective dynamic titration protocol, able to discriminate components **R** in a mixture by the rate constants k_{+1}^A and k_{-1}^A of their reaction with the photoswitchable reagent, viewed as the titrating

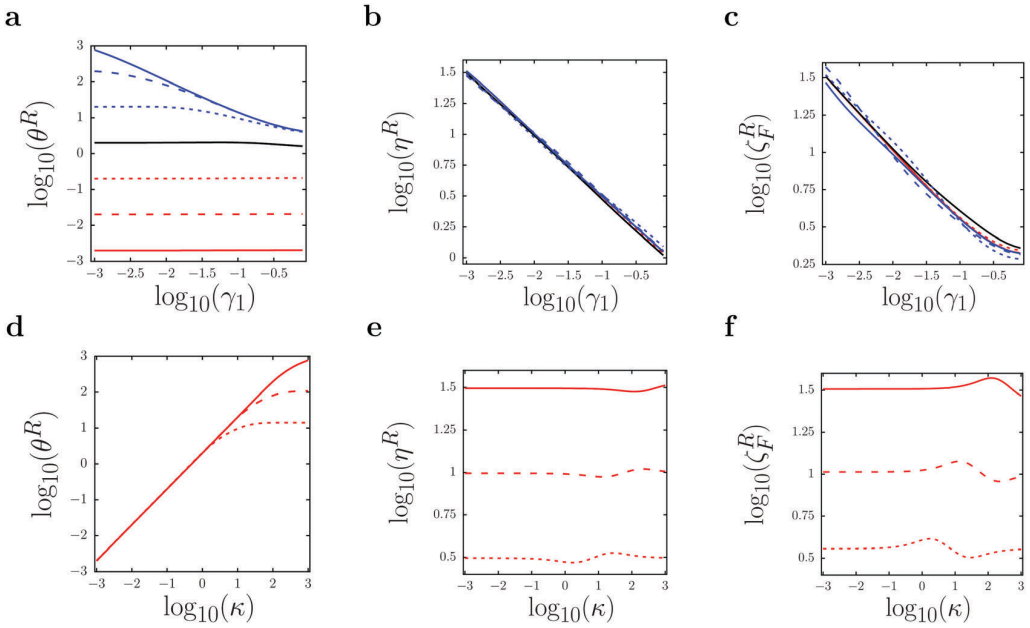

Fig. 4 Two-color system. Dependence of the resonant values of the control parameters on γ_1 (ratio of forward and backward photochemical isomerization rate constants corresponding to the light intensity I_1^0) and κ (ratio of complexation and isomerization rate constants). Dependence of (a) θ^R, (b) η^R, (c) ζ_F^R on γ_1 for several fixed values of κ equal to 10^{-3} (red solid line), 10^{-2} (red dashed line), 10^{-1} (red dotted line), 1 (black solid line), 10^1 (blue dotted line), 10^2 (blue dashed line), 10^3 (blue solid line). Dependence of (d) θ^R, (e) η^R, (f) ζ_F^R on κ for several fixed values of γ_1 equal to 10^{-3} (red solid line), 10^{-2} (red dashed line), 10^{-1} (red dotted line). The numerical computations are performed for a fixed value of ζ_R = 0.1 (dimensionless concentration of the titrated species) and with variable $\gamma_2 = 1/\gamma_1$.

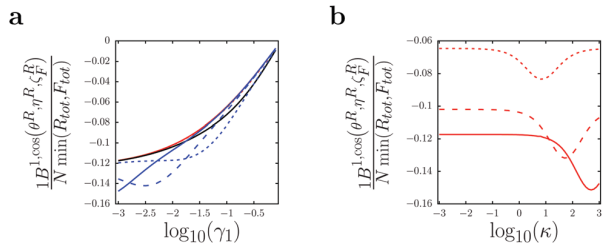

Fig. 5 Two-color system. (a) Dependence of the resonant out-of-phase amplitude of oscillation of concentration $1B^{1,\cos}(\theta^R,\eta^R,\zeta_F^R)/N\min(R_{\text{tot}},F_{\text{tot}})$ on γ_1 for several fixed values of κ equal to 10^{-3} (red solid line), 10^{-2} (red dashed line), 10^{-1} (red dotted line), 1 (black solid line), 10^1 (blue dotted line), 10^2 (blue dashed line), 10^3 (blue solid line). (b) Dependence of the resonant out-of-phase amplitude on κ for several fixed values of γ_1 equal to 10^{-3} (red solid line), 10^{-2} (red dashed line), 10^{-1} (red dotted line). The numerical computations are performed for a fixed value of ζ_R = 0.1 and with variable $\gamma_2 = 1/\gamma_1$.

reagent. Focussing on a targeted component, we suggest to tune the control parameters and maximize the amplitude of the out-of-phase response of its associated bound state **1B**. Indeed, resonant or optimized values of the parameters ζ_R, ζ_F, θ, and η provide a significant observable for **1B** proportional to the total concentration R_{tot} of the targeted species while eliminating the contributions from the other mixture components. According to Tables 1 and 3, choosing ζ_R, ζ_F, θ, and η imposes constraints on the concentrations R_{tot} and F_{tot} of the targeted component and the titrating reagent, the angular frequency ω of the forced illumination oscillations, and the illumination intensities I^0 in a one-color system and I_1^0 and I_2^0 in a two-color system. In a user-friendly approach, we derive the optimized expressions of the dimensioned control parameters and design an experimental titrating protocol.

6.1 Setting the concentrations of the targeted component and the titrating reagent

We assume that the total concentration R_{tot} of the target cannot be tuned but is significantly lower than the tunable total concentration of the photoswitchable reagent F_{tot}. We further assume that $R_{\text{tot}} \ll K_{\text{d}}$ which leads to simpler expressions of the illumination control parameters presented in the following.

We use eqn (57) and (59) to relate the resonant value F_{tot}^R to the dimensioned parameters of the targeted component. We obtain for the one-color system

$$F_{\text{tot}}^R \simeq K_{\text{d}}\sqrt{1+\frac{\sigma_{12}}{\sigma_{21}}} \tag{63}$$

and for the two-color system

$$F_{\text{tot}}^R \simeq K_{\text{d}}\sqrt{\left(1+\frac{\sigma_{12,1}}{\sigma_{21,1}}\right)\left(1+\frac{\sigma_{12,2}}{\sigma_{21,2}}\right)} \tag{64}$$

where $(\sigma_{12}, \sigma_{21})$ and $(\sigma_{12,1}, \sigma_{21,1}, \sigma_{12,2}, \sigma_{21,2})$ are specific to the photoswitchable reagent and $K_{\text{d}} = k_{-1}^A/k_{+1}^A$ is the thermodynamic dissociation constant specific to the couple formed by the photoswitchable reagent and the targeted component.

6.2 Setting the illumination parameters

The control parameters associated with illumination are the frequency ω and the light intensities, I^0 in a one-color system and I_1^0 and I_2^0 in a two-color system.

6.2.1 One-color system. Using eqn (48), (49) and (52), valid in the approximation $R_{\mathrm{tot}} \ll F_{\mathrm{tot}}$, we find the following resonant values for the one-color system

$$\omega^R \simeq k_{21}^{\mathcal{A}}\left(1+\sqrt{1+\frac{\sigma_{12}}{\sigma_{21}}}\right), \quad \text{for} \quad k_{-1}^{\mathcal{A}} \gg k_{21}^{\mathcal{A}} \tag{65}$$

$$\omega^R \simeq 2k_{-1}^{\mathcal{A}}, \quad \text{for } k_{-1}^{\mathcal{A}} \ll k_{21}^{\mathcal{A}} \tag{66}$$

$$I^{0,R} \simeq \frac{k_{21}^{\mathcal{A}}}{\sqrt{\sigma_{21}(\sigma_{12}+\sigma_{21})}} \tag{67}$$

Only eqn (66) links the resonant value of the angular frequency with the specific kinetics of the target. The other resonance conditions on the illumination parameters only involve the kinetics of the titrating reagent, which is common to all the titrated species. Extracted from eqn (58), the optimized amplitude is given by

$$1B^{1,\cos}\left(\omega^R, I^{0,R}, F_{\mathrm{tot}}^R\right) \simeq \frac{R_{\mathrm{tot}}}{8\sqrt{\frac{\sigma_{21}}{\sigma_{12}}}\left(2\sqrt{\frac{\sigma_{21}}{\sigma_{12}}\left(\frac{\sigma_{21}}{\sigma_{12}}+1\right)}+2\frac{\sigma_{21}}{\sigma_{12}}+1\right)} \tag{68}$$

6.2.2 Two-color system. In a two-color system, we use the resonant values of the dimensionless parameters given in eqn (48), (49) and (55), valid in the approximation $R_{\mathrm{tot}} \ll F_{\mathrm{tot}}$ and obtain

$$\omega^R \simeq \sqrt{\sigma_{21,2}\left(\sigma_{12,2}+\sigma_{21,2}\right)}\left(\sqrt{1+\frac{\sigma_{12,1}}{\sigma_{21,1}}} + \sqrt{1+\frac{\sigma_{12,2}}{\sigma_{21,2}}}\right)I_2^0, \quad \text{for} \quad k_{-1}^{\mathcal{A}} \gg \sigma_{21,2}I_2^0 \tag{69}$$

$$\omega^R \simeq 2k_{-1}^{\mathcal{A}}, \quad \text{for } k_{-1}^{\mathcal{A}} \ll \sigma_{21,2}I_2^0 \tag{70}$$

$$\left(\frac{I_1^0}{I_2^0}\right)^R \simeq \sqrt{\frac{(\sigma_{12,2}+\sigma_{21,2})\sigma_{21,2}}{(\sigma_{12,1}+\sigma_{21,1})\sigma_{21,1}}} \tag{71}$$

As for the one-color system, only the resonant value of the angular frequency is related to the kinetics of the target according to eqn (70). The optimized amplitude is deduced from eqn (60)

$$1B^{1,\cos}\left(\omega^R, \left(I_1^0/I_2^0\right)^R, F_{\mathrm{tot}}^R\right) \simeq \frac{NR_{\mathrm{tot}}\left(\frac{\sigma_{12,1}}{\sigma_{21,1}}-\frac{\sigma_{12,2}}{\sigma_{21,2}}\right)}{8\left(\sqrt{\frac{\sigma_{12,1}}{\sigma_{21,1}}+1}+\sqrt{\frac{\sigma_{12,2}}{\sigma_{21,2}}+1}\right)^2} \tag{72}$$

Choosing to scale the light intensity I_1^0 and the angular frequency ω by the light intensity I_2^0 is arbitrary, the roles of I_1^0 and I_2^0 being symmetrical. Interestingly, optimization of the illumination parameters imposes two conditions whereas the experimentalist has three degrees of freedom, I_1^0, I_2^0, and ω. The method is therefore very flexible. The resonance condition on the illumination intensities does not independently set I_1^0 and I_2^0, but sets the ratio $\left(\frac{I_1^0}{I_2^0}\right)^R$. In the case of fast complexation compared to isomerization, increasing the illumination intensities leads to increasing the angular frequency, whereas the angular frequency remains unchanged otherwise. In addition, the choice of I_2^0 determines the rate-limiting step: small I_2^0 values lead to slower photoisomerization and large I_2^0 values lead to slower complexation.

Comparing $k_{-1}^{\mathcal{A}}$ to $k_{21}^{\mathcal{A}}$ in the case of the one-color system and to $\sigma_{21,2}I_2^0$ in the case of the two-color system amounts to comparing the relaxation times of photoisomerization (reaction (1)) and complexation (reaction (2)). The expressions of the resonant angular frequency given in eqn (65) and (69) are obtained when photoisomerization is the rate-limiting step. Conversely, eqn (66) and (70) are obtained when complexation is the rate-determining step. Eqn (65) and (66) for the one-color system can be written

$$\omega^R \simeq k_{21}^{\mathcal{A}} + I^{0,R}(\sigma_{12}+\sigma_{21}), \quad \text{for } k_{-1}^{\mathcal{A}} \gg k_{21}^{\mathcal{A}} \tag{73}$$

$$\omega^R \simeq k_{+1}^{\mathcal{A}}1F^0(I^{0,R},F_{\mathrm{tot}}^R) + k_{-1}^{\mathcal{A}}, \quad \text{for } k_{-1}^{\mathcal{A}} \ll k_{21}^{\mathcal{A}} \tag{74}$$

and eqn (65) and (66) for the two-color system lead to

$$\omega^R \simeq \left(\left(\sigma_{12,1}+\sigma_{21,1}\right)\left(\frac{I_1^0}{I_2^0}\right)^R + \left(\sigma_{12,2}+\sigma_{21,2}\right)\right)I_2^0, \quad \text{for } k_{-1}^{\mathcal{A}} \gg \sigma_{21,2}I_2^0 \tag{75}$$

$$\omega^R \simeq k_{+1}^{\mathcal{A}}1F^0((I_1^0/I_2^0)^R, F_{\mathrm{tot}}^R) + k_{-1}^{\mathcal{A}}, \quad \text{for } k_{-1}^{\mathcal{A}} \ll \sigma_{21,2}I_2^0 \tag{76}$$

Hence, in the two limit cases, the resonant angular frequency is equal to the inverse of the relaxation time of the rate-limiting step, exactly as in a chemical scheme with a single step.[11,53,54] Moreover, when complexation is slower than isomerization, the value of the angular frequency, tuned to discriminate the targeted component, is the same in the two-color system (eqn (70)) as in the one-color system (eqn (66)).

It is worth noting that the resonance conditions setting light intensity $I^{0,R}$ or $(I_1^0/I_2^0)^R$ according to eqn (67) and (71) impose

$$k_{12}^0(I^{0,R})1F^0(I^{0,R},F_{\mathrm{tot}}^R) \simeq k_{21}^0(I^{0,R})2F^0(I^{0,R},F_{\mathrm{tot}}^R) \tag{77}$$

for the one-color system and

$$k_{12}^0((I_1^0/I_2^0)^R)1F^0((I_1^0/I_2^0)^R,F_{\mathrm{tot}}^R) \simeq k_{21}^0((I_1^0/I_2^0)^R)2F^0((I_1^0/I_2^0)^R,F_{\mathrm{tot}}^R) \tag{78}$$

for the two-color system, where the rate constants are given in eqn (11)–(14) and the steady concentrations in eqn (19), (20) and (22) for resonant values of light intensity and total concentration of the photoswitchable reagent. Hence, the photoisomerization reaction is at equilibrium when the control parameters are resonant. Similarly, the resonance conditions setting the

concentration F^R_{tot} of the photoswitchable reagent according to eqn (63) and (64) lead to

$$1F^0(I^{0,R},F^R_{tot}) \simeq K_d \quad (79)$$

$$1B^0(I^{0,R},F^R_{tot}) \simeq R^0(I^{0,R},F^R_{tot}) \simeq R_{tot}/2 \quad (80)$$

for the one-color system and

$$1F^0((I^0_1/I^0_2)^R,F^R_{tot}) \simeq K_d \quad (81)$$

$$1B^0((I^0_1/I^0_2)^R,F^R_{tot}) \simeq R^0((I^0_1/I^0_2)^R,F^R_{tot}) \simeq R_{tot}/2 \quad (82)$$

for the two color system. Thus, the complexation reaction is at equilibrium for resonant values of the control parameters.

In summary, the optimized conditions bring out specific links between the kinetics of the target and the control parameters. From eqn (63) and (67) and eqn (64) and (71), it comes out that both the unbinding rate constant k^A_{-1} and the thermodynamic dissociation constant $K_d = k^A_{-1}/k^A_{+1}$ are discriminating parameters for both the one- and two-color systems. In both cases, k^A_{-1} only affects the choice of the angular frequency ω^R while K_d affects the choice of the concentration F^R_{tot} of the titrating reagent. From eqn (68) and (72), the optimized out-of-phase is proportional to the total concentration of the titrated species R_{tot}.

6.3 The light-assisted dynamic titration in action

In view of the preceding results, we design a protocol relevant to discriminate a targeted species **R** against interfering compounds. The choice of the titrating species sets the photoisomerization cross-sections and the thermal isomerization rate constant. For both the one- and two-color systems, we propose a titrating protocol using k^A_{+1} and k^A_{-1} as discriminating parameters, for a given choice of the titrating reagent. The total concentration of the titrating species F^R_{tot} is set according to eqn (63) and (64): the ratio of rate constants, $K_d = k^A_{-1}/k^A_{+1}$, of the targeted species specifies the total concentration F^R_{tot}. The angular frequency ω^R is set according to either eqn (65) and (69) or eqn (66) and (70), depending on the value of the unbinding rate constant k^A_{-1}. The light intensity $I^{0,R}$ or the ratio $(I^0_1/I^0_2)^R$ is set to the resonant value given in eqn (67) and (71).

Fig. 6a for the one-color system and Fig. 6b for the two-color system display isodensity curves associated with the out-of-phase amplitude of **1B** for three targeted species with different unbinding rate constants k^A_{-1} in the (ω,I^0) space and the $(\omega,I^0_1/I^0_2)$ space, respectively. For targeted species with different k^A_{-1} but the same value of the dissociation constant K_d, the position of the resonance with respect to I^0 and I^0_1/I^0_2 is the same for all the three targeted species, whereas the position of the resonance with respect to ω varies with the unbinding rate constant of the targeted species. Kinetic discrimination is efficient provided that $k^A_{-1} < k^A_{21}$ for the one-color system and $k^A_{-1} < \sigma_{21,2}I^0_2$ for the two-color system. Hence, the choice of the titrating agent has to be adapted to the targeted species for dynamic titration to be successful.

Fig. 6c for the one-color system and Fig. 6d for the two-color system show how the isodensity curves associated with the

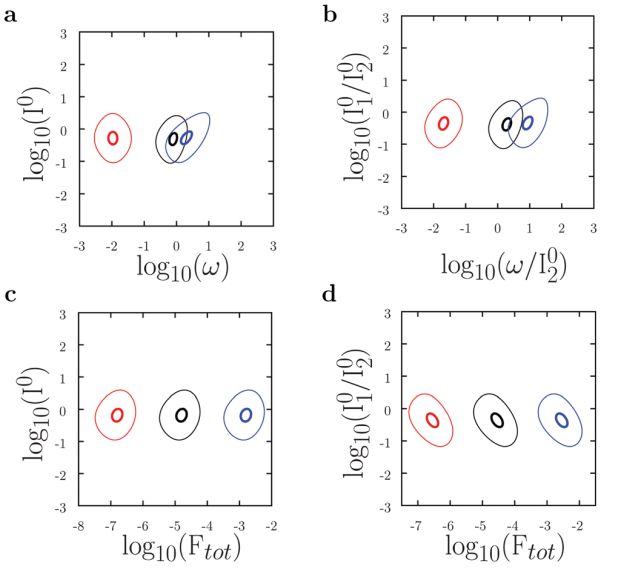

Fig. 6 Isodensity curves corresponding to 50% (thin line) and 95% (thick line) of the resonant out-of-phase amplitude $1B^{1,cos}/N\min(R_{tot},F_{tot})$, optimized with respect to the three control parameters, for $R_{tot} = 0.1K_d$. (a and c) One-color system: $\sigma_{12} = \sigma_{21} = 1$ in arbitrary units, $k^A_{21} = 1\ s^{-1}$. (a) $k^A_{-1} = 10^{-2}\ s^{-1}$ (red), $k^A_{-1} = 1\ s^{-1}$ (black), and $k^A_{-1} = 10^{2}\ s^{-1}$ (blue), for $K_d = 100$ nM, in the (ω,I^0) space, (c) $K_d = 1$ nM (red), $K_d = 10^2$ nM (black), and $K_d = 10^4$ nM (blue), for $k^A_{-1} = 10^{-1}\ s^{-1}$, in the (F_{tot},I^0) space, (b and d) two-color system: $\sigma_{12,1} = \sigma_{21,2} = 1$ in arbitrary units, $\sigma_{12,2} = \sigma_{21,1} = 5$ in arbitrary units. (b) $k^A_{-1}/I^0_2 = 10^{-2}\ s^{-1}$ (red), $k^A_{-1}/I^0_2 = 1\ s^{-1}$ (black), and $k^A_{-1}/I^0_2 = 10^{2}\ s^{-1}$ (blue), for $K_d = 100$ nM, in the $(\omega/I^0_2,I^0_1/I^0_2)$ space, (d) $K_d = 1$ nM (red), $K_d = 10^2$ nM (black), and $K_d = 10^4$ nM (blue), $k^A_{-1}/I^0_2 = 10^{-1}\ s^{-1}$, in the $(F_{tot},I^0_1/I^0_2)$ space.

observable move in the (F_{tot}, I^0) space and the $(F_{tot}, I^0_1/I^0_2)$ space, respectively, when the thermodynamic dissociation constant K_d of the targeted species changes. For targeted species with different values of the dissociation constant but the same value of the unbinding rate constant k^A_{-1}, the position of the resonance with respect to I^0 or I^0_1/I^0_2 is the same for all K_d values. On the contrary, the position of the resonance with respect to F_{tot} significantly varies for the investigated values of K_d. Hence, kinetic discrimination for targets with different k^A_{+1} values will be efficient.

It is worth noting that the protocol is also well adapted to discriminating targeted species with both different values of k^A_{+1} and k^A_{-1}, using the resonance conditions on F^R_{tot} and ω^R. When complexation is slower than photoisomerization, the resonance condition setting ω^R involves k^A_{-1} and the condition setting F^R_{tot} involves K_d, *i.e.* k^A_{+1} when k^A_{-1} has already been singularized by the choice of ω^R. Then the titrating protocol involves the values of both the forward and backward rate constants and not only the equilibrium constant K_d: the protocol fully deserves the title of dynamic titration protocol. However, when complexation is faster than photoisomerization, the resonance condition imposing ω^R does not involve k^A_{-1}, as shown in eqn (65) and (69). In this case, the protocol belongs to the class of standard titrations relying on the variation of the equilibrium constant of reaction between titrated and titrating species.

Table 5 Summary of the analytical expressions of the control parameters associated with the dynamic titration protocol in one- and two-color systems

One-color system	Two-color system
Fixed parameters associated with the titrating reagent	
σ_{12}, σ_{21}	$\sigma_{12,1}$, $\sigma_{12,2}$, $\sigma_{21,1}$, $\sigma_{21,2}$
k_{21}^{Λ}	k_{21}^{Λ} negligible
Illumination modulation	
$I(t) = I^0[1 + \varepsilon\sin(\omega t)]$	$I_1(t) = I_1^0[1 + n_1\varepsilon\sin(\omega t)]$ $I_2(t) = I_2^0[1 + n_2\varepsilon\sin(\omega t)]$
Total concentrations	
$R_{tot} \ll K_d$	$R_{tot} \ll K_d$
$F_{tot}^R \simeq K_d\sqrt{\frac{\sigma_{12}+\sigma_{21}}{\sigma_{21}}}$	$F_{tot}^R \simeq K_d\sqrt{\left(1+\frac{\sigma_{12,1}}{\sigma_{21,1}}\right)\left(1+\frac{\sigma_{12,2}}{\sigma_{21,2}}\right)}$
Illumination parameters	
$I^{0,R} \simeq \frac{k_{21}^{\Lambda}}{\sqrt{\sigma_{21}(\sigma_{12}+\sigma_{21})}}$	$\left(\frac{I_1^0}{I_2^0}\right)^R \simeq \sqrt{\frac{(\sigma_{12,2}+\sigma_{21,2})\sigma_{21,2}}{(\sigma_{12,1}+\sigma_{21,1})\sigma_{21,1}}}$
If $k_{-1}^{\Lambda} \gg k_{21}^{\Lambda}$, $\omega^R \simeq k_{21}^{\Lambda} + I^{0,R}(\sigma_{12}+\sigma_{21})$	If $k_{-1}^{\Lambda} \gg \sigma_{21,2}I_2^0$, $\omega^R \simeq \left((\sigma_{12,1}+\sigma_{21,1})\left(\frac{I_1^0}{I_2^0}\right)^R + (\sigma_{12,2}+\sigma_{21,2})\right)I_2^0$
If $k_{-1}^{\Lambda} \ll k_{21}^{\Lambda}$, $\omega^R = 2k_{-1}^{\Lambda}$	If $k_{-1}^{\Lambda} \ll \sigma_{21,2}I_2^0$, $\omega^R = 2k_{-1}^{\Lambda}$

The conditions on the control parameters to be imposed to implement the dynamic titration protocol are summarized in Table 5 for one- and two- color systems.

7 Conclusion

A dynamic titration method is proposed for compounds that can react with a reversibly photoswitchable reagent. The principle relies on applying light modulation which imposes forced concentration oscillations. We have chosen to detect the out-of-phase amplitude of concentration oscillations. This observable presents satisfying properties for dynamic titration because it is proportional to the total concentration of a species of interest and takes appreciable values only for the targeted species. Singularizing a targeted species amounts to setting the control parameters to resonant values that optimize the observable. The resonance conditions consist in adjusting the period of the forced illumination to the relaxation time of the slowest reaction. Moreover they impose that both reactions, photoisomerization and complexation, are at equilibrium at leading order: at the resonance, the chemical system obeys detailed balance. We have derived user-friendly analytical expressions that relate the resonant control parameters to the kinetics of the titrated/titrating couple. The validity of the analytical predictions has been numerically checked. Using these results, we have proposed an experimental protocol able to dynamically titrate any targeted species, provided that the photoswitchable reagent has been adequately chosen.

From an experimental point of view, the implementation of the titration protocol requests to preliminarily study the kinetics of photoswitching and complexation which can be accomplished with standard photochemical and stopped-flow methods. Then, collecting data should not be a problem and data processing is expected to be easy.

The present titration protocol relying on periodic light excitation should yield a better signal-to-noise ratio than titration protocols relying on thermodynamic equilibrium or on the analysis of the response to a jump like in a standard dynamic titration.[12] Indeed although the observable reaches half the value of the steady concentration in the most favorable case, lock-in detection acts as a band-filter around the resonant angular frequency, which efficiently filters the noise spectrum. As such, this titration protocol should find useful applications in analysis and imaging under demanding conditions.

Conflicts of interest

There are no conflicts to declare.

References

1 B. N. G. Giepmans, S. R. Adams, M. H. Ellisman and R. Y. Tsien, *Science*, 2006, **312**, 217–224.
2 A. Valm, S. Cohen, W. Legant, J. Melunis, U. Hershberg, E. Wait, A. Cohen, M. Davidson, E. Betzig and J. Lippincott-Schwartz, *Nature*, 2017, **546**, 162–167.
3 R. Weissleder and M. Nahrendorf, *Proc. Natl. Acad. Sci. U. S. A.*, 2015, **112**, 14424–14428.
4 H. Grecco, S. Imtiaz and E. Zamir, *Cytometry, Part A*, 2016, **89**, 761–775.
5 J. Livet, T. A. Weissman, H. Kang, R. W. Draft, J. Lu, R. A. Bennis, J. R. Sanes and J. W. Lichtman, *Nature*, 2007, **450**, 56–61.
6 A. Valm, R. Oldenbourg and G. Borisy, *PLoS One*, 2016, **11**, e0158495.
7 S. Pontes-Quero, L. Heredia, V. Casquero-Garcia, M. Fernandez-Chacon, W. Luo, A. Hermoso, M. Bansal, I. Garcia-Gonzalez, M. Sanchez-Munoz, J. Perea, A. Galiana-Simal, I. Rodriguez-Arabaolaza, S. Del Olmo-Cabrera, S. Rocha,

L. Criado-Rodriguez, G. Giovinazzo and R. Benedito, *Cell*, 2017, **170**, 800–814.
8 M. J. Gerdes, C. J. Sevinsky, A. Sood, S. Adak, M. O. Bello, A. Bordwell, A. Can, A. Corwin, S. Dinn, R. J. Filkins, D. Hollman, V. Kamath, S. Kaanumalle, K. Kenny, M. Larsen, M. Lazare, Q. Li, C. Lowes, C. C. McCulloch, E. McDonough, M. C. Montalto, Z. Pang, J. Rittscher, A. Santamaria-Pang, B. D. Sarachan, M. L. Seel, A. Seppo, K. Shaikh, Y. Sui, J. Zhang and F. Ginty, *Proc. Natl. Acad. Sci. U. S. A.*, 2013, **110**, 11982–11987.
9 P. Liberali, B. Snijder and L. Pelkmans, *Nat. Rev. Genet.*, 2015, **16**, 18–32.
10 R. Winkler-Oswatitsch and M. Eigen, *Angew. Chem., Int. Ed. Engl.*, 1979, **18**, 20–49.
11 J. Quérard, T. Le Saux, A. Gautier, D. Alcor, V. Croquette, A. Lemarchand, C. Gosse and L. Jullien, *ChemPhysChem*, 2016, **17**, 1396–1413.
12 M. Eigen and L. de Mayer, *Relaxation Methods in Techniques of Organic Chemistry*, Wiley, New York, 1963.
13 C. F. Bernasconi, *Relaxation kinetics*, Academic Press, New York, 1976.
14 H. Strehlow and W. Knoche, *Fundamentals of chemical relaxation*, Weinheim, New York, 1977.
15 B. Nölting, *Protein folding kinetics*, Springer, Berlin, 2006.
16 J. F. Eccleston, S. R. Martin and M. J. Schilstra, *Methods Cell Biol.*, 2008, **84**, 445–477.
17 V. Petrov, Q. Ouyang and H. L. Swinney, *Nature*, 1997, **388**, 655–657.
18 D. Baurecht and U. P. Fringeli, *Rev. Sci. Instrum.*, 2001, **72**, 3782–3792.
19 D. Baurecht, I. Porth and U. P. Fringeli, *Vib. Spectrosc.*, 2002, **30**, 85–92.
20 V. P. Zhdanov, *Surf. Sci. Rep.*, 2004, **55**, 1–48.
21 J. Dushoff, J. B. Plotkin, S. A. Levin and D. J. Earn, *Proc. Natl. Acad. Sci. U. S. A.*, 2004, **101**, 16915–16916.
22 M. D. McDonnell and D. Abbott, *PLoS Comput. Biol.*, 2009, **5**, e1000348.
23 H. Berthoumieux, C. Antoine, L. Jullien and A. Lemarchand, *Phys. Rev. E: Stat., Nonlinear, Soft Matter Phys.*, 2009, **79**, 021906.
24 I. Schoen, H. Krammer and D. Braun, *Proc. Natl. Acad. Sci. U. S. A.*, 2009, **106**, 21649–61654.
25 K. Zrelli, T. Barilero, E. Cavatore, H. Berthoumieux, T. Le Saux, V. Croquette, A. Lemarchand, C. Gosse and L. Jullien, *Anal. Chem.*, 2011, **83**, 2476–2484.
26 M. Platkov and M. Gruebele, *J. Chem. Phys.*, 2014, **141**, 035103.
27 K. Dave, A. Davtyan, G. A. Papoian, M. Gruebele and M. Platkov, *ChemPhysChem*, 2016, **17**, 1341–1348.
28 A. Davtyan, M. Platkov, M. Gruebele and G. A. Papoian, *ChemPhysChem*, 2016, **17**, 1305–1313.
29 H. Berthoumieux, L. Jullien and A. Lemarchand, *Phys. Rev. E: Stat., Nonlinear, Soft Matter Phys.*, 2007, **76**, 056112.
30 H. Berthoumieux, C. Antoine and A. Lemarchand, *J. Chem. Phys.*, 2009, **131**, 084106.
31 A. Lemarchand, H. Berthoumieux, L. Jullien and C. Gosse, *J. Phys. Chem. A*, 2012, **116**, 8455–8463.
32 F. Closa, C. Gosse, L. Jullien and A. Lemarchand, *J. Chem. Phys.*, 2013, **138**, 244109.
33 F. Closa, C. Gosse, L. Jullien and A. Lemarchand, *J. Chem. Phys.*, 2015, **142**, 174108.
34 A. Gautier, C. Gauron, M. Volovitch, D. Bensimon, L. Jullien and S. Vriz, *Nat. Chem. Biol.*, 2014, **10**, 533–541.
35 P. Wang, J. Querard, S. Maurin, S. S. Nath, T. Le Saux, A. Gautier and L. Jullien, *Chem. Sci.*, 2013, **4**, 2865–2873.
36 M. A. Plamont, E. Billon-Denis, S. Maurin, C. Gauron, F. M. Pimenta, C. G. Specht, J. Shi, J. Quérard, B. Pan, J. Rossignol, K. Moncoq, N. Morellet, M. Volovitch, E. Lescop, Y. Chen, A. Triller, S. Vriz, T. Le Saux, L. Jullien and A. Gautier, *Proc. Natl. Acad. Sci. U. S. A.*, 2016, **133**, 497–502.
37 F. M. Pimenta, G. Chiappetta, T. Le Saux, J. Vinh, L. Jullien and A. Gautier, *Sci. Rep.*, 2017, **7**, 12316.
38 H. Bouas-Laurent and H. Dürr, *Pure Appl. Chem.*, 2001, **73**, 639–665.
39 M. S. Wang, G. Xu, Z. J. Zhang and G. C. Guo, *Chem. Commun.*, 2010, **46**, 361–376.
40 T. Fukaminato, *J. Photochem. Photobiol., C*, 2011, **12**, 177–208.
41 S. van de Linde and M. Sauer, *Chem. Soc. Rev.*, 2014, **43**, 1076–1087.
42 D. Bourgeois and V. Adam, *IUBMB Life*, 2012, **64**, 482–491.
43 X. X. Zhou and M. Z. Lin, *Curr. Opin. Chem. Biol.*, 2013, **17**, 682–690.
44 H. M. Bandara and S. C. Burdette, *Chem. Soc. Rev.*, 2012, **41**, 1809–1825.
45 M. Dong, A. Babalhavaeji, S. Samanta, A. A. Beharry and G. A. Woolley, *Acc. Chem. Res.*, 2015, **48**, 2662–2670.
46 D. Bleger and S. Hecht, *Angew. Chem., Int. Ed.*, 2015, **54**, 11338–11349.
47 J. Widengren and P. Schwille, *J. Phys. Chem. A*, 2000, **104**, 6416–6428.
48 G. T. Dempsey, M. Bates, W. E. Kowtoniuk, D. R. Liu, R. Y. Tsien and X. Zhuang, *J. Am. Chem. Soc.*, 2009, **131**, 18192–18193.
49 H. Tian and S. Yanga, *Chem. Soc. Rev.*, 2004, **33**, 85–97.
50 K. Matsuda and M. Irie, *J. Photochem. Photobiol., C*, 2004, **5**, 169–182.
51 C. Yun, J. You, J. Kim, J. Huh and E. Kim, *J. Photochem. Photobiol., C*, 2009, **10**, 111–129.
52 R. Klajn, *Chem. Soc. Rev.*, 2014, **43**, 148–184.
53 J. Quérard, T. Z. Markus, M. A. Plamont, C. Gauron, P. Wang, A. Espagne, M. Volovitch, S. Vriz, V. Croquette, A. Gautier, T. Le Saux and L. Jullien, *Angew. Chem., Int. Ed.*, 2015, **127**, 2671–2675.
54 J. Quérard, R. Zhang, Z. Kelemen, M. A. Plamont, X. Xie, R. Chouket, I. Roemgens, Y. Korepina, S. Albright, E. Ipendey, M. Volovitch, H. L. Sladitschek, P. Neveu, L. Gissot, A. Gautier, J. D. Faure, V. Croquette, T. Le Saux and L. Jullien, *Nat. Commun.*, 2017, **8**, 969.

Chapter 4

Comparison of discrimination protocols based on dynamic contrast

During my PhD, I have designed several discrimination protocols relying on dynamic contrast, which exhibit similarities with other state-of-the-art protocols. In this chapter, I compare the different protocols and point out the specificity of my approach.

4.1 Comparison of LIGHTNING and optical lock-in detection (OLID)

The optical lock-in detection protocol (OLID)[58] is comparable to the Light-tunable tImegated readinG-out of pHotocycles for mulTiplexed fluorescence ImagiNG protocol (LIGHTNING). Both protocols have similar illumination conditions, i.e. constant light which activates the kinetics of the reversibly photoswitchable fluorophore leading to the variation of the fluorescence evolution. They both harness the kinetics of fluorescence evolution without hypothesis on the underlying chemical network and the number of exponential components. They both use cross-correlation data analysis between the fluorescence signal $I_F(t)$ and a reference.

In OLID, the reference fluorescence evolution $R(t)$ is the average signal from a chosen few pixels.[58,72] A cross-correlation coefficient ρ is computed for each pixel according to

$$\rho = \frac{\int \left(I_F(t) - \langle I_F(t)\rangle\right)\left(R(t) - \langle R(t)\rangle\right) dt}{\sigma_{I_F}\sigma_R} \tag{4.1}$$

where σ_{I_F} and σ_R are the standard deviations of the fluorescence intensity and the reference signal, respectively.

The original paper[58] does not provide information on the boundaries of the integral. The integration is probably performed over the entire acquisition time. Due to the

adopted normalization, the cross-correlation coefficient ρ is a number between 0 and 1. A pixel associated with a large value of ρ is likely to contain the fluorophore chosen as the reference. However, the value of ρ does not provide the amount of fluorophore in the pixel. OLID protocol has been improved to become quantitative. To this goal, Du *et al.* and Abbandonato *et al.* exploit the difference between the maximum and the minimum fluorescence intensity.[72–74] For example, in the case of a monotonously decreasing fluorescence evolution, the difference between the initial and final fluorescence intensities is proportional to the amount of fluorophore.

The computation of a spectrum of characteristic times used in LIGHTNING and detailed in section 2.4.2 resembles the determination of cross-correlation used in OLID. The spectrum $S(l)$ is obtained by cross-correlating the fluorescence evolution with an exponential function $\exp(-t/10^l)$ between 0 and 3.25×10^l, l being the decimal logarithm of a characteristic time. Unlike OLID, which provides a single number using Eq. 4.1, LIGHTNING exploits the variation of the cross-correlation coefficient $S(l)$ with the characteristic time l over a wide interval. Hence the fluorescence kinetics is highlighted over the entire investigated timescale. The choice of the integral boundaries has an impact on the result of the cross-correlation computation. The boundaries of integration in Eq. 2.103 are chosen in such a way that the extremum of the spectrum of characteristic times is observed for the characteristic time of the monoexponential fluorescence evolution.

LIGHTNING proposes two methods of data processing, curve fitting and determination of the spectrum of characteristic times, that provide mutual testing. Both methods directly give the characteristic time and the associated pre-exponential factor. The normalization condition of the spectrum is different from OLID and preserves the proportionality to the amount of fluorophore. Although the current implementation of LIGHTNING is not quantitative, quantitative information could be retrieved from curve fitting as well as spectra of characteristic times. Both data processing methods exploit the entire range of fluorescence evolution. Hence the potential use of LIGHTNING as a quantitative protocol could lead to an accurate evaluation of the amount of fluorophore even for noisy fluorescence data.

To conclude, OLID and LIGHTNING exploit the computation of cross-correlations. Both protocols are based on the comparison of the signal with a reference. However they differ on a number of issues. Using LIGHTNING and tuning light intensities, we exploit the richness of a reaction photocycle by probing kinetically independent regimes. Compared to the unidimensional character of OLID, LIGHTNING provides multidimensional

information which increases its discrimination power. In addition, a quantitative version of LIGHTNING could be developed and would provide accurate results.

4.2 Comparison of HIGHLIGHT and synchronously amplified fluorescence imaging recovery (SAFIRe)

Several discrimination protocols exploit periodic illuminations. The pHase-sensItive imaGing of reversibly pHotoactivatable Labels after modulatIon of activatinG ligHT (HIGHLIGHT) protocol most resembles the Synchronously amplified fluorescence imaging recovery protocol (SAFIRe), which also exploits periodic illuminations. Both protocols exploit Fourier analysis of fluorescence evolution for reversibly photoswitchable fluorophores under modulated light at the angular frequency ω.

In SAFIRe the Fourier transform of the fluorescence signal is computed. The Fourier amplitude $c_1 = \sqrt{a_1^2 + b_1^2}$ of the peak at angular frequency ω is extracted where a_1 and b_1 are the quadrature and in-phase amplitudes at the fundamental frequency, respectively.[45,68,75] Contrary to the quadrature Fourier amplitude used in HIGHLIGHT, the Fourier amplitude c_1 does not display a resonance but only a low-pass filter behavior with respect to the excitation frequency. The inflection point of the function $c_1(\omega)$ corresponds to the cutoff frequency and occurs when the frequency is equal to the inverse of the characteristic time of the investigated reversibly photoswitchable fluorophore. In a sample containing two reversibly photoswitchable fluorophores, the contribution to fluorescence of the faster reversibly photoswitchable fluorophore (associated with a small characteristic time, i.e. a large cutoff frequency) is eliminated but the contribution of the slowest fluorophore (associated with a large characteristic time, i.e. a small cutoff frequency) cannot be extracted.[45] SAFIRe suffers from the weakness of a low-pass filter.

In HIGHLIGHT, Fourier amplitudes are extracted using phase-sensitive detection with respect to light excitation. At the fundamental frequency HIGHLIGHT exploits the quadrature Fourier amplitude which displays a resonance with respect to the angular frequency ω and also the mean light intensity. In a mixture of several reversibly photoswitchable fluorophores, the contributions of faster and slower fluorophores than a target are eliminated when the control parameters meet the resonance conditions of the target. In contrast to SAFIRe, HIGHLIGHT exploits the Fourier amplitudes of fluorescence oscillations not only at the fundamental frequency but also at the harmonic frequencies. At each order HIGHLIGHT selects the Fourier amplitude which has a resonance behavior.

Although SAFIRe and HIGHLIGHT have similarities, SAFIRe does not take full advantage of the information contained in the response of a fluorophore to periodic illumination. Using resonance phenomena and phase-sensitive detection, HIGHLIGHT exploits optimized Fourier amplitudes leading to a multidimensional kinetic signature of the targeted reversibly photoswitchable fluorophore. Obviously, the implementation of HIGHLIGHT requires prior determination of the resonance conditions of the used reversibly photoswitchable fluorophores and assumes that these conditions are experimentally accessible.

4.3 Comparison of LIGHTNING and HIGHLIGHT implemented on RSFPs

Both protocols, LIGHTNING and HIGHLIGHT, have been implemented using RSFPs as reversibly photoswitchable fluorophores. We used low and high light intensity regimes in the constant illumination protocol, LIGHTNING, but only low light intensity in the modulated illumination protocol, HIGHLIGHT. Figure 4.1 displays the LIGHTNING kinetic fingerprint and the HIGHLIGHT quadrature Fourier amplitudes at the fundamental frequency for the 22 RSFPs characterized in section 2.5 in their respective discrimination spaces.

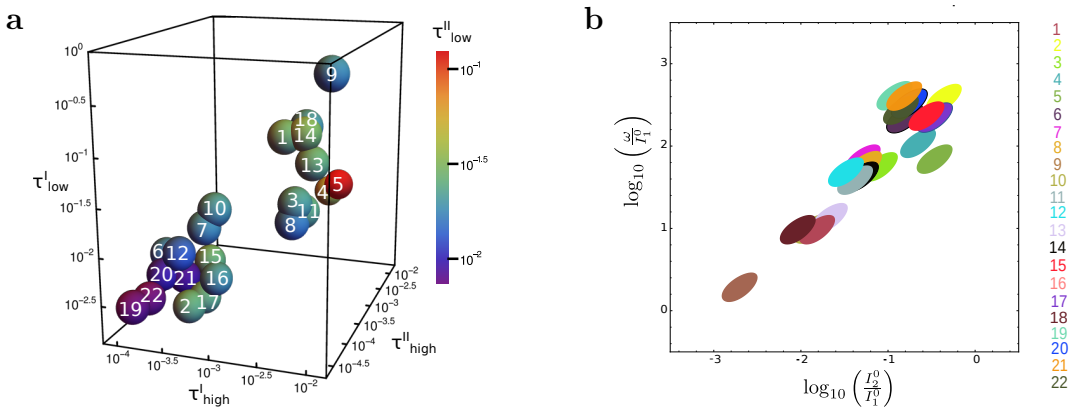

Figure 4.1: **a**: LIGHTNING kinetic fingerprint of the 22 RSFPs. The radius of the spheres are related to the uncertainty on the determination of the characteristic times. **b**: HIGHLIGHT discrimination map of the 22 RSFPs using the quadrature Fourier amplitudes at the fundamental frequency. The areas correspond to signal higher than 95 % of its absolute maximal value. Numbers from **1** to **22** are referring to the 22 RSFPs characterized in section 2.5.

LIGHTNING harnesses four dimensions of discrimination, the characteristic times ob-

tained under the four constant illuminations. The hypervolume of the signal of one RSFP in the discrimination space is about 0.003, which is due to uncertainty on the determination of the characteristic times. Up to 20 noncolocalized out of the 22 characterized RSFPs are discriminatable using LIGHTNING. When no more than two RSFPs are colocalized, 10 out of the same 22 RSFPs can still be discriminated.[132] In preliminary experiments of RSFP-labeled bacteria, kinetics is essentially the same as in solution. However the characteristic times are more dispersed than in solution, presumably due to either the sample preparation or the dispersion of RSFP environment. This feature presently increases the hypervolume that characterizes an RSFP in the discrimination space up to 0.1 which decreases the number of discriminatable RSFPs. Work is in progress and improvements are expected.

HIGHLIGHT harnesses two dimensions of discrimination, scaled frequency ω/I_1^0 and scaled mean illumination intensity I_2^0/I_1^0 in the case of illumination at $\lambda_1 = 488$ nm and $\lambda_2 = 405$ nm. In the control parameter space $(\omega/I_1^0, I_2^0/I_1^0)$ the area around the resonance conditions of an RSFP is imposed by the intrinsic width of the resonance peak, much larger than the experimental uncertainty on the kinetic parameters and the control parameters. For a modulation at $\lambda_1 = 488$ nm, the width at mid-height of the resonance peak of the Fourier amplitudes is 1.4, 1.0, and 0.7 for the first, second, and third orders, respectively. According to the experiments performed on biological samples in our group, no significant shift nor widening of the resonances have been observed with respect to the behavior observed in RSFP solutions. Under single sine-wave modulation, 4 and 5 RSFPs out of the 22 RSFPs are discriminatable using the first- and second-order Fourier amplitudes, respectively.

To conclude, although it may yield a lower signal-to-noise ratio, LIGHTNING has a better RSFP discriminatory power than HIGHLIGHT. HIGHLIGHT has been implemented on a two-state mechanism. In the case of RSFPs, assuming that kinetics is governed by a two-state model imposes upper boundaries to the range of exploitable light intensities. Moreover the RSFPs have very similar cross sections at the wavelength $\lambda_2 = 405$ nm, making the cross sections at the wavelength $\lambda_1 = 480$ nm the only discriminating parameter in HIGHLIGHT. However, using the principles of HIGHLIGHT is not intrinsically limited to two-state mechanisms. The application to richer kinetics was carried out in the case of a titration reaction coupled with a reversibly photo-activatable step.

4.4 Comparison of discrimination protocols using constant and modulated illuminations

A general comparison of the imaging protocols relying on constant and modulated illumination can be drawn beyond the implementation on RSFPs. Each protocol applies to many photochemical systems with a sufficient level of complexity. In the following we consider a photo-activatable system non necessarily reversible.

The protocol principle Both imaging protocols harness the kinetics of photo-activatable system, which possesses thermal reaction steps and species of different brightnesses. The fluorescence evolution is recorded under either several constant illuminations or a modulated, not necessarily sine-wave, illumination. For a constant illumination, the characteristic times and the associated amplitudes are extracted, e.g. using curve fitting or a spectrum of characteristic times. The sampling interval and the acquisition time of the fluorescence evolution impact the result of data analysis. For a modulated illumination, in-phase and quadrature Fourier amplitudes are extracted at the fundamental frequency and the harmonic frequencies. In this case, a single experiment leads to several observables.

Implementation - Kinetic characterization Both imaging protocols require preliminary characterization of the kinetics of the photochemical species. A theoretical analysis is possible only if the reactive mechanism is known. For the constant illumination protocol, the theoretical interpretation of the extracted characteristic time can be challenging but is not necessary for discrimination purposes. For the modulated illumination protocol, analytical expressions of Fourier amplitudes can be obtained by perturbation using the modulation amplitude as a "small" parameter. Then a resonance behavior can be sought and analytical or numerical expressions of the resonance conditions obtained. If the reaction mechanism is unknown, an experimental approach is always possible and resonance conditions can be determined empirically.

Kinetic signature Figure 4.2 displays the kinetic signature of a photoactivatable fluorophore for both imaging protocols. For the constant illumination protocol, the kinetic signature consists of the set of independent characteristic times, $(\tau_1, ..., \tau_i)$, associated with various light intensities at possibly different wavelengths. Similar kinetic signatures can be obtained in the full range of light intensities belonging to the same regime, i.e. provided

that the same reduced mechanism describing kinetics is valid. Experimental implementation is therefore flexible. The uncertainty on the determination of the characteristic times leads to an hypervolume around the signature.

For the modulated illumination protocol, kinetics is characterized by a set of control parameters, for example the angular frequency ω, the total concentration C_{tot}, the mean light intensities I_1^0 and I_2^0, for which the considered Fourier amplitude is resonant. Implementation requires that the control parameters can be experimentally tuned to obey the resonance conditions. As a resonance corresponds to a zero derivative, the control parameters are loosely defined at the resonance. This feature offers a small flexibility to fulfill the resonance conditions but it also decreases the accuracy with which a set of control parameters values is associated with a given photoactivatable fluorophore. It is worth noting that, depending on the mechanism, a Fourier amplitude at a given order may present several extrema, a single extremum, or even none with respect to some control parameters. The rich behavior of the Fourier amplitudes has advantages and drawbacks. In particular, the existence of zero lines between extrema of opposite signs can be harnessed as demonstrated in section 3.2. However the loss of any extremum prevents from using the considered Fourier amplitude.

For both protocols, the kinetic signature is a hypervolume due to the uncertainty on the measured quantities. For the modulated illumination protocol, the intrinsic width of the resonance significantly increases the size of the hyper-volume associated with the kinetic signature.

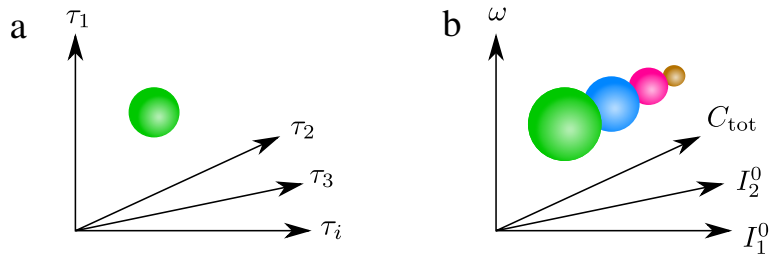

Figure 4.2: **a**: Kinetic signature in the space of characteristic times with constant illumination. **b**: Kinetic signatures associated with various Fourier amplitudes in the space of control parameters with modulated illumination.

Data acquisition Several experiments with various control parameter values are necessary to record a single kinetic signature for the constant illumination protocol whereas it is recorded using a single experiment for the modulated illumination protocol for which

several Fourier amplitudes can be extracted. For both protocols, the acquisition time is similar, being related to the characteristic times of the kinetics. The constant illumination protocol has limitations due to the sampling interval and the acquisition time. For the modulated illumination protocol, the experimentally accessible range of control parameters may prevent from reaching the resonance conditions. Due to the lock-in amplification intrinsic to Fourier analysis, the modulated illumination protocol leads to good signal-to-noise ratios.

Discrimination Once kinetic data have been collected for a sample containing an unknown photoactivatable fluorophore, identification of the fluorophore remains to be done. The discriminating spaces of both protocols can be harnessed in different ways. For the constant illumination protocol, a Euclidean distance between the kinetic signature of a reference and the characteristic times of the sample can be defined. A cut-off distance can be used to assign the identity of the photoactivatable fluorophore in the sample. Methods of map segmentation, like Voronoï diagrams, could also be implemented to assign a univocal hypervolume around each reference in the case of a cut-off distance larger than the distance between two references.

For the modulated illumination protocol, the presence or the absence of a given photoactivatable fluorophore is deduced from the Fourier amplitudes at the resonance conditions of the photoactivatable fluorophore, without further development. This method applies when each fluorophore contributes in a similar way to the fluorescence signal. The resonance peak being not a rectangular pulse, a fluorophore present in large concentration for not rigorous resonant conditions may lead to the same signal as a fluorophore in small concentration but exactly at resonance. Apart from this restriction, the modulated illumination protocol straightforwardly provides quantitative information since the Fourier amplitudes are proportional to the amount of fluorophore.

Eventually implementing machine learning algorithms could increase the discrimination capabilities of both protocols. They would be especially relevant for the modulated illumination protocol by taking into account all Fourier amplitudes with or without resonant behavior.

Pixel colocalization With constant illumination, the protocol implemented to analyze the experimental data for noncolocalized species must be adapted if several chemical species occupy the same pixel. Colocalized species may not be discriminatable beyond

a given number. These limitations are not encountered with modulated illumination. Unlike with constant illumination, the modulated illumination protocol straightforwardly extends to colocalized species.

Optical sectioning power Both protocols have intrinsic optical sectioning capabilities, which are limited by the hypervolume of the kinetic signature. In this respect, the constant illumination is therefore more efficient than the modulated illumination protocol.

Conclusion Both protocols have complementary merits. To summarize, the constant illumination protocol has the larger discriminatory power whereas the modulated illumination protocol provides observables with a better signal-to-noise ratio.

Chapter 5

Conclusion and perspectives

5.1 A kinetic approach to characterize reversible photoswitching

During my PhD I have studied the kinetics of reversibly photoswitchable fluorophores and in particular reversibly photoswitchable fluorescent proteins (RSFPs) to develop discrimination methods.

The classical approach to get kinetic information on photochemical species is have been thoroughly investigate their light-induced mechanisms. Such detailed studies are performed using complementary techniques of time-resolved spectroscopies for a few reversibly photoswitchable fluorophores (RSFPs[104–107,133,134] and organic photochromes[49,135]). They evidence that photoswitching involves many species and both light and thermally-driven steps covering a broad range of timescales. These studies produce a wealth of kinetic information but they are time consuming, expensive, and not routinely performed in a non specialized laboratory.

Implementing kinetics-based discrimination protocols does not require the full characterization of kinetics. Our group has developed an optical instrument called photoswitchometer which automatically records and analyzes a sequence of fluorescence evolutions for a reversibly photoswitchable fluorophore under several constant illuminations. A major advantage of the photoswitchometer is to cover a wide range of light intensities. The setup imposes few constraints on the sample making it easily adaptable to biology. Lot of kinetic information, primarily directed to the end-users of fluorescence imaging, can be retrieved quickly and affordably, using a much simpler setup than those used in spectroscopy. However in the case of a solution of fluorophore, diffusion in the illuminated region may make interpretation difficult. We determined the time window in which

diffusion can be neglected. Hence we obtained an upper bound to the experimentally accessible characteristic times.

Extracting relevant kinetic information from fluorescence evolution is not straightforward. I contributed to adapting methods of signal processing well-suited for multiexponential behaviors. On the one hand, monoexponential curve fitting was used to extract minimal but robust kinetic information. On the other hand, spectra of characteristic times have revealed kinetics without prior knowledge of the mechanism. Building a spectrum of characteristic times proved to be a powerful tool to investigate kinetics. The two methods complement and justify each other.

Using these methods and literature, I proposed a reaction scheme qualitatively accounting for the observed fluorescence evolutions of RSFPs in a given time window and a large range of light intensities. The proposed reaction mechanism does not pretend to account for all the elementary steps involved in the complex kinetics of RSFPs. Reduced mechanisms valid in specific intervals of light intensities were determined. Kinetic information on the bright to dark light-driven transition of the RSFPs exhibiting negative photochromism, which is difficult to access by most available time-resolved techniques, has been extracted. The number of relevant species, the network of reactions connecting them, and the photochemical or thermal nature of the steps have been made precise. Assigning the chemical nature of the species could not be done using only the kinetic data provided by the photoswitchometer. However it has been achieved using spectroscopic results found in the literature. Indeed kinetic information deduced from fluorescence evolution is not as complete as information deduced from spectroscopic studies.

The kinetics of twenty-two RSFPs has been investigated. Information on their photoswitching has been summarized by a small number of quantities, isomerization cross sections and characteristic times. We have used the results to discriminate RSFPs, but they can find many other applications on a variety of optical setups.

5.2 Kinetics-based protocols of fluorophore discrimination

Light has been used to reveal kinetics of reversibly photoswitchable fluorophores engaged in complex mechanisms. Discrimination protocols using either constant light or modulated light have been designed.

The method called Light-tunable tIme-gated readinG-out of pHotocycles for mulTi-

plexed fluorescence ImagiNG (LIGHTNING) uses several constant light illuminations. We found four illumination conditions associated with different kinetic regimes of RSFPs. For each kinetic regime, fluorescence evolution is characterized by a single characteristic time. Hence, probing RSFP kinetics in the four illumination conditions provides a four-dimensional kinetic fingerprint. Discrimination is performed in the four-dimensional space of the characteristic times by finding the RSFP, among all referenced RSFPs, whose kinetic fingerprint matches the fingerprint of the sample. Our results show that up to 20 out of 22 noncolocalized RSFPs can be discriminated. When no more than two RSFPs contribute to a given fluorescence signal, LIGHTNING is able to discriminate 10 out of 22 RSFPs. In addition I theoretically showed that LIGHTNING contains intrinsically optical sectioning power, i.e. the ability to observe the fluorescence emitted by a thin slice of the sample. This feature could be attractive for 3D fluorescence imaging. The analysis of the evolution of fluorescence in a homogeneous solution significantly pushes forward the limits of dynamic contrast in fluorescence imaging.

Light modulations have also been used to take advantage of the kinetics of reversibly photoswitchable fluorophores. Forced dynamical systems are known to exhibit resonance phenomena that are *a priori* suitable for discrimination. The resonance conditions link the parameters controlling illumination and the kinetic parameters of the reversibly photoswitchable fluorophore. Tuning the control parameters to target a given fluorophore optimizes its fluorescence response and nearly eliminates the responses of fluorophores with different kinetic properties. I considered sine-wave oscillating illuminations and determined analytical resonance conditions for two types of reversibly photoswitchable systems.

In the continuation of the OPIOM approach, PHase-sensItive imaGing of reversibly pHotoswitchable Labels after modulatIon of activatinG ligHT (HIGHLIGHT) applies to a mechanism with a single reaction step. I determined analytical expressions of the Fourier amplitudes of fluorescence oscillations at the fundamental and harmonic frequencies. At each order, either the in-phase or the quadrature Fourier amplitude with respect to the excitation light exhibits resonance phenomena in the space of the control parameters (angular frequency of modulation and mean light intensities). From the second order, the Fourier amplitudes display two resonance peaks separated by a zero line. This feature is particularly valuable in the context of discrimination since the contribution of a given reversibly photoswitchable fluorophore to the fluorescence signal vanishes when the control parameters obey the zero line condition. Experiments performed in our group for a

large amplitude of light modulation have validated the theoretical predictions. Using a wide-field epifluorescence setup, three RSFPs have been selectively imaged by judiciously exploiting the zero lines of the second order Fourier amplitudes of some RSFPs and the resonances of others. As for LIGHTNING, the HIGHLIGHT protocol contains an intrinsic optical sectioning ability.

I showed that discrimination harnessing resonance phenomena induced by light modulation is possible for other reaction mechanisms, in particular in the case of a system coupling a titration step and a photoswitching step. Dynamic titration protocols have been proposed.

In conclusion, both fluorescence imaging protocols have complementary merits. LIGHTNING has a larger discriminatory power. HIGHLIGHT provides better quality images due to lock-in amplification and can be straightforwardly extended to colocalized fluorophores.

5.3 Perspectives

The design of kinetics-based discrimination methods and fluorescence imaging protocols deserves further developments.

A first development deals with improving data processing for the discrimination methods using constant and modulated illumination. In the case of LIGHTNING, several characteristic times could be extracted from a single fluorescence evolution. The amplitudes of the exponential terms associated with the characteristic times could constitute additional dimensions of discrimination. Illumination at a third wavelength could be used to add new discriminative dimensions. For example, a red-shifted illumination could be used to excite the triplet of the bright state and reveal yet unexplored steps.

Moreover the RSFP identification could be achieved by other methods than the evaluation of the distance between the fingerprints of sample and a reference in the discrimination space. Methods such as map segmentation of the discrimination space for example using Voronoï diagrams[136] or machine learning algorithms could be implemented to further improve discrimination. Machine learning algorithms seem especially attractive for HIGHLIGHT since a single experiment delivers several observables, the Fourier amplitudes at different orders. In addition the learning process could be facilitated using the already determined analytical expressions of the Fourier amplitudes.

A second development concerns the adaptation of HIGHLIGHT and LIGHTNING to other setups of fluorescence microscopy than wide-field setups. We are especially inter-

ested in light scanning microscopes, e.g. confocal microscopes and scanning light-sheet microscopes, which are already available in most imaging platforms of biology departments with light sources covering the range of intensities necessary to LIGHTNING implementation.

A last development concerns the extension of the discrimination methods to other fluorescent labels than RSFPs. In particular the fluorescent labels popular in the community of biologists could be investigated. Simple fluorescent proteins (FPs) presently harnessed for spectral discrimination provide an attractive perspective. Interestingly, a reversible photoswitching phenomenon involving a triplet state has been reported for FPs.[110] Dynamic contrast methods, and in particular LIGHTNING and HIGHLIGHT, will probably be able to make use of the photoswitching kinetics of FPs while keeping available the spectral discrimination dimension. The already existing families of FPs suggest that a large number of FPs with sufficiently different kinetics could be found. The photoswitchometer may prove to be useful to characterize the kinetics of FPs.

Bibliography

[1] Kevin M Marks and Garry P Nolan. Chemical labeling strategies for cell biology. *Nature methods*, 3(8):591–596, 2006.

[2] Kevin M Dean and Amy E Palmer. Advances in fluorescence labeling strategies for dynamic cellular imaging. *Nature chemical biology*, 10(7):512, 2014.

[3] Elizabeth A Specht, Esther Braselmann, and Amy E Palmer. A critical and comparative review of fluorescent tools for live-cell imaging. *Annual review of physiology*, 79:93–117, 2017.

[4] Steven L Jacques. Optical properties of biological tissues: a review. *Physics in Medicine & Biology*, 58(11):R37, 2013.

[5] Anna Croce and Giovanni Bottiroli. Autofluorescence spectroscopy and imaging: A tool for biomedical research and diagnosis. *European journal of histochemistry : EJH*, 58:2461, 12 2014.

[6] Ben NG Giepmans, Stephen R Adams, Mark H Ellisman, and Roger Y Tsien. The fluorescent toolbox for assessing protein location and function. *science*, 312(5771):217–224, 2006.

[7] Liu Zhe, D. Lavis Luke, and Betzig Eric. Imaging live-cell dynamics and structure at the single-molecule level. *Molecular Cell*, 58(4):644 – 659, 2015.

[8] Markus Grabolle, Sara Cavaliere-Jaricot, Roland Nitschke, and Thomas Nann. Quantum dots versus organic dyes as fluorescent labels. *Nature Methods*, 5:763–776, 2008.

[9] Luke D Lavis and Ronald T Raines. Bright ideas for chemical biology. *ACS chemical biology*, 3(3):142–155, 2008.

[10] Luke D. Lavis and Ronald T. Raines. Bright building blocks for chemical biology. *ACS Chemical Biology*, 9(4):855–866, 2014.

[11] Osamu Shimomura, Frank H. Johnson, and Yo Saiga. Extraction, purification and properties of Aequorin, a bioluminescent protein from the luminous hydromedusan, Aequorea. *Journal of Cellular and Comparative Physiology*, 59(3):223–239, 1962.

[12] Douglas C. Prasher, Virginia K. Eckenrode, William W. Ward, Frank G. Prendergast, and Milton J. Cormier. Primary structure of the aequorea victoria green-fluorescent protein. *Gene*, 111(2):229 – 233, 1992.

[13] M. Chalfie, Y. Tu, G. Euskirchen, W. W. Ward, and D. C. Prasher. Green fluorescent protein as a marker for gene expression. *Science*, 263:802–805, 1994.

[14] Dmitriy M. Chudakov, Mikhail V. Matz, Sergey Lukyanov, and Konstantin A. Lukyanov. Fluorescent proteins and their applications in imaging living cells and tissues. *Physiological Reviews*, 90:1103–1163, 2010.

[15] Erik A. Rodriguez, Robert E. Campbell, John Y. Lin, Michael Z. Lin, Atsushi Miyawaki, Amy E. Palmer, Xiaokun Shu, Jin Zhang, and Roger Y. Tsien. The growing and glowing toolbox of fluorescent and photoactive proteins. *Trends in Biochemical Sciences*, 42(2):111 – 129, 2017.

[16] Wataru Tomosugi, Tomoki Matsuda, Tomomi Tani, Tomomi Nemoto, Ippei Kotera, Kenta Saito, Kazuki Horikawa, and Takeharu Nagai. An ultramarine fluorescent protein with increased photostability and ph insensitivity. *Nature methods*, 6(2):351–354, 2009.

[17] Oksana M. Subach, Illia S. Gundorov, Masami Yoshimura, Fedor V. Subach, Jinghang Zhang, David Gruenwald, Ekaterina A. Souslova, Dmitriy M. Chudakov, and Vladislav V. Verkhusha. Conversion of red fluorescent protein into a bright blue probe. *Chemistry and Biology*, 15:1116–1124, 2008.

[18] Hui-wang Ai, J. Nathan Henderson, S.James Remington, and Robert E. Campbell. Directed evolution of a monomeric, bright and photostable version of clavularia cyan fluorescent protein: structural characterization and applications in fluorescence imaging. *Biochemical Journal*, 400(3):531–540, 2006.

[19] Karen S. Sarkisyan, Alexander S. Goryashchenko, Peter V. Lidsky, Dmitry A. Gorbachev, Nina G. Bozhanova, Andrey Yu. Gorokhovatsky, Alina R. Pereverzeva, Alina P. Ryumina, Victoria V. Zherdeva, Alexander P. Savitsky, Kyril M. Solntsev, Andreas S.

Bommarius, George V. Sharonov, Jake R. Lindquist, Mikhail Drobizhev, Thomas E. Hughes, Aleksander Rebane, Konstantin A. Lukyanov, and Alexander S. Mishin. Green fluorescent protein with anionic tryptophan-based chromophore and long fluorescence lifetime. *Biophysical Journal*, 109:380 – 389, 2015.

[20] Hiofan Hoi, Elizabeth S. Howe, Yidan Ding, Wei Zhang, Michelle A. Baird, Brittney R. Sell, John R. Allen, Michael W. Davidson, and Robert E. Campbell. An engineered monomeric Zoanthus sp. yellow fluorescent protein. *Chemistry and Biology*, 20:1296 – 1304, 2013.

[21] Nathan C Shaner, Robert E Campbell, Paul A Steinbach, Ben N G Giepmans, Amy E Palmer, and Roger Y Tsien. Improved monomeric red, orange and yellow fluorescent proteins derived from Discosoma sp. red fluorescent protein. *Nature Biotechnology*, 22:1567–1572, 2004.

[22] Daphne S Bindels, Lindsay Haarbosch, Laura van Weeren, Marten Postma, Katrin E Wiese, Marieke Mastop, Sylvain Aumonier, Guillaume Gotthard, Antoine Royant, Mark A Hink, and Theodorus W J Gadella Jr. mScarlet: a bright monomeric red fluorescent protein for cellular imaging. *Nature Methods*, 14:53–56, 2016.

[23] Gabriela Matela, Peng Gao, Gernot Guigas, Antonia F. Eckert, Karin Nienhaus, and G. Ulrich Nienhaus. A far-red emitting fluorescent marker protein mGarnet2 for microscopy and STED nanoscopy. *Chem. Commun.*, 53:979–982, 2017.

[24] Daria M. Shcherbakova, Mikhail Baloban, Alexander V. Emelyanov, Michael Brenowitz, Peng Guo, and Vladislav V. Verkhusha. Bright monomeric near-infrared fluorescent proteins as tags and biosensors for multiscale imaging. *Nature communications*, 7:12405, 2016.

[25] Kevin M Dean and Amy E Palmer. Advances in fluorescence labeling strategies for dynamic cellular imaging. *Nature Chemical Biology*, 10:512–522, 2014.

[26] Jens Rietdorf, editor. *Spectral Imaging and Linear Unmixing in Light Microscopy*. Springer Berlin Heidelberg, Berlin, Heidelberg, 2005.

[27] Timo Zimmermann, Jens Rietdorf, and Rainer Pepperkok. Spectral imaging and its applications in live cell microscopy. *FEBS Letters*, 546(1):87–92, 2003.

[28] Farzad Fereidouni, Arjen N. Bader, and Hans C. Gerritsen. Spectral phasor analysis allows rapid and reliable unmixing of fluorescence microscopy spectral images. *Opt. Express*, 20(12):12729–12741, 2012.

[29] Leonel Malacrida, Soledad Astrada, Arturo Briva, Mariela Bollati-Fogollin, Enrico Gratton, and Luis Bagatolli. Spectral phasor analysis of LAURDAN fluorescence in live A549 lung cells to study the hydration and time evolution of intracellular lamellar body-like structures:. *Biochimica et Biophysica Acta (BBA) - Biomembranes*, 1858:2625–2635, 2016.

[30] Francesco Cutrale, Vikas Trivedi, Le A Trinh, Chi-Li Chiu, John M Choi, Marcela S Artiga, and Scott E Fraser. Hyperspectral phasor analysis enables multiplexed 5d in vivo imaging. *Nature methods*, 14(2):149, 2017.

[31] R. Winkler-Oswatitsch and M. Eigen. The art of titration. from classical end points to modern differential and dynamic analysis. *Angew. Chem. Intl. Ed.*, 18:20–49, 1979.

[32] Mikhail Y. Berezin and Samuel Achilefu. Fluorescence lifetime measurements and biological imaging. *Chemical Reviews*, 110(5):2641–2684, 2010.

[33] Britta Seefeldt, Robert Kasper, Thorsten Seidel, Philip Tinnefeld, Karl-Josef Dietz, Mike Heilemann, and Markus Sauer. Fluorescent proteins for single-molecule fluorescence applications. *Journal of Biophotonics*, 1(1):74–82, 2008.

[34] Dayong Jin and James A. Piper. Time-gated luminescence microscopy allowing direct visual inspection of lanthanide-stained microorganisms in background-free condition. *Anal. Chem.*, 83:2294–2300, 2011.

[35] Ryan M. Rich, Dorota L. Stankowska, Badri P. Maliwal, Thomas Just Sørensen, Bo W. Laursen, Raghu R. Krishnamoorthy, Zygmunt Gryczynski, Julian Borejdo, Ignacy Gryczynski, and Rafal Fudala. Elimination of autofluorescence background from fluorescence tissue images by use of time-gated detection and the AzaDiOxaTriAngulenium (ADOTA) fluorophore. *Analytical and Bioanalytical Chemistry*, 405:2065–2075, 2013.

[36] Ryan M. Rich, Mark Mummert, Zygmunt Gryczynski, Julian Borejdo, Thomas Just Sørensen, Bo W. Laursen, Zeno Foldes-Papp, Ignacy Gryczynski, and Rafal Fudala. Elimination of autofluorescence in fluorescence correlation spectroscopy using the AzaDiOxaTriAngulenium (ADOTA) fluorophore in combination with time-correlated

single-photon counting (TCSPC). *Analytical and Bioanalytical Chemistry*, 405:4887–4894, 2013.

[37] Blake C. Fleischer, Jeffrey T Petty, J. C. Hsiang, and Robert M Dickson. Optically activated delayed fluorescence. *The journal of physical chemistry letters*, 8 15:3536–3543, 2017.

[38] Kai Zhang, Hauyee Chang, Aihua Fu, A. Paul Alivisatos, and Haw Yang. Continuous distribution of emission states from single CdSe/ZnS quantum dots. *Nano Letters*, 6:843–847, 2006.

[39] Joseph R. Lakowicz, Henryk Szmacinski, Kazimierz Nowaczyk, Klaus W. Berndt, and Michael Jonson. Fluorescence lifetime imaging. *Analytical Biochemistry*, 202:316–330, 1992.

[40] P. I. Bastiaens and A. Squire. Fluorescence lifetime imaging microscopy: spatial resolution of biochemical processes in the cell. *Trends in Cell Biology*, 9:48–52, 1999.

[41] Thomas Niehörster, Anna Löschberger, Ingo Gregor, Benedikt Krämer, Hans-Jürgen Rahn, Matthias Patting, Felix Koberling, Jörg Enderlein, and Markus Sauer. Multi-target spectrally resolved fluorescence lifetime imaging microscopy. *Nature methods*, 13(3):257–262, 2016.

[42] Sebastian van de Linde and Markus Sauer. How to switch a fluorophore: from undesired blinking to controlled photoswitching. *Chemical Society Reviews*, 43(4):1076–1087, 2014.

[43] Elizabeth A Jares-Erijman and Thomas M Jovin. Fret imaging. *Nature biotechnology*, 21(11):1387–1395, 2003.

[44] Chris I Richards, Jung-Cheng Hsiang, Andrew M Khalil, Nathan P Hull, and Robert M Dickson. Fret-enabled optical modulation for high sensitivity fluorescence imaging. *Journal of the American Chemical Society*, 132(18):6318–6323, 2010.

[45] J.-C. Hsiang, A. E. Jablonski, and R. M. Dickson. Optically modulated fluorescence bioimaging: Visualizing obscured fluorophores in high background. *Acc. Chem. Res.*, 47:1545–1554, 2014.

[46] George H Patterson and Jennifer Lippincott-Schwartz. A photoactivatable gfp for selective photolabeling of proteins and cells. *Science*, 297(5588):1873–1877, 2002.

[47] Jörg Wiedenmann, Sergey Ivanchenko, Franz Oswald, Florian Schmitt, Carlheinz Röcker, Anya Salih, Klaus-Dieter Spindler, and G Ulrich Nienhaus. Eosfp, a fluorescent marker protein with uv-inducible green-to-red fluorescence conversion. *Proceedings of the National Academy of Sciences*, 101(45):15905–15910, 2004.

[48] G. T. Dempsey, M. Bates, W. E. Kowtoniuk, D. R. Liu, R. Y. Tsien, and X. Zhuang. Photoswitching mechanism of cyanine dyes. *J. Am. Chem. Soc.*, 131:18192–18193, 2009.

[49] T. Fukaminato. Single-molecule fluorescence photoswitching : Design and synthesis of photoswitchable fluorescent molecules. *J. Photochem. Photobiol. C : Photochem. Rev.*, 12:177–208, 2011.

[50] D. Bourgeois and V. Adam. Reversible photoswitching in fluorescent proteins : A mechanistic view. *IUBMB Life*, 64:482–491, 2012.

[51] X. X. Zhou and M. Z. Lin. Photoswitchable fluorescent proteins: ten years of colorful chemistry and exciting applications. *Curr. Opin. Chem. Biol.*, 17:682–690, 2013.

[52] Ryoko Ando, Hideaki Mizuno, and Atsushi Miyawaki. Regulated fast nucleocytoplasmic shuttling observed by reversible protein highlighting. *Science*, 306:1370–1373, 2004.

[53] M. Andresen, A. C. Stiel, S. Trowitzsch, G. Weber, C. Eggeling, M. C. Wahl, S. W. Hell, and S. Jakobs. Structural basis for reversible photoswitching in Dronpa. *Proc. Natl. Acad. Sci. U. S. A.*, 104:13005–13009, 2007.

[54] Satoshi Habuchi, Ryoko Ando, Peter Dedecker, Wendy Verheijen, Hideaki Mizuno, Atsushi Miyawaki, and Johan Hofkens. Reversible single-molecule photoswitching in the GFP-like fluorescent protein Dronpa. *Proceedings of the National Academy of Sciences*, 102:9511–9516, 2005.

[55] Andre C. Stiel, Simon Trowitzsch, Gert Weber, Martin Andresen, Christian Eggeling, Stefan W. Hell, Stefan Jakobs, and Markus C. Wahl. 1.8 å bright-state structure of the reversibly switchable fluorescent protein Dronpa guides the generation of fast switching variants. *Biochemical Journal*, 402(1):35–42, 2007.

[56] Ryoko Ando, Cristina Flors, Hideaki Mizuno, Johan Hofkens, and Atsushi Miyawaki. Highlighted generation of fluorescence signals using simultaneous two-color irradiation on Dronpa mutants. *Biophysical Journal*, 92:97–99, 2007.

[57] Martin Andresen, Andre C Stiel, Jonas Folling, Dirk Wenzel, Andreas Schonle, Alexander Egner, Christian Eggeling, Stefan W Hell, and Stefan Jakobs. Photoswitchable fluorescent proteins enable monochromatic multilabel imaging and dual color fluorescence nanoscopy. *Nature Biotechnology*, 26:1035–1040, 2008.

[58] G. Marriott, S. Mao, T. Sakata, J. Ran, D. K. Jackson, C. Petchprayoon, T. J. Gomez, E. Warp, O. Tulyathan, H. L. Aaron, E. Y. Isacoff, and Y. Yan. Optical lock-in detection imaging microscopy for contrast-enhanced imaging in living cells. *Proc. Natl. Acad. Sci. U. S. A.*, 105:17789–17794, 2008.

[59] Amy E Jablonski, Jung-Cheng Hsiang, Pritha Bagchi, Nathan Hull, Chris I Richards, Christoph J Fahrni, and Robert M Dickson. Signal discrimination between fluorescent proteins in live cells by long-wavelength optical modulation. *The journal of physical chemistry letters*, 3(23):3585–3591, 2012.

[60] Amy E. Jablonski, Russell B. Vegh, J. C. Hsiang, Bettina R Bommarius, Yen-Cheng Chen, Kyril M Solntsev, Andreas S. Bommarius, Laren M. Tolbert, and Robert M Dickson. Optically modulatable blue fluorescent proteins. *J. Am. Chem. Soc.*, 135 44:16410–7, 2013.

[61] Yen-Cheng Chen, Amy E Jablonski, Irina Issaeva, Daisy Bourassa, Jung-Cheng Hsiang, Christoph J Fahrni, and Robert M Dickson. Optically modulated photoswitchable fluorescent proteins yield improved biological imaging sensitivity. *Journal of the American Chemical Society*, 137(40):12764–12767, 2015.

[62] J. Quérard, T.-Z. Markus, M.-A. Plamont, C. Gauron, P. Wang, A. Espagne, M. Volovitch, S. Vriz, V. Croquette, A. Gautier, T. Le Saux, and L. Jullien. Photoswitching kinetics and phase-sensitive detection add discriminative dimensions for selective fluorescence imaging. *Angew. Chem. Int. Ed.*, 127:2671–2675, 2015.

[63] J. Quérard, R. Zhang, Z. Kelemen, M.-A. Plamont, X. Xie, R. Chouket, I. Roemgens, Y. Korepina, S. Albright, E. Ipendey, M. Volovitch, H. L. Sladitschek, P. Neveu, L. Gissot, A. Gautier, J.-D. Faure, V. Croquette, T. Le Saux, and L. Jullien. Resonant

out-of-phase fluorescence microscopy and remote imaging overcome spectral limitations. *Nat. Comm.*, 8:969, 2017.

[64] Antony Orth, Richik N. Ghosh, Emma R. Wilson, Timothy Doughney, Hannah Brown, Philipp Reineck, Jeremy G. Thompson, and Brant C. Gibson. Super-multiplexed fluorescence microscopy via photostability contrast. *Biomed. Opt. Express*, 9(7):2943–2954, 2018.

[65] Tor Sandén, Gustav Persson, Per Thyberg, Hans Blom, and Jerker Widengren. Monitoring kinetics of highly environment sensitive states of fluorescent molecules by modulated excitation and time-averaged fluorescence intensity recording. *Analytical chemistry*, 79(9):3330–3341, 2007.

[66] Tor Sandén, Gustav Persson, and Jerker Widengren. Transient state imaging for microenvironmental monitoring by laser scanning microscopy. *Analytical chemistry*, 80(24):9589–9596, 2008.

[67] J. Widengren. Fluorescence-based transient state monitoring for biomolecular spectroscopy and imaging. *J. R. Soc. Interface*, 7:1135–1144, 2010.

[68] C. I. Richards, J.-C. Hsiang, and R. M. Dickson. Synchronously amplified fluorescence image recovery (SAFIRe). *J. Phys. Chem. B*, 114:660–665, 2010.

[69] J. Quérard, A. Gautier, T. Le Saux, and L. Jullien. Expanding discriminative dimensions for analysis and imaging. *Chem. Sci.*, 6:2968–2978, 2015.

[70] Ruikang Zhang, Raja Chouket, Marie-Aude Plamont, Zsolt Kelemen, Agathe Espagne, Alison G Tebo, Arnaud Gautier, Lionel Gissot, Jean-Denis Faure, Ludovic Jullien, Vincent Croquette, and Thomas Le Saux. Macroscale fluorescence imaging against autofluorescence under ambient light. *Light: Science & Applications*, 7(1):97, 2018.

[71] Ruikang Zhang, Raja Chouket, Alison G. Tebo, Marie-Aude Plamont, Zsolt Kelemen, Lionel Gissot, Jean-Denis Faure, Arnaud Gautier, Vincent Croquette, Ludovic Jullien, and Thomas Le Saux. A simple imaging protocol for autofluorescence elimination and optical sectioning in fluorescence endomicroscopy. *Optica*, 6:972–980, 2019.

[72] Gan Du, Gerard Marriott, and Yuling Yan. An improved optical lock-in detection method for contrast-enhanced imaging in living cells. In *2010 4th International Conference on Bioinformatics and Biomedical Engineering*, pages 1–5. IEEE, 2010.

[73] Liangxing Wu, Yingrui Dai, Xiaoli Jiang, Chutima Petchprayoon, Jessie E Lee, Tao Jiang, Yuling Yan, and Gerard Marriott. High-contrast fluorescence imaging in fixed and living cells using optimized optical switches. *PloS one*, 8(6):e64738, 2013.

[74] Gerardo Abbandonato, Barbara Storti, Giovanni Signore, Fabio Beltram, and Ranieri Bizzarri. Quantitative optical lock-in detection for quantitative imaging of switchable and non-switchable components. *Microscopy Research and Technique*, 79(10):929–937, 2016.

[75] Chris I Richards, Jung-Cheng Hsiang, Dulal Senapati, Sandeep Patel, Junhua Yu, Tom Vosch, and Robert M Dickson. Optically modulated fluorophores for selective fluorescence signal recovery. *Journal of the American Chemical Society*, 131(13):4619–4621, 2009.

[76] Chris I. Richards, Jung Cheng Hsiang, and Robert M. Dickson. Synchronously Amplified Fluorescence Image Recovery (SAFIRe). *The Journal of Physical Chemistry B*, 114:660–665, 2010.

[77] C. Fan, J.-C. Hsiang, and R. M. Dickson. Optical modulation and selective recovery of Cy5 fluorescence. *ChemPhysChem*, 13:1023–1029, 2012.

[78] Chaoyang Fan, Jung-Cheng Hsiang, Amy E Jablonski, and Robert M Dickson. All-optical fluorescence image recovery using modulated stimulated emission depletion. *Chemical science*, 2(6):1080–1085, 2011.

[79] Murilo S Baptista, Tiago P Silva, José C Sartorelli, Iberê L Caldas, and Epaminondas Rosa Jr. Phase synchronization in the perturbed chua circuit. *Physical Review E*, 67(5):056212, 2003.

[80] Wenming Zhang and Guang Meng. Nonlinear dynamical system of micro-cantilever under combined parametric and forcing excitations in mems. *Sensors and Actuators A: Physical*, 119(2):291–299, 2005.

[81] Yen Cheng Chen and Robert M Dickson. Improved fluorescent protein contrast and discrimination by optically controlling dark state lifetimes. *The journal of physical chemistry letters*, 8:733–736, 2017.

[82] Raja Chouket, Agnès Pellissier-Tanon, Annie Lemarchand, Agathe Espagne, Thomas Le Saux, and Ludovic Jullien. Dynamic contrast with reversibly photoswitchable fluorescent labels for imaging living cells. *Chemical Science*, 11(11):2882–2887, 2020.

[83] Raja Chouket, Agnès Pellissier-Tanon, Annie Lemarchand, Agathe Espagne, Thomas Le Saux, and Ludovic Jullien. Dynamic contrast for overcoming spectral interferences in fluorescence imaging. *Journal of Physics: Photonics*, 2020.

[84] R. Chouket, R. Zhang, A. Pellissier-Tanon, A. Lemarchand, A. Espagne, T. Le Saux, and L. Jullien. Out-of-phase imaging after optical modulation (opiom) for multiplexed fluorescence imaging under adverse optical conditions. In *Multiplexed Imaging*. Springer, to appear.

[85] R. Chouket, A. Espagne, L. Jullien, A. Lemarchand, T. Le Saux, and A. Pellissier-Tanon. Method and apparatus for detecting a photochemically active chemical species in a sample, September 18 2019. Patent application EP19306120.7.

[86] R. Chouket, V. Croquette, A. Espagne, L. Jullien, A. Lemarchand, T. Le Saux, A. Pellissier-Tanon, L. Signon Colonna Bozzi, and R. Zhang. Apparatus for performing photochemical measurements on a liquid or liquid-containing sample, November 24 2019. Patent application EP19306385.6.

[87] R. Chouket, V. Croquette, A. Espagne, L. Jullien, A. Lemarchand, T. Le Saux, A. Pellissier-Tanon, and R. Zhang. Method for detecting a reversible photoswitchable chemical species in a sample, December 17 2019. Patent application EP19306658.6.

[88] Agnès Pellissier-Tanon, Raja Chouket, Thomas Le Saux, Ludovic Jullien, and Annie Lemarchand. Light-assisted dynamic titration: from theory to an experimental protocol. *Physical Chemistry Chemical Physics*, 20(37):23998–24010, 2018.

[89] Nicolaas Godfried Van Kampen. Elimination of fast variables. *Physics Reports*, 124(2):69–160, 1985.

[90] Alexander N Gorban and Iliya V Karlin. Method of invariant manifold for chemical kinetics. *Chemical Engineering Science*, 58(21):4751–4768, 2003.

[91] Alexander N Gorban, Ovidiu Radulescu, and Andrei Y Zinovyev. Asymptotology of chemical reaction networks. *Chemical Engineering Science*, 65(7):2310–2324, 2010.

[92] Dimitris A Goussis. Quasi steady state and partial equilibrium approximations: their relation and their validity. *Combustion Theory and Modelling*, 16(5):869–926, 2012.

[93] AN Gorban. Model reduction in chemical dynamics: slow invariant manifolds, singular perturbations, thermodynamic estimates, and analysis of reaction graph. *Current Opinion in Chemical Engineering*, 21:48–59, 2018.

[94] Neil Fenichel. Geometric singular perturbation theory for ordinary differential equations. *Journal of differential equations*, 31(1):53–98, 1979.

[95] Simon J Fraser. The steady state and equilibrium approximations: A geometrical picture. *The Journal of chemical physics*, 88(8):4732–4738, 1988.

[96] Joseph R Murdoch. What is the rate-limiting step of a multistep reaction? *Journal of Chemical Education*, 58(1):32, 1981.

[97] Keith J Laidler. Rate controlling step: A necessary or useful concept? *Journal of Chemical Education*, 65(3):250, 1988.

[98] Sebastian Kozuch and Jan ML Martin. The rate-determining step is dead. long live the rate-determining state! *ChemPhysChem*, 12(8):1413–1418, 2011.

[99] Max Bodenstein. Eine theorie der photochemischen reaktionsgeschwindigkeiten. *Zeitschrift für physikalische Chemie*, 85(1):329–397, 1913.

[100] T Turanyi, AS Tomlin, and MJ Pilling. On the error of the quasi-steady-state approximation. *The Journal of Physical Chemistry*, 97(1):163–172, 1993.

[101] Lee A Segel. On the validity of the steady state assumption of enzyme kinetics. *Bulletin of mathematical biology*, 50(6):579–593, 1988.

[102] Lee A Segel and Marshall Slemrod. The quasi-steady-state assumption: a case study in perturbation. *SIAM review*, 31(3):446–477, 1989.

[103] Leonor Michaelis and Maude L Menten. The kinetics of the inversion effect. *Biochem. Z*, 49:333–369, 1913.

[104] Mark M Warren, Marius Kaucikas, Ann Fitzpatrick, Paul Champion, J Timothy Sage, and Jasper J Van Thor. Ground-state proton transfer in the photoswitching reactions of the fluorescent protein dronpa. *Nature communications*, 4(1):1–8, 2013.

[105] Dheerendra Yadav, Fabien Lacombat, Nadia Dozova, Fabrice Rappaport, Pascal Plaza, and Agathe Espagne. Real-time monitoring of chromophore isomerization and deprotonation during the photoactivation of the fluorescent protein dronpa. *The Journal of Physical Chemistry B*, 119(6):2404–2414, 2015.

[106] Jacques-Philippe Colletier, Michel Sliwa, François-Xavier Gallat, Michihiro Sugahara, Virginia Guillon, Giorgio Schirò, Nicolas Coquelle, Joyce Woodhouse, Laure Roux, Guillaume Gotthard, et al. Serial femtosecond crystallography and ultrafast absorption spectroscopy of the photoswitchable fluorescent protein irisfp. *The Journal of Physical Chemistry Letters*, 7(5):882–887, 2016.

[107] Nicolas Coquelle, Michel Sliwa, Joyce Woodhouse, Giorgio Schirò, Virgile Adam, Andrew Aquila, Thomas RM Barends, Sébastien Boutet, Martin Byrdin, Sergio Carbajo, et al. Chromophore twisting in the excited state of a photoswitchable fluorescent protein captured by time-resolved serial femtosecond crystallography. *Nature Chemistry*, 10(1):31–37, 2018.

[108] Sergey P Laptenok, Agnieszka A Gil, Christopher R Hall, Andras Lukacs, James N Iuliano, Garth A Jones, Gregory M Greetham, Paul Donaldson, Atsushi Miyawaki, Peter J Tonge, et al. Infrared spectroscopy reveals multi-step multi-timescale photoactivation in the photoconvertible protein archetype dronpa. *Nature chemistry*, 10(8):845–852, 2018.

[109] A Espagne. in progress.

[110] Martin Byrdin, Chenxi Duan, Dominique Bourgeois, and Klaus Brettel. A long-lived triplet state is the entrance gateway to oxidative photochemistry in green fluorescent proteins. *Journal of the American Chemical Society*, 140(8):2897–2905, 2018.

[111] Andrei A Istratov and Oleg F Vyvenko. Exponential analysis in physical phenomena. *Review of Scientific Instruments*, 70(2):1233–1257, 1999.

[112] Kenneth Levenberg. A method for the solution of certain non-linear problems in least squares. *Quarterly of applied mathematics*, 2(2):164–168, 1944.

[113] Donald W Marquardt. An algorithm for least-squares estimation of nonlinear parameters. *Journal of the society for Industrial and Applied Mathematics*, 11(2):431–441, 1963.

[114] GL Miller, JV Ramirez, and DAH Robinson. A correlation method for semiconductor transient signal measurements. *Journal of Applied Physics*, 46(6):2638–2644, 1975.

[115] SW Provencher. An eigenfunction expansion method for the analysis of exponential decay curves. *The Journal of Chemical Physics*, 64(7):2772–2777, 1976.

[116] PM Henry, JM Meese, JW Farmer, and CD Lamp. Frequency-scanned deep-level transient spectroscopy. *Journal of applied physics*, 57(2):628–630, 1985.

[117] G Ferenczi, J Boda, and T Pavelka. Isothermal frequency scan dlts. *physica status solidi (a)*, 94(2):K119–K124, 1986.

[118] L' Stuchlíková, L Harmatha, V Nagl, and M Gaži. Determination of deep-level parameters by isothermal deep-level transient spectroscopy with optical excitation. *physica status solidi (a)*, 138(1):241–248, 1993.

[119] AA Istratov. New correlation procedure for the improvement of resolution of deep level transient spectroscopy of semiconductors. *Journal of applied physics*, 82(6):2965–2968, 1997.

[120] AA Istratov. The resolution limit of traditional correlation functions for deep level transient spectroscopy. *Review of scientific instruments*, 68(10):3861–3865, 1997.

[121] AA Istratov, OF Vyvenko, H Hieslmair, and ER Weber. Critical analysis of weighting functions for the deep level transient spectroscopy of semiconductors. *Measurement Science and Technology*, 9(3):477, 1998.

[122] Luca Gammaitoni, Peter Hänggi, Peter Jung, and Fabio Marchesoni. Stochastic resonance. *Reviews of modern physics*, 70(1):223, 1998.

[123] L Gammaitoni, F Marchesoni, E Menichella-Saetta, and S Santucci. Stochastic resonance in bistable systems. *Physical Review Letters*, 62(4):349, 1989.

[124] Roland Bartussek, Peter Hänggi, and Peter Jung. Stochastic resonance in optical bistable systems. *Physical Review E*, 49(5):3930, 1994.

[125] Peter Jung and Peter Talkner. Suppression of higher harmonics at noise induced resonances. *Physical Review E*, 51(3):2640, 1995.

[126] Gerhard Schmid and Peter Hänggi. Controlling nonlinear stochastic resonance by harmonic mixing. *Physica A: Statistical Mechanics and its Applications*, 351(1):95–105, 2005.

[127] Damien Alcor, Vincent Croquette, Ludovic Jullien, and Annie Lemarchand. Molecular sorting by stochastic resonance. *Proceedings of the National Academy of Sciences*, 101(22):8276–8280, 2004.

[128] Pengcheng Wang, Jérôme Querard, Sylvie Maurin, Sarang S Nath, Thomas Le Saux, Arnaud Gautier, and Ludovic Jullien. Photochemical properties of spinach and its use in selective imaging. *Chemical Science*, 4(7):2865–2873, 2013.

[129] Marie-Aude Plamont, Emmanuelle Billon-Denis, Sylvie Maurin, Carole Gauron, Frederico M Pimenta, Christian G Specht, Jian Shi, Jérôme Quérard, Buyan Pan, Julien Rossignol, et al. Small fluorescence-activating and absorption-shifting tag for tunable protein imaging in vivo. *Proceedings of the National Academy of Sciences*, 113(3):497–502, 2016.

[130] Frederico M Pimenta, Giovanni Chiappetta, Thomas Le Saux, Joëlle Vinh, Ludovic Jullien, and Arnaud Gautier. Chromophore renewal and fluorogen-binding tags: a match made to last. *Scientific reports*, 7(1):1–8, 2017.

[131] J. Quérard, T. Le Saux, A. Gautier, D. Alcor, V. Croquette, A. Lemarchand, C. Gosse, and L. Jullien. Kinetics of reactive modules adds discriminative dimensions for selective cell imaging. *ChemPhysChem*, 17:1396–1413, 2016.

[132] A Pellissier-Tanon, R Chouket, A Espagne, T LeSaux, A Lemarchand, and L Jullien. in progress.

[133] E. Fron, M. Van der Auweraer, J. Hofkens, and P. Dedecker. Excited state dynamics of photoswitchable fluorescent protein padron. *J. Phys. Chem. B*, 117:16422–16427, 2013.

[134] Andras Lukacs, Allison Haigney, Richard Brust, Kiri Addison, Michael Towrie, Gregory M. Greetham, Garth A. Jones, Atsushi Miyawaki, Peter J. Tonge, and Stephen R. Meech. Protein photochromism observed by ultrafast vibrational spectroscopy. *The Journal of Physical Chemistry B*, 117(40):11954–11959, 2013.

[135] E. Barrez, G. Laurent, C. Pavageau, M. Sliwa, and R. Metivier. Comparative photophysical investigation of doubly-emissive photochromic-fluorescent diarylethenes. *Phys. Chem. Chem. Phys.*, 20:2470–2479, 2018.

[136] Koichi Kise, Akinori Sato, and Motoi Iwata. Segmentation of page images using the area voronoi diagram. *Computer Vision and Image Understanding*, 70(3):370–382, 1998.

Appendix A

Supporting information of the manuscript: Extra kinetic dimensions for fluorescence imaging (LIGHTNING)

A1 Materials and methods

A1.1 Materials

A1.1.1 Development of Skylan serials

We have previously reported that a serial of RSFPs with versatile properties could be obtained by site-saturation mutagenesis of the first amino acid of the chromophore triplet (XYG) in a photo-convertible fluorescent protein (PCFP).[1] Using the same strategy, we developed new RSFPs based on the PCFP mEos3.1, which can be denoted as Skylan-X (X represents the α-amino-acid at 62, the first one of the chromophore triplet). Among which two: Skylan-S[2] (herein Skylan-SVF) and Skylan-NS[3] (herein Skylan-LVF) had been reported for their optimal performance in live super-resolution microscopy. Next, to further diversify the photoswitching kinetics of Skylan-X, we did site-directed mutagenesis at 157 and 173, which had been proven to affect the brightness[4] and photoswitching kinetics.[5] All the mutants were then sequenced, and the plasmids were extracted and transformed into Escherichia coli strain BL21 (DE3). The clones were analyzed by a widefield upright fluorescence microscope (Stereo Discovery V8, Carl Zeiss) with blue light generated by the X-cite 120PC (mercury lamp) equipped with proper filter set. Then these mutants were analyzed by our home-made wield-field microscope to confirm its photo-switchable properties under 488-nm and 405-nm lasers. At last, 11 mutants with high fluorescent brightness and high on-off contrast were selected for this study.

A1.1.2 Plasmids

The plasmids for bacterial expression of variants from Skylan-NS,[3] rsFolder, and rsEGFP2[6] were provided by Pingyong Xu and Dominique Bourgeois, respectively. The members of the Skylan serials are denoted as Skylan-XXX (X represents the α-amino acid at position 62, 157, 173 respectively).

The numbering adopted for the RSFPs in this manuscript is provided below together with the sequences of the genes coding for these proteins:

- **1**: Dronpa.[7]

  ATGGTGAGTGTGATTAAACCAGACATGAAGATCAAGCTGCGTATGGAAGGCGCT
  GTAAATGGACACCCGTTCGCGATTGAAGGAGTTGGCCTTGGGAAGCCTTTCGAG
  GGAAAACAGAGTATGGACCTTAAAGTCAAAGAAGGCGGACCTCTGCCTTTCGCC
  TATGACATCTTGACAACTGTGTTCTGTTACGGCAACAGGGTATTCGCCAAATAC
  CCAGAAAATATAGTAGACTATTTCAAGCAGTCGTTTCCTGAGGGCTACTCTTGG
  GAACGAAGCATGAATTACGAAGACGGGGGCATTTGTAACGCGACAAACGACATA

ACCCTGGATGGTGACTGTTATATCTATGAAATTCGATTTGATGGTGTGAACTTT
CCTGCCAATGGTCCAGTTATGCAGAAGAGGACTGTGAAATGGGAGCCATCCACT
GAGAAATTGTATGTGCGTGATGGAGTGCTGAAGGGTGATGTTAACATGGCTCTG
TCGCTTGAAGGAGGTGGCCATTACCGATGTGACTTCAAAACTACTTATAAAGCT
AAGAAGGTTGTCCAGTTGCCAGACTATCACTTTGTGGACCACCACATTGAGATT
AAAAGCCACGACAAAGATTACAGTAATGTTAATCTGCATGAGCACGCCGAAGCG
CATTCTGAGCTGCCGAGGCAGGCCAAG;

- **2**: Dronpa-2.[8]

ATGGTGAGTGTGATTAAACCAGACATGAAGATCAAGCTGCGTATGGAAGGCGCT
GTAAATGGACACCCGTTCGCGATTGAAGGAGTTGGCCTTGGGAAGCCTTTCGAG
GGAAAACAGAGTATGGACCTTAAAGTCAAAGAAGGCGGACCTCTGCCTTTCGCC
TATGACATCTTGACAACTGTGTTCTGTTACGGCAACAGGGTATTCGCCAAATAC
CCAGAAAATATAGTAGACTATTTCAAGCAGTCGTTTCCTGAGGGCTACTCTTGG
GAACGAAGCATGAATTACGAAGACGGGGGCATTTGTAACGCGACAAACGACATA
ACCCTGGATGGTGACTGTTATATCTATGAAATTCGATTTGATGGTGTGAACTTT
CCTGCCAATGGTCCAGTTATGCAGAAGAGGACTGTGAAATGGGAGCCATCCACT
GAGAAATTGTATGTGCGTGATGGAGTGCTGAAGGGTGATGTTAACACGGCTCTG
TCGCTTGAAGGAGGTGGCCATTACCGATGTGACTTCAAAACTACTTATAAAGCT
AAGAAGGTTGTCCAGTTGCCAGACTATCACTTTGTGGACCACCACATTGAGATT
AAAAGCCACGACAAAGATTACAGTAATGTTAATCTGCATGAGCACGCCGAAGCG
CATTCTGAGCTGCCGAGGCAGGCCAAG;

- **3**: Dronpa-3.[9]

ATGGTGAGTGTGATTAAACCAGACATGAAGATCAAGCTGCGTATGGAAGGCGCT
GTAAATGGACACCCGTTCGCGATTGAAGGAGTTGGCCTTGGGAAGCCTTTCGAG
GGAAAACAGAGTATGGACCTTAAAGTCAAAGAAGGCGGACCTCTGCCTTTCGCC
TATGACATCTTGACAACTGTGTTCTGTTACGGCAACAGGGTATTCGCCAAATAC
CCAGAAAATATAGTAGACTATTTCAAGCAGTCGTTTCCTGAGGGCTACTCTTGG
GAACGAAGCATGAATTACGAAGACGGGGGCATTTGTAACGCGACAAACGACATA
ACCCTGGATGGTGACTGTTATATCTATGAAATTCGATTTGATGGTGTGAACTTT
CCTGCCAATGGTCCAGTTATGCAGAAGAGGACTGTGAAATGGGAGCCATCCACT
GAGAAATTGTATGTGCGTGATGGAGTGCTGAAGGGTGATATTAACGCCGCTCTG
TCGCTTGAAGGAGGTGGCCATTACCGATGTGACTTCAAAACTACTTATAAAGCT
AAGAAGGTTGTCCAGTTGCCAGACTATCACTTTGTGGACCACCACATTGAGATT

AAAAGCCACGACAAAGATTACAGTAATGTTAATCTGCATGAGCACGCCGAAGCG
CATTCTGAGCTGCCGAGGCAGGCCAAGTAA;

- **4**: Kohinoor.[10]

ATGAGTGTGATTAAACCAGACATGAAGATCAAGCTGCGTATGGAAGGCGCTGTA
AATGGACACCCGTTCGCGATTGAAGGAGTTGGCCTTGGGAAGCCTTTCGAGGGA
AAACAGAGTATGGACCTTAAAGTCAAAGAAGGCGGACCTCTGCCTTTCGCCTAT
GACATCTTGACAATGGCCTTCTGTTACGGCAACAGGGTATTCGCCAAATACCCA
GAAAATATAGTAGATTATTTCAAGCAGTCGTTTCCTGAGGGCTACTCTTGGGAA
CGAAGCATGATTTACGAAGACGGGGGCATTTGTATCGCGACAAACGACATAACC
CTGGATGGTGACTGTTATATCTATGAAATTCGATTTGATGGTGTGAACTTTCCT
GCCAATGGTCCAGTTATGCAGAAGAGGACTGTGAAATGGGAGCCATCCACTGAG
AAATTGTATGTGCGTGATGGAGTGCTGAAGAGCGATGGCAATTACGCTCTGTCG
CTTGAAGGAGGTGGCCACTACCGATGTGACTCCAAAACTACTTATAAAGCTAAG
AAGGTTGTCCAGTTGCCAGACTATCACGATGTGGTCCACCACATTGAGATTAAA
AGCCACGACAGAGATTACAGTAATGTTAATCTGCATGAGCATGCCGAAGCGCAT
TCTGGGCTGCCGAGGCAGGCCAAGTAA;

- **5**: Padron.[11]

ATGAGTGTGATTAAACCAGACATGAAGATCAAGCTGCGTATGGAAGGCGCTGTA
AATGGACACCCGTTCGCGATTGAAGGAGTTGGCCTTGGGAAGCCTTTCGAGGGA
AAACAGAGTATGGACCTTAAAGTCAAAGAAGGCGGACCTCTGCCTTTCGCCTAT
GACATCTTGACAATGGCGTTCTGTTACGGCAACAGGGTATTCGCCAAATACCCA
GAAAATATAGTAGACTATTTCAAGCAGTCGTTTCCTGAGGGCTACTCTTGGGAA
CGAAGCATGATTTACGAAGACGGGGGCATTTGTAACGCGACAAACGACATAACC
CTGGATGGTGACTGTTATATCTATGAAATTCGATTTGATGGTGTGAACTTTCCT
GCCAATGGTCCAGTTATGCAGAAGAGGACTGTGAAATGGGAGCTATCCACTGAG
AAATTGTATGTGCGTGATGGAGTGCTGAAGTCTGATGGTAACTACGCTCTGTCG
CTTGAAGGAGGTGGCCATTACCGATGTGACTTCAAAACTACTTATAAAGCTAAG
AAGGTTGTCCAGTTGCCAGACTATCACTCTGTGGACCACCACATTGAGATTAAA
AGCCACGACAAAGATTACAGTAATGTTAATCTGCATGAGCATGCCGAAGCGCAT
TCTGAGCTGCCGAGGCAGGCCAAG;

- **6**: rsEGFP2.[12]

ATGGTGAGCAAGGGCGAGGAGCTGTTCACCGGGGTGGTGCCCATCCTGGTCGAG
CTGGACGGCGACGTAAACGGCCACAAGTTCAGCGTGTCCGGCGAGGGCGAGGGC

GATGCCACCTACGGCAAGCTGACCCTGAAGTTCATCTGCACCACCGGCAAGCTG
CCCGTGCCCTGGCCCACCCTCGTGACCACCCTGGCCTACGGCGTGCTGTGCTTC
AGCCGCTACCCCGACCACATGAAGCAGCACGACTTCTTCAAGTCCGCCATGCCC
GAAGGCTACGTCCAGGAGCGCACCATCTTCTTCAAGGACGACGGCAACTACAAG
ACCCGCGCCGAGGTGAAGTTCGAGGGCGACACCCTGGTGAACCGCATCGAGCTG
AAGGGCATCGACTTCAAGGAGGACGGCAACATCCTGGGGCACAAGCTGGAGTAC
AACTACAACAGCCACAACGTCTATATCATGGCCGACAAGCAGAAGAACGGCATC
AAGTCTAACTTCAAGATCCGCCACAACATCGAGGACGGCAGCGTGCAGCTCGCC
GACCACTACCAGCAGAACACCCCCATCGGCGACGGCCCCGTGCTGCTGCCCGAC
AACCACTACCTGAGCACCCAGTCCAAGCTGAGCAAAGACCCCAACGAGAAGCGC
GATCACATGGTCCTGCTGGAGTTCGTGACCGCCGCCGGGATCACTCTCGGCATG
GACGAGCTGTACAAG;

- **7**: rsFastLime.[8,11]

ATGGTGAGTGTGATTAAACCAGACATGAAGATCAAGCTGCGTATGGAAGGCGCT
GTAAATGGACACCCGTTCGCGATTGAAGGAGTTGGCCTTGGGAAGCCTTTCGAG
GGAAAACAGAGTATGGACCTTAAAGTCAAAGAAGGCGGACCTCTGCCTTTCGCC
TATGACATCTTGACAACTGTGTTCTGTTACGGCAACAGGGTATTCGCCAAATAC
CCAGAAAATATAGTAGACTATTTCAAGCAGTCGTTTCCTGAGGGCTACTCTTGG
GAACGAAGCATGAATTACGAAGACGGGGGCATTTGTAACGCGACAAACGACATA
ACCCTGGATGGTGACTGTTATATCTATGAAATTCGATTTGATGGTGTGAACTTT
CCTGCCAATGGTCCAGTTATGCAGAAGAGGACTGTGAAATGGGAGCCATCCACT
GAGAAATTGTATGTGCGTGATGGAGTGCTGAAGGGTGATGGTAACATGGCTCTG
TCGCTTGAAGGAGGTGGCCATTACCGATGTGACTTCAAAACTACTTATAAAGCT
AAGAAGGTTGTCCAGTTGCCAGACTATCACTTTGTGGACCACCACATTGAGATT
AAAAGCCACGACAAAGATTACAGTAATGTTAATCTGCATGAGCACGCCGAAGCG
CATTCTGAGCTGCCGAGGCAGGCCAAG;

- **8**: Skylan-MVF.

CATCATCATCATCATCATGGTATGGCTAGCATGACTGGTGGACAGCAAATGGGT
CGGGATCTGTACGACGATGACGATAAGGATCGATGGGGATCCATGAGTGCGATT
AAGCCAGACATGAAGATCAAACTCCGTATGGAAGGCAACGTAAACGGGCACCAC
TTTGTGATCGACGGAGATGGTACAGGCAAGCCTTTTGAGGGAAAACAGAGTATG
GATCTTGAAGTCAAAGAGGGCGGACCTCTGCCTTTTGCCTTTGATATCCTGACC
ACTGCATTCATGTACGGCAACAGGGTATTCGCCAAATATCCAGACAACATACAA

GACTATTTTAAGCAGTCGTTTCCTAAGGGGTATTCGTGGGAACGAAGCTTGACT
TTCGAAGACGGGGGCATTTGCAACGCCAGAAACGACATAACAATGGAAGGGGAC
ACTTTCTATAATAAAGTTCGATTTTATGGTACCAACTTTCCCGCCAATGGTCCA
GTTATGCAGAAGAAGACGCTGAAATGGGAGCCCTCCACTGAGAAAATGTATGTG
CGTGATGGAGTGCTGACGGGTGATGTAGAGATGGCTTTGTTGCTTGAAGGAAAT
GCCCATTACCGATGTGACTTCAGAACTACTTACAAAGCTAAGGAGAAGGGTGTC
AAGTTACCAGGCGCCCACTTTGTGGACCACTGCATTGAGATTTTAAGCCATGAC
AAAGATTACAACAAGGTTAAGCTGTATGAGCATGCTGTTGCTCATTCTGGATTG
CCTGACAATGCCAGACGATAA;

- **9**: Skylan-SVF.

CATCATCATCATCATCATGGTATGGCTAGCATGACTGGTGGACAGCAAATGGGT
CGGGATCTGTACGACGATGACGATAAGGATCGATGGGGATCCATGAGTGCGATT
AAGCCAGACATGAAGATCAAACTCCGTATGGAAGGCAACGTAAACGGGCACCAC
TTTGTGATCGACGGAGATGGTACAGGCAAGCCTTTTGAGGGAAAACAGAGTATG
GATCTTGAAGTCAAAGAGGGCGGACCTCTGCCTTTTGCCTTTGATATCCTGACC
ACTGCATTCTCCTACGGCAACAGGGTATTCGCCAAATATCCAGACAACATACAA
GACTATTTTAAGCAGTCGTTTCCTAAGGGGTATTCGTGGGAACGAAGCTTGACT
TTCGAAGACGGGGGCATTTGCAACGCCAGAAACGACATAACAATGGAAGGGGAC
ACTTTCTATAATAAAGTTCGATTTTATGGTACCAACTTTCCCGCCAATGGTCCA
GTTATGCAGAAGAAGACGCTGAAATGGGAGCCCTCCACTGAGAAAATGTATGTG
CGTGATGGAGTGCTGACGGGTGATGTAGAGATGGCTTTGTTGCTTGAAGGAAAT
GCCCATTACCGATGTGACTTCAGAACTACTTACAAAGCTAAGGAGAAGGGTGTC
AAGTTACCAGGCGCCCACTTTGTGGACCACTGCATTGAGATTTTAAGCCATGAC
AAAGATTACAACAAGGTTAAGCTGTATGAGCATGCTGTTGCTCATTCTGGATTG
CCTGACAATGCCAGACGATAA;

- **10**: Skylan-LVF.

CATCATCATCATCATCATGGTATGGCTAGCATGACTGGTGGACAGCAAATGGGT
CGGGATCTGTACGACGATGACGATAAGGATCGATGGGGATCCATGAGTGCGATT
AAGCCAGACATGAAGATCAAACTCCGTATGGAAGGCAACGTAAACGGGCACCAC
TTTGTGATCGACGGAGATGGTACAGGCAAGCCTTTTGAGGGAAAACAGAGTATG
GATCTTGAAGTCAAAGAGGGCGGACCTCTGCCTTTTGCCTTTGATATCCTGACC
ACTGCATTCCTGTACGGCAACAGGGTATTCGCCAAATATCCAGACAACATACAA
GACTATTTTAAGCAGTCGTTTCCTAAGGGGTATTCGTGGGAACGAAGCTTGACT

TTCGAAGACGGGGGCATTTGCAACGCCAGAAACGACATAACAATGGAAGGGGAC
ACTTTCTATAATAAAGTTCGATTTTATGGTACCAACTTTCCCGCCAATGGTCCA
GTTATGCAGAAGAAGACGCTGAAATGGGAGCCCTCCACTGAGAAAATGTATGTG
CGTGATGGAGTGCTGACGGGTGATGTAGAGATGGCTTTGTTGCTTGAAGGAAAT
GCCCATTACCGATGTGACTTCAGAACTACTTACAAAGCTAAGGAGAAGGGTGTC
AAGTTACCAGGCGCCCACTTTGTGGACCACTGCATTGAGATTTTAAGCCATGAC
AAAGATTACAACAAGGTTAAGCTGTATGAGCATGCTGTTGCTCATTCTGGATTG
CCTGACAATGCCAGACGATAA;

- **11**: Skylan-EVF.

CATCATCATCATCATCATGGTATGGCTAGCATGACTGGTGGACAGCAAATGGGT
CGGGATCTGTACGACGATGACGATAAGGATCGATGGGGATCCATGAGTGCGATT
AAGCCAGACATGAAGATCAAACTCCGTATGGAAGGCAACGTAAACGGGCACCAC
TTTGTGATCGACGGAGATGGTACAGGCAAGCCTTTTGAGGGAAAACAGAGTATG
GATCTTGAAGTCAAAGAGGGCGGACCTCTGCCTTTTGCCTTTGATATCCTGACC
ACTGCATTCGAGTACGGCAACAGGGTATTCGCCAAATATCCAGACAACATACAA
GACTATTTTAAGCAGTCGTTTCCTAAGGGGTATTCGTGGGAACGAAGCTTGACT
TTCGAAGACGGGGGCATTTGCAACGCCAGAAACGACATAACAATGGAAGGGGAC
ACTTTCTATAATAAAGTTCGATTTTATGGTACCAACTTTCCCGCCAATGGTCCA
GTTATGCAGAAGAAGACGCTGAAATGGGAGCCCTCCACTGAGAAAATGTATGTG
CGTGATGGAGTGCTGACGGGTGATGTAGAGATGGCTTTGTTGCTTGAAGGAAAT
GCCCATTACCGATGTGACTTCAGAACTACTTACAAAGCTAAGGAGAAGGGTGTC
AAGTTACCAGGCGCCCACTTTGTGGACCACTGCATTGAGATTTTAAGCCATGAC
AAAGATTACAACAAGGTTAAGCTGTATGAGCATGCTGTTGCTCATTCTGGATTG
CCTGACAATGCCAGACGATAA;

- **12**: Skylan-VVF.

CATCATCATCATCATCATGGTATGGCTAGCATGACTGGTGGACAGCAAATGGGT
CGGGATCTGTACGACGATGACGATAAGGATCGATGGGGATCCATGAGTGCGATT
AAGCCAGACATGAAGATCAAACTCCGTATGGAAGGCAACGTAAACGGGCACCAC
TTTGTGATCGACGGAGATGGTACAGGCAAGCCTTTTGAGGGAAAACAGAGTATG
GATCTTGAAGTCAAAGAGGGCGGACCTCTGCCTTTTGCCTTTGATATCCTGACC
ACTGCATTCGTGTACGGCAACAGGGTATTCGCCAAATATCCAGACAACATACAA
GACTATTTTAAGCAGTCGTTTCCTAAGGGGTATTCGTGGGAACGAAGCTTGACT
TTCGAAGACGGGGGCATTTGCAACGCCAGAAACGACATAACAATGGAAGGGGAC

ACTTTCTATAATAAAGTTCGATTTTATGGTACCAACTTTCCCGCCAATGGTCCA
GTTATGCAGAAGAAGACGCTGAAATGGGAGCCCTCCACTGAGAAAATGTATGTG
CGTGATGGAGTGCTGACGGGTGATGTAGAGATGGCTTTGTTGCTTGAAGGAAAT
GCCCATTACCGATGTGACTTCAGAACTACTTACAAAGCTAAGGAGAAGGGTGTC
AAGTTACCAGGCGCCCACTTTGTGGACCACTGCATTGAGATTTTAAGCCATGAC
AAAGATTACAACAAGGTTAAGCTGTATGAGCATGCTGTTGCTCATTCTGGATTG
CCTGACAATGCCAGACGATAA;

- **13**: Skylan-MIF.

CATCATCATCATCATCATGGTATGGCTAGCATGACTGGTGGACAGCAAATGGGT
CGGGATCTGTACGACGATGACGATAAGGATCGATGGGGATCCATGAGTGCGATT
AAGCCAGACATGAAGATCAAACTCCGTATGGAAGGCAACGTAAACGGGCACCAC
TTTGTGATCGACGGAGATGGTACAGGCAAGCCTTTTGAGGGAAAACAGAGTATG
GATCTTGAAGTCAAAGAGGGCGGACCTCTGCCTTTTGCCTTTGATATCCTGACC
ACTGCATTCATGTACGGCAACAGGGTATTCGCCAAATATCCAGACAACATACAA
GACTATTTTAAGCAGTCGTTTCCTAAGGGGTATTCGTGGGAACGAAGCTTGACT
TTCGAAGACGGGGGCATTTGCAACGCCAGAAACGACATAACAATGGAAGGGGAC
ACTTTCTATAATAAAGTTCGATTTTATGGTACCAACTTTCCCGCCAATGGTCCA
GTTATGCAGAAGAAGACGCTGAAATGGGAGCCCTCCACTGAGAAAATGTATGTG
CGTGATGGAGTGCTGACGGGTGATATTGAGATGGCTTTGTTGCTTGAAGGAAAT
GCCCATTACCGATGTGACTTCAGAACTACTTACAAAGCTAAGGAGAAGGGTGTC
AAGTTACCAGGCGCCCACTTTGTGGACCACTGCATTGAGATTTTAAGCCATGAC
AAAGATTACAACAAGGTTAAGCTGTATGAGCATGCTGTTGCTCATTCTGGATTG
CCTGACAATGCCAGACGATAA;

- **14**: Skylan-SIF.

CATCATCATCATCATCATGGTATGGCTAGCATGACTGGTGGACAGCAAATGGGT
CGGGATCTGTACGACGATGACGATAAGGATCGATGGGGATCCATGAGTGCGATT
AAGCCAGACATGAAGATCAAACTCCGTATGGAAGGCAACGTAAACGGGCACCAC
TTTGTGATCGACGGAGATGGTACAGGCAAGCCTTTTGAGGGAAAACAGAGTATG
GATCTTGAAGTCAAAGAGGGCGGACCTCTGCCTTTTGCCTTTGATATCCTGACC
ACTGCATTCTCCTACGGCAACAGGGTATTCGCCAAATATCCAGACAACATACAA
GACTATTTTAAGCAGTCGTTTCCTAAGGGGTATTCGTGGGAACGAAGCTTGACT
TTCGAAGACGGGGGCATTTGCAACGCCAGAAACGACATAACAATGGAAGGGGAC
ACTTTCTATAATAAAGTTCGATTTTATGGTACCAACTTTCCCGCCAATGGTCCA

GTTATGCAGAAGAAGACGCTGAAATGGGAGCCCTCCACTGAGAAAATGTATGTG
CGTGATGGAGTGCTGACGGGTGATATTGAGATGGCTTTGTTGCTTGAAGGAAAT
GCCCATTACCGATGTGACTTCAGAACTACTTACAAAGCTAAGGAGAAGGGTGTC
AAGTTACCAGGCGCCCACTTTGTGGACCACTGCATTGAGATTTTAAGCCATGAC
AAAGATTACAACAAGGTTAAGCTGTATGAGCATGCTGTTGCTCATTCTGGATTG
CCTGACAATGCCAGACGATAA;

- **15**: Skylan-MVS.

CATCATCATCATCATCATGGTATGGCTAGCATGACTGGTGGACAGCAAATGGGT
CGGGATCTGTACGACGATGACGATAAGGATCGATGGGGATCCATGAGTGCGATT
AAGCCAGACATGAAGATCAAACTCCGTATGGAAGGCAACGTAAACGGGCACCAC
TTTGTGATCGACGGAGATGGTACAGGCAAGCCTTTTGAGGGAAAACAGAGTATG
GATCTTGAAGTCAAAGAGGGCGGACCTCTGCCTTTTGCCTTTGATATCCTGACC
ACTGCATTCATGTACGGCAACAGGGTATTCGCCAAATATCCAGACAACATACAA
GACTATTTTAAGCAGTCGTTTCCTAAGGGGTATTCGTGGGAACGAAGCTTGACT
TTCGAAGACGGGGGCATTTGCAACGCCAGAAACGACATAACAATGGAAGGGGAC
ACTTTCTATAATAAAGTTCGATTTTATGGTACCAACTTTCCCGCCAATGGTCCA
GTTATGCAGAAGAAGACGCTGAAATGGGAGCCCTCCACTGAGAAAATGTATGTG
CGTGATGGAGTGCTGACGGGTGATGTAGAGATGGCTTTGTTGCTTGAAGGAAAT
GCCCATTACCGATGTGACTCCAGAACTACTTACAAAGCTAAGGAGAAGGGTGTC
AAGTTACCAGGCGCCCACTTTGTGGACCACTGCATTGAGATTTTAAGCCATGAC
AAAGATTACAACAAGGTTAAGCTGTATGAGCATGCTGTTGCTCATTCTGGATTG
CCTGACAATGCCAGACGATAA;

- **16**: Skylan-SVS.

CATCATCATCATCATCATGGTATGGCTAGCATGACTGGTGGACAGCAAATGGGT
CGGGATCTGTACGACGATGACGATAAGGATCGATGGGGATCCATGAGTGCGATT
AAGCCAGACATGAAGATCAAACTCCGTATGGAAGGCAACGTAAACGGGCACCAC
TTTGTGATCGACGGAGATGGTACAGGCAAGCCTTTTGAGGGAAAACAGAGTATG
GATCTTGAAGTCAAAGAGGGCGGACCTCTGCCTTTTGCCTTTGATATCCTGACC
ACTGCATTCTCCTACGGCAACAGGGTATTCGCCAAATATCCAGACAACATACAA
GACTATTTTAAGCAGTCGTTTCCTAAGGGGTATTCGTGGGAACGAAGCTTGACT
TTCGAAGACGGGGGCATTTGCAACGCCAGAAACGACATAACAATGGAAGGGGAC
ACTTTCTATAATAAAGTTCGATTTTATGGTACCAACTTTCCCGCCAATGGTCCA
GTTATGCAGAAGAAGACGCTGAAATGGGAGCCCTCCACTGAGAAAATGTATGTG

CGTGATGGAGTGCTGACGGGTGAtGTAGAGATGGCTTTGTTGCTTGAAGGAAAT
GCCCATTACCGATGTGACTCCAGAACTACTTACAAAGCTAAGGAGAAGGGTGTC
AAGTTACCAGGCGCCCACTTTGTGGACCACTGCATTGAGATTTTAAGCCATGAC
AAAGATTACAACAAGGTTAAGCTGTATGAGCATGCTGTTGCTCATTCTGGATTG
CCTGACAATGCCAGACGATAA;

- **17**: Skylan-LVS.

CATCATCATCATCATCATGGTATGGCTAGCATGACTGGTGGACAGCAAATGGGT
CGGGATCTGTACGACGATGACGATAAGGATCGATGGGGATCCATGAGTGCGATT
AAGCCAGACATGAAGATCAAACTCCGTATGGAAGGCAACGTAAACGGGCACCAC
TTTGTGATCGACGGAGATGGTACAGGCAAGCCTTTTGAGGGAAAACAGAGTATG
GATCTTGAAGTCAAAGAGGGCGGACCTCTGCCTTTTGCCTTTGATATCCTGACC
ACTGCATTCCTGTACGGCAACAGGGTATTCGCCAAATATCCAGACAACATACAA
GACTATTTTAAGCAGTCGTTTCCTAAGGGGTATTCGTGGGAACGAAGCTTGACT
TTCGAAGACGGGGGCATTTGCAACGCCAGAAACGACATAACAATGGAAGGGGAC
ACTTTCTATAATAAAGTTCGATTTTATGGTACCAACTTTCCCGCCAATGGTCCA
GTTATGCAGAAGAAGACGCTGAAATGGGAGCCCTCCACTGAGAAAATGTATGTG
CGTGATGGAGTGCTGACGGGTGATGTAGAGATGGCTTTGTTGCTTGAAGGAAAT
GCCCATTACCGATGTGACTCCAGAACTACTTACAAAGCTAAGGAGAAGGGTGTC
AAGTTACCAGGCGCCCACTTTGTGGACCACTGCATTGAGATTTTAAGCCATGAC
AAAGATTACAACAAGGTTAAGCTGTATGAGCATGCTGTTGCTCATTCTGGATTG
CCTGACAATGCCAGACGATAA;

- **18**: Skylan-SLF.

CATCATCATCATCATCATGGTATGGCTAGCATGACTGGTGGACAGCAAATGGGT
CGGGATCTGTACGACGATGACGATAAGGATCGATGGGGATCCATGAGTGCGATT
AAGCCAGACATGAAGATCAAACTCCGTATGGAAGGCAACGTAAACGGGCACCAC
TTTGTGATCGACGGAGATGGTACAGGCAAGCCTTTTGAGGGAAAACAGAGTATG
GATCTTGAAGTCAAAGAGGGCGGACCTCTGCCTTTTGCCTTTGATATCCTGACC
ACTGCATTCTCCTACGGCAACAGGGTATTCGCCAAATATCCAGACAACATACAA
GACTATTTTAAGCAGTCGTTTCCTAAGGGGTATTCGTGGGAACGAAGCTTGACT
TTCGAAGACGGGGGCATTTGCAACGCCAGAAACGACATAACAATGGAAGGGGAC
ACTTTCTATAATAAAGTTCGATTTTATGGTACCAACTTTCCCGCCAATGGTCCA
GTTATGCAGAAGAAGACGCTGAAATGGGAGCCCTCCACTGAGAAAATGTATGTG
CGTGATGGAGTGCTGACGGGTGATCTGGAGATGGCTTTGTTGCTTGAAGGAAAT

GCCCATTACCGATGTGACTTCAGAACTACTTACAAAGCTAAGGAGAAGGGTGTC
AAGTTACCAGGCGCCCACTTTGTGGACCACTGCATTGAGATTTTAAGCCATGAC
AAAGATTACAACAAGGTTAAGCTGTATGAGCATGCTGTTGCTCATTCTGGATTG
CCTGACAATGCCAGACGATAA;

- **19**: rsFolder.

ATGGTAAGCAAGGGCGAGGAGCTGTTCACCGGCGTGGTGCCAATCCTGGTGGAG
CTGGATGGCGATGTGAACGGCCACAAGTTTAGCGTGCGCGGCGAGGGCGAGGGC
GATGCTACCAACGGCAAGCTGACCCTGAAGTTTATCTGCACCACCGGCAAGCTG
CCGGTGCCGTGGCCAACCCTGGTGACCACCCTGGCCTACGGCGTGCTGTGCTTT
TCCCGCTACCCGGATCACATGAAGCGCCACGACTTTTTCAAGAGCGCCaTGCCG
GAGGGCTACGTGCAgGAGCGCACCATCaGCTTCAAGGATGACGGCACCTACAAG
ACCCGCGCTGAGGTGAAGTTTGAGGGCGATACCCTGGTGAACCGCATCGAGCTG
AAGGGCATCgACTTTAAGGAGGATGGCAACATCCTGGGCCACAAGCTGGAGTAC
AACTTTAACAGCCaCAACGTGTACATCACCGCCGAcaACGAGAAGAACGGCATC
AAGAGCAACTTCAAgATCCGCCACaAaCGTGGAGGATGGCTCCgTgCaGCTGGC
CGAcCACTACCagcaGAACACCCCAATCGGcgATGGCCCGGtGCTGCTGcCAGA
CAACCACTACCTGAgCACCCaGaGcaAGCTgAGCaAgGACCCgaAACGAgAAgc
gCGACCaCaTGgTGCtGCtGGAgTTtGTGA;

- **20**: rsFolder2.

ATGGTAAGCAAGGGCGAGGAGCTGTTCACCGGCGTGGTGCCAATCCTGGTGGAG
CTGGATGGCGATGTGAACGGCCACAAGTTTAGCGTGCGCGGCGAGGGCGAGGGC
GATGCTACCAACGGCAAGCTGACCCTGAAGTTTATCTGCACCACCGGCAAGCTG
CCGGTGCCGTGGCCAACCCTGGTGACCACCCTGGCCTACGGCGTGCTGTGCTTT
TCCCGCTACCCGGATCACATGAAGCGCCACGACTTTTTCAAGAGCGCCATGCCG
GAGGGCTACGTGCAGGAGCGCACCATCAGCTTCAAGGATGACGGCACCTACAAG
ACCCGCGCTGAGGTGAAGTTTGAGGGCGATACCCTGGTGAACCGCATCGAGCTG
AAGGGCATCGACTTTAAGGAGGATGGCAACATCCTGGGCCACAAGCTGGAGTAC
AACTATAACAGCCACAACGTGTACATCACCGCCGACAAGCAGAAGAACGGCATC
AAGAGCAACTTCAAGATCCGCCACAACGTGGAGGAtGGCTCCGtGCaGCTGGCC
GAcCACTACCAGCAGAACACCCCAATCGGCGATGGCCCGGTGCTGCTGCCAGAC
AACCACTACCTGaGCACCCAGAgCAAGCTGAgCAaGGAcCCGAACGAGAAGcGC
GACCACATGgtGCTGCTGgAgTTTGTGACCGCTGCTGGCATCaCCCACgGcATG
GATGAgCTGTaCAAGGgATCCGGCTGCTaA;

- **21**: rsFolder2 V151A.

  ATGGTAAGCAAGGGCGAGGAGCTGTTCACCGGCGTGGTGCCAATCCTGGTGGAG
  CTGGATGGCGATGTGAACGGCCACAAGTTTAGCGTGCGCGGCGAGGGCGAGGGC
  GATGCTACCAACGGCAAGCTGACCCTGAAGTTTATCTGCACCACCGGCAAGCTG
  CCGGTGCCGTGGCCAACCCTGGTGACCACCCTGGCCTACGGCGTGCTGTGCTTT
  TCCCGCTACCCGGATCACATGAAGCGCCACGACTTTTTCAAGAGCGCCATGCCG
  GAGGGCTACGTGCAGGAGCGCACCATCAGCTTCAAGGATGACGGCACCTACAAG
  ACCCGCGCTGAGGTGAAGTTTGAGGGCGATACCCTGGTGAACCGCATCGAGCTG
  AAGGGCATCGACTTTAAGGAGGATGGCAACATCCTGGGCCACAAGCTGGAGTAC
  AACTATAACAGCCACAACGCGTACATCACCGCCGACAAGCAGAAGAACGGCATC
  AAGAGCAACTTCAAGATCCGCCACAACGTGGAGGATGGCTCCGTGCAGCTGGCC
  GACCACTACCAGCAGAACACCCCAATCGGCGATGGCCCGgtgCTGCTGCCAGaC
  AACCACTACCTGAGCACCcAGAGCAAGCTGAGCAAGGACCcGAACGAGAAGCGC
  GACCACATGGTGCTGCTGGAGTTTGTGACCGCTGCTGGCATCACCCACGGCATG
  GATGAGCTGTACAAGGGATCCGGCTGCTAA;

- **22**: rsEGFP2 V151L.

  ATGGTGAGCAAGGGCGAGGagCTGTTCACCGGGGTGGTGCCCATCCTGGTCGAG
  CTGGACGGCGACGTAAACGGCCACAAGTTCAGCGTGTCCGGCGAGGGCGAGGGC
  GATGCCACCTACGGCAAGCTGACCCTGAAGTTCATCTGCACCACCGGCAAGCTG
  CCCGTGCCCTGGCCCACCCTCGTGACCACCCTGGCCTACGGCGTGCTGTGCTTC
  AGCCGCTACCCCGACCACATGAAGCAGCACGACTTCTTCAAGTCCGCCATGCCC
  GAAGGCTACGTCCAGGAGCGCACCATCTTCTTCAAGGACGACGGCAACTACAAG
  ACCCGCGCCGAGGTGAAGTTCGAGGGCGACACCCTGGTGAACCGCATCGAGCTG
  AAGGGCATCGACTTCAAGGAGGACGGCAACATCCTGGGGCACAAGCTGGAGTAC
  AACTACAACAGCCACAACCTCTATATCATGGCCGACAAGCAGAAGAACGGCATC
  AAGTCTAACTTCAAGATCCGCCACAACATCGAGGACGGCAGCGTGCAGCTCGCC
  GACCACTACCAGCAGAACACCCCCATCGGCGACGGCCCCGTGCTGCTGCCCGAC
  AACCACTACCTGAGCACCCAGTCCAAGCTGAGCAAAGACCCCAACGAGAAGCGC
  GATCACATGGTCCTGCTGGAGTTCGTGACCGCCGCcGGgATCACTCTCGGCATG
  GACGAGCTGTACAAGTAA.

A1.1.3 Protein production and purification

The plasmids expressing proteins with an N-terminal hexahistidine tag were transformed in E. coli BL21 strain. Cells were grown in Terrific Broth (TB) at 37°C. The expression was induced at 30°C

or 16°C by addition of isopropyl β-*D*-1-thio-galactopyranoside (IPTG) to a final concentration of 1 mM at OD(600)=0.6. The cells were harvested after 16 h of expression and lysed by sonication in lysis buffer (50 mM PBS with 150 mM NaCl at pH 7.4, 5 mg/ml DNAse, 5 mM $MgCl_2$ and 1 mM phenylmethylsulfonyl fluoride (PMSF), and a cocktail of protease inhibitors (Sigma Aldrich; S8830)). After lysis, the mixture was incubated on ice for 2 h for DNA digestion. The insoluble material was removed by centrifugation and the supernatant was incubated overnight with Ni-NTA agarose beads (Thermo Fisher) at 4°C in a rotator-mixer. The protein loaded Ni-NTA column was washed twice with 20 column volumes of N1 buffer (50 mM PBS, 300 mM NaCl, 30 mM imidazole, pH 7.4) and twice N2 buffer (50 mM PBS, 150 mM NaCl, 10 mM imidazole, pH 7.4). The bound protein was eluted with N3 buffer (150 mM PBS pH 7.4, 300 mM imidazole). The protein fractions were eventually dialyzed with cassette Slide-A-Lyzer Dialysis Cassettes (Thermo Fisher) against 50 mM PBS, 150 mM NaCl pH 7.4.

A1.2 Spectroscopic measurements

UV/Vis absorption spectra were recorded on a UV/Vis spectrophotometer (Cary 300 UV-Vis, Agilent Technologies, Santa Clara, CA) at $20\,^{\circ}\mathrm{C}$ equipped with a Peltier 1×1 thermostatic cell holder (Agilent Technologies). Samples (45 μL) were contained in 0.3 cm $\times$ 0.3 cm (light path) quartz cuvettes (Hellma Optics, Jena, Germany). Fluorescence measurements were acquired on a LPS 220 spectrofluorometer (PTI, Monmouth Junction, NJ), equipped with a TLC50 cuvette holder (Quantum Northwest, Liberty Lake, WA) thermoregulated at $25\,^{\circ}\mathrm{C}$.The normalized absorption and emission spectra of the 22 RSFPs, which have been investigated in this study are provided in Fig.A6.

A1.3 Measurements of the rate constant associated with thermal relaxation after photoswitching

In order to study the thermal relaxation after phoisomerization upon illumination at $\lambda_1 = 488$ nm, we used the fluorimeter to record the fluorescence emission from 5 μM RSFP solutions upon applying a series of light pulses at 480 nm up to reach the photostationary state using a LED (M470-L4, Thorlabs, NJ; filtered at 480 $\pm$ 20 nm (FF480-40, Semrock, Rochester, NY)) separated by increasing delays in the dark (denoted "illumination" III in subsection A7.1.3). Since we adopted a regime of low light intensity in which a two-state model is relevant to account for the RSFP photoswitching behavior, we could satisfactorily use an exponential fitting function to account for the decay of the fluorescence signal occurring during each light pulse and accordingly extract its value at the initial time of each light pulse (see subsection A7.1.3). We eventually retrieved the

thermal relaxation rate constant k_{21}^{Δ} from applying a monoexponential fitting function (see Eq. (A64)) to the dependence of the values of the fluorescence signal at the initial time of each light pulse on the delay (see Fig.A7–A9). The results are provided in Tab.A3.

A1.4 Description of the photoswitchometer

A1.4.1 Specification

Myriads of illuminations can be considered for LIGHTNING implementation. In order to minimize the acquisition time, it is necessary to recognize the minimal set of illuminations, which generate time series of the RSFs fluorescence signal under control of different steps of their photocycle over a given kinetic window. To address this concern with RSFPs, we designed and built a specific optical instrument , which we denominated "photoswitchometer". Equipped with synchronized detectors, it integrates two sets of light sources (Light Emitting Diodes – LEDs – and lasers for low and high regimes of light intensities, respectively) at the wavelengths $\lambda_1 = 488$ nm and $\lambda_2 = 405$ nm, which have been spectrally tuned to photoswitch green RSFPs. The photoswitchometer automatically records and analyzes in a few minutes the fluorescence response from a RSFP solution exposed to homogeneous illumination at a series of light intensities covering 5 orders of magnitude (up to a few hundreds of ein.m^{-2}.s^{-1} – 10^4 W/cm^2 range) with microseconds time resolution;

A1.4.2 Configuration for acquiring the RSFP photoswitching information

The measurement cell To facilitate automated analysis, we tailored the geometry of illumination in order to control the fluorescence evolution by the light- and thermally-driven reactions without any significant interference of diffusion over the whole range of light intensities (see subsection A7.2). The RSFP solution is sandwiched in a 80 μm-thick measurement cell, which is put on a 0.4 mm thick copper disk. This metal holder is mounted on an aluminum block thermostated at $25 \pm 0.2\,^{\circ}\mathrm{C}$ with two thermoelectric Peltier devices (CP 1.0-63-05L-RTV, Melcor, Trenton, NJ). The stage temperature is monitored with a TCS610 thermistor (Wavelength Electronics, Bozeman, MT) and the feedback loop is driven by a MPT10000 temperature controller (Wavelength Electronics, Bozeman, MT).

Light sources The photoswichometer integrates two stages enabling us to illuminate the samples with Light Emitting Diodes (LEDs) or modulated laser diodes. Overall these light sources equip the photoswitchometer with light intensities covering five orders of magnitude (from 0.5 W.cm^{-2} to 50 kW.cm^{-2}).

The LEDs illumination stage The LED illumination stage integrates a blue color LED (M470L4, Thorlabs, NJ) filtered at $\lambda_1 = 480 \pm 20$ nm (FF01-480-40, Semrock, Rochester, NY) and a UV LED (M405L3, Thorlabs, NJ) filtered at 405 ± 20 nm (ET 405/20x, Chroma Technologies, Bellows Falls, VT) as light sources. The current driving each LED is regulated by a LED driver (DC 4104, Thorlabs, NJ) operated in the external control mode and driven by the two analog outputs of a ADC card (usb-1604hs-2ao, Measurement Computing, Norton, MA) used for data acquisition or a waveform generator. A light condenser (ACL25416U, Thorlabs, Newton, NJ, $f = 16$ mm) is placed just after each LED to collimate light and both light beams are combined with a dichroic mirror (T425LPXR, Chroma Technologies, Bellows Falls, VT). A second lens ($f = 100$ mm) is used to focus the light at the back focal plane of the objective after being reflected by the dichroic filter (FF506-Di-03, Semrock, Rochester, NY). Thanks to two consecutive beam splitters (30:70, EBP1, Thorlabs and 50:50, CCM1-BS013/M, Thorlabs) and a lens (AC254-150, $f = 150$ mm), part of the fluorescence emission at 525 ± 15 nm (FF525-30, Semrock, Rochester, NY) is focused on a multipixel photocounter (C13366-1350GA, Hamamatsu Photonics K.K., Hamamatsu City, Japan) used to measure fluorescence signals and on a CMOS sensor of a camera (3060cp, iDS, Obersulm, Germany) used to control the alignment of the beams and image the illuminated sample. Triggering and synchronization of light illuminations and data acquisitions is controlled by a Labview 2010 program (National Instruments, Austin, TX).

The laser diodes illumination stage The beams of the laser diodes at $\lambda_1 = 488$ nm (LBX serie, Oxxius, Lannion, France) and $\lambda_2 = 405$ nm (06-01 Serie, Cobolt, Solna, Sweden) are first enlarged with a beam expander comprising two achromatic lenses (AC254-100-A, Thorlabs, Newton, NJ, f=100 mm and AC254-050-A, Thorlabs, Newton, NJ f=50 mm). A second afocal system made of two lenses (LA1213-A, Thorlabs, NJ, f=50 mm and LA1289-A, Thorlabs, NJ f=30 mm) is inserted in the 405 nm lightpath to correct possible chromatic aberrations of the imaging objective and improve the illumination homogeneity. The enlarged beams are combined with a dichroic mirror (T425LPXR, Chroma, Bellows Falls, VT) before the central part of the beams is selected with an iris (SM1D12CZ, Thorlabs, NJ, US), and focused with an achromatic lens (AC254-200-A, f=200 mm, Thorlabs, NJ ,US) on the rear focal plane of a 50X objective (MPLFLN, NA 0.8, Olympus Corporation, Tokyo, Japan) after passing through a dichroic filter (FF506-Di-03, Semrock, Rochester, NY). The iris is conjugated to the focal plan of the objective, so that the size of the illuminated area can be adjusted by tuning the aperture of the iris. Thanks to a 30:70 beam splitter, 70 % of the collected fluorescence emission at 525 ± 15 nm (FF525-30, Semrock, Rochester, NY) is focused with a lens (AC254-50, Thorlabs, f= 50 mm) on the aperture of a 100 μm pinhole

mounted in front of a photomultiplier tube (H10492-013, Hamamatsu Photonics K.K., Hamamatsu City, Japan) used to measure fluorescence signals while 15 % of the collected fluorescence emission is focused on a CMOS sensor of a camera (3060cp, iDS, Obersulm, Germany) used to image the illuminated sample with a lens (AC254-150, f=150 mm). Triggering and synchronization of light illuminations and data acquisitions is controlled by a Labview 2010 program (National Instruments, Austin, TX). In this system, the laser sources are triggered by a waveform generator (33612 A, Keysight Technologies) either in analogue (488 nm; accepting an arbitrary 0-5 V input signal) or in digital (405 nm) mode.

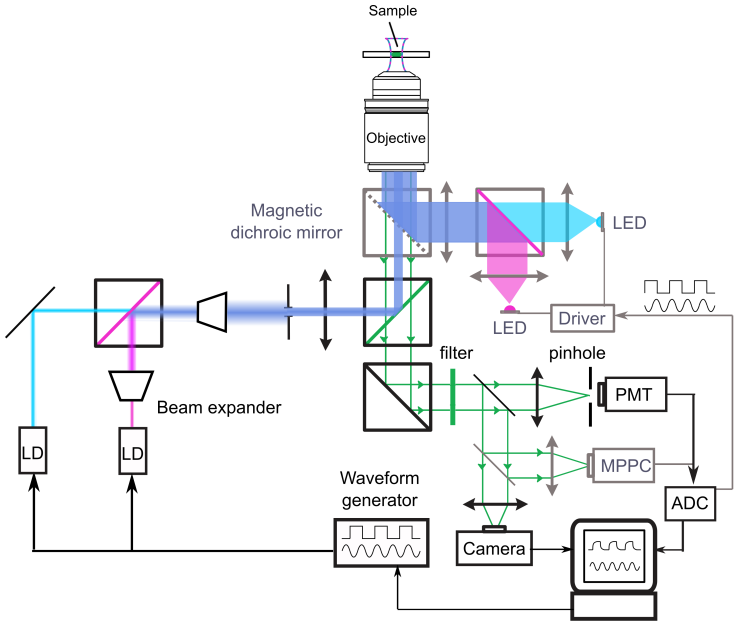

Figure A1: Scheme of the photoswitchometer designed for automated acquisition of the photoswitching kinetic information of RSFPs in liquid solutions. Light-emitting diodes and lasers diode modules are controlled with a waveform generator or the analog outputs of a data acquisition card (ADC) and deliver sequences of modulated homogeneous illumination at the sample with 1-10^5 W/cm^2 intensities and 1-10^6 Hz frequencies at $\lambda_1 = 488$ nm and $\lambda_2 = 405$ nm. Fluorescence is retrieved with synchronized detectors. The components involving LEDs and lasers for illuminations are displayed in gray and black, respectively . ADC: analog digital converter; MPPC: multipixel photon counter; PMT: photomultiplier tube; LD: Laser diode.

Temporal characterization of the illumination profiles To characterize the temporal resolution of the photoswitchometer, we recorded the time response of the signal detected by the photomultiplier upon switching on and off the light sources. Fig. A2a–d display the results. The time resolution of the photoswitchometer is limited by the time resolution of the photomultiplier when switching on and off the laser light sources at both λ_1= 488 nm and λ_2= 405 nm ($\simeq$ 1 μs). In contrast, the time resolution of the photoswitchometer is limited by the light sources when using

the LEDs. Switching on and off the light sources respectively generates signal changes at 9.6 and 1.7 μs time scales at λ_1= 488 nm (5.7 and 1.1 μs at λ_2= 405 nm, respectively).

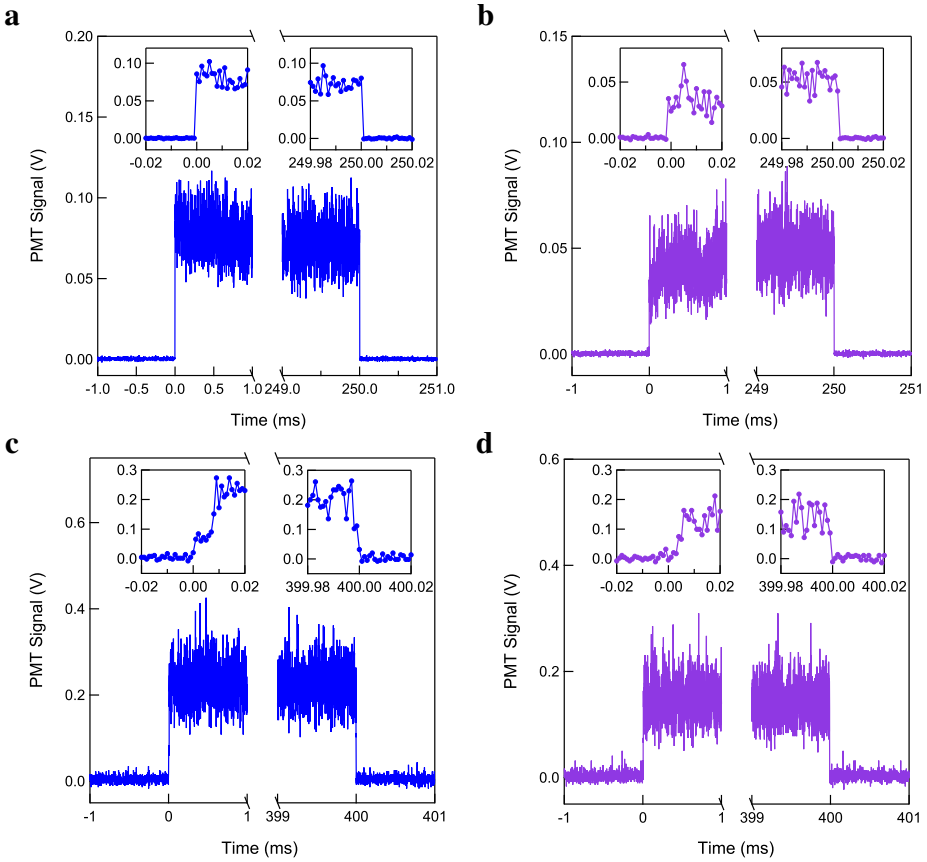

Figure A2: *Characterization of the temporal resolution of the photoswitchometer.* Time response of the signal detected by the photomultiplier upon switching on and off the lasers (**a**,**b**) and the LEDs (**c**,**d**) at λ_1= 488 nm (**a**,**c**) and λ_2= 405 nm (**b**,**d**).

A1.4.3 Calibration of light intensities

LEDs We relied on the photoswitching kinetics of a photochemically well-characterized RSFP (Dronpa-2 at pH 7.4) for measuring light intensities at which the kinetics is well-accounted with a two-state model (see section A7). We could show that such an actinometric measurement is photochemically reliable up to 10 ein.m^{-2}.s^{-1} light intensities at the wavelengths $\lambda_1 = 488$ nm and $\lambda_2 = 405$ nm respectively.

The calibration of the light intensities exploits light jumps on Dronpa-2 samples (typically a 10 μM Dronpa-2 solution in pH 7.4 PBS buffer):

- As a preliminary step of the calibration protocol, the Dronpa-2 solution is illuminated with the 405 nm LED ($I_2 = 0.01$ ein.m^{-2}.s^{-1} for 2 min) to secure that Dronpa-2 is initially in its thermodynamically stable state C_1;

- Then the sample is illuminated at constant light intensity I_1 at $\lambda_1 = 488$ nm (this first illumination is associated with the exponent I) and the evolution of the fluorescence signal is collected. The decay is adjusted by:

$$I_F^{\mathrm{I}} = I_F^{\mathrm{I}}(0) + A^{\mathrm{I}} \left[1 - \exp\left(-\frac{t}{\tau^{\mathrm{I}}} \right) \right] \tag{A1}$$

  The time τ^{I} is used as a fitting parameter and the intensity I_1 is retrieved according to (see Eq.(A49))

$$I_1 = \frac{\dfrac{1}{\tau^{\mathrm{I}}} - k_{21}^{\Delta}}{\Sigma_1} \tag{A2}$$

  where the reference values of the rate constant for thermal return after reversible fluorescence photoswitching ($k_{21}^{\Delta} = 0.014$ s^{-1}) and the sum of the photoswitching cross sections ($\Sigma_1 = 196$ m^{2}mol^{-1}) at the wavelength λ_1 are given in reference;[13]

- In a second step, while maintaining constant illumination I_1 at the wavelength $\lambda_1 = 488$ nm, the sample is submitted to a light jump of intensity I_2 at the wavelength $\lambda_2 = 405$ nm (this second illumination protocol is associated with the exponent II). The exponential fluorescence recovery is recorded and adjusted using

$$I_F^{\mathrm{II}} = I_F^{\mathrm{II}}(0) + A^{\mathrm{II}} \left[1 - \exp\left(-\frac{t}{\tau^{\mathrm{II}}} \right) \right] \tag{A3}$$

  where the time τ^{II} is used as a fitting parameter and the intensity I_2 can be retrieved from (see Eq.(A58))

$$I_2^{\mathrm{II}} = \frac{\dfrac{1}{\tau^{\mathrm{II}}} - \Sigma_1 I_1 - k_{21}^{\Delta}}{\Sigma_2} \tag{A4}$$

  where the reference value of the sum of the photoswitching cross sections ($\Sigma_2 = 413$ m^{2}mol^{-1}) at the wavelength λ_2 is given in reference.[13]

Lasers The calibrations of the light from the lasers were performed with a power meter (PM100A, Thorlabs, NJ, US) by measuring the dependence of the laser output power on the applied input (tension voltage – in V – for the 488 nm laser and input power – in mW – for the 405 nm laser). We observed a linear dependence (i) with the 488 nm laser source between 0.12 and 4.6 V (see Fig.A3a) and (ii) with the 405 nm laser diode between 2 mW and 100 mW (see Fig.A3b) and adopted the corresponding ranges to perform all the subsequent experiments.

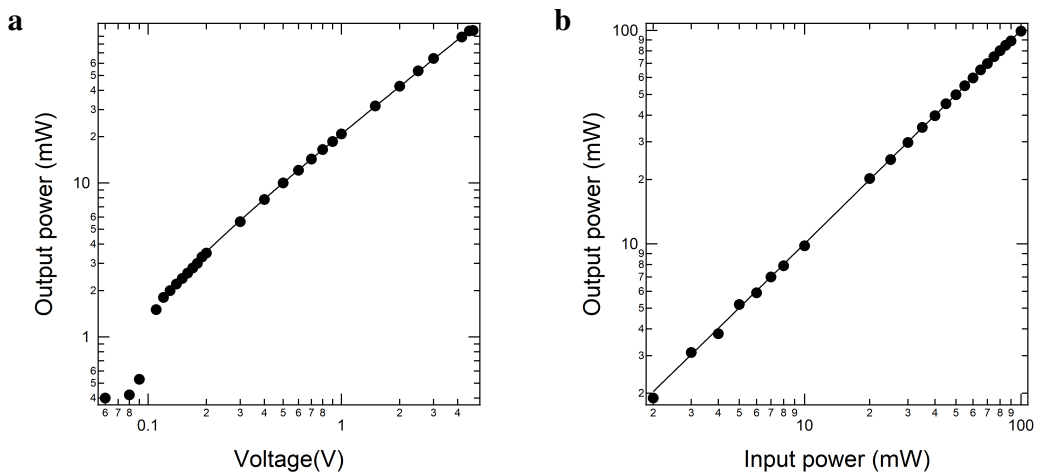

Figure A3: *Calibration of the output power of the lasers*. Dependence of the laser output power on the applied input (tension voltage – in V – for the 488 nm laser – **a** – and input power – **b**, in mW – for the 405 nm laser).

In particular, these calibrations have been used to validate the continuity of the illumination when switching from the LEDs to the lasers for illumination since the maximum of LED intensity matches the lower laser intensity once the later is decreased with an optical absorptive density (NE10A-A Thorlabs, Newton, NJ, OD=1).

A1.5 Protocols of acquisition of the RSFP kinetic fingerprints

A1.5.1 Acquisition of the RSFP photochemical behavior

The protocol to acquire the kinetic fingerprint of RSFPs as a set of characteristic times associated with illuminations leading to non-redundant kinetic behaviors has been set up for acquisition of the RSFP photochemical behavior. It includes: (i) Recording the time series of the RSFP fluorescence signal under several illumination conditions at different light intensities; (ii) Extracting a single characteristic time from each time evolution of the RSFP fluorescence signal; (iii) Analyzing the dependence of the inverse of the characteristic time in each illumination condition on the associated light intensities; (iv) Retaining the characteristic times at different typical light intensities to account for the RSFP kinetics when the characteristic times showed different regimes of light intensity dependence.

The photoswitchometer has been automated to enable the fast screening of the green RSFPs. Data acquisition is automated with LabVIEW and includes the external control of the outputs (square wave, cycle duration, average voltage, duty cycle,...) of the two waveform generators.

Two illuminations denoted I and II have been used to characterize the photoswitching kinetics of the RSFPs. The photoswitchometer applies constant light at the wavelength $\lambda_1 = 488$ nm and

periodic square-wave light at the wavelength $\lambda_2 = 405$ nm during three periods (see Fig. A4). The light at $\lambda_2 = 405$ nm is turned off during the first half periods, which generates the time windows of illumination I involving constant light at $\lambda_1 = 488$ nm. In contrast, it is turned on during the second half periods, which generates the time windows of illumination II involving constant lights at both $\lambda_1 = 488$ nm and $\lambda_2 = 405$ nm. The fluorescence evolution is recorded at 525 nm.

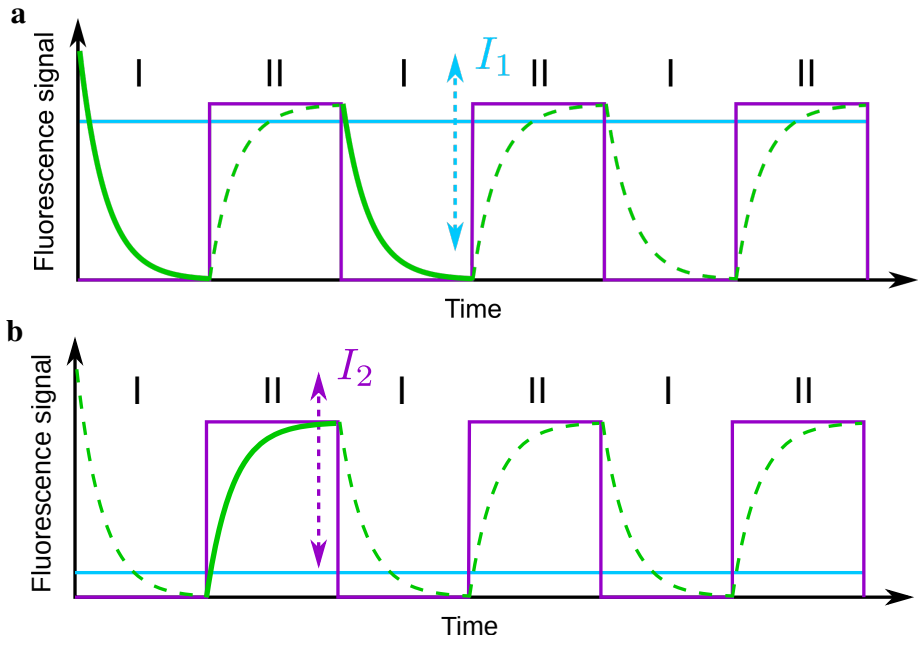

Figure A4: *Illumination experiments devoted to the photochemical characterization of the RSFPs*. The photoswitchometer records the fluorescence evolution upon applying three periods of illumination, which involves constant light at the wavelength $\lambda_1 = 488$ nm (blue) and square-wave light at the wavelength $\lambda_2 = 405$ nm (purple) by using either LEDs or lasers. The first (second, resp.) half period corresponds to illumination I (II, resp.). Two series of photochemical experiments have been performed (see Fig. A14–A35a,b): **a**: Variable light intensity I_1 at the wavelength $\lambda_1 = 488$ nm and fixed light intensity at the wavelength $\lambda_2 = 405$ nm. Among the three periods of fluorescence acquisition (dashed green line), the first (for LIGHTNING imaging) or third (for acquisition of the photoswitching kinetic information of RSFPs) half periods (solid green line) under illumination I have been analyzed; **b**: Fixed light intensity at the wavelength $\lambda_1 = 488$ nm and variable light intensity I_2 at the wavelength $\lambda_2 = 405$ nm. Among the three periods of fluorescence acquisition (dashed green line), the second half period (solid green line) under illumination II is analyzed.

Data acquisition has proceeded in two steps:

- In a preliminary step, we determined the time window over which the two-color photoactivation of the RSFPs is fully reversible. Illuminations I and II were applied using strong LED lights (Fig. A10–A13). In order to roughly delimit two kinetic regimes involving fast and slow variations of the fluorescence signal, the fluorescence evolution I_F^i observed for the two illuminations $i = \mathrm{I}, \mathrm{II}$ has been analyzed using an unsupervised biexponential fitting function

over the whole time window

$$I_F^{\mathrm{i}}(t) = A_{fast}^{\mathrm{i}} \exp(-t/\tau_{fast}^{\mathrm{i}}) + A_{slow}^{\mathrm{i}} \exp(-t/\tau_{slow}^{\mathrm{i}}) + I_F^{\mathrm{i}}(\infty) \quad \text{(A5)}$$

The values of the fast and slow relaxation times, τ_{fast}^{i} and τ_{slow}^{i}, have been extracted.

τ_{fast}^{i} provides a signature of reversible fluorescence photoswitching whereas τ_{slow}^{i} presumably originates from extinction at a longer timescale, leading to an estimate of the cross sections for reversible fluorescence photoswitching or light-driven extinction (see Eq.(A49) for $i = \mathrm{I}$, Eq.(A58) for $i = \mathrm{II}$; compare the cross sections $\Sigma_{1,fast}$ and $\Sigma_{2,fast}$ in Tab. A2 and Σ_1 and Σ_2 in Tab. A3). For all the RFSPs and both wavelengths, the ratios of the cross sections of reversible photoswitching and long-term extinction were found greater than 10^3. Hence we could define a wide time window in which reversible photoswitching is not perturbed by light-driven long-term extinction;

- In a second step, the two illuminations I and II involving LED and laser lights were used to establish the RSFP photoswitching signature for several tens of light intensities in a broad range covering the 10^{-3}–10^{2} ein.m^{-2}.s^{-1} (see Fig. A14–A35a,b). The value of the half-period has been set at 5 s for all RSFPs upon LED illumination. At all investigated LED intensities, this time window is both larger than a few times the order of magnitude of the fast relaxation time τ_{fast}^{i} deduced in the preliminary step and narrow enough to neglect long-term extinction. In contrast, the value of the half-period was further down scaled proportionally to the inverse of light intensity upon laser illumination for diffusion to remain negligible in the time evolution of the fluorescence signal (see section A7.2) (see Fig. A14–A35c–f). In the course of our experiments, we noticed that the fluorescence decay observed for illumination I during the first half period exhibited a larger amplitude for high I_1 intensities than during the following odd half periods. The detailed interpretation of this behavior is left for another publication. In the present report, we processed the data from the first and the third half periods for three RSFPs (**1**, **2**, and **6** exhibiting distinct photochemical behavior). Fig. A5a–c show that despite the difference of their amplitudes, the fluorescence decays observed during the first and the third half periods of application of illumination I exhibit similar characteristic times so as to be equally used to establish the kinetic fingerprint of the RSFPs. Whereas the third half period has been used for data processing during our subsequent experiments to be at steady-state, the first half period should be more favorable in providing a better signal-to-noise-ratio for LIGHTNING imaging of RSFPs.

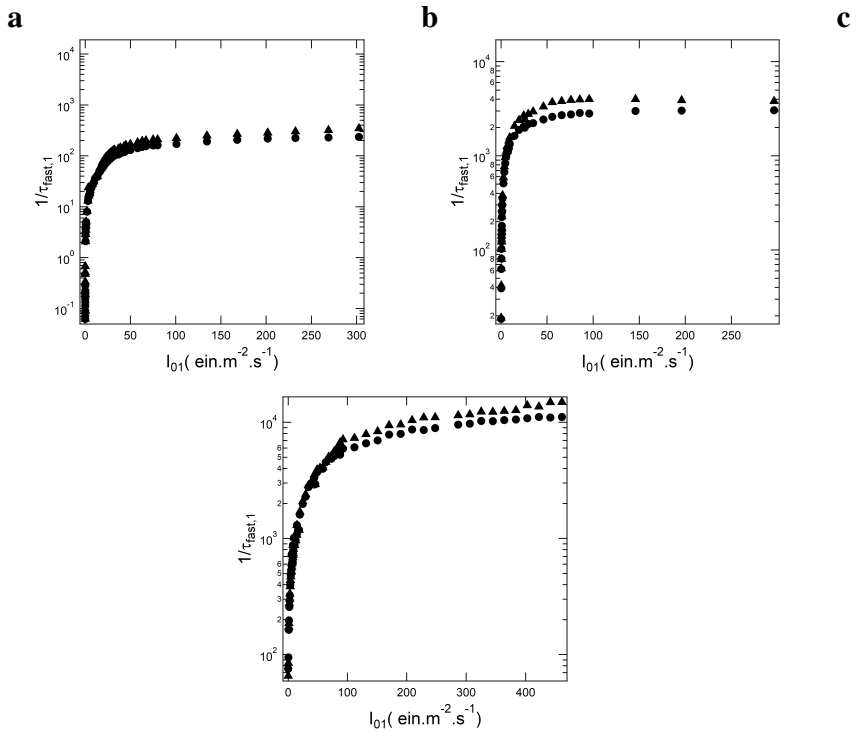

Figure A5: Dependence of the inverse of the characteristic times $1/\tau^I$ of **1** (**a**), **2** (**b**), and **6** (**c**) obtained from analyzing the fluorescence decays during the first (triangle) and the third (disk) half periods of application of illumination I.

A1.5.2 Acquisition of the RSFP kinetic fingerprints for LIGHTNING imaging

This series of experiments has been performed on a series of 6 μm-thick 10 μM RSFP solutions sandwiched between two 170 μm-thick glass slides and on agarose pads of RSFP-labeled Escherichia coli by using the photoswitchometer in the LIGHTNING imaging mode. We recorded images from a 20 μm-wide circular field of view at 1 kHz frequency upon illuminations I_{low} ($I_{1,low} = 2$ ein.m^{-2}.s^{-1}), II_{low} ($I_{1,low} = 2$ ein.m^{-2}.s^{-1} and $I_{2,low} = 0.2$ ein.m^{-2}.s^{-1}), I_{high} ($I_{1,high} = 50$ ein.m^{-2}.s^{-1}), and II_{high} ($I_{1,high} = 50$ ein.m^{-2}.s^{-1} and $I_{2,high}$ =20 ein.m^{-2}.s^{-1}).

A1.6 Data processing

The analysis of the fluorescence evolution (see Section A4) used two independent protocols for the determination of the characteristic times of the kinetic fingerprint. The method based on spectra of relaxation times is reported in Section A5 and the data analysis was automated using Matlab. The monoexponential reduction of fluorescence evolution regardless of the complexity of kinetics is described in Section A6 and data analysis was automated using Igor Pro.

The fluorescence evolution under illumination I was monotonous for all RSFPs. We first used the unsupervised monoexponential fitting function given in Eq.(A46) over the whole acquisition

window to extract a first guess of the characteristic time τ^{I}. We then restricted the time window to [0, $5\tau^{\mathrm{I}}$] in order to extract the final τ^{I} values using the same monoexponential fitting function. For illumination II, we used the same protocol as for illumination I for sufficiently low light intensities such that the fluorescence evolution is monotonous. From the light intensities for which the fluorescence evolution displays an extremum, we first restricted the lower and upper limits of the analyzed time window to the times respectively associated with the initial and extremum values of the fluorescence signal. Then we proceeded by applying the monoexponential fitting function given in Eq.(A55) over the delimited time window in order to extract the value of τ^{II}.

The spectra of relaxation times have been computed from Eq.(A22) by using the fluorescence data collected over the whole acquisition window for a given illumination. The absolute maximum is determined for illumination I and the absolute minimum for illumination II, except for the RSFPs **4** and **5** for which the opposite procedure is applied. The abscissa of the absolute extrema provide the relaxation times τ^{I} and τ^{II} for illumination I and II, respectively. For all investigated RSFPs the spectra of relaxation time admits an extremum in the acquisition window defining a single characteristic time without ambiguity and legitimating the use of a monoexponential reduction.

For both methods used to determine the characteristic times, data processing ends up by plotting the inverse of the photoswitching relaxation times $1/\tau^{\mathrm{I}}$ versus the light intensity I_1 at the wavelength $\lambda_1 = 488$ nm and $1/\tau^{\mathrm{II}}$ versus the light intensity I_2 at the wavelength $\lambda_2 = 405$ nm (see Fig. A14–A35c–f).

In the regime of low light intensities, the fluorescence evolution is satisfactorily accounted by a two-state kinetic model (see section A7). The reaction rate being limited by the photochemical step, $1/\tau^{\mathrm{i}}_{low}$ for $i = \mathrm{I}, \mathrm{II}$ linearly depends on light intensity (see Eqs.(A49,A58)). The slope of $1/\tau^{\mathrm{I}}_{low}$ versus I_1 provides the cross section Σ_1 and the slope of $1/\tau^{\mathrm{II}}_{low}$ versus I_2 provides the cross section Σ_2. In a high intensity regime where thermal steps impact the reaction rate, the inverse of the relaxation times $1/\tau^{\mathrm{I}}_{high}$ and $1/\tau^{\mathrm{II}}_{high}$ exhibit no or a weaker dependence on the light intensities.

The cutoff intensity I_1^c (I_2^c, resp.) delimiting the two regimes was defined as the intensity for which the inverse of the characteristic time $1/\tau^{\mathrm{I}}$ ($1/\tau^{\mathrm{II}}$, resp.) departs from 33% (20%, resp.) from the prediction of the two-state model $\Sigma_1 I_1^c$ ($\Sigma_1 I_1^c + \Sigma_2 I_2^c$, resp.). The values of the characteristic times in both intensity regimes provide non-redundant information. We set the intensity value $I_{1,low}$ ($I_{2,low}$, resp.) for which the kinetics of all RSFPs is driven by photochemistry at λ_1 (λ_2, resp.). Specifically we chose the value of $I_{1,low}$ ($I_{2,low}$, resp.) as the value of the lowest cutoff intensity I_1^c (I_2^c, resp.) obtained from all RSFPs. We fixed the intensity value $I_{1,high}$ ($I_{2,high}$, resp.) at the highest available intensity. Hence, for the series of photochemical experiments on the 22 investigated RSFPs with the photoswitchometer in its configuration displayed in Fig.A1, we adopted the values

of light intensities $I_{1,low} = 2$ ein.m^{-2}.s^{-1} for regime I$_{low}$, $I_{1,high} = 200$ ein.m^{-2}.s^{-1} for I$_{high}$, $I_{1,low} = 2$ ein.m^{-2}.s^{-1} and $I_{2,low} = 0.1$ ein.m^{-2}.s^{-1} for II$_{low}$, and $I_{1,high} = 200$ ein.m^{-2}.s^{-1} and $I_{2,high} = 90$ ein.m^{-2}.s^{-1} for II$_{high}$.

For all RSFPs we eventually extracted the two characteristic times τ^{I}_{low} and τ^{II}_{low} in the low intensity regime of illuminations I and II and the two characteristic times τ^{I}_{high} and $\tau^{\mathrm{II}}_{high}$ in the high intensity regime. The set of the four characteristic times (τ^{I}_{low}, τ^{II}_{low}, τ^{I}_{high}, $\tau^{\mathrm{II}}_{high}$) constitutes the LIGHTNING kinetic fingerprint of reversible photoswitching for the RSFPs. Tab. A4 sums up the results.

A1.7 Definition of a set of distinguishable RSFPs

A1.7.1 Sorting algorithms

Optimizing the discriminating power of LIGHTNING requires choosing the most distant RSFPs. We have implemented two algorithms to rank N RSFPs according to their distance between pairs. The distances d_{ij} between all pairs (i, j) of RSFPs

$$d_{ij} = \sqrt{\Sigma_{k=1}^{n} \left(l_{ki} - l_{kj}\right)^2} \tag{A6}$$

are computed in the space of n discriminative dimensions, where l_{ki} and l_{kj} are the decimal logarithms of the k^{th} characteristic time of RSFP i and RSFP j, respectively.

Selection of the most distant RSFPs within sets of RSFPs We first determined optimized subsets $s'(m)$ of m RSFPs for $m = 2, ..., N$. The minimum distances $d_{\min}$ between pairs are computed for all subsets of m RSFPs included in $s(N)$. The subset $s'(m)$ with the maximum value of $d_{\min}$ is selected.

Selection of the most distant RSFPs within inclusive subsets of an RSFP set As shown in Tab. A5, the relation $s'(m) \subset s'(m+1)$ is not necessarily observed for $s'(m)$ and $s'(m+1)$. This absence may be a drawback for end-users who would like to use a same set of RSFPs in order to discriminate various numbers of its members. Hence we have also implemented the following efficient algorithm including three-body interactions to rank N RSFPs according to their distance between pairs.

The procedure followed to generate an ordered list of RSFPs begins with sorting pairs by increasing distances and sequentially eliminating the RSFP which is the closest to two other RSFPs. Specifically, the pair associated with the smallest distance in the set $s(N)$ of N RSFPs is denoted (i, j). The closest RSFP to i different from j is denoted k and the closest RSFP to j different from

i is denoted l. If the distance d_{ik} is smaller than d_{jl}, the RSFP i is the closest RSFP to two RSFPs. The rank assigned to the RSFP i in the ordered list is equal to the number N of RSFPs in the set $s(N)$. Then the RSFP i is removed from the set $s(N)$ leading to the set $s(N-1)$ of $N-1$ RSFPs. The procedure is repeated until the set $s(2)$ has been built. Rankings 1 and 2 are assigned to the two RSFPs of the remaining pair $s(2)$.

A1.7.2 Evaluation of the cutoff distance

Discrimination between two RSFPs is possible if their distance is larger than the cutoff distance d_c imposed by the experimental accuracy Δd_{ij} on the distance d_{ij} induced by the uncertainty Δl_{ki} on the logarithm of the characteristic times l_{ki}. Differentiating Eq.(A6), we find

$$\Delta d_{ij} = \frac{1}{d_{ij}} \Sigma_{k=1}^{n} \mid l_{ki} - l_{kj} \mid \Delta \mid l_{ki} - l_{kj} \mid . \tag{A7}$$

Introducing the maximum uncertainty $M = \max_{k,i} (\Delta l_{ki})$ on the determination of the kinetic fingerprint $\{l_{ki}\}$, we have $\Delta \mid l_{ki} - l_{kj} \mid \leq 2M$. Hence Eq.(A7) reads

$$\Delta d_{ij} \leq 2MX. \tag{A8}$$

with $X^2 = 1 + 2\Sigma_{k=1}^{n} \Sigma_{k'=k+1}^{n} \mid l_{ki} - l_{kj} \mid\mid l_{k'i} - l_{k'j} \mid / d_{ij}^2$ Regardless of the value of $\mid l_{ki} - l_{kj} \mid$, the inequality

$$2\Sigma_{k=1}^{n} \Sigma_{k'=k+1}^{n} \mid l_{ki} - l_{kj} \mid\mid l_{k'i} - l_{k'j} \mid \leq (n-1) \Sigma_{k=1}^{n} (l_{ki} - l_{kj})^2 \tag{A9}$$

is observed, leading to $X \leq \sqrt{n}$. Using Eq.(A8) we find $\Delta d_{ij} \leq d_c$ where the cutoff distance obeys

$$d_c = 2M\sqrt{n} \tag{A10}$$

The cutoff distance between two RSFPs depends on two parameters, the number n of discriminating dimensions and the uncertainty M on the determination of the logarithm of the characteristic times. The protocol used to evaluate M is described in section (A8.3).

A2 Supplementary Figures

A2.1 Absorption and fluorescence emission spectra of the RSFPs

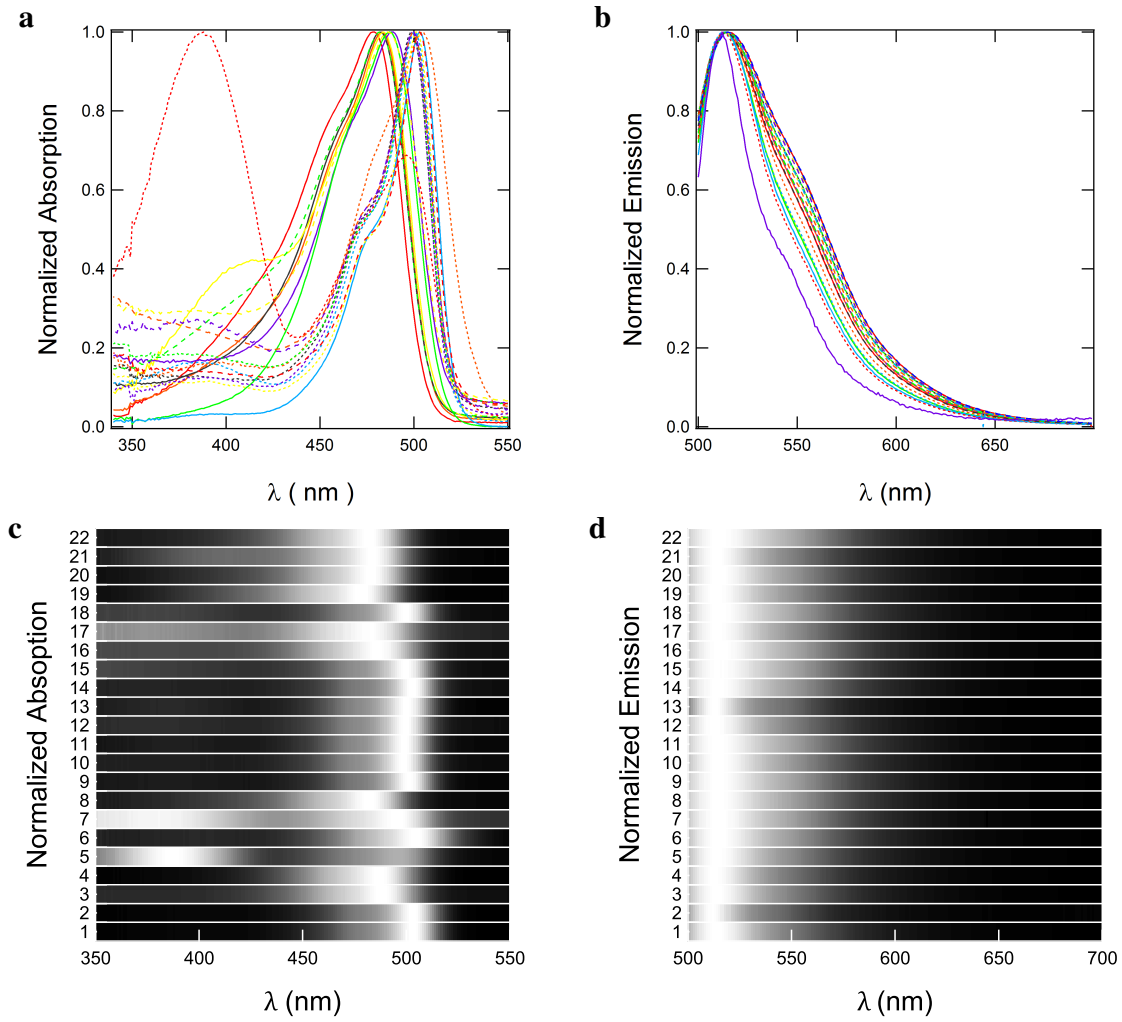

Figure A6: Normalized absorption (**a**,**c**) and emission (**b**,**d**; λ_{exc} = 488 nm) spectra of the 22 RSFPs, which have been investigated in this study. In **c** and **d**, the grey scale is linear between 0 and 1. RSFP solutions: 5 μM in pH 7.4 PBS (50 mM sodium phosphate, 150 mM NaCl); T = 298 K.

A2.2 Measurement of the rate constant k_{21}^{Δ} associated with the thermally driven relaxation of the photoswitched RSFPs

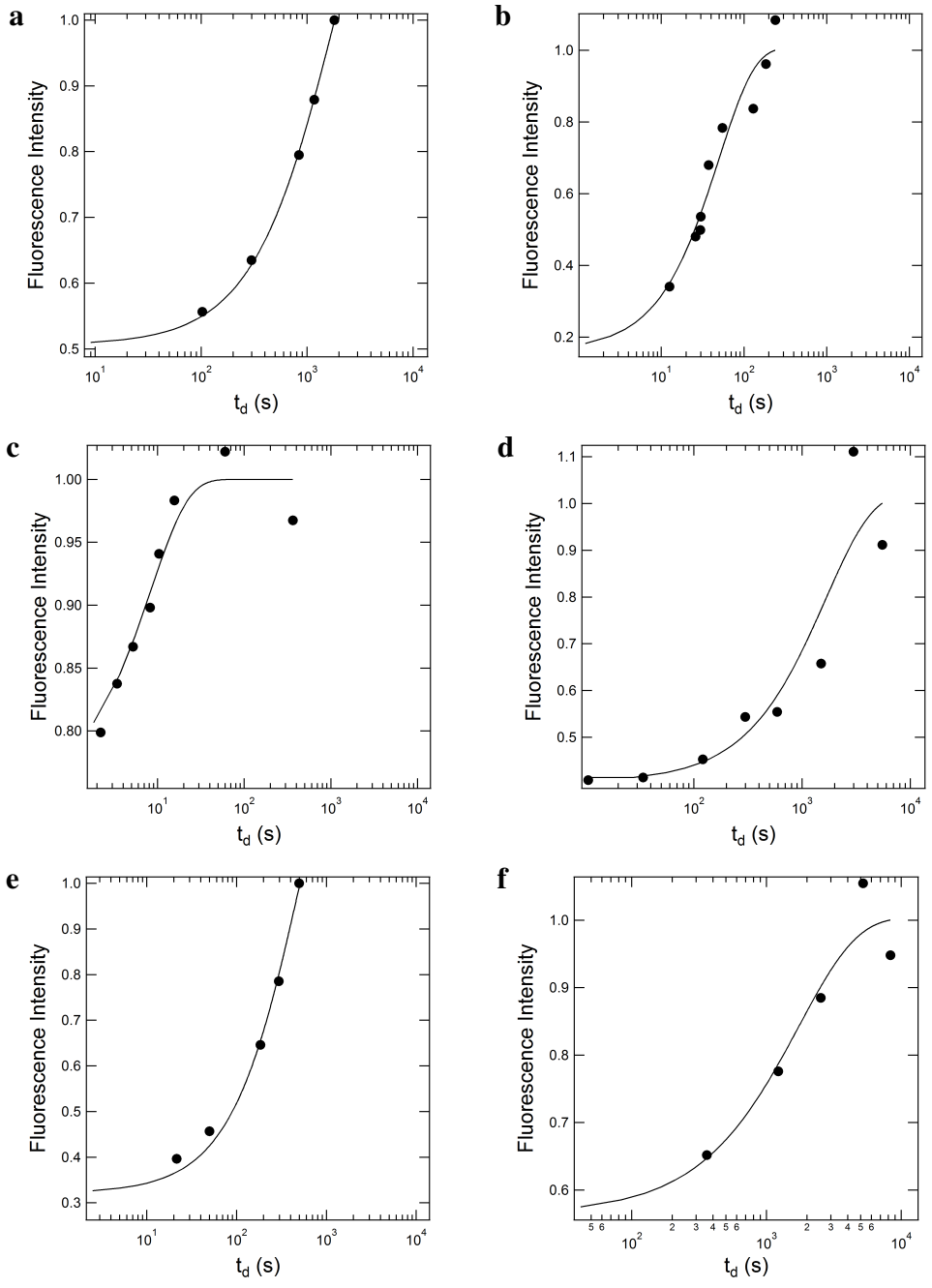

Figure A7: Dependence of the normalized fluorescence emission at the initial time of each light pulse on the delay t_d between two pulses at 480 nm (in a regime of low light intensity in which a two-state model is relevant to account for the photoswitching behavior). **a**: **1**; **b**: **2**; **c**: **3**; **d**: **6**; **e**: **7**; **f**: **8**. RSFP solutions: 8 μM in pH 7.4 PBS (50 mM sodium phosphate, 150 mM NaCl); T = 298 K.

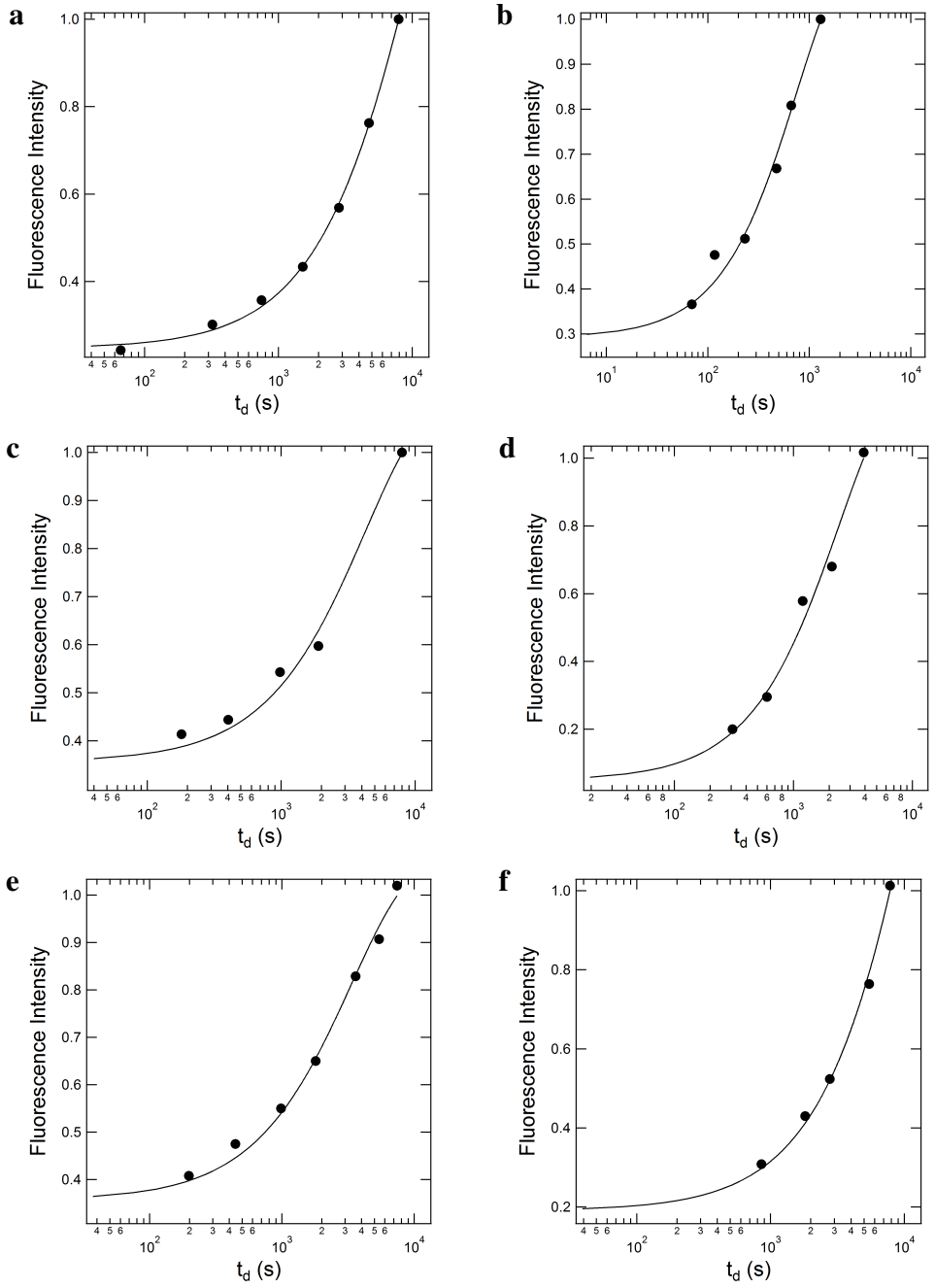

Figure A8: Dependence of the normalized fluorescence emission at the initial time of each light pulse on the delay t_d between two pulses at 480 nm (in a regime of low light intensity in which a two-state model is relevant to account for the photoswitching behavior). **a**: **9**; **b**: **10**; **c**: **11**; **d**: **12**; **e**: **13**; **f**: **14**. RSFP solutions: 8 μM in pH 7.4 PBS (50 mM sodium phosphate, 150 mM NaCl); T = 298 K.

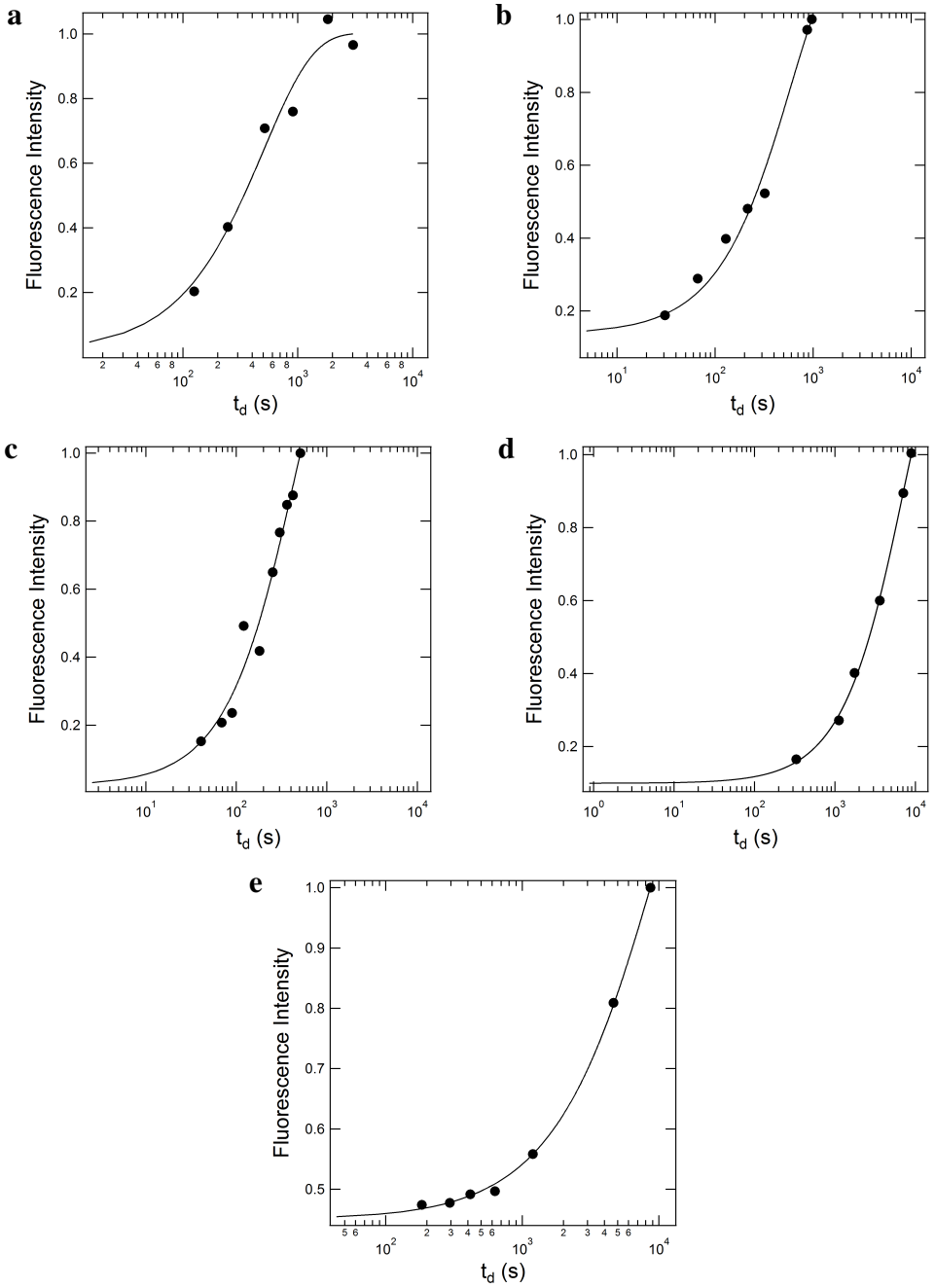

Figure A9: Dependence of the normalized fluorescence emission at the initial time of each light pulse on the delay t_d between two pulses at 480 nm (in a regime of low light intensity in which a two-state model is relevant to account for the photoswitching behavior). **a**: **15**; **b**: **16**; **c**: **17**; **d**: **18**; **e**: **21**. RSFP solutions: 8 μM in pH 7.4 PBS (50 mM sodium phosphate, 150 mM NaCl); T = 298 K.

A2.3 Photochemical characterization of the RSFPs

A2.3.1 Preliminary illumination experiments on the RSFPs

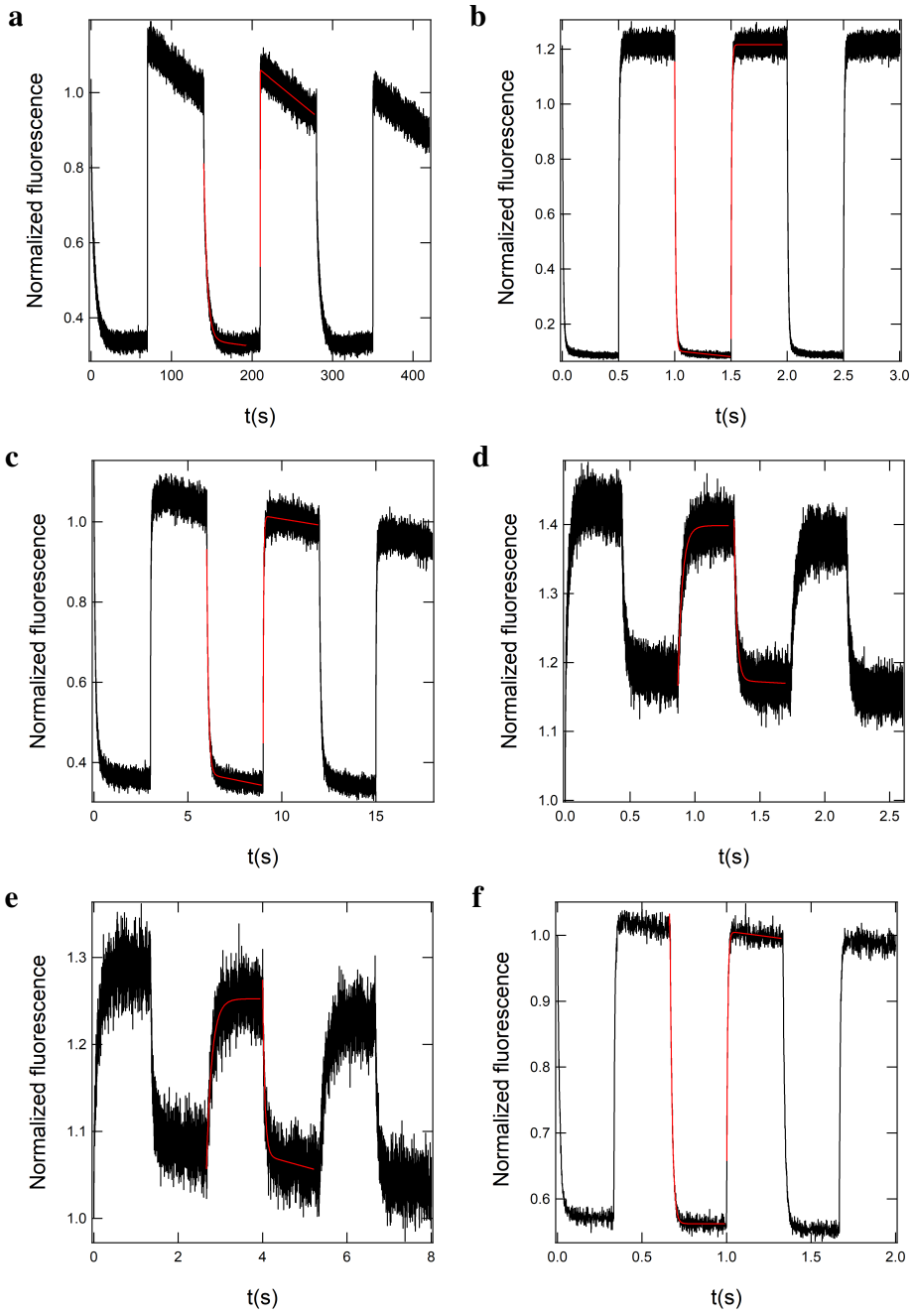

Figure A10: Preliminary analysis of fluorescence photoswitching for **1** (**a**), **2** (**b**), **3** (**c**), **4** (**d**), **5** (**e**), **6** (**f**). Evolution of fluorescence intensity upon continuous illumination of intensity I_1 at $\lambda_1 = 488$ nm and square-wave illumination of intensity I_2 at $\lambda_2 = 405$ nm yielding two different illumination regimes I ($I_1 = 0.6$ ein.m^{-2}.s^{-1}) and II ($I_1 = 0.6$ ein.m^{-2}.s^{-1} and $I_2 = 0.1$ ein.m^{-2}.s^{-1}). Solid black line: Experimental data; solid red line: Biexponentional fitting function with Eq.(A5). RSFP solutions: 20 μM in pH 7.4 PBS (50 mM sodium phosphate, 150 mM NaCl); T = 298 K.

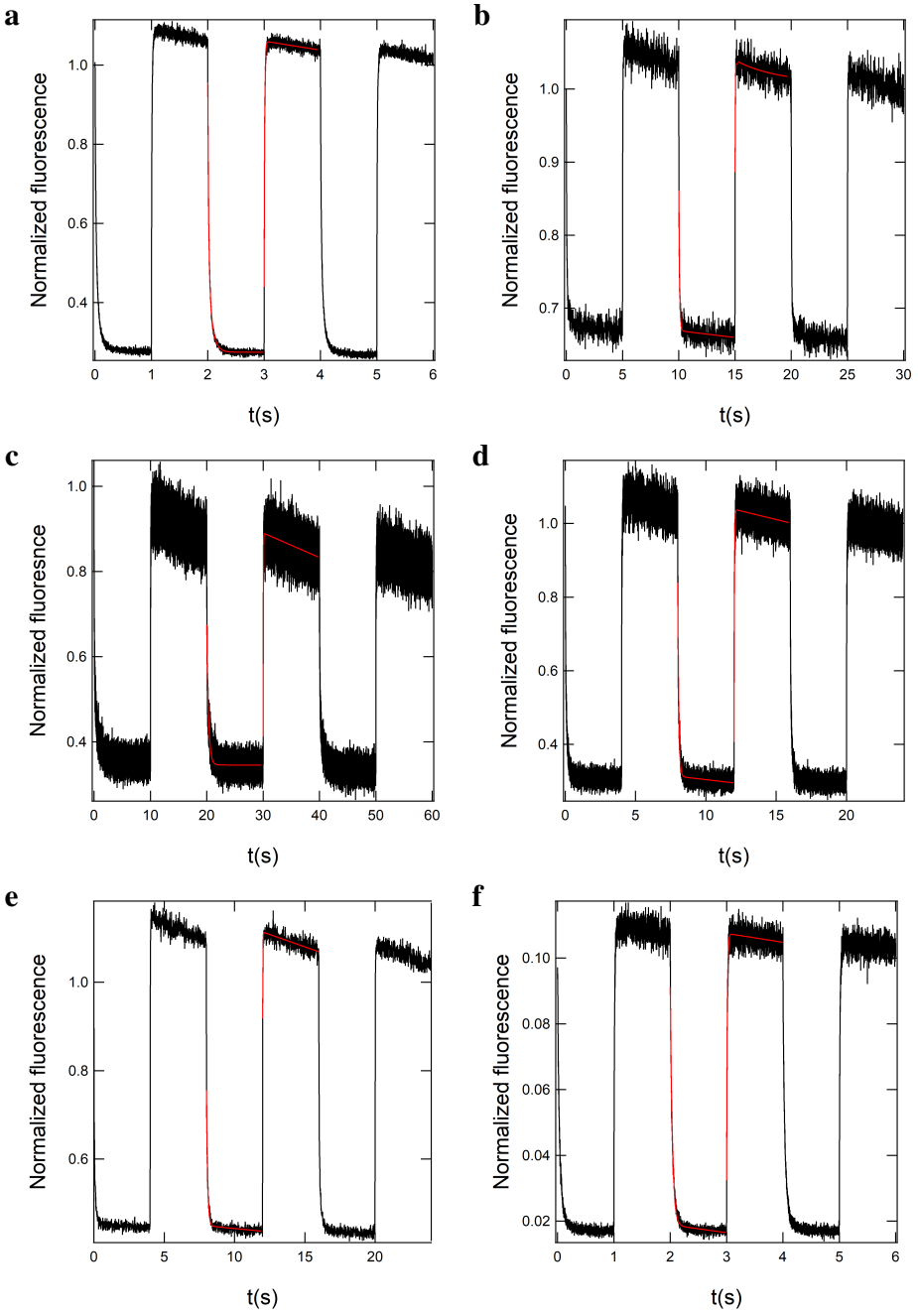

Figure A11: Preliminary analysis of fluorescence photoswitching for **7** (**a**), **8** (**b**), **9** (**c**), **10** (**d**), **11** (**e**), **12** (**f**). Evolution of fluorescence intensity upon continuous illumination of intensity I_1 at $\lambda_1 = 488$ nm and square-wave illumination of intensity I_2 at $\lambda_2 = 405$ nm yielding two different illumination regimes I ($I_1 = 0.6$ ein.m^{-2}.s^{-1} – except for **8** where it is 0.4 ein.m^{-2}.s^{-1}) and II ($I_1 = 0.6$ ein.m^{-2}.s^{-1} – except for **8** where it is 0.4 ein.m^{-2}.s^{-1} – and $I_2 = 0.1$ ein.m^{-2}.s^{-1}). Solid black line: Experimental data; solid red line: Biexponentional fitting function with Eq.(A5). RSFP solutions: 20 μM in pH 7.4 PBS (50 mM sodium phosphate, 150 mM NaCl); T = 298 K.

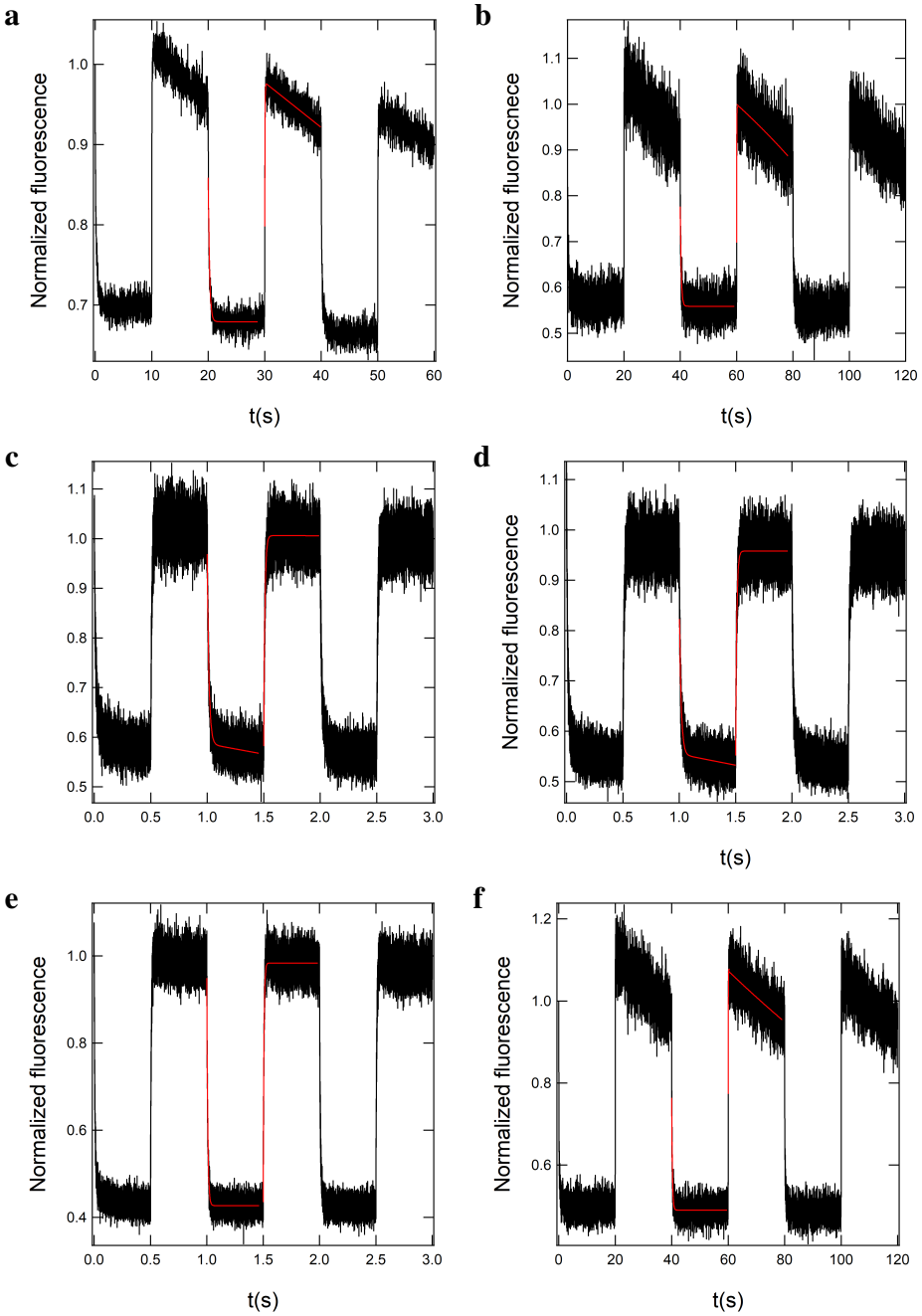

Figure A12: Preliminary analysis of fluorescence photoswitching for **13** (**a**), **14** (**b**), **15** (**c**), **16** (**d**), **17** (**e**), **18** (**f**). Evolution of fluorescence intensity upon continuous illumination of intensity I_1 at $\lambda_1 = 488$ nm and square-wave illumination of intensity I_2 at $\lambda_2 = 405$ nm yielding two different illumination regimes I ($I_1 = 0.6$ ein.m^{-2}.s^{-1} – except for **13** where it is 0.5 ein.m^{-2}.s^{-1}) and II ($I_1 = 0.6$ ein.m^{-2}.s^{-1} – except for **13** where it is 0.5 ein.m^{-2}.s^{-1} – and $I_2 = 0.1$ ein.m^{-2}.s^{-1}). Solid black line: Experimental data; solid red line: Biexponentional fitting function with Eq.(A5). RSFP solutions: 20 μM in pH 7.4 PBS (50 mM sodium phosphate, 150 mM NaCl); T = 298 K.

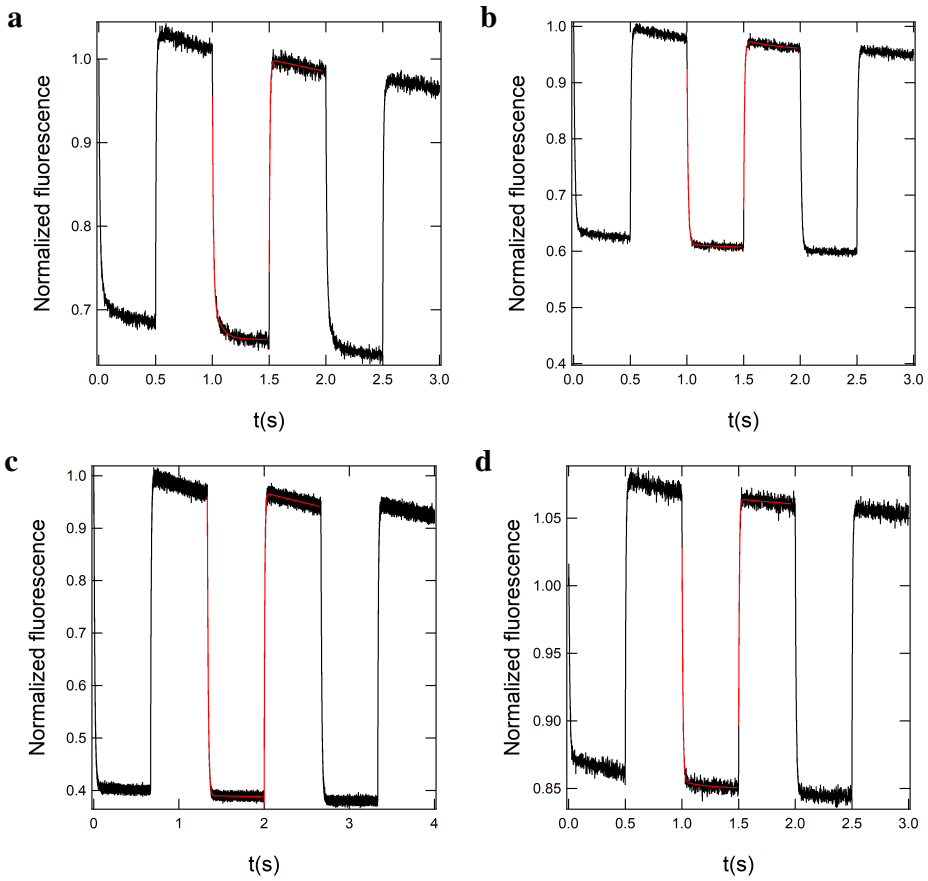

Figure A13: Preliminary analysis of fluorescence photoswitching for **19** (**a**), **20** (**b**), **21** (**c**), **22** (**d**). Evolution of fluorescence intensity upon continuous illumination of intensity I_1 at $\lambda_1 = 488$ nm and square-wave illumination of intensity I_2 at $\lambda_2 = 405$ nm yielding two different illumination regimes I ($I_1 = 0.6$ ein.m^{-2}.s^{-1}) and II ($I_1 = 0.6$ ein.m^{-2}.s^{-1} and $I_2 = 0.1$ ein.m^{-2}.s^{-1} – except for **20** where it is 0.08 ein.m^{-2}.s^{-1}). Solid black line: Experimental data; solid red line: Biexponentional fitting function with Eq.(A5). RSFP solutions: 20 μM in pH 7.4 PBS (50 mM sodium phosphate, 150 mM NaCl); T = 298 K.

A2.3.2 Final illumination experiments

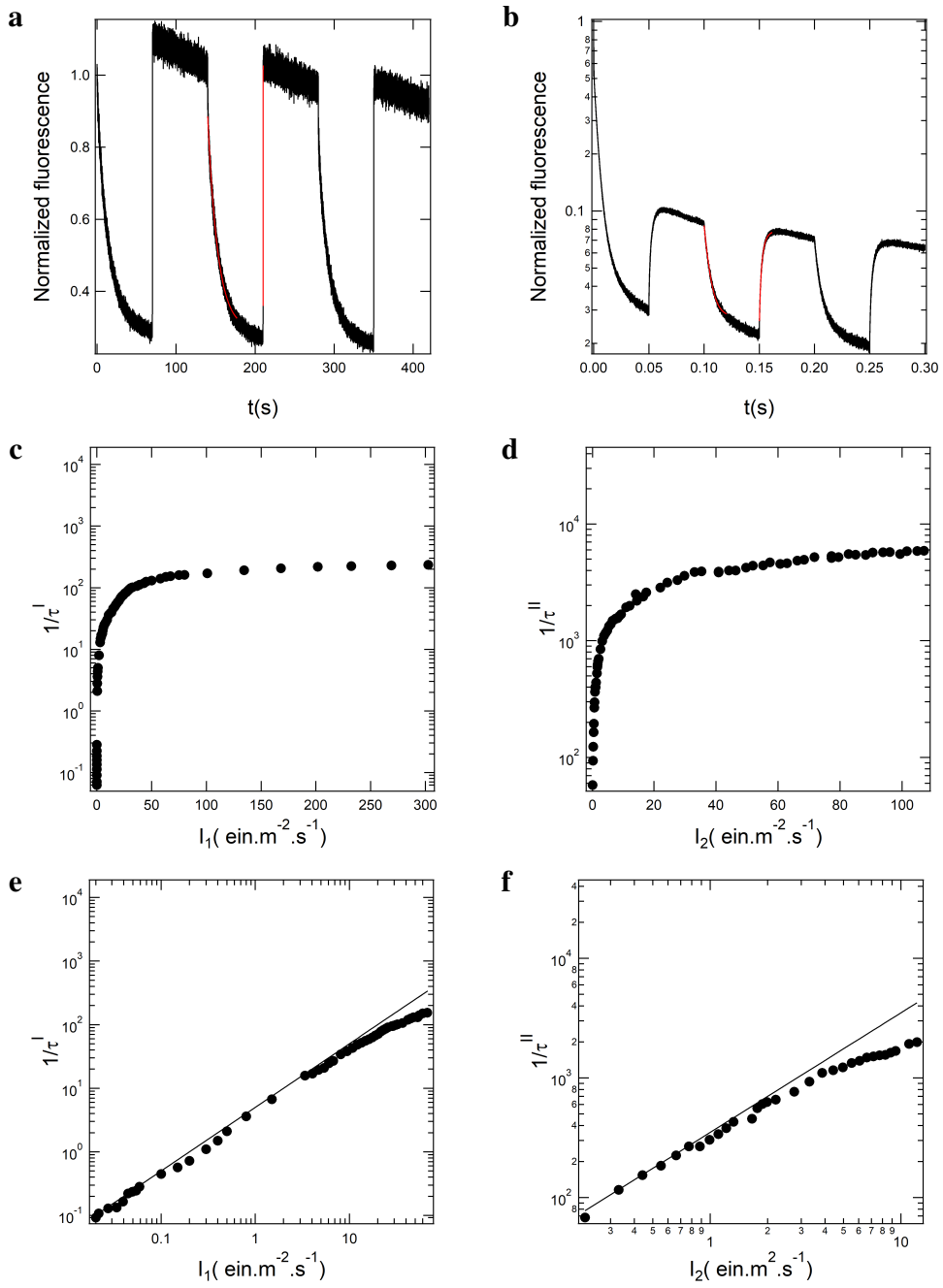

Figure A14: Kinetic analysis of **1** photoswitching at 20 μM in pH 7.4 PBS (50 mM sodium phosphate, 150 mM NaCl); T = 298 K. **a**, **b**: Evolution of fluorescence intensity upon continuous illumination of intensity I_1 at $\lambda_1 = 488$ nm and square-wave illumination of intensity I_2 at $\lambda_2 = 405$ nm (**a**: Illumination I $I_1 = 0.05$ ein.m^{-2}.s^{-1}, $I_2 = 0.1$ ein.m^{-2}.s^{-1}; **b**: $I_1 = 200$ ein.m^{-2}.s^{-1}, $I_2 = 3$ ein.m^{-2}.s^{-1}). Black line: experimental data; red line: fitting functions according to Eq.(A46) and Eq.(A55); **c**: Illumination I: Inverse of the relaxation time $1/\tau^{\mathrm{I}}$ (disks) versus light intensity I_1 at $\lambda_1 = 488$ nm, **d**: Illumination II: Inverse of the relaxation time $1/\tau^{\mathrm{II}}$ (disks) versus light intensity I_2 at $\lambda_2 = 405$ nm; **e**: Magnification of **c** at low light intensity. Solid line: linear fitting function yielding the photoswitching cross section Σ_1, **f**: Magnification of **d** at low light intensity. Solid line: linear fitting function yielding the photoswitching cross section Σ_2.

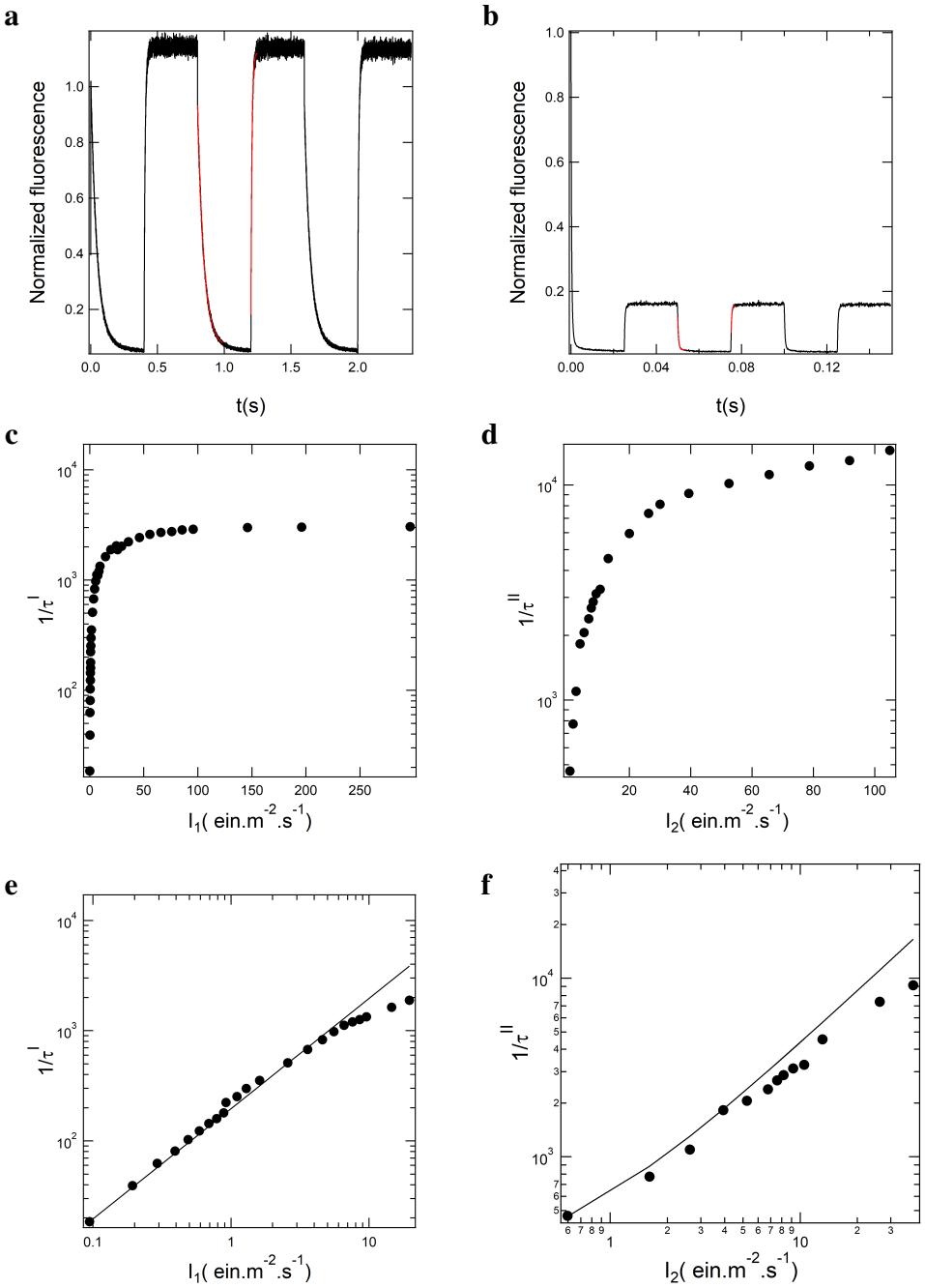

Figure A15: Kinetic analysis of **2** photoswitching at 20 μM in pH 7.4 PBS (50 mM sodium phosphate, 150 mM NaCl); T = 298 K. **a**, **b**: Evolution of fluorescence intensity upon continuous illumination of intensity I_1 at $\lambda_1 = 488$ nm and square-wave illumination of intensity I_2 at $\lambda_2 = 405$ nm (**a**: $I_1 = 0.05$ ein.m^{-2}.s^{-1}, $I_2 = 0.1$ ein.m^{-2}.s^{-1}; **b**: $I_1 = 200$ ein.m^{-2}.s^{-1}, $I_2 = 3$ ein.m^{-2}.s^{-1}). Black line: experimental data; red line: fitting functions according to Eq.(A46) and Eq.(A55); **c**: Illumination I: Inverse of the relaxation time $1/\tau^{\mathrm{I}}$ (disks) versus light intensity I_1 at $\lambda_1 = 488$ nm, **d**: Illumination II: Inverse of the relaxation time $1/\tau^{\mathrm{II}}$ (disks) versus light intensity I_2 at $\lambda_2 = 405$ nm; **e**: Magnification of **c** at low light intensity. Solid line: linear fitting function yielding the photoswitching cross section Σ_1, **f**: Magnification of **d** at low light intensity. Solid line: linear fitting function yielding the photoswitching cross section Σ_2.

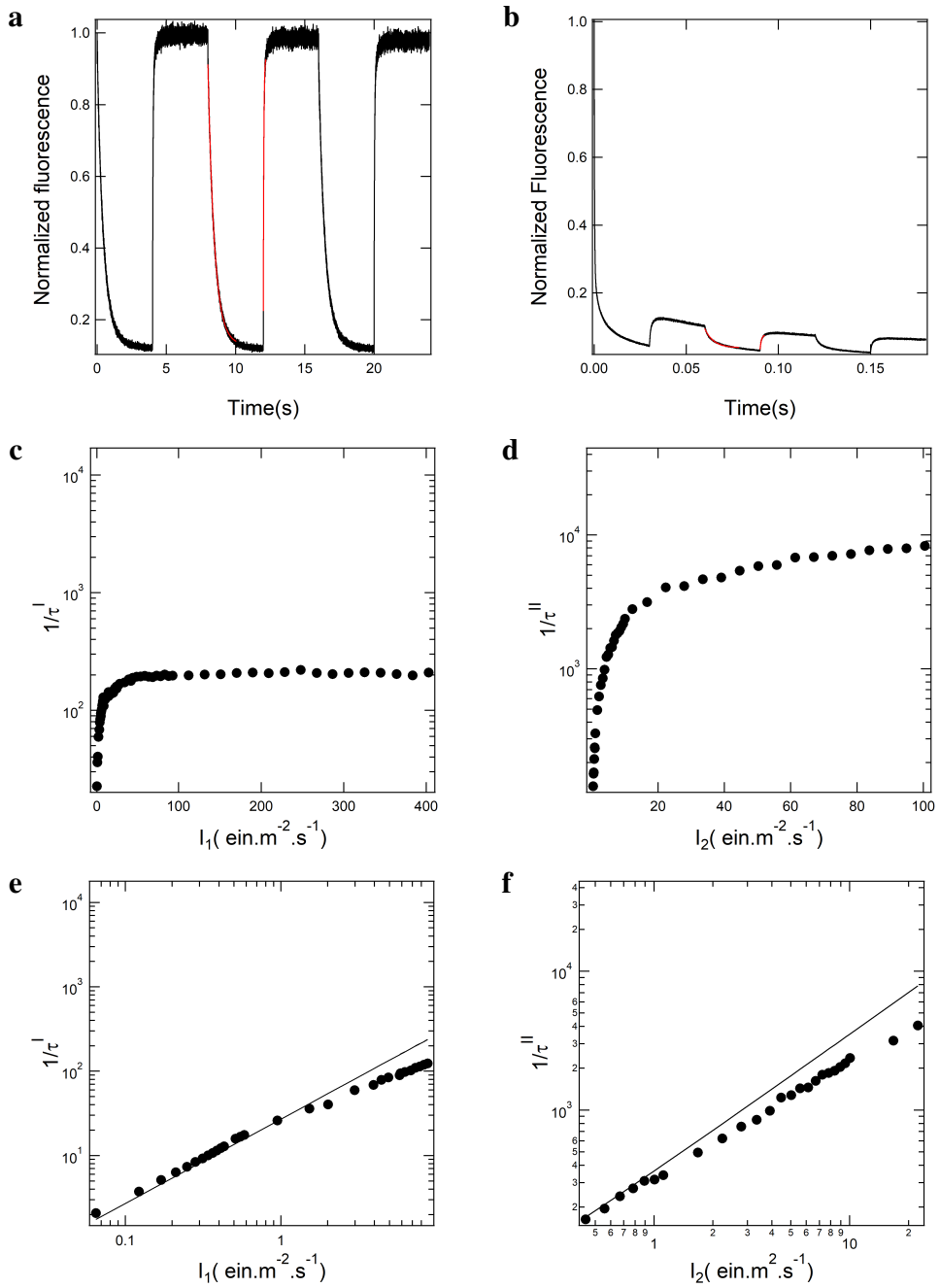

Figure A16: Kinetic analysis of **3** photoswitching at 20 μM in pH 7.4 PBS (50 mM sodium phosphate, 150 mM NaCl); T = 298 K. **a**, **b**: Evolution of fluorescence intensity upon continuous illumination of intensity I_1 at $\lambda_1 = 488$ nm and square-wave illumination of intensity I_2 at $\lambda_2 = 405$ nm (**a**: $I_1 = 0.05$ ein.m^{-2}.s^{-1}, $I_2 = 0.1$ ein.m^{-2}.s^{-1}; **b**: $I_1 = 200$ ein.m^{-2}.s^{-1}, $I_2 = 3$ ein.m^{-2}.s^{-1}). Black line: experimental data; red line: fitting functions according to Eq.(A46) and Eq.(A55); **c**: Illumination I: Inverse of the relaxation time $1/\tau^{\mathrm{I}}$ (disks) versus light intensity I_1 at $\lambda_1 = 488$ nm, **d**: Illumination II: Inverse of the relaxation time $1/\tau^{\mathrm{II}}$ (disks) versus light intensity I_2 at $\lambda_2 = 405$ nm; **e**: Magnification of **c** at low light intensity. Solid line: linear fitting function yielding the photoswitching cross section Σ_1, **f**: Magnification of **d** at low light intensity. Solid line: linear fitting function yielding the photoswitching cross section Σ_2.

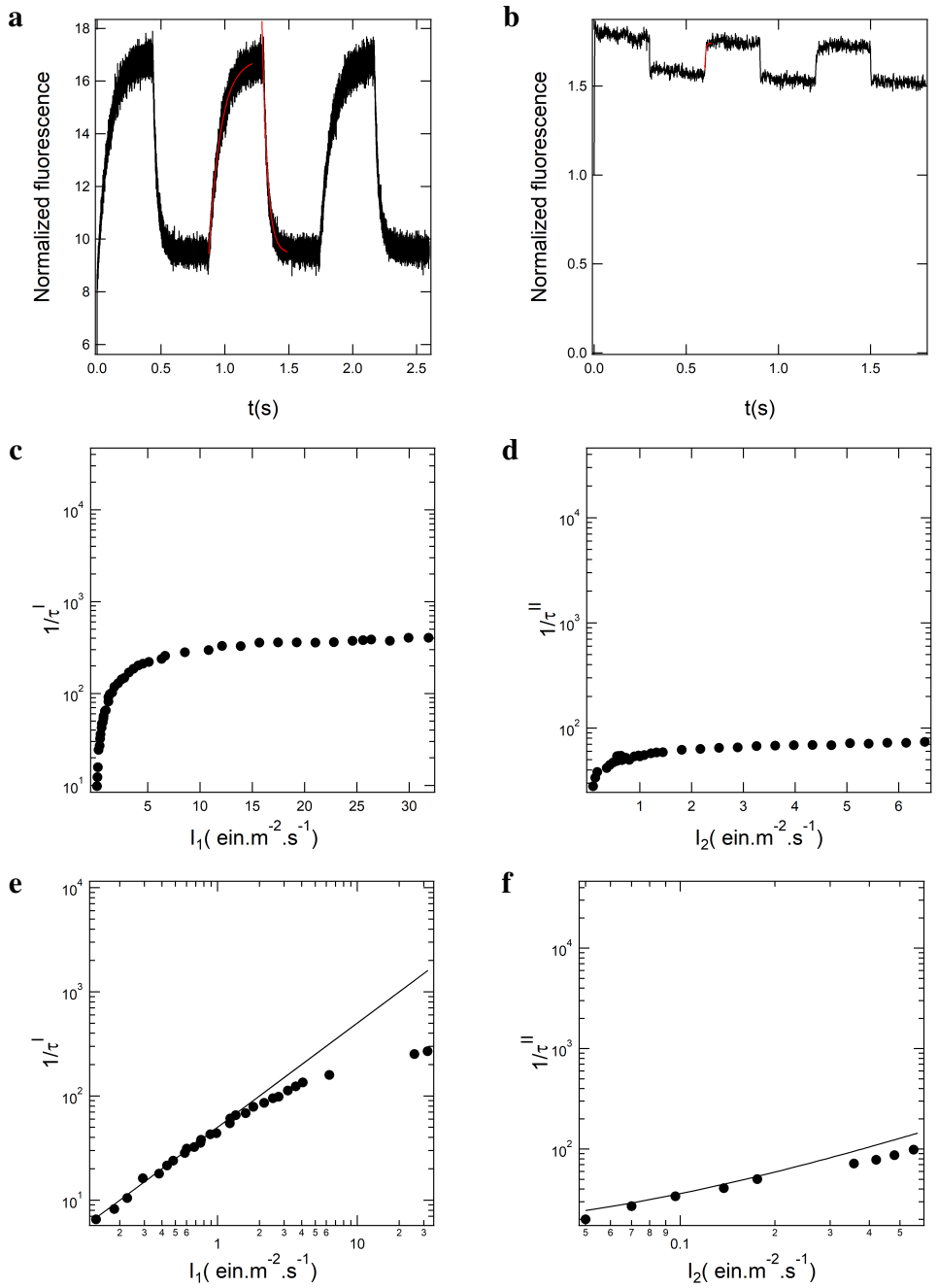

Figure A17: Kinetic analysis of **4** photoswitching at 20 μM in pH 7.4 PBS (50 mM sodium phosphate, 150 mM NaCl); T = 298 K. **a**, **b**: Evolution of fluorescence intensity upon continuous illumination of intensity I_1 at $\lambda_1 = 488$ nm and square-wave illumination of intensity I_2 at $\lambda_2 = 405$ nm (**a**: $I_1 = 0.05$ ein.m^{-2}.s^{-1}, $I_2 = 0.1$ ein.m^{-2}.s^{-1}; **b**: $I_1 = 200$ ein.m^{-2}.s^{-1}, $I_2 = 3$ ein.m^{-2}.s^{-1}). Black line: experimental data; red line: fitting functions according to Eq.(A46) and Eq.(A55); **c**: Illumination I: Inverse of the relaxation time $1/\tau^{\mathrm{I}}$ (disks) versus light intensity I_1 at $\lambda_1 = 488$ nm, **d**: Illumination II: Inverse of the relaxation time $1/\tau^{\mathrm{II}}$ (disks) versus light intensity I_2 at $\lambda_2 = 405$ nm; **e**: Magnification of **c** at low light intensity. Solid line: linear fitting function yielding the photoswitching cross section Σ_1, **f**: Magnification of **d** at low light intensity. Solid line: linear fitting function yielding the photoswitching cross section Σ_2.

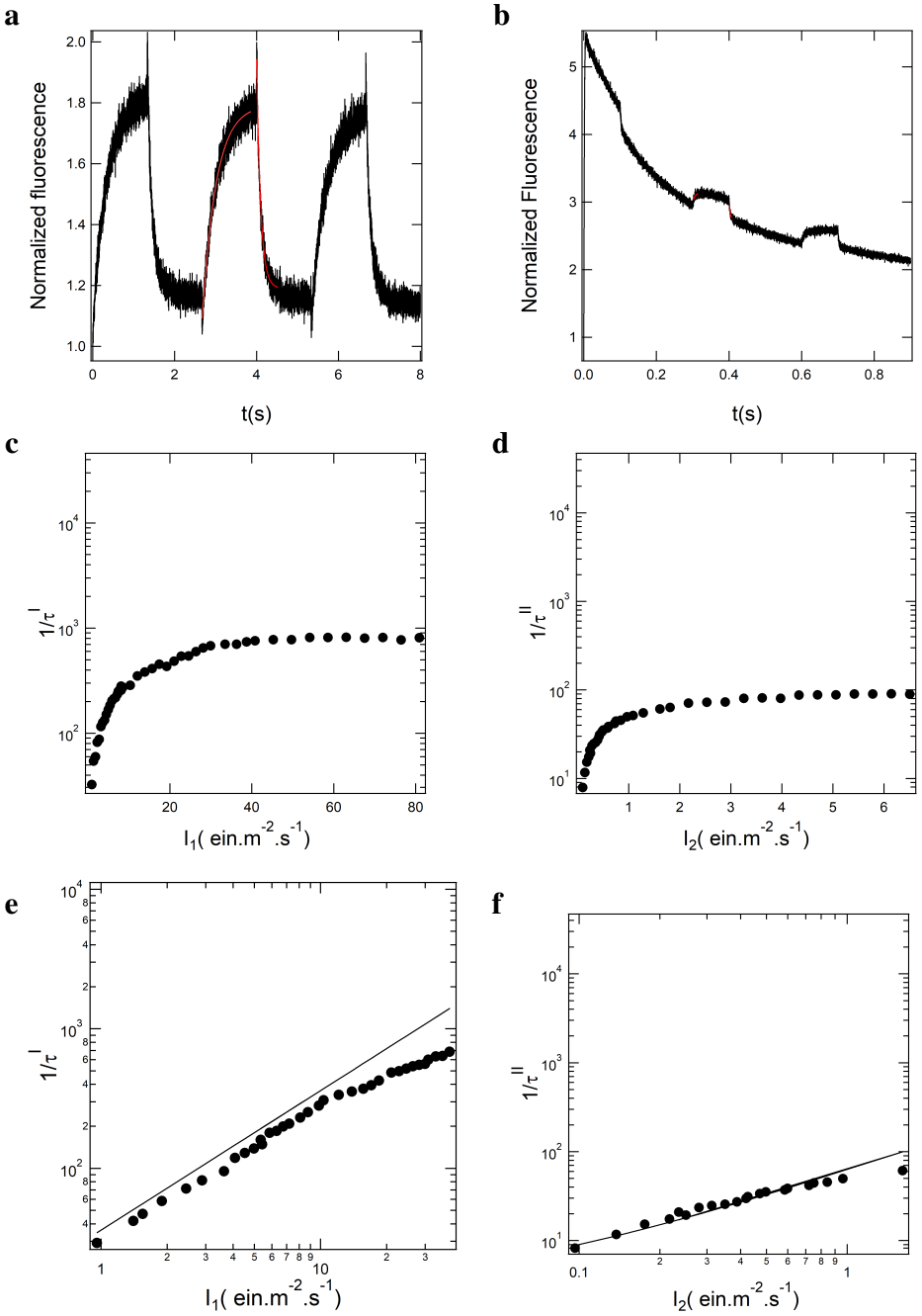

Figure A18: Kinetic analysis of **5** photoswitching at 20 μM in pH 7.4 PBS (50 mM sodium phosphate, 150 mM NaCl); T = 298 K. **a**, **b**: Evolution of fluorescence intensity upon continuous illumination of intensity I_1 at $\lambda_1 = 488$ nm and square-wave illumination of intensity I_2 at $\lambda_2 = 405$ nm (**a**: $I_1 = 0.05$ ein.m^{-2}.s^{-1}, $I_2 = 0.1$ ein.m^{-2}.s^{-1}; **b**: $I_1 = 200$ ein.m^{-2}.s^{-1}, $I_2 = 3$ ein.m^{-2}.s^{-1}). Black line: experimental data; red line: fitting functions according to Eq.(A46) and Eq.(A55); **c**: Illumination I: Inverse of the relaxation time $1/\tau^{\mathrm{I}}$ (disks) versus light intensity I_1 at $\lambda_1 = 488$ nm, **d**: Illumination II: Inverse of the relaxation time $1/\tau^{\mathrm{II}}$ (disks) versus light intensity I_2 at $\lambda_2 = 405$ nm; **e**: Magnification of **c** at low light intensity. Solid line: linear fitting function yielding the photoswitching cross section Σ_1, **f**: Magnification of **d** at low light intensity. Solid line: linear fitting function yielding the photoswitching cross section Σ_2.

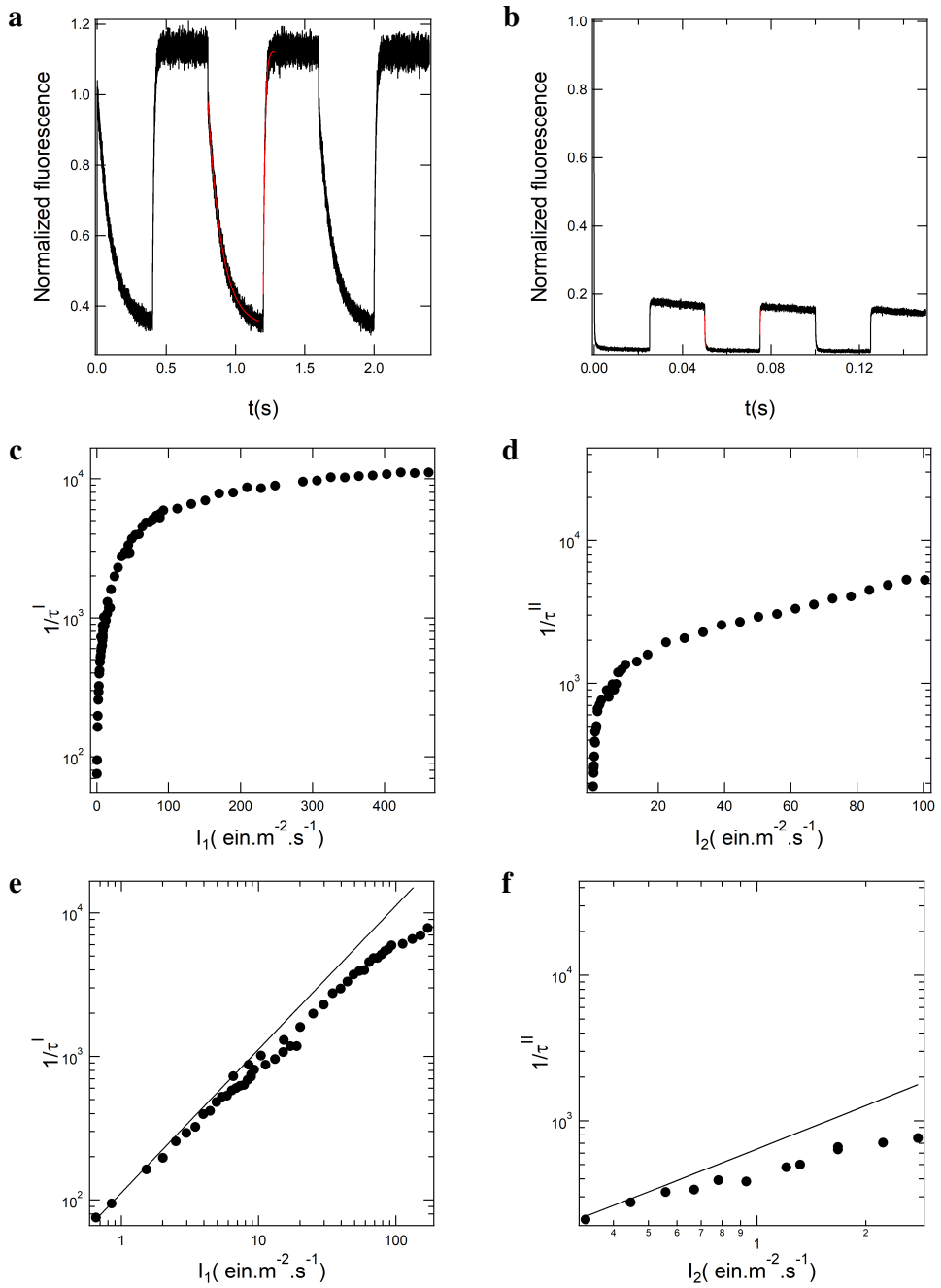

Figure A19: Kinetic analysis of **6** photoswitching at 20 μM in pH 7.4 PBS (50 mM sodium phosphate, 150 mM NaCl); T = 298 K. **a**, **b**: Evolution of fluorescence intensity upon continuous illumination of intensity I_1 at $\lambda_1 = 488$ nm and square-wave illumination of intensity I_2 at $\lambda_2 = 405$ nm (**a**: $I_1 = 0.05$ ein.m^{-2}.s^{-1}, $I_2 = 0.1$ ein.m^{-2}.s^{-1}; **b**: $I_1 = 200$ ein.m^{-2}.s^{-1}, $I_2 = 3$ ein.m^{-2}.s^{-1}). Black line: experimental data; red line: fitting functions according to Eq.(A46) and Eq.(A55); **c**: Illumination I: Inverse of the relaxation time $1/\tau^{\mathrm{I}}$ (disks) versus light intensity I_1 at $\lambda_1 = 488$ nm, **d**: Illumination II: Inverse of the relaxation time $1/\tau^{\mathrm{II}}$ (disks) versus light intensity I_2 at $\lambda_2 = 405$ nm; **e**: Magnification of **c** at low light intensity. Solid line: linear fitting function yielding the photoswitching cross section Σ_1, **f**: Magnification of **d** at low light intensity. Solid line: linear fitting function yielding the photoswitching cross section Σ_2.

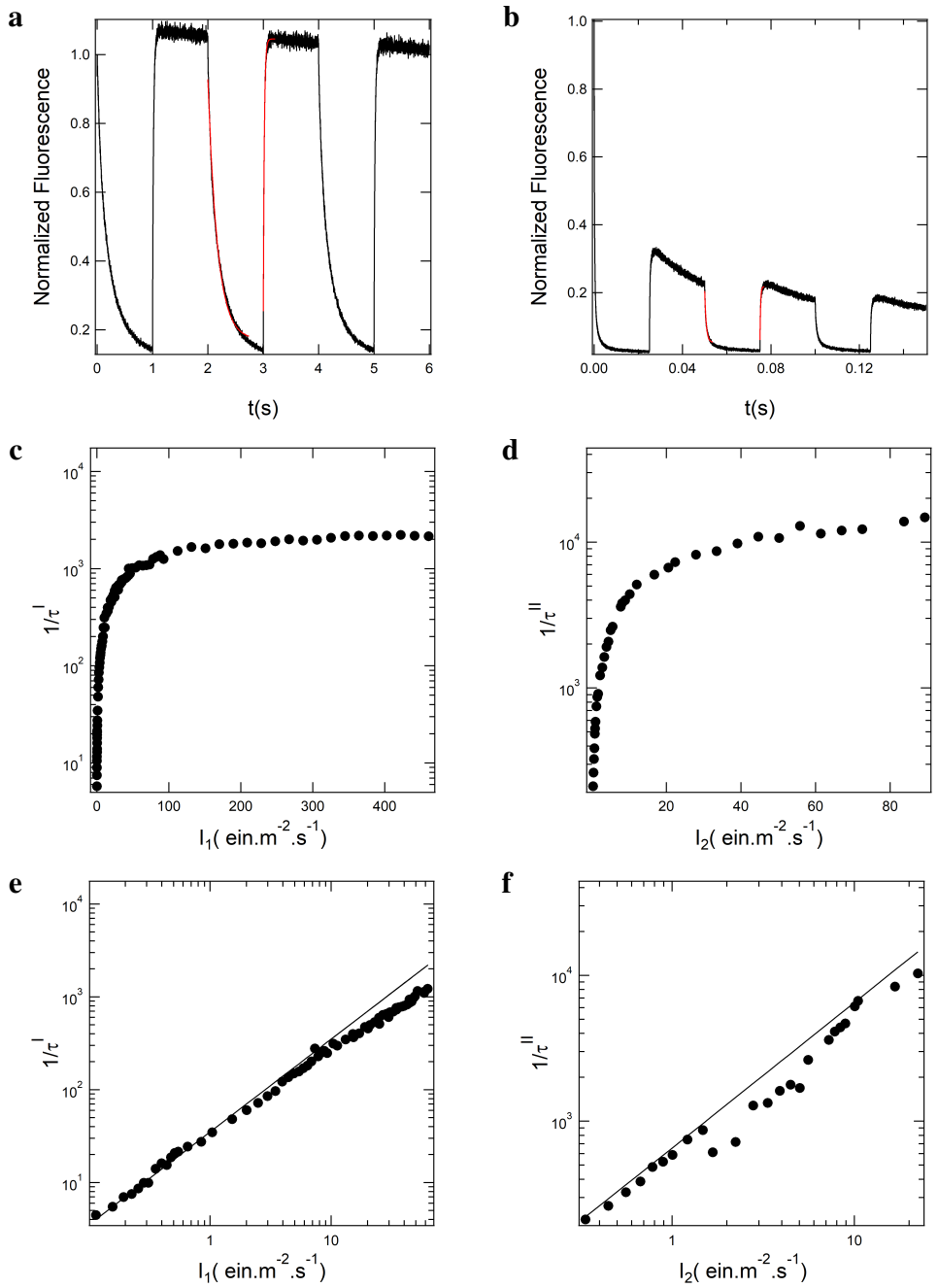

Figure A20: Kinetic analysis of **7** photoswitching at 20 μM in pH 7.4 PBS (50 mM sodium phosphate, 150 mM NaCl); T = 298 K. **a**, **b**: Evolution of fluorescence intensity upon continuous illumination of intensity I_1 at $\lambda_1 = 488$ nm and square-wave illumination of intensity I_2 at $\lambda_2 = 405$ nm (**a**: $I_1 = 0.05$ ein.m^{-2}.s^{-1}, $I_2 = 0.1$ ein.m^{-2}.s^{-1}; **b**: $I_1 = 200$ ein.m^{-2}.s^{-1}, $I_2 = 3$ ein.m^{-2}.s^{-1}). Black line: experimental data; red line: fitting functions according to Eq.(A46) and Eq.(A55); **c**: Illumination I: Inverse of the relaxation time $1/\tau^{\mathrm{I}}$ (disks) versus light intensity I_1 at $\lambda_1 = 488$ nm, **d**: Illumination II: Inverse of the relaxation time $1/\tau^{\mathrm{II}}$ (disks) versus light intensity I_2 at $\lambda_2 = 405$ nm; **e**: Magnification of **c** at low light intensity. Solid line: linear fitting function yielding the photoswitching cross section Σ_1, **f**: Magnification of **d** at low light intensity. Solid line: linear fitting function yielding the photoswitching cross section Σ_2.

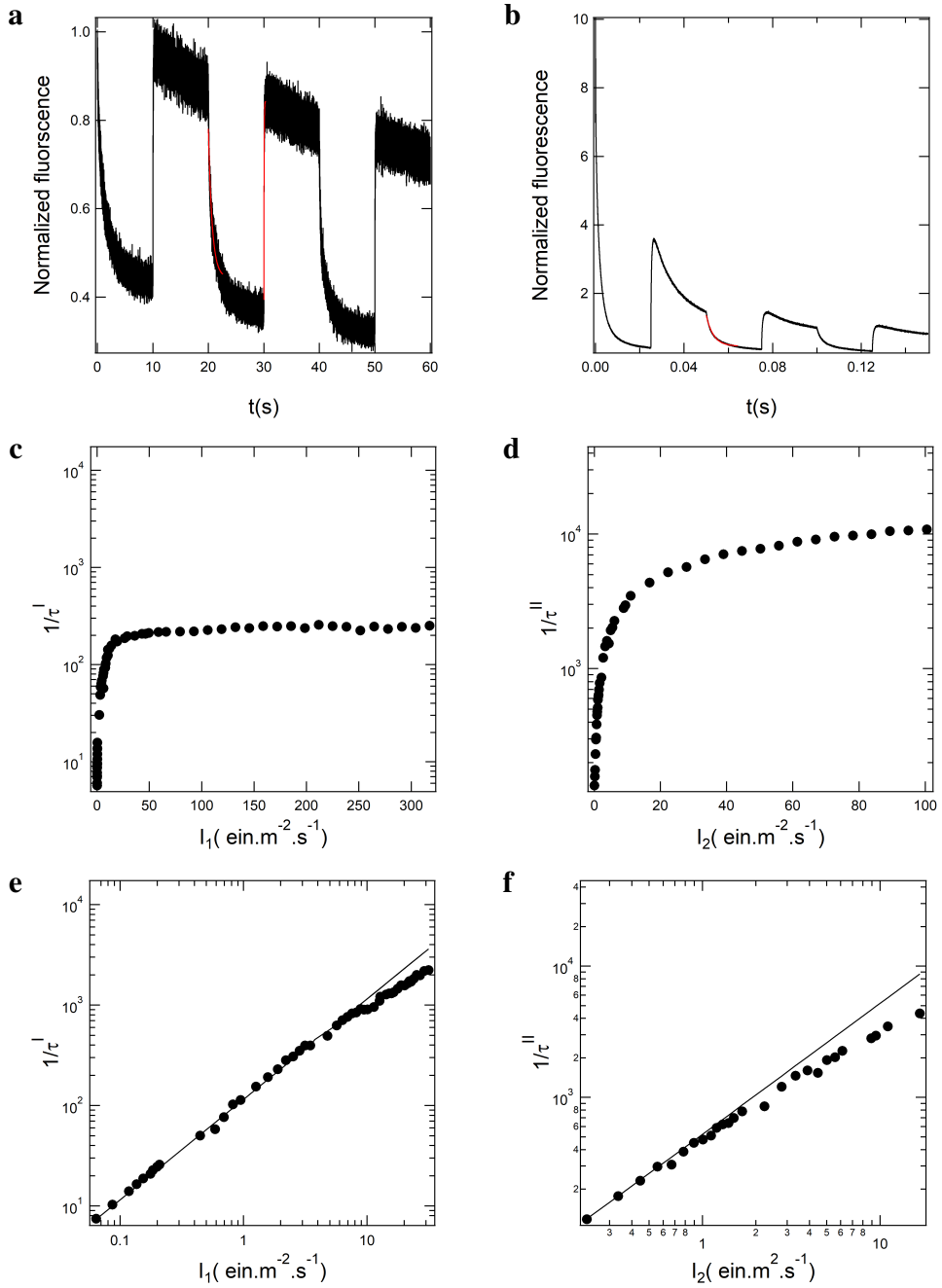

Figure A21: Kinetic analysis of **8** photoswitching at 20 μM in pH 7.4 PBS (50 mM sodium phosphate, 150 mM NaCl); T = 298 K. **a**, **b**: Evolution of fluorescence intensity upon continuous illumination of intensity I_1 at $\lambda_1 = 488$ nm and square-wave illumination of intensity I_2 at $\lambda_2 = 405$ nm (**a**: $I_1 = 0.05$ ein.m^{-2}.s^{-1}, $I_2 = 0.1$ ein.m^{-2}.s^{-1}; **b**: $I_1 = 200$ ein.m^{-2}.s^{-1}, $I_2 = 3$ ein.m^{-2}.s^{-1}). Black line: experimental data; red line: fitting functions according to Eq.(A46) and Eq.(A55); **c**: Illumination I: Inverse of the relaxation time $1/\tau^{\mathrm{I}}$ (disks) versus light intensity I_1 at $\lambda_1 = 488$ nm, **d**: Illumination II: Inverse of the relaxation time $1/\tau^{\mathrm{II}}$ (disks) versus light intensity I_2 at $\lambda_2 = 405$ nm; **e**: Magnification of **c** at low light intensity. Solid line: linear fitting function yielding the photoswitching cross section Σ_1, **f**: Magnification of **d** at low light intensity. Solid line: linear fitting function yielding the photoswitching cross section Σ_2.

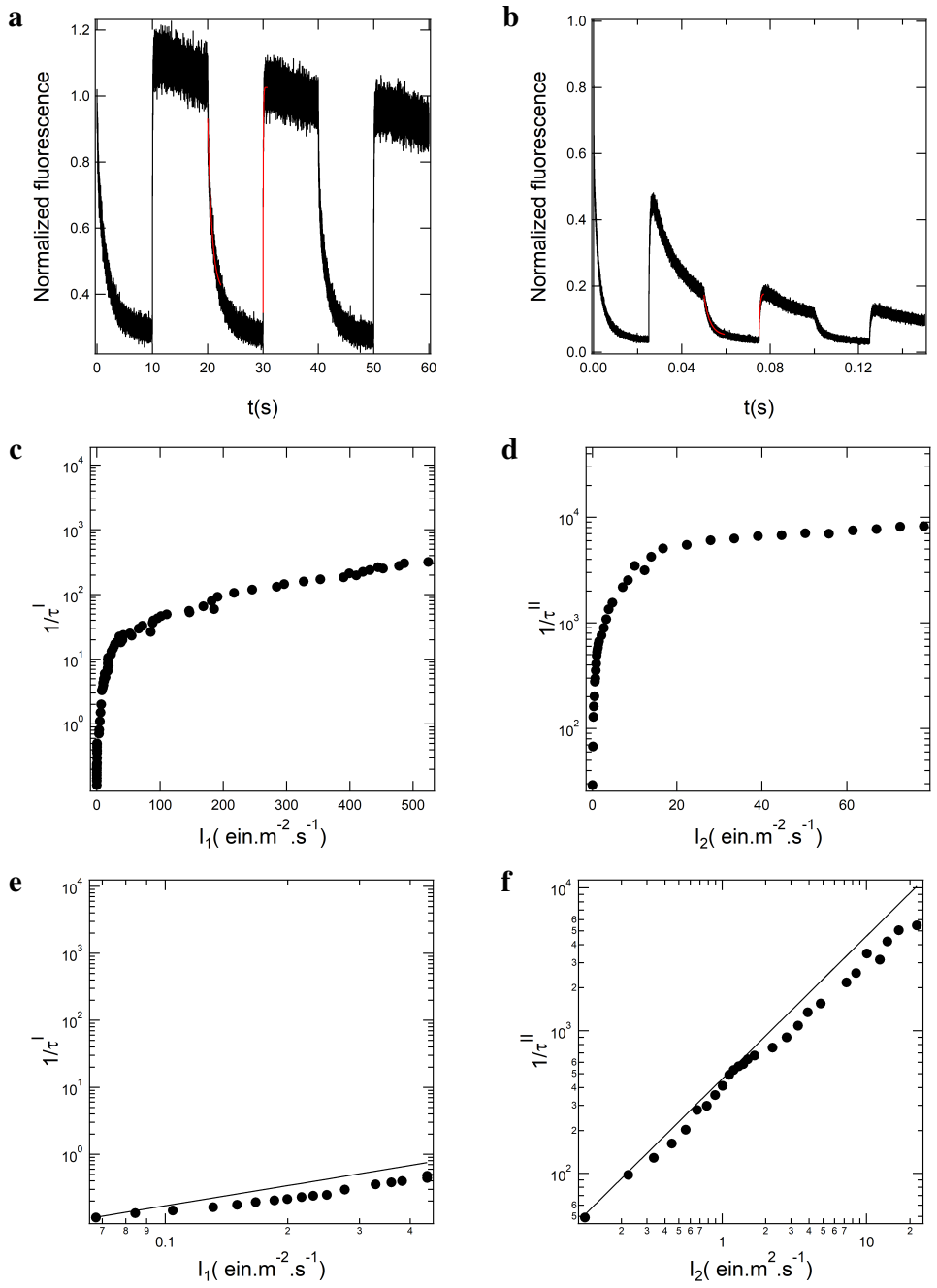

Figure A22: Kinetic analysis of **9** photoswitching at 20 μM in pH 7.4 PBS (50 mM sodium phosphate, 150 mM NaCl); T = 298 K. **a**, **b**: Evolution of fluorescence intensity upon continuous illumination of intensity I_1 at $\lambda_1 = 488$ nm and square-wave illumination of intensity I_2 at $\lambda_2 = 405$ nm (**a**: $I_1 = 0.05$ ein.m^{-2}.s^{-1}, $I_2 = 0.1$ ein.m^{-2}.s^{-1}; **b**: $I_1 = 200$ ein.m^{-2}.s^{-1}, $I_2 = 3$ ein.m^{-2}.s^{-1}). Black line: experimental data; red line: fitting functions according to Eq.(A46) and Eq.(A55); **c**: Illumination I: Inverse of the relaxation time $1/\tau^{\mathrm{I}}$ (disks) versus light intensity I_1 at $\lambda_1 = 488$ nm, **d**: Illumination II: Inverse of the relaxation time $1/\tau^{\mathrm{II}}$ (disks) versus light intensity I_2 at $\lambda_2 = 405$ nm; **e**: Magnification of **c** at low light intensity. Solid line: linear fitting function yielding the photoswitching cross section Σ_1, **f**: Magnification of **d** at low light intensity. Solid line: linear fitting function yielding the photoswitching cross section Σ_2.

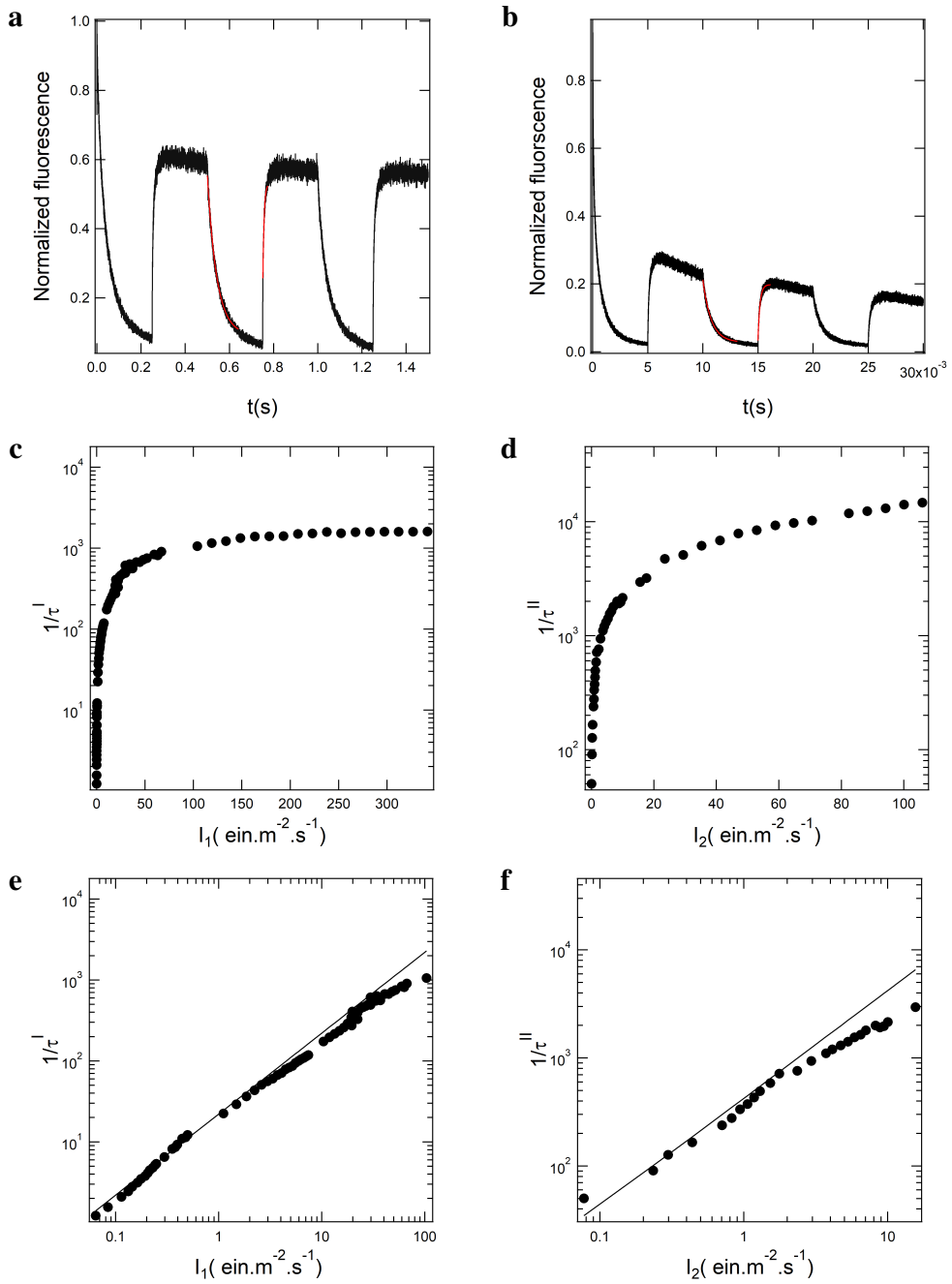

Figure A23: Kinetic analysis of **10** photoswitching at 20 μM in pH 7.4 PBS (50 mM sodium phosphate, 150 mM NaCl); T = 298 K. **a**, **b**: Evolution of fluorescence intensity upon continuous illumination of intensity I_1 at $\lambda_1 = 488$ nm and square-wave illumination of intensity I_2 at $\lambda_2 = 405$ nm (**a**: $I_1 = 0.05$ ein.m^{-2}.s^{-1}, $I_2 = 0.1$ ein.m^{-2}.s^{-1}; **b**: $I_1 = 200$ ein.m^{-2}.s^{-1}, $I_2 = 3$ ein.m^{-2}.s^{-1}). Black line: experimental data; red line: fitting functions according to Eq.(A46) and Eq.(A55); **c**: Illumination I: Inverse of the relaxation time $1/\tau^{\mathrm{I}}$ (disks) versus light intensity I_1 at $\lambda_1 = 488$ nm, **d**: Illumination II: Inverse of the relaxation time $1/\tau^{\mathrm{II}}$ (disks) versus light intensity I_2 at $\lambda_2 = 405$ nm; **e**: Magnification of **c** at low light intensity. Solid line: linear fitting function yielding the photoswitching cross section Σ_1, **f**: Magnification of **d** at low light intensity. Solid line: linear fitting function yielding the photoswitching cross section Σ_2.

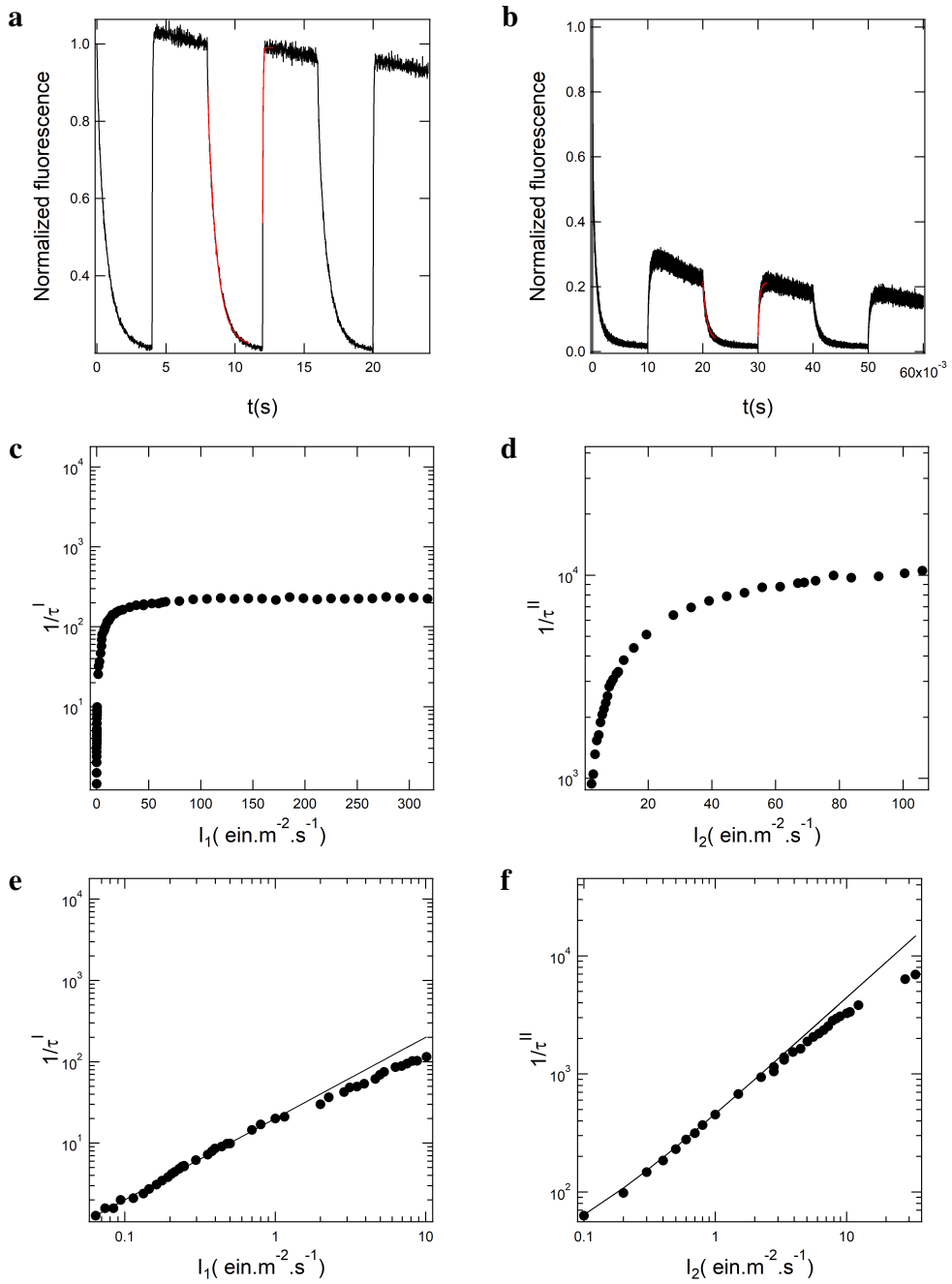

Figure A24: Kinetic analysis of **11** photoswitching at 20 μM in pH 7.4 PBS (50 mM sodium phosphate, 150 mM NaCl); T = 298 K. **a**, **b**: Evolution of fluorescence intensity upon continuous illumination of intensity I_1 at $\lambda_1 = 488$ nm and square-wave illumination of intensity I_2 at $\lambda_2 = 405$ nm (**a**: $I_1 = 0.05$ ein.m^{-2}.s^{-1}, $I_2 = 0.1$ ein.m^{-2}.s^{-1}; **b**: $I_1 = 200$ ein.m^{-2}.s^{-1}, $I_2 = 3$ ein.m^{-2}.s^{-1}). Black line: experimental data; red line: fitting functions according to Eq.(A46) and Eq.(A55); **c**: Illumination I: Inverse of the relaxation time $1/\tau^{\mathrm{I}}$ (disks) versus light intensity I_1 at $\lambda_1 = 488$ nm, **d**: Illumination II: Inverse of the relaxation time $1/\tau^{\mathrm{II}}$ (disks) versus light intensity I_2 at $\lambda_2 = 405$ nm; **e**: Magnification of **c** at low light intensity. Solid line: linear fitting function yielding the photoswitching cross section Σ_1, **f**: Magnification of **d** at low light intensity. Solid line: linear fitting function yielding the photoswitching cross section Σ_2.

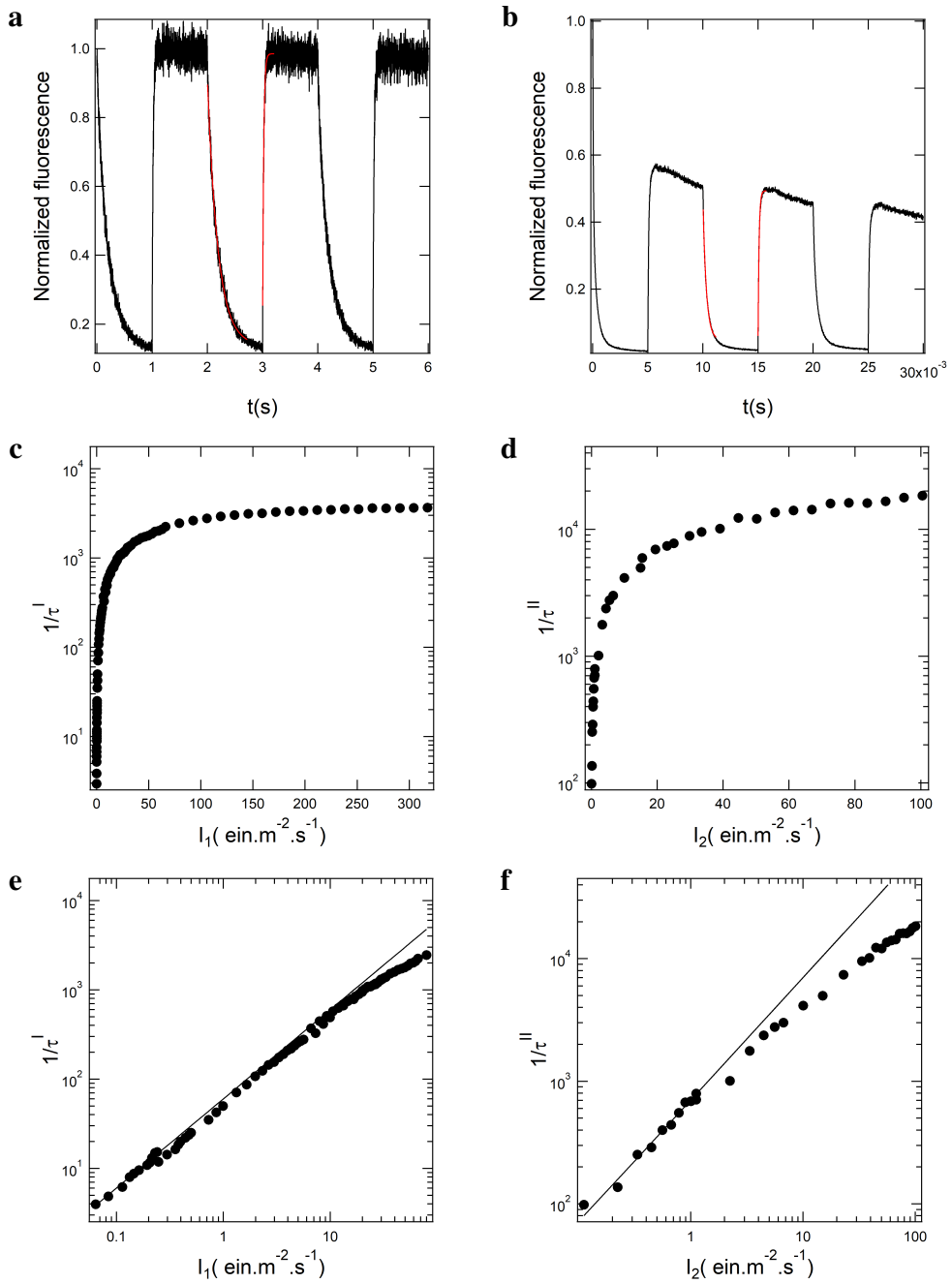

Figure A25: Kinetic analysis of **12** photoswitching at 20 μM in pH 7.4 PBS (50 mM sodium phosphate, 150 mM NaCl); T = 298 K. **a**, **b**: Evolution of fluorescence intensity upon continuous illumination of intensity I_1 at $\lambda_1 = 488$ nm and square-wave illumination of intensity I_2 at $\lambda_2 = 405$ nm (**a**: $I_1 = 0.05$ ein.m^{-2}.s^{-1}, $I_2 = 0.1$ ein.m^{-2}.s^{-1}; **b**: $I_1 = 200$ ein.m^{-2}.s^{-1}, $I_2 = 3$ ein.m^{-2}.s^{-1}). Black line: experimental data; red line: fitting functions according to Eq.(A46) and Eq.(A55); **c**: Illumination I: Inverse of the relaxation time $1/\tau^{\mathrm{I}}$ (disks) versus light intensity I_1 at $\lambda_1 = 488$ nm, **d**: Illumination II: Inverse of the relaxation time $1/\tau^{\mathrm{II}}$ (disks) versus light intensity I_2 at $\lambda_2 = 405$ nm; **e**: Magnification of **c** at low light intensity. Solid line: linear fitting function yielding the photoswitching cross section Σ_1, **f**: Magnification of **d** at low light intensity. Solid line: linear fitting function yielding the photoswitching cross section Σ_2.

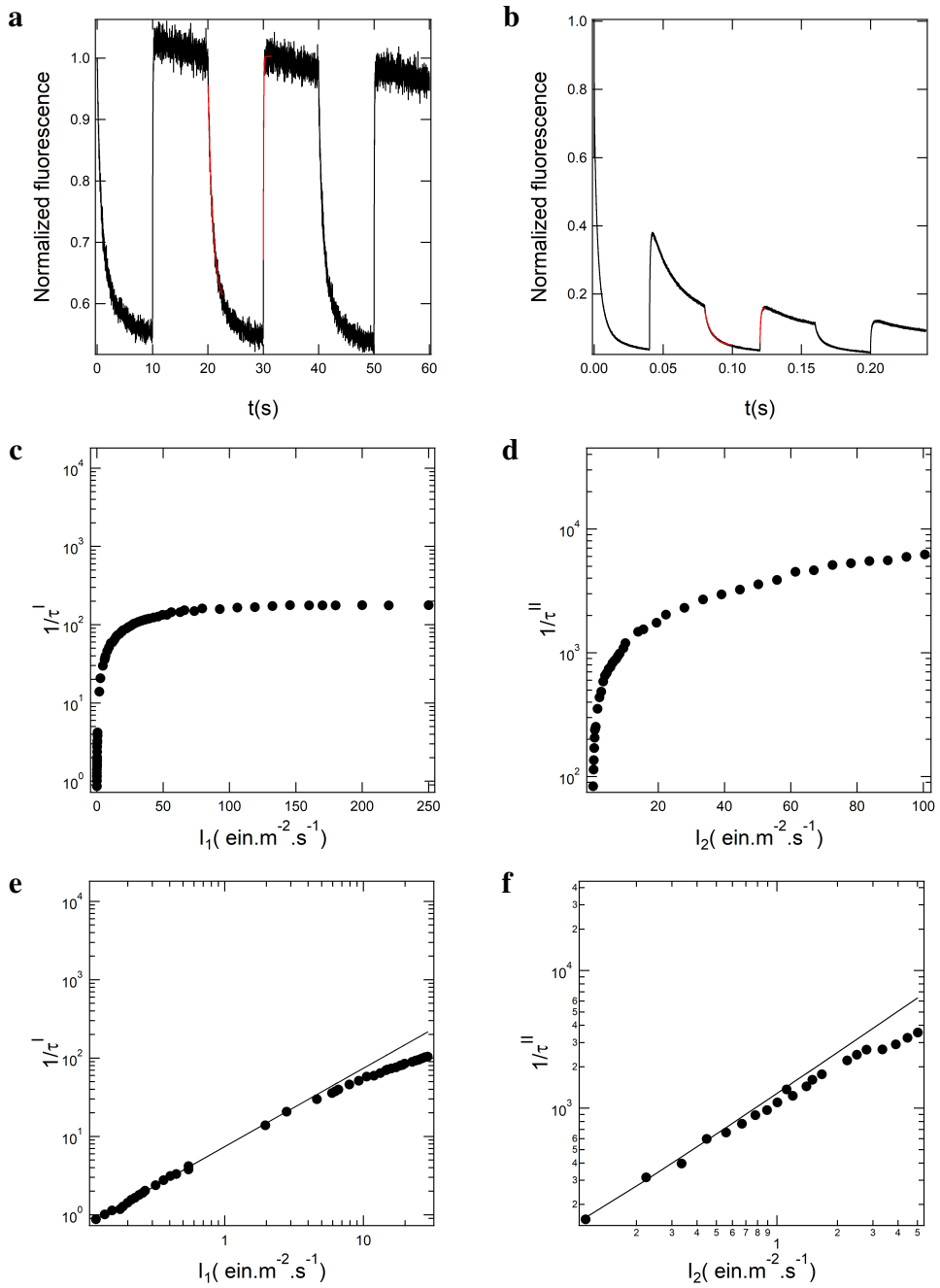

Figure A26: Kinetic analysis of **13** photoswitching at 20 μM in pH 7.4 PBS (50 mM sodium phosphate, 150 mM NaCl); T = 298 K. **a**, **b**: Evolution of fluorescence intensity upon continuous illumination of intensity I_1 at $\lambda_1 = 488$ nm and square-wave illumination of intensity I_2 at $\lambda_2 = 405$ nm (**a**: $I_1 = 0.05$ ein.m^{-2}.s^{-1}, $I_2 = 0.1$ ein.m^{-2}.s^{-1}; **b**: $I_1 = 200$ ein.m^{-2}.s^{-1}, $I_2 = 3$ ein.m^{-2}.s^{-1}). Black line: experimental data; red line: fitting functions according to Eq.(A46) and Eq.(A55); **c**: Illumination I: Inverse of the relaxation time $1/\tau^{\mathrm{I}}$ (disks) versus light intensity I_1 at $\lambda_1 = 488$ nm, **d**: Illumination II: Inverse of the relaxation time $1/\tau^{\mathrm{II}}$ (disks) versus light intensity I_2 at $\lambda_2 = 405$ nm; **e**: Magnification of **c** at low light intensity. Solid line: linear fitting function yielding the photoswitching cross section Σ_1, **f**: Magnification of **d** at low light intensity. Solid line: linear fitting function yielding the photoswitching cross section Σ_2.

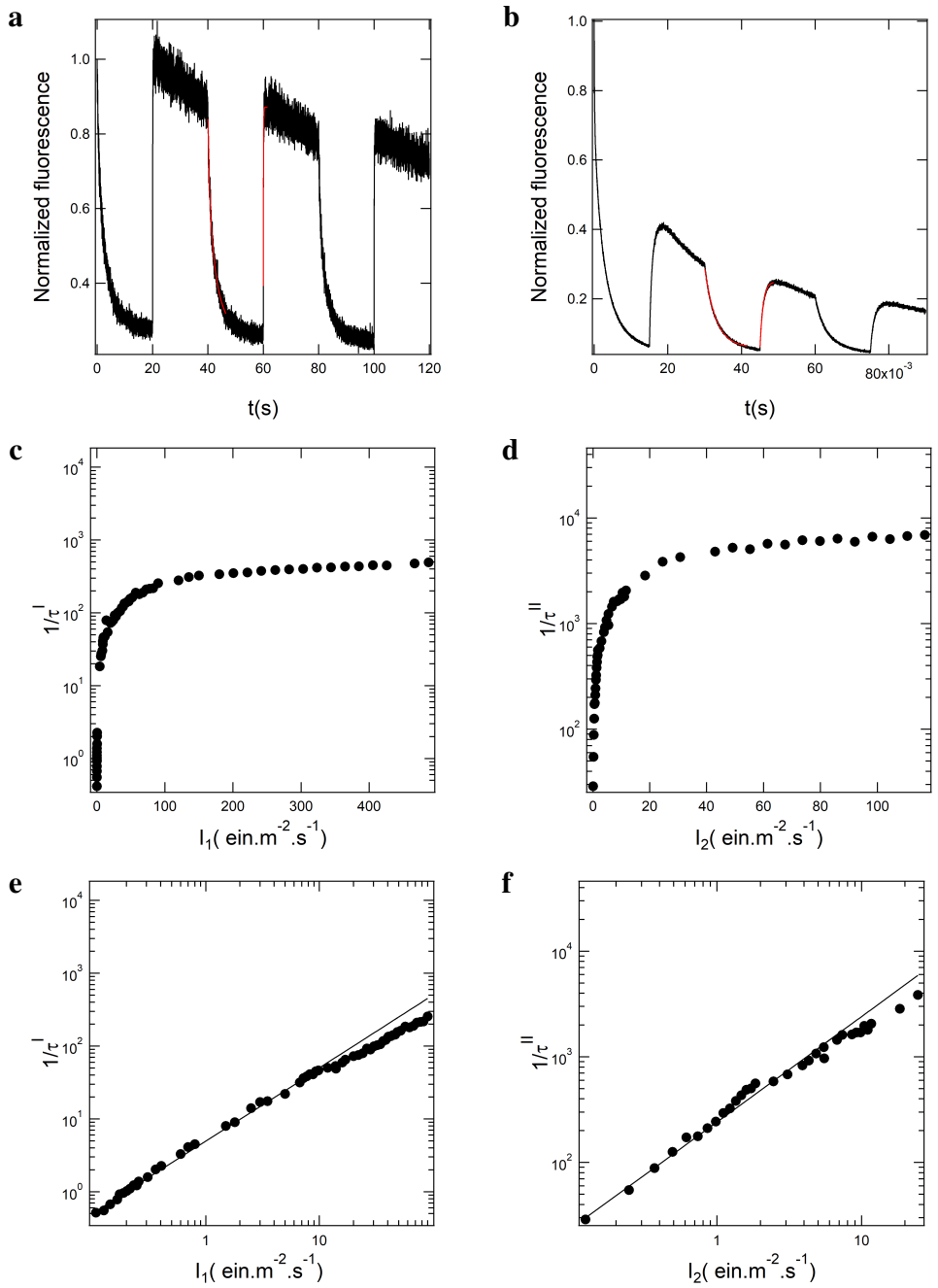

Figure A27: Kinetic analysis of **14** photoswitching at 20 μM in pH 7.4 PBS (50 mM sodium phosphate, 150 mM NaCl); T = 298 K. **a**, **b**: Evolution of fluorescence intensity upon continuous illumination of intensity I_1 at $\lambda_1 = 488$ nm and square-wave illumination of intensity I_2 at $\lambda_2 = 405$ nm (**a**: $I_1 = 0.05$ ein.m^{-2}.s^{-1}, $I_2 = 0.1$ ein.m^{-2}.s^{-1}; **b**: $I_1 = 200$ ein.m^{-2}.s^{-1}, $I_2 = 3$ ein.m^{-2}.s^{-1}). Black line: experimental data; red line: fitting functions according to Eq.(A46) and Eq.(A55); **c**: Illumination I: Inverse of the relaxation time $1/\tau^{\mathrm{I}}$ (disks) versus light intensity I_1 at $\lambda_1 = 488$ nm, **d**: Illumination II: Inverse of the relaxation time $1/\tau^{\mathrm{II}}$ (disks) versus light intensity I_2 at $\lambda_2 = 405$ nm; **e**: Magnification of **c** at low light intensity. Solid line: linear fitting function yielding the photoswitching cross section Σ_1, **f**: Magnification of **d** at low light intensity. Solid line: linear fitting function yielding the photoswitching cross section Σ_2.

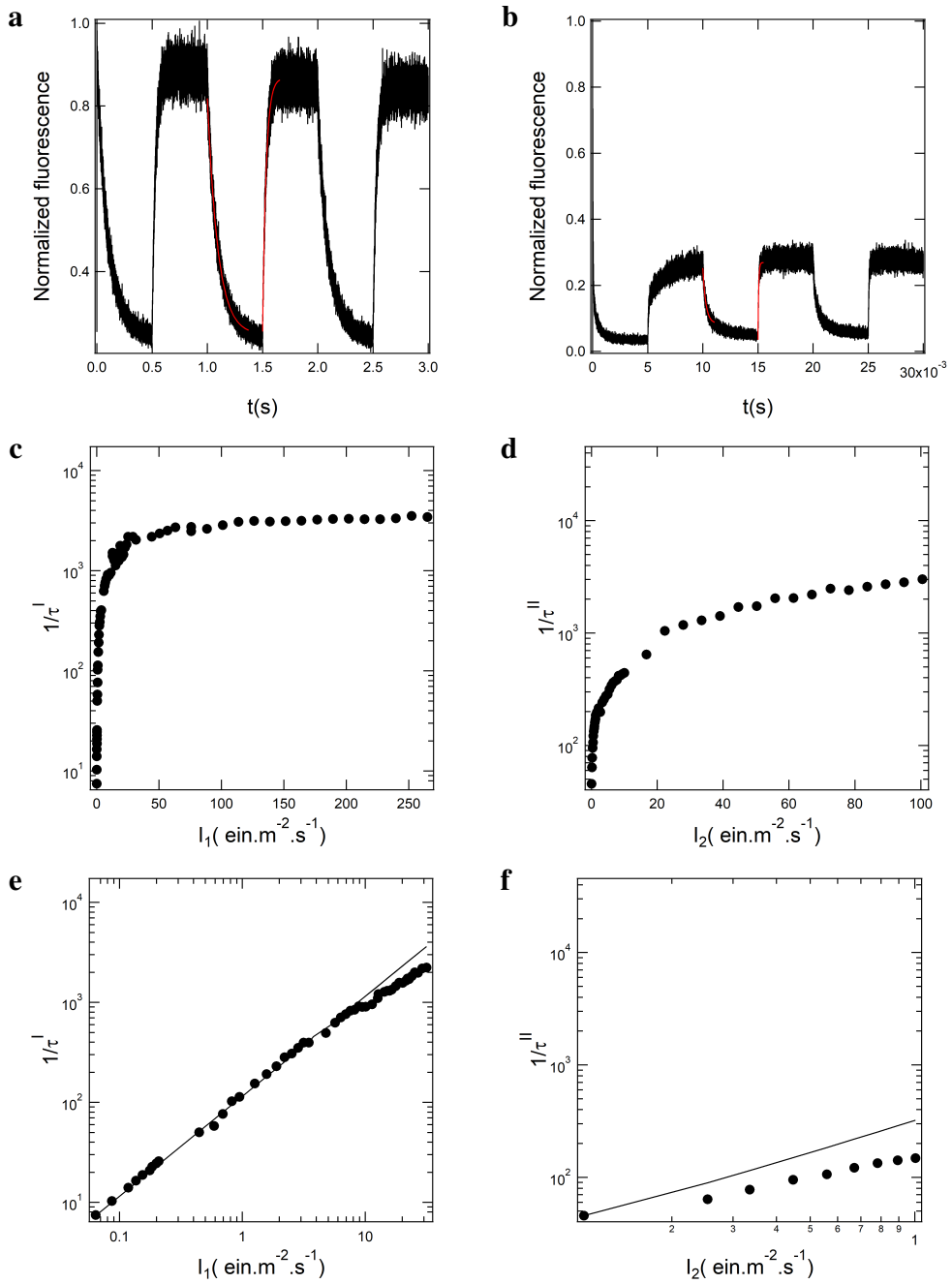

Figure A28: Kinetic analysis of **15** photoswitching at 20 μM in pH 7.4 PBS (50 mM sodium phosphate, 150 mM NaCl); T = 298 K. **a**, **b**: Evolution of fluorescence intensity upon continuous illumination of intensity I_1 at $\lambda_1 = 488$ nm and square-wave illumination of intensity I_2 at $\lambda_2 = 405$ nm (**a**: $I_1 = 0.05$ ein.m^{-2}.s^{-1}, $I_2 = 0.1$ ein.m^{-2}.s^{-1}; **b**: $I_1 = 200$ ein.m^{-2}.s^{-1}, $I_2 = 3$ ein.m^{-2}.s^{-1}). Black line: experimental data; red line: fitting functions according to Eq.(A46) and Eq.(A55); **c**: Illumination I: Inverse of the relaxation time $1/\tau^{\mathrm{I}}$ (disks) versus light intensity I_1 at $\lambda_1 = 488$ nm, **d**: Illumination II: Inverse of the relaxation time $1/\tau^{\mathrm{II}}$ (disks) versus light intensity I_2 at $\lambda_2 = 405$ nm; **e**: Magnification of **c** at low light intensity. Solid line: linear fitting function yielding the photoswitching cross section Σ_1, **f**: Magnification of **d** at low light intensity. Solid line: linear fitting function yielding the photoswitching cross section Σ_2.

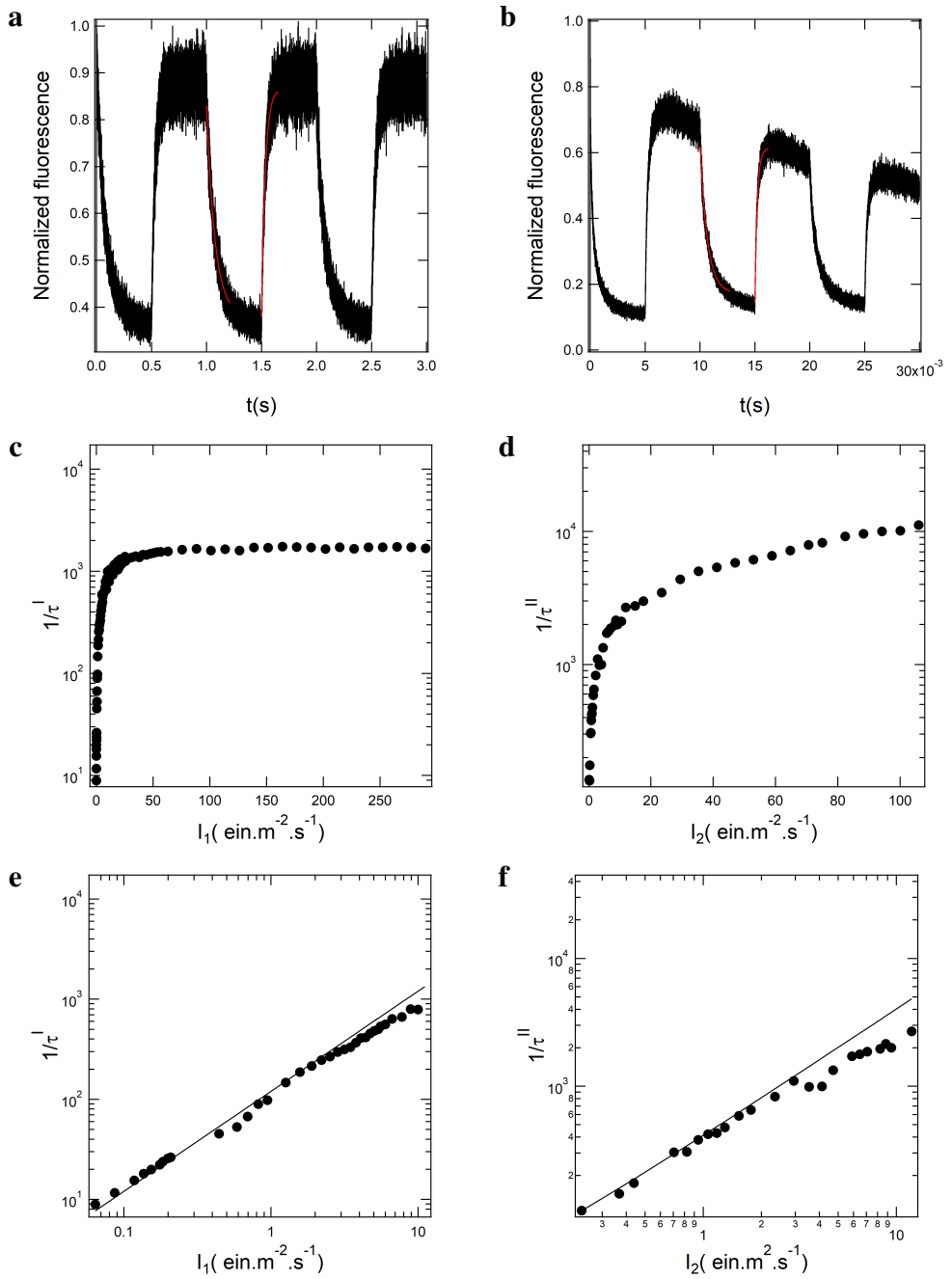

Figure A29: Kinetic analysis of **16** photoswitching at 20 μM in pH 7.4 PBS (50 mM sodium phosphate, 150 mM NaCl); T = 298 K. **a**, **b**: Evolution of fluorescence intensity upon continuous illumination of intensity I_1 at $\lambda_1 = 488$ nm and square-wave illumination of intensity I_2 at $\lambda_2 = 405$ nm (**a**: $I_1 = 0.05$ ein.m^{-2}.s^{-1}, $I_2 = 0.1$ ein.m^{-2}.s^{-1}; **b**: $I_1 = 200$ ein.m^{-2}.s^{-1}, $I_2 = 3$ ein.m^{-2}.s^{-1}). Black line: experimental data; red line: fitting functions according to Eq.(A46) and Eq.(A55); **c**: Illumination I: Inverse of the relaxation time $1/\tau^{\mathrm{I}}$ (disks) versus light intensity I_1 at $\lambda_1 = 488$ nm, **d**: Illumination II: Inverse of the relaxation time $1/\tau^{\mathrm{II}}$ (disks) versus light intensity I_2 at $\lambda_2 = 405$ nm; **e**: Magnification of **c** at low light intensity. Solid line: linear fitting function yielding the photoswitching cross section Σ_1, **f**: Magnification of **d** at low light intensity. Solid line: linear fitting function yielding the photoswitching cross section Σ_2.

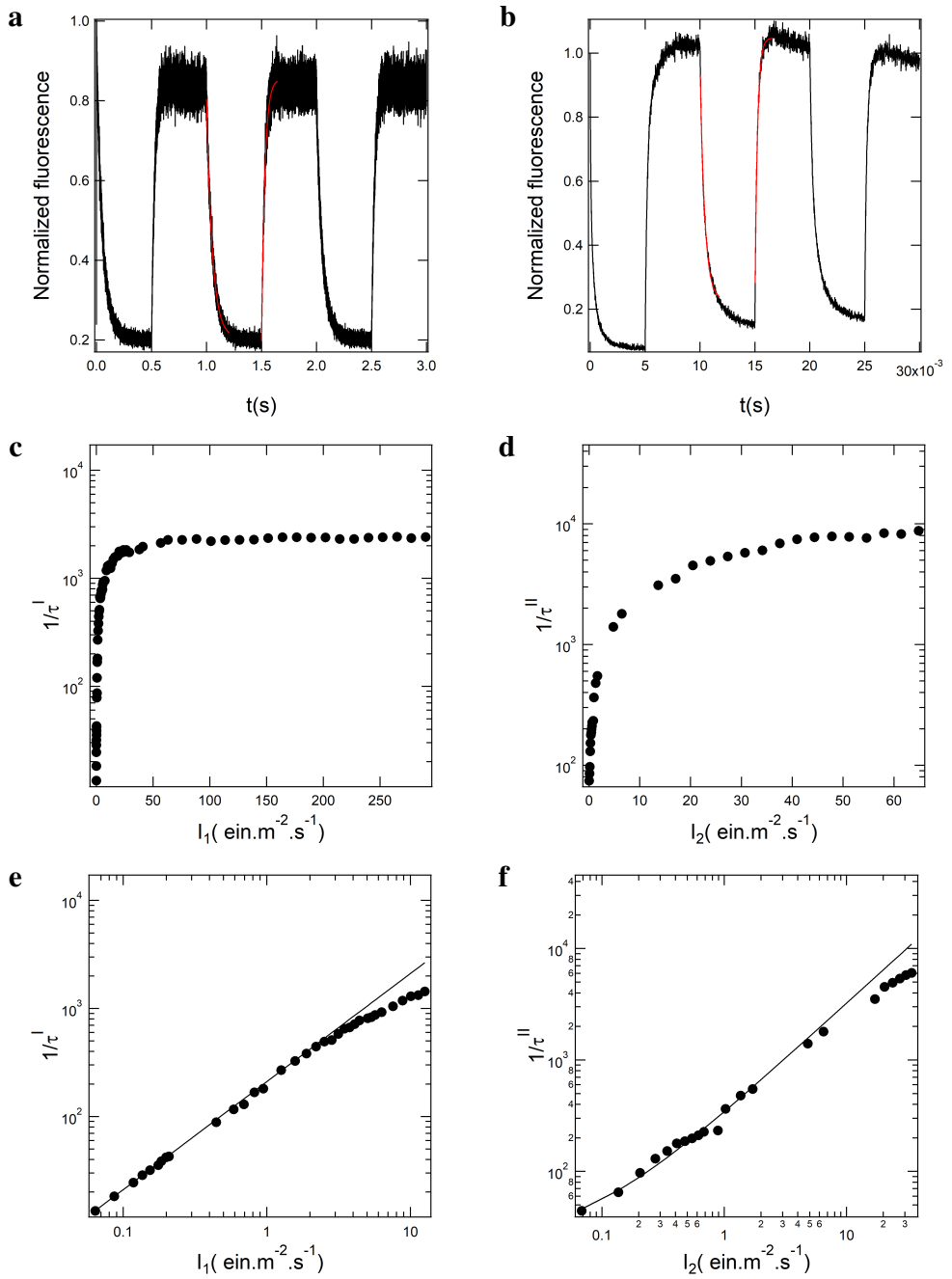

Figure A30: Kinetic analysis of **17** photoswitching at 20 μM in pH 7.4 PBS (50 mM sodium phosphate, 150 mM NaCl); T = 298 K. **a**, **b**: Evolution of fluorescence intensity upon continuous illumination of intensity I_1 at $\lambda_1 = 488$ nm and square-wave illumination of intensity I_2 at $\lambda_2 = 405$ nm (**a**: $I_1 = 0.05$ ein.m^{-2}.s^{-1}, $I_2 = 0.1$ ein.m^{-2}.s^{-1}; **b**: $I_1 = 200$ ein.m^{-2}.s^{-1}, $I_2 = 3$ ein.m^{-2}.s^{-1}). Black line: experimental data; red line: fitting functions according to Eq.(A46) and Eq.(A55); **c**: Illumination I: Inverse of the relaxation time $1/\tau^{\mathrm{I}}$ (disks) versus light intensity I_1 at $\lambda_1 = 488$ nm, **d**: Illumination II: Inverse of the relaxation time $1/\tau^{\mathrm{II}}$ (disks) versus light intensity I_2 at $\lambda_2 = 405$ nm; **e**: Magnification of **c** at low light intensity. Solid line: linear fitting function yielding the photoswitching cross section Σ_1, **f**: Magnification of **d** at low light intensity. Solid line: linear fitting function yielding the photoswitching cross section Σ_2.

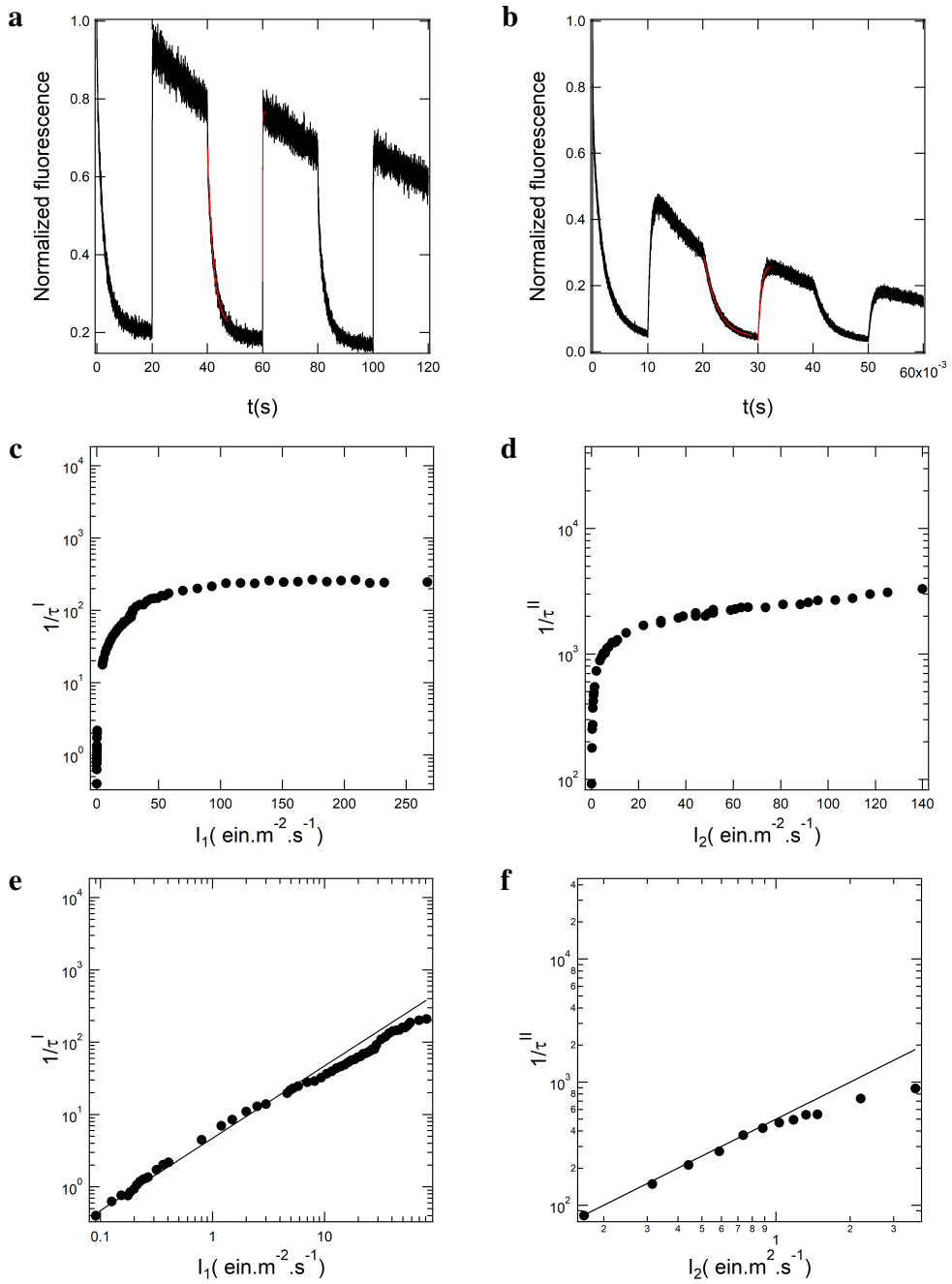

Figure A31: Kinetic analysis of **18** photoswitching at 20 μM in pH 7.4 PBS (50 mM sodium phosphate, 150 mM NaCl); T = 298 K. **a**, **b**: Evolution of fluorescence intensity upon continuous illumination of intensity I_1 at $\lambda_1 = 488$ nm and square-wave illumination of intensity I_2 at $\lambda_2 = 405$ nm (**a**: $I_1 = 0.05$ ein.m^{-2}.s^{-1}, $I_2 = 0.1$ ein.m^{-2}.s^{-1}; **b**: $I_1 = 200$ ein.m^{-2}.s^{-1}, $I_2 = 3$ ein.m^{-2}.s^{-1}). Black line: experimental data; red line: fitting functions according to Eq.(A46) and Eq.(A55); **c**: Illumination I: Inverse of the relaxation time $1/\tau^{\mathrm{I}}$ (disks) versus light intensity I_1 at $\lambda_1 = 488$ nm, **d**: Illumination II: Inverse of the relaxation time $1/\tau^{\mathrm{II}}$ (disks) versus light intensity I_2 at $\lambda_2 = 405$ nm; **e**: Magnification of **c** at low light intensity. Solid line: linear fitting function yielding the photoswitching cross section Σ_1, **f**: Magnification of **d** at low light intensity. Solid line: linear fitting function yielding the photoswitching cross section Σ_2.

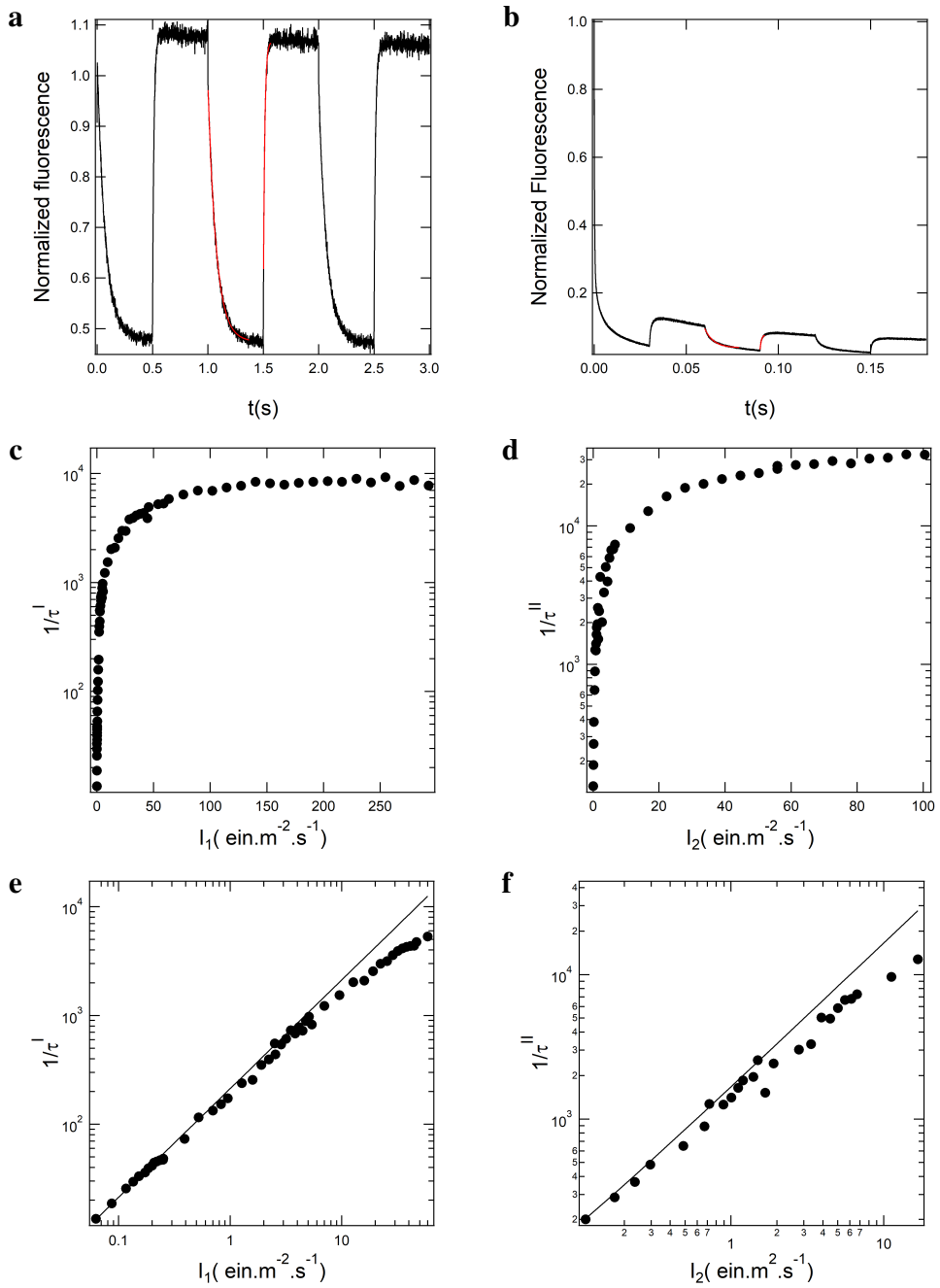

Figure A32: Kinetic analysis of **19** photoswitching at 20 μM in pH 7.4 PBS (50 mM sodium phosphate, 150 mM NaCl); T = 298 K. **a**, **b**: Evolution of fluorescence intensity upon continuous illumination of intensity I_1 at $\lambda_1 = 488$ nm and square-wave illumination of intensity I_2 at $\lambda_2 = 405$ nm (**a**: $I_1 = 0.05$ ein.m^{-2}.s^{-1}, $I_2 = 0.1$ ein.m^{-2}.s^{-1}; **b**: $I_1 = 200$ ein.m^{-2}.s^{-1}, $I_2 = 3$ ein.m^{-2}.s^{-1}). Black line: experimental data; red line: fitting functions according to Eq.(A46) and Eq.(A55); **c**: Illumination I: Inverse of the relaxation time $1/\tau^{\mathrm{I}}$ (disks) versus light intensity I_1 at $\lambda_1 = 488$ nm, **d**: Illumination II: Inverse of the relaxation time $1/\tau^{\mathrm{II}}$ (disks) versus light intensity I_2 at $\lambda_2 = 405$ nm; **e**: Magnification of **c** at low light intensity. Solid line: linear fitting function yielding the photoswitching cross section Σ_1, **f**: Magnification of **d** at low light intensity. Solid line: linear fitting function yielding the photoswitching cross section Σ_2.

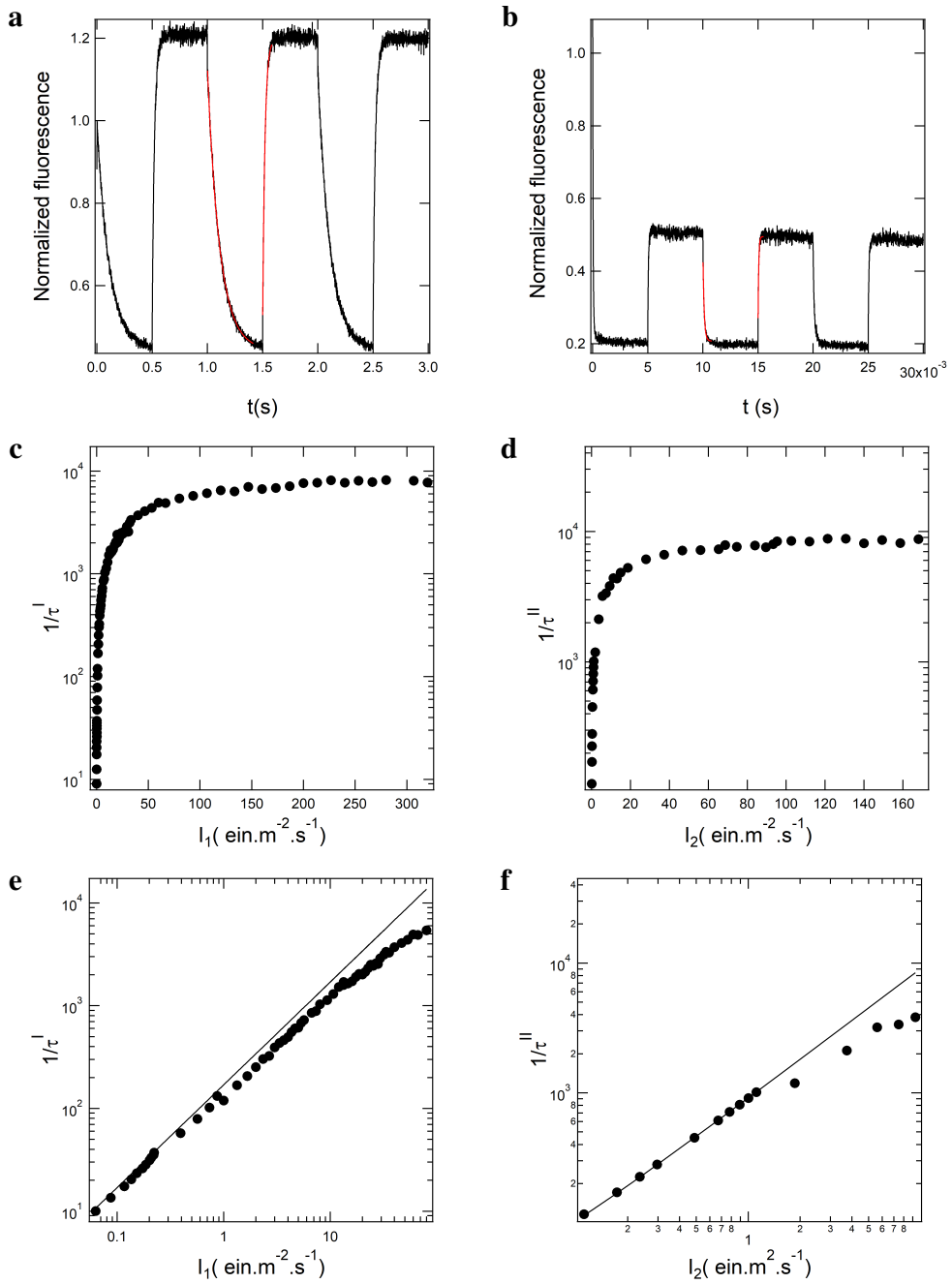

Figure A33: Kinetic analysis of **20** photoswitching at 20 μM in pH 7.4 PBS (50 mM sodium phosphate, 150 mM NaCl); T = 298 K. **a**, **b**: Evolution of fluorescence intensity upon continuous illumination of intensity I_1 at $\lambda_1 = 488$ nm and square-wave illumination of intensity I_2 at $\lambda_2 = 405$ nm (**a**: $I_1 = 0.05$ ein.m^{-2}.s^{-1}, $I_2 = 0.1$ ein.m^{-2}.s^{-1}; **b**: $I_1 = 200$ ein.m^{-2}.s^{-1}, $I_2 = 3$ ein.m^{-2}.s^{-1}). Black line: experimental data; red line: fitting functions according to Eq.(A46) and Eq.(A55); **c**: Illumination I: Inverse of the relaxation time $1/\tau^{\mathrm{I}}$ (disks) versus light intensity I_1 at $\lambda_1 = 488$ nm, **d**: Illumination II: Inverse of the relaxation time $1/\tau^{\mathrm{II}}$ (disks) versus light intensity I_2 at $\lambda_2 = 405$ nm; **e**: Magnification of **c** at low light intensity. Solid line: linear fitting function yielding the photoswitching cross section Σ_1, **f**: Magnification of **d** at low light intensity. Solid line: linear fitting function yielding the photoswitching cross section Σ_2.

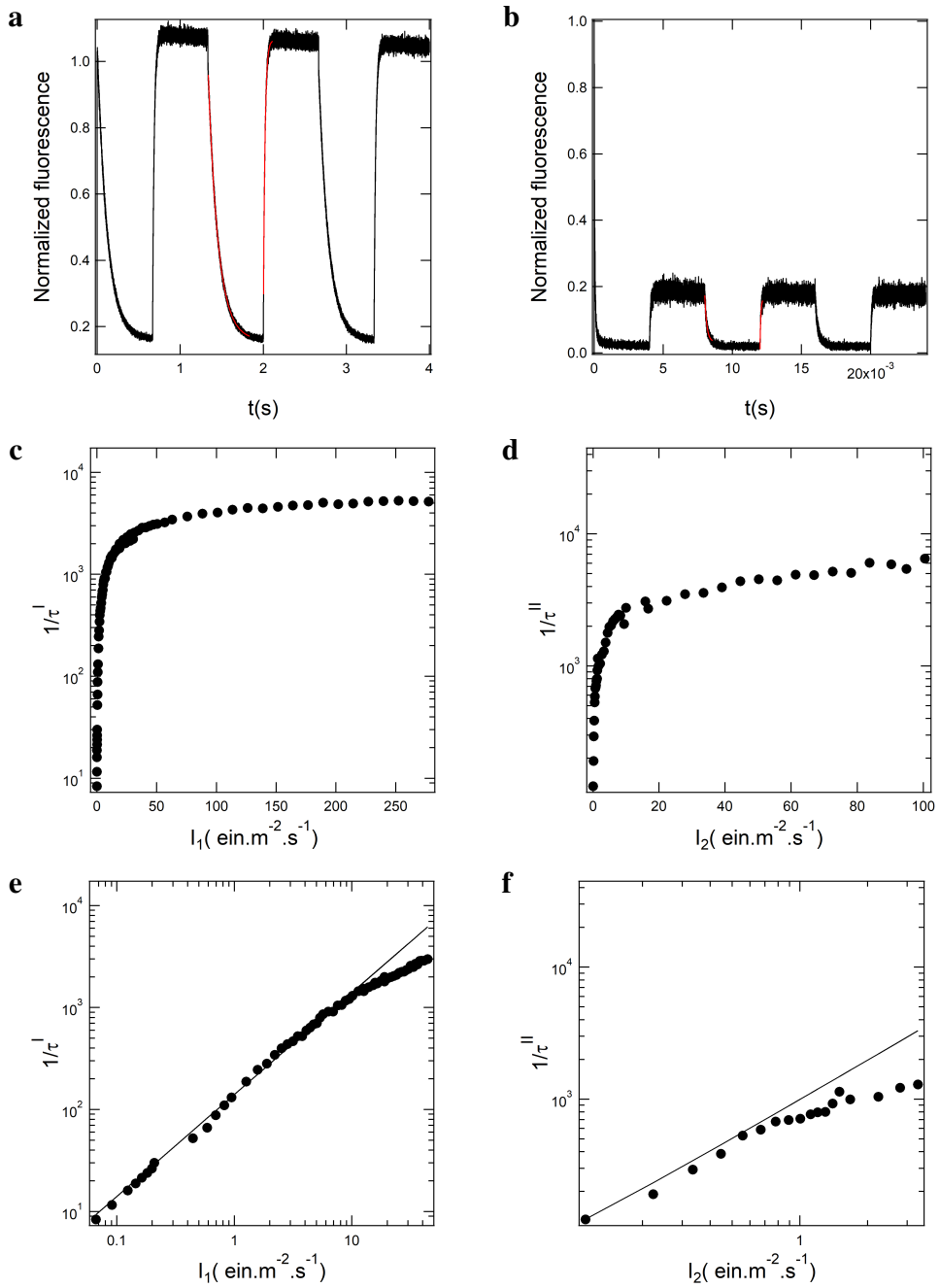

Figure A34: Kinetic analysis of **21** photoswitching at 20 μM in pH 7.4 PBS (50 mM sodium phosphate, 150 mM NaCl); T = 298 K. **a**, **b**: Evolution of fluorescence intensity upon continuous illumination of intensity I_1 at $\lambda_1 = 488$ nm and square-wave illumination of intensity I_2 at $\lambda_2 = 405$ nm (**a**: $I_1 = 0.05$ ein.m^{-2}.s^{-1}, $I_2 = 0.1$ ein.m^{-2}.s^{-1}; **b**: $I_1 = 200$ ein.m^{-2}.s^{-1}, $I_2 = 3$ ein.m^{-2}.s^{-1}). Black line: experimental data; red line: fitting functions according to Eq.(A46) and Eq.(A55); **c**: Illumination I: Inverse of the relaxation time $1/\tau^{\mathrm{I}}$ (disks) versus light intensity I_1 at $\lambda_1 = 488$ nm, **d**: Illumination II: Inverse of the relaxation time $1/\tau^{\mathrm{II}}$ (disks) versus light intensity I_2 at $\lambda_2 = 405$ nm; **e**: Magnification of **c** at low light intensity. Solid line: linear fitting function yielding the photoswitching cross section Σ_1, **f**: Magnification of **d** at low light intensity. Solid line: linear fitting function yielding the photoswitching cross section Σ_2.

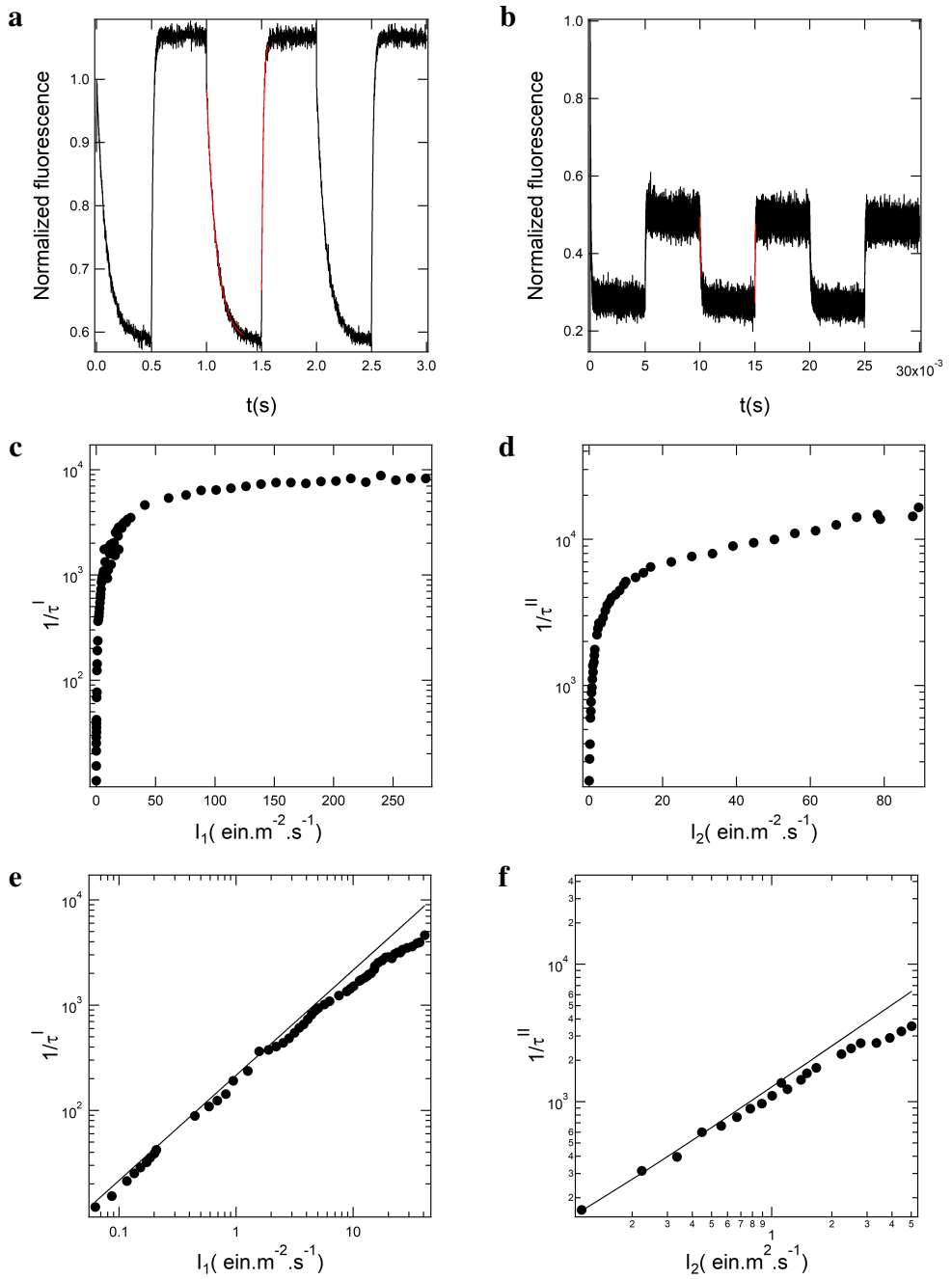

Figure A35: Kinetic analysis of **22** photoswitching at 20 μM in pH 7.4 PBS (50 mM sodium phosphate, 150 mM NaCl); T = 298 K. **a**, **b**: Evolution of fluorescence intensity upon continuous illumination of intensity I_1 at $\lambda_1 = 488$ nm and square-wave illumination of intensity I_2 at $\lambda_2 = 405$ nm (**a**: $I_1 = 0.05$ ein.m^{-2}.s^{-1}, $I_2 = 0.1$ ein.m^{-2}.s^{-1}; **b**: $I_1 = 200$ ein.m^{-2}.s^{-1}, $I_2 = 3$ ein.m^{-2}.s^{-1}). Black line: experimental data; red line: fitting functions according to Eq.(A46) and Eq.(A55); **c**: Illumination I: Inverse of the relaxation time $1/\tau^{\mathrm{I}}$ (disks) versus light intensity I_1 at $\lambda_1 = 488$ nm, **d**: Illumination II: Inverse of the relaxation time $1/\tau^{\mathrm{II}}$ (disks) versus light intensity I_2 at $\lambda_2 = 405$ nm; **e**: Magnification of **c** at low light intensity. Solid line: linear fitting function yielding the photoswitching cross section Σ_1, **f**: Magnification of **d** at low light intensity. Solid line: linear fitting function yielding the photoswitching cross section Σ_2.

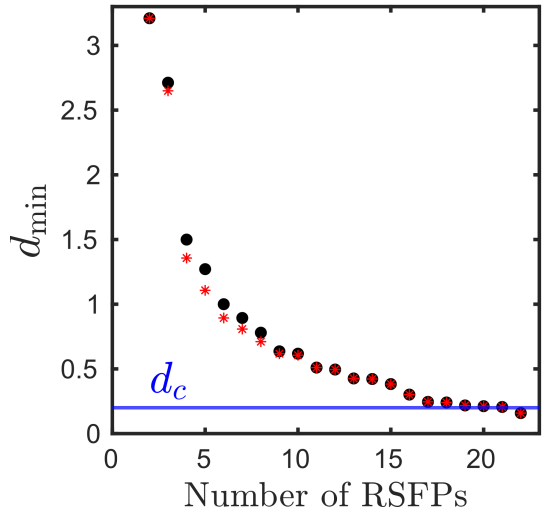

Figure A36: *The LIGHTNING discriminatory power.* Minimum distance between pairs for optimized subsets of RSFPs versus cardinal m of the subsets. Deducing the threshold d_c from the experimental uncertainty on the determination of the characteristic times, the condition $d_{\min} \geq d_c$ fixes the overall number of discriminatable representatives within a RSFP set (here 20 among the 22 RSFPs **1**–**22**).

A3 Supplementary Tables

A3.1 Photophysical properties of the RSFPs

Table A1: *Photophysical properties of the 22 investigated RSFPs as measured in this study.* λ_{max} and $\varepsilon(\lambda_{max})$ are the wavelength of maximal absorption and the molar absorption coefficient at λ_{max}, and λ_{em} and Φ_F are the wavelength of maximal emission and quantum yield of fluorescence. Solvent: pH=7.4 PBS (50 mM PBS, 150 mM NaCl).

RSFP	λ_{max} (nm)	$\varepsilon(\lambda_{max})$ ($M^{-1}.cm^{-1}$)	λ_{em} (nm)	Φ_F
1	503	80000	514	0.8
2	488	75000	512	0.2
3	487	55000	514	0.4
4	488	20000	513	–
5	505	40000	514	–
6	482	45000	514	0.4
7	496	35000	515	0.5
8	501	60000	514	0.7
9	499	95000	514	0.7
10	499	65000	514	0.7
11	500	85000	514	0.6
12	500	60000	513	0.6
13	503	105000	514	0.7
14	500	80000	514	0.6
15	486	50000	515	0.5
16	484	60000	515	0.2
17	483	50000	514	0.4
18	500	63000	515	0.5
19	479	55000	513	0.2
20	483	60000	515	0.3
21	484	50000	514	0.2
22	482	65000	515	0.2

A3.2 Photochemical properties of the RSFPs

Table A2: *Results of the preliminary illumination experiments to evidence fast reversible fluorescence photoswitching vs slow light-driven fluorescence extinction for the 22 investigated RSFPs.* $\Sigma_{j,fast}$ and $\Sigma_{j,slow}$ designate the cross sections associated with a fast and slow fluorescence photoswitching, respectively, as extracted from τ^{i}_{fast} and τ^{i}_{slow} obtained using Eq.(A5) as a fitting function to the fluorescence decays (the exponent $i = \mathrm{I}, \mathrm{II}$ refers to the two illuminations I and II) (see Eq.(A49) for I and Eq.(A58) for II). Solvent: pH=7.4 PBS (50 mM PBS, 150 mM NaCl).

RSFP	$\Sigma_{1,fast}$ (m^2/mol)	$\Sigma_{1,slow}$ (m^2/mol)	$\frac{\Sigma_{1,fast}}{\Sigma_{1,slow}}$	$\Sigma_{2,fast}$ (m^2/mol)	$\Sigma_{2,slow}$ (m^2/mol)	$\frac{\Sigma_{2,fast}}{\Sigma_{2,slow}}$
1	4.5 ± 0.7	6.10^{-4}	$(8.3 \pm 0.4)\times10^{3}$	315±10	$(6.3 \pm 0.1)\times10^{-4}$	$(2.2 \pm 0.4)\times10^{4}$
2	199 ± 10	7.10^{-3}	$(3.6 \pm 0.2)\times10^{4}$	431±20	$(7.3 \pm 0.2)\times10^{-3}$	$(7.1 \pm 0.2)\times10^{4}$
3	27 ± 3	2.10^{-3}	$(2.4 \pm 0.3)\times10^{4}$	326±30	$(2.2 \pm 0.1)\times10^{-3}$	$(1.4 \pm 0.3)\times10^{4}$
4	65 ± 2	6.10^{-3}	$(1.2 \pm 0.1)\times10^{4}$	240±15	$(7.6 \pm 0.1)\times10^{-3}$	$(1.5 \pm 0.1)\times10^{3}$
5	31 ± 3	5.10^{-4}	$(5.7 \pm 0.4)\times10^{4}$	75±8	$(6.4 \pm 0.3)\times10^{-4}$	$(2.4 \pm 0.2)\times10^{3}$
6	125 ± 12	9.10^{-4}	$(13.4 \pm 0.9)\times10^{4}$	700±20	$(1.5 \pm 0.1)\times10^{-3}$	$(3.2 \pm 0.1)\times10^{4}$
7	40 ± 5	3.10^{-3}	$(1.5 \pm 0.4)\times10^{4}$	680±30	$(3.4 \pm 0.2)\times10^{-3}$	$(5.3 \pm 0.1)\times10^{3}$
8	30 ± 8	4.10^{-4}	$(7.3 \pm 0.4)\times10^{4}$	560±20	$(4.2 \pm 0.3)\times10^{-4}$	$(1.2 \pm 0.5)\times10^{4}$
9	1.5 ± 0.3	2.10^{-4}	$(1.3 \pm 0.1)\times10^{4}$	490±30	$(2.2 \pm 0.4)\times10^{-4}$	$(1.8 \pm 0.7)\times10^{4}$
10	21 ± 2	2.10^{-4}	$(9.3 \pm 0.1)\times10^{4}$	425 ± 10	$(2.5 \pm 0.2)\times10^{-4}$	$(1.1 \pm 0.6)\times10^{4}$
11	20 ± 3	2.10^{-4}	$(12.6 \pm 0.8)\times10^{4}$	493±15	$(1.3 \pm 0.1)\times10^{-4}$	$(5.4 \pm 0.2)\times10^{4}$
12	45 ± 7	2.10^{-3}	$(2.2 \pm 0.4)\times10^{4}$	760±40	$(2.3 \pm 0.1)\times10^{-3}$	$(1.5 \pm 0.7)\times10^{4}$
13	7.3 ± 0.1	2.10^{-4}	$(3.1 \pm 0.2)\times10^{4}$	320±10	$(2.7 \pm 0.1)\times10^{-4}$	$(2.8 \pm 0.6)\times10^{4}$
14	5.7 ± 0.1	2.10^{-4}	$(2.8 \pm 0.3)\times10^{4}$	330±20	$(2.4 \pm 0.1)\times10^{-4}$	$(4.1 \pm 0.4)\times10^{4}$
15	97 ± 12	2.10^{-3}	$(4.3 \pm 0.2)\times10^{4}$	300±30	$(3.5 \pm 0.3)\times10^{-3}$	$(9.4 \pm 0.5)\times10^{4}$
16	110 ± 20	3.10^{-3}	$(4.6 \pm 0.3)\times10^{4}$	415±25	$(2.7 \pm 0.1)\times10^{-3}$	$(1.8 \pm 0.1)\times10^{4}$
17	200 ± 15	1.10^{-4}	$(10.1 \pm 0.8)\times10^{4}$	330±30	$(2.3 \pm 0.4)\times10^{-4}$	$(11.3 \pm 0.4)\times10^{4}$
18	5.4 ± 0.2	1.10^{-3}	$(4.2 \pm 0.4)\times10^{4}$	450±40	$(1.2 \pm 0.1)\times10^{-4}$	$(4.5 \pm 0.3)\times10^{4}$
19	190 ± 10	3.10^{-3}	$(7.2 \pm 0.6)\times10^{4}$	1400±250	$(2.6 \pm 0.2)\times10^{-3}$	$(1.4 \pm 0.2)\times10^{4}$
20	160 ± 21	3.10^{-3}	$(5.3 \pm 0.2)\times10^{4}$	920±20	$(3.7 \pm 0.1)\times10^{-3}$	$(7.6 \pm 0.3)\times10^{3}$
21	150 ± 8	7.10^{-3}	$(2.1 \pm 0.4)\times10^{4}$	1010±40	$(8.2 \pm 0.4)\times10^{-3}$	$(1.4 \pm 0.1)\times10^{3}$
22	200 ± 17	5.10^{-3}	$(4.1 \pm 0.3)\times10^{4}$	1250±30	$(6.3 \pm 0.2)\times10^{-3}$	$(1.4 \pm 0.2)\times10^{4}$

Table A3: *Kinetic signatures of the 22 investigated RSFPs in the investigated time windows.* Σ_1 and Σ_2 are the cross sections for reversible fluorescence photoswitching at $\lambda_1 = 488$ and $\lambda_2 = 405$ nm, respectively. k_{21}^{Δ} is the rate constant for thermally-driven back isomerization of the photoswitched state. τ_{high}^{I} and $\tau_{high}^{\mathrm{II}}$ are the characteristic times obtained at the highest light intensities accessible with the photoswitchometer in the regime of high light intensity (illumination I: $I_1 = 200$ ein.m^{-2}.s^{-1}; illumination II: $I_1 = 200$ ein.m^{-2}.s^{-1} and $I_2 = 90$ ein.m^{-2}.s^{-1}). I_1^c and I_2^c are the cutoff light intensities at λ_1 and λ_2 at which the inverse of the characteristic times $1/\tau^{\mathrm{I}}$ and $1/\tau^{\mathrm{II}}$ depart from the two-states model predictions by 33% and 20%, respectively. Solvent: pH=7.4 PBS (50 mM PBS, 150 mM NaCl).

RSFP	Σ_1 (m^2/mol)	Σ_2 (m^2/mol)	$10^4 \times k_{21}^{\Delta}$ (s^{-1})	τ_{high}^{I} (s)	$\tau_{high}^{\mathrm{II}}$ (s)	I_1^c (ein/m^2.s)	I_2^c (ein/m^2.s)
1	5.1±0.5	350±20	5 ± 1	(4.52±0.09)×10^{-3}	(1.85±0.04)×10^{-4}	36 ± 2	4.3 ± 0.1
2	198±8	415±30	200 ± 50	(3.34±0.01)×10^{-4}	(7.73±0.02)×10^{-5}	8.2 ± 0.5	9.4 ± 0.2
3	30±5	350±18	1300 ± 300	(4.84±0.08)×10^{-3}	(1.25±0.03)×10^{-4}	4.6 ± 0.1	3.47 ± 0.05
4	70±10	230±22	0 ± 6	(2.56±0.07)×10^{-3}	(1.13±0.02)×10^{-2}	6.3 ± 0.5	1.23 ± 0.01
5	36±2	70±10	0 ± 8	(3.57±0.08)×10^{-3}	(9.25±0.02)×10^{-3}	35 ± 2	0.8 ± 0.1
6	112±9	670±45	6 ± 2	(1.17±0.05)×10^{-4}	(2.14±0.02)×10^{-4}	83 ± 15	3.1 ± 0.8
7	32±3	650±50	20 ± 10	(5.44±0.02)×10^{-4}	(6.74±0.03)×10^{-5}	36 ± 4	8.14 ± 0.02
8	33±2	515±30	6 ± 1	(4.23±0.03)×10^{-3}	(9.5±0.1)×10^{-5}	4.1 ± 0.2	4.2 ± 0.5
9	1.2 ±0.1	465±25	0.8 ± 0.2	(5.95±0.02)×10^{-3}	(1.25±0.02)×10^{-4}	2.2 ± 0.5	0.9 ± 0.1
10	25±4	420±30	10 ± 10	(6.8±0.1)×10^{-4}	(7.75±0.03)×10^{-5}	35 ± 6	0.27 ± 0.01
11	21±1	440±21	20 ± 10	(3.82±0.07)×10^{-3}	(1.12±0.01)×10^{-4}	6.3 ± 0.2	10 ± 4
12	50±6	730±43	4 ± 2	(3.1±0.2)×10^{-4}	(6.23±0.02)×10^{-5}	40 ± 5	3.12 ± 0.02
13	7.4±0.2	300±12	3 ± 1	(5.63±0.02)×10^{-3}	(1.75±0.03)×10^{-4}	35 ± 6	1.18 ± 0.03
14	6.1±0.3	300±31	20 ± 10	(2.92±0.05)×10^{-3}	(1.84±0.02)×10^{-4}	20 ± 3	8.42 ± 0.05
15	115±6	310±28	20 ± 10	(3.14±0.02)×10^{-4}	(3.64±0.03)×10^{-4}	7.1 ± 0.3	0.45 ± 0.07
16	120±11	400±37	20 ± 10	(6.25±0.04)×10^{-4}	(9.83±0.02)×10^{-5}	6.3 ± 0.1	3.45 ± 0.08
17	212±6	320±10	30 ± 10	(4.26±0.03)×10^{-4}	(1.27±0.02)×10^{-4}	3.4 ± 0.1	2.15 ± 0.07
18	5.1±0.3	483±24	0 ± 3	(3.82±0.01)×10^{-3}	(3.82±0.06)×10^{-4}	41 ± 3	1.32 ± 0.04
19	212±8	1670±120	–†	(1.21±0.06)×10^{-4}	(3.15±0.01)×10^{-5}	25 ± 5	1.15 ± 0.02
20	170±10	900±85	–†	(1.34±0.07)×10^{-4}	(1.35±0.04)×10^{-4}	5±2	0.83 ± 0.01
21	144±35	930±66	1.1 ± 0.3	(2.15±0.03)×10^{-4}	(1.73±0.01)×10^{-4}	2.5 ± 0.1	3.4 ± 0.2
22	212±10	1260±100	–†	(1.36±0.08)×10^{-4}	(6.17±0.02)×10^{-5}	1.7 ± 0.2	2.5 ± 0.4

† Too slow to be reliably measured.

A4 Fluorescence evolution of an RSF

A4.1 General expressions of the concentrations

We consider an RSF engaged in a photocycle involving n_s states $\mathrm{C_i}$ and first-order reactions

$$\mathrm{C_i} \underset{k_{ji}}{\overset{k_{ij}}{\rightleftharpoons}} \mathrm{C_j} \tag{A11}$$

where $i = 1, ..., n_s$, $j = 1, ..., n_s$, and $i \neq j$. The rate constants k_{ij} are associated with thermal or photochemical steps. The dynamics of the system is governed by the system of equations

$$\frac{\mathrm{d}C_1}{\mathrm{d}t} = -\left(k_{12} + k_{13} + ... + k_{1n_s}\right) C_1 + k_{21}C_2 + k_{31}C_3 + ... + k_{n_s1}C_n \tag{A12}$$

$$\frac{\mathrm{d}C_2}{\mathrm{d}t} = k_{12}C_1 - \left(k_{21} + k_{23} + ... + k_{2n_s}\right) C_2 + k_{32}C_3 + ... + k_{n_s2}C_n \tag{A13}$$

$$... \tag{A14}$$

$$\frac{\mathrm{d}C_n}{\mathrm{d}t} = k_{1n_s}C_1 + k_{2n_s}C_2 + k_{3n_s}C_3 + ... - \left(k_{n_s1} + k_{n_s2} + ... + k_{n_s(n_s-1)}\right) C_n \tag{A15}$$

which yields the conservation relation $\Sigma_{i=1}^{n_s} C_i(t) = \Sigma_{i=1}^{n_s} C_i^0$ where C_i^0 are the initial concentrations.

The linear system given in Eqs.(A12–A15) can be written in matrix form

$$\frac{\mathrm{d}\mathbf{C}}{\mathrm{d}t} = \mathbf{K}\mathbf{C} \tag{A16}$$

with the vector $\mathbf{C}$ and the matrix $\mathbf{K}$

$$\mathbf{C} = \begin{pmatrix} C_1 \\ C_2 \\ . \\ . \\ C_n \end{pmatrix}, \tag{A17}$$

$$\mathbf{K} = \begin{pmatrix} -\left(k_{12} + k_{13} + ... + k_{1n_s}\right) & k_{21} & ... & k_{n_s1} \\ k_{12} & -\left(k_{21} + k_{23} + ... + k_{2n_s}\right) & ... & k_{n_s2} \\ . & . & ... & . \\ . & . & ... & . \\ . & . & ... & . \\ k_{1n_s} & k_{2n_s} & ... & -\left(k_{n_s1} + k_{n_s2} + ... + k_{n_s(n_s-1)}\right) \end{pmatrix} \tag{A18}$$

The matrix $\mathbf{K}$ has n_s eigenvalues, one of which is zero.[14] Considering the case where the eigenvalues are real, negative and denoted by $-1/\tau_i$, they are ordered according to $0 < \tau_1 < \tau_2 < ... < \tau_{n_s-1}$. The Gerschgorin's circle theorem has been used to show that the eigenvalues are bounded and obey[14]

$$0 \leq \frac{1}{\tau_i} \leq 2 \max_i(\Sigma_{j=1, j\neq i}^{n_s} k_{ij}). \tag{A19}$$

Eq.(A16) is straightforwardly solved in the eigenvector basis. By using the change-of-basis matrix and the initial conditions, we find that the concentrations C_i are sums of exponential terms involving the eigenvalues

$$C_i = \Sigma_{j=1}^{n_s-1} r_{ij} \exp\left(-\frac{t}{\tau_j}\right) + s_{\mathrm{i}}. \tag{A20}$$

where the preexponential factors r_{ij} and the constant s_{i} depend on the rate constants and the initial conditions.

A4.2 General expressions of the fluorescence signal

The RSF fluorescence signal $I_F(t)$ originates from summing the individual contributions of the n_s RSF states associated with brightness Q_i and concentrations C_i

$$I_F(t) = \Sigma_{i=1}^{n_s} Q_i I C_i = \Sigma_{j=1}^{n_s-1} U_j \exp\left(-\frac{t}{\tau_j}\right) + W \tag{A21}$$

with $U_j = \Sigma_{i=1}^{n_s} Q_i I r_{ij}$ and $W = \Sigma_{i=1}^{n_s} Q_i I s_{\mathrm{i}}$ for a light excitation of intensity I. As shown in Eq.(A21), the RSF fluorescence signal exhibits a multiexponential time dependence.

A5 Spectrum of the relaxation times of RSF fluorescence evolution

A5.1 Generating a spectrum

A spectrum of relaxation times has been used to characterize the kinetics of RSFPs. The spectrum is built by correlating the fluorescence evolution $I_F(t)$ with a function $f_l(t)$ where the parameter l is the decimal logarithm of a relaxation time[15–22]

$$S(l) = \frac{\int_0^{\beta 10^l} \left(I_F(t) - \langle I_F(t)\rangle\right)\left(f_l(t) - \langle f_l(t)\rangle\right) dt}{\int_0^{\beta 10^l} \left(e^{-\frac{t}{10^l}} - \langle e^{-\frac{t}{10^l}}\rangle\right)\left(f_l(t) - \langle f_l(t)\rangle\right) dt} \tag{A22}$$

The average $\langle\rangle$ represents the integration between 0 and $\beta 10^l$. The value of the parameter β depends on the function $f_l(t)$. The denominator is a normalization condition.

When the fluorescence intensity is a monoexponential function associated with a relaxation time τ_F

$$I_F(t) = \left(I_F^0 - I_F^\infty\right)\exp\left(-t/\tau_F\right) + I_F^\infty \tag{A23}$$

the value of β is chosen to ensure that the spectrum $S(l)$ possesses an extremum for $l_F = \log(\tau_F)$ as shown in Fig. A37. Due to the chosen normalization, the amplitude of the extremum $S(l_F)$ is equal

to the preexponential factor $I_F^0 - I_F^\infty$. The sign of the preexponential factor determines the nature of the extremum, a positive factor leading to a maximum and a negative factor leading to a minimum of $S(l)$. When the fluorescence evolution $I_F(t)$ is not correctly described by a monoexponential function but behaves as a sum of $n_s - 1$ exponential terms, the spectrum of the relaxation times displays between one and $n_s - 1$ extrema.

The spectra of relaxation times can be computed for different choices of the function $f_l(t)$. The fluorescence evolution $I_F(t)$ being a linear combination of exponential functions (see section A4), the choice $f_l(t) = e^{-\frac{t}{10^l}}$ is intuitive. The correlation with an exponential is known to produce spectra with broad peaks i.e. a moderate time resolution but little sensitivity to the signal-to-noise ratio of the fluorescence signal.[21,22] In order to characterize the kinetics of fluorescence photoswitching of an RSF under a given illumination by a single quantity, we chose to compute the spectrum using the exponential correlator and look for the absolute extremum of the spectrum. For the exponential correlator we find $\beta = 3.25$.

The analytical expression of the spectrum $S(l)$ for the monoexponential fluorescence evolution $I_F(t)$ given in Eq.(A23) is given by

$$S(l) = \left(I_F^0 - I_F^\infty\right) \frac{\exp\left(-3.25 \times 10^{l-l_F}\right)\left(1.38 + 1.20 \times 10^{l-l_F}\right) - 1.38 + 3.28 \times 10^{l-l_F}}{10^{l-l_F}\left(1 + 10^{l-l_F}\right)} \quad \text{(A24)}$$

As shown in Fig. A37a,b, the peak of the spectrum is symmetrical with respect to the extremum and its width at half height equals $\Delta l = 1.4$. The logarithm of the relaxation time l has to differ by more than 1.5 from l_F for the corresponding spectrum value $S(l)$ to be smaller than 10% of the amplitude $S(l_F)$ of the extremum.

The generalization to a linear combination of exponential functions is straightforward.

In the case where the fluorescence intensity $I_F(t)$ is a sum of two exponential terms with identical prefactors p and different characteristic times $\tau_F < \tau_{F'}$, the spectrum has either one or two extrema. The spectrum shows one or two maxima if the prefactors are positive and one or two minima if the prefactors are negative. If $l_{F'} - l_F < 1.1$, the spectrum has a single extremum for l between l_F and $l_{F'}$. In this case, the amplitude of the extremum is between $1.3p$ and $2p$. On the contrary, if $l_{F'} - l_F > 1.1$, the spectrum has two extrema. If $l_{F'} - l_F > 1.7$, the abscissa of the extrema differ from l_F and $l_{F'}$ by less than 5%. Moreover, the values of the spectrum associated with the extrema are less than 7% larger than the prefactor p.

For a fluorescence intensity $I_F(t)$ equal to the difference of two exponential terms with identical prefactors and characteristic times $\tau_F < \tau_{F'}$, the spectrum has always one maximum and one minimum. If $l_{F'} - l_F > 1.7$, then the abscissa of the extrema differ from l_F and $l_{F'}$ by less than 4%. In addition, the amplitudes of the extrema are less than 6% smaller than the prefactor.

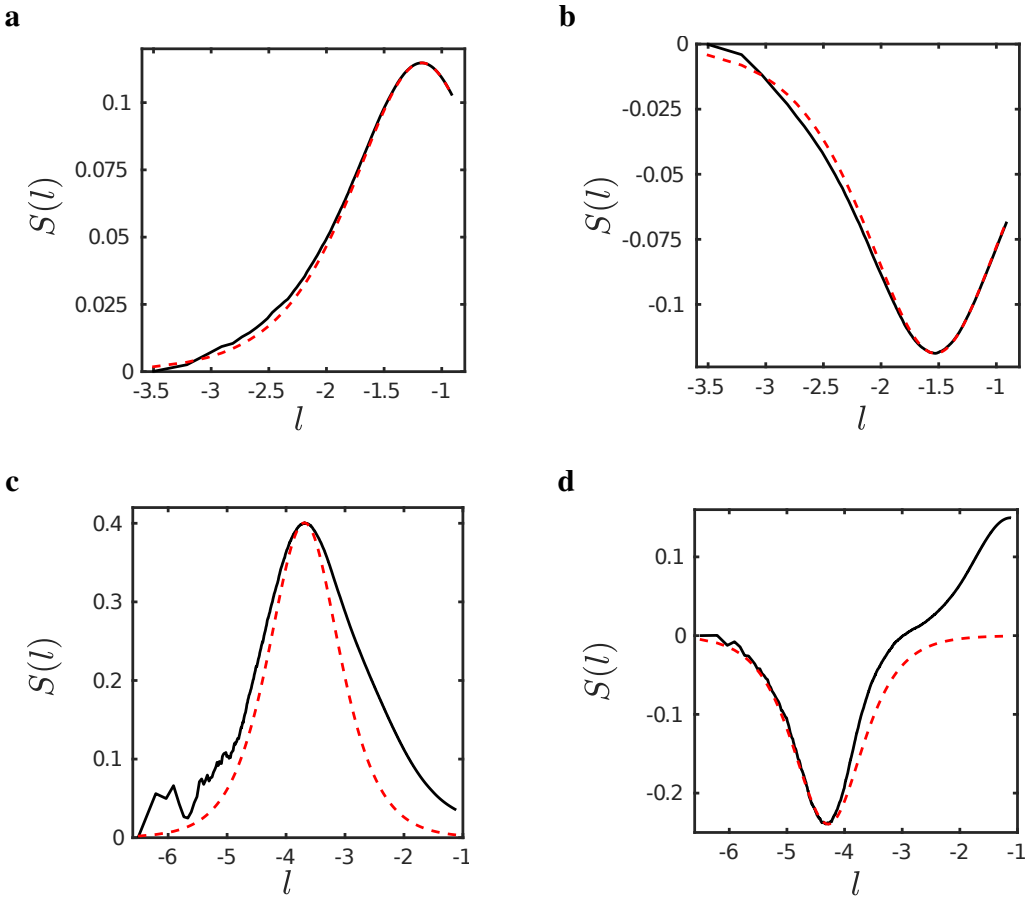

Figure A37: Spectra of the relaxation times associated with the RSFP **2**. The solid lines are obtained by computing $S(l)$ for the experimental fluorescence evolution $I_F(t)$. The dashed red lines are obtained when replacing $I_F(t)$ by a monoexponential function with the relaxation time associated with the absolute extremum of the spectrum built from the experimental fluorescence evolution. **a**: Illumination I with $I_{1,low} = 0.23$ Ein.m^{-2}.s^{-1} at the wavelength $\lambda_1 = 488$ nm; **b**: Illumination II with $I_1 = 0.07$ Ein.m^{-2}.s^{-1} at the wavelength $\lambda_1 = 488$ nm and $I_{2,low} = 0.10$ Ein.m^{-2}.s^{-1} at the wavelength $\lambda_2 = 405$ nm; **c**: Illumination I with $I_{1,high} = 128.8$ Ein.m^{-2}.s^{-1} at the wavelength $\lambda_1 = 488$ nm; **d**: Illumination II with $I_1 = 0.15$ Ein.m^{-2}.s^{-1} at the wavelength $\lambda_1 = 488$ nm and $I_{2,high} = 106$ Ein.m^{-2}.s^{-1} at the wavelength $\lambda_2 = 405$ nm.

In the general case of non identical prefactors the position of the absolute extremum is close to the characteristic time of the exponential associated with the largest prefactor.

A5.2 Application to RSFPs

Figure A37 displays the spectra of the relaxation times obtained for the RSFP **2** in four illuminations. The spectrum directly deduced from Eq.(A22) for the experimental fluorescence evolution $I_F(t)$ is referred to as the experimental spectrum and the spectrum obtained when replacing $I_F(t)$ by a monoexponential function with a relaxation time matching the extremum observed in the experimental spectrum is called the predicted spectrum.

For the low light intensities used to obtain Figs. A37a and A37b, the photochemical reactions are rate-limiting steps and an excellent match between the experimental and predicted spectra is observed. This agreement proves that, in these low light intensity regimes, the characteristic times deduced by reducing $I_F(t)$ to a monoexponential function (see section A6) are properly evaluated. Hence, for sufficiently low light intensities, a single characteristic time or equivalently a two-state model is sufficient to adequately describe the kinetics of fluorescence photoswitching.

For the high light intensities used to obtain Figs. A37c and A37d, the reaction rate depends on some thermal steps. The asymmetrical broadening of the experimental spectrum in Fig. A37c accounts for at least a biexponential behavior with close relaxation times but different preexponential factors. Nevertheless the value of the characteristic time deduced from a monoexponential reduced function satisfactorily coincides with the position of the maximum of the experimental spectrum. The experimental spectrum in Fig. A37d exhibits a minimum, an inflection point, and a maximum at the largest τ values. However the good agreement between the minima of the experimental and predicted spectra still validates the use of a monoexponential reduced function to $I_F(t)$.

More generally, only one extremum was observed for all studied RSFPs for illumination I: a minimum for **4** and **5** and a maximum for the other 20 RSFPs, as expected from their respective positive and negative photochromism. In contrast, for illumination II, we characterized the RSFPs by the minimum of the spectrum (maximum for **4** and **5**, resp.) observed at all light intensities and ignored the maximum (minimum for **4** and **5**, resp.) which could be observed at the highest light intensities. As mentioned above, the perturbation of the extremum by a second relaxation time of the fluorescence photoswitching remains small when the two relaxation times are sufficiently different or sufficiently close, or when the preexponential factor associated with the second relaxation time is sufficiently small. One of these conditions is always met for all considered RSFPs.

In conclusion to this section, the position of the extremum obtained by directly computing the spectrum of relaxation times from the experimental fluorescence evolution $I_F(t)$ is close to the

position of the extremum of the spectrum obtained by reducing the data to a monoexponential function. Excellent match has always been observed in the low intensity regime. Less than a factor of 2 between the characteristic times extracted from the spectrum and the monoexponential reduction of the fluorescence evolution has been obtained in the high intensity regime, which is satisfactory for the purpose of discrimination. The two data processing methods lead to similar behaviors of the inverse of the characteristic time versus the light intensity. Linear increase at low light intensity and saturation at high light intensity are observed in both cases as shown in Figs.A38 and A39. The agreement between the two data processing methods validates the monoexponential reduction of fluorescence evolution.

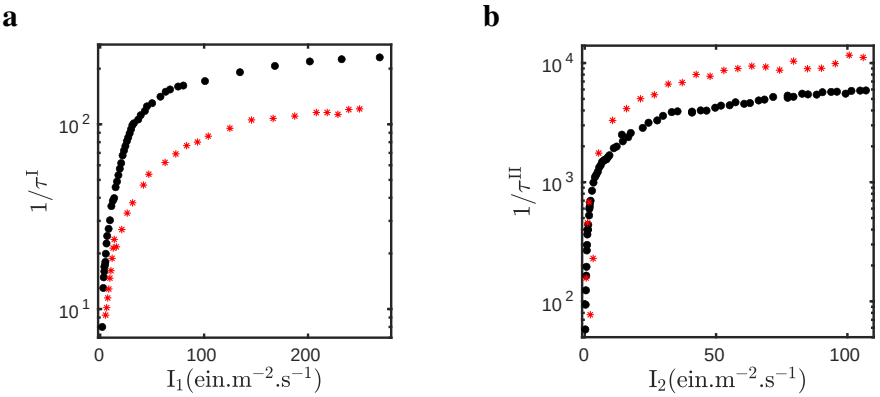

Figure A38: Kinetic characterization of RSFP **1** at 20 μM in pH=7.4 PBS (50 mM sodium phosphate, 150 mM NaCl); T = 298 K. **a**: Illumination I: Inverse of the relaxation time $1/\tau^{\mathrm{I}}$ versus light intensity I_1 at $\lambda_1 = 488$ nm, **b**: Illumination II: Inverse of the relaxation time $1/\tau^{\mathrm{II}}$ versus light intensity I_2 at $\lambda_2 = 405$ nm. The relaxation times have been extracted using either the extremum of the spectrum of characteristic times (red star) or monoexponential fitting (black disk).

A6 Monoexponential reduction of RSF fluorescence evolution

In this section, we propose a simple protocol for processing RSF kinetics and apply the results to the fluorescence evolution obtained for the illuminations I and II.

A6.1 A kinetic filter

Choosing a time window around a targeted time scale plays the role of a kinetic filter for fluorescence evolution. According to the concentration evolution of RSFs engaged in first-order reactions between n_s states, the fluorescence evolution is a linear combination of exponential terms (see Eq.(A21)). Focusing on the dynamics occurring at a time scale amounts to selecting the small

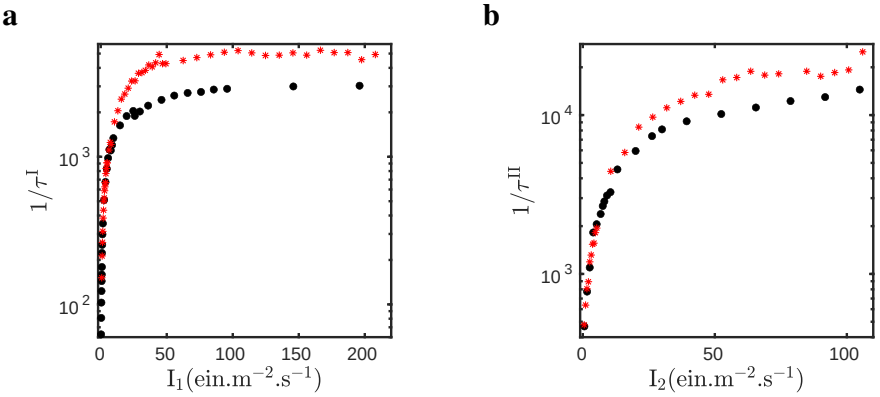

Figure A39: Kinetic characterization of RSFP **2** at 20 μM in pH=7.4 PBS (50 mM sodium phosphate, 150 mM NaCl); T = 298 K. **a**: Illumination I: Inverse of the relaxation time $1/\tau^{\mathrm{I}}$ versus light intensity I_1 at $\lambda_1 = 488$ nm, **b**: Illumination II: Inverse of the relaxation time $1/\tau^{\mathrm{II}}$ versus light intensity I_2 at $\lambda_2 = 405$ nm. The relaxation times have been extracted using either the extremum of the spectrum of characteristic times (red star) or monoexponential fitting (black disk).

number of exponential terms associated with relaxation times close to this time scale. Two situations are mainly encountered:

- A single relaxation time τ_a is close to the targeted time scale. For a time t close to τ_a, the exponential terms associated with the m first relaxation times obeying $\tau_i < \tau_a$ are negligible with respect to $\exp(-t/\tau_a)$. At the same time scale, the other $n_s - m - 2$ exponential terms can be considered constant. Consequently the fluorescence evolution is close to

$$I_F = U_a \exp\left(-\frac{t}{\tau_a}\right) + W_a \tag{A25}$$

  with $W_a = W + \Sigma_{i=n_s-m-2}^{n_s} U_i$ where W and U_i are defined under Eq.(A21). In this case, the effect of the kinetic filter legitimates using the following monoexponential reduction

$$I_F \simeq \left(I_F^0 - I_F^\infty\right) \exp\left(-\frac{t}{\tau}\right) + I_F^\infty \tag{A26}$$

- If two relaxation times $\tau_a < \tau_b$ are close to the targeted time scale, the observed fluorescence evolution is biexponential

$$I_F = U_a \exp\left(-\frac{t}{\tau_a}\right) + U_b \exp\left(-\frac{t}{\tau_b}\right) + W_b \tag{A27}$$

  with $W_b = W + \Sigma_{i=n_s-m-3}^{n_s} U_i$. The observed behavior depends on the sign of the product $U_a U_b$ of the preexponential factors:

  – If $U_a U_b > 0$, fluorescence evolution is monotonous. We then assume that Eq.(A27) can be approximated by the monoexponential function given in Eq.(A26). The initial

$(t = 0)$ and final $(t \to \infty)$ conditions on I_F lead to

$$I_F^0 \simeq U_a + U_b + W_b \tag{A28}$$

$$I_F^\infty \simeq W_b \tag{A29}$$

Substituting Eqs.(A28,A29) into Eq.(A26), we perform a first-order expansion of the exponential terms of Eq.(A27) around $t = 0$ and obtain

$$\tau \simeq \frac{\tau_a \tau_b (U_a + U_b)}{U_a \tau_b + U_b \tau_a} \tag{A30}$$

Hence the fluorescence evolution can be approximated by a monoexponential function with a characteristic time between τ_a and τ_b.

– If $U_a U_b < 0$, fluorescence evolution displays an extremum and the relaxation time τ_a is associated with the first part of the evolution before the extremum whereas τ_b is associated with the second part of the evolution. We consider the case where the extremum is a maximum, i.e.

$$0 < \tau_a < \tau_b \tag{A31}$$

$$0 < U_b <\mid U_a \mid \tag{A32}$$

$$U_a + U_b + W_b > 0 \tag{A33}$$

The extension to the case of a minimum is straightforward. According to Eq.(A27), the maximum of the fluorescence evolution

$$I_F^{\max} = U_a \exp\left(-\frac{t^{\max}}{\tau_a}\right) + U_b \exp\left(-\frac{t^{\max}}{\tau_b}\right) + W_b \tag{A34}$$

is reached at time

$$t^{\max} = \frac{\tau_a \tau_b}{\tau_b - \tau_a} \ln\left(\frac{\mid U_a \mid \tau_b}{U_b \tau_a}\right) \tag{A35}$$

Substituting Eq.(A35) into Eq.(A34), we perform a first-order expansion of $I_F^{\max}$ with respect to the parameter τ_a/τ_b and obtain

$$I_F^{\max} \simeq U_b \left[1 - \frac{\tau_a}{\tau_b} \ln\left(\frac{\mid U_a \mid \tau_b}{U_b \tau_a}\right)\right] + W_b \tag{A36}$$

We approximate the first part of the evolution before the maximum by a monoexponential function of characteristic time τ reaching $I_F^{\max}$ for $t \to \infty$

$$I_F \simeq \left(I_F^0 - I_F^{\max}\right) \exp\left(-\frac{t}{\tau}\right) + I_F^{\max} \tag{A37}$$

in which I_F^0 is given in Eq.(A28) and $I_F^{\max}$ in Eq.(A34). We perform a first-order expansion of the exponential terms around $t = 0$ in the biexponential expression of I_F given in Eq.(A27) and in the monoexponential reduced function given in Eq.(A37) and obtain the following relation between the fitting parameter τ and the relaxation times τ_a and τ_b

$$\tau \simeq \tau_a \left[1 + \frac{U_b \tau_a}{U_a \tau_b} \ln \left(\frac{\mid U_a \mid \tau_b}{U_b \tau_a} \right) \right] \tag{A38}$$

The conditions given in Eqs.(A31,A32) ensure that $\tau < \tau_a$. The correction to τ_a is small provided that $\tau_a \ll \tau_b$ and $U_b \ll \mid U_a \mid$. This result supports the choice of a monoexponential reduced function for the increasing part of the fluorescence evolution before the maximum.

This subsection gives the conditions for which it is legitimate to use a monoexponential reduced function to the fluorescence evolution. It is essential to choose a time window in which the evolution is monotonous. The reduction procedure provides a characteristic time close to the relaxation times of the kinetics at the targeted time scale.

A6.2 Application to RSFPs

In the case of RSFPs, the previously studied cases have been encountered. For illuminations I and II and for sufficiently low light intensities the kinetics of RSFPs is well-described by a two-state model and monoexponential reduction to fluorescence evolution using Eq.(A26) is fully justified. The fluorescence data are processed over the entire acquisition window. For illumination I and high light intensities, the fluorescence evolution is described by a linear combination of at least two exponential functions with negative prefactors for RSFPs **4** and **5**, and positive prefactors for the 20 others. It can be approximated by the monoexponential reduced function given in Eq.(A26). The estimated characteristic time is between the smallest relaxation time and the largest one selected by the kinetic filter. This assessment is sufficiently accurate for the purpose of RSFPs discrimination. For illumination II and high light intensities, the fluorescence evolution displays a minimum for $t = t^{\max}$ for RSFPs **4** and **5**, and a maximum for the 20 others. Nevertheless a monoexponential reduced function can be used to account for the first part of the curve before the maximum provided that fluorescence evolution does not too strongly depart from a monotonous behavior. The processed time window is restricted to $[0, t^{\max}]$. Then the characteristic time deduced from the fitting protocol is close to the smallest relaxation time selected by the kinetic filter.

A7 Design of the measurement cell of the photoswitchometer

In this section, we first derive the expressions of the fluorescence evolution in a two-state system. Then we make precise geometrical constraints on the measurement cell of the photoswitchometer for which diffusion may be neglected.

We adopt the two-state exchange

$$\mathrm{C}_1 \underset{k_{21}^i}{\overset{k_{12}^i}{\rightleftharpoons}} \mathrm{C}_2 \tag{A39}$$

where the state C_1 is photochemically converted into the state C_2 at rate constant k_{12}^{i} from which it can relax back to the state C_1 at the rate constant k_{21}^{i} including photochemical and thermally-driven contributions. The exponent $i = \mathrm{I}, \mathrm{II}, \mathrm{III}$ refers to the illuminations I, II, and III. We further introduce $K_{12}^{\mathrm{i}} = k_{12}^{\mathrm{i}}/k_{21}^{\mathrm{i}}$.

A7.1 Fluorescence evolution in a homogeneous system

We assume that the system is homogeneous at any time of its evolution. The evolution of the concentrations C_1^{i} and C_2^{i} of the two species C_1 and C_2 for each illumination i is then given by

$$\frac{\mathrm{d}C_1^{\mathrm{i}}}{\mathrm{d}t} = -k_{12}^{\mathrm{i}} C_1^{\mathrm{i}} + k_{21}^{\mathrm{i}} C_2^{\mathrm{i}} \tag{A40}$$

with the conservation relation $C_1^{\mathrm{i}} + C_2^{\mathrm{i}} = C_{\mathrm{tot}}$, where C_{tot} is the total concentration.

A7.1.1 Illumination I

For illumination I, under light intensity I_1 at the wavelength λ_1, the initial condition is $C_1^{\mathrm{I}} = C_{\mathrm{tot}}$. The concentrations C_1^{I} and C_2^{I} obey

$$C_2^{\mathrm{I}} - C_2^{\mathrm{I},\infty} = C_1^{\mathrm{I},\infty} - C_1^{\mathrm{I}} = -C_2^{\mathrm{I},\infty} \exp\left(-\frac{t}{\tau^{\mathrm{I}}}\right) \tag{A41}$$

where

$$C_1^{\mathrm{I},\infty} = \frac{1}{1 + K_{12}^{\mathrm{I}}} C_{\mathrm{tot}} \tag{A42}$$

$$C_2^{\mathrm{I},\infty} = \frac{K_{12}^{\mathrm{I}}}{1 + K_{12}^{\mathrm{I}}} C_{\mathrm{tot}} \tag{A43}$$

are the steady concentrations reached at large time and

$$\tau^{\mathrm{I}} = \frac{1}{k_{12}^{\mathrm{I}} + k_{21}^{\mathrm{I}}} \tag{A44}$$

designates the relaxation time of the photochemical conversion of the two species C_1 and C_2. The fluorescence emission results from the individual contributions of the species C_1 and C_2. For the

sake of simplicity, we assume that only one species, supposed to be C_1, has a non-negligible brightness Q. The results can be straightforwardly extended to the general case. The fluorescence intensity can be written

$$I_F^{\mathrm{I}} = QC_1^{\mathrm{I}} I_1 \tag{A45}$$

Using Eqs.(A41-A43), we find

$$\frac{I_F^{\mathrm{I}}}{I_F^{\mathrm{I},0}} = 1 + \frac{QC_{\mathrm{tot}} I_1}{I_F^{\mathrm{I},0}} \frac{K_{12}^{\mathrm{I}}}{1 + K_{12}^{\mathrm{I}}} \left[\exp\left(-\frac{t}{\tau^{\mathrm{I}}} \right) - 1 \right] \tag{A46}$$

where $I_F^{\mathrm{I},0}$ is the initial fluorescence intensity.

In the case of RSFPs and at low light intensity I_1 the two-state model (A39) satisfactorily accounts for the observed fluorescence photoswitching. Denoting by $\sigma_{12,1}$ ($\sigma_{21,1}$, resp.) the molecular cross section for the photoisomerization $C_1 \rightarrow C_2$ ($C_2 \rightarrow C_1$, resp.) driven at wavelength λ_1 and by k_{21}^{Δ} the thermal part of the rate constant for the backward step $C_2 \rightarrow C_1$, we have

$$k_{12}^{\mathrm{I}} = \sigma_{12,1} I_1 \tag{A47}$$

$$k_{21}^{\mathrm{I}} = \sigma_{21,1} I_1 + k_{21}^{\Delta} \tag{A48}$$

The relaxation time given in Eq.(A44) is rewritten

$$\tau^{\mathrm{I}} = \frac{1}{\Sigma_1 I_1 + k_{21}^{\Delta}} \tag{A49}$$

where $\Sigma_1 = \sigma_{12,1} + \sigma_{21,1}$ is the sum of cross sections at the wavelength λ_1. Eq.(A49) shows that $1/\tau^{\mathrm{I}}$ exhibits a linear dependence on the light intensity I_1.

A7.1.2 Illumination II

For illumination II, under light intensities I_1 at the wavelength λ_1 and I_2 at the wavelength λ_2, the initial condition is the steady state reached at the end of illumination I, $C_1^{\mathrm{II}} = C_1^{\mathrm{I},\infty}$. The concentrations C_1^{II} and C_2^{II} obey

$$C_2^{\mathrm{II}} - C_2^{\mathrm{II},\infty} = C_1^{\mathrm{II},\infty} - C_1^{\mathrm{II}} = \left(C_2^{\mathrm{I},\infty} - C_2^{\mathrm{II},\infty} \right) \exp\left(-\frac{t}{\tau^{\mathrm{II}}} \right) \tag{A50}$$

where

$$C_1^{\mathrm{II},\infty} = \frac{1}{1 + K_{12}^{\mathrm{II}}} C_{\mathrm{tot}} \tag{A51}$$

$$C_2^{\mathrm{II},\infty} = \frac{K_{12}^{\mathrm{II}}}{1 + K_{12}^{\mathrm{II}}} C_{\mathrm{tot}} \tag{A52}$$

are the steady concentrations reached at large time and

$$\tau^{\mathrm{II}} = \frac{1}{k_{12}^{\mathrm{II}} + k_{21}^{\mathrm{II}}} \tag{A53}$$

designates the relaxation time of the photochemical conversion of the two species C_1 and C_2. The brightness at the wavelength λ_2 is assumed to be much smaller than the one at the wavelength λ_1.[13] Using the same assumptions as the ones made for illumination I, we obtain the fluorescence intensity

$$I_F^{\mathrm{II}} = QC_1^{\mathrm{II}} I_1 \tag{A54}$$

Using Eqs.(A50-A52), we find

$$\frac{I_F^{\mathrm{II}}}{I_F^{\mathrm{II},0}} = 1 + \frac{QC_{\mathrm{tot}} I_1}{I_F^{\mathrm{II},0}} \left(\frac{K_{12}^{\mathrm{II}}}{1 + K_{12}^{\mathrm{II}}} - \frac{K_{12}^{\mathrm{I}}}{1 + K_{12}^{\mathrm{I}}} \right) \left[\exp\left(-\frac{t}{\tau^{\mathrm{II}}} \right) - 1 \right] \tag{A55}$$

where $I_F^{\mathrm{II},0}$ is the initial fluorescence intensity.

For RSFPs at low light intensities I_1 and I_2, the two-state model (A39) can be used to account for the observed fluorescence photoswitching. Introducing $\sigma_{12,2}$ and $\sigma_{21,2}$ as the molecular cross sections for photoisomerization steps driven at wavelength λ_2, one has

$$k_{12}^{\mathrm{II}} = \sigma_{12,1} I_1 + \sigma_{12,2} I_2 \tag{A56}$$

$$k_{21}^{\mathrm{II}} = \sigma_{21,1} I_1 + \sigma_{21,2} I_2 + k_{21}^{\Delta} \tag{A57}$$

The relaxation time given in Eq.(A53) is rewritten

$$\tau^{\mathrm{II}} = \frac{1}{\Sigma_1 I_1 + \Sigma_2 I_2 + k_{21}^{\Delta}} \tag{A58}$$

where $\Sigma_2 = \sigma_{12,2} + \sigma_{21,2}$ is the sum of cross sections at the wavelength λ_2. Eq.(A58) shows that $1/\tau^{\mathrm{II}}$ exhibits a linear dependence on the light intensity I_2.

A7.1.3 Illumination III

For the illumination III which has been used to measure the rate constant associated to thermal relaxation of the photoswitched RSFPs, the initial condition is the steady state reached at the end of illumination I, $C_1^{\mathrm{III}} = C_1^{\mathrm{I},\infty}$. The concentrations C_1^{III} and C_2^{III} obey

$$C_2^{\mathrm{III}} - C_2^{\mathrm{III},\infty} = C_1^{\mathrm{III},\infty} - C_1^{\mathrm{III}} = \left(C_2^{\mathrm{I},\infty} - C_2^{\mathrm{III},\infty} \right) \exp\left(-\frac{t}{\tau^{\mathrm{III}}} \right) \tag{A59}$$

where

$$C_1^{\mathrm{III},\infty} = \frac{1}{1 + K_{12}^{\mathrm{III}}} C_{\mathrm{tot}} \tag{A60}$$

$$C_2^{\mathrm{III},\infty} = \frac{K_{12}^{\mathrm{III}}}{1 + K_{12}^{\mathrm{III}}} C_{\mathrm{tot}} \tag{A61}$$

are the steady concentrations reached at large time and

$$\tau^{\mathrm{III}} = \frac{1}{k_{12}^{\mathrm{III}} + k_{21}^{\mathrm{III}}} \tag{A62}$$

designates the relaxation time of the photochemical conversion of the two species C_1 and C_2. Using the same assumptions as the ones made for illumination I, we obtain the fluorescence intensity

$$I_F^{\mathrm{III}} = QC_1^{\mathrm{III}} I_1 \tag{A63}$$

Using Eqs.(A59–A61), we find

$$\frac{I_F^{\mathrm{III}}}{I_F^{\mathrm{III},0}} = 1 + \frac{QC_{\mathrm{tot}} I_1}{I_F^{\mathrm{III},0}} \left(\frac{K_{12}^{\mathrm{III}}}{1 + K_{12}^{\mathrm{III}}} - \frac{K_{12}^{\mathrm{I}}}{1 + K_{12}^{\mathrm{I}}} \right) \left[\exp\left(-\frac{t}{\tau^{\mathrm{III}}} \right) - 1 \right] \tag{A64}$$

where $I_F^{\mathrm{III},0}$ is the initial fluorescence intensity.

In the presence of the weak light at the wavelength λ_1 required to read out the RSFP signal after variable delays without any light, one has

$$k_{12}^{\mathrm{III}} \simeq 0 \tag{A65}$$

$$k_{21}^{\mathrm{III}} \simeq k_{21}^{\Delta} \tag{A66}$$

The relaxation time given in Eq.(A62) is rewritten

$$\tau^{\mathrm{III}} \simeq \frac{1}{k_{21}^{\Delta}}. \tag{A67}$$

A7.2 Impact of diffusion

Our home-built photoswichometer was designed to illuminate the samples with light intensities covering five orders of magnitude (from 0.5 W.cm^{-2} to 50 kW.cm^{-2}). Whereas for low light intensities we could rely on LED delivering homogeneous illumination in a large volume, we had to focus laser beams to reach the higher light intensities. In the case of a small illuminated cell, the fluorescence evolution may adopt a non-trivial decay due to the diffusion of the fluorophore outside the illuminated cell. The design of the photoswitchometer is compatible with the acquisition of the photoswitching properties of RSFs in solid samples. However, it was interesting to make it as well relevant for measurements in solution. Indeed diffusion can refresh a solution between successive experiments which avoids long-term extinction. Fluorescence evolution including the effect of diffusion could be theoretically treated to extract the photochemical information sought for. Nevertheless this computation would not be easily prone to data processing and would slow down the automatic acquisition of the photochemical information in the widest range of illumination intensities. Hence we designed experimental conditions in which the contribution of diffusion could be neglected.

Without loss of generality, we restrict the analysis of diffusion effect to illumination i=I. The rate constants in Eq.(A39) are written k_{12} and k_{21}. We establish below the evolution of the concentrations of C_1 and C_2 in two different geometries of the illuminated measuring cell. In the first case, we apply a 3D-model in which illumination is restricted to a sphere. In the second situation, we apply a 2D-model in which illumination occurs within a cylinder. The most favorable geometry of the illuminated cell of the photoswitchometer is then made precise.

A7.2.1 Spherical illumination

In the first model, we assume that illumination is homogeneous within a sphere of radius r_0 and vanishes out of the illuminated sphere within the whole solution envisioned as a spherical reservoir of radius R containing the species C_1 at concentration $C_{\rm tot}$. We adopt $r_0 = 0.3$ μm and $R = 2.2$ μm which are experimentally relevant. As expected for the investigated fluorescent proteins, the species C_1 and C_2 are supposed to diffuse in the reactor with the same diffusion coefficient D so that their concentrations obey the conservation relation $C_1 + C_2 = C_{\rm tot}$.

We deal with a reaction-diffusion system with spherical symmetry. In the illuminated cell, the dynamics is governed by

$$\frac{\partial C_1}{\partial t} = -(k_{12} + k_{21})C_1 + k_{21}C_{\rm tot} + D\left[\frac{\partial^2 C_1}{\partial r^2} + \frac{2}{r}\frac{\partial C_1}{\partial r}\right] \tag{A68}$$

where r is the radial coordinate. The change of variable

$$u = r[C_1 - C_1^{h,\infty}], \tag{A69}$$

where $C_1^{h,\infty} = \frac{k_{21}C_{\rm tot}}{k_{12}+k_{21}}$ is the steady state obtained upon homogeneous illumination, leads to[23]

$$\frac{\partial u}{\partial t} = -(k_{12} + k_{21})u + D\frac{\partial^2 u}{\partial r^2} \tag{A70}$$

for which the boundary condition $u(r = 0, t) = 0$ holds for all time t. The initial condition is $u(r, t = 0) = r(C_{\rm tot} - C_1^{h,\infty})$. An analogous equation is used outside the illuminated cell where $k_{12} = 0$. Our goal is to determine the range of rate constants in which diffusion can be neglected.

In the absence of diffusion, the dynamics of the system is given by

$$\frac{{\rm d}C_1^h}{{\rm d}t} = -(k_{12} + k_{21})C_1^h + k_{21}C_{\rm tot} \tag{A71}$$

leading to the exponential decay

$$C_1^h = \frac{C_{\rm tot}}{k_{12} + k_{21}}\left[k_{12}\exp(-(k_{12} + k_{21})t) + k_{21}\right] \tag{A72}$$

We define the time τ^∞ at which the concentration of species C_1 reaches the stationary value $C_1^{h,\infty}$ to within 1 percent in the absence of diffusion. Following Eq.(A72), we find

$$\tau^\infty = \frac{-1}{k_{12}+k_{21}} \ln\left(\frac{0.01 k_{21}}{k_{12}}\right) \tag{A73}$$

where we assume $k_{21} \leq k_{12}$. Eq.(A70) inside the illuminated cell and the analogous equation with $k_{12} = 0$ outside the illuminated cell are discretized and numerically solved until time reaches τ^∞. We investigated the following parameter range: $1\ \text{s}^{-1} \leq k_{12} \leq 10^7\ \text{s}^{-1}$, $1\ \text{s}^{-1} \leq k_{21} \leq 10^5\ \text{s}^{-1}$ with $k_{21} \leq k_{12}$, $30\ \mu\text{m}^2\text{s}^{-1} \leq D \leq 300\ \mu\text{m}^2\text{s}^{-1}$, which is consistent with RSFs properties.

The stationary spatial profile $C_1(r, \tau^\infty)$ is compared to the prediction $C_1^{h,\infty}$ in Fig. A40 for different values of k_{12}. In the spherical geometry and for such parameter values, diffusion induces an important bias, which decreases without disappearing as the rate constant k_{12} increases in the investigated range.

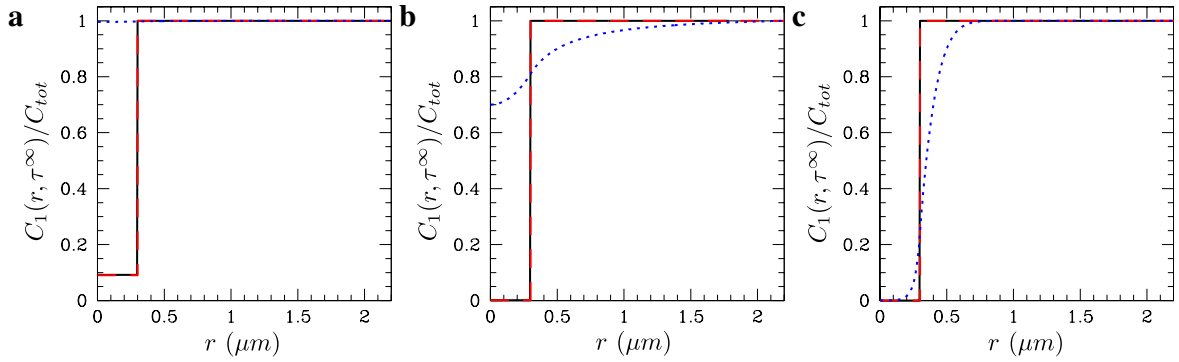

Figure A40: Scaled stationary spatial profiles $C_1(r, \tau^\infty)/C_{\text{tot}}$ for species C_1 deduced from the numerical integration of Eq.(A70) in the spherical geometry (blue dotted line), the numerical integration of Eq.(A77) in the cylindrical geometry (black dashed line), and the prediction $C_1^{h,\infty}$ (red dashed line) for $r_0 = 0.3\ \mu$m, $R = 2.2\ \mu$m, $k_{21} = 1\ \text{s}^{-1}$, $D = 100\ \mu\text{m}^2\ \text{s}^{-1}$ with k_{12} (s^{-1})= 10 (**a**), 10^3 (**b**), 10^5 (**c**).

Without loss of generality, we assume that only species C_1 has a non vanishing brightness Q. The fluorescence signal $I_F = QI_1I_F'$ is proportional to the integral of the concentration C_1 over the illuminated volume

$$I_F' = \int_0^{r_0} C_1 4\pi r^2 \mathrm{d}r \tag{A74}$$

where $C_1 = C_{\text{tot}} - C_2$ is deduced from Eqs.(A69) and (A70).

The evolution of fluorescence I_F is compared to the prediction without diffusion, $C_1^h V$, where C_1^h is given in Eq.(A72) and $V = \frac{4}{3}\pi r_0^3$ is the volume of the illuminated cell. Fig. A41 displays the fluorescence evolution for different values of the rate constant k_{12}. The difference between the

results in the presence and absence of diffusion markedly depends on k_{12}. As already mentioned, the deviation is reduced as k_{12} increases.

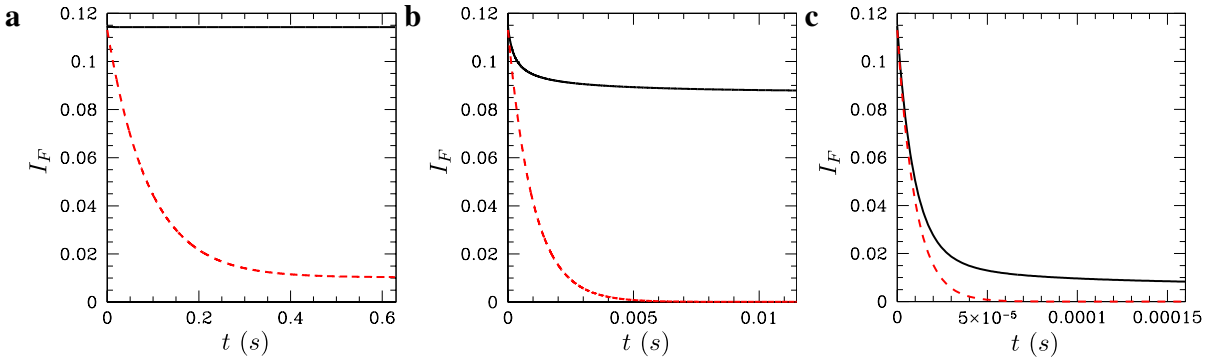

Figure A41: Spherical geometry: Fluorescence evolution I_F for species C_1 deduced from the numerical integration of Eq.(A70) and integration over the volume $V = \frac{4}{3}\pi r_0^3$ of the illuminated cell (black solid line) and from exponential decay $C_1^h V$ predicted by Eq.(A72) upon homogeneous illumination (red dashed line) for the parameter values given in the caption of Fig. A40 and $Q = I_1 = 1$.

If the signal-to-noise ratio remains sufficient when integrating the concentration C_1 over a sphere of radius $r_0/2$ instead of the radius r_0 of the illuminated zone, the results are improved for $k_{12} = 10^5$ s^{-1} as shown in Fig. A42. The same scale was chosen in Fig. A41c and Fig. A42 to better highlight the loss of signal strength due to the integration of the concentration over a smaller volume. Nevertheless, this strategy is useless for $k_{12} \leq 10^3$ s^{-1}, since the concentration at $r_0/2$ is extremely far from the prediction without diffusion, as shown in Fig. A40a and Fig. A40b.

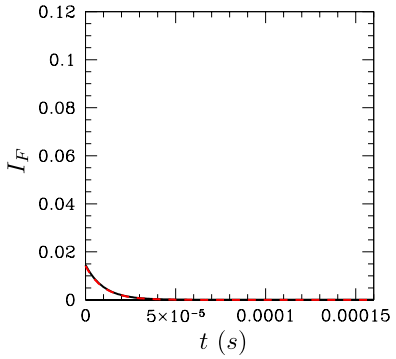

Figure A42: Spherical geometry: Same caption as for Fig. A41c ($k_{12} = 10^5$ s^{-1}) for the fluorescence evolution obtained by integration of the concentration C_1 over a sphere of radius $r_0/2$ instead of r_0.

A more quantitative evaluation of the discrepancy between the results with and without diffusion is given in Fig. A43 for variable rate constants and two values of the diffusion coefficient. The difference between the signal and the exponentially-decaying solution obtained upon homogeneous

illumination is computed according to:

$$J = \frac{\int_{t=0}^{\tau^\infty}(I'_F - C_1^h V)dt}{(C_{\rm tot} - C_1^{h,\infty})V\tau^\infty} \tag{A75}$$

where $C_1^h(t)$ is given in Eq.(A72). The deviation J tends to 1 when the rate constant k_{12} is small compared to the typical frequency $\frac{D}{r_0^2}$ and vanishes for sufficiently large values of k_{12}. As expected, J is smaller and the results are improved for a smaller value of the diffusion coefficient. Interestingly, J does not sensitively depend on the rate constant k_{21}.

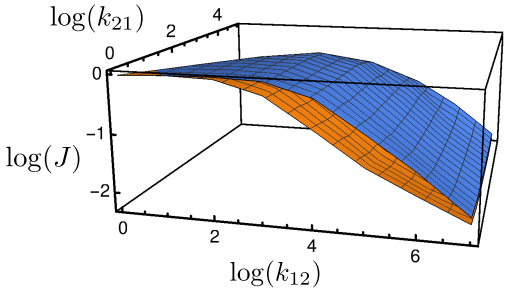

Figure A43: Spherical geometry: Decimal logarithm $\log(J)$ of the deviation between the results with and without diffusion versus $\log(k_{12})$ and $\log(k_{21})$ for $D = 300$ μm^2 s^{-1} (blue) and $D = 30$ μm^2 s^{-1} (orange).

According to Fig. A43, the determination of the relaxation time using the exponential decay without diffusion is valid to within a few percent in a spherical reactor for $r_0 = 0.3$ μm and $D \simeq 100$ μm^2 s^{-1} if the rate constant k_{12} of the photochemical step is larger than or equal to 10^7 s^{-1}, which is very restrictive. More generally, we introduce the cutoff rate constant

$$k_{12}^c \simeq 10^4 \frac{D}{r_0^2} \tag{A76}$$

where D is the diffusion coefficient of the different species and r_0, the typical length of the illuminated cell. Diffusion is negligible to within a few percent in the spherical geometry provided that $k_{12} \geq k_{12}^c$ with k_{12}^c given in Eq.(A76). Even with a larger cell of radius $r_0 = 10$ μm, the condition would become $k_{12} \geq 10^4$ s^{-1}, which remains constraining.

A7.2.2 Cylindrical illumination

In the second model, we assume that illumination is homogeneous within a cylinder of radius r_0 and height h and vanishes out of the illuminated zone within the whole solution envisioned as a cylindrical reservoir of radius R containing the species C_1 at concentration $C_{\rm tot}$. With respect to the experimental conditions, we adopt $h = 80$ μm, $r_0 = 0.3$ μm, and $R = 2.2$ μm in order to establish the comparison with the results derived in the spherical geometry.

In the illuminated cell, the dynamics is governed by

$$\frac{\partial C_1}{\partial t} = -(k_{12}+k_{21})C_1 + k_{21}C_{\rm tot} + D\left[\frac{\partial^2 C_1}{\partial r^2} + \frac{1}{r}\frac{\partial C_1}{\partial r}\right] \tag{A77}$$

The same equation with $k_{12} = 0$ holds outside the illuminated cell. We introduce the same change of variable $u(r,t) = r(C_1 - C_1^{h,\infty})$ as in the case of spherical symmetry, because the boundary condition $u(r=0,t) = 0$ is convenient and makes it possible to solve 1D equations. The equations for u inside and outside the illuminated zone are solved in an infinite cylinder in contact with a reservoir of species C_1. The stationary profiles obtained in the cylindrical reactor are given in Fig. A44 and superimposed on the predictions without diffusion. The results perfectly agree with the homogeneously illuminated solution $C_1^{h,\infty}$, even for the small rate constant value $k_{12} = 10$ s^{-1}. It is to be noted that the results are obtained for an infinite cylindrical reactor which certainly overestimates their quality. However, the predictions remain valid for a cylinder of height h about 10 times larger than the radius r_0. This condition is fully obeyed for the considered parameters leading to $h/r_0 \simeq 270$.

The fluorescence evolution $I_F = QI_1I_F'$ given in Fig. A44 for $k_{12} = 10$ s^{-1} results from integrating the concentration C_1 over a cylinder of radius r_0 and height h according to

$$I_F' = h\int_0^{r_0} C_1 2\pi r \mathrm{d}r \tag{A78}$$

Due to the larger volume of the cylinder compared to the sphere of the same radius, the fluorescence evolution in Fig. A44 begins with a larger amplitude than the fluorescence evolution in Fig. A41. In Fig. A44, the fluorescence series I_F taking into account or not diffusion are superimposed even for the small value $k_{12} = 10$ s^{-1} of the rate constant and the small radius $r_0 = 0.3$ μm of the illuminated cell.

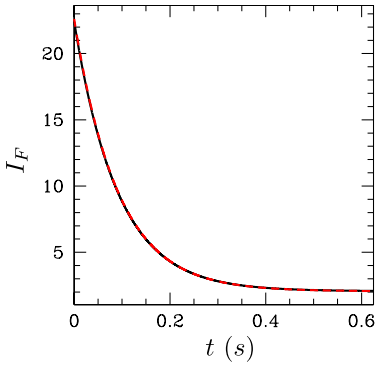

Figure A44: Cylindrical geometry: Evolution of the signal S for species C_1 deduced from the numerical integration of Eq.(A77) and integration over the volume $V = \pi(r_0)^2 h$ of the illuminated zone (blue solid line) and exponential decay $C_1^h V$ predicted by Eq.(A72) upon homogeneous illumination (red dashed line) for $k_{12} = 10$ s^{-1}, $h = 80$ μm, and $Q = I_1 = 1$. The values of the other parameters are given in the caption of Fig.A40.

The difference J between the fluorescence series with and without diffusion defined in Eq.(A75) is equal to 1.2% for $k_{12} = 10^3$ s^{-1}, $r_0 = 0.3$ μm, and $D = 100$ μm^2 s^{-1}. Hence, in the cylindrical geometry, we find that the cutoff rate constant obeys

$$k_{12}^c \simeq \frac{D}{r_0^2} \tag{A79}$$

Diffusion is negligible inside the illuminated cell for $k_{12} \geq k_{12}^c$ and whatever k_{21}. Comparing Eqs.(A76) and (A79), we conclude that the cylindrical geometry, with an illuminated cell of height larger than its radius, is much more favorable than the spherical geometry.

A7.2.3 Conclusion

Based on the above results, our experiments have been performed in a cylindrical reactor of radius $R = 70$ μm and height $h = 80$ μm. When using laser illumination, the smallest measured rate constant k_{12} for the investigated RSFPs was 1 s^{-1} and the largest was 10^5 s^{-1}. The radius of the illuminated cylinder was chosen equal to $r_0 = 10$ μm, which guarantees a cutoff rate constant $k_{12}^c \simeq 1$ s^{-1} for a diffusion coefficient $D = 100$ μm^2 s^{-1} while preserving the homogeneity of the illuminated cell. For further precautions, the fluorescence signal has been integrated over a cylinder of radius $r_0/2$ instead of r_0. Under these conditions, the effect of diffusion was entirely negligible over the full range of experimental values of the rate constants.

A8 The LIGHTNING discriminatory power

This section reports on the evaluation of the kinetic fingerprint of the RSFPs, the minimal distance among sets of RSFPs, and the cutoff distance d_c, which are reported in the Main Text for the photoswitchometer configuration devoted to acquire the kinetic information on RSFP photoswitching.

A8.1 The LIGHTNING kinetic fingerprint of RSFPs

Tab. A4 sums up the $\{\tau_{low}^{\mathrm{I}}, \tau_{low}^{\mathrm{II}}, \tau_{high}^{\mathrm{I}}, \tau_{high}^{\mathrm{II}}\}$ sets, which have been obtained with the photoswitchometer in the configuration displayed in Fig.A1 for the 22 investigated RSFPs at 15–20 μM concentrations.

Table A4: *Kinetic fingerprints* $\{\tau^{\mathrm{I}}_{low}, \tau^{\mathrm{II}}_{low}, \tau^{\mathrm{I}}_{high}, \tau^{\mathrm{II}}_{high}\}$ *of the 22 RSFPs.* The characteristic times τ^{I}_{low} and τ^{II}_{low} have been measured with the photoswitchometer in the configuration displayed in Fig.A1 in the regime of low light intensity with illumination I_{low}: $I_1 = 2$ ein.m^{-2}.s^{-1} and illumination II_{low}: $I_1 = 2$ ein.m^{-2}.s^{-1} and $I_2 = 0.1$ ein.m^{-2}.s^{-1} whereas the characteristic times τ^{I}_{high} and $\tau^{\mathrm{II}}_{high}$ were obtained at the highest light intensities accessible with the photoswitchometer in the regime of high light intensity with illumination I_{high}: $I_1 = 200$ ein.m^{-2}.s^{-1}; illumination II_{high}: $I_1 = 200$ ein.m^{-2}.s^{-1} and $I_2 = 90$ ein.m^{-2}.s^{-1}. Solvent: pH=7.4 PBS (50 mM PBS, 150 mM NaCl). T = 298 K.

RSFP	τ^{I}_{low} (s)	τ^{II}_{low} (s)	τ^{I}_{high} (s)	$\tau^{\mathrm{II}}_{high}$ (s)
1	$(1.4\pm0.3)\times10^{-1}$	$(3.15\pm0.01)\times10^{-2}$	$(4.52\pm0.09)\times10^{-3}$	$(1.83\pm0.04)\times10^{-4}$
2	$(2.2\pm0.1)\times10^{-3}$	$(2.53\pm0.05)\times10^{-2}$	$(3.34\pm0.01)\times10^{-4}$	$(7.73\pm0.02)\times10^{-5}$
3	$(2.57\pm0.05)\times10^{-2}$	$(2.4\pm0.03)\times10^{-2}$	$(4.84\pm0.08)\times10^{-3}$	$(1.25\pm0.03)\times10^{-4}$
4	$(1.12\pm0.08)\times10^{-2}$	$(4.26\pm0.03)\times10^{-2}$	$(2.56\pm0.07)\times10^{-3}$	$(1.13\pm0.02)\times10^{-2}$
5	$(1.42\pm0.01)\times10^{-2}$	$(1.23\pm0.02)\times10^{-1}$	$(3.57\pm0.08)\times10^{-3}$	$(9.25\pm0.02)\times10^{-3}$
6	$(5.1\pm0.3)\times10^{-2}$	$(1.67\pm0.01)\times10^{-2}$	$(1.17\pm0.05)\times10^{-4}$	$(2.14\pm0.02)\times10^{-4}$
7	$(1.7\pm0.4)\times10^{-2}$	$(1.84\pm0.02)\times10^{-2}$	$(5.44\pm0.02)\times10^{-4}$	$(6.74\pm0.03)\times10^{-5}$
8	$(2.11\pm0.08)\times10^{-2}$	$(1.61\pm0.04)\times10^{-2}$	$(4.23\pm0.03)\times10^{-3}$	$(9.5\pm0.1)\times10^{-5}$
9	$(5.8\pm0.1)\times10^{-1}$	$(1.84\pm0.02)\times10^{-2}$	$(5.95\pm0.02)\times10^{-3}$	$(1.25\pm0.02)\times10^{-4}$
10	$(2.53\pm0.15)\times10^{-2}$	$(2.14\pm0.02)\times10^{-2}$	$(6.8\pm0.1)\times10^{-4}$	$(7.75\pm0.03)\times10^{-5}$
11	$(3.16\pm0.03)\times10^{-2}$	$(2.23\pm0.03)\times10^{-2}$	$(3.82\pm0.07)\times10^{-3}$	$(1.12\pm0.01)\times10^{-4}$
12	$(8.6\pm0.1)\times10^{-3}$	$(1.46\pm0.05)\times10^{-2}$	$(3.1\pm0.2)\times10^{-4}$	$(6.23\pm0.02)\times10^{-5}$
13	$(7.1\pm0.4)\times10^{-2}$	$(2.66\pm0.03)\times10^{-2}$	$(5.63\pm0.02)\times10^{-3}$	$(1.75\pm0.03)\times10^{-4}$
14	$(1.36\pm0.05)\times10^{-1}$	$(2.84\pm0.01)\times10^{-2}$	$(2.92\pm0.05)\times10^{-3}$	$(1.84\pm0.02)\times10^{-4}$
15	$(4.2\pm0.1)\times10^{-3}$	$(2.61\pm0.03)\times10^{-2}$	$(3.14\pm0.02)\times10^{-4}$	$(3.64\pm0.03)\times10^{-4}$
16	$(4.3\pm0.1)\times10^{-2}$	$(1.82\pm0.06)\times10^{-2}$	$(6.25\pm0.04)\times10^{-4}$	$(9.83\pm0.01)\times10^{-5}$
17	$(2.45\pm0.03)\times10^{-3}$	$(2.55\pm0.01)\times10^{-2}$	$(4.26\pm0.03)\times10^{-4}$	$(1.27\pm0.02)\times10^{-4}$
18	$(1.45\pm0.07)\times10^{-2}$	$(2.14\pm0.04)\times10^{-2}$	$(3.82\pm0.01)\times10^{-3}$	$(3.82\pm0.06)\times10^{-4}$
19	$(2.6\pm0.1)\times10^{-3}$	$(7.64\pm0.03)\times10^{-3}$	$(1.21\pm0.03)\times10^{-4}$	$(3.15\pm0.04)\times10^{-5}$
20	$(3.6\pm0.1)\times10^{-3}$	$(9.52\pm0.02)\times10^{-3}$	$(1.31\pm0.07)\times10^{-4}$	$(1.35\pm0.04)\times10^{-4}$
21	$(3.25\pm0.02)\times10^{-4}$	$(8.77\pm0.02)\times10^{-3}$	$(2.15\pm0.07)\times10^{-4}$	$(1.73\pm0.01)\times10^{-4}$
22	$(2.7\pm0.1)\times10^{-3}$	$(7.45\pm0.01)\times10^{-3}$	$(1.36\pm0.08)\times10^{-4}$	$(6.17\pm0.02)\times10^{-5}$

A8.2 The LIGHTNING minimal distance among sets of RSFPs

The preceding results have been exploited to choose and rank RSFPs within the set of the $N = 22$ studied RSFPs by implementing the sorting algorithms reported in paragraph A1.7.1. The optimized subsets $s'(m)$ and $s(m)$ of m RSFPs for $m = 2, ..., N$ subsets are given in Tab. A5.

As shown in Tab. A5, the relation $s'(m) \subset s'(m+1)$ is not necessarily observed for $s'(m)$ and $s'(m+1)$. This observation has motivated to introduce the alternative sorting algorithm including three-body interactions, which does not suffer from this limitation. The two sorting algorithms lead to similar results even if the relation $s(m) \subset s(m+1)$ is not necessarily observed for $s'(m)$ and $s'(m+1)$. The set $s(m)$ is obtained from $s'(m)$ by replacing some RSFs with close ones.

Table A5: Optimized subsets $s'(m)$ and $s(m)$ of m RSFPs for $m = 2, ..., 22$ using the kinetic signature given in Tab. A4 and the maximum value of the minimum distance between pairs.

m	$s'(m)$	$s(m)$
2	(**5**,**19**)	(**5**,**19**)
3	(**4**,**9**,**19**)	**9**
4	(**4**,**6**,**8**,**9**)	**10**
5	(**3**,**4**,**9**,**15**,**19**)	**15**
6	(**3**,**4**,**7**,**9**,**15**,**19**)	**18**
7	(**4**,**6**,**7**,**8**,**9**,**18**,**19**)	**8**
8	(**3**,**4**,**6**,**9**,**10**,**16**,**18**,**19**)	**2**
9	(**1**,**2**,**3**,**4**,**7**,**9**,**15**,**19**,**20**)	**12**
10	(**1**,**2**,**3**,**4**,**9**,**10**,**12**,**15**,**19**,**20**)	**21**
11	(**1**,**2**,**3**,**4**,**5**,**6**,**9**,**10**,**12**,**15**,**22**)	**4**
12	(**2**,**4**,**5**,**6**,**8**,**9**,**10**,**12**,**13**,**15**,**18**,**22**)	**13**
13	(**2**,**3**,**4**,**5**,**6**,**9**,**10**,**12**,**13**,**15**,**18**,**21**,**22**)	**6**
14	(**2**,**3**,**4**,**5**,**6**,**9**,**10**,**12**,**13**,**15**,**16**,**18**,**21**,**22**)	**16**
15	(**2**,**3**,**4**,**5**,**6**,**9**,**10**,**12**,**13**,**14**,**15**,**16**,**18**,**21**,**22**)	**14**
16	(**1**,**2**,**3**,**4**,**5**,**6**,**9**,**10**,**12**,**13**,**15**,**16**,**18**,**19**,**21**,**22**)	**22**
17	(**1**,**2**,**3**,**4**,**5**,**6**,**9**,**10**,**12**,**13**,**15**,**16**,**18**,**19**,**20**,**21**,**22**)	**20**
18	(**1**,**2**,**3**,**4**,**5**,**6**,**8**,**9**,**10**,**12**,**13**,**15**,**16**,**18**,**19**,**20**,**21**,**22**)	**3**
19	(**1**,**2**,**3**,**4**,**5**,**6**,**8**,**9**,**10**,**12**,**13**,**14**,**15**,**16**,**18**,**19**,**20**,**21**,**22**)	**1**
20	(**1**,**2**,**3**,**4**,**5**,**6**,**7**,**8**,**9**,**10**,**12**,**13**,**14**,**15**,**16**,**18**,**19**,**20**,**21**,**22**)	**7**
21	(**1**,**2**,**3**,**4**,**5**,**6**,**7**,**8**,**9**,**10**,**12**,**13**,**14**,**15**,**16**,**17**,**18**,**19**,**20**,**21**,**22**)	**17**
22	(**1**,**2**,**3**,**4**,**5**,**6**,**7**,**8**,**9**,**10**,**11**,**12**,**13**,**14**,**15**,**16**,**17**,**18**,**19**,**20**,**21**,**22**)	**11**

In a purpose of comparison with the results we previously obtained with Speed OPIOM,[13] we use as well the sorting algorithms to choose and rank RSFPs within the reduced set of the $N = 7$ RSFPs **1**–**7**. The optimized subsets $s'(m)$ and $s(m)$ of m RSFPs for $m = 2, ..., N$ subsets are given in Tab. A6.

Table A6: Optimized subsets $s'(m)$ and $s(m)$ of m RSFPs for $m = 2, ..., 7$ using the kinetic signature given in Tab. A4 and the maximum value of the minimum distance between pairs.

m	$s'(m)$	$s(m)$
2	(**2**,**5**)	(**5**,**6**)
3	(**1**,**2**,**4**)	**3**
4	(**3**,**5**,**6**,**7**)	**1**
5	(**1**,**3**,**5**,**6**,**7**)	**7**
6	(**1**,**2**,**3**,**4**,**6**,**7**)	**2**
7	(**1**,**2**,**3**,**4**,**5**,**6**,**7**)	**4**

The comparison of the data provided in Tab. A5 and A6 shows that the ranking of the RSFPs

may be slightly affected by the removal of an RSFP in the initial set.

A8.3 The LIGHTNING cutoff distance d_c

A8.3.1 d_c evaluation

The paragraph A1.7.2 has shown that the cutoff distance d_c depends on the maximum uncertainty M of the experimental measurements. d_c has been evaluated with the photoswitchometer in the optical configuration displayed in Fig. A1 by recording with the photomultiplier the time series of the fluorescence originating from a cylindrical volume (80 μm-high and 10 μm-radius) of 15–20 μM RSFP solutions upon illuminations I_{low}, II_{low}, I_{high}, and II_{high}. Fluorescence evolution has been recorded 500 times for each discriminative dimension k for the RSFPs i =**2**,**6**. The characteristic times have been extracted using the spectrum approach and a monoexponential reduction. The corresponding distributions of l_{ki} are given in Fig. A45 and A46.

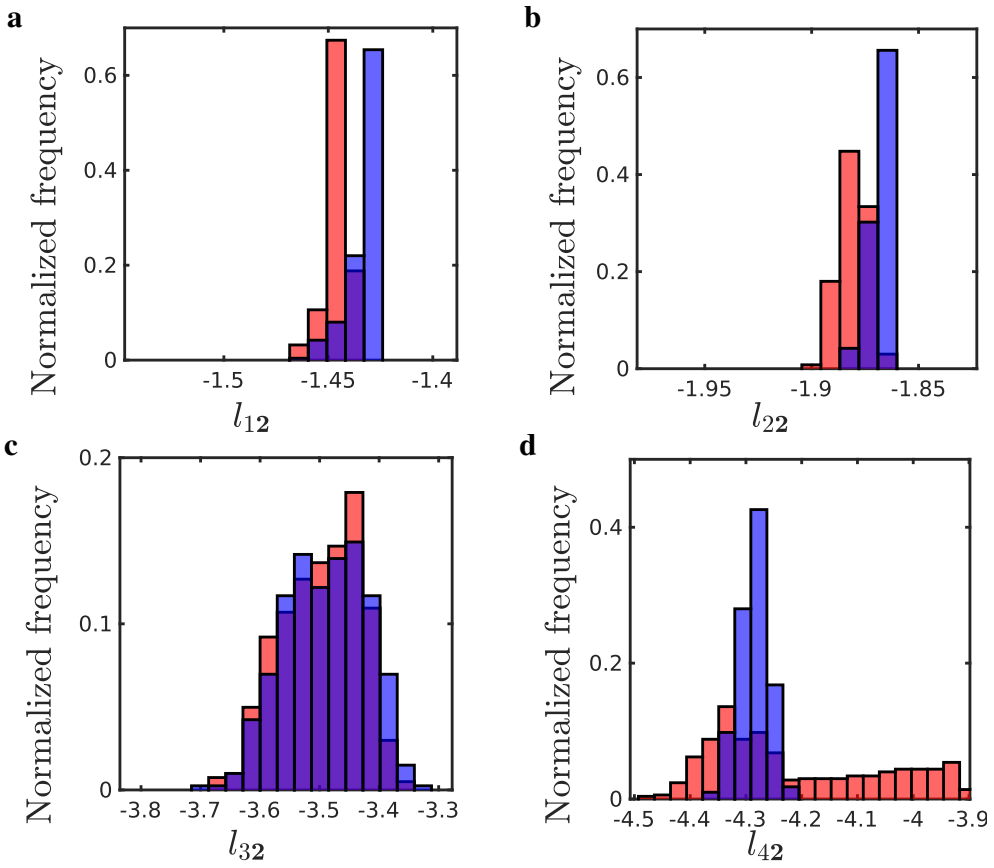

Figure A45: Histograms of the decimal logarithm of the characteristic times l_{12} (**a**, $I_1 = 0.16$ ein.m^{-2}.s^{-1}), l_{22} (**b**, $I_1 = 0.18$ ein.m^{-2}.s^{-1}, $I_2 = 0.18$ ein.m^{-2}.s^{-1}), l_{32} (**c**, $I_1 = 228.8$ ein.m^{-2}.s^{-1}), and l_{42} (**d**, $I_1 = 0.275$ ein.m^{-2}.s^{-1}, $I_2 = 100.7$ ein.m^{-2}.s^{-1}) of RSFP **2** deduced from 500 experiments by recording with the photomultiplier the changes of the fluorescence signal originating from a cylindrical volume (80 μm-high and 10 μm-radius) of 15 μM solution of RSFP **2** in pH 7.4 PBS (50 mM sodium phosphate, 150 mM NaCl) for each discriminative dimension using the spectrum approach (red) and a monoexponential reduction (blue). The characteristic times are expressed in seconds.

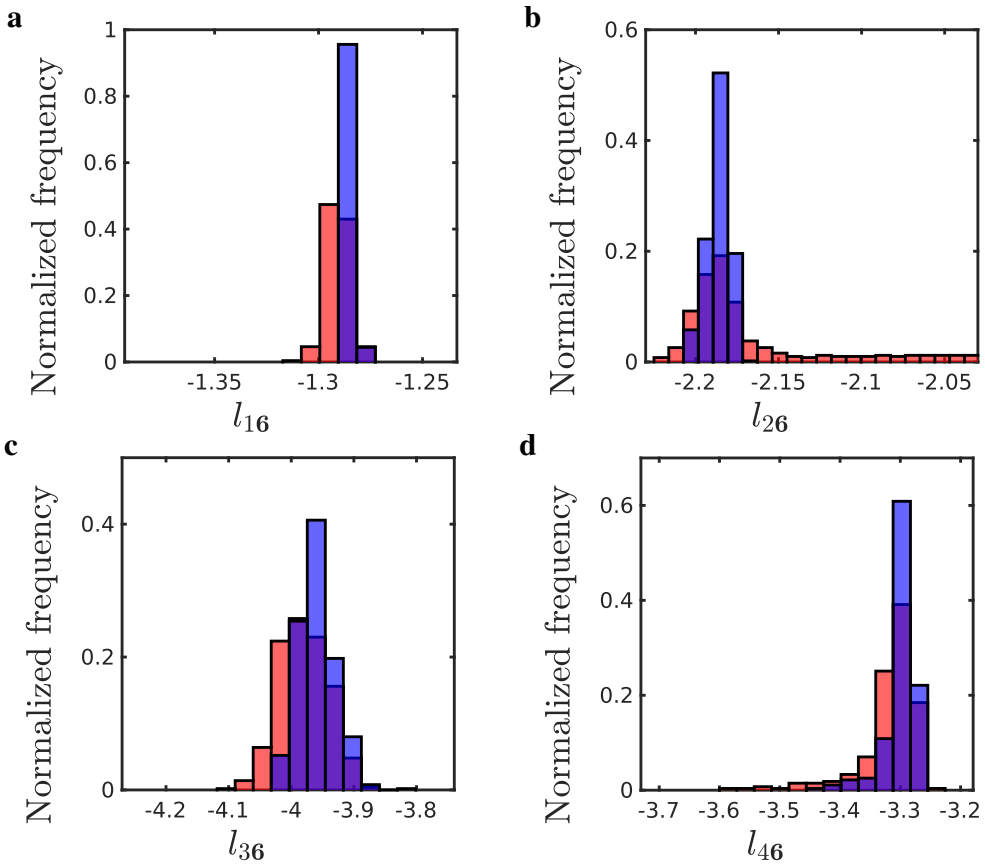

Figure A46: Histograms of the decimal logarithm of the characteristic times l_{16} (**a**, $I_1 = 0.18$ ein.m^{-2}.s^{-1}), l_{26} (**b**, $I_1 = 0.18$ ein.m^{-2}.s^{-1}, $I_2 = 0.18$ ein.m^{-2}.s^{-1}), l_{36} (**c**, $I_1 = 249.6$ ein.m^{-2}.s^{-1}), and l_{46} (**d**, $I_1 = 0.175$ ein.m^{-2}.s^{-1}, $I_2 = 95.4$ ein.m^{-2}.s^{-1}) of RSFP **6** deduced from 500 experiments by recording with the photomultiplier the changes of the fluorescence signal originating from a cylindrical volume (80 μm-high and 10 μm-radius) of 20 μM solution of RSFP **6** in pH 7.4 PBS (50 mM sodium phosphate, 150 mM NaCl) for each discriminative dimension using the spectrum approach (red) and a monoexponential reduction (blue). The characteristic times are expressed in seconds.

Both methods provide similar mean values $\langle l_{ki} \rangle$ and standard deviations σ_{ki} of the distributions as shown in Tab. A7 and A8. When the mean characteristic time is smaller than ten times the sampling time of the fluorescence evolution, the standard deviations deduced from the spectra are slightly larger than the values obtained using the monoexponential reduction.

Table A7: RSFP **2**: Properties of the distribution functions of the decimal logarithm of the characteristic times deduced from two methods of data processing. The mean value $\langle l_{k\mathbf{2}} \rangle$ of the decimal logarithm of the characteristic time and the standard deviation $\sigma_{k\mathbf{2}}$ have been computed using 500 experiments by recording with the photomultiplier the changes of the fluorescence signal originating from a cylindrical volume (80 μm-high and 10 μm-radius) of 15 μM solution of RSFP **2** in pH 7.4 PBS (50 mM sodium phosphate, 150 mM NaCl) for the four discrimination dimensions $k = 1, 2, 3, 4$. The characteristic times are expressed in seconds. The values of the light intensities are given in the caption of Fig. A45.

	Spectrum		Monoexponential reduction	
	$\langle l_{k\mathbf{2}} \rangle$	$\sigma_{k\mathbf{2}}$	$\langle l_{k\mathbf{2}} \rangle$	$\sigma_{k\mathbf{2}}$
$l_{1\mathbf{2}}$	-1.4454	0.0050	-1.4343	0.0065
$l_{2\mathbf{2}}$	-1.8806	0.0063	-1.8693	0.0035
$l_{3\mathbf{2}}$	-3.4977	0.0652	-3.4910	0.0677
$l_{4\mathbf{2}}$	-4.2090	0.1534	-4.2851	0.0267

Table A8: Same caption as in Tab. A7 for 20 μM solution of RSFP **6**. The values of the light intensities are given in the caption of Fig. A46.

	Spectrum		Monoexponential reduction	
	$\langle l_{k\mathbf{6}} \rangle$	$\sigma_{k\mathbf{6}}$	$\langle l_{k\mathbf{6}} \rangle$	$\sigma_{k\mathbf{6}}$
$l_{1\mathbf{6}}$	-1.2905	0.0055	-1.2844	0.0016
$l_{2\mathbf{6}}$	-2.1295	0.0906	-2.1862	0.0066
$l_{3\mathbf{6}}$	-3.9803	0.0385	-3.9595	0.0286
$l_{4\mathbf{6}}$	-3.3176	0.0500	-3.2987	0.0254

For illuminations I_{low} and II_{low} and the two investigated RSFPs i =**2**,**6**, we found $\sigma_{1i} \simeq \sigma_{2i} \simeq 0.007$ whereas $\sigma_{3i} \simeq \sigma_{4i} \simeq 0.05$ for illuminations I_{high} and II_{high}. Based on the order of magnitude of the standard deviations of the distributions of l_{ki}, we assigned the value $M = 0.05$ to the uncertainty. Then we used Eq.(A10) to derive $d_c = 0.2$ since $n = 4$ in the case of RSFPs.

A8.3.2 Discussion

Under the present experimental conditions involving a large number of RSFP molecules in a same environment contained in the observed volume (so as to give rise to an excellent signal-to-noise-ratio) as well as the high frequency of the acquisition of the fluorescence signal (so as to provide many data points), we questioned whether the standard deviations of the distributions $l_{k\mathbf{i}}$ reported in Tab. A7 and A8 could originate from some instabilities of our instrumental setup. To evaluate the latter possibility, we collected a fraction of the light from the LEDs at 480 and 405 nm, and from the lasers at 488 and 405 nm and measured their intensity as a function of the number of acquisitions under the conditions, which had been used to build the histograms in Fig. A45 and A46. Fig. A47 and A48 display the results.

Fig. A47a,b and A48a,b demonstrate that light intensity at the focal plane encounters evolution over the acquisition window, which had been used to build the histograms in Fig. A45 and A46. The observed drift is more pronounced with the lasers than with the LEDs, which interestingly correlates with the higher standard deviations observed for the distributions of $l_{3\mathbf{i}}$ and $l_{4\mathbf{i}}$ than for the distributions of $l_{1\mathbf{i}}$ and $l_{2\mathbf{i}}$ (see the data extracted from monoexponential reduction in Tab. A7 and A8). To quantitatively evaluate this correlation, we computed the average values and the standard deviations observed for the distributions of the decimal logarithm of the light intensity of the LEDs and the lasers displayed in Fig. A47c,d and A48c,d. The results are shown in Tab. A9.

Table A9: Average values $< I >$ and standard deviations σ_I observed for the distributions of the decimal logarithm of the light intensity of the LEDs and the lasers displayed in Fig. A47c,d and A48c,d. The light intensities have been experimentally extracted in Volt and are in arbitrary units.

Light source	$< I >$	σ_I
LED 480 nm	-2.3072	0.0035
LED 405 nm	-2.1461	0.0023
Laser 480 nm	-0.8301	0.0115
Laser 405 nm	-1.6386	0.0224

The standard deviations of the distributions of the decimal logarithm of the light intensity of the LEDs and the lasers are in fair agreement with the standard deviations extracted from the distribution functions of the decimal logarithm of the characteristic times for **2** and **6** (see the data extracted from monoexponential reduction in Tab. A7 and A8). This observation led us to conclude that the $M = 0.05$ uncertainty value extracted from our measurements (and correspondingly the $d_c = 0.2$ value) is an upper value, which may be limited by our instrumental setup.

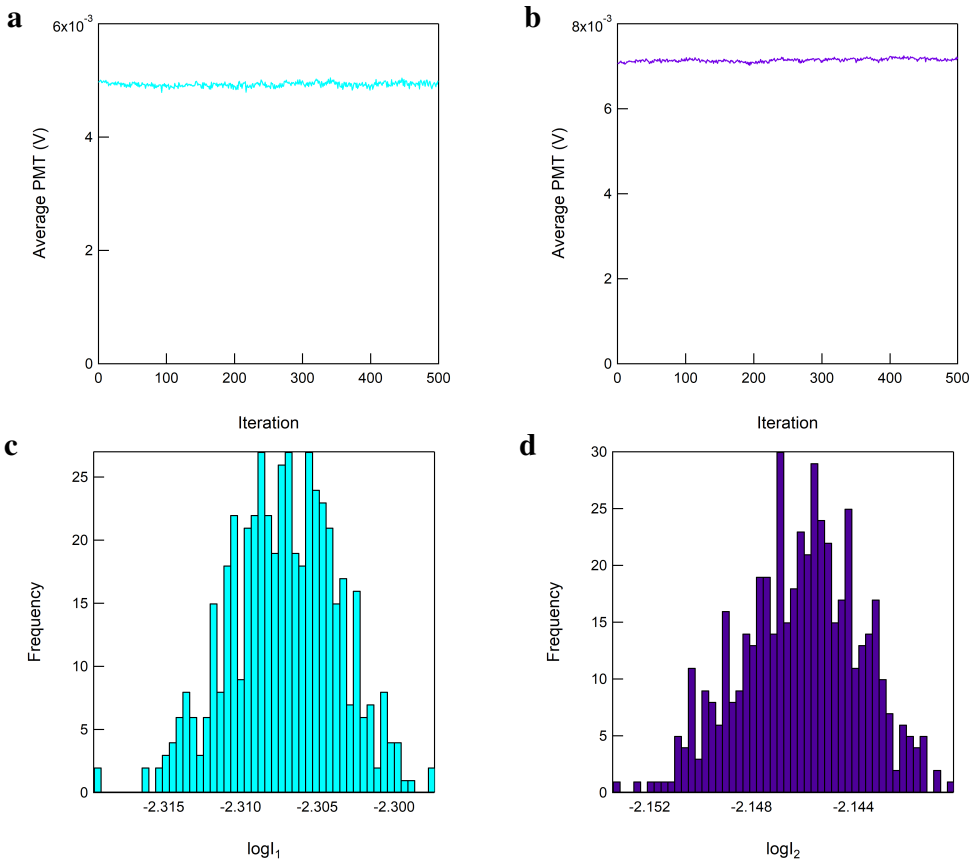

Figure A47: *Characterization of the stability of the LED light sources over 500 successive acquisitions*. **a**,**b**: Evolution of the light intensity of the LEDs at 480 (**a**) and 405 (**b**) nm with the number of acquisitions; **c**,**d**: Histograms of the decimal logarithm of the light intensity of the LEDs at 480 (**c**) and 405 (**d**) nm.

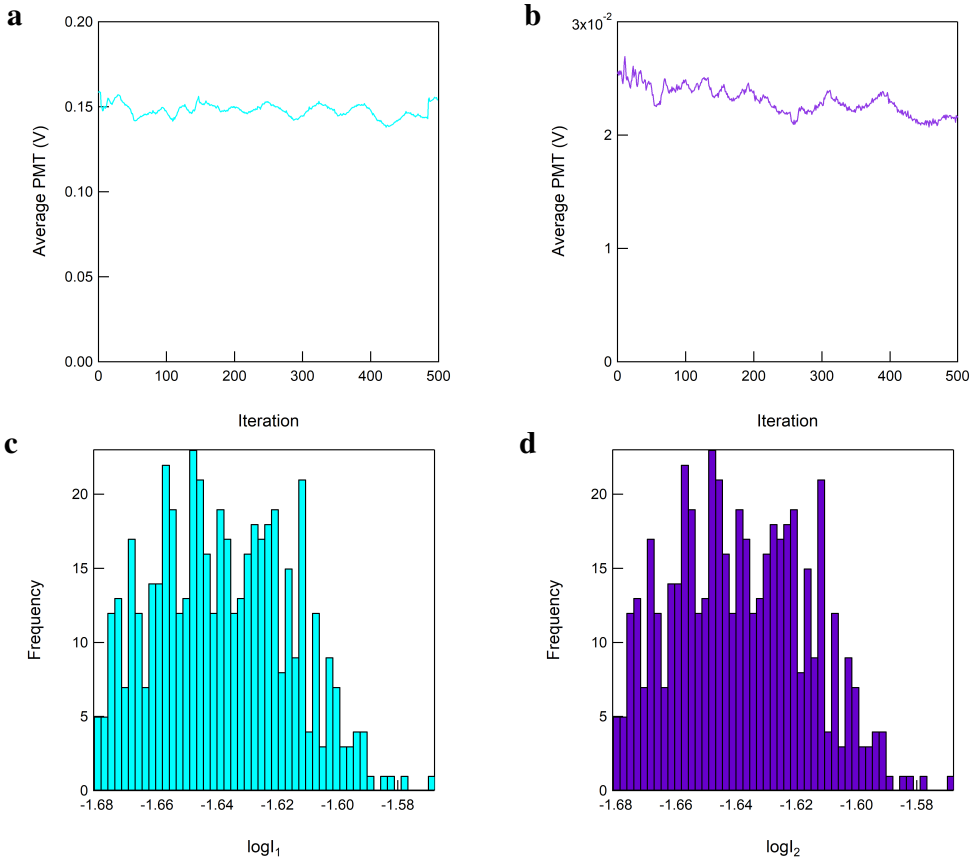

Figure A48: *Characterization of the stability of the laser light sources over 500 successive acquisitions*. **a**,**b**: Evolution of the light intensity of the lasers at 488 (**a**) and 405 (**b**) nm with the number of acquisitions; **c**,**d**: Histograms of the decimal logarithm of the light intensity of the lasers at 488 (**c**) and 405 (**d**) nm.

A8.4 Colocalization of RSFPs

LIGHTNING can discriminate and recognize not only an RSF but several co-localized RSFs as well. In the following, we assume that the sample contains m RSFs and illustrate the discrimination and recognition of two RSFs, which can be colocalized in a same pixel. Our approach can be generalized to a larger number of colocalized RSFs.

The fluorescence properties of the pixel are compared to the one of pairs (i, j) of RSFs to determine whether i, j, or both i and j are present in the pixel. For a given pair (i, j), we use the kinetic fingerprints given in Tab.A4 to determine the most discriminating dimension k for which the 1-dimensional distance $d_{ij}^k = \max_{k'}(\mid l_{k'i} - l_{k'j} \mid)$ is maximum, where $l_{k'i}$ is the decimal logarithm of the characteristic time of the RSF i under illumination k'. We also rank the corresponding characteristic times leading for example to $\tau_{ki} < \tau_{kj}$. Then we use the monoexponential fitting function $U \exp\left(-\frac{t}{\tau}\right) + W$ to the experimental fluorescence evolution I_F^k under illumination k in

the interval $[\tau_{kj}, 5\tau_{kj}]$ to evaluate whether RSF j is present. The lower bound of the interval is found to be the smallest value minimizing the possible impact of exponential functions associated with the shorter characteristic time τ_{ki} without significant detrimental effect on the determination of the longer characteristic time τ_{kj}. The procedure provides the prefactor U_{ka} and the characteristic time τ_{ka}, i.e. l_{ka}. The presence of RSF j is asserted if the 1-dimensional distance $d_{ja}^k = \mid l_{kj} - l_{ka} \mid$ is smaller than a well-defined cutoff distance d_c. The biexponential fitting function $U \exp\left(-\frac{t}{\tau}\right) + U_{ka} \exp\left(-\frac{t}{\tau_{ka}}\right) + W$ to I_F^k, with U_{ka} and τ_{ka} set at the values previously deduced, is used in the interval $[0, 5\tau_{ki}]$ to evaluate whether RSF i is present. The procedure provides the prefactor U_{kb} and the characteristic time τ_{kb}, i.e. l_{kb}. Similarly the presence of RSF i is asserted if $d_{ib}^k < d_c$. The fluorescence evolution is analyzed $m(m-1)/2$ times to conclude for all possible pairs, which is sufficient and may be redundant to determine if each RSF is present in the pixel.

The cutoff distance d_c does not anymore depend only on the uncertainty M on the determination of the kinetic fingerprint as for non colocalized RSFs but it also involves an error e on the determination of the characteristic times from applying the preceding fitting protocol. It becomes $d_c = M + e$. We previously estimated M in subsection A8.3 for experimentally relevant noise levels. When checking if the pair (i, j) is present in the pixel, the error e on the determination of the characteristic times τ_{ka} and τ_{kb} increases as the distance d_{ij}^k decreases. The method is as accurate as for non colocalized RSFs when the characteristic times of the two checked RSFs typically differ by an order of magnitude. An upper bound of e can be obtained by taking the lower bound $d_{\min}$ of d_{ij}^k in an optimized subset $s'(m)$. Hence the error e depends on the number m of considered RSFs in $s'(m)$.

To evaluate the dependence of e on m, we first implemented an analogous sorting algorithm as in section A8.2 to generate subsets of RSFs as distant as possible by computing the minimum distances $d_{\min} = \max_{s'(m)}(\min_{i,j}(d_{ij}^k))$ between pairs (i, j) for all subsets $s'(m)$ of m RSFs. This sorting protocol has been applied to RSFPs. Among the 22 studied RSFPs, only two RSFPs, **4** and **5**, are positive photoswitchers. The colocalization of positive and negative photoswitchers may blur the fluorescence signal. We therefore considered the 20 negative photoswitchers. The sorting results are given in Tab. A10 and Fig. A49.

In order to estimate e for the considered sorting of RSFPs, we analyzed a designed signal accounting for the fluorescence evolution of a pixel containing RSF i of characteristic time τ_{ki} and RSF j of characteristic time τ_{kj} under illumination k. We further assumed that the contribution of an RSF to the fluorescence intensity is adequately described by a monoexponential function and the two preexponential factors are equal. The fluorescence evolution was generated with an additive

Table A10: Optimized subsets $s'(m)$ of m RSFPs for $m = 2, ..., 20$ using the kinetic signature given in Tab. A4 and the minimum distance $d_{\min}$ between pairs.

m	$s'(m)$
2	(**2**,**9**)
3	(**6**,**8**,**9**)
4	(**3**,**9**,**15**,**19**)
5	(**3**,**9**,**10**,**15**,**19**)
6	(**1**,**3**,**6**,**10**,**16**,**19**)
7	(**3**,**6**,**9**,**10**,**14**,**16**,**19**)
8	(**1**,**3**,**6**,**9**,**10**,**12**,**17**,**22**)
9	(**1**,**2**,**3**,**6**,**9**,**10**,**12**,**15**,**19**)
10	(**2**,**3**,**6**,**9**,**10**,**12**,**14**,**15**,**18**,**22**)
11	(**1**,**2**,**3**,**6**,**9**,**10**,**12**,**15**,**18**,**19**,**22**)
12	(**2**,**3**,**6**,**9**,**10**,**12**,**13**,**14**,**15**,**18**,**19**,**22**)
13	(**2**,**3**,**6**,**9**,**10**,**12**,**13**,**14**,**15**,**16**,**18**,**19**,**22**)
14	(**1**,**2**,**3**,**6**,**9**,**10**,**12**,**13**,**15**,**16**,**18**,**19**,**21**,**22**)
15	(**1**,**2**,**3**,**6**,**9**,**10**,**12**,**13**,**14**,**15**,**16**,**18**,**19**,**21**,**22**)
16	(**1**,**2**,**3**,**6**,**9**,**10**,**12**,**13**,**14**,**15**,**16**,**18**,**19**,**20**,**21**,**22**)
17	(**1**,**2**,**3**,**6**,**7**,**9**,**10**,**12**,**13**,**14**,**15**,**16**,**18**,**19**,**20**,**21**,**22**)
18	(**1**,**2**,**6**,**7**,**8**,**9**,**10**,**11**,**12**,**13**,**14**,**15**,**16**,**18**,**19**,**20**,**21**,**22**)
19	(**1**,**2**,**6**,**7**,**8**,**9**,**10**,**11**,**12**,**13**,**14**,**15**,**16**,**17**,**18**,**19**,**20**,**21**,**22**)
20	(**1**,**2**,**3**,**6**,**7**,**8**,**9**,**10**,**11**,**12**,**13**,**14**,**15**,**16**,**17**,**18**,**19**,**20**,**21**,**22**)

Gaussian white noise $\epsilon\xi(t)$

$$I_F^k = \exp\left(-\frac{t}{\tau_{ki}}\right) + \exp\left(-\frac{t}{\tau_{kj}}\right) + \epsilon\xi(t) \tag{A80}$$

with $\tau_{ki} < \tau_{kj}$, $\langle\xi(t)\rangle = 0$, $\langle\xi(t)\xi(t')\rangle = \delta(t-t')$, and the value $\epsilon = 0.05$ is experimentally relevant.

We determined the mean values $\langle l_{ka}\rangle$, $\langle l_{kb}\rangle$ and the standard deviations σ_{ka}, σ_{kb} from a statistics over 1000 realizations of the noisy signal I_F^k for $l_{ki} = 0$ and $l_{kj} = d_{\min}$ where $d_{\min}$ is given in Fig. A49. The longer characteristic time τ_{kb} is more precisely determined than the shorter characteristic time τ_{ka} and the error is estimated by $e =\mid l_{ki} - \langle l_{ka}\rangle \mid +\sigma_{ka}$. Knowing that the minimum distance $d_{\min}$ depends on the optimized subset $s'(m)$, the error e depends on m. As shown in Fig. A49a, we found $e = 0.037m$ in the considered conditions. Using $M = 0.05$ as in subsection A8.3, we retrieved $d_c = 0.037m + 0.05$.

For all checked pairs (i', j') of an optimized subset $s'(m)$ and any j', the presence of a given RSFP i in pixel is unambiguously asserted if $d^k_{i'a} > d_c$ and $d^k_{i'b} > d_c$, $\forall i' \neq i$, and $d^k_{ia} < d_c$ and $d^k_{ib} < d_c$. Similarly the presence of a given colocalized pair (i, j) such that $\tau_{ki} < \tau_{kj}$ is asserted if $d^k_{i'b} > d_c$ and $d^k_{j'a} > d_c$, $\forall i' \neq i, j' \neq j$, and $d^k_{ib} < d_c$ and $d^k_{ja} < d_c$. Since the presence of a given RSFP i is checked in all trials involving it in a pair, the procedure may lead to distance values

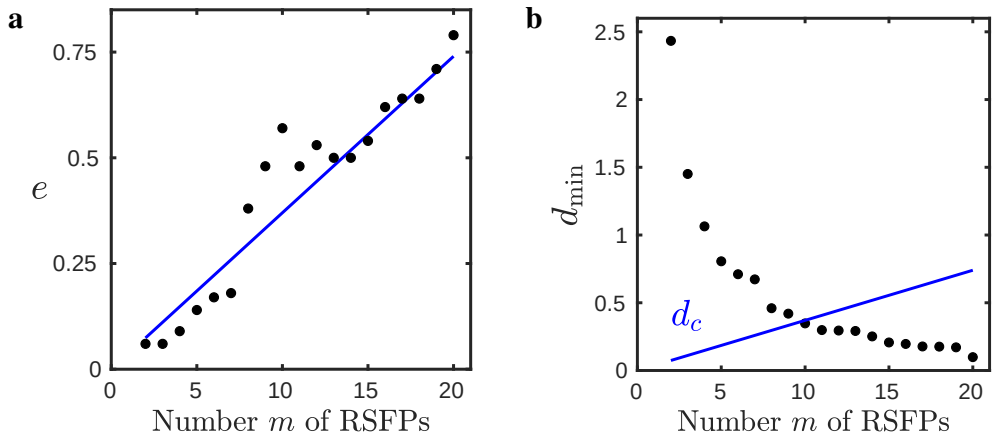

Figure A49: *The LIGHTNING discriminatory power of colocalized RSFPs*. **a**: Error e on the determination of each characteristic time of two colocalized RSFPs deduced from a designed noisy fluorescence evolution versus number m of possible RSFPs in the sample. The blue line $e = 0.037m$ fits the results. **b**: Minimum distance $d_{\min}$ between pairs for optimized subsets $s'(m)$ of RSFPs versus cardinal m of the subsets. The threshold $d_c = e + 0.05$ is deduced from the uncertainty on the determination of the characteristic time of a colocalized RSFP and a non colocalized RSFP. The condition $d_{\min} \geq d_c$ fixes the overall number of discriminatable colocalized RSFPs.

leading to an inconsistent conclusion. The conclusion of the presence of an RSFP is more likely to be undecided for a shorter characteristic time.

The presence of any pair of colocalized RSFPs in a sample containing m RSFPs can be asserted if $d_{\min}$ is larger than the cutoff distance d_c. As shown in Fig. A49b up to 9 RSFPs can be discriminated in these conditions.

A9 LIGHTNING for imaging

A9.1 Specifications

In this section, we specifically address the exploitation of LIGHTNING for imaging in wide-field microscopy. Several considerations have to be taken into account for optimal implementation:

- To get maximal temporal resolution, the acquisition duration should be minimal for each explored discriminative dimension (which generates an individual discriminating characteristic time);

- The sequential acquisitions to retrieve the LIGHTNING distance (which yields the overall set of characteristic times used to measure the distances d_{ij}) should be optimally integrated to obtain maximal fluorescence changes along each discriminative dimension in a minimal duration.

The illumination conditions in the regimes of low and high light intensities are obtained by tuning the light intensities I_1 and I_2 in order to make the changes of the fluorescence signal to be under kinetic control of the photochemical activation (see Fig. A50a) and of at least a thermal step (see Fig. A50b), respectively. In order to reach the highest temporal resolution, the intensities are fixed at their highest values in their respective regimes. Hence the light intensities $I_{1,low}$ and $I_{2,low}$ should remain below the cutoff light intensities I_1^c and I_2^c for all the imaged RSFPs (see Tab. A3) whereas $I_{1,high}$ and $I_{2,high}$ should be fixed at the highest accessible values in the high intensity one. We eventually retained the following illuminations: I_{low} ($I_{1,low} = 2$ ein.m^{-2}.s^{-1}), II_{low} ($I_{1,low} = 2$ ein.m^{-2}.s^{-1} and $I_{2,low} = 0.2$ ein.m^{-2}.s^{-1}), I_{high} ($I_{1,high} = 50$ ein.m^{-2}.s^{-1}), and II_{high} ($I_{1,high} = 50$ ein.m^{-2}.s^{-1} and $I_{2,high}$ =20 ein.m^{-2}.s^{-1}).

LIGHTNING implementation for fluorescence imaging of RSFPs necessitates the integration of the four conditions of illumination yielding the set $\left(\tau_{low}^{\mathrm{I}}, \tau_{low}^{\mathrm{II}}, \tau_{high}^{\mathrm{I}}, \tau_{high}^{\mathrm{II}}\right)$. To benefit from the largest amplitudes of fluorescence changes under the four conditions of illuminations, we propose to have initially all the RSFPs in their thermodynamically stable state and to apply the sequence 1) $\{I_{1,low}\}$, 2) $\{I_{1,low}$,$I_{2,low}\}$, 3) $\{I_{1,high}\}$, and 4) $\{I_{1,high}$,$I_{2,high}\}$ upon fixing the duration of acquisition along each discriminative dimension to five times the characteristic time of the slowest RSFP.

A9.2 Optimization of acquisition and data processing

LIGHTNING exploits the time response of the RSF fluorescence to several changes of illuminations. Up to this point, these illuminations have been assumed to be constant (e.g. constant light at $\lambda_1 = 488$ nm in illumination I, or constant lights at $\lambda_1 = 488$ nm and $\lambda_2 = 405$ nm in illumination II) with instantaneous reading out of the flux of emitted fluorescence photons. However, these conditions are not met in real imaging instruments: the emitted fluorescence photons are collected over a collecting time t_c fixed by the acquisition frequency of the detecting device. Whereas fast-responding detectors are compatible with acquisition frequencies higher than 1 MHz (like the photomultipliers used for acquiring the RSFP photochemical fingerprints), cameras can typically acquire images up to 1 kHz. More precisely, they collect photons over a frame time t_c down to 1 ms and the acquired frame is then transferred in a time t_d. The time delay t_d is much shorter than the frame acquisition time t_c. With RSFPs, the fluorescence signal does not significantly change at the t_d timescale so as to be neglected in the analysis of the time series of fluorescence used to extract the characteristic times. The sequential acquisition of the fluorescence signal over t_c-wide windows yielding discrete amounts of data points for LIGHTNING processing interrogates the optimization of acquisition and processing of data (see Fig. A50).

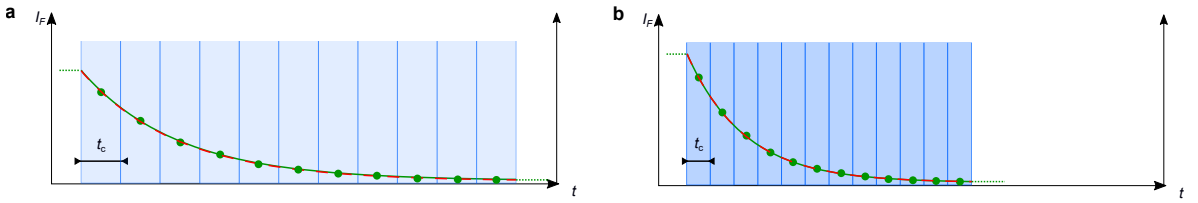

Figure A50: Illustration of LIGHTNING implementation for wide-field imaging of RSFPs. The illumination is maintained constant and the emitted photons are collected over successive time windows of width t_c. With a camera, the image built during t_c is then transferred in a time $t_d \ll t_c$ so as to be neglected in the figure. The time series of fluorescence signals (averaged over t_c) retraces the kinetics of the photoactivation step in a regime of low light intensity (**a**) whereas it integrates the kinetics of thermal steps in a regime of high light intensity (**b**). Dashed green line: Time evolution of the concentrations in the bright states of the RSFP; Green disks: Collected fluorescence signals over t_c; Dashed red line: Time profile of the fluorescence signal extracted from analyzing the fluorescence evolution upon applying illumination and used to extract the characteristic times along each discriminative dimension. Illumination I of RSFPs exhibiting negative photochromisms at $\lambda_1 = 488$ nm is used for illustration.

To address this issue, we simulated the effect of noise on a typical fluorescence evolution and studied the influence of the collecting time t_c on the determination of the characteristic time. The product νt_c, where ν is the number of analyzed fluorescence data, was constant and equal to the considered time window for extracting the characteristic time. Hence the smaller t_c, the wider the fluctuation of the number of collected photons. More precisely, noise varies as $1/\sqrt{t_c}$, i.e. $\sqrt{\nu}$. We considered a monoexponential decay $I_F(t) = \exp(-t/\tau_F)$ where $\tau_F = 1$ in arbitrary units (a. u.) with an additive Gaussian white noise $\epsilon\xi(t)$ with $\epsilon = 0.0032\sqrt{\nu}$, $\langle\xi(t)\rangle = 0$, and $\langle\xi(t)\xi(t')\rangle = \delta(t - t')$, which was representative of the experimental noise properties for a concentration of 20 μM when using the photomultiplier detecting system. 1000 decays have been generated over a time window of 10 a. u. for each t_c value. Typically we analyzed $\nu = 1001$ data points for $t_c = 0.01$ and $\nu = 5$ data points for $t_c = 2$. The characteristic times were determined using both a monoexponential reduction over a time window of 5 a. u. and a spectrum of relaxation times over 10 a. u. The variations of the mean value $\langle l\rangle$ and the standard deviation σ_l of the decimal logarithm of the characteristic time with respect to the number ν of analyzed data points are given in Fig. A51 for the two methods of data processing.

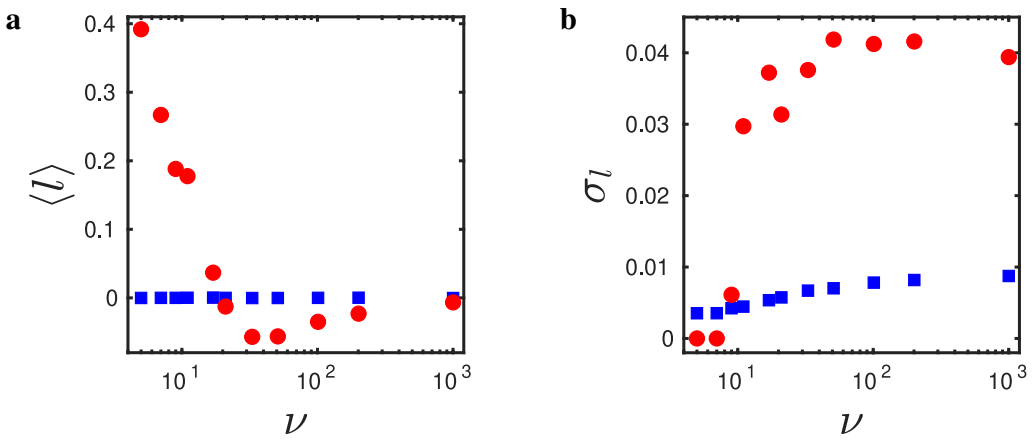

Figure A51: Mean values $\langle l \rangle = \langle \log(\tau) \rangle$ (**a**) and standard deviations σ_l (**b**) of the decimal logarithm of the characteristic times τ versus amount ν of data points used to sample 1000 noisy exponential decays $\exp(-t/\tau_F) + \epsilon\xi(t)$ over the same time window. $\xi(t)$ is a Gaussian white noise of zero mean and unit variance, $\epsilon = 0.0032\sqrt{\nu}$, and $\tau_F = 1$ a. u. The blue squares give the results of a monoexponential reduction and the red circles are deduced from a spectrum approach.

In both cases, the effect of noise remains small and the standard deviation σ_l is smaller than 0.01 using a monoexponential reduction and smaller than 0.04 using the spectrum approach. The results provided by the fitting approach are excellent. The mean value $\langle l \rangle$ agrees with $\log(\tau_F) = 0$ to within 0.01% for all ν. The standard deviation σ_l even decreases as the amount ν of analyzed data decreases due to the decrease of noise amplitude. Whereas the fitting approach leads to continuous values of l, the maximum of the spectrum is only found in discrete values of l. For more than 11 analyzed data points, the spectrum approach provides a good evaluation of the characteristic time with a satisfying accuracy. For $\nu < 11$ searching for the maximum of the spectrum always leads to the same value as l because the time step in logarithmic units is larger than the noise-induced uncertainty about l. Hence, the standard deviation σ_l vanishes but the value of $\langle l \rangle$ is far from $\log(\tau_F) = 0$. Due to the large number of analyzed data points, analogous results are obtained when considering a logarithmic increase of t_c to sample fluorescence evolution.

From this series of simulations, we concluded that LIGHTNING should preferentially exploit a monoexponential reduction instead of the spectrum approach and favor a lower amount of data points with individual lower level of noise to analyze the data over a time window of five times a rough evaluation of the characteristic time.

A9.3 LIGHTNING photon budget and duration of acquisition

In this subsection, we address the photon budget and the acquisition duration of LIGHTNING, which determines its signal-to-noise ratio and temporal resolution respectively.

Computation We computed the number of detected photons emitted from a pixel of volume V containing a RSF at a variable concentration $C(t)$ under illuminations i =I, II. For the sake of simplicity we considered that only excitation of intensity I_1 at the wavelength λ_1 leads to fluorescence emission and assumed the following monoexponential decay for the concentration $C^{\mathrm{I}}(t) = C_{tot}\exp(-t/\tau^{\mathrm{I}})$ for illumination I and $C^{\mathrm{II}}(t) = C_{tot}\left(1-\exp(-t/\tau^{\mathrm{II}})\right)$ for illumination II. The brightness can be written in the form $Q = \epsilon(\lambda_1)\Phi_F$ where $\epsilon(\lambda_1)$ is the molar absorption coefficient at the wavelength λ_1 and Φ_F the quantum yield of RSF fluorescence. The collection factor of the objective is denoted by ρ. To derive orders of magnitude, we adopted $C_{tot} = 1$ μM, a cubic pixel of length 0.3 μm and $\rho = 0.25$. We chose RSFPs **1** and **2** as typical examples of proteins associated with small and large cross sections of photoisomerization, respectively. The absorption coefficients and the fluorescence quantum yields of RSFPs **1** and **2** are given in Tab. A1, the cross sections in Tab. A3, and the values of the characteristic times τ^{I}_{low}, τ^{II}_{low}, τ^{I}_{high}, and $\tau^{\mathrm{II}}_{high}$ and the corresponding intensities I_1 in Tab. A4.

In the case of continuous illumination, the numbers of photons $n^i_{h\nu}$ detected during five times the characteristic time τ^{i} for illuminations i =I, II are obtained by integrating the fluorescence intensity between 0 and $5\tau^{\mathrm{i}}$ leading to

$$n^{\mathrm{I}}_{h\nu} = \epsilon(\lambda_1)\Phi_F I_1 \rho V C_{tot}\tau^{\mathrm{I}}\left(1-e^{-5}\right) \tag{A81}$$

$$n^{\mathrm{II}}_{h\nu} = \epsilon(\lambda_1)\Phi_F I_1 \rho V C_{tot}\tau^{\mathrm{II}}\left(4+e^{-5}\right) \tag{A82}$$

For given illumination and detection conditions, the number of detected photons is about four times larger during a fluorescence increase than a decay. We determined the number of detected photons during fluorescence evolution using Eqs.(A81,A82). The results are given in Tabs. A11 and A12.

Table A11: Evaluation of the number of detected photons $n^i_{h\nu}$ for RSFP **1** under the continuous illumination conditions i = I_{low}, II_{low}, I_{high}, II_{high} at intensity I_1 at the wavelength $\lambda_1 = 488$ nm. τ^{i} is the characteristic time associated with fluorescence evolution under illuminations i. The parameters values are $C_{tot} = 1$ μM, $V = 0.027$ μm^3, $\rho = 0.25$, $\epsilon(\lambda_1) = 80000$ M^{-1}.cm^{-1}, $\Phi_F = 0.8$.

Illumination	I_1	τ^{i}	$n^i_{h\nu}$
	(ein.m^{-2}.s^{-1})	(ms)	
I_{low}	2	140	7 236
II_{low}	2	31	6 464
I_{high}	200	4.5	23 260
II_{high}	200	0.18	3 754

Discussion

Table A12: Evaluation of the number of detected photons $n^i_{h\nu}$ for RSFP **2** under the continuous illumination conditions $i = \mathrm{I}_{low}$, II_{low}, I_{high}, II_{high} at intensity I_1 at the wavelength $\lambda_1 = 488$ nm. τ^{i} is the characteristic time associated with fluorescence evolution under illuminations i. The parameters values are $C_{tot} = 1$ μM, $V = 0.027$ μm^3, $\rho = 0.25$, $\epsilon(\lambda_1) = 75000$ M^{-1}.cm^{-1}, $\Phi_F = 0.2$.

Illumination	I_1	τ^{i}	$n^i_{h\nu}$
	(ein.m^{-2}.s^{-1})	(ms)	
I_{low}	2	2.2	27
II_{low}	2	25	1 222
I_{high}	200	0.33	400
II_{high}	200	0.077	376

Photon budget The signal-to-noise ratio when recording the RSF fluorescence evolution upon successive illuminations affects the cutoff distance d_c. In order to evaluate the regime of RSF concentration down to which LIGHTNING would be relevant for effective highly multiplexed fluorescence imaging, we estimated the number of detected photons for experimentally relevant conditions. We considered two representative RSFPs associated with small and large characteristic times. Our data predict that the typical numbers of photons extracted from a (0.3 μm)^3-pixel at micromolar concentration for each characteristic time is about 100 and 5000 for the fast and slow RSFPs, respectively. This number of detected photons with LIGHTNING is essentially similar to the order of magnitude obtained with a non-photoswitchable fluorophore exhibiting similar photophysical features. Indeed, the number of detected photons is reduced by a factor of 5 in the case of illumination I and a factor of 5/4 in the case of illumination II. More photons are detected for RSFPs associated with large values of the product $I_1\tau^{\mathrm{i}}$, i.e. small cross sections such as for RSFP **1**.

Acquisition duration The duration of the experiments allowing us to determine the kinetic fingerprint of an RSFP for continuous illumination is equal to five times the sum of the four characteristic times. According to Tabs. A11 and A12, we obtain 878 ms for RSFP **1** and 138 ms for RSFP **2**. Hence, in the optimization of the choice of an RSFP, the number of detected photons is balanced by the duration of the acquisition.

Beyond the preceding derivation which demonstrates that LIGHTNING should enable real time imaging at acquisition frequency compatible with observation of many important biological phenomena, it is worth making explicit that LIGHTNING significantly expands dynamic contrast. Indeed the time domain has been already proposed to complement the spectral domain in order to improve the multiplexing capabilities in fluorescence imaging.[13,31–38] Yet the reported imaging protocols exploiting dynamic contrast cannot favorably respond to the growing demand of quantitative

biology in simultaneously imaging tens of chemical species at an acceptable frequency of image acquisition. Indeed they exploit only one relaxation time of reversible light excitation for dynamic contrast. Hence, to enable their reliable discrimination without any subtraction nor deconvolution, two fluorescent labels must typically exhibit relaxation times of their signal differing by a factor of ten. Distinguishing N labels would imply that their dynamics spread over a $10^N\tau_{min}$-wide time window, where τ_{min} designates the relaxation time of the RSF responding the fastest to light variation. Consequently $T = 10^N\tau_{min}$ fixes the duration of an image acquisition. Hence, as soon as N would become large enough (e.g. 10, a number which has been reached in the present series of experiments), T would become excessively long and the frequency of image acquisition would not be anymore compatible with the observation of living biological samples, not to mention that it would be highly demanding to find a library of labels with such a broad range of relaxation times. Taking for illustration a library of 10 distinguishable RSFs and τ_{min} in the 1 ms range as presently evaluated with RSFPs (see Tab. A4) yields $T \simeq 10^7$ s, which is excessively long.

LIGHTNING introduces an innovative and totally unprecedented approach to overcome the preceding limitation. By adopting labels engaged in rich photocycles which can be probed by applying illuminations in various regimes of light intensities, LIGHTNING does not anymore exploit one but $n > 1$ ($n = 4$ in the present implementation) characteristic times for dynamic contrast. Discrimination between two labels still requires characteristic times to differ by a factor of ten but in at least one among the n discriminative dimensions. Hence the overall discriminative window necessary to image N labels can be shared among the n dimensions so as to possibly reduce to $10^{N/n}$ the width of the time windows along each discriminative dimension. Overall acquisition time now becomes $T = \sum_{k=1}^{n} 10^{N/n}\tau_{min,k}$ where $\tau_{min,k}$ designates the characteristic time of the RSF responding at the fastest to light variation along the dimension k. By assuming that $\tau_{min,k}$ does not depend on the discriminative dimension, using n dimensions for discrimination makes possible to increase the frequency of image acquisition by a factor of $10^{N(1-1/n)}/n$. Taking again a library of 10 distinguishable RSFs with $n = 4$ dimensions and $\tau_{min,k}$ = 1 ms for all k, one has $T \simeq 1.3$ s and an increase of the frequency of image acquisition by an impressive factor of 8×10^6.

References

[1] H. Chang, M. Zhang, W. Ji, J. Chen, Y. Zhang, B. Liu, J. Lu, J. Zhang, P. Xu, and T. Xu. A unique series of reversibly switchable fluorescent proteins with beneficial properties for various applications. *Proc. Natl. Acad. Sci. U. S. A.*, 109:4455–4460.

[2] Xi Zhang, Xuanze Chen, Zhiping Zeng, Mingshu Zhang, Yujie Sun, Peng Xi, Jianxin Peng,

and Pingyong Xu. Development of a reversibly switchable fluorescent protein for super-resolution optical fluctuation imaging (sofi). *ACS Nano*, 9(3):2659–2667, 2015. PMID: 25695314.

[3] Xi Zhang, Mingshu Zhang, Dong Li, Wenting He, Jianxin Peng, Eric Betzig, and Pingyong Xu. Highly photostable, reversibly photoswitchable fluorescent protein with high contrast ratio for live-cell superresolution microscopy. *Proc. Nat. Acad. Sci.*, 113:10364–10369, 2016.

[4] Mingshu Zhang, Hao Chang, Yongdeng Zhang, Junwei Yu, Lijie Wu, Wei Ji, Juanjuan Chen, Bei Liu, Jingze Lu, Yingfang Liu, et al. Rational design of true monomeric and bright photoactivatable fluorescent proteins. *Nature methods*, 9(7):727–729, 2012.

[5] D. Bourgeois and V. Adam. Reversible photoswitching in fluorescent proteins : A mechanistic view. *IUBMB Life*, 64:482–491, 2012.

[6] Mariam El Khatib, Alexandre Martins, Dominique Bourgeois, Jacques-Philippe Colletier, and Virgile Adam. Rational design of ultrastable and reversibly photoswitchable fluorescent proteins for super-resolution imaging of the bacterial periplasm. *Scientific Reports*, 6:18459, 2016.

[7] R. Ando, H. Mizuno, and A. Miyawaki. Regulated fast nucleocytoplasmic shuttling observed by reversible protein highlighting. *Science*, 306:1370–1373, 2004.

[8] A. C. Stiel, S. Trowitzsch, G. Weber, M. Andresen, C. Eggeling, S. W. Hell, S. Jakobs, and M. C. Wahl. 1.8 å bright-state structure of the reversibly switchable fluorescent protein Dronpa guides the generation of fast switching variants. *Biochem. J.*, 402:35–42, 2007.

[9] R. Ando, C. Flors, H. Mizuno, J. Hofkens, and A. Miyawaki. Highlighted generation of fluorescence signals using simultaneous two-color irradiation on Dronpa mutants. *Biophys. J.*, 92:L97 – L99, 2007.

[10] D. K. Tiwari, Y. Arai, M. Yamanaka, T. Matsuda, M. Agetsuma, M. Nakano, K. Fujita, and T. Nagai. A fast-and positively photoswitchable fluorescent protein for ultralow-laser-power RESOLFT nanoscopy. *Nat. Meth.*, 12:515–518, 2015.

[11] M. Andresen, A. C. Stiel, J. Follig, D. Wenzel, A. Schoenle, A. Egner, C. Eggeling, S. W. Hell, and S. Jakobs. Photoswitchable fluorescent proteins enable monochromatic multilabel imaging and dual color fluorescence nanoscopy. *Nat. Biotech.*, 26:1035–1040, 2008.

[12] T. Grotjohann, I. Testa, M. Reuss, T. Brakemann, C. Eggeling, S. W. Hell, and S. Jakobs. rsEGFP2 enables fast RESOLFT nanoscopy of living cells. *ELife*, 1, 2012.

[13] J. Quérard, R. Zhang, Z. Kelemen, M.-A. Plamont, X. Xie, R. Chouket, I. Roemgens, Y. Korepina, S. Albright, E. Ipendey, M. Volovitch, H. L. Sladitschek, P. Neveu, L. Gissot, A. Gautier, J.-D. Faure, V. Croquette, T. Le Saux, and L. Jullien. Resonant out-of-phase fluorescence microscopy and remote imaging overcome spectral limitations. *Nat. Comm.*, 8:969, 2017.

[14] D. Summers and J. M. W. Scott. Systems of first-order chemical reactions. *Mathl. Comput. Modelling*, 10:901–909, 1988.

[15] A. A. Istratov and O. F. Vyvenko. Exponential analysis in physical phenomena. *Rev. Sci. Instrum.*, 70:1233–1257, 1999.

[16] G. L. Miller, J. V. Ramirez, and D. A. H. Robinson. A correlation method for semiconductor transient signal measurements. *J. Appl. Phys.*, 46:2638–2644, 1975.

[17] S. W. Provencher. An eigenfunction expansion method for the analysis of exponential decay curves. *J. Chem. Phys.*, 64:2772–2777, 1976.

[18] P. M. Henry, J. M. Meese, J. W. Farmer, and C. D. Lamp. Frequency-scanned deep-level transient spectroscopy. *J. Appl. Phys.*, 57:628–630, 1985.

[19] J. Ferenczi, J. Boda, and T. Pavelka. Isothermal frequency scan dlts. *Phys. Status Solidi A*, 94:K119–K124, 1986.

[20] L. Stuchlikova, L. Harmatha, V. Nagl, and M. Gazi. Determination of deep-level parameters by isothermal deep-level transient spectroscopy with optical excitation. *Phys. Status Solidi A*, 138:K241–K248, 1993.

[21] A. A. Istratov. The resolution limit of traditional correlation functions for deep-level transient spectroscopy. *Rev. Sci. Instrum.*, 68:3861–3865, 1997.

[22] A. A. Istratov. New correlation procedure for rthe improvement of resolution of deep-level transient spectroscopy of semiconductors. *J. Appl. Phys.*, 82:2965–2968, 1997.

[23] J Crank. *The Mathematics of Diffusion (2nd edn)*. Oxford University Press, Oxford, 1975.

[24] P. G. Wilmann, K. Turcic, J. M. Battad, M. C.J. Wilce, R. J. Devenish, M. Prescott, and J. Rossjohn. The 1.7 $\AA$ crystal structure of Dronpa : A photoswitchable green fluorescent protein. *J. Mol. Biol.*, 364:213 – 224, 2006.

[25] N. Coquelle, M. Sliwa, J. Woodhouse, G. Schiro, V. Adam, A. Aquila, T. R. M. Barends, S. Boutet, M. Byrdin, S. Carbajo, E. De la Mora, R. B. Doak, M. Feliks, F. Fieschi, L. Foucar, V Guillon, M. Hilpert, M. S. Hunter, S. Jakobs, J. E. Koglin, G. Kovacsova, T. J. Lane, B. L, M. Liang, K. Nass, J. Ridard, J. S. Robinson, C. M. Roome, Ruckebusch C., M. Seaberg, M. Thepaut, M. Cammarata, I. Demachy, M. Field, R. L. Shoeman, D. Bourgeois, J. P. Colletier, I. Schlichting, and M. Weik. Chromophore twisting in the excited state of a photoswitchable fluorescent protein captured by time-resolved serial femtosecond crystallography. *Nat. Chem.*, 10:31–37, 2017.

[26] Christopher Hutchison, Violeta Cordon-Preciado, Rhodri Morgan, Takanori Nakane, Josie Ferreira, Gabriel Dorlhiac, Alvaro Sanchez-Gonzalez, Allan Johnson, Ann Fitzpatrick, Clyde Fare, et al. X-ray free electron laser determination of crystal structures of dark and light states of a reversibly photoswitching fluorescent protein at room temperature. *International journal of molecular sciences*, 18(9):1918, 2017.

[27] M. Andresen, A. C. Stiel, S. Trowitzsch, G. Weber, C. Eggeling, M. C. Wahl, S. W. Hell, and S. Jakobs. Structural basis for reversible photoswitching in Dronpa. *Proc. Natl. Acad. Sci. U. S. A.*, 104:13005–13009, 2007.

[28] D. Yadav, F. Lacombat, N. Dozova, F. Rappaport, P. Plaza, and A. Espagne. Real-time monitoring of chromophore isomerization and deprotonation during the photoactivation of the fluorescent protein dronpa. *J. Phys. Chem. B*, 119:2404–2414, 2015.

[29] J. P. Colletier, M. Sliwa, F. X. Gallat, M. Sugahara, V. Guillon, G. Schiro, N. Coquelle, J. Woodhouse, L. Roux, G. Gotthard, A. Royant, L. M. Uriarte, C. Ruckebusch, Y. Joti, M. Byrdin, E. Mizohata, E. Nango, T. Tanaka, K. Tono, M. Yabashi, V. Adam, M. Cammarata, I. Schlichting, D. Bourgeois, and M. Weik. Serial femtosecond crystallography and ultrafast absorption spectroscopy of the photoswitchable fluorescent protein irisfp. *J. Phys. Chem. Lett.*, 7:882–887, 2016.

[30] M. M. Warren, M. Kaucikas, A. Fitzpatrick, P. Champion, J. T. Sage, and J. J. van Thor. Ground-state proton transfer in the photoswitching reactions of the fluorescent protein dronpa. *Nat. Comm.*, 4:1461, 2013.

[31] J. R. Lakowicz, H. Szmacinski, K. Nowaczyk, K. W. Berndt, and M. L. Johnson. Fluorescence lifetime imaging. *Anal. Biochem.*, 202:316–330, 1992.

[32] P. I. Bastiaens and A. Squire. Fluorescence lifetime imaging microscopy: spatial resolution of biochemical processes in the cell. *Trends Cell Biol.*, 9:48–52, 1999.

[33] G. Marriott, S. Mao, T. Sakata, J. Ran, D. K. Jackson, C. Petchprayoon, T. J. Gomez, E. Warp, O. Tulyathan, H. L. Aaron, E. Y. Isacoff, and Y. Yan. Optical lock-in detection imaging microscopy for contrast-enhanced imaging in living cells. *Proc. Natl. Acad. Sci. U. S. A.*, 105:17789–17794, 2008.

[34] C. I. Richards, J.-C. Hsiang, and R. M. Dickson. Synchronously amplified fluorescence image recovery (SAFIRe). *J. Phys. Chem. B*, 114:660–665, 2010.

[35] J.-C. Hsiang, A. E. Jablonski, and R. M. Dickson. Optically modulated fluorescence bioimaging: Visualizing obscured fluorophores in high background. *Acc. Chem. Res.*, 47:1545–1554, 2014.

[36] J. Widengren. Fluorescence-based transient state monitoring for biomolecular spectroscopy and imaging. *J. R. Soc. Interface*, 7:1135–1144, 2010.

[37] J. Quérard, T.-Z. Markus, M.-A. Plamont, C. Gauron, P. Wang, A. Espagne, M. Volovitch, S. Vriz, V. Croquette, A. Gautier, T. Le Saux, and L. Jullien. Photoswitching kinetics and phase-sensitive detection add discriminative dimensions for selective fluorescence imaging. *Angew. Chem. Int. Ed.*, 127:2671–2675, 2015.

[38] R. Zhang, R. Chouket, M.-A. Plamont, Z. Kelemen, A. Espagne, A. G. Tebo, A. Gautier, L. Gissot, J.-D. Faure, L. Jullien, V. Croquette, and T. Le Saux. Macroscale fluorescence imaging against autofluorescence under ambient light. *Light: Science & Applications*, 7:97, 2018.

Appendix B

Supporting information of the manuscript: Resonances of reversibly photoactivatable labels responding to high amplitude light modulation for selective analysis and imaging (HIGHLIGHT)

B1 Kinetic analysis of the two-state model

B1.1 A two-state model with external forcing

The dynamical behavior of a reversibly photoswitchable label is assumed to be reliably described by the two-state exchange

$$C_1 \underset{k_2}{\overset{k_1}{\rightleftharpoons}} C_2 \tag{B1}$$

where the state C_1 is photochemically converted into the state C_2 under illumination I_1 at the wavelength λ_1. The conversion of C_2 into C_1 occurs under illumination I_2 at the wavelength λ_2 or by a slower thermally-driven process which is neglected if I_2 does not vanish. Introducing a light modulation at the wavelength λ_i of mean value I_i^0 and large amplitude α_i of order 1 at the angular frequency ω according to

$$I_i = I_i^0 \left[1 + \alpha_i \sin(\omega t)\right] \tag{B2}$$

and assuming that the photochemical rate constants are proportional to light intensity yields

$$k_i = k_i^0 \left[1 + \alpha_i \sin(\omega t)\right] \tag{B3}$$

for $i = 1, 2$.

Two cases are considered. The case (i) associated with a single modulation corresponds to either case (i1) associated with the modulation of I_1, i.e. $\alpha_1 = \alpha$ and $\alpha_2 = 0$, or case (i2) associated with the modulation of I_2, i.e. $\alpha_1 = 0$ and $\alpha_2 = \alpha$. In the following we illustrate case (i1). By symmetry case (i2) is deduced from case (i1) by exchanging the intensities I_1 and I_2, i.e. the rate constants k_1 and k_2, and exchanging the concentrations C_1 and C_2. The case (ii) is associated with two modulations in antiphase, i.e. $\alpha_1 = \alpha$ and $\alpha_2 = -\alpha$.

The evolution of the concentration C_1 is given by

$$\frac{\mathrm{d}C_1}{\mathrm{d}t} = -(k_1 + k_2) C_1 + k_2 C_{tot} \tag{B4}$$

where the total concentration obeys

$$C_{tot} = C_1 + C_2 \tag{B5}$$

We define the dimensionless deviation

$$c = \frac{C_1^0 - C_1}{C_{tot}} \tag{B6}$$

to the steady-state $C_1^0 = C_{tot}/(1 + K^0)$ with

$$K^0 = \frac{k_1^0}{k_2^0}. \tag{B7}$$

Using Eqs.(B4,B6) we find in case (i1)

$$\tau^0 \frac{\mathrm{d}c}{\mathrm{d}t} = -c + \alpha \left[\frac{K^0}{(1+K^0)^2} - \frac{K^0}{1+K^0} c \right] \sin(\omega t) \tag{B8}$$

and in case (ii)

$$\tau^0 \frac{\mathrm{d}c}{\mathrm{d}t} = -c + \alpha \left[\frac{2K^0}{(1+K^0)^2} - \frac{K^0-1}{1+K^0} c \right] \sin(\omega t) \tag{B9}$$

The description of the kinetics of a photoswitchable system under modulated illumination enters into the framework of forced dynamical systems. Many applications are found in the domain of electrical circuits and micro-electral-mechanical systems (MEMS).[1,2]

Beyond the relaxation time

$$\tau^0 = \frac{1}{k_1^0 + k_2^0} \tag{B10}$$

the system enters into a permanent regime in which the deviation $C = cC_{\mathrm{tot}}$ to the steady state is periodic and expressed using a Fourier series

$$C = a_0 + \sum_{n=1}^{+\infty} \left[a_n \cos(n\omega t) + b_n \sin(n\omega t) \right] \tag{B11}$$

where a_0 is the mean value of c and a_n and b_n designate the quadrature and in-phase amplitudes of concentration oscillation of the n-th harmonics.

B1.2 Single modulation at the wavelength λ_1 - case (i1) - or λ_2 - case (i2)

B1.2.1 Analytical derivation of the amplitudes of concentration oscillation

Substituting for c from Eq.(B11) into Eq.(B8), we cancel the terms in front of the sine and cosine at each order n and find the following linear equations

$$a_0 = -\frac{\alpha K^0}{2(1+K^0)} b_1 \tag{B12}$$

$$a_1 \theta = b_1 - \frac{\alpha K^0 C_{\mathrm{tot}}}{(1+K^0)^2} - \frac{\alpha K^0}{2(1+K^0)} (a_2 - 2a_0) \tag{B13}$$

$$b_1 \theta = -a_1 - \frac{\alpha K^0}{2(1+K^0)} b_2 \tag{B14}$$

$$a_n n\theta = b_n - \frac{\alpha K^0}{2(1+K^0)} (a_{n+1} - a_{n-1}) \quad \text{for} \quad n > 1 \tag{B15}$$

$$b_n n\theta = -a_n - \frac{\alpha K^0}{2(1+K^0)} (b_{n+1} - b_{n-1}) \quad \text{for} \quad n > 1 \tag{B16}$$

where

$$\theta = \omega \tau^0 \tag{B17}$$

The Fourier amplitudes a_n and b_n scale as α^n for $n \geq 1$. At leading order in α, the recurrence equations given in Eqs.(B12-B16) yield

$$a_0 \simeq -\alpha \frac{K^0}{2(1+K^0)} b_1 \tag{B18}$$

$$a_1 \simeq -\alpha \frac{K^0}{(1+K^0)^2} \frac{\theta}{1+\theta^2} C_{\text{tot}} \tag{B19}$$

$$b_1 \simeq \alpha \frac{K^0}{(1+K^0)^2} \frac{1}{1+\theta^2} C_{\text{tot}} \tag{B20}$$

$$a_n \simeq \alpha \frac{K^0}{2(1+K^0)(1+n^2\theta^2)} \left(n\theta a_{n-1} + b_{n-1}\right) \quad \text{for} \quad n > 1 \tag{B21}$$

$$b_n \simeq -\alpha \frac{K^0}{2(1+K^0)(1+n^2\theta^2)} \left(a_{n-1} - n\theta b_{n-1}\right) \quad \text{for} \quad n > 1 \tag{B22}$$

The explicit expressions of the amplitudes of concentration oscillation up to the fourth order are

$$a_0 \simeq -\alpha^2 \frac{(K^0)^2}{2(1+K^0)^3} \frac{1}{1+\theta^2} C_{\text{tot}} \tag{B23}$$

$$a_2 \simeq \alpha^2 \frac{(K^0)^2}{2(1+K^0)^3} \frac{1-2\theta^2}{(1+\theta^2)(1+4\theta^2)} C_{\text{tot}} \tag{B24}$$

$$b_2 \simeq \alpha^2 \frac{(K^0)^2}{2(1+K^0)^3} \frac{3\theta}{(1+\theta^2)(1+4\theta^2)} C_{\text{tot}} \tag{B25}$$

$$a_3 \simeq \alpha^3 \frac{(K^0)^3}{2^2(1+K^0)^4} \frac{6\theta(1-\theta^2)}{(1+\theta^2)(1+4\theta^2)(1+9\theta^2)} C_{\text{tot}} \tag{B26}$$

$$b_3 \simeq -\alpha^3 \frac{(K^0)^3}{2^2(1+K^0)^4} \frac{1-11\theta^2}{(1+\theta^2)(1+4\theta^2)(1+9\theta^2)} C_{\text{tot}} \tag{B27}$$

$$a_4 \simeq -\alpha^4 \frac{(K^0)^4}{2^3(1+K^0)^5} \frac{1-35\theta+24\theta^2}{(1+\theta^2)(1+4\theta^2)(1+9\theta^2)(1+16\theta^2)} C_{\text{tot}} \tag{B28}$$

$$b_4 \simeq -\alpha^4 \frac{(K^0)^4}{2^3(1+K^0)^5} \frac{10\theta(1-5\theta^2)}{(1+\theta^2)(1+4\theta^2)(1+9\theta^2)(1+16\theta^2)} C_{\text{tot}} \tag{B29}$$

with a_1 and b_1 given in Eqs.(B19,B20).

The amplitudes of concentration oscillation depend on two parameters, the equilibrium constant K^0 and the scaled angular frequency θ. Assuming that, for a given order $n-1$, we have

$$a_{n-1} = \alpha^{n-1} \frac{(K^0)^{n-1}}{2^{n-1}(1+K^0)^n} \frac{f_{n-1}(\theta)}{\Pi_{k=1}^{n-1}(1+k^2\theta^2)} C_{\text{tot}} \tag{B30}$$

$$b_{n-1} = \alpha^{n-1} \frac{(K^0)^{n-1}}{2^{n-1}(1+K^0)^n} \frac{g_{n-1}(\theta)}{\Pi_{k=1}^{n-1}(1+k^2\theta^2)} C_{\text{tot}} \tag{B31}$$

where $f_{n-1}(\theta)$ and $g_{n-1}(\theta)$ are polynomial functions independent of K^0 , we use Eqs.(B21,B22) to show that Eqs.(B30,B31) are valid at order n and consequently at all order. In order to determine the extrema of the amplitudes of concentration oscillation, we first derive Eqs.(B30,B31) with

respect to K^0 and obtain the resonant value $K_n^{0R} = n$ for the equilibrium constant at order n. The polynomial functions $f_{2k+1}(\theta)$ associated with odd orders and $g_{2k}(\theta)$ associated with even orders vanish for $\theta = 0$ contrary to $f_{2k}(\theta)$ and $g_{2k+1}(\theta)$. The amplitudes of concentration oscillation a_{2k+1} and b_{2k} display a pronounced extremum contrary to a_{2k} and b_{2k+1} which behave as a low-pass filter with respect to θ. The resonant value θ_n^R of the scaled angular frequency is close to $1/(2n-1)$.

B1.2.2 Numerical derivation of the amplitudes of concentration oscillation

Equations (B12-B16) involve an infinite number of Fourier amplitudes and their numerical solution requires a truncation. We studied the convergence of the solution of the four first orders using truncation at increasing values of n. Considering the Fourier amplitudes up to $n = 5$ is enough to observe the desired convergence. The resonances shown in Fig. B1 are associated with the values given in Tab. B1.

The amplitudes of concentration oscillation with extrema do not have the same sign, a_1 and b_4 being negative and b_2 and a_3 positive. The greater the order, the less symmetric the resonance peak and the smaller its width at half maximum. For a large modulation of light excitation $\alpha = 1$, the value of the amplitudes at the resonance decrease by less than a factor of 2 as the order n increases. The resonant values K_n^{0R} of the equilibrium constant increase with the order n whereas the resonant values θ_n^R of the scaled angular frequency decrease. The analytical expressions underestimate the peak displacement as the order changes and they overestimate the decrease of the amplitude at the resonance and the width at half maximum.

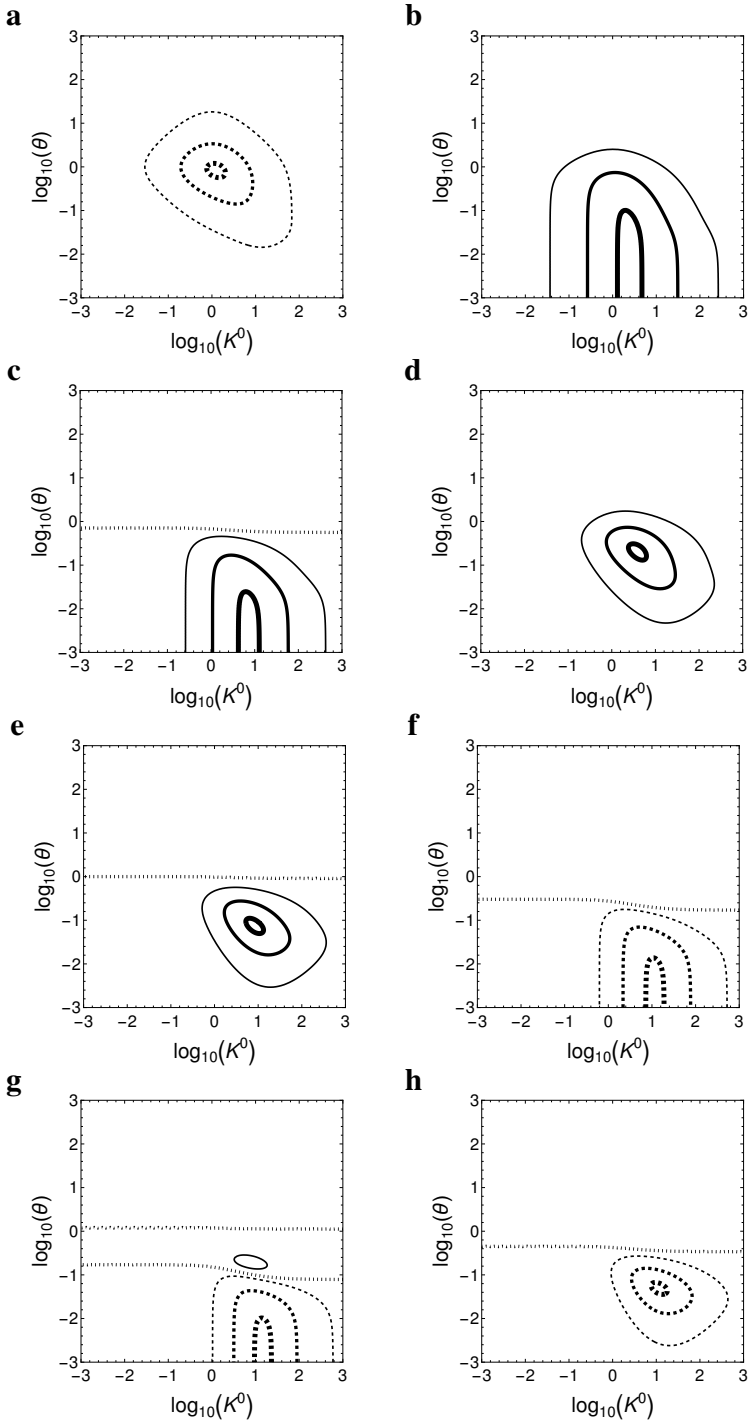

Figure B1: Amplitudes of concentration oscillation driven by single modulation at the wavelength λ_1 (case (i1)) or λ_2 (case (i2)) and of fluorescence oscillation driven by single modulation at the wavelength λ_2 (case (i2)) deduced from the numerical solutions of Eqs.(B12-B16) truncated at the fifth order for $\alpha = 1$. (a): a_1, (b): b_1, (c): a_2, (d): b_2, (e): a_3, (f): b_3, (g): a_4, (h): b_4. The parameter values for which the amplitudes are equal to 0 are represented by a dotted line. The other contour lines are set at 95 % (thick lines), 50 % (medium lines), and 10 % (thin lines) of the extremum value reached in the represented parameter domain, the positive values being associated with a plain line and the negative values with a dashed line.

B1.3 Two modulations in antiphase - case (ii)

B1.3.1 Analytical expression of the amplitudes of concentration oscillation

Following the same method as in section B1.2.1 for a single modulation, we find the following linear equations for the amplitudes of concentration oscillation in the case of two modulations in antiphase

$$a_0 = -\frac{\alpha(K^0-1)}{2(1+K^0)}b_1 \tag{B32}$$

$$a_1\theta = b_1 - \frac{2\alpha K^0 C_{\rm tot}}{(1+K^0)^2} - \frac{\alpha(K^0-1)}{2(1+K^0)}(a_2-2a_0) \tag{B33}$$

$$b_1\theta = -a_1 - \frac{\alpha(K^0-1)}{2(1+K^0)}b_2 \tag{B34}$$

$$a_n n\theta = b_n - \frac{\alpha(K^0-1)}{2(1+K^0)}(a_{n+1}-a_{n-1}) \quad \text{for} \quad n>1 \tag{B35}$$

$$b_n n\theta = -a_n - \frac{\alpha(K^0-1)}{2(1+K^0)}(b_{n+1}-b_{n-1}) \quad \text{for} \quad n>1 \tag{B36}$$

The explicit expressions of the amplitudes of concentration oscillation up to the fourth order are

$$a_0 \simeq -\alpha^2\frac{K^0(K^0-1)}{2(1+K^0)^3}\frac{1}{1+\theta^2}C_{\rm tot} \tag{B37}$$

$$a_1 \simeq -2\alpha\frac{K^0}{(1+K^0)^2}\frac{\theta}{1+\theta^2}C_{\rm tot} \tag{B38}$$

$$b_1 \simeq 2\alpha\frac{K^0}{(1+K^0)^2}\frac{1}{1+\theta^2}C_{\rm tot} \tag{B39}$$

$$a_2 \simeq \alpha^2\frac{K^0(K^0-1)}{2(1+K^0)^3}\frac{1-2\theta^2}{(1+\theta^2)(1+4\theta^2)}C_{\rm tot} \tag{B40}$$

$$b_2 \simeq \alpha^2\frac{K^0(K^0-1)}{2(1+K^0)^3}\frac{3\theta}{(1+\theta^2)(1+4\theta^2)}C_{\rm tot} \tag{B41}$$

$$a_3 \simeq \alpha^3\frac{K^0(K^0-1)^2}{2^2(1+K^0)^4}\frac{6\theta(1-\theta^2)}{(1+\theta^2)(1+4\theta^2)(1+9\theta^2)}C_{\rm tot} \tag{B42}$$

$$b_3 \simeq -\alpha^3\frac{K^0(K^0-1)^2}{2^2(1+K^0)^4}\frac{1-11\theta^2}{(1+\theta^2)(1+4\theta^2)(1+9\theta^2)}C_{\rm tot} \tag{B43}$$

$$a_4 \simeq -\alpha^4\frac{K^0(K^0-1)^3}{2^3(1+K^0)^5}\frac{1-35\theta+24\theta^2}{(1+\theta^2)(1+4\theta^2)(1+9\theta^2)(1+16\theta^2)}C_{\rm tot} \tag{B44}$$

$$b_4 \simeq -\alpha^4\frac{K^0(K^0-1)^3}{2^3(1+K^0)^5}\frac{10\theta(1-5\theta^2)}{(1+\theta^2)(1+4\theta^2)(1+9\theta^2)(1+16\theta^2)}C_{\rm tot} \tag{B45}$$

The amplitudes of concentration oscillation a_1 and b_1 at the first order given in Eq.(B38,B39) driven by two modulations in antiphase are twice the amplitudes of concentration oscillation a_1 and b_1 given in Eq.(B19,B20) driven by a single modulation.

Table B1: Amplitudes R of concentration oscillation with extrema driven by single modulation at the wavelength λ_1 (case (i1)) or at the wavelength λ_2 (case (i2)) and of fluorescence oscillation driven by single modulation at the wavelength λ_2 (case (i2)), resonant parameter values K_n^{0R} and θ_n^R up to the fourth order deduced from the numerical solutions of Eqs.(B12-B16) truncated at the fifth order for $\alpha = 1$.

Order	R	K_n^{0R}	θ_n^R
1	a_1^R	1.24	0.84
2	b_2^R	3.83	0.21
3	a_3^R	8.25	0.07
4	b_4^R	11.55	0.05

Using a similar mathematical induction as in case (i1), we show that for all orders n the amplitudes obey

$$a_n = \alpha^n \frac{K^0(K^0-1)^{n-1}}{2^n(1+K^0)^{n+1}} \frac{f_n(\theta)}{\Pi_{k=1}^n (1+k^2\theta^2)} C_{\rm tot} \quad \text{(B46)}$$

$$b_n = \alpha^n \frac{K^0(K^0-1)^{n-1}}{2^n(1+K^0)^{n+1}} \frac{g_n(\theta)}{\Pi_{k=1}^n (1+k^2\theta^2)} C_{\rm tot} \quad \text{(B47)}$$

where $f_n(\theta)$ and $g_n(\theta)$ are the same polynomial functions independent of K^0 as in Eqs.(B30,B31) leading in particular to the same behavior in θ. The resonant value of the equilibrium constant $K_n^{0R} = n \pm \sqrt{n^2-1}$ at order n is deduced from Eqs.(B46,B47). The amplitude a_1 displays a single extremum of coordinates (K_1^{0R}, θ_1^R). From the second order the amplitudes a_{2k+1} and b_{2k} possess two extrema $(K_n^{0R_1}, \theta_n^R)$ and $(K_n^{0R_2}, \theta_n^R)$ associated with the same resonant value of θ identical to the value obtained in case (i1). The amplitudes a_{2k} and b_{2k+1} behave as a low-pass filter with respect to θ.

B1.3.2 Numerical derivation of the amplitudes of concentration oscillation

Figure B2 displays the amplitudes of concentration oscillation in the (K^0, θ) space obtained using a numerical solution of Eqs.(B32-B36) truncated at the fifth order. Tab. B2 gives the amplitudes R with extrema and the resonant parameter values deduced from the numerical approach.

The amplitudes of odd order display a mirror symmetry with respect to the $K^0 = 1$-plane in the $(\log_{10}(K^0), \log_{10}(\theta))$ space. The amplitudes of even order display a mirror antisymmetry with respect to the $K^0 = 1$-plane. The greater the order, the smaller the width of the resonance peak at half maximum. For a large modulation of light excitation $\alpha = 1$, the absolute amplitudes at the extremum decrease by less than a factor of 2 when the order n increases by 1 from $n = 2$. A more severe decrease of about a factor of 3 is observed when switching from $n = 1$ to $n = 2$.

The resonant values in K^0 obey $K_n^{0R_1} < K_1^{0R} < K_n^{0R_2}$ for $n > 1$. The values $K_n^{0R_1}$ and θ_n^R decrease as the order n increases. On the contrary $K_n^{0R_2}$ increases as n increases. The analytical expressions underestimate the resonance displacement as the order changes and they overestimate the decrease of the amplitude at the extremum and the width at half maximum of the peak.

Table B2: Amplitudes R of concentration oscillation with extrema driven by two modulations in antiphase (case (ii)), resonant parameter values K_1^{0R} and θ_1^R, $K_n^{0R_1}$, $K_n^{0R_2}$ and $\theta_n^{R_1} = \theta_n^{R_2}$ up to the fourth order deduced from the numerical solutions of Eqs.(B32-B36) truncated at the fifth order for $\alpha = 1$.

Order	R	K_1^{0R}		θ_1^R
1	a_1^R	1.00		1.00
Order	R	$K_n^{0R_1}$	$K_n^{0R_2}$	$\theta_n^{R_1} = \theta_n^{R_2}$
2	$b_2^{R_1}$, $b_2^{R_2}$	0.15	6.60	0.24
3	$a_3^{R_1}$, $a_3^{R_2}$	0.07	15.04	0.08
4	$b_4^{R_1}$, $b_4^{R_2}$	0.04	22.36	0.05

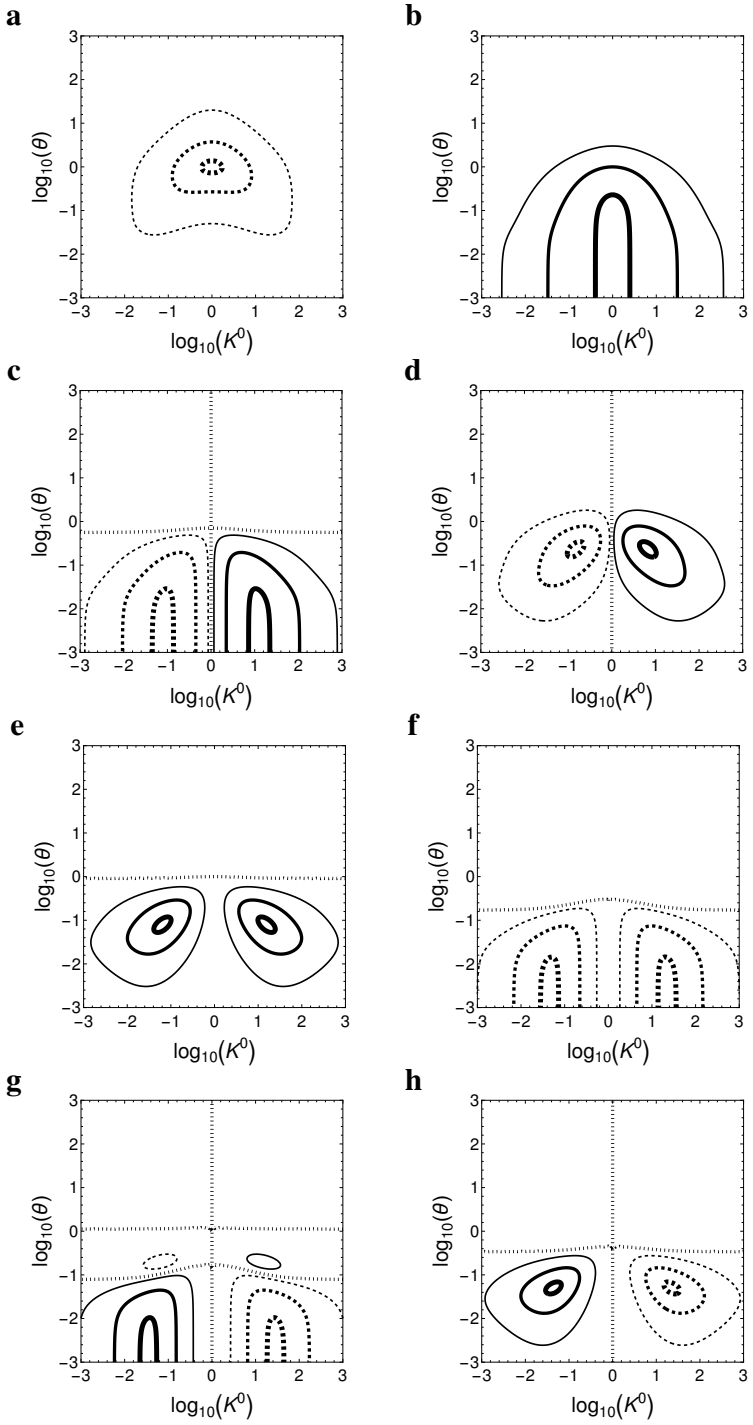

Figure B2: Amplitudes of concentration oscillation driven by two modulations in antiphase (case (ii)) deduced from the numerical solutions of Eqs.(B32-B36) truncated at the fifth order for $\alpha = 1$. (a): a_1, (b): b_1, (c): a_2, (d): b_2, (e): a_3, (f): b_3, (g): a_4, (h): b_4. The parameter values for which the amplitudes are equal to 0 are represented by a dotted line. The other contour lines are set at 95 % (thick lines), 50 % (medium lines), and 10 % (thin lines) of the extremum value reached in the represented parameter domain, the positive values being associated with a plain line and the negative values with a dashed line.

Figure B3 displays the variation of the amplitudes R of concentration oscillation with extrema, the surface S at half maximum of the peak in the $(\log_{10}(K^0), \log_{10}(\theta))$ space, and the ratio R/S with respect to the order n for case (i1) (single modulation) and case (ii) (two modulations in antiphase). The decrease of the surface S shows the increase of the resonance sharpness as the order increases. Nevertheless the decrease of the amplitude R is faster than the decrease of the surface S. However the ratio R/S reaches a plateau at large n. A balance has to be found between signal strength and resonance sharpness. The analytical results underestimate the amplitudes at the extremum and the surfaces at half maximum. Except for the first order, for which the amplitude associated with case (ii) is much larger than the amplitude of case (i1), both cases lead to close resonance properties.

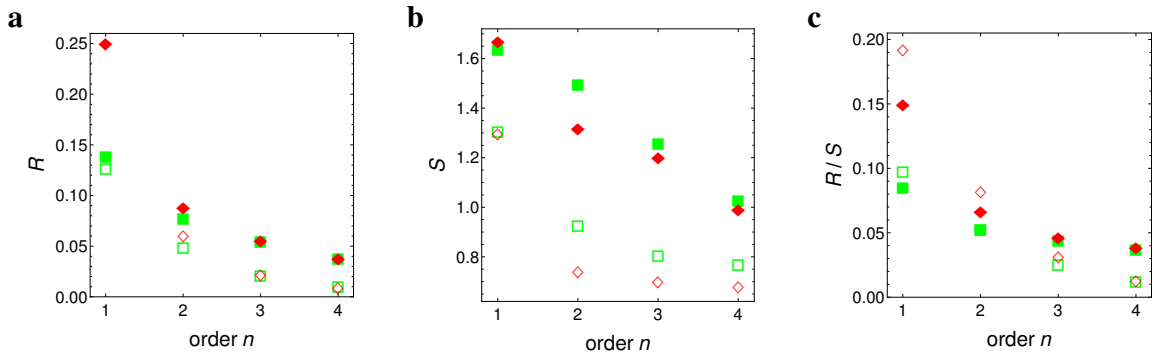

Figure B3: (a) Absolute amplitudes R of concentration oscillation at the extremum defined in Tabs. B1 and B2, (b) surface S at half maximum of the peak in the $(\log_{10}(K^0), \log_{10}(\theta))$ space, and (c) ratio R/S versus order n for $\alpha = 1$. The green squares correspond to a single modulation associated with case (i1), the red diamonds to two modulations in antiphase associated with case (ii), the open symbols to the analytical results, and the solid symbols to the numerical results. Total concentration $C_{\text{tot}} = 1$.

B2 Evolution of fluorescence intensity

In this section we address the case where the observable is fluorescence intensity. For the sake of simplicity, we consider a single significant brightness Q for a single species C_i for i equals 1 or 2 at the wavelength λ_1. We introduce the scaled fluorescence intensity

$$I_{\text{F}} = \frac{I_1 C_i}{I_1^0 C_{tot}} \tag{B48}$$

where $i = 1$ for negative photoswitchable fluorophores and $i = 2$ for positive photoswitchable fluorophores. Whereas C_1 is fluorescent for negative photoswitchable fluorophores, C_2 is fluorescent for positive ones. Contrary to the concentration the fluorescence intensity is not symmetrical with respect to the exchange of the light intensities I_1 and I_2.

The fluorescence intensity is expressed using a Fourier series

$$I_{\mathrm{F}} = I_{\mathrm{F}}^0 + \sum_{n=1}^{+\infty} \left[A_n \cos\left(n\omega t\right) + B_n \sin\left(n\omega t\right)\right] \tag{B49}$$

where I_{F}^0 is the mean fluorescence intensity and A_n and B_n designate the quadrature and in-phase amplitudes of fluorescence oscillation of the n-th harmonics.

Using Eqs.(B6,B48) we obtain

$$I_{\mathrm{F}} = \frac{I_1\left(C_1^0 - C\right)}{I_1^0} \tag{B50}$$

for negative photoswitchers and

$$I_{\mathrm{F}} = \frac{I_1\left(C_{tot} - C_1^0 + C\right)}{I_1^0} \tag{B51}$$

for positive photoswitchers.

Substituting for I_{F} from Eq.(B49), I_1 from Eq.(B2), and c from Eq.(B11) into Eq.(B50), we cancel the terms in front of the sine and cosine at each order n and find the following linear equations

$$\begin{aligned}
I_{\mathrm{F}}^0 &= \frac{C_{\mathrm{tot}}}{1+K^0} - a_0 - \frac{\alpha_1}{2} b_1 && \text{(B52)}\\
A_1 &= -a_1 - \frac{\alpha_1}{2} b_2 && \text{(B53)}\\
B_1 &= -b_1 + \alpha_1 \left(\frac{C_{\mathrm{tot}}}{1+K^0} - a_0 + \frac{1}{2} a_2\right) && \text{(B54)}\\
A_n &= -a_n + \frac{\alpha_1}{2}\left(b_{n-1} - b_{n+1}\right) && \text{(B55)}\\
B_n &= -b_n - \frac{\alpha_1}{2}\left(a_{n-1} - a_{n+1}\right) && \text{(B56)}
\end{aligned}$$

for negative photoswitchers. Substituting for I_{F} from Eq.(B49), I_1 from Eq.(B2), and c from Eq.(B11) into Eq.(B51), we obtain

$$\begin{aligned}
I_{\mathrm{F}}^0 &= \frac{K^0 C_{\mathrm{tot}}}{1+K^0} + a_0 + \frac{\alpha_1}{2} b_1 && \text{(B57)}\\
A_1 &= a_1 + \frac{\alpha_1}{2} b_2 && \text{(B58)}\\
B_1 &= b_1 + \alpha_1 \left(\frac{K^0 C_{\mathrm{tot}}}{1+K^0} + a_0 - \frac{1}{2} a_2\right) && \text{(B59)}\\
A_n &= a_n - \frac{\alpha_1}{2}\left(b_{n-1} - b_{n+1}\right) && \text{(B60)}\\
B_n &= b_n + \frac{\alpha_1}{2}\left(a_{n-1} - a_{n+1}\right) && \text{(B61)}
\end{aligned}$$

for positive photoswitchers. Except for I_{F}^0 and B_1, the amplitudes of fluorescence oscillation for positive and negative photoswitchers only differ by their sign. When the light intensity I_1 at the

wavelength λ_1 is not modulated, i.e. in case (i2) with $\alpha_1 = 0$ and $\alpha_2 = \alpha$, the amplitudes of fluorescence oscillation, A_n and B_n, are equal to the amplitudes a_n and b_n of concentration oscillations. When the light intensity I_1 at the wavelength λ_1 is modulated, i.e. in case (i1) with $\alpha_1 = \alpha$ and $\alpha_2 = 0$ and in case (ii) with $\alpha_1 = \alpha$ and $\alpha_2 = -\alpha$, the amplitudes A_n and B_n are linear combination of amplitudes a_n and b_n either with or without extremum.

B2.1 Single modulation at the wavelength λ_1 - case (i1)

The case (i1) is associated with a single modulation of light intensity I_1 at the wavelength λ_1 i.e. $\alpha_1 = \alpha, \alpha_2 = 0$. Substituting for the amplitudes of concentration oscillation from Eqs.(B19,B20,B23-B29) into Eqs.(B52-B61) for the Fourier amplitudes A_n and B_n, we obtain approximate analytical expressions for the amplitudes of fluorescence oscillation. Using Eqs.(B57-B59) and numerical solutions of the amplitudes of concentration oscillation a_n and b_n after truncation of Eqs.(B12-B16) at the fifth order, we obtain numerical solutions of the amplitudes of fluorescence oscillation. The numerical results are given in Fig. B4. The first-order amplitude A_1 is very close to a_1 showing a single resonance denoted by the exponent R. From the second order, the odd quadrature amplitudes A_{2k+1} and even in-phase amplitudes B_{2k} have resonances but display a richer behavior than the corresponding amplitudes a_{2k+1} and b_{2k} of the concentrations. In particular they present two peaks associated with opposite signs, implying that the amplitudes vanish on a specific line in the (K^0, θ) space. The resonance associated with the peak of larger amplitude in absolute value is denoted by an exponent R_1 and the smaller peak with R_2. Table B3 gives the characteristics of the resonances. Due to the presence of two peaks the amplitudes of fluorescence oscillation are smaller than the corresponding amplitudes of the concentrations.

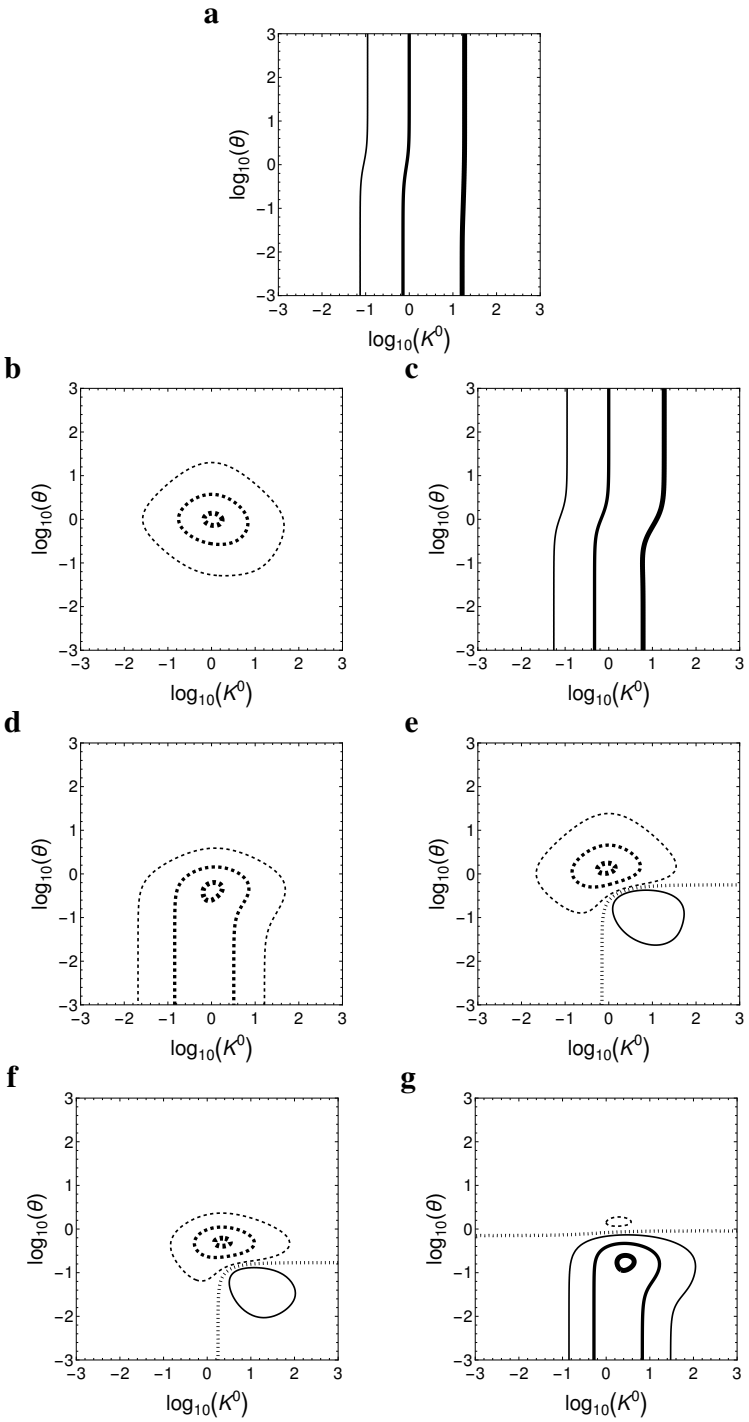

Figure B4: Amplitudes of fluorescence oscillation driven by single modulation at the wavelength λ_1 (case (i1)) deduced from the numerical solutions of Eqs.(B12-B16) truncated at the fifth order and introduced in Eqs.(B57-B61) for positive photoswitchers and $\alpha = 1$. (a): I_{F}^0, (b): A_1, (c): B_1, (d): A_2, (e): B_2, (f): A_3, (g): B_3. The parameter values for which the amplitudes are equal to 0 are represented by a dotted line. The other contour lines are set at 95 % (thick lines), 50 % (medium lines), and 10 % (thin lines) of the extremum value reached in the represented parameter domain, the positive values being associated with a plain line and the negative values with a dashed line.

Table B3: Amplitudes R of fluorescence oscillation with extrema driven by the single modulation at the wavelength λ_1 (case (i1)), resonant parameter values K_1^{0R} and θ_1^R, $K_n^{0R_1}$, $K_n^{0R_2}$, $\theta_n^{R_1}$, and $\theta_n^{R_2}$ up to the third order deduced from the numerical solutions of Eqs.(B12-B16) truncated at the fifth order and introduced in Eqs.(B57-B61) for positive photoswitchers and $\alpha = 1$.

Order	R	K_1^{0R}		θ_1^R	
1	A_1^R	1.08		1.00	
Order	R	$K_n^{0R_1}$	$K_n^{0R_2}$	$\theta_n^{R_1}$	$\theta_n^{R_2}$
2	$B_2^{R_1}$, $B_2^{R_2}$	0.88	5.16	1.33	0.18
3	$A_3^{R_1}$, $A_3^{R_2}$	2.22	12.21	0.50	0.05

B2.2 Single modulation at the wavelength λ_2 - case (i2)

The case (i2) is associated with a single modulation of light intensity I_2 at the wavelength λ_2 i.e. $\alpha_1 = 0$, $\alpha_2 = \alpha$. The amplitudes of fluorescence oscillation, A_n and B_n, are equal to the amplitudes a_n and b_n of concentration oscillations. The results are given in Fig. B1 and Tab. B1 after exchanging the intensities I_1 and I_2 and the concentrations C_1 and C_2.

B2.3 Two modulations in antiphase - case (ii)

The case (ii) is associated with two antiphase modulations of light intensities I_1 at the wavelength λ_1 and I_2 at the wavelength λ_2, i.e. $\alpha_1 = \alpha$ and $\alpha_2 = -\alpha$. Following the same method as in section B2.1, we find the analytical and numerical expressions of the amplitudes A_n and B_n of fluorescence oscillation. Fig. B5 displays the numerical results. Unlike the amplitudes of concentration oscillation, the amplitudes of fluorescence oscillation do not have a mirror symmetry. At the first order the amplitude A_1 is similar to the concentration amplitude a_1. From the second order the odd quadrature amplitudes A_{2k+1} and even in-phase amplitudes B_{2k} display two resonances. Contrary to the amplitudes a_{2k+1} and b_{2k}, the two amplitudes A_{2k+1} and B_{2k} have always opposite signs and different absolute values. The amplitudes having two resonances vanish along a specific line in the (K^0, θ) space. The resonance associated with the peak of larger amplitude in absolute value is denoted by an exponent R_1 and the smaller peak by R_2. Table B4 gives the coordinates of the resonances.

Table B4: Amplitudes R of fluorescence oscillation with extrema driven by two modulations in antiphase (case (ii)), resonant parameter values K_1^{0R} and θ_1^R, $K_n^{0R_1}$, $K_n^{0R_2}$, $\theta_n^{R_1}$, and $\theta_n^{R_2}$ up to the third order deduced from the numerical solutions of Eqs.(B32-B36) truncated at the fifth order and introduced in Eqs.(B57-B61) for positive photoswitchers and $\alpha = 1$.

Order	R	K_1^{0R}		θ_1^R	
1	A_1^R	0.80		0.97	
Order	R	$K_n^{0R_1}$	$K_n^{0R_2}$	$\theta_n^{R_1}$	$\theta_n^{R_2}$
2	$B_2^{R_1}$, $B_2^{R_2}$	0.21	10.06	0.33	0.18
3	$A_3^{R_1}$, $A_3^{R_2}$	0.07	3.96	0.09	0.50

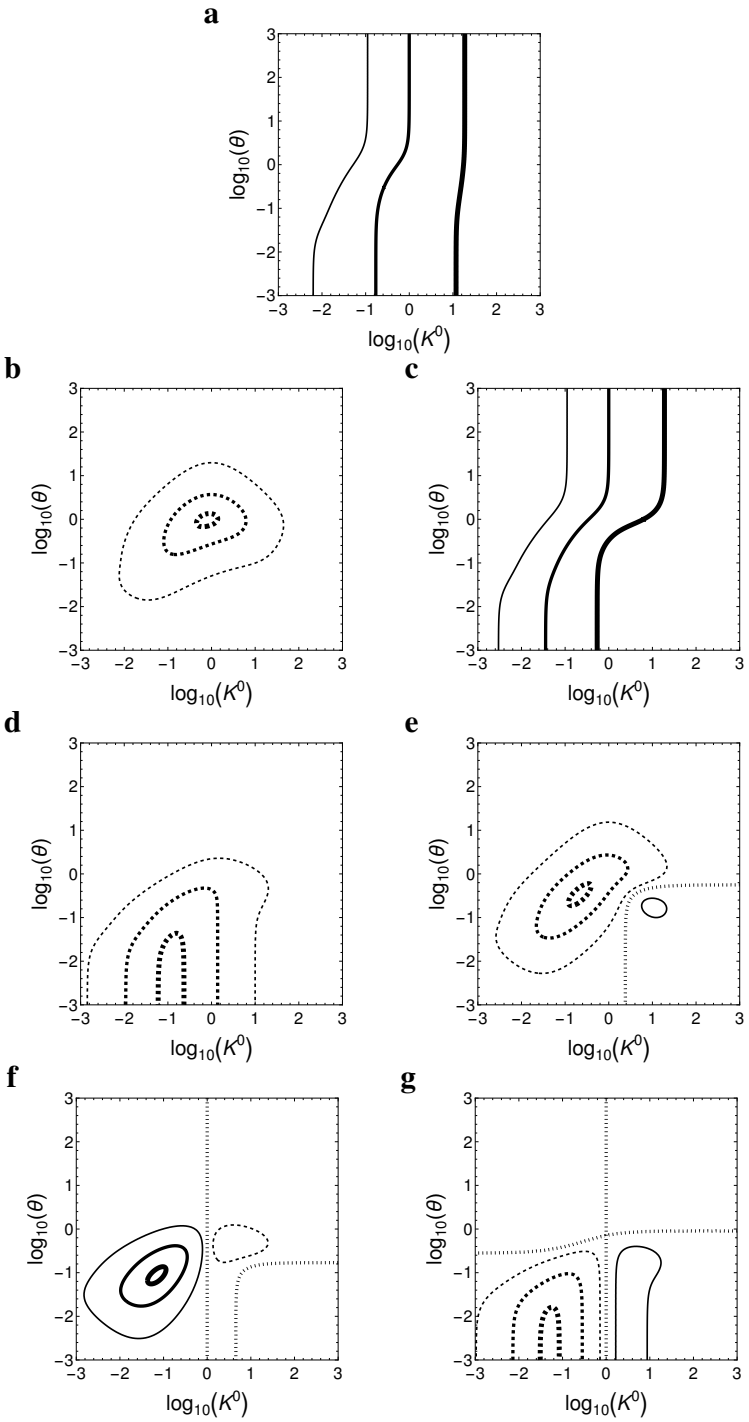

Figure B5: Amplitudes of fluorescence oscillation driven by two modulations in antiphase (case (ii)) deduced from the numerical solutions of Eqs.(B32-B36) truncated at the fifth order and introduced in Eqs.(B57-B61) for positive photoswitchers and $\alpha = 1$. (a): I_F^0, (b): A_1, (c): B_1, (d): A_2, (e): B_2, (f): A_3, (g): B_3. The parameter values for which the amplitudes are equal to 0 are represented by a dotted line. The other contour lines are set at 95 % (thick lines), 50 % (medium lines), and 10 % (thin lines) of the extremum value reached in the represented parameter domain, the positive values being associated with a plain line and the negative values with a dashed line.

Figure B6 displays the variation of the amplitudes R of fluorescence oscillation with extrema, the surface S at half maximum of the peaks in the $(\log_{10}(K^0), \log_{10}(\theta))$ space, and the ratio R/S with respect to the order n for case (i1) (single modulation at λ_1), case (i2) (single modulation at λ_2), and case (ii) (two modulations in antiphase). The analytical results underestimate the amplitudes at the extremum and the surfaces at half maximum. Regardless of the order n, the resonance R_1 of larger amplitude is significantly greater for two modulations than for a single modulation, case (i2) being slightly more favorable than case (i1). Contrary to the resonance R_1, the resonance R_2 of smaller amplitude does not sensitively decrease as the order increases from $n = 2$. The surface at half width S is anomalously large in the case (ii) for $n = 2$. Interestingly for case (i1) and resonance R_1, the decrease of S as n increases is more marked than in the other cases. The ratio R/S of the amplitude at the extremum and the surface at half width accounts for the sharpness of the resonance and remains nearly constant in all cases when switching from $n = 2$ to $n = 3$.

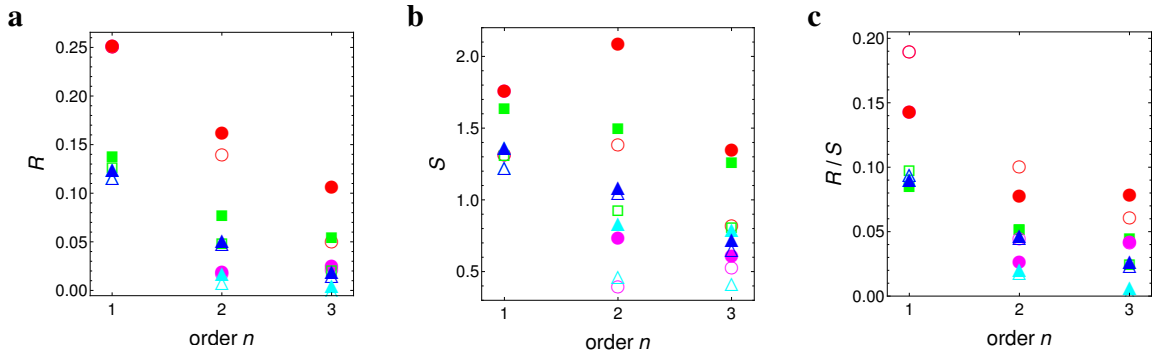

Figure B6: (a) Absolute amplitudes R of fluorescence oscillation at the extremum defined in Tabs. B1, B3, and B4, (b) surface S at half maximum of the peaks in the $(\log_{10}(K^0), \log_{10}(\theta))$ space, and (c) ratio R/S versus order n for $\alpha = 1$. The green squares correspond to the resonance R associated with a single modulation and case (i2). The blue and cyan triangles correspond to a single modulation associated with case (i1) and the red and magenta circles to two modulations in antiphase associated with case (ii). The blue triangles and the red circles correspond to the resonance R_1 of larger amplitude. The cyan triangles and the magenta circles correspond to the resonance R_2 of smaller amplitude. The open and solid symbols are associated with the analytical and numerical results, respectively. Total concentration $C_{\text{tot}} = 1$.

B3 Application to the discrimination of reversibly photoswitchable species

As shown in Eqs.(B8,B9,B50,B51), the analysis of the resonant behaviors of the amplitudes of concentration or fluorescence oscillation reveals the minimal number of dimensionless independent parameters. However the discrimination of several reversibly photoswitchable species requires

switching from the two dimensionless parameters, K^0 and θ, to two experimentally relevant control parameters chosen among the mean light intensities I_1^0 and I_2^0 and the angular frequency ω.

The mean value of the photochemical rate constant of the forward reaction given in Eq.(B1) is assumed to be given by

$$k_1^0 = \sigma_1 I_1^0 \tag{B62}$$

where σ_1 is the cross section and I_1^0, the mean light intensity at the wavelength λ_1. For a single modulation at the wavelength λ_1 (case (i1)) two subcases are considered depending on the values of the mean light intensity I_2^0 at the wavelength λ_2. Case (i1a) corresponds to a vanishing light intensity I_2^0 leading to a thermal rate constant

$$k_2^0 = k^\Delta \tag{B63}$$

The properties of the photochemical system are then set by the two control parameters I_1^0 and ω. Case (i1b) corresponds to a sufficiently large light intensity I_2^0 such that

$$\sigma_2 I_2^0 \gg k^\Delta \tag{B64}$$

leading to

$$k_2^0 = \sigma_2 I_2^0 \tag{B65}$$

where σ_2 is the cross section at the wavelength λ_2. If the condition given in Eq.(B64) is obeyed, the rate constant k_2^0 is given by Eq.(B65) for cases (i2) and (ii). In cases (i1b), (i2) and (ii) we choose I_2^0/I_1^0 and ω/I_1^0 as the two independent control parameters.

Using Eqs.(B7,B10,B17) the control parameters are related to the dimensionless parameters K^0 and θ according to

$$I_1^0 = K^0 \frac{k^\Delta}{\sigma_1} \tag{B66}$$

$$\omega = \theta \left(1 + K^0\right) k^\Delta \tag{B67}$$

for case (i1a). Similarly, for cases (i1b), (i2) and (ii) we obtain

$$\frac{I_2^0}{I_1^0} = \frac{1}{K^0} \frac{\sigma_1}{\sigma_2} \tag{B68}$$

$$\frac{\omega}{I_1^0} = \theta \left(1 + \frac{1}{K^0}\right) \sigma_1 \tag{B69}$$

The resonant values of K^0 and θ at order n are given in Tabs. B1, B2, B3, B4. Resonant control parameter values are obtained in case (i1a) and the other cases by substituting for the resonant

values of K^0 and θ into Eqs. (B66,B67) and Eqs. (B68,B69), respectively. The amplitudes of concentration and fluorescence oscillation for the representative photoswitchable species Dronpa-2 in the cases (i1a), (i1b), (i2), and (ii) are given in Figs. B7 and B8 in the control parameter space. The typical behaviors observed in the dimensionless space are recovered in the control parameter space (I_1^0, ω) or $(I_2^0/I_1^0, \omega/I_1^0)$. In particular we numerically proved that the amplitudes at the extremum and the surfaces at half maximum of the resonance peak are unchanged. Hence Figs. B3 and B6 remain relevant in the control parameter spaces. The gap between the resonant parameter values of two photoswitchable species only depends on the values of their kinetic properties (cross sections σ_1 and σ_2 and thermal rate constant k^{Δ}) but not on the order n of the harmonics and little on the number of modulated lights.

The Fourier amplitudes with extrema are well-suited observables for discrimination purposes. The parameters that control illumination can be tuned to maximize the contribution of the target and minimize the contributions of interfering species. The n^{th}-order Fourier amplitude of fluorescence oscillation with extrema is further referred to a HIGHLIGHT-n signal. Specifically we harness the resonance properties of A_1 = HIGHLIGHT-1, B_2 = HIGHLIGHT-2, and A_3 = HIGHLIGHT-3. A small width at half maximum is favorable provided that the associated resonant value is large enough to be experimentally detectable. Following Fig. B6 the width of the resonance peak is smaller for cases (i1a) and (i1b). However these cases are associated with the smallest amplitudes and requires a good signal-to-noise ratio. The optimization of both the signal-to-noise ratio and the sharpness of the resonance is obtained for case (ii). Cases (i1b), (i2) and (ii) have advantages with respect to case (i1a). Indeed, the mean light intensity I_1^0 is a fully adjustable parameter that can be chosen large leading to large values of k_1^0. Due to larger values of k_1^0 and k_2^0, cases (i1b), (i2) and (ii) enable faster acquisition than case (i1a), the acquisition time of concentration or fluorescence evolution being of the order of $1/\tau^0$ with τ^0 given in Eq.(B10). Choosing large values of I_1^0 also optimizes the signal-to-noise ratio of fluorescence intensity. Case (i2) leads to a single resonance at each order and consequently no zero line in the control parameter space. Contrary to case (i2), both cases (i1b) and (ii) show zero lines from the second order.

Figure B9 gives the resonance maps at orders $n = 1, 2, 3$ for cases (i1b) and (ii) and three well-chosen RSFPs (Dronpa, Dronpa-2, and rsFastlime). Interestingly from the experimental point of view, the zero line of one RSFP goes through the resonance of another RSFP and the resonance conditions of orders 1 and 2 nearly coincide in case (i1b). The situation is not as favorable in case (ii) for the chosen RSFPs. We therefore chose case (i1b) to implement the following experimental protocol. For the sake of simplicity we extract the Fourier amplitudes at various orders from the fluorescence evolution recorded for a single control parameter set associated with the resonant

condition of the first-order amplitude. Three fluorescence evolutions are recorded for different control parameter values coinciding with the resonance condition of Dronpa, then rsFastLime, and finally Dronpa-2. For each acquisition the first-order quadrature amplitude of fluorescence oscillation and the second-order in-phase amplitude are extracted. At the resonance condition of Dronpa, the detected amplitude contains the contributions of both Dronpa and rsFastLime to the first order whereas the contribution of Dronpa is isolated in the second-order amplitude. Indeed the zero line of the second order amplitude of rsFastLime meets the resonance condition of Dronpa and the resonance condition of Dronpa-2 are sufficiently different for the contribution of Dronpa-2 to be negligible. Similarly, the contribution of Dronpa-2 to the second-order amplitude vanishes in the resonance condition of rsFastLime associated with a point on the zero line of Dronpa-2. The contribution of Dronpa can be neglected. Finally, the contribution of Dronpa-2 is retrieved for its resonance condition, the contributions of Dronpa and rsFastLime being negligible.

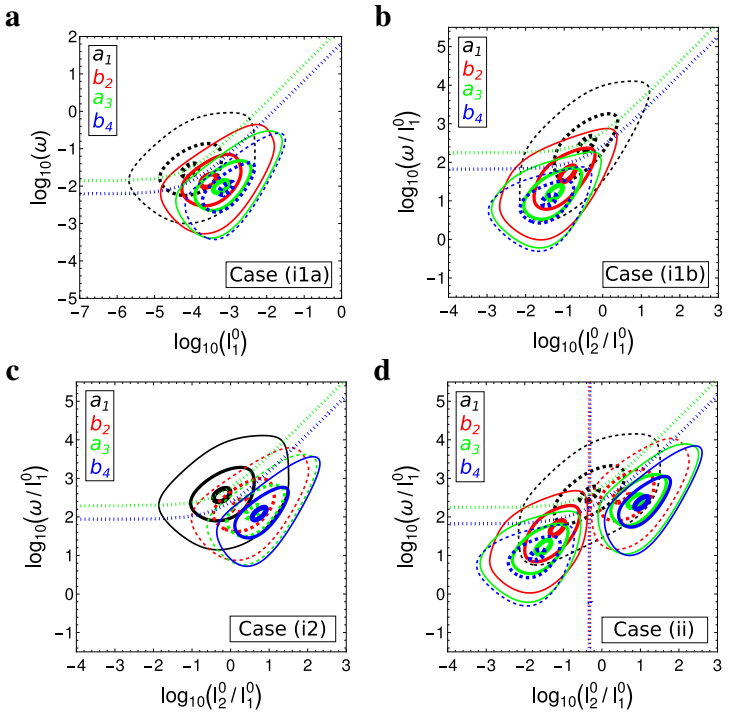

Figure B7: Amplitudes a_1, b_2, a_3, and b_4 of concentration oscillation for the RSFP Dronpa-2 driven by one modulation at the wavelength λ_1 with $I_2^0 = 0$ (a: case (i1a)), with $I_2^0 \neq 0$ (b: case (i1b)), at the wavelength λ_2 with $I_1^0 \neq 0$ (c: case (i2)), and two modulations in antiphase (d: case (ii)). The results are deduced from the numerical solutions of Eqs.(B12-B16) for cases (i1a), (i1b), (i2) and Eqs.(B32-B36) for case (ii) truncated at the fifth order. The zero lines are represented by dotted lines. The other contour lines correspond to 95 % (thick lines), 50 % (medium lines), and 10 % (thin lines) of the extremum value, the positive values being associated with a solid line and the negative values with a dashed line. $\sigma_1 = 196$ m^2.mol^{-1}, $\sigma_2 = 413$ m^2.mol^{-1}, $k^\Delta = 14 \times 10^{-3}$ s^{-1}, and $\alpha = 1$.

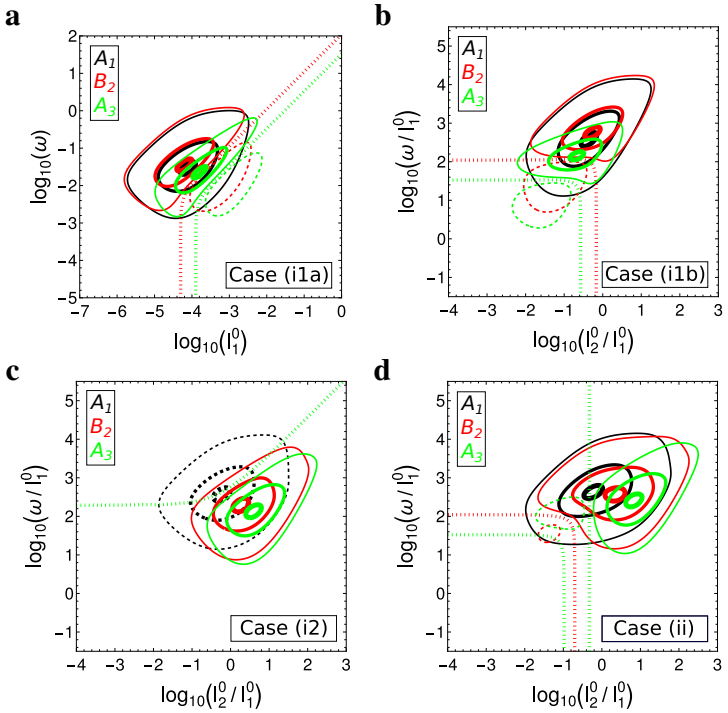

Figure B8: Amplitudes A_1, B_2, and A_3 of fluorescence oscillation for the RSFP Dronpa-2 driven by one modulation at the wavelength λ_1 with $I_2^0 = 0$ (a: case (i1a)), with $I_2^0 \neq 0$ (b: case (i1b)), at the wavelength λ_2 with $I_1^0 \neq 0$ (c: case (i2)), and two modulations in antiphase (d: case (ii)). The results are deduced from Eqs.(B52-B56) in which the amplitudes of concentration oscillation are numerical solutions of Eqs.(B12-B16) for cases (i1a), (i1b), (i2) and Eqs.(B32-B36) for case (ii) truncated at the fifth order. The zero lines are represented by dotted lines. The other contour lines correspond to 95 % (thick lines), 50 % (medium lines), and 10 % (thin lines) of the extremum value, the positive values being associated with a solid line and the negative values with a dashed line. $\sigma_1 = 196$ m^2.mol^{-1}, $\sigma_2 = 413$ m^2.mol^{-1}, $k^{\Delta} = 14 \times 10^{-3}$ s^{-1}, and $\alpha = 1$.

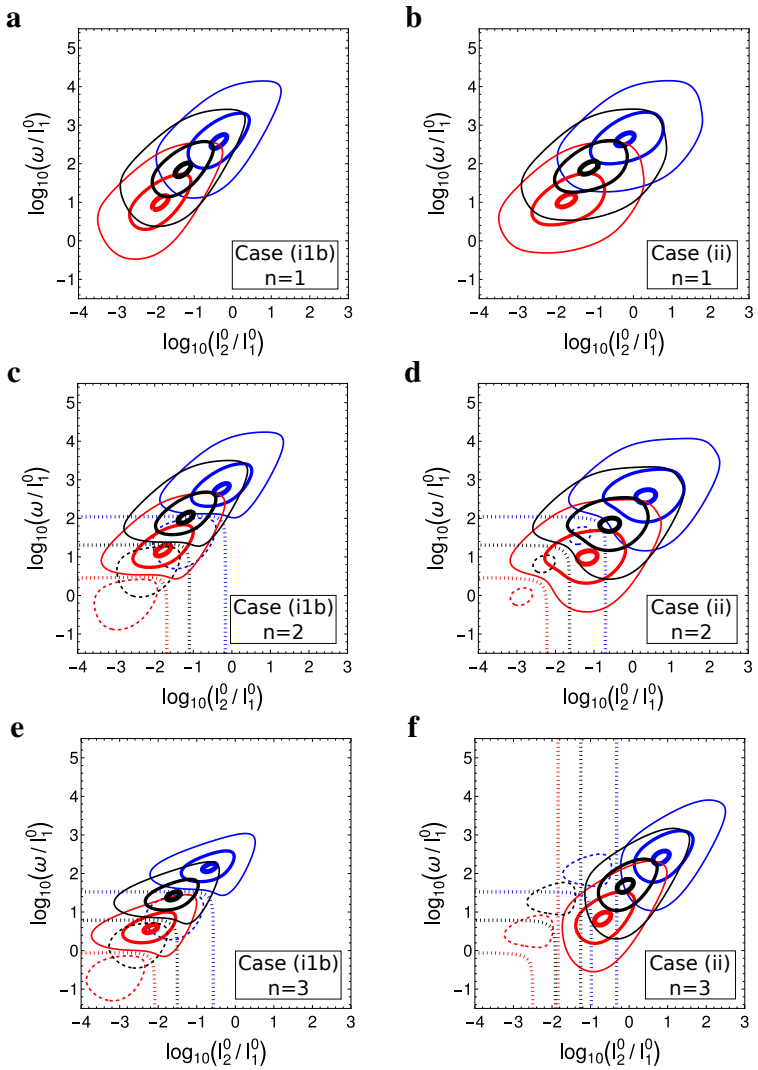

Figure B9: Discrimination of Dronpa-2, rsFastlime, and Dronpa. Amplitudes A_1 (a, b), B_2 (c, d), and A_3 (e, f) of fluorescence oscillation for the RSFPs Dronpa-2 (blue), rsFastLime (black), and Dronpa (red) driven by one modulation at the wavelength λ_1 with $I_2^0 \neq 0$ (a, c, e: case (i1b)) and two modulations in antiphase (b, d, f: case (ii)). The results are deduced from Eqs.(B52-B56) in which the amplitudes of concentration oscillation are numerical solutions of Eqs.(B12-B16) for case (i1b) and Eqs.(B32-B36) for case (ii) truncated at the fifth order. The zero lines are represented by dotted lines. The other contour lines correspond to 95 % (thick lines), 50 % (medium lines), and 10 % (thin lines) of the extremum value, the positive values being associated with a solid line and the negative values with a dashed line. $\sigma_1 = 196$ m^2.mol^{-1}, $\sigma_2 = 413$ m^2.mol^{-1} for Dronpa-2, $\sigma_1 = 36$ m^2.mol^{-1}, $\sigma_2 = 648$ m^2.mol^{-1} for rsFastLime, $\sigma_1 = 5.1$ m^2.mol^{-1}, $\sigma_2 = 354.5$ m^2.mol^{-1} for Dronpa, and $\alpha = 1$.

B4 Materials and Methods

B4.1 Protein production and purification

The genes encoding Dronpa-2 and Dronpa-3 were kindly provided by Stefan Jakobs and Atsushi Miyawaki respectively. The genes encoding Dronpa and rsFastLime were kindly provided by Agathe Espagne. The plasmids expressing the fluorescent proteins carrying an N-terminal hexahistidine tag were transformed in E. coli BL21 strain. Cells were grown in Terrific Broth (TB) at 37°C. The expression was induced at 30°C by addition of isopropyl β-*D*-1-thio-galactopyranoside (IPTG) to a final concentration of 1 mM at OD(600)=0.6. The cells were harvested after 16 h of expression and lysed by sonication in Lysis buffer (50 mM PBS with 150 mM NaCl at pH 7.4, 5 mg/ml DNAse, 5 mM $MgCl_2$ and 1 mM phenylmethylsulfonyl fluoride (PMSF), and a cocktail of protease inhibitor (Sigma Aldrich; S8830)). After lysis, the mixture was incubated on ice for 2 h for DNA digestion. The insoluble material was removed by centrifugation and the supernatant was incubated overnight with Ni-NTA agarose beads (Thermo-fisher) at 4°C in a rotator-mixer. The protein loaded Ni-NTA column was washed twice with 20 column volumes of N1 buffer (50 mM PBS, 300 mM NaCl, 30 mM imidazole, pH 7.4) and twice N2 buffer (50 mM PBS, 150 mM NaCl, 10 mM imidazole, pH 7.4). The bound protein was subsequently eluted with N3 buffer (150 mM PBS pH 7.4, 300 mM imidazole). The protein fractions were eventually dialyzed with cassette Slide-A-Lyzer Dialysis Cassettes (Thermofisher) against 50 mM PBS, 150 mM NaCl pH 7.4.

B4.2 Mammalian cell culture and transfection

U2OS cells were incubated at 37°C in a 5% CO_2 in air atmosphere with McCoy's 5A Medium complemented with 10% fetal bovine serum (FBS). Cells were transiently transfected with Genejuice (Merck) according to the manufacturer protocol then washed with Dulbecco's phosphate buffered saline (DPBS) and fixed with 2% paraformaldehyde (PFA) solution.

B4.3 Reagents and solutions

B4.3.1 General

pH 7.4 PBS buffer (50 mM sodium phosphate, 150 mM NaCl) used for all experiments was made up using purified water (Direct-Q 5 apparatus; Millipore, Billerica, MA). By assimilating activity and concentration, the proton concentration of the solutions was directly measured after calibration of the pH meter (Standard pH meter PHM210, Radiometer Analytical equipped with a Radiometer Analytical PHC3359-8 combination pH electrode; Hach, Loveland, CO).

B4.3.2 RSFP solutions

The concentrations of the purified RSFP solutions were determined with a UV-spectrophotometer (Agilent Technologies, Santa Clara, CA). The UV-Vis absorption spectrum of the denaturated RSFP solution in 1 M NaOH was recorded from 400 to 600 nm in a 55 μL quartz cuvette with 1.5 mm light path (Hellma Optics, Jena, Germany). The RSFP concentration was extracted from the absorbance at 447 nm by using 44000 $M^{-1} \cdot cm^{-1}$ for the molar absorption coefficient of the deprotonated chromophore.[3] The RSFP solution was subsequently diluted with a PBS buffer (50 mM phosphate, 150 mM NaCl, pH 7.4) to give the RSFP solution at the desired concentration.

B4.3.3 Microfluidic device

The microdevice was composed of a circular glass coverslip (0.17 mm thick, 40 mm diameter; Menzel-Glaser, Braunschweig, Germany) and a PDMS stamp (RTV615; General Electrics, Fairfield, CT) including four 250 μm $\times$ 125 μm $\times$ 20 μm chambers separated by 100 μm $\times$ 20 μm walls. Each chamber was connected to a sample reservoir punched in the PDMS stamp through a 40 μm $\times$ 20 μm channel. Before assembly, the coverslip and the PDMS stamp were rinsed with ethanol and dried under a nitrogen flow. The bottom glass surface of the microdevice was placed on a 0.4 mm thick copper disk in which a 8 mm hole had been opened for further observation with the objective. To fill the micro-chambers with appropriate solutions, the air dissolved in the PDMS was pumped for 3 min at 50 mbar at room temperature and sample solutions were added to each reservoir, which resulted in the autonomous and controlled loading of the device.

B4.4 Epifluorescence setup for multiplexed imaging

We used a home-built epifluorescence microscopy setup. The samples were illuminated using a LXZ1-PB01 LED (Philips Lumileds) filtered at 480$\pm$20 nm (F480-40; Semrock, Rochester, NY) and a LHUV-0405 (Philips Lumileds) LED filtered at 405$\pm$20 nm (F405-40; Semrock, Rochester, NY) as light sources. Each LED was supplied by a LED driver (LEDD1B, Thorlabs, Newton, NJ). Light levels were sampled with an Arduino compatible card (Teensy 3.5, PJRC). A lens (ACL2520U; Thorlabs, Newton, NJ, $f = 20$ mm) was placed just after each diode to collimate the light sources. The two light beams were next combined thanks to a dichroic mirror (T425LPXR, Chroma, Bellows Falls, VT) and a second pair of lenses was used to focus the light at the back focal plane of the objective after being reflected by the dichroic filter (Di-FF506, Semrock, Rochester, NY). Fluorescence images at 525$\pm$15 nm (F525-30; Semrock, Rochester, NY) were acquired for the microdevices with a 10$\times$ fluar (NA 0.5, Carl Zeiss AG, Feldbach, Switzerland) objective and

for cell imaging with a 50× UPlanApo (NA 0.8, Olympus Corporation, Tokyo, Japan) objective. Objectives were mounted on a home-built microscope equipped with a Luca-R CCD camera (Andor Technology, Belfast,UK).

B4.5 Epifluorescence setup with inhomogeneous illumination

B4.5.1 Description

This home-built epi-fluorescence imaging system has been designed to validate the intrinsic optical sectioning effect of HIGHLIGHT by artificially introducing a controllable chromatic aberration between the two excitation wavelengths at 480 and 405 nm (see Fig.B10a). The system integrates two colored LEDs (LXZ1-PB01, centered at 480 nm and LHUV-0400, centered at 405 nm, Lumileds, NL) as excitation sources, in order to generate a large focal field around the focal plane. Each LED is triggered by a LED driver (DC 4104, Thorlabs, NJ, US). Light from each source is first collimated by lens L1 (AC254-200-A, $f = 200$ mm, Thorlabs, NJ, US) and then reduced by a quasi-afocal system consisting of two lenses (L2: LA1134-A, $f = 60$ mm, L3: LC2679-A, $f = -30$ mm, Thorlabs, Newton, NJ). The reduced beams are combined by a dichroic mirror (T425LPXR, Chroma, Bellows Falls, VT) and then focused by a convergent lens L4 (LA1131-A, $f = 50$ mm, Thorlabs, NJ, US). The focal plane of L4 is conjugated to the focal plane of the objective (UPLSAPO60XW, 60×, NA 1.2, Olympus Corporation, Tokyo, Japan), with the help of the tube lens system L5 and L6 (AC254-200-A, $f = 200$ mm, Thorlabs, NJ, US). The objective along with the tube lenses L5 and L6 gives a total magnitude of 100:3, forming an illuminated area of 15 μm at the sample. The position of the imaging plan after L4 can be effectively changed by slightly moving the element L3 back and forth along the optical axis, which makes it possible to defocus each wavelength independently from the focal plane of the objective. According to software simulation, a displacement of the element L3 by 1 mm gives rise to a defocus of 4 μm at the focal plane of the objective. The fluorescence signal from the sample is separated from the excitation lights with another dichroic mirror (T505LPXR, Chroma, Bellows Falls, VT) and then recorded by a CCD camera (Luca-R Andor Technology, Belfast, UK).

B4.5.2 Inhomogeneous illumination

Model of light profile The light distribution along the optical axis around the intermediate image on the focal plane in a medium of refractive index n was computed by making several approximations:

- The intensity of the image is considered to be constant across the image plane. This results from the uniformity of the LED source itself;

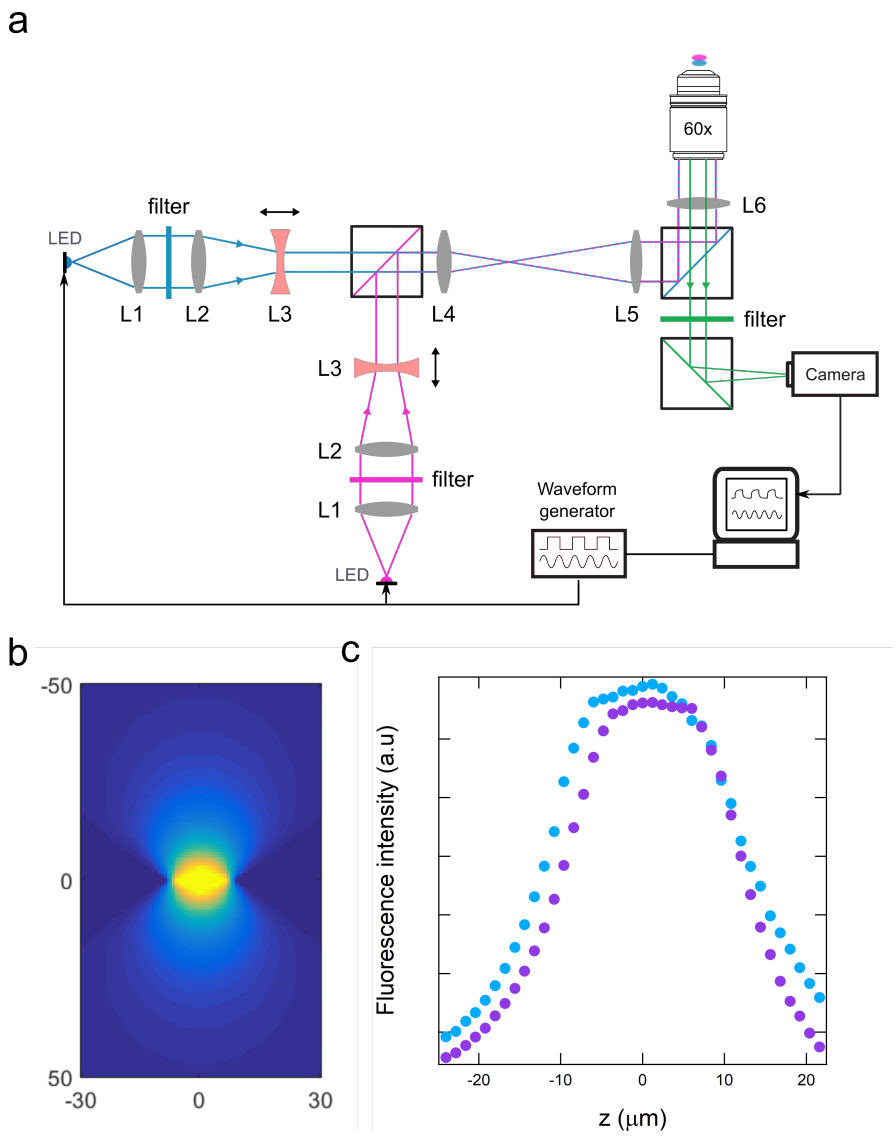

Figure B10: *Fluorescence imaging microscope for evidencing HIGHLIGHT optical sectioning*. **a**: Optical layout of the microscope and its interface to a PC-based synchronized modulation and imaging acquisition system. This epi-fluorescence imaging system is designed for manual defocusing of the two wavelengths at 480 (in blue) and 405 (in violet) nm; **b**: Simulation of the excitation light intensity in cylindrical coordinates. Essentially similar at 480 and 405 nm, it exhibits strong homogeneous light intensity over a square-based bipyramidal shape with 15 μm diameter and 15 μm height, which acts as a large pixel. Illumination is predicted to be laterally restricted in the focal plane and to axially decay over ten μm from the focal plane; **c**: Dependence of the normalized light intensity at 480 (blue disks) and 405 (violet disks) nm measured along the optical axis.

- The radiance L of the image is angularly constant within the aperture angle of the objective, because the LED source can be considered as a lambertian source;
- Assuming that the geometric aberration of the system is negligible, the light intensity distribution is symmetrical to the image plane (mirror symmetry, $I(-z) = I(+z)$).

We first analyzed the spatial profile of the light intensity around the focal plane of the objective, where a round shaped image of the LED source with a R_0 radius is projected. Since the light distribution is rotationally symmetric to the optical axis and mirrorly symmetric to the focal plane, we only computed the light irradiance I at medium points (r, z) identified by their cylindrical coordinates with origin set at the center of the focal plane (see Fig. B11).

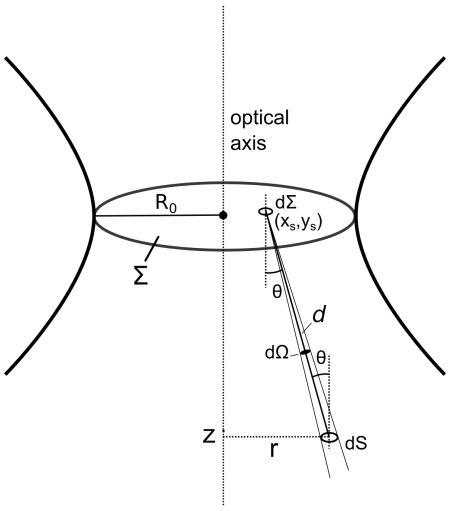

Figure B11: Schematic representation of the simulated excitation light intensity.

One has

$$I(r,z) = \frac{\mathrm{d}\Phi_F(r,z)}{\mathrm{d}S} \tag{B70}$$

where r is the distance to the optical axis of the system, z is the distance to the focal plane, and $\Phi_F(r,z)$ is the photon flux passing through an element of area $\mathrm{d}S$ at (r,z).

When analyzing the points (r,z) close to the image in the focal plane ($z \sim 2R_0$), the intermediate image is considered as a surface source Σ. Each element of surface $\mathrm{d}\Sigma$ at $(x_s, y_s, 0)$ is considered Lambertian within an acceptance angle θ_m. The radiance can be expressed as:

$$L(\theta) = \begin{cases} L_s & \theta \leqslant \theta_m \\ 0 & \theta > \theta_m \end{cases}$$

where θ is the angle between the light ray and the normal of the surface Σ. The acceptance angle is defined by the numerical aperture of the objective in use, NA$= n\sin(\theta_m) = 1.2$, where n is the refractive index of the medium around the fiber.

The flux received by $\mathrm{d}S$ at (r,z) from the source element $\mathrm{d}\Sigma$ at $(x_s, y_s, 0)$ is:

$$\mathrm{d}^2\Phi_F = L(\theta)10^{-\frac{d}{d_c}}\mathrm{d}^2G = L(\theta)10^{-\frac{d}{d_c}}\frac{\mathrm{d}S\mathrm{d}\Sigma\cos^2\theta}{d^2} = L(\theta)10^{-\frac{d}{d_c}}\frac{\mathrm{d}S\mathrm{d}\Sigma\cos^4\theta}{z^2} \tag{B71}$$

where d_c is a typical length. In Eq.(B71), G is the *etendue* defined as

$$\mathrm{d}^2G = \mathrm{d}\Sigma\cos\theta\mathrm{d}\Omega_\Sigma = \frac{\mathrm{d}\Sigma\mathrm{d}S\cos^2\theta}{d^2} \tag{B72}$$

where d is the distance between $\mathrm{d}\Sigma$ and $\mathrm{d}S$, and $\cos\theta = \frac{z}{d} = \frac{z}{\sqrt{(r-x_s)^2+y_s^2+z^2}}$ (see Fig. B11).

Finally we get the irradiance at (r,z) from the entire surface Σ:

$$\begin{aligned} I(r,z) &= \frac{\mathrm{d}\Phi_F(r,z)}{\mathrm{d}S} = \frac{1}{\mathrm{d}S}\int_\Sigma \mathrm{d}^2\Phi_F(r,z) \\ &= \frac{1}{\mathrm{d}S}\int_\Sigma \frac{L(\theta)\mathrm{d}\Sigma\mathrm{d}S\cos^2\theta}{d^2}10^{-\frac{d}{d_c}} = \int_\Sigma \frac{L(\theta)\cos^4\theta}{z^2}10^{-\frac{d}{d_c}}\mathrm{d}\Sigma \end{aligned} \tag{B73}$$

Calculation of the Pre-HIGHLIGHT and HIGHLIGHT-n signals for the model of inhomogeneous light profile We neglect possible chromatic aberration of the fluorescence microscope and assume that the medium exhibits similar absorption and scattering of light at the two wavelengths. Consequently illuminations have the same spatial dependence at both wavelengths and the ratio $I_2^0(r,z)/I_1^0(r,z)$ is constant. In the following, we consider that the HIGHLIGHT-1 resonance condition is fulfilled in the focal plane on the optical axis ($r = z = 0$). According to Eqs. (B68,B69) for $K^0 = \theta = 1$ we have

$$\frac{I_2^0(r,z)}{I_1^0(r,z)} = \frac{\sigma_1}{\sigma_2} \tag{B74}$$

$$\frac{\omega}{I_1^0(0,0)} = 2\sigma_1 \tag{B75}$$

The condition given in Eq. (B75) is not obeyed apart from the intersection between the optical axis and the focal plane. The HIGHLIGHT-n signals display a better axial selectivity than the Pre-HIGHLIGHT signal.

The spatial dependence of the Pre-HIGHLIGHT and HIGHLIGHT-n signals are computed using Eqs. (B19,B20,B23–B29) and Eqs. (B52–B56). The dependence of the parameters K^0 and θ is deduced from Eqs. (B68,B69) and the light profile is given in Eq. (B73) with an experimentally evaluated typical length d_c. The results are given in Fig. B12. The areas in which the HIGHLIGHT-n signals are significant are smaller than in the Pre-HIGHLIGHT signal. With the present setup which projects the contributions of all fluorophores located along the optical axis, the HIGHLIGHT-n signals are dominated by the contributions of the fluorophores located close to the focal plane as shown in Figure 4.

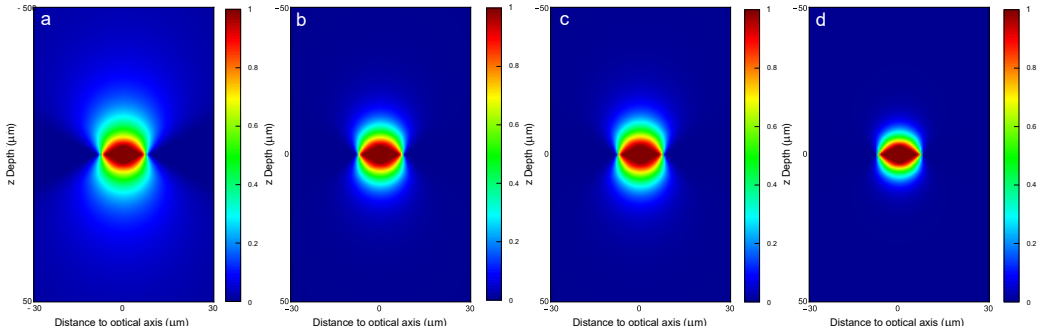

Figure B12: Spatial dependence of the scaled Pre-HIGHLIGHT (**a**), HIGHLIGHT-1 (**b**), HIGHLIGHT-2 (**c**) and HIGHLIGHT-3 (**d**) signals after introducing the light profiles in the analytical expressions of the HIGHLIGHT signals with sine-wave light modulation at $\lambda_1 = 480$ nm and constant light at $\lambda_2 = 405$ nm.

B4.5.3 Characterization of the illumination profile

In order to study the excitation profiles from the LEDs at $\lambda_1 = 488$ nm and $\lambda_2 = 405$ nm, we imaged a 2 μm-thick layer of 5 μM fluorescein solution in pH 7.4 PBS buffer (sandwiched between two 170 μm-thick glass plates) at different axial positions ranging from 0 to 21.6 μm. Fig. B10c has been obtained after measuring the signal emission intensity for each axial position.

B4.5.4 Samples for confocality validation

Dronpa-2-containing samples of defined thickness have been obtained by sandwiching Dronpa-2 solutions between two 170 μm-thick glass slides, which have been treated with air plasma cleaner to increase their surface hydrophilicity. In order to control the sample thicknesses below the 20 μm range, we used either polystyrene beads (carboxylate microsphere, Polybead, Polysciences Inc, Us) or magnetic polystyrene beads (Magnetic polystyrene particles micromer, Micromer-M, Micromod, Germany) with 4, 6, 12 and 20 μm diameters as spacers. The commercial suspension of beads was first diluted in PBS to the thousandth. Then the resulting suspension was uniformly suspended by sonicating. It was eventually mixed with the Dronpa-2 solution for sandwiching. In order to get the 50, 80, and 120 μm sample thicknesses, we exploited a double sided tape as home-made imaging spacer and a 120 μm-thick commercially available spacer (SecureSeal, Sigma-Aldrich, Grace Bio-Lab, USA).

B4.6 Generation of pure sine-wave light modulation

Light emitted from a LED was modulated sinusoidally and filtered with a bandpass filter (ZET 405-20x, Chroma Technology, Bellows Falls, VT, for the violet LED or ET 480-20x, Chroma Technology for the blue LED). An optical fiber (M38L01, Thorlabs, Newton, NJ) was used to collect

part of the emitted light that was next focused with a $f = 40$ mm lens onto the sensor of a silicon photomultiplier module (C13366-3050GA, Hamamatsu Photonics K.K., Hamamatsu City, Japan). Light levels were sampled with an Arduino compatible card (Teensy 3.5, PJRC) which calculated the Fourier Transform of the silicon photomultiplier signal to retrieve the harmonic content of the modulated light. The first harmonics up to the 10^{th} order were introduced with a 180° phase shift in the voltage modulation delivered by a DAC output of the Teensy 3.5 which controlled the electric current delivered by a LED driver (LEDD1B, Thorlabs) to the LED chip. After a few iterations (typically 10), the harmonic content of modulated light emitted from the LED chip was efficiently damped: the amplitude of each harmonics was measured independently by our EM-CCD camera (Luca-R, Andor Technology, Belfast, Northern Ireland) and was found to be less than 0.75% of the amplitude term at fundamental frequency.

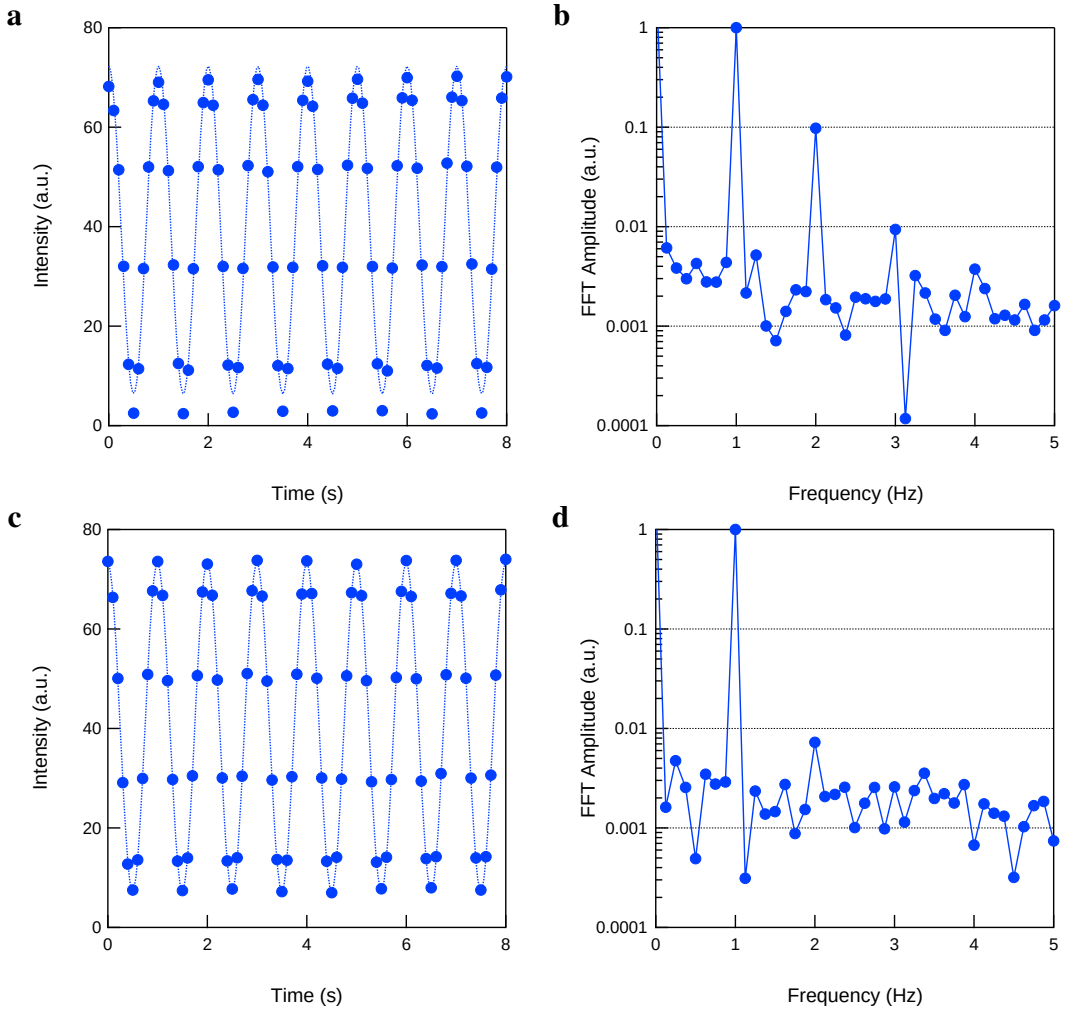

Figure B13: Generation of pure sine-wave light from the LED at 480 nm. **a**,**c**: Evolution of the light intensity of the modulated LED light before (**a**) and after (**c**) harmonic correction of the sine-wave tension from the generator supplying the LED; **b**,**d**: Fourier transforms of the signals displayed in **a**,**c**.

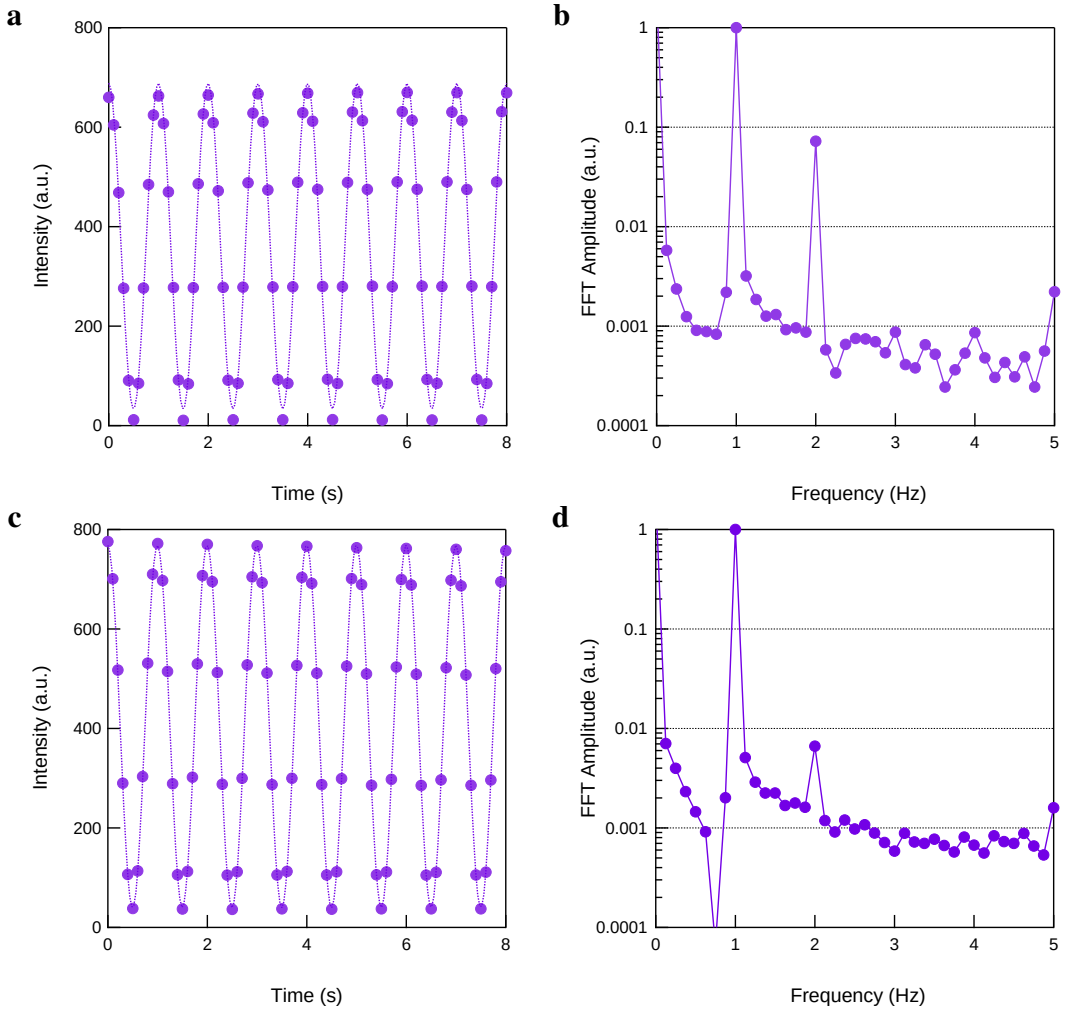

Figure B14: Generation of pure sine-wave light from the LED at 405 nm. **a**,**c**: Evolution of the light intensity of the modulated LED light before (**a**) and after (**c**) harmonic correction of the sine-wave tension from the generator supplying the LED; **b**,**d**: Fourier transforms of the signals displayed in **a**,**c**.

B4.7 Video acquisition

In the imaging experiments, we record films for m periods of light modulation (m is an integer). The acquisition frequency of the camera is set to obtain $2N$ (N is an integer) frames per period of modulation. Thus the acquisition frequency is $f_s = 2Nf_m$, where f_m is the modulation frequency of the excitation light. The fluorescence emission acquired at pixel (x,y) of the k^{th} frame is equal

to

$$I_{\mathrm{F}}(x,y,k) = T_s\Bigg(I_F^0(x,y) + \sum_{n=1}^{N}\Bigg\{B_n(x,y)\sin\left[\frac{\pi n f_s}{N}\left(\frac{k}{f_s}+\phi_{\mathrm{acq}}\right)\right] + A_n(x,y)\cos\left[\frac{\pi n f_s}{N}\left(\frac{k}{f_s}+\phi_{\mathrm{acq}}\right)\right]\Bigg\}\Bigg) \tag{B76}$$

where $T_s = \frac{1}{f_s}$ is the exposure time of one frame, $B_n(x,y)$ and $A_n(x,y)$ are the n-th in-phase and quadrature Fourier amplitudes of the fluorescence signal oscillating around the average value $I_F^0(x,y)$. The phase ϕ_{acq} may originate from distinct starting times for the light modulation and the acquisition of the camera and can be easily calibrated using the fluorescence emission from instantaneously responding fluorophores (such as EGFP or Fluorescein).

Pre-processing is performed to compensate for possible photobleaching of fluorophores. Assuming that photobleaching linearly decays, we evaluate the compensation factor $K(x,y)$ from the average of two successive periods

$$K(x,y) = \frac{\langle I_F(x,y,k)\rangle_{k=2N}^{4N-1} - \langle I_F(x,y,k)\rangle_{k=0}^{2N-1}}{2N} \tag{B77}$$

Then the frames of the same two periods are corrected according to

$$I_F^{\mathrm{corr}}(x,y,k) = I_F(x,y,k) - K(x,y)\times k \tag{B78}$$

The procedure is repeated for the whole video.

The Pre-HIGHLIGHT image $I_F^0(x,y)$ is calculated by averaging the frames over the whole film

$$I_F^0(x,y) = \frac{f_s}{2mN}\sum_{k=0}^{2\mathrm{mN}-1} I_F^{\mathrm{corr}}(x,y,k) \tag{B79}$$

The HIGHLIGHT-n signals are retrieved according to

$$A_1 = \frac{f_s}{mN}\sum_{k=0}^{2\mathrm{mN}-1}\left\{I_F^{\mathrm{corr}}(x,y,k)\times\cos\left[\frac{\pi f_s}{N}\left(\frac{k}{f_s}+\phi_{\mathrm{acq}}\right)\right]\right\} \tag{B80}$$

$$B_2 = \frac{f_s}{mN}\sum_{k=0}^{2\mathrm{mN}-1}\left\{I_F^{\mathrm{corr}}(x,y,k)\times\sin\left[2\frac{\pi f_s}{N}\left(\frac{k}{f_s}+\phi_{\mathrm{acq}}\right)\right]\right\} \tag{B81}$$

$$A_3 = \frac{f_s}{mN}\sum_{k=0}^{2\mathrm{mN}-1}\left\{I_F^{\mathrm{corr}}(x,y,k)\times\cos\left[3\frac{\pi f_s}{N}\left(\frac{k}{f_s}+\phi_{\mathrm{acq}}\right)\right]\right\}. \tag{B82}$$

In section B4.9, we provide the Matlab code, which we used to compute the HIGHLIGHT-n signals in our imaging experiments.

B4.8 Calibration of light intensities

HIGHLIGHT implementation requires knowing the intensity of the two excitation lights at 480 and 405 nm in the sample in order to set the control parameters at the resonance condition for the targeted RSFP. Instead of using a powermeter, we relied on the photoswitching kinetics of a photochemically well-characterized RSFP (Dronpa-2 at pH 7.4) for measuring light intensities at which the kinetics is well-accounted by a two-state model (see section B1). Such an actinometric measurement is photochemically reliable up to 10 ein.m^{-2}.s^{-1} light intensities at the wavelengths $\lambda_1 = 480$ nm and $\lambda_2 = 405$ nm respectively. The calibration of the light intensities exploits light jumps on Dronpa-2 samples (calibrating sample: 6 μm-thick layer of 20 μM Dronpa-2 solution in pH 7.4 PBS buffer sandwiched between two 130 μm-thick glass slides). We use the reported values of $\sigma_1 = 196$ m^{2}mol^{-1}, $\sigma_2 = 413$ m^{2}mol^{-1}, and $k^\Delta = 0.014$ s^{-1} for Dronpa-2.[5]

- As a preliminary step of the calibration protocol, the Dronpa-2 solution is illuminated with the 405 nm LED ($I_2^0 = 0.01$ ein.m^{-2}.s^{-1} for 2 min) to secure that Dronpa-2 is initially in its thermodynamically stable state C_1.

- In a first step, the sample is submitted to constant light intensity I_1^0 at $\lambda_1 = 480$ nm. Dronpa-2 switches from the bright state C_1 to the dark state C_2 (see Fig. B15a). The evolution of fluorescence is averaged over space and compared to

$$I_{\mathrm{F}}(t) = A + B \exp\left(-\frac{t}{\tau}\right) \tag{B83}$$

  where A, B, and τ are used as fitting parameters. Using Eqs. (B10,B62,B63) relating the characteristic time and the rate constants, we obtain the light intensity at the wavelength λ_1

$$I_1^0 = \frac{1}{\sigma_1}\left(\frac{1}{\tau} - k^\Delta\right) \tag{B84}$$

- In a second step, while maintaining constant the illumination I_1^0 at the wavelength $\lambda_1 = 480$ nm, we submit the sample to to a constant light I_2^0 at the wavelength $\lambda_2 = 405$ nm in order to drive the C_2 to C_1 reaction and recover fluorescence (see Fig. B15b). The fluorescence evolution is averaged space and compared to the fitting function given in Eq. (B83) leading to an evaluation of the characteristic time τ. Using Eqs. (B10,B62,B63,B65) relating the characteristic time and the rate constants, we obtain the light intensity at the wavelength λ_2

$$I_2^0 = \frac{1}{\sigma_2}\left(\frac{1}{\tau} - k^\Delta - \sigma_1 I_1^0\right) \tag{B85}$$

  where the light intensity I_1 has been evaluated in the first step.

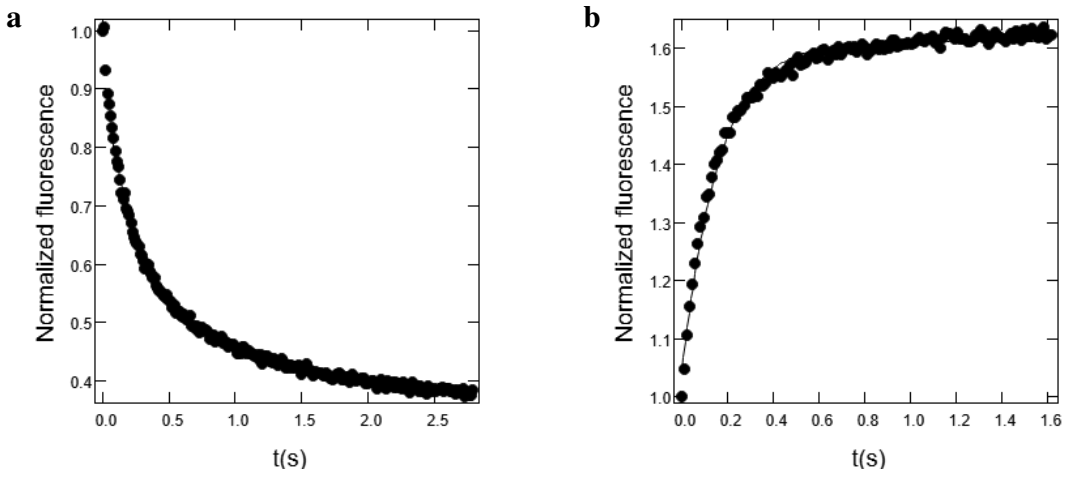

Figure B15: Calibration of the light intensities using the photoisomerization kinetics of Dronpa-2. **a**: Fluorescence evolution of a 20 μM Dronpa-2 solution in pH 7.4 PBS buffer submitted to illumination at $\lambda_1 = 480$ nm ($I_1^0 = 4.8 \times 10^{-2}$ Ein.m^{-2}s^{-1}); **b**: Fluorescence evolution of a 20 μM Dronpa-2 solution in pH 7.4 PBS buffer submitted to illumination at both $\lambda_1 = 480$ and $\lambda_2 = 405$ nm ($I_1^0 = 1.6 \times 10^{-2}$ Ein.m^{-2}s^{-1} and $I_2^0 = 7.6 \times 10^{-3}$ Ein.m^{-2}s^{-1}). Disks: Experimental data; solid lines: Fitting function given in Eq. (B83). $T = 298$ K.

B4.9 Matlab code for extracting the HIGHLIGHT signals

```
function [IF0,IF1in,IF1out,IF2in,IF2out,Phase]=highlight(filename,period,phi_acq,n_per,skip_per)
% Computes pre-HIGHLIGHT (IF0) and HIGHLIGHT responses IF1out and IF2in
% We assume movie acquired is already loaded in matlab as 'filename'
% (as camera manufacturers usually provide code to import files)
% 'period' is the period of the light excitation at fundamental frequency in frame number
% 'phi_acq' is the phase delay between the dates of camera recording
% and light excitation previously calibrated at first order with fluorescein or EGFP
% 'n_per' is the total number of periods used for calculation,
% an even number of periods is considered (typically 8)
% 'skip_per' is the number of periods to skip before calculation

npts = period*n_per;
first = skip_per*period;
[X,Y,Z] = size(filename);
Holder = zeros(X,Y,npts);
IF1in = zeros(X,Y);
IF1out = zeros(X,Y);
IF2in = zeros(X,Y);
IF2out = zeros(X,Y);

for i=1:npts
     Holder(:,:,i)=filename(:,:,i+first);
end

%%%%%%%%%%%%%%%%%%%%%%%%%%%%%%%%%%%%%%%%%%%%%%%%%%%%%%%%%%%%%%%%%%%
%%  Photobleaching correction assuming a linear decay
%%%%%%%%%%%%%%%%%%%%%%%%%%%%%%%%%%%%%%%%%%%%%%%%%%%%%%%%%%%%%%%%%%%

% Calculate the average signal over the first half of 2n periods
```

```
 linePoint1=mean(Holder(:,:,1:((npts)/2)),3);
%Calculate the average signal over the last half of 2n periods
 linePoint2=mean(Holder(:,:,((npts)/2+1):end),3);
% Calculate the slope B(x,y)
 slope=(linePoint2-linePoint1)/(npts/2);
%Correction for photobleaching
  for i=1:npts
     Holder(:,:,i)=(Holder(:,:,i)-slope.*i);
  end

%%%%%%%%%%%%%%%%%%%%%%%%%%%%%%%%%%%%%%%%%%%%%%%%%%%%%%%%%%%%%%%%
%%  Data processing
%%%%%%%%%%%%%%%%%%%%%%%%%%%%%%%%%%%%%%%%%%%%%%%%%%%%%%%%%%%%%%%%

% Compute pre-HIGHLIGHT image
IF0=mean(Holder,3); % pre-HIGHLIGHT image

% Compute HIGHLIGHT images
for i=1:npts
    IF1in(:,:)= (IF1in(:,:) + ((Holder(:,:,i)).*sin(2*pi*(i-1)/period + phi_acq)));
    IF1out(:,:)= (IF1out(:,:) + ((Holder(:,:,i)).*cos(2*pi*(i-1)/period + phi_acq)));
    IF2in(:,:) = (IF2in(:,:) + (Holder(:,:,i)).*sin(4*pi*(i-1)/period + 2*phi_acq));
    IF2out(:,:) = (IF2out(:,:) + (Holder(:,:,i)).*cos(4*pi*(i-1)/period + 2*phi_acq));
end

IF1in = 2.*IF1in./npts; % HIGHLIGHT 1in image
IF1out = 2.*IF1out./npts; % HIGHLIGHT 1out image
IF2in = 2.*IF2in./npts; % HIGHLIGHT 2in image
IF2out = 2.*IF2out./npts; % HIGHLIGHT 2out image
Phase = atan(IF1out./IF1in); %to calibrate phase with Fluorescein or EGFP


%%%%%%%%%%%%%%%%%%%%%%%%%%%%%%%%%%%%%%%%%%%%%%%%%%%%%%%%%%%%%%%%
%%  Display Pre-HIGHLIGHT
%%%%%%%%%%%%%%%%%%%%%%%%%%%%%%%%%%%%%%%%%%%%%%%%%%%%%%%%%%%%%%%%

CameraDark = 508.12; %Black level of the camera, Change to match your model
IF0=IF0-CameraDark; %We substract the black level
figure;imagesc(IF0);colormap(gray(4096));colorbar;axis equal tight;

%%%%%%%%%%%%%%%%%%%%%%%%%%%%%%%%%%%%%%%%%%%%%%%%%%%%%%%%%%%%%%%%
%%  Display HIGHLIGHT
%%%%%%%%%%%%%%%%%%%%%%%%%%%%%%%%%%%%%%%%%%%%%%%%%%%%%%%%%%%%%%%%

%Generate 1in image
figure;imagesc(IF1in);colormap(gray(4096));colorbar;
%Generate 1out image
figure;imagesc(IF1out);colormap(gray(4096));colorbar;
%Generate 2in image
figure;imagesc(IF2in);colormap(gray(4096));colorbar;
%Generate 2out image
figure;imagesc(IF2out);colormap(gray(4096));colorbar;
end
```

B4.10 Cell imaging

This series of experiments has been performed using sine-wave modulation of large amplitude (100%) at $\lambda_1 = 480$ nm and constant light at $\lambda_2 = 405$ nm. The fluorescence intensity $I_{\rm F}(x, y, t)$ of each pixel was analyzed with Eqs.(B79–B82) to provide the $I_F^0(x, y)$ (pre-HIGHLIGHT) and the $A_1(x, y)$ (HIGHLIGHT-1), $B_2(x, y)$ (HIGHLIGHT-2), $A_3(x, y)$ (HIGHLIGHT-3) images. To reduce noise, the images have been spatially averaged over a 3-pixel square. The acquisition parameters used for HIGHLIGHT imaging of cells are reported in Tab. B6.

B4.11 Confocal experiments

The images displayed in Fig. 4a–f and Fig. B21a–f devoted to evidence intrinsic HIGHLIGHT optical sectioning were recorded for a 10-μM Dronpa-2 solution in pH 7.4 PBS buffer for different sample thicknesses z using sine-wave modulation of large amplitude (100%) at $\lambda_1 = 480$ nm ($\lambda_2 = 405$ nm, resp.) and constant light at $\lambda_2 = 405$ nm ($\lambda_1 = 480$ nm, resp.). The dependence of the signal intensities on z shown in Fig. 4g and Fig. B21g have been obtained after spatial averaging of the images over a region of interest of 400 pixels (equivalent to a square of 6 μm in the sample).

B4.12 Photochemical parameters of the RSFPs

Table B5: Photochemical parameters of Dronpa, Dronpa-2, Dronpa-3, and rsFastLime at pH 7.5 and at 37 °C. σ_1 and σ_2 designate the photoswitching cross sections from the bright state C_1 (dark state C_2, resp.) to the dark state C_2 (bright state C_1, resp.) at $\lambda_1 = 480$ nm ($\lambda_2 = 405$ nm, resp.).[5]

RSFP	σ_1 ($m^2.mol^{-1}$)	σ_1 ($m^2.mol^{-1}$)
Dronpa	5,1	354,5
Dronpa-2	196	413
Dronpa-3	29	331
rsFastLime	36	648

B4.13 Acquisition parameters used for the HIGHLIGHT experiments

The acquisition parameters used in the HIGHLIGHT experiments are reported in Tab. B6.

B4.14 Softwares

Data treatment, image analysis and theoretical computations were performed using Igor Pro (WaveMetrics), MATLAB (The MathWorks), Gnuplot and Mathematica (Wolfram Research) softwares.

Table B6: Acquisition parameters used to image RSFPs at 25°C in Fig. 2, 3, 4 of the Main Text and Fig. B17, B18, B19, B20, and B21 of the Supporting Information. f_s and f_m refer to the sampling rate and the modulation frequency of the excitation lights. $\alpha = 1$ for all experiments.

Figure	Periods	f_s (Hz)	f_m (Hz)	ω (rad.s^{-1})	I_1^0 (Ein.m^{-2}.s^{-1})	I_2^0 (Ein.m^{-2}.s^{-1})
2e–h	10	12	1	6.3	1.6×10^{-2}	7.6×10^{-2}
2e–h;3c,g,k;4;B19;B20e–h;B21	10	12	1	6.3	1.6×10^{-2}	7.6×10^{-3}
2e–h	10	12	1	6.3	1.6×10^{-2}	7.6×10^{-4}
2e–h	10	12	1	6.3	1.6×10^{-2}	7.6×10^{-5}
2e–h	10	1.20	0.1	0.6	1.6×10^{-2}	7.6×10^{-3}
2e–h	10	12	1	6.3	1.6×10^{-2}	7.6×10^{-3}
2e–h	10	120	10	63	1.6×10^{-2}	7.6×10^{-3}
3b,f,j	40	0.3	0.025	0.16	1.5×10^{-2}	2.2×10^{-4}
3d,h,i;B18	10	12	1	6.3	8.7×10^{-2}	4.8×10^{-3}
B17	10	12	1	6.3	0.1	9.4×10^{-3}
B20a–d	10	12	1	6.3	8.7×10^{-2}	4.8×10^{-3}

B5 Supplementary Figures

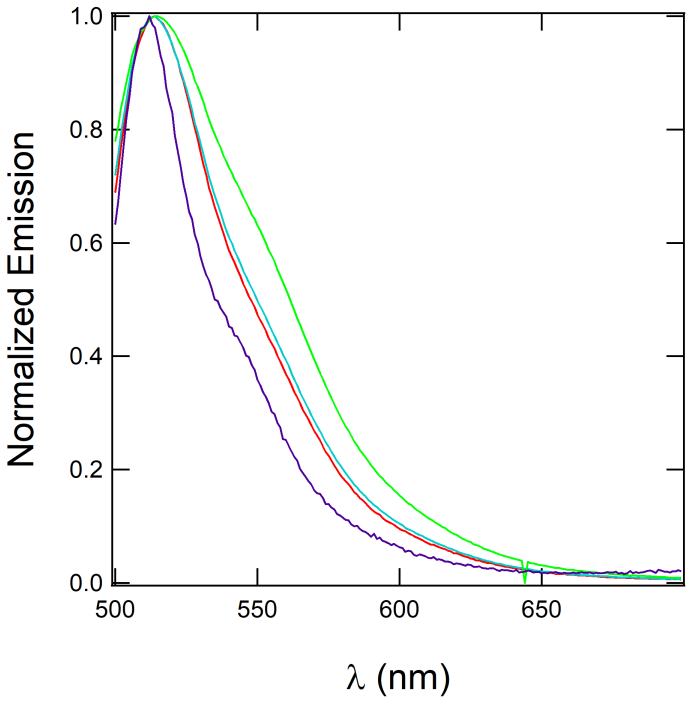

Figure B16: Normalized emission (λ_{exc} = 488 nm) spectra of 5 μM solutions in pH 7.4 PBS (50 mM sodium phosphate, 150 mM NaCl) of the 4 RSFPs : Dronpa (red), Dronpa-3 (blue), rsFastLime (green), and Dronpa-2 (violet); T = 298 K.

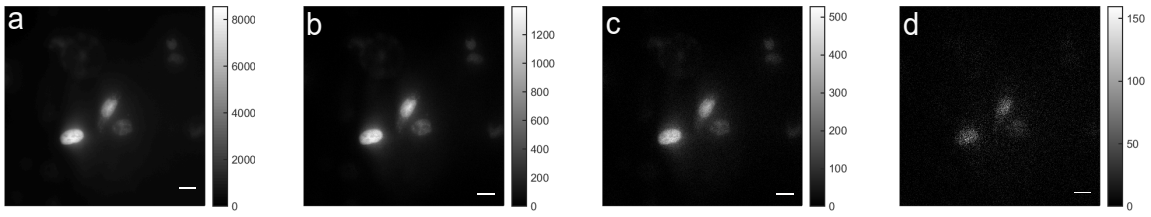

Figure B17: HIGHLIGHT-n discrimination of Dronpa-3. Pre-HIGHLIGHT (**a**), HIGHLIGHT-1 (**b**), HIGHLIGHT-2 (**c**), HIGHLIGHT-3 (**d**) images of Dronpa-3. System: Fixed U2OS cells expressing H2B-Dronpa-3 (at the nucleus). The images were recorded at 298 K. Scale bars: 10 μm. See Tab. B6 in Supporting Information for the acquisition conditions.

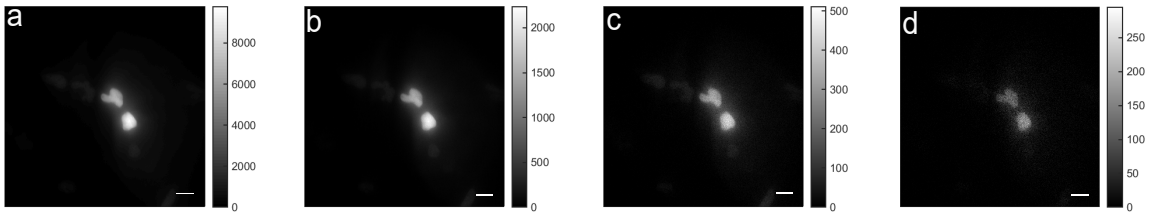

Figure B18: HIGHLIGHT-n discrimination of rsFastLime. Pre-HIGHLIGHT (**a**), HIGHLIGHT-1 (**b**), HIGHLIGHT-2 (**c**), HIGHLIGHT-3 (**d**) image of rsFastLime. System: Fixed U2OS cells expressing H2B-rsFastLime (at the nucleus). The images were recorded at 298 K. Scale bars: 10 μm. See Tab. B6 in Supporting Information for the acquisition conditions.

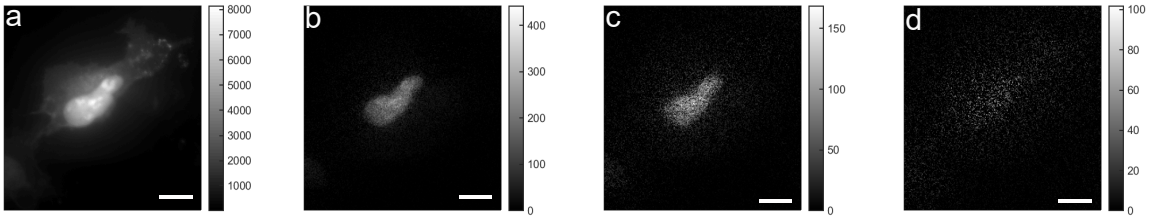

Figure B19: *HIGHLIGHT-n eliminate spectral interferences*. Pre-HIGHLIGHT (**a**), HIGHLIGHT-1 (**b**), HIGHLIGHT-2 (**c**), HIGHLIGHT-3 (**d**) images of Dronpa-2 and EGFP. System: Fixed U2OS cells expressing H2B-Dronpa-2 (at the nucleus) and Lyn11-EGFP (at the cell membrane). The images were recorded at 298 K. Scale bars: 10 μm. See Tab. B6 in Supporting Information for the acquisition conditions.

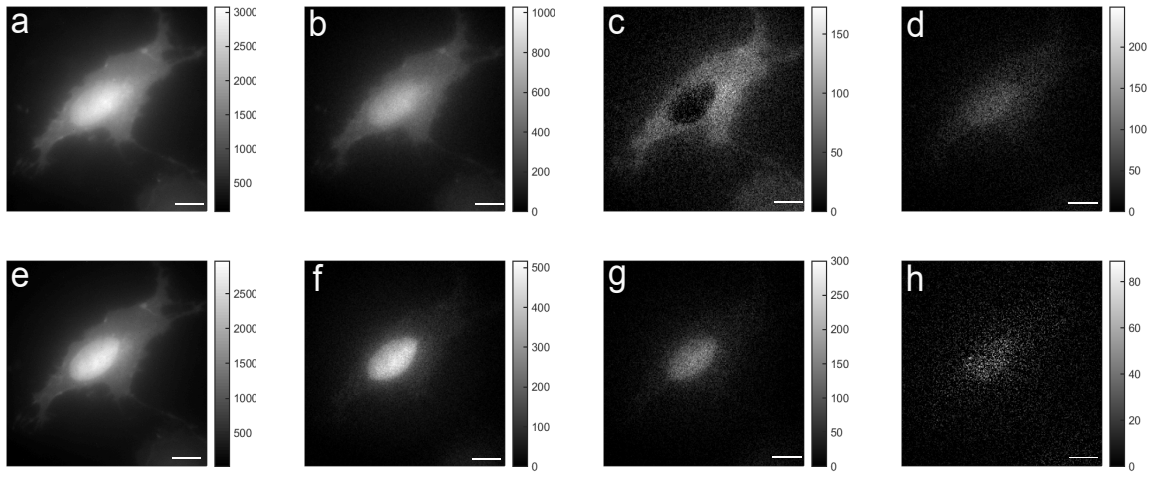

Figure B20: *HIGHLIGHT-2 discriminates distinct spectrally similar RSFPs*. Pre-HIGHLIGHT (**a**,**e**), HIGHLIGHT-1 (**b**,**f**), HIGHLIGHT-2 (**c**,**g**), HIGHLIGHT-3 (**d**,**h**) images of Dronpa-2 and rsFastLime. System: Fixed U2OS cells expressing H2B-Dronpa-2 (at the nucleus) and Lyn11-rsFastLime (at the cell membrane). The images were recorded at 298 K. Scale bars: 10 μm. See Tab. B6 in Supporting Information for the acquisition conditions.

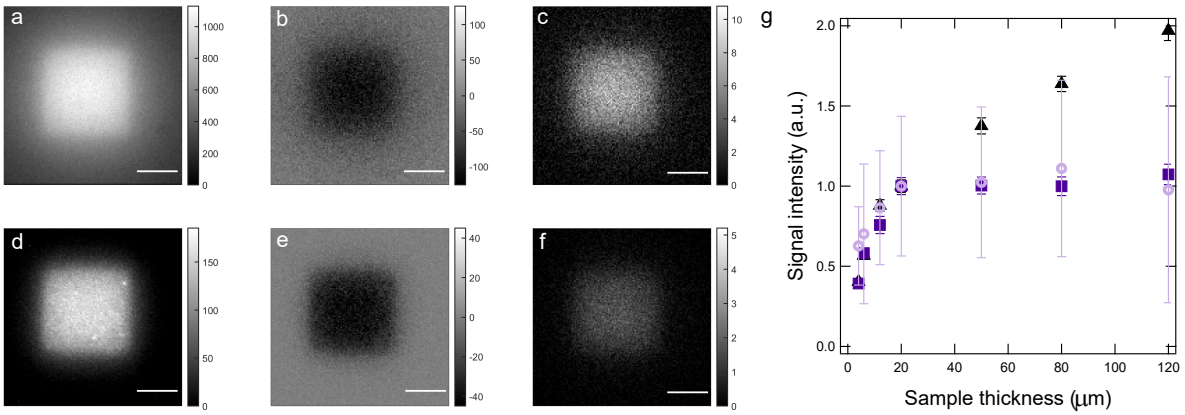

Figure B21: *Optical sectioning power of HIGHLIGHT*. Pre-HIGHLIGHT (**a**,**d**), HIGHLIGHT-1 (**b**,**e**), -2 (**c**,**f**) images of a 10-μM Dronpa-2 solution of thickness 120 μm (**a–c**) and 4 μm (**d–f**) obtained with an optical setup using coaxial light profiles spatially decaying over 10 μm from a homogeneously illuminated 15-μm edge octahedron. Scale bar: 10 μm; **g**: Pre-HIGHLIGHT (black triangles), HIGHLIGHT-1 (deep violet squares), -2 (light violet circles) signals versus thickness z of the sample for a 10-μM Dronpa-2 solution. The mean signal intensities and the error bars are obtained using spatial averages of the images over a 6-μm square. See Tab. B6 in Supporting Information for the acquisition conditions with sine-wave light at $\lambda_2 = 405$ nm and constant light at $\lambda_1 = 480$ nm.

References

[1] M. Baptista, T. Silva, J. Sartorelli, I. Caldas, L. Iberê, and E. Rosa, Phase synchronization in the perturbed Chua circuit, *Physical Review E*, **2003**, *67*, 056212.

[2] W. Zhang and G. Meng, Nonlinear dynamical system of micro-cantilever under combined parametric and forcing excitations in MEMS,*Sensors and Actuators A: Physical*, **2005**, *119*, 291–299.

[3] S. Kredel, K. Nienhaus, F. Oswald, M. Wolff, S. Ivanchenko, F. Cymer, A. Jeromin, F. J. Michel, K.-D. Spindler, R. Heilker, G. U. Nienhaus, J. Wiedenmann, Optimized and far-red-emitting variants of fluorescent protein eqfp611, *Chemistry Biology*, **2008**, *15*, 224–233.

[4] J. Querard, A. Gautier, T. Le Saux, L. Jullien, Expanding discriminative dimensions for analysis and imaging, *Chem. Sci.*, **2015**, *6*, 2968–2978.

[5] J. Querard, R. Zhang, Z. Kelemen, M.-A. Plamont, X. Xie, R. Chouket, I. Roemgens, Y. Korepina, S. Albright, E. Ipendey, M. Volovitch, H. L. Sladitschek, P. Neveu, L. Gissot, A. Gautier, J.-D. Faure, V. Croquette, T. Le Saux, L. Jullien, Resonant out-of-phase fluorescence microscopy and remote imaging overcome spectral limitations, *Nat. Commun.*, **2017**, *8*, 969.

Agnès Pellissier-Tanon – Thèse de doctorat – 2020

Discrimination cinétique de marqueurs fluorescents réversiblement photocommutables

Resumé : Le multiplexage ou imagerie simultanée de dizaines d'espèces dans une cellule, est un défi pour la biologie quantitative. Deux protocoles d'imagerie, LIGHTNING et HIGHLIGHT, exploitant la cinétique riche de photocycles comprenant des étapes photochimiques et thermiques, ont été conçus et appliqués à des protéines fluorescentes réversiblement photocommutables (RSFP). Dans LIGHTNING, 4 temps caractéristiques définissant la signature cinétique d'une RSFP sont extraits de l'évolution de la fluorescence pour 4 conditions d'illumination constante donnant accès à 4 dynamiques indépendantes. Des mécanismes chimiques réduits sont dérivés pour les 4 conditions d'illumination. Deux RSFP sont distinguées si la distance entre leurs signatures cinétiques est plus grande qu'une distance de coupure liée à la précision expérimentale. 20 RSFP parmi les 22 étudiées sont discriminées. Dans HIGHLIGHT, des fluorophores reversiblement photocommutables sont soumis à un éclairement sinusoïdal. A chaque harmonique, l'amplitude de Fourier en phase ou en quadrature des oscillations de fluorescence présente une résonance dans l'espace des paramètres de contrôle, fréquence d'excitation et intensités lumineuses moyennes. Des conditions de résonance reliant les paramètres de contrôle et les paramètres caractérisant la cinétique sont explicitées. Le choix des paramètres de contrôle permet d'optimiser la réponse d'un fluorophore tout en éliminant celle des fluorophores de cinétiques différentes. Les deux protocoles ont des mérites complémentaires. LIGHTNING a un pouvoir discriminant plus important et HIGHLIGHT fournit des images de meilleure qualité grâce à une détection synchrone.

Mots clés : Imagerie de fluorescence multiplexée, protéines fluorescentes réversiblement photocommutables, analyse multiexponentielle, élimination de variables rapides, système dynamique forcé, résonance.

Kinetics-based discrimination of reversibly photoswitchable fluorescent labels

Abstract : Multiplexing, i.e. simultaneously imaging tens of chemical species in a cell, is a challenge for quantitative biology. To this aim, two imaging protocols, LIGHTNING and HIGHLIGHT, exploiting the kinetics of rich photocycles including photochemical and thermal steps are introduced and applied to reversibly photoswitchable fluorescent proteins (RSFPs). In LIGHTNING, four characteristic times defining the kinetic signature of an RSFP are extracted from fluorescence evolution in four constant illumination regimes granting access to four independent dynamics. Reduced chemical mechanisms derived for the four illumination regimes qualitatively account for fluorescence evolution. Two RSFPs can be distinguished provided that the distance between their 4-D kinetic signature is larger than a cutoff distance related to experimental accuracy. 20 RSFPs out of the 22 investigated RSFPs are discriminated. In HIGHLIGHT, reversibly photoactivatable fluorophores are submitted to sine-wave illumination. At each harmonics, either the in-phase or the quadrature Fourier amplitude of fluorescence oscillations exhibits a resonance in the space of control parameters formed by the excitation frequency and the mean light intensities. Resonance conditions relating the control parameters and parameters characterizing kinetics are made explicit. Tuning the control parameters to target a given fluorophore optimizes its fluorescence response and nearly eliminates the responses of fluorophores with different kinetic properties. Both protocols have complementary merits. LIGHTNING has a larger discriminatory power and HIGHLIGHT provides better quality images due to lock-in amplification.

Keywords : Multiplexed fluorescence imaging, reversibly photoswitchable fluorescent proteins, multiexponential analysis, elimination of fast variables, forced dynamical system, resonance.